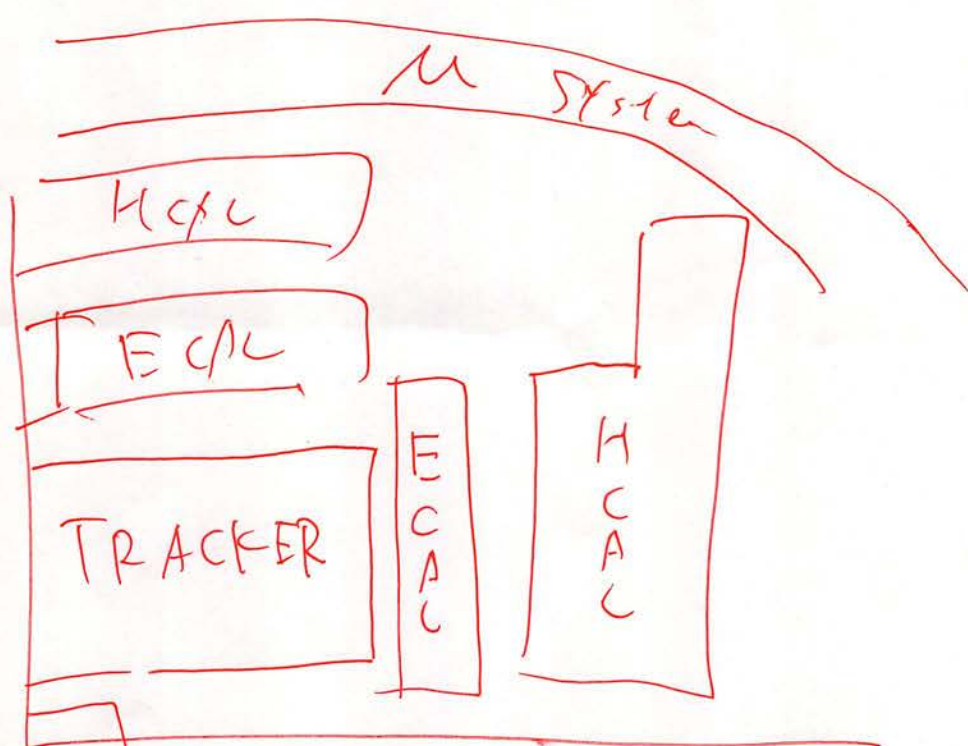
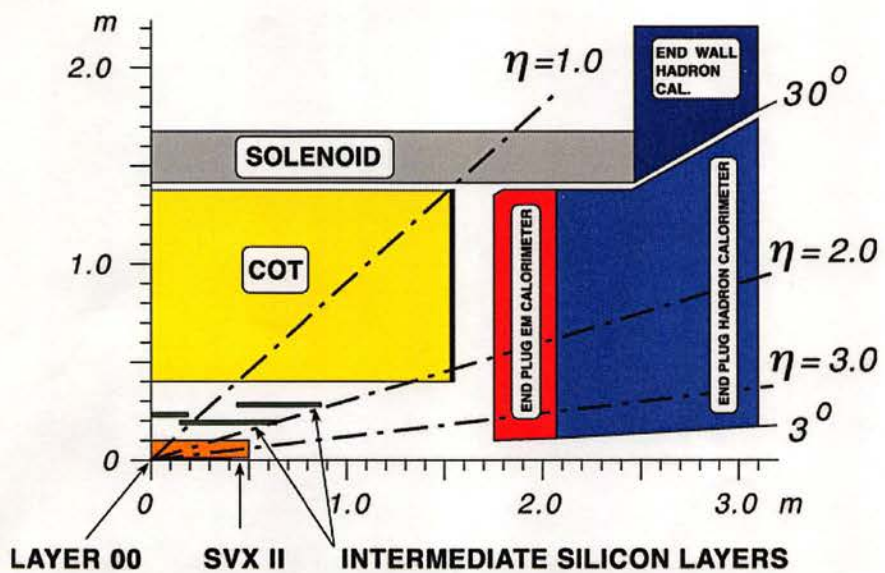
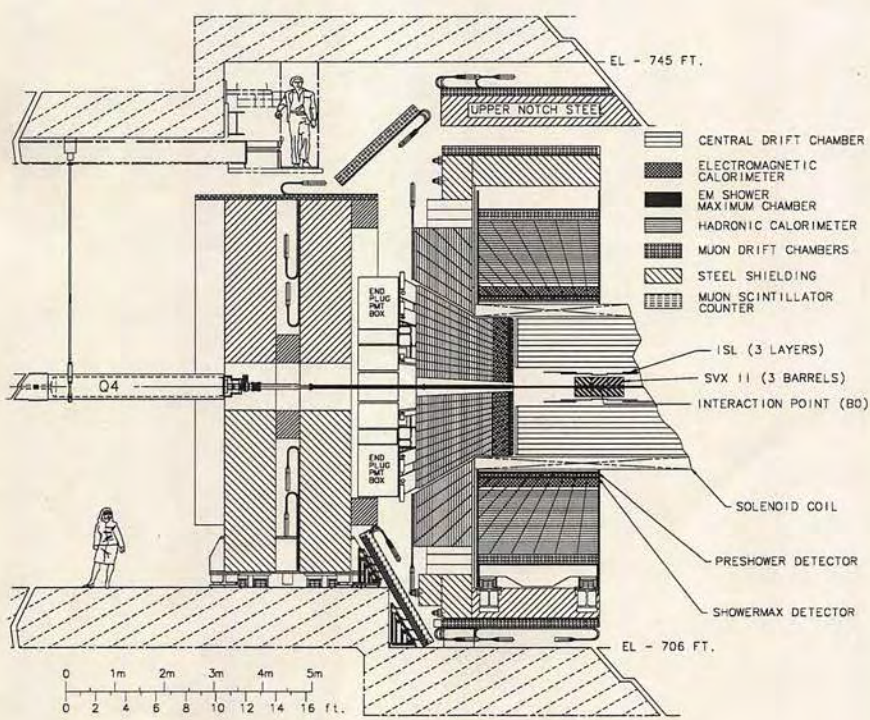
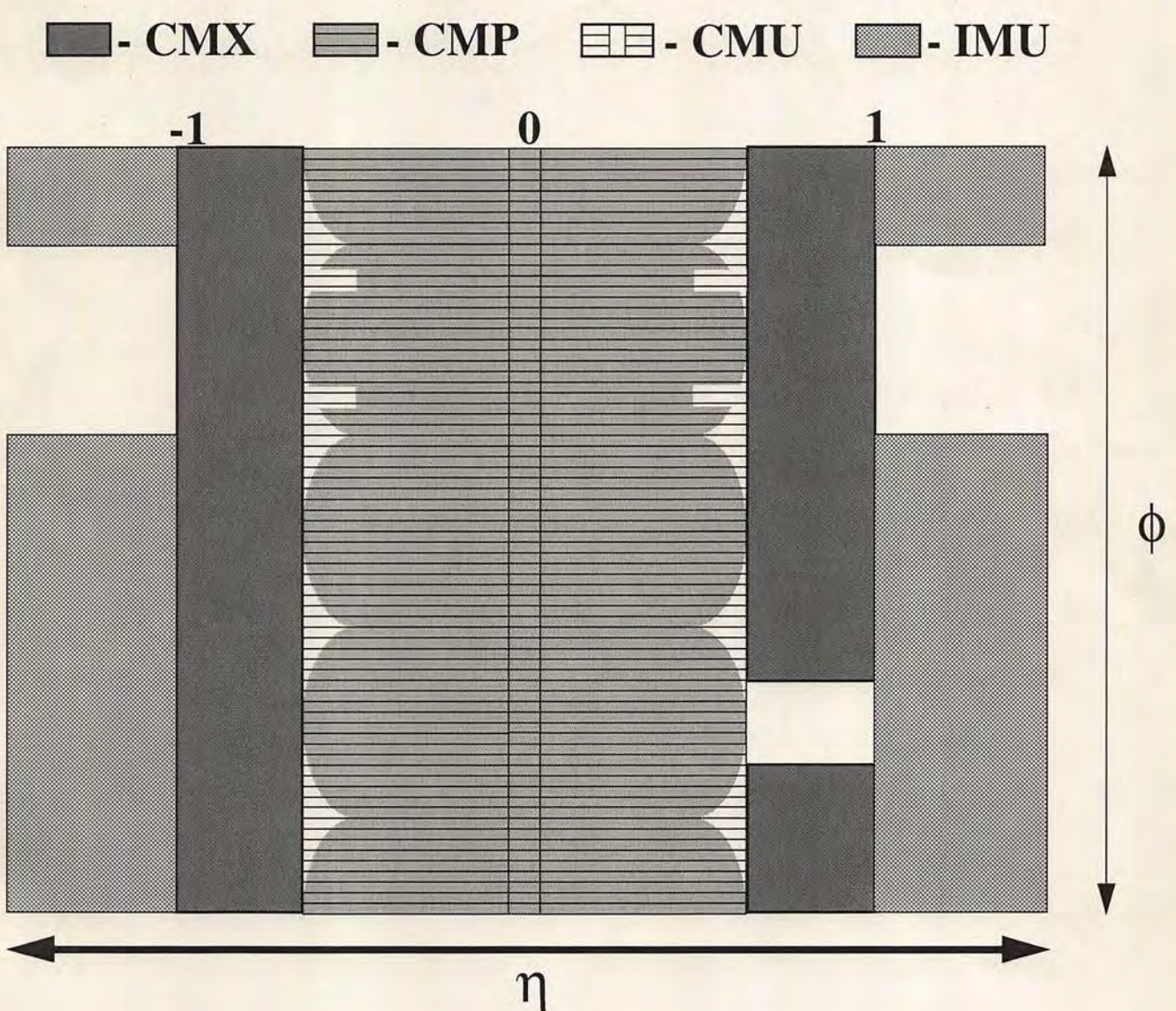


A



B





④ Tevatron Combined Result [1007.3178]

| | | | | | | | |
|----------|------|------|------|--------|----------------------------|-------------------|--|
| RunI | Pub. | CDF | lj | -2.5% | 0.1 fb | 174.80 ± 2.61 | $[172.5 \pm 2.1]$ |
| | | | ll | -0.5 | | | |
| | | | jj | -0.7 | | | |
| DO | | lj | 1.3 | | | | |
| | | ll | 0.2 | | | | |
| II | Pub. | CDF | jj | 10.5 @ | 2.9 fb | 174.80 ± 2.61 | $\frac{5.8 \text{ fb}}{172.5 \pm 2.1}$ |
| | | | trk | -0.5 | 1.9 fb | ± 6.94 | |
| II | Pre. | DO | lj | 26.2 @ | 3.6 fb | 173.75 ± 1.80 | |
| | | | ll | -2.1 | | ± 3.80 | |
| | | CDF | lj | 70.0 @ | 5.6 fb | 173.00 ± 1.24 | |
| | | | ll | -1.8 | 4.8 fb | ± 3.79 | |
| Combined | | | jj | | 175.2 ± 2.6 | | |
| | | | lj | | 173.0 ± 1.1 | | |
| | | | ll | | 171.1 ± 2.5 | | |
| Total | | | | | $173.32 \pm 0.56 \pm 0.89$ | stat | syst |

⑤ DØ Combined [DØ NOTE 6189 (2011. 4. 25)]

| | | | | |
|----|------|-----------------------|------------------|---|
| I | lj | 0.13 fb ⁻¹ | 180.1 ± 5.3 | ^{4.08} _{0.25} |
| I | ll | 0.13 | 168.9 ± 12.8 | |
| II | lj | 3.6 | 174.94 ± 1.5 | ^{89.74} |
| II | ll | 5.4 | 173.97 ± 3.1 | ^{9.93} → <u>175.8 ± 1.4</u> |

arXiv:1001.3181v1 [hep-ex] 1 July 2010

FERMI NATIONAL ACCELERATOR LABORATORY

FERMILAB-TM-2466-E
TEVEWWG/top 2010/07
CDF Note 10210
DØ Note 6090
July 2010

Combination of CDF and DØ results on the mass of the top quark using up to 5.6 fb^{-1} of data

The Tevatron Electroweak Working Group¹
for the CDF and DØ Collaborations

Abstract

We summarize the top-quark mass measurements from the CDF and DØ experiments at Fermilab. We combine published Run I (1992–1996) measurements with the most precise published and preliminary Run II (2001–present) measurements using up to 5.6 fb^{-1} of data. Taking uncertainty correlations properly into account, and adding in quadrature the statistical and systematic uncertainties, the resulting preliminary Tevatron average mass of the top quark is $m_{\text{top}} = 173.3 \pm 1.1 \text{ GeV}/c^2$.

¹The Tevatron Electroweak Working Group can be contacted at tev-ewwg@fnal.gov.
More information can be found at <http://tevewwg.fnal.gov>.

1 Introduction

This note reports the Tevatron average top-quark mass obtained by combining the most precise published and preliminary measurements of the top-quark mass, m_{top} .

The experiments CDF and DØ, taking data at the Tevatron proton-antiproton collider located at the Fermi National Accelerator Laboratory, have made several direct experimental measurements of the top-quark mass, m_{top} . The pioneering measurements were based on about 100 pb^{-1} of Run I data [1 - 12] collected from 1992 to 1996, and include results from the $t\bar{t} \rightarrow W^+ bW^- \bar{b} \rightarrow qq' bqq'\bar{b}$ (all-j), $t\bar{t} \rightarrow W^+ bW^- \bar{b} \rightarrow \ell\nu bqq'\bar{b}$ ($l+j$)², and $t\bar{t} \rightarrow W^+ bW^- \bar{b} \rightarrow \ell^+\nu b\ell^-\bar{\nu}\bar{b}$ (di-l) decay channels. Several more measurements have been performed in Run II (2001 - present) in all decay modes. The Run II measurements considered here are the most recent results in the $l+j$, di-l, and all-j channels using $1.9 - 5.6 \text{ fb}^{-1}$ of data and improved analysis techniques [13 – 20].

With respect to the March 2009 combination [21], the preliminary Run II CDF measurement in the $l+j$ channel has been updated using 5.6 fb^{-1} of data, and improved analysis technique [14]. The now published Run II CDF measurement in the di-l channel [22] has been substituted with a more precise preliminary result that uses 4.8 fb^{-1} of data [13]. Also, the Run II measurements in the all-j channel, and the measurement based on charged particle tracking have been published [15, 16]. The DØ Run II measurements are unchanged. The Tevatron average top-quark mass is thus obtained by combining five published Run I measurements [2, 3, 5, 7, 10, 11] with two published Run II CDF results [15, 16], two preliminary Run II CDF results [13, 14] and two preliminary Run II DØ results [18 – 20]. The combination takes into account the statistical and systematic uncertainties and their correlations using the method of Refs. [23, 24] and supersedes previous combinations [25, 26, 27, 28, 29, 30, 31, 21]. The definition and evaluation of the systematic uncertainties and the understanding of the correlations among channels, experiments, and Tevatron runs, is the outcome of many years of joint work between the CDF and DØ collaborations.

The input measurements and uncertainty categories used in the combination are detailed in Sections 2 and 3, respectively. The correlations used in the combination are discussed in Section 4 and the resulting Tevatron average top-quark mass is given in Section 5. A summary and outlook are presented in Section 6.

²Here $\ell = e$ or μ . Decay channels with explicit tau lepton identification are presently under study and are not yet used for measurements of the top-quark mass. Decays with $\tau \rightarrow e, \mu$ are included in the direct $W \rightarrow e$ and $W \rightarrow \mu$ channels.

2 Input Measurements

For this combination eleven measurements of m_{top} are used: five published Run I results, two published Run II results, and four preliminary Run II results, all reported in Table 1. In general, the Run I measurements all have relatively large statistical uncertainties and their systematic uncertainties are dominated by the total jet energy scale (JES) uncertainty. In Run II both CDF and DØ take advantage of the larger $t\bar{t}$ samples available and employ new analysis techniques to reduce both these uncertainties. In particular, the Run II DØ analysis in the l+j channel and the Run II CDF analyses in the l+j and all-j channels constrain the response of light-quark jets using the kinematic information from $W \rightarrow qq'$ decays (*in situ* calibration). Residual JES uncertainties associated with p_T and η dependencies as well as uncertainties specific to the response of b -jets are treated separately. The Run II CDF and DØ di-l measurements and the CDF measurement of Ref. [16] use a JES determined from external calibration samples. Some parts of the associated uncertainty are correlated with the Run I JES uncertainty as noted below.

The DØ Run II l+j analysis uses the JES determined from the external calibration derived from γ +jets events as an additional Gaussian constraint to the *in situ* calibration. Therefore the total resulting JES uncertainty is split into one part emerging from the *in situ* calibration and another part emerging from the external calibration.

To do that, the measurement without external JES constraint has been combined iteratively with a pseudo-measurement using the method of Refs. [23, 24] which uses only the external calibration in a way that the combination give the actual total JES uncertainty. The splitting obtained in this way is used to assess the statistical part of the JES uncertainty, and the part of the JES uncertainty coming from the external calibration constraint [32].

The analysis technique developed by CDF and referred to as “trk” uses both the mean decay-length from b -tagged jets and the mean lepton transverse momentum to determine the top-quark mass in l+j candidate events. While the statistical sensitivity is not as good as the more traditional methods, this technique has the advantage that since it uses primarily tracking information, it is almost entirely independent of JES uncertainties. As the statistics of this sample continue to grow, this method is expected to offer a cross-check of the top-quark mass largely independent of the dominant JES systematic uncertainty. The statistical correlation between an earlier version of the trk analysis and a traditional Run II CDF l+j measurement was studied using Monte Carlo signal-plus-background pseudo-experiments which correctly account for the sample overlap and was found to be consistent with zero (to within <1%) independent of the assumed top-quark mass.

The DØ Run II l+j result is a combination of the published Run IIa (2002–2005) measurement [17] with 1 fb^{-1} of data and the preliminary result obtained with 2.6 fb^{-1} Run IIb (2006–2007) dataset.

Table 1: Summary of the measurements used to determine the Tevatron average m_{top} . Integrated luminosity ($\int \mathcal{L} dt$) has units in fb^{-1} , and all other numbers are in GeV/c^2 . The uncertainty categories and their correlations are described in the Sec. 3. The total systematic uncertainty and the total uncertainty are obtained by adding the relevant contributions in quadrature. The new measurements utilized here are the two CDF preliminary results in the last column.

| | Run I published | | | | | Run II published | | Run II preliminary | | | |
|-----------------------|-----------------|-------|-------|-------|-------|------------------|--------|--------------------|--------|--------|--------|
| | CDF | | DØ | | | CDF | | DØ | | CDF | |
| | all-j | l+j | di-l | l+j | di-l | all-j | trk | l+j | di-l | l+j | di-l |
| $\int \mathcal{L} dt$ | 0.1 | 0.1 | 0.1 | 0.1 | 0.1 | 2.9 | 1.9 | 3.6 | 3.6 | 5.6 | 4.8 |
| Result | 186.0 | 176.1 | 167.4 | 180.1 | 168.4 | 174.80 | 175.30 | 173.75 | 174.66 | 173.00 | 170.56 |
| iJES | - | - | - | - | - | 1.64 | - | 0.47 | - | 0.58 | - |
| aJES | - | - | - | - | - | - | - | 0.91 | 1.32 | - | - |
| bJES | 0.6 | 0.6 | 0.8 | 0.7 | 0.7 | 0.21 | 0.0 | 0.07 | 0.26 | 0.26 | 0.35 |
| cJES | 3.0 | 2.7 | 2.6 | 2.0 | 2.0 | 0.49 | 0.60 | 0.0 | 0.0 | 0.27 | 2.01 |
| dJES | 0.3 | 0.7 | 0.6 | 0.0 | 0.0 | 0.08 | 0.0 | 0.84 | 1.46 | 0.01 | 0.64 |
| rJES | 4.0 | 3.4 | 2.7 | 2.5 | 1.1 | 0.21 | 0.10 | 0.0 | 0.0 | 0.41 | 1.98 |
| LepPt | 0.0 | 0.0 | 0.0 | 0.0 | 0.0 | - | 1.10 | 0.18 | 0.32 | 0.14 | 0.31 |
| Signal | 1.8 | 2.6 | 2.8 | 1.1 | 1.8 | 0.23 | 1.60 | 0.45 | 0.65 | 0.21 | 0.36 |
| Backgd | 1.7 | 1.3 | 0.3 | 1.0 | 1.1 | 0.35 | 1.60 | 0.08 | 0.08 | 0.34 | 0.27 |
| Fit | 0.6 | 0.0 | 0.7 | 0.6 | 1.1 | 0.67 | 1.40 | 0.21 | 0.51 | 0.10 | 0.05 |
| MC | 0.8 | 0.1 | 0.6 | 0.0 | 0.0 | 0.31 | 0.60 | 0.58 | 1.00 | 0.37 | 0.57 |
| UN/MI | - | - | - | 1.3 | 1.3 | - | - | - | - | - | - |
| CR | - | - | - | - | - | 0.41 | 0.40 | 0.41 | 0.41 | 0.37 | 0.61 |
| MHI | - | - | - | - | - | 0.17 | 0.70 | 0.05 | 0.00 | 0.10 | 0.27 |
| Syst | 5.7 | 5.3 | 4.9 | 3.9 | 3.6 | 1.99 | 3.10 | 1.60 | 2.43 | 1.06 | 3.09 |
| Stat | 10.0 | 5.1 | 10.3 | 3.6 | 12.3 | 1.70 | 6.20 | 0.83 | 2.92 | 0.65 | 2.19 |
| Total | 11.5 | 7.3 | 11.4 | 5.3 | 12.8 | 2.61 | 6.94 | 1.80 | 3.80 | 1.24 | 3.79 |

The DØ Run II di-l result is itself a combination of two results using different techniques but partially overlapping dilepton datasets [19, 20].

Table 1 also lists the uncertainties of the results, subdivided into the categories described in the next Section. The correlations between the inputs are described in Section 4.

3 Uncertainty Categories

We employ the same uncertainty categories as used for the previous Tevatron average [21]. They are divided such that sources of systematic uncertainty that share the same or similar origin are combined. For example, the “Signal” category discussed below includes the uncertainties from initial state radiation (ISR), final state radiation (FSR), and parton density functions (PDF)—all of which affect the modeling of the $t\bar{t}$ signal. Some systematic uncertainties have been broken down into multiple categories in order to accommodate specific types of correlations. For example, the jet energy scale (JES) uncertainty is subdivided into six components in order to more accurately accommodate our best estimate of the relevant correlations.

Statistics: The statistical uncertainty associated with the m_{top} determination.

iJES: That part of the JES uncertainty which originates from *in situ* calibration procedures and is uncorrelated among the measurements. In the combination reported here, it corresponds to the statistical uncertainty associated with the JES determination using the $W \rightarrow qq'$ invariant mass in the CDF Run II l+j and all-j measurements and DØ Run II l+j measurement. Residual JES uncertainties arising from effects not considered in the *in situ* calibration are included in other categories.

aJES: That part of the JES uncertainty which originates from differences in detector electromagnetic over hadronic (e/h) response between b -jets and light-quark jets. This category also includes uncertainties associated with the jet identification and resolution, trigger and b -jets tagging. It is specific to the DØ Run II measurements and is uncorrelated with the DØ Run I and CDF measurements.

bJES: That part of the JES uncertainty which originates from uncertainties specific to the modeling of b -jets and which is correlated across all measurements. For both CDF and DØ this includes uncertainties arising from variations in the semileptonic branching fractions, b -fragmentation modeling, and differences in the color flow between b -jets and light-quark jets. These were determined from Run II studies but back-propagated to the Run I measurements, whose rJES uncertainties (see below) were then corrected in order to keep the total JES uncertainty constant.

cJES: That part of the JES uncertainty which originates from modeling uncertainties correlated across all measurements. Specifically it includes the modeling uncertainties associated with light-quark fragmentation and out-of-cone corrections. For DØ Run II measurements, it is included in the dJES category.

dJES: That part of the JES uncertainty which originates from limitations in the data samples used for calibrations and which is correlated between measurements within the same data-taking period, such as Run I or Run II, but not between experiments. For CDF this corresponds to uncertainties associated with the η -dependent JES corrections which are

estimated using di-jet data events. For DØ this includes uncertainties in the calorimeter response for light jets, uncertainties from p_T - and η -dependent JES corrections and from the sample dependence of using γ +jets data samples to derive the JES.

rJES: The remaining part of the JES uncertainty which is correlated between all measurements of the same experiment independently from the data-taking period, but which is uncorrelated between experiments. For CDF, this is dominated by uncertainties in the calorimeter response to light-quark jets, and also includes small uncertainties associated with the multiple interaction and underlying event corrections. For DØ Run II measurements, it is included in the dJES category.

LepPt: The systematic uncertainty arising from uncertainties in the scale of lepton transverse momentum measurements. This is an important uncertainty for CDF’s track-based measurement. It was not considered as a source of systematic uncertainty in the Run I measurements.

Signal: The systematic uncertainty arising from uncertainties in the $t\bar{t}$ modeling which is correlated across all measurements. This includes uncertainties from variations in the ISR, FSR, and PDF descriptions used to generate the $t\bar{t}$ Monte Carlo samples that calibrate each method. For DØ it also includes the uncertainty from higher order corrections evaluated from a comparison of $t\bar{t}$ samples generated by MC@NLO [33] and ALPGEN [34], both interfaced to HERWIG [35, 36] for the simulation of parton showers and hadronization.

Background: Uncertainty in modeling the background sources. They are correlated between all measurements in the same channel, and include uncertainties on the background composition and shape. In particular uncertainties associated with the modeling of the QCD multijet background using data in the all-j and 1+j channels, uncertainties associated with the modeling of the Drell-Yan background in the di-l channel, and uncertainties associated with variations of the factorization scale used to model W +jets background are included.

Fit: The systematic uncertainty arising from any source specific to a particular fit method, including the finite Monte Carlo statistics available to calibrate each method. For DØ this uncertainty also includes the uncertainties from modeling of the QCD multijet background determined from data and dominated by limited statistics.

Monte Carlo (MC): The systematic uncertainty associated with variations of the physics model used to calibrate the fit methods and which is correlated across all measurements. It includes variations observed when substituting PYTHIA [37–39] (Run I and Run II) or ISAJET [40] (Run I) for HERWIG [35, 36] when modeling the $t\bar{t}$ signal.

Uranium Noise and Multiple Interactions (UN/MI): This is specific to DØ and includes the uncertainty arising from uranium noise in the DØ calorimeter and from the multiple interaction corrections to the JES. For DØ Run I these uncertainties were sizable, while

for Run II, owing to the shorter calorimeter electronics integration time and *in situ* JES calibration, these uncertainties are negligible.

Color Reconnection (CR): The systematic uncertainty arising from a variation of the phenomenological description of color reconnection between final state particles [41, 42]. This is obtained taking the difference between PYTHIA 6.4 tune “Apro” and PYTHIA 6.4 tune “ACRpro” that only differ only in the color reconnection model. Monte Carlo generators which explicitly include different CR models for hadron collisions have recently become available. This was not possible in Run I; these measurements therefore do not include this source of systematic uncertainty.

Multiple Hadron Interactions (MHI): The systematic uncertainty arising from a mismodeling of the distribution of the number of collisions per Tevatron bunch crossing owing to the steady increase in the collider instantaneous luminosity during data-taking. This uncertainty has been separated from other sources to account for the fact that it is uncorrelated with D \emptyset measurements.

These categories represent the current preliminary understanding of the various sources of uncertainty and their correlations. We expect these to evolve as we continue to probe each method’s sensitivity to the various systematic sources with ever improving precision. Variations in the assignment of uncertainties to the uncertainty categories, in the back-propagation of the bJES uncertainties to Run I measurements, in the approximations made to symmetrize the uncertainties used in the combination, and in the assumed magnitude of the correlations, have all a negligible impact ($\ll 0.1 \text{ GeV}/c^2$) in the combined m_{top} and total uncertainty.

4 Correlations

The following correlations are used for the combination:

- The uncertainties in the Statistical, Fit, and iJES categories are taken to be uncorrelated among the measurements.
- The uncertainties in the aJES, dJES, LepPt and MHI categories are taken to be 100% correlated among all Run I and all Run II measurements within the same experiment, but uncorrelated between Run I and Run II and uncorrelated between the experiments.
- The uncertainties in the rJES and UN/MI categories are taken to be 100% correlated among all measurements within the same experiment but uncorrelated between the experiments.
- The uncertainties in the Background category are taken to be 100% correlated among all measurements in the same channel.

Table 2: The matrix of correlation coefficients used to determine the Tevatron average top-quark mass.

| | Run I published | | | | | Run II published | | Run II preliminary | | | |
|--------------|-----------------|------|-------|------|------|------------------|------|--------------------|------|------|------|
| | CDF | | DØ | | | CDF | | DØ | | CDF | |
| | l+j | di-l | all-j | l+j | di-l | all-j | trk | l+j | di-l | l+j | di-l |
| CDF-l+j | 1.00 | - | - | - | - | - | - | - | - | - | - |
| CDF-I di-l | 0.29 | 1.00 | - | - | - | - | - | - | - | - | - |
| CDF-I all-j | 0.32 | 0.19 | 1.00 | - | - | - | - | - | - | - | - |
| DØ-I l+j | 0.26 | 0.15 | 0.14 | 1.00 | - | - | - | - | - | - | - |
| DØ-I di-l | 0.11 | 0.08 | 0.07 | 0.16 | 1.00 | - | - | - | - | - | - |
| CDF-II all-j | 0.15 | 0.10 | 0.12 | 0.10 | 0.05 | 1.00 | - | - | - | - | - |
| CDF-II trk | 0.16 | 0.08 | 0.07 | 0.12 | 0.05 | 0.06 | 1.00 | - | - | - | - |
| DØ-II l+j | 0.10 | 0.08 | 0.06 | 0.07 | 0.04 | 0.10 | 0.11 | 1.00 | - | - | - |
| DØ-II di-l | 0.07 | 0.06 | 0.05 | 0.04 | 0.03 | 0.07 | 0.07 | 0.52 | 1.00 | - | - |
| CDF-II l+j | 0.36 | 0.19 | 0.23 | 0.20 | 0.07 | 0.19 | 0.19 | 0.22 | 0.15 | 1.00 | - |
| CDF-II di-l | 0.48 | 0.28 | 0.35 | 0.23 | 0.11 | 0.21 | 0.12 | 0.11 | 0.08 | 0.43 | 1.00 |

- The uncertainties in the bJES, cJES, Signal, CR, and MC categories are taken to be 100% correlated among all measurements.

Using the inputs from Table 1 and the correlations specified here, the resulting matrix of total correlation coefficients is given in Table 2.

The measurements are combined using a program implementing two independent methods: a numerical χ^2 minimization and the analytic best linear unbiased estimator (BLUE) method [23, 24]. The two methods are mathematically equivalent, and are also equivalent to the method used in an older combination [43]. It has been checked that they give identical results for the combination. The BLUE method yields the decomposition of the uncertainty on the Tevatron m_{top} average in terms of the uncertainty categories specified for the input measurements [24].

5 Results

The combined value for the top-quark mass is: $m_{\text{top}} = 173.32 \pm 0.56 \text{ (stat)} \pm 0.89 \text{ (syst) } \text{GeV}/c^2$. Adding the statistical and systematic uncertainties in quadrature yields a total uncertainty of $1.06 \text{ GeV}/c^2$, corresponding to a relative precision of 0.61% on the top-quark mass. Rounding off to two significant digits in the uncertainty, the combination provides $m_{\text{top}} = 173.3 \pm 1.1 \text{ GeV}/c^2$. It has a χ^2 of 6.1 for 10 degrees of freedom, which corresponds to a probability of 81%, indicating good agreement among all the input measurements. The breakdown of the uncertainties is shown in Table 3. The total JES uncertainty is $\pm 0.61 \text{ GeV}/c^2$ with $\pm 0.46 \text{ GeV}/c^2$ coming from its statistical component and $\pm 0.40 \text{ GeV}/c^2$ from the nonstatistical component. The total statistical uncertainty is $\pm 0.56 \text{ GeV}/c^2$.

The pull and weight for each of the inputs are listed in Table 4. The input measurements and the resulting Tevatron average mass of the top quark are summarized in Fig. 1.

Table 3: Summary of the Tevatron combined average m_{top} . The uncertainty categories are described in the text. The total systematic uncertainty and the total uncertainty are obtained by adding the relevant contributions in quadrature.

| Tevatron combined values (GeV/c^2) | |
|---|--------|
| m_{top} | 173.32 |
| iJES | 0.46 |
| aJES | 0.21 |
| bJES | 0.20 |
| cJES | 0.13 |
| dJES | 0.19 |
| rJES | 0.15 |
| LepPt | 0.10 |
| Signal | 0.19 |
| Background | 0.23 |
| Fit | 0.11 |
| MC | 0.40 |
| UN/MI | 0.02 |
| CR | 0.39 |
| MHI | 0.08 |
| Systematics | 0.89 |
| Statistics | 0.56 |
| Total | 1.06 |

The weights of some of the measurements are negative. In general, this situation can occur if the correlation between two measurements is larger than the ratio of their total uncertainties.

Table 4: The pull and weight for each of the inputs used to determine the Tevatron average mass of the top quark. See Reference [23] for a discussion of negative weights.

| | Run I published | | | | | Run II published | | | Run II preliminary | | | |
|------------|-----------------|-------|-------|-------|-------|------------------|-------|-------|--------------------|-------|-------|--|
| | CDF | | | DØ | | CDF | | DØ | | CDF | | |
| | l+j | di-l | all-j | l+j | di-l | all-j | trk | l+j | di-l | l+j | di-l | |
| Pull | +0.38 | -0.52 | +1.11 | +1.30 | -0.39 | +0.62 | +0.29 | +0.29 | +0.37 | -0.50 | -0.76 | |
| Weight [%] | -2.5 | -0.5 | -0.7 | +1.3 | +0.2 | +10.5 | -0.5 | +26.2 | -2.1 | +70.0 | -1.8 | |

Table 5: Summary of the combination of the 11 measurements by CDF and DØ in terms of three physical quantities, the mass of the top quark in the all-j $m_{\text{top}}^{\text{all-j}}$, l+j m_{top}^{l+j} , and di-l $m_{\text{top}}^{\text{di-l}}$ decay channels.

| Parameter | Value (GeV/c^2) | Correlations | | |
|---------------------------------|----------------------------|---------------------------------|------------------------|--------------------------------|
| | | $m_{\text{top}}^{\text{all-j}}$ | m_{top}^{l+j} | $m_{\text{top}}^{\text{di-l}}$ |
| $m_{\text{top}}^{\text{all-j}}$ | 175.2 ± 2.6 | 1.00 | | |
| m_{top}^{l+j} | 173.0 ± 1.1 | 0.20 | 1.00 | |
| $m_{\text{top}}^{\text{di-l}}$ | 171.1 ± 2.5 | 0.19 | 0.48 | 1.00 |

This is indeed the case here. In these instances the less precise measurement will usually acquire a negative weight. While a weight of zero means that a particular input is effectively ignored in the combination, a negative weight means that it affects the resulting m_{top} central value and helps reduce the total uncertainty.

Although no input has an anomalously large pull and the χ^2 from the combination of all measurements indicates that there is good agreement among them, it is still interesting to also fit for the top-quark mass in the all-j, l+j, and di-l channels separately. We use the same methodology, inputs, uncertainty categories, and correlations as described above, but fit the three physical observables, $m_{\text{top}}^{\text{all-j}}$, m_{top}^{l+j} , and $m_{\text{top}}^{\text{di-l}}$ separately. The results of these combinations are shown in Table 5.

Using the results of Table 5 we calculate the chi-squared consistency between any two channels, including all correlations, as $\chi^2(\text{di-l/l+j})=0.75$, $\chi^2(\text{l+j/all-j})=0.68$, and $\chi^2(\text{all-j/di-l})=1.58$. These correspond to chi-squared probabilities of 38%, 68%, and 21%, respectively, and indicate that the determinations of m_{top} from the three different final states are consistent with each another.

Mass of the Top Quark

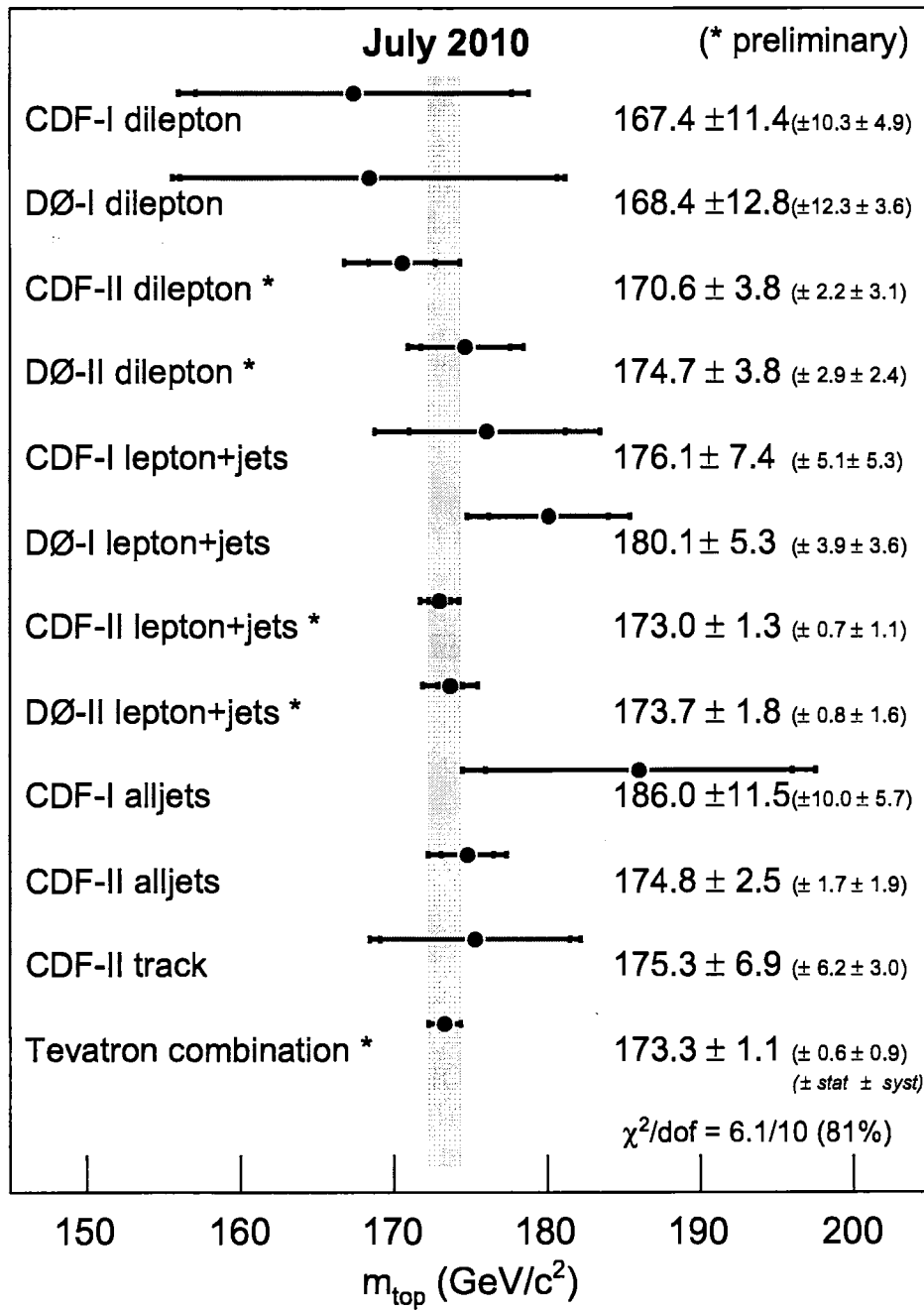


Figure 1: Summary of the input measurements and resulting Tevatron average mass of the top-quark.

6 Summary

A preliminary combination of measurements of the mass of the top quark from the Tevatron experiments CDF and DØ is presented. The combination includes five published Run I measurements, two published Run II measurements, and four preliminary Run II measurements. Taking into account the statistical and systematic uncertainties and their correlations, the preliminary result for the Tevatron average is: $m_{\text{top}} = 173.32 \pm 0.56 \text{ (stat)} \pm 0.89 \text{ (syst)} \text{ GeV}/c^2$, where the total uncertainty is obtained assuming Gaussian systematic uncertainties. Adding in quadrature the statistical and systematic uncertainties yields a total uncertainty of $1.06 \text{ GeV}/c^2$, corresponding to a relative precision of 0.61% on the top-quark mass. Rounding off the uncertainty to two significant digits, the combination provides $m_{\text{top}} = 173.3 \pm 1.1 \text{ GeV}/c^2$.

The central value is $0.20 \text{ GeV}/c^2$ higher than our March 2009 average of $m_{\text{top}} = 173.12 \pm 1.26 \text{ GeV}/c^2$, while the relative precision has improved by 15% with respect to the previous Tevatron average.

The mass of the top quark is now known with a relative precision of 0.61%, limited by the systematic uncertainties, which are dominated by the jet energy scale uncertainty. This source of systematic uncertainty is expected to improve as larger datasets are collected since analysis techniques constrain the jet energy scale using kinematical information from $W \rightarrow qq'$ decays. It can be expected that with the full Run II dataset the top-quark mass will be known to an accuracy better than the one presented in this paper. To reach this level of precision further work will focus on a better understanding of b -jet modeling, and in the uncertainties in the signal and background simulations.

7 Acknowledgments

We thank the Fermilab staff and the technical staffs of the participating institutions for their vital contributions. This work was supported by DOE and NSF (USA), CONICET and UBA-CyT (Argentina), CNPq, FAPERJ, FAPESP and FUNDUNESP (Brazil), CRC Program, CFI, NSERC and WestGrid Project (Canada), CAS and CNSF (China), Colciencias (Colombia), MSMT and GACR (Czech Republic), Academy of Finland (Finland), CEA and CNRS/IN2P3 (France), BMBF and DFG (Germany), Ministry of Education, Culture, Sports, Science and Technology (Japan), World Class University Program, National Research Foundation (Korea), KRF and KOSEF (Korea), DAE and DST (India), SFI (Ireland), INFN (Italy), CONACyT (Mexico), NSC (Republic of China), FASI, Rosatom and RFBR (Russia), Slovak R&D Agency (Slovakia), Ministerio de Ciencia e Innovación, and Programa Consolider-Ingenio 2010 (Spain), The Swedish Research Council (Sweden), Swiss National Science Foundation (Switzerland), FOM (The Netherlands), STFC and the Royal Society (UK), and the A.P. Sloan Foundation (USA).

References

- [1] F. Abe *et al.*, [CDF Collaboration] Phys. Rev. Lett. **80** (1998) 2779, [hep-ex/9802017](#);
- [2] F. Abe *et al.*, [CDF Collaboration] Phys. Rev. Lett. **82** (1999) 271, [hep-ex/9810029](#);
- [3] F. Abe *et al.*, [CDF Collaboration] Erratum: Phys. Rev. Lett. **82** (1999) 2808, [hep-ex/9810029](#);
- [4] B. Abbott *et al.*, [DØ Collaboration] Phys. Rev. Lett. **80** (1998) 2063, [hep-ex/9706014](#);
- [5] B. Abbott *et al.*, [DØ Collaboration] Phys. Rev. **D60** (1999) 052001, [hep-ex/9808029](#);
- [6] F. Abe *et al.*, [CDF Collaboration] Phys. Rev. Lett. **80** (1998) 2767, [hep-ex/9801014](#);
- [7] The CDF Collaboration, T. Affolder *et al.*, Phys. Rev. **D63** (2001) 032003, [hep-ex/0006028](#);
- [8] S. Abachi *et al.*, [DØ Collaboration] Phys. Rev. Lett. **79** (1997) 1197, [hep-ex/9703008](#);
- [9] B. Abbott *et al.*, [DØ Collaboration] Phys. Rev. **D58** (1998) 052001, [hep-ex/9801025](#);
- [10] V. M. Abazov *et al.*, [DØ Collaboration] Nature **429** (2004) 638, [hep-ex/0406031](#);
- [11] F. Abe *et al.*, [CDF Collaboration] Phys. Rev. Lett. **79** (1997) 1992;
- [12] V. M. Abazov *et al.*, [DØ Collaboration] Phys. Lett. **B606** (2005) 25, [hep-ex/0410086](#);
- [13] T. Aaltonen *et al.*, [CDF Collaboration] CDF Conference Note 10033;
- [14] T. Aaltonen *et al.* [CDF Collaboration], CDF Conference Note 10198;
- [15] T. Aaltonen *et al.* [CDF Collaboration], Phys. Rev. D **81** (2010) 052011
[arXiv:1002.0365](#);
- [16] T. Aaltonen *et al.* [CDF Collaboration], Phys. Rev. D **81** (2010) 032002;
[arXiv:0910.0969](#);
- [17] V .M. Abazov *et al.*, [DØ Collaboration] Phys. Rev. Lett. **101** (2008) 182001;
[arXiv:0807.2141](#);
- [18] V .M. Abazov *et al.*, [DØ Collaboration] DØ Conference Note 5877;
- [19] V .M. Abazov *et al.*, [DØ Collaboration] DØ Conference Note 5897;
- [20] V .M. Abazov *et al.*, [DØ Collaboration] DØ Conference Note 5745;
- [21] The CDF Collaboration, the DØ Collaboration and the Tevatron Electroweak Working Group, [arXiv:0903.2503](#);

- [22] T. Aaltonen *et al.* [CDF Collaboration], Phys. Rev. Lett. **102**, 152001 (2009) [arXiv:0807.4652](#);
- [23] L. Lyons, D. Gibaut, and P. Clifford, Nucl. Instrum. Meth. **A270** (1988) 110;
- [24] A. Valassi, Nucl. Instrum. Meth. **A500** (2003) 391;
- [25] The CDF Collaboration, the DØ Collaboration, and the Tevatron Electroweak Working Group, [hep-ex/0404010](#);
- [26] The CDF Collaboration, the DØ Collaboration, and the Tevatron Electroweak Working Group, [hep-ex/0507091](#);
- [27] The CDF Collaboration, the DØ Collaboration, and the Tevatron Electroweak Working Group, [hep-ex/0603039](#);
- [28] The CDF Collaboration, the DØ Collaboration, and the Tevatron Electroweak Working Group, [hep-ex/0608032](#);
- [29] The CDF Collaboration, the DØ Collaboration, and the Tevatron Electroweak Working Group, [hep-ex/0703034](#);
- [30] The CDF Collaboration, the DØ Collaboration, and the Tevatron Electroweak Working Group, [arXiv:0803.1683](#);
- [31] The CDF Collaboration, the DØ Collaboration, and the Tevatron Electroweak Working Group, [arXiv:0808.1089](#);
- [32] V. M. Abazov *et al.*, [DØ Collaboration] DØ-note 5900-CONF;
- [33] S. Frixione and B. Webber, JHEP **029** (2002) 0206, [hep-ph/0204244](#);
- [34] M. L. Mangano, M. Moretti, F. Piccinini, R. Pittau, and A. D. Polosa, JHEP **07** (2003) 001, [hep-ph/0206293](#);
- [35] G. Marchesini *et al.*, Comput. Phys. Commun. **67** (1992) 465;
- [36] G. Corcella *et al.*, JHEP **01** (2001) 010, [hep-ph/0011363](#);
- [37] H.-U. Bengtsson and T. Sjostrand, Comput. Phys. Commun. **46** (1987) 43;
- [38] T. Sjostrand, Comput. Phys. Commun. **82** (1994) 74;
- [39] T. Sjostrand *et al.*, Comput. Phys. Commun. **135** (2001) 238, [hep-ph/0010017](#);
- [40] F. E. Paige and S. D. Protopopescu, BNL Reports 38034 and 38774 (1986) unpublished;
- [41] P. Z. Skands and D. Wicke, Eur. Phys. J. C **52** (2007) 133 [hep-ph/0703081](#);
- [42] P. Z. Skands, [arXiv:0905.3418](#);
- [43] The Top Averaging Collaboration, L. Demortier *et al.*, FERMILAB-TM-2084 (1999).

◦ CDF top quark mass measurements

CDF NOTE 10444

(2011, S. 10)

Combined : $\left\{ \begin{array}{l} 110 \text{ pb}^{-1} @ 1.8 \text{ TeV ECR} \quad (\text{Run I}) \\ 5.8 \text{ fb}^{-1} @ 1.96 \text{ TeV} \quad (\text{Run II}) \end{array} \right.$

$$\Rightarrow 172.70 \pm 0.63 \text{ stat} \pm 0.89 \text{ GeV}_{\text{syst}}$$

$$= 172.70 \pm 1.09 \text{ GeV} \quad (0.63\%)$$

$\oplus_{\text{Syst. 12}}^{\text{Syst. 12}}$
Top quark combined

Channel: HAD $t\bar{t} \rightarrow b\bar{b} + 4\gamma$
 LJT $t\bar{t} \rightarrow b\bar{b} + l\nu jj$
 DIL $t\bar{t} \rightarrow b\bar{b} + l^+l^- \nu\bar{\nu}$
 $E_T + \text{JETS}$

| | uncertainty | weight |
|---------|----------------------------------|---------|
| Run I: | L JT. 7.3 GeV | -2.65 |
| | D IL 11.4 | -0.46 |
| | H AD 11.5 | -0.99 |
| Run II: | L JT 1.24 | 76.52 @ |
| | D IL 3.79 | -2.78 |
| | H AD 2.06 | 19.25 @ |
| | $E_T + \text{Jets}$ 2.56 | 10.65 |
| | $L_{xy} + P_T^{\text{lep}}$ 6.90 | 0.46 |

Syst. unc. (110 fb) JES on chain \rightarrow JES_{sys}

* uncertainties

• Stat.

• iJES: JES stat. unc. in
in-situ $W \rightarrow \ell\ell'$ calibration

• bJES: b-jet modeling syst.

• cJES: OOC syst. in JES (L7,8)

• dJES: RC syst. in JES (L1)

• rJES: Cal response, UE, MI in JES (L4,5,6)

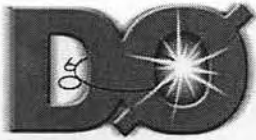
(• Lepton P_T syst.)• Signal: $t\bar{t}$ modeling syst; ISR, FSR, PDF• Generator: syst. included variation of
pyt. Her. & ALP.

• BG syst.

• Method: Syst. of B-tag eff.
Stat of MC

• Color Reconnection syst.

• Multiple had interaction:
Bunch modeling syst.



DØ Note 6189

Combination of the DØ top quark mass measurements

The DØ Collaboration
URL <http://www-d0.fnal.gov>
(Dated: April 25, 2011)

We present a combination of the top quark mass measurements performed by the DØ experiment in lepton plus jets ($\ell + \text{jets}$) and dilepton ($\ell\ell$) channels. The combined result yields:

$$\begin{aligned}m_{\text{top}} &= 175.08 \pm 0.77 \text{ (stat)} \pm 1.25 \text{ (syst)} \text{ GeV}, \\m_{\text{top}} &= 175.08 \pm 1.47 \text{ (stat + syst)} \text{ GeV}.\end{aligned}$$

Result for winter 2011 conferences

I. INTRODUCTION

The combination of top quark mass (m_{top}) measurements presented in this note includes the best D \emptyset measurements from Run I of the Tevatron in the dilepton [1] and $\ell + \text{jets}$ [2] channels, and the most recent Run II measurements in the dilepton [3] channel using 5.4 fb^{-1} and the $\ell + \text{jets}$ [4, 5] channel with 3.6 fb^{-1} of data. This combination supersedes the previous result [6].

II. METHOD AND INPUTS

We use the BLUE [7] method to combine of the m_{top} measurements following the same procedure, using essentially the same classes of uncertainties and the same program as used to compute the Tevatron average of m_{top} [8].

Table I summarizes the measurements and the corresponding statistical and systematic uncertainties that enter the combination. The categories of uncertainties represent the current understanding of the sources of uncertainty and their correlations. We expect these to evolve as we continue to probe the sensitivity of each method to each source of uncertainties with greater precision. We give below a short explanation for what these categories contain (see [8] for further details).

iJES: That part of the jet energy scale (JES) uncertainty which originates from in situ calibration procedures and is of statistical origin. To properly take into account the correlation between the $\ell + \text{jets}$ and dilepton channels, it also contains the flavor dependent jet response systematic uncertainty for the $\ell + \text{jets}$ channel.

aJES: That part of the JES uncertainty which originates from differences in detector response between b -jets and light-quark jets for the dilepton channel.

bJES: That part of the JES uncertainty which originates from uncertainties specific to the Monte Carlo (MC) modeling of b -jets like variations of the semileptonic branching fractions or b -fragmentation modeling.

cJES: That part of the JES uncertainty which originates from MC modeling uncertainties associated with light-quark fragmentation and out-of-cone corrections. For Run II measurements, it is included in the dJES category.

dJES: That part of the JES uncertainty which originates from limitations in the data samples used for calibrations. It includes uncertainties in the calorimeter response for light jets, and uncertainties from p_T - and η -dependent JES corrections.

rJES: The remaining part of the JES uncertainty. For Run II measurements, it is included in the dJES category.

Detector Modeling: The systematic uncertainty arising from uncertainties in the modeling of the detector in the MC simulation. This includes uncertainties from jet resolution and identification.

Lepton pt: The systematic uncertainty arising from uncertainties in the scale of lepton transverse momentum and lepton momentum resolution measurements.

Signal Modeling: The systematic uncertainty arising from uncertainties in the $t\bar{t}$ modeling. This includes uncertainties from variations of the ISR, FSR, the choice of PDF and from higher order corrections.

Background from MC: The uncertainty in modeling the background sources measured using MC simulation. This includes uncertainties from the modeling of the $W+\text{jets}$ background in the $\ell + \text{jets}$ channel.

Background from Data: The uncertainty in modeling the background sources evaluated from data. This includes uncertainties on the signal fraction, trigger and b -jet identification.

Method: The systematic uncertainty arising from any source specific to a particular fit method, including the finite MC statistics available to calibrate each method.

Color Reconnection (CR): The systematic uncertainty arising from a variation of the phenomenological description of color reconnection between final state particles.

Multiple Hadron Interactions (MHI): The systematic uncertainty arising from a mismodeling of the distribution of the number of collisions per Tevatron bunch crossing.

Uranium Noise and Multiple Interactions (UN/MI): This is specific to DØ Run I measurements and includes the uncertainty arising from uranium noise in the calorimeter and from the multiple interaction corrections to the JES.

For the current combination, we introduced some modifications to the categories specified in [8]. The category "MC" has been merged with the "Signal Modeling" as they have the same correlation (fully correlated between among measurements) and similar physical origin. The category "Fit" of Ref. [8] has been given a more appropriate name "Method". A new category, "Detector Modeling", has been introduced for systematic uncertainties related to detector resolution and reconstruction effects that are correlated among all measurements in the same experiment. In Ref. [8], to ensure proper correlation for these modeling uncertainties, they were included to "aJES", despite that they were not related to the jet energy scale. The category "Background" has been split into "Background from MC" and "Background from Data". This has no impact on the present combination, but will be used to properly take into account the correlations with CDF measurements. In particular, "Background from MC" is expected to be fully correlated between the same CDF and DØ channels, while "Background from Data" will be correlated only for measurements in the same channel within the same experiment for the same data taking period. These changes are expected to take effect for the next computation of the Tevatron average m_{top} . A summary of the correlations between the different systematic categories is shown in Table II.

As discussed in Ref. [5], uncertainties for the Run IIa measurement in the $\ell + \text{jets}$ channel [4] have been updated. In particular, uncertainties associated with the model for hadronization, higher-order corrections, modeling of color reconnection, and the momentum scale for leptons have been re-examined for the $\ell + \text{jets}$ result of Ref. [4]. Also, the central value of this measurement was shifted by 1.28 GeV, following the estimation of the flavor dependence of jet energy corrections in MC events [5].

The $\ell + \text{jets}$ measurement uses the matrix element method with an in-situ jet energy calibration. In addition, it takes advantage of an externally determined jet energy scale calibration to achieve the highest precision. To take into account correlations among different sources of systematic uncertainty, the uncertainty on JES is separated into two parts, one arising from the in-situ calibration, and the other from the standard JES. This separation is unchanged since the previous combination, and is documented in Ref. [6].

The combined Run IIa and Run IIb measurement in the $\ell + \text{jets}$ channel yields [5]:

$$m_{\text{top}}^{\ell+\text{jets}} = 174.94 \pm 0.83 \text{ (stat)} \pm 1.24 \text{ (syst)} \text{ GeV.}$$

The dilepton mass measurement entering this combination also uses the matrix element technique [3] for the ee , $e\mu$ and $\mu\mu$ channels both for Run IIa and Run IIb, leading to:

$$m_{\text{top}}^{\ell\ell} = 173.97 \pm 1.83 \text{ (stat)} \pm 2.45 \text{ (syst)} \text{ GeV.}$$

The assignment of uncertainties to different categories is influenced by two factors: the nature of the source and the treatment of correlations defined for combining the mass measurements from the Tevatron [8]. A summary of the assignment of the systematic uncertainties of the input measurements from Run II into the categories defined above is shown in Table III.

III. RESULTS

Combining the $\ell + \text{jets}$ and $\ell\ell$ measurements from Run I and Run II, we obtain:

$$m_{\text{top}} = 175.08 \pm 0.77 \text{ (stat)} \pm 1.25 \text{ (syst)} \text{ GeV or } m_{\text{top}} = 175.08 \pm 1.47 \text{ (stat + syst)} \text{ GeV.}$$

Table IV summarizes the weights of individual measurements. The χ^2 for the combination is 1.5 for 3 degrees of freedom, which corresponds to a probability of 68% of getting a larger value of χ^2 . A breakdown of uncertainties on the combined result is given in Table V.

Figure 1 displays a summary of the input m_{top} measurements and the combined DØ result, as well as the Tevatron average and the top quark mass extracted by DØ from the measurement of the $t\bar{t}$ cross section [11].

We thank the staffs at Fermilab and collaborating institutions, and acknowledge support from the DOE and NSF (USA); CEA and CNRS/IN2P3 (France); FASI, Rosatom and RFBR (Russia); CNPq, FAPERJ, FAPESP and FUNDUNESP (Brazil); DAE and DST (India); Colciencias (Colombia); CONACyT (Mexico); KRF and KOSEF (Korea); CONICET and UBACyT (Argentina); FOM (The Netherlands); STFC and the Royal Society (United

| | Run I | | Run II | |
|-------------------|----------------------|----------------|----------------------|----------------|
| | $\ell + \text{jets}$ | $\ell\ell$ | $\ell + \text{jets}$ | $\ell\ell$ |
| Luminosity | 130 pb $^{-1}$ | 130 pb $^{-1}$ | 3.6 fb $^{-1}$ | 5.4 fb $^{-1}$ |
| m_{top} | 180.1 GeV | 168.4 GeV | 174.94 GeV | 173.97 GeV |
| iJES | 0.0 | 0.0 | 0.53 | 0.00 |
| aJES | 0.0 | 0.0 | 0.00 | 1.57 |
| bJES | 0.7 | 0.7 | 0.07 | 0.40 |
| cJES | 2.0 | 2.0 | 0.00 | 0.00 |
| dJES | 0.0 | 0.0 | 0.63 | 1.50 |
| rJES | 2.5 | 1.1 | 0.00 | 0.00 |
| Det. Modeling | 0.0 | 0.0 | 0.36 | 0.33 |
| Lepton pt | 0.0 | 0.0 | 0.18 | 0.49 |
| Signal Modeling | 1.1 | 1.8 | 0.72 | 0.74 |
| Bkg from MC | 1.0 | 1.1 | 0.18 | 0.00 |
| Bkg from Data | 0.0 | 0.0 | 0.23 | 0.47 |
| Method | 0.6 | 1.1 | 0.16 | 0.10 |
| CR | 0.0 | 0.0 | 0.28 | 0.10 |
| MHI | 0.0 | 0.0 | 0.05 | 0.00 |
| UN/MI | 1.3 | 1.3 | 0.00 | 0.00 |
| syst. uncertainty | 3.9 | 3.6 | 1.24 | 2.45 |
| stat. uncertainty | 3.6 | 12.3 | 0.83 | 1.83 |
| total | 5.3 | 12.8 | 1.50 | 3.06 |

TABLE I: Inputs to the combination of m_{top} measurements at DØ, with uncertainties specified in GeV.

| | Run I | | Run II | |
|-----------------|----------------------|------------|----------------------|------------|
| | $\ell + \text{jets}$ | $\ell\ell$ | $\ell + \text{jets}$ | $\ell\ell$ |
| iJES | | | | |
| aJES | | | x | x |
| bJES | x | x | x | x |
| cJES | x | x | x | x |
| dJES | | | x | x |
| rJES | x | x | x | x |
| Det. Modeling | x | x | x | x |
| Lepton pt | | | x | x |
| Signal Modeling | x | x | x | x |
| Bkg from MC | x | o | x | o |
| Bkg from Data | | | | |
| Method | | | | |
| CR | | | x | x |
| MHI | | | x | x |
| UN/MI | x | x | x | x |
| statistical | | | | |

TABLE II: Summary of correlations among sources of uncertainties. An x or o within any category indicates the uncertainties that are 100% correlated, and no symbol indicates absence of correlation.

Kingdom); MSMT and GACR (Czech Republic); CRC Program and NSERC (Canada); BMBF and DFG (Germany); SFI (Ireland); The Swedish Research Council (Sweden); and CAS and CNSF (China).

-
- [1] DØ Collaboration, B. Abbott et al., Phys. Rev. Lett. **80**, 2063 (1998), DØ Collaboration, B. Abbott et al., Phys. Rev. D **60**, 052001 (1999).
 - [2] DØ Collaboration, V. Abazov et al., Nature **429**, 638 (2004).
 - [3] DØ Collaboration, V. Abazov et al., “Precise Measurement of the Top Quark Mass in the Dilepton Channel at DØ”, to be submitted to PRL.
 - [4] DØ Collaboration, V. Abazov et al., “Precise measurement of the top quark mass from lepton+jets events at DØ”, Phys. Rev. Lett. **101**, 182001 (2008).

| | Run II $\ell + \text{jets}$ | Run II $\ell\ell$ |
|-----------------|--|---|
| iJES | part of in-situ JES ⊕ Data-MC jet response | 0 |
| aJES | 0 | b/light response |
| bJES | b -modeling | b -quark modeling |
| cJES | 0 | 0 |
| dJES | part of in-situ JES ⊕ Residual JES | JES |
| rJES | 0 | 0 |
| Det. Modeling | Jet ID ⊕ Jet resolution | Jet resolution |
| Lepton pt | Lepton momentum scale | Lepton pt scale ⊕ muon resolution |
| Signal Modeling | Hadronization ⊕ Higher order effects ⊕ ISR/FSR ⊕ PDF | Hadronization/Higer Order ⊕ ISR/FSR ⊕ PDF |
| Bkg from MC | $W+\text{jets}$ heavy flavor scale factor ⊕ Background modeling | 0 |
| Bkg from Data | Multijet contamination ⊕ Signal fraction ⊕ b -tagging ⊕ trigger | Signal fraction |
| Method | MC calibration | MC calibration |
| CR | Color reconnection | Color reconnection |
| MHI | Multiple hadron interactions | 0 |
| UN/MI | 0 | 0 |

TABLE III: Summary of the assignments of the systematic uncertainties in Ref. [5] and [3] in term of the Tevatron categories defined in Ref. [8]. In each category, the quadratic sum of the assigned uncertainties is performed.

| | Run I | | Run II | |
|--------|----------------------|------------|----------------------|------------|
| | $\ell + \text{jets}$ | $\ell\ell$ | $\ell + \text{jets}$ | $\ell\ell$ |
| weight | 4.08 % | 0.25 % | 89.74 % | 5.93 % |

TABLE IV: Summary of contributing weights for the individual measurements.

- [5] DØ Collaboration, V. Abazov et al., “Precise measurement of the top quark mass from lepton+jets events at DØ”, to be submitted to PRD.
- [6] “Combination of the DØ top quark mass measurements”, DØ note 5900-CONF
- [7] L. Lyons, D. Gibaut and P. Clifford, Nucl. Instrum. and Methods A **270**, 110 (1988) and A. Valassi, Nucl. Instrum. and Methods A **500**, 391 (2003).
- [8] CDF and DØ Collaborations, “Combination of CDF and DØ results on the mass of the top quark using up to 5.6 fb⁻¹ of data”, DØ note 6090-CONF, arXiv:1007.3178
- [9] CDF Note 6804, http://hep.uchicago.edu/~hslee/ISR/cdf6804_ISR_DY.ps
- [10] L. Lyons, D. Gibaut, and P. Clifford, “How to combine correlated estimates of a single physical quantity”, Nucl. Instrum. Meth. A**270** 110 (1988)
- [11] DØ Collaboration, V. Abazov et al., “Combination and interpretation of $t\bar{t}$ cross section measurements with the DØ detector”, DØ note 5907-CONF

| | all channels |
|-----------------|--------------|
| iJES | 0.48 |
| aJES | 0.09 |
| bJES | 0.12 |
| cJES | 0.09 |
| dJES | 0.65 |
| rJES | 0.11 |
| Det. Modeling | 0.35 |
| Lepton pt | 0.19 |
| Signal Modeling | 0.74 |
| Bkg from MC | 0.20 |
| Bkg from Data | 0.21 |
| Method | 0.14 |
| CR | 0.26 |
| MHI | 0.05 |
| UN/MI | 0.06 |
| systematic | 1.25 |
| statistical | 0.77 |
| total | 1.47 |

TABLE V: Breakdown of systematic uncertainties on the combined DØ m_{top} measurement, with uncertainties given in GeV.

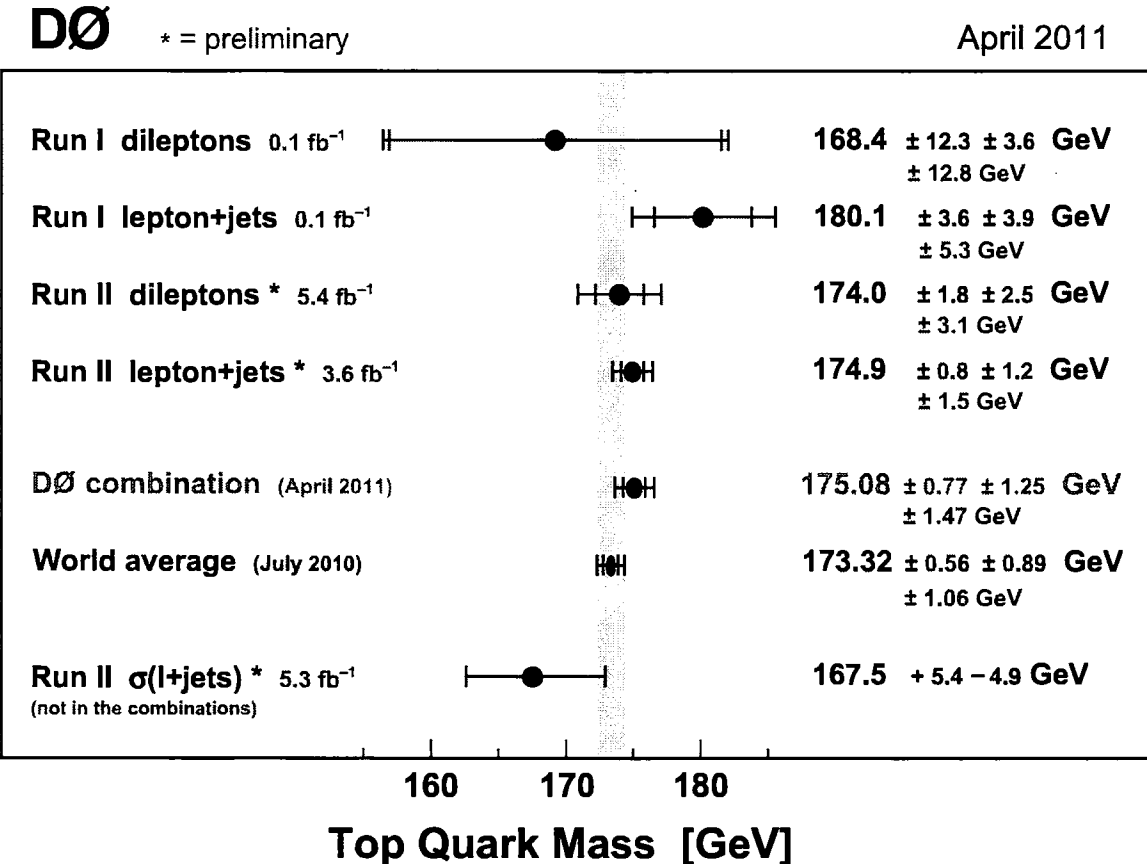


FIG. 1: A summary of the m_{top} measurements used for the DØ combination along with the DØ combination result, the Tevatron average of m_{top} and the top quark mass extracted from the cross section measurement. This extracted m_{top} value is not used in the combinations.



O

CDF note 10444

Combination of CDF top quark mass measurements (Winter 2011)

The CDF Collaboration
URL <http://www-cdf.fnal.gov>
(Dated: March 10, 2011)

We summarize the CDF measurements of the top-quark mass, M_{top} , performed analyzing 110 pb^{-1} of data collected at 1.8 TeV center of mass collision energy (Run I), and as much as 5.8 fb^{-1} of data collected at 1.96 TeV (Run II). We combine the most precise CDF published and preliminary results to obtain $M_{top} = 172.70 \pm 0.63 \text{ (stat)} \pm 0.89 \text{ (syst)} \text{ GeV}/c^2$ which corresponds to a total uncertainty of $1.09 \text{ GeV}/c^2$. The combination provides a relative precision $\Delta M_{top}/M_{top}$ of 0.63%. Rounding off to two significant digits, the combination yields $M_{top} = 172.7 \pm 1.1 \text{ (stat + syst)} \text{ GeV}/c^2$. This result includes the new top mass in all-hadronic channel and the first time determined mass in $\cancel{E}_T + \text{Jets}$ sample.

Preliminary Results for Winter 2011 Conferences

I. INTRODUCTION

We combine the CDF published top-quark mass results from the Tevatron run at 1.8 TeV center of mass collision energy (Run I) performed analyzing 110 pb^{-1} of data [1-3] with two published [4,5] and three preliminary results [6,7,8] that use up to 5.8 fb^{-1} of data collected at the Tevatron run at 1.96 TeV center of mass energy (Run II).

Results from the $t\bar{t} \rightarrow qq'bgg'b$ (HAD), $t\bar{t} \rightarrow \ell\nu qq'b\bar{b}$ (LJT), and $t\bar{t} \rightarrow \ell^+\nu b\ell^-\bar{\nu}\bar{b}$ (DIL) final states are included. For first time, additional measurement of the top quark mass from $\cancel{E}_T + \text{Jets}$ is used in the combination. It is statistically independent from LJT, DIL and HAD. These measurements are combined accounting for statistical and systematic correlations using the method of reference [9].

Relative to the previous CDF combination reported in [10], this combination includes updates of the Run II analyses in the HAD channel (5.8 fb^{-1}) and new result in the $\cancel{E}_T + \text{Jets}$ channel (5.7 fb^{-1}). Still, the Summer 2010 measurement in the LJT channel using Matrix Element technique keeps the single most precise result, with a 0.72% relative precision on $\Delta M_{top}/M_{top}$, more precise than the '09 Tevatron top mass combination [11].

The uncertainty categories used in the combination are detailed in Section II while the input measurements themselves are summarized in Section III. The correlations used in the combination are discussed in Section IV and the resulting top-quark mass is given in Section V. Section VI summarizes the results obtained.

II. UNCERTAINTY CATEGORIES

The uncertainty categories did not change from the previous CDF combination [10] and they correspond to the same uncertainty categories as used for the Tevatron world average [11]. They have evolved to include a detailed breakdown of the various sources of uncertainty and aim to lump together sources of systematic uncertainty that share the same or similar origin. For example, the "Signal" category discussed below includes the uncertainties from initial state radiation (ISR), final state radiation (FSR), and parton distribution functions (PDF) - all of which affect the modeling of the $t\bar{t}$ signal. The dominant systematic, the jet energy scale (JES) uncertainty, is sub-divided into several components ("levels") in order to more accurately accommodate our best estimate of the relevant correlations [12]. Additional categories have been added in order to accommodate specific types of correlations. Each uncertainty category is discussed below.

Statistical: The statistical uncertainty associated with the M_{top} determination.

iJES: The statistical uncertainty on the JES arising from the in-situ $W \rightarrow qq'$ calibration alone. Residual JES uncertainties, which arise from effects not considered in the in-situ calibration, are included in the Method category below.

aJES: This is specific to DØ Run II and is only included here in order to be consistent with reference [11].

bJES: The systematic uncertainty specific to the modeling of b-jets. This includes uncertainties arising from variations in the semi-leptonic branching fraction, b-fragmentation modeling, and differences in the color flow between b-quark jets and light-quark. This is usually labeled "B Jet" for CDF Run II analyses.

cJES: The systematic uncertainty on the JES arising from the modeling of the out-of-cone corrections. This is the quadrature sum of the L7 and L8 JES uncertainties for CDF Run II analyses.

dJES: The systematic uncertainty on the JES arising from the relative corrections. This is the L1 JES uncertainties for CDF Run II analyses.

rJES: The systematic uncertainty on the JES arising from the modeling of the calorimeter response, the underlying event, and the multiple interaction corrections. This is the quadrature sum of the L4, L5, and L6 JES uncertainties for CDF Run II analyses.

Lepton P_T : The systematic uncertainty arising from uncertainties in the scale of the lepton transverse momentum measurements. This is an important uncertainty in the analysis with minimal dependence on the jet energy scale. It was not considered a source of systematic uncertainty in the Run I measurements.

Signal: The systematic uncertainty arising from uncertainties in the modeling of the $t\bar{t}$ signal including variations in the ISR, FSR, and PDF descriptions used to generate the $t\bar{t}$ Monte Carlo samples that calibrate each method.

Generator: The systematic uncertainty associated with variations of the physics model used to calibrate the fit methods and correlated across all measurements. It includes variations observed when substituting Pythia [13–15] (Run I and Run II) or ISAJET [16] (Run I) for HERWIG [17, 18] when modeling the $t\bar{t}$ signal.

Uranium noise and multiple interactions (UN/MI): This is specific to DØ Run I and is only included here in order to be consistent with reference [11].

Background: The systematic uncertainty arising from uncertainties in modeling the dominant background sources, including q^2 variations. This is the quadrature sum of the “Background Shape” and “Background normalization” uncertainties for most CDF Run II analyses.

Method: The systematic uncertainty arising from any source specific to a particular fit method, including the variations in B-tagging efficiency and the finite Monte Carlo statistics available to calibrate each method. This is the quadrature sum of the “Method”, “B-tag”, and “MC Statistics” categories for most CDF Run II analyses.

Color Reconnections (CR): The systematic uncertainty arising from a variation of the phenomenological description of color reconnection between final state particles [19]. This is obtained taking the difference between PYTHIA 6.4 tune “Apro” and PYTHIA 6.4 tune “ACRpro” that only includes a change in the color reconnection model. Monte Carlo generators which explicitly include CR models for hadron collisions have recently become available. This was not possible in Run I and these measurements do not include this source of systematic uncertainty.

Multiple Hadron Interactions (MHI): The systematic uncertainty arising from a mismodeling of the distribution of number of collision per bunch crossing due to the change in the collider instantaneous luminosity during data-taking. It has been separated from other sources to account for the fact that it is uncorrelated with DØ’s measurements.

These categories represent the current preliminary understanding of the various uncertainty categories and their correlations. We expect these to evolve as we continue to probe each method’s sensitivity to the various systematic sources with ever improving precision. Small variations in the assignment of uncertainties to the uncertainty categories and in the correlations assumed negligibly affect the combination.

III. INPUT MEASUREMENTS

For this combination we use eight measurements: three published Run I [1–3] results, two published Run II results [4,5] and three preliminary Run II results [6,7,8]. They are summarized in Table I. The correlations between the various inputs are described in the next section. Based on studies described in reference [20] the statistical correlation between the $L_{xy} + P_T^{lep}$ and LJT inputs is set to zero in the combination. Variations of ± 0.5 , which cover the full range observed in these studies, negligibly affect the combination reported here. Additionally, the new measurement from the $E_T + \text{Jets}$ sample is treated as statistically uncorrelated with the other samples.

There are other CDF measurements in the LJT, DIL, HAD, and minimal-JES-dependence channels. We have chosen to include in this combination the analysis methods which yielded the best *expected* sensitivity for each channel. The channels themselves are statistically independent of each other and are treated as such.

For the $L_{xy} + P_T^{lep}$ measurement, we include the systematic uncertainty associated with the potential mis-modeling of the background decay length distribution in the “Method” category, as it is a source of uncertainty unique to this method.

For the Run I measurements, we back propagate the systematic uncertainty specific to B-jets (bJES) as determined in Run II and then correct the Run I absolute corrections (rJES) to keep the total JES uncertainty constant. We perform a series of cross-check to probe the robustness of the result. We propagate using the estimation of the color reconnection systematic performed in Run II back to Run I measurements as well, finding no noticeable difference in the combination. Another cross-check is to back-propagate the Lepton P_T systematic back to Run I results; again, no noticeable difference was found in the combination. Variations of the above assumptions were explored and found to negligibly affect the final value.

IV. CORRELATIONS

The following correlations are used when making the combination:

| Input | Run II Published | | | Run II Preliminary | | | Run I Published | | |
|------------------------------|------------------|----------------------|--------|--------------------|------------------------------|-------|-----------------|-------|--|
| | LJT | $L_{xy} + P_T^{lep}$ | DIL | HAD | $\cancel{E}_T + \text{Jets}$ | LJT | DIL | HAD | |
| M_{top} | 173.00 | 170.70 | 170.56 | 172.47 | 172.32 | 176.1 | 167.4 | 186.0 | |
| Statistical | 0.65 | 6.30 | 2.19 | 1.43 | 1.80 | 5.1 | 10.3 | 10.0 | |
| iJES | 0.58 | 0.0 | 0.0 | 0.95 | 1.54 | - | - | - | |
| aJES | - | - | - | - | - | - | - | - | |
| bJES | 0.26 | 0.0 | 0.35 | 0.15 | 0.29 | 0.6 | 0.8 | 0.6 | |
| cJES | 0.27 | 0.06 | 2.01 | 0.24 | 0.20 | 2.7 | 2.6 | 3.0 | |
| dJES | 0.01 | 0.02 | 0.64 | 0.04 | 0.05 | 0.7 | 0.6 | 0.3 | |
| rJES | 0.41 | 0.11 | 1.98 | 0.38 | 0.45 | 3.4 | 2.7 | 4.0 | |
| Lepton P_T | 0.14 | 1.20 | 0.31 | - | 0.00 | - | - | - | |
| Signal | 0.21 | 0.86 | 0.36 | 0.22 | 0.29 | 2.6 | 2.8 | 1.8 | |
| Generator | 0.37 | 0.30 | 0.57 | 0.48 | 0.65 | 0.1 | 0.6 | 0.8 | |
| UN/MI | - | - | - | - | - | - | - | - | |
| Background | 0.34 | 1.70 | 0.27 | 0.75 | 0.12 | 1.3 | 0.3 | 1.7 | |
| Method | 0.10 | 1.13 | 0.05 | 0.38 | 0.14 | 0.0 | 0.7 | 0.6 | |
| Color Reconnections | 0.37 | 0.40 | 0.61 | 0.32 | 0.20 | - | - | - | |
| Multiple Hadron Interactions | 0.10 | 0.70 | 0.27 | 0.08 | 0.16 | - | - | - | |
| Statistical | 0.65 | 6.20 | 2.19 | 1.43 | 1.80 | 5.1 | 10.3 | 10.0 | |
| Systematics | 1.06 | 3.10 | 3.09 | 1.49 | 1.82 | 5.3 | 4.9 | 5.7 | |
| Total | 1.24 | 6.90 | 3.79 | 2.06 | 2.56 | 7.3 | 11.4 | 11.5 | |

TABLE I: The measurements used to determine the CDF combined top-quark mass. All numbers are in units of GeV/c^2 . The uncertainty categories and their correlations are defined in the text. Some of the systematic sources were not accounted for in Run I measurements, due to them being negligible with respect to the actual measurements.

- The uncertainties in the Statistical, Method, and iJES categories are taken to be uncorrelated among the measurements.
- The uncertainties in the aJES, dJES, Lepton P_T and Multiple Hadron Interaction categories are taken to be 100% correlated among all Run I and all Run II measurements, but uncorrelated between Run I and Run II.
- The uncertainties in the Background category are taken to be 100% correlated among all measurements in the same channel.
- The uncertainties in the bJES, cJES, rJES, Signal, Generator and Color Reconnection categories are taken to be 100% correlated among all measurements.

Using the inputs from Table I and the correlations specified here, the resulting matrix of total correlation coefficients is given in Table II.

To help quantify how sensitive the combination is to these assumptions we vary some of these correlations and redo the combination. In Summer 2010 combination, we changed all correlations that were set to be 100%, to a 50% value and found a shift in the combined M_{top} of less than $50\text{ MeV}/c^2$, and a change in precision of less than $10\text{ MeV}/c^2$. We also varied the statistical correlation for the two very different LJT analyses from 0% to 50%, and found a shift and change in precision less than $10\text{ MeV}/c^2$.

| | Run II Published | | | Run II Preliminary | | | Run I Published | | |
|------------------------------|------------------|----------------------|------|--------------------|------------------------------|------|-----------------|-----|--|
| | LJT | $L_{xy} + P_T^{lep}$ | DIL | HAD | $\cancel{E}_T + \text{Jets}$ | LJT | DIL | HAD | |
| LJT | 1 | | | | | | | | |
| $L_{xy} + P_T^{lep}$ | 0.15 | 1 | | | | | | | |
| DIL | 0.43 | 0.06 | 1 | | | | | | |
| HAD | 0.24 | 0.04 | 0.24 | 1 | | | | | |
| $\cancel{E}_T + \text{Jets}$ | 0.22 | 0.04 | 0.21 | 0.14 | 1 | | | | |
| LJT | 0.36 | 0.04 | 0.47 | 0.17 | 0.16 | 1 | | | |
| DIL | 0.20 | 0.03 | 0.28 | 0.11 | 0.10 | 0.29 | 1 | | |
| HAD | 0.23 | 0.15 | 0.35 | 0.18 | 0.13 | 0.32 | 0.19 | 1 | |

TABLE II: The resulting matrix of total correlation coefficients used to determine the CDF combined top quark mass.

V. RESULTS

Using the measurements of Table I and the correlations of Section IV the CDF combined top mass is

$$M_{top} = 172.70 \pm 0.63 \text{ (stat)} \pm 0.89 \text{ (syst) GeV}/c^2 \quad (1)$$

$$= 172.70 \pm 1.09 \text{ GeV}/c^2 \quad (2)$$

with $\chi^2/dof = 3.4/7$, which corresponds to a chi-squared probability of about 85%, indicating good agreement among all the input measurements. The combined value is $0.4 \text{ GeV}/c^2$ lower than the previous CDF combination [10], due to an downward shift in the mass determination in the Run, II HAD channel [8]. It is also $0.3 \text{ GeV}/c^2$ lower than [4] due to lower masses in HAD and E_T +Jets.

This CDF-only combination has a relative precision of $\Delta M_{top}/M_{top} = 0.63\%$. The combined value presented here improves the precision by 13% with respect to the single most precise measurement [5]. This CDF combination improves the precision on M_{top} by 6% with respect to the previous CDF best determination [10].

The method of reference [9] decomposes the total uncertainty into the contributions from the various uncertainty categories; the results can be found in Table III.

| Results | CDF combined values |
|--------------|---------------------|
| M_{top} | 172.70 |
| iJES | 0.51 |
| aJES | - |
| bJES | 0.23 |
| cJES | 0.11 |
| dJES | 0.02 |
| rJES | 0.24 |
| Lepton P_T | 0.10 |
| Signal | 0.13 |
| Generator | 0.42 |
| UM | - |
| Background | 0.27 |
| Fit | 0.11 |
| CR | 0.35 |
| MHI | 0.11 |
| Syst. | 0.89 |
| Stat. | 0.63 |
| Total | 1.09 |

TABLE III: Summary of the Tevatron combined world average M_{top} . The error categories are described in the text. The total systematic uncertainty and the total uncertainty are obtained by adding the relevant contributions in quadrature. All numbers are in units of GeV/c^2 .

The corresponding pull and weight for each of the inputs are listed in Table IV.

| | Run II Published | | | Run II Preliminary | | | Run I Published | | |
|------------|------------------|----------------------|-------|--------------------|-------------|-------|-----------------|-------|--|
| | LJT | $L_{xy} + P_T^{lep}$ | DIL | HAD | E_T +Jets | LJT | DIL | HAD | |
| Pull | 0.51 | -0.30 | -0.59 | -0.13 | -0.16 | 0.47 | -0.47 | 1.16 | |
| Weight (%) | +76.52 | 0.46 | -2.78 | 19.25 | 10.65 | -2.65 | -0.46 | -0.99 | |

TABLE IV: The pull and weight for each of the inputs used to determine the CDF combined top quark mass.

The input measurements, the output combination and the χ^2/dof are summarized in Figure 2.

The weights of some of the measurements are negative. In general, this situation can occur if the correlation between two measurements is larger than the ratio of their total uncertainties. This is indeed the case here. In these instances the less precise measurement will usually acquire a negative weight. While a weight of zero means that a particular input is effectively ignored in the combination, a negative weight means that it affects the resulting central value and helps reduce the total uncertainty. See Reference [22] for further discussion of negative weights. To visualize the weight each measurement carries in the combination, weights have been divided by the sum of the modulo of all the input measurements weights. The result is shown in Figure 1.

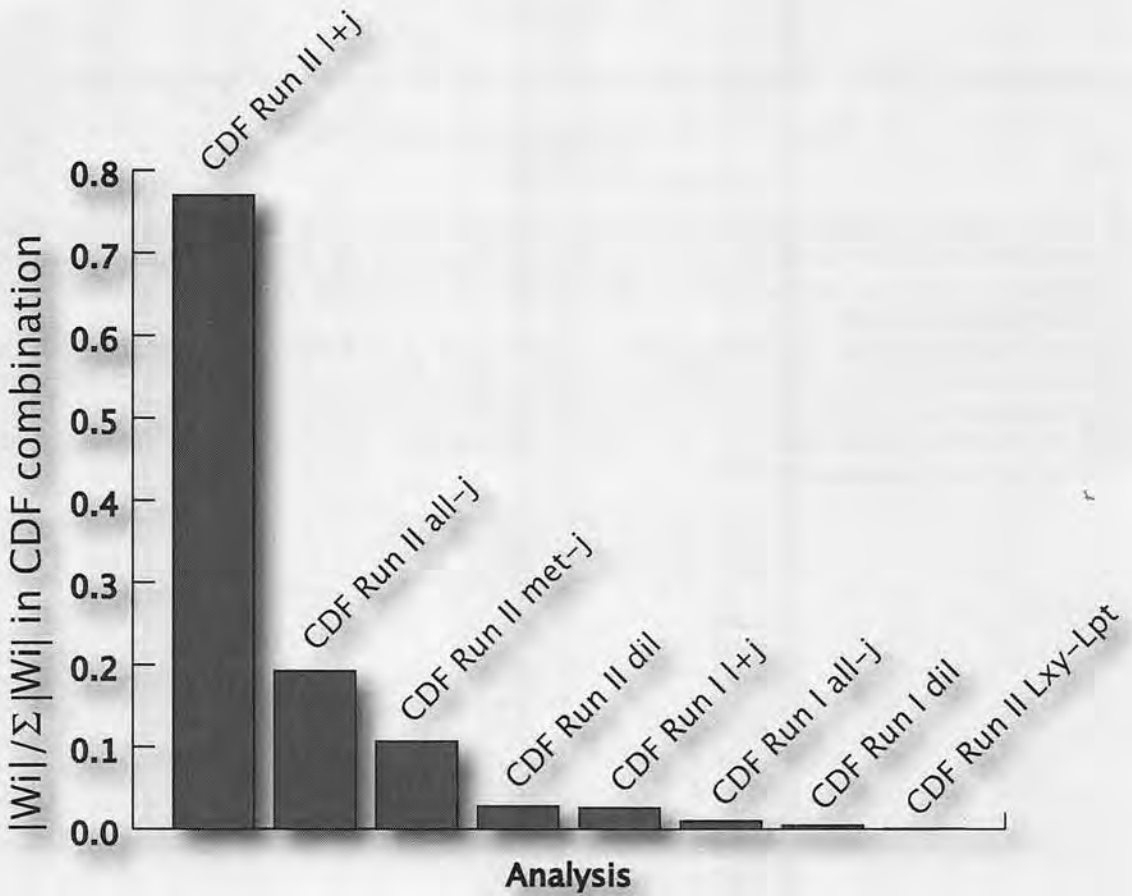


FIG. 1: Relative weights of the input measurements in the combination. The relative weights have been obtained dividing each measurement weight by the sum over all measurements of the modulo of their weights.

Although the chi-squared from the combination of all measurements indicates that there is good agreement among them, and no input has an anomalously large pull, it is still interesting to also fit for the top mass in the LJT, DIL, HAD and $\cancel{E}_T + \text{jets}$ channels separately. We use the same methodology and include the systematic correlations among the measurements as described in Section IV. The results are shown in Table V.

Using the expression in reference [21] we calculate the following chi-squares $\chi^2(LJT - DIL) = 1.62/1$, $\chi^2(LJT - HAD) = 0.02/1$, $\chi^2(LJT - \cancel{E}_T + \text{jets}) = 0.07/1$, $\chi^2(DIL - HAD) = 1.07/1$, $\chi^2(DIL - \cancel{E}_T + \text{jets}) = 0.69/1$ and $\chi^2(HAD - \cancel{E}_T + \text{jets}) = 0.02/1$. These correspond to chi-squared probabilities of 20%, 89%, 79%, 30%, 41%, 89% respectively, and indicate that all channels are reasonably consistent with each other.

| | fit value (GeV/ c^2) | correlations | | | |
|------------------------------|-------------------------|--------------|--------|--------|------------------------------|
| | | M(LJT) | M(DIL) | M(HAD) | $\cancel{E}_T + \text{Jets}$ |
| M(LJT) | 172.69 ± 1.20 | 1 | | | |
| M(DIL) | 168.77 ± 3.31 | 0.38 | 1 | | |
| M(HAD) | 172.43 ± 2.04 | 0.22 | 0.22 | 1 | |
| $\cancel{E}_T + \text{Jets}$ | 172.00 ± 2.53 | 0.19 | 0.17 | 0.12 | 1 |

TABLE V: The results of a fit to determine the top-quark mass in the three final states separately.

Using only the Run II measurements of Table I and the correlations of Section IV the CDF combined Run II top mass is

$$M_{top} = 172.97 \pm 1.12 \text{ GeV}/c^2 \quad (3)$$

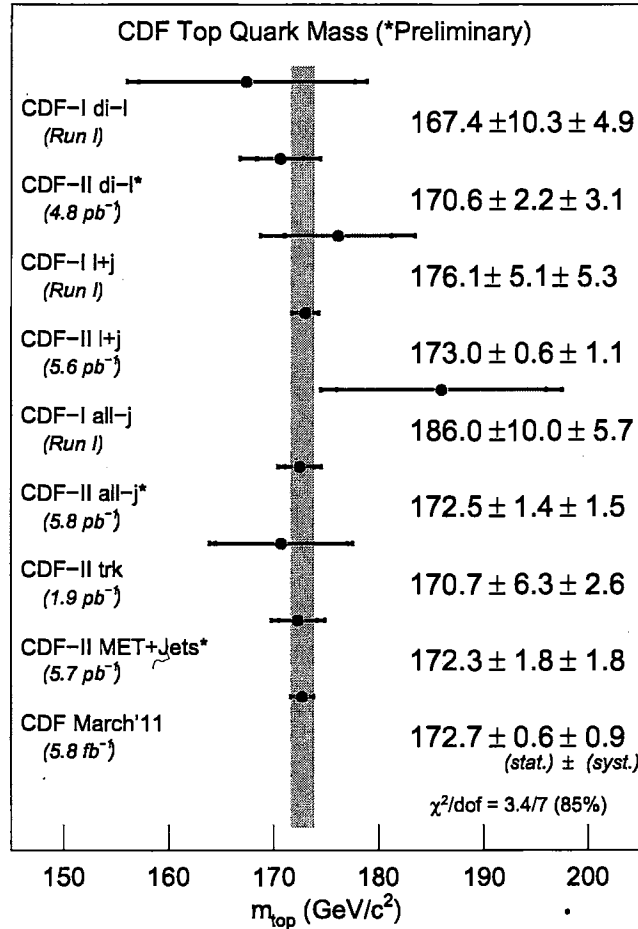


FIG. 2: A summary of the input measurements utilized in this combination, and the resulting CDF combined top-quark mass. The preliminary results are the ones that carry the asterisk sign. All other results have been published.

with $\chi^2/\text{dof} = 0.678/4$, which corresponds to a chi-squared probability of about 95%, indicating good agreement among all the input measurements. The combined value is $300 \text{ MeV}/c^2$ higher than the Run I plus Run II CDF combination, and has only $20 \text{ MeV}/c^2$ larger uncertainty.

VI. CONCLUSION

We have combined CDF Run I and Run II top-quark mass measurements from four final states, LJT, DIL, HAD and \cancel{E}_T to get a CDF combined top-quark mass of $172.70 \pm 1.09 \text{ GeV}/c^2$. In this combination, for first time, a new sample of $\cancel{E}_T + \text{Jets}$ events was used. This CDF-only combination has thus a relative precision of $\Delta M_{top}/M_{top} = 0.63\%$. This corresponds to a relative improvement of 7% with respect to the previous CDF combination [10] and 3% worse with respect to the previous 2010 Tevatron combination [11]. Rounding off to two significant digits, the combination yields $M_{top} = 172.7 \pm 1.1(\text{stat} + \text{syst}) \text{ GeV}/c^2$.

Acknowledgments

We thank the Fermilab staff and the technical staffs of the participating institutions for their vital contributions. This work was supported by the U.S. Department of Energy and National Science Foundation; the Italian Istituto Nazionale di Fisica Nucleare; the Ministry of Education, Culture, Sports, Science and Technology of Japan; the Natural Sciences and Engineering Research Council of Canada; the National Science Council of the Republic of China; the Swiss National Science Foundation; the A.P. Sloan Foundation; the Bundesministerium für Bildung und Forschung, Germany; the World Class University Program, the National Research Foundation of Korea; the Science and Technology Facilities Council and the Royal Society, UK; the Institut National de Physique Nucléaire et Physique des Particules/CNRS; the Russian Foundation for Basic Research; the Ministerio de Ciencia e Innovación, and Programa Consolider-Ingenio 2010, Spain; the Slovak R&D Agency; and the Academy of Finland.

- [1] CDF Collaboration, F. Abe *et al.*, Phys. Rev. Lett. **80**, (1998) 2779;
- [2] CDF Collaboration, F. Abe *et al.*, Phys. Rev. **D63**, (2001) 032003;
- [3] CDF Collaboration, F. Abe *et al.*, Phys. Rev. Lett. **79**, (1997) 1992;
- [4] T. Aaltonen *et al.* [The CDF Collaboration], Phys. Rev. D **81** (2010) 032002;
- [5] T. Aaltonen *et al.* [The CDF Collaboration], Phys. Rev. Lett. **105** (2010) 252001;
- [6] T. Aaltonen *et al.* [The CDF Collaboration], CDF Conference Note 10273;
- [7] T. Aaltonen *et al.* [The CDF Collaboration], CDF Conference Note 10433;
- [8] T. Aaltonen *et al.* [The CDF Collaboration], CDF Conference Note 104xx;
- [9] L. Lyons, D. Gibaut, and P. Clifford, Nucl. Instrum. Meth. **A270** (1988) 110;
A. Valassi, Nucl. Instrum. Meth. **A500** (2003) 391;
- [10] M. Datta, D. Glenzinski, F. Margaroli, G. Velev [The CDF collaboration], CDF Conference Note 10210;
- [11] Tevatron Electroweak Working Group, [The CDF and D0 Collaborations], arXiv:0903.2503;
- [12] A. Bhatti *et al.*, Nucl. Instrum. Meth. A **566** (2006) 375;
- [13] H.-U. Bengtsson and T. Sjostrand, Comput. Phys. Commun. **46** (1987) 43;
- [14] T. Sjostrand, Comput. Phys. Commun. **82** (1994) 74;
- [15] T. Sjostrand *et al.*, Comput. Phys. Commun. **135** (2001) 238;
- [16] F. E. Paige and S. D. Protopopescu, BNL Reports 38034 and 38774 (1986) unpublished;
- [17] G. Marchesini *et al.*, Comput. Phys. Commun. **67** (1992) 465;
- [18] G. Corcella *et al.*, JHEP **01** (2001) 010;
- [19] P. Z. Skands, arXiv:0905.3418;
- [20] T. Aaltonen *et al.* [The CDF Collaboration], CDF Conference Note 8222;
- [21] For two measurements, x and y , we calculate their consistency using $\chi^2 = (x-y)^2/\sigma_{x-y}^2$, where $\sigma_{x-y}^2 = \sigma_x^2 + \sigma_y^2 - 2\rho_{xy}\sigma_x\sigma_y$, where ρ_{xy} is the (x,y) correlation coefficient;
- [22] L. Lyons, D. Gibaut, and P. Clifford, Nucl. Instrum. Meth. **A270** (1988) 110.

(2)

$$P_T^{\text{PARTON}} = \frac{(P_T^{\text{JET}} \times C_\eta - C_{\text{MI}}) \times C_{\text{Abs}}}{P_T^{\text{PARTICLE}}} - C_{\text{UE}} + C_{\text{OOC}}$$

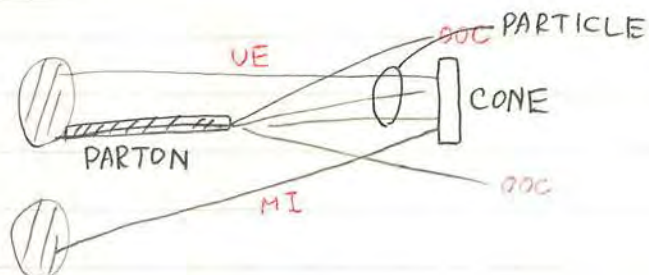
(71)

Diagram illustrating the components of the equation:

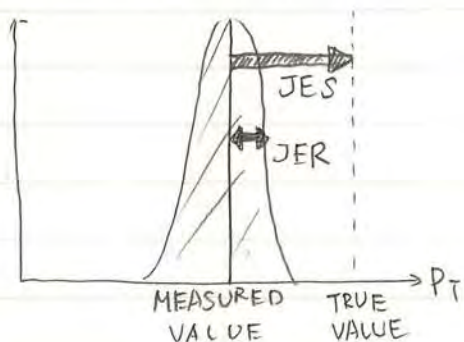
- P_T^{PARTICLE} : Measured in Calo
- η -dependent correction: $P_T^{\text{JET}} \times C_\eta$
- multiple interactions: C_{MI}
- Jet energy scale: C_{Abs}
- underlying event correction: C_{UE}
- out of cone correction: C_{OOC}
- indep. of detector: C_{OOC}

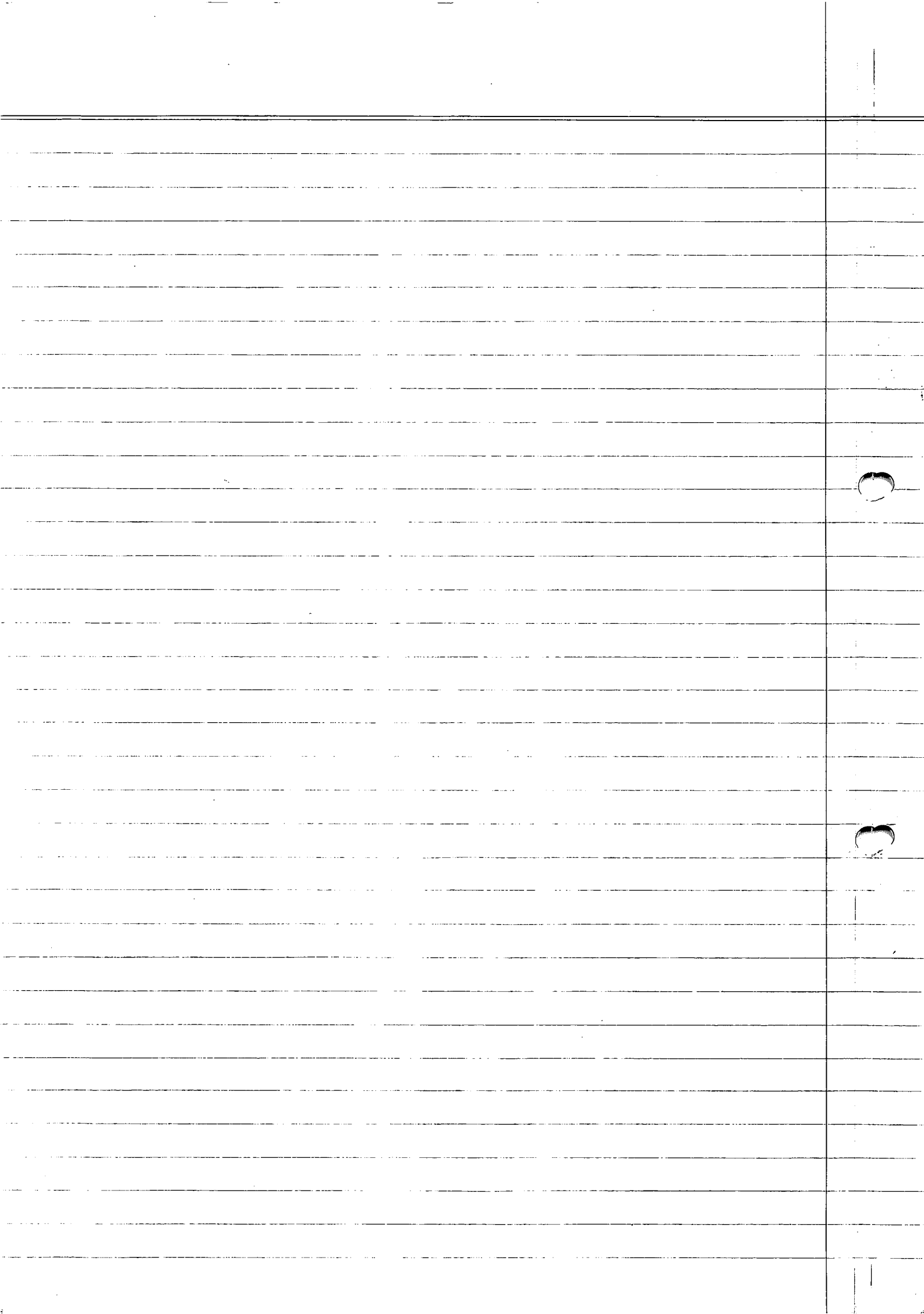
"計った結果を η について調整した上で
他の $p\bar{p}$ 散乱から来る寄りを引いたもの" $\times C_{\text{Abs}} = \text{Calo に } \lambda, \tau \text{ で} \text{した}$
uniform 粒子の P_T

"Calorimeter Cone に λ, τ でした 粒子の P_T から
spectator particle を引いた
Cone に λ, τ でした 粒子を足したもの" = PARTON の P_T .



ALSO THERE IS "JET ENERGY RESOLUTION"!





High- P_T Physics: from the Tevatron to the LHC

Tommaso Dorigo

Dipartimento di Fisica “G.Galilei”, Via Marzolo 8, 35131 Padova, Italy

E-mail: dorigo@pd.infn.it

Abstract. The CDF and DØ collaborations at the Tevatron have been producing exquisite precision measurements on high- P_T physics with their large datasets of $p\bar{p}$ collisions. During the few years that divide us from the start of operation of the Large Hadron Collider experiments at CERN, a lot can be done besides improving the measurement of accessible observable quantities, to prepare the ground for an easier and more successful exploitation of the forthcoming LHC collisions.

Foreword

Allow me to start these proceedings by thanking the organizers of the Corfu 2005 conference for their effort, and for putting together a successful mix of topical conferences and schools in a lovely venue. The relaxed atmosphere, the careful organization, and the beautiful setting conspired to make the meeting a productive and very pleasant one.

The present document summarizes the review I gave in Corfu last September on the status of high transverse momentum physics at the Tevatron. The review focused primarily on measurements which are both of current interest at the Tevatron, and of future relevance in the forthcoming years, when a migration of experience, analytical effort, and eventually results will occur towards CERN, where the Large Hadron Collider (LHC) is being built.

In my talk I did not make any attempt at being exhaustive in the choice of discussed topics –I did not deal with QCD measurements or exotic searches– nor in the coverage of those I did discuss. I also felt free to upset the usual balance of an equal share of advertisement of the results of the two Tevatron collider experiments: I cited mostly analyses performed by CDF, which I of course know more in detail, being a member of that collaboration.

The same approach will be offered here. I however made my best to provide updated results, where CDF or DØ produced anything new since September 2005. My excuses are herewith offered in advance to anybody who feels their favourite analysis has been neglected: this is by no means a complete review of current results, nor a showroom of the best ones, but rather a discussion of general topics that appear of relevance in the few years that will bridge us from the Tevatron to the LHC era.

It is indeed of paramount importance for the future of high-energy physics in the 21st century to not only treasure the experience gathered by analysing 2 TeV proton-antiproton collisions during the last 20 years at the Tevatron, but also to identify well in advance those aspects that make a difference when going from 2 to 14 TeV, and specifically the ones which will be most critical for a successful exploitation of the LHC data.

Of course, several studies have been carried out in the past with the above goal in mind. The present, however, provides us with Tevatron data in large amounts, and the statistical precision with which CDF and DØ are measuring physical quantities is now forcing the two experiments into putting a major effort in investigating new ways to reduce the by now dominant systematic uncertainties.

Now is therefore as good a time as any to summarize the status of our learning curve in the preparations for the LHC era.

1. Introduction

1.1. The present

The Tevatron accelerator has been subjected at the turn of the millennium to a massive upgrade, with the construction of an entirely new ring, the Main Injector, and several improvements in the facility producing and storing antiprotons – the most challenging part of the whole project.

A sketch of the Run II setup of the Tevatron accelerating complex is shown in Fig. 1.

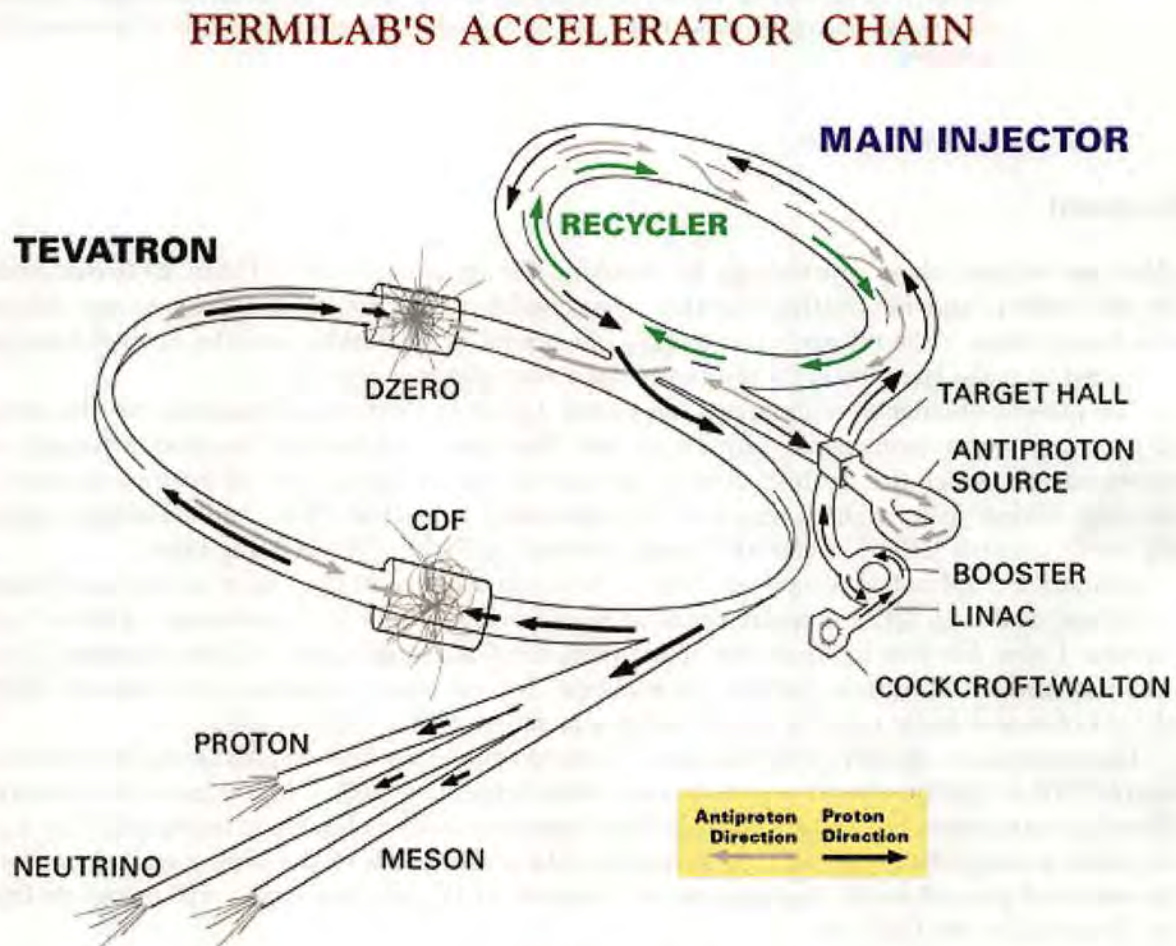


Figure 1. Sketch of the Tevatron accelerator facility.

A modest increase in beam energy –from 900 to 980 GeV– was the by-product of an upgrade of the accelerating cavities. The Tevatron upgrade did not aim at achieving the maximum

possible center-of-mass energy so much as at securing the best operating conditions which would guarantee the machine to consistently deliver the highest possible instantaneous luminosity, a crucial ingredient to keep hopes alive for a Higgs boson discovery, and for the measurement of mixing parameters of B_s mesons, the other main goal for Run II of the CDF and D \emptyset experiments –now successfully achieved. The 9% increase in center-of-mass energy does grant a $\sim 25\%$ increase in production rate of heavy particles such as the top quark or the Higgs boson, but the impact that a larger number of protons and antiprotons and a faster rate of data collection have on the discovery reach of the Tevatron experiments in Run II is more dramatic. The Tevatron has recently surpassed the peak luminosity of $1.8 \times 10^{32} \text{ cm}^{-2} \text{ s}^{-1}$ (see Fig. 2), and has been consistently delivering steady beam to the experiments. An integrated luminosity of about 1.5 fb^{-1} per experiment has been collected at the time of writing.

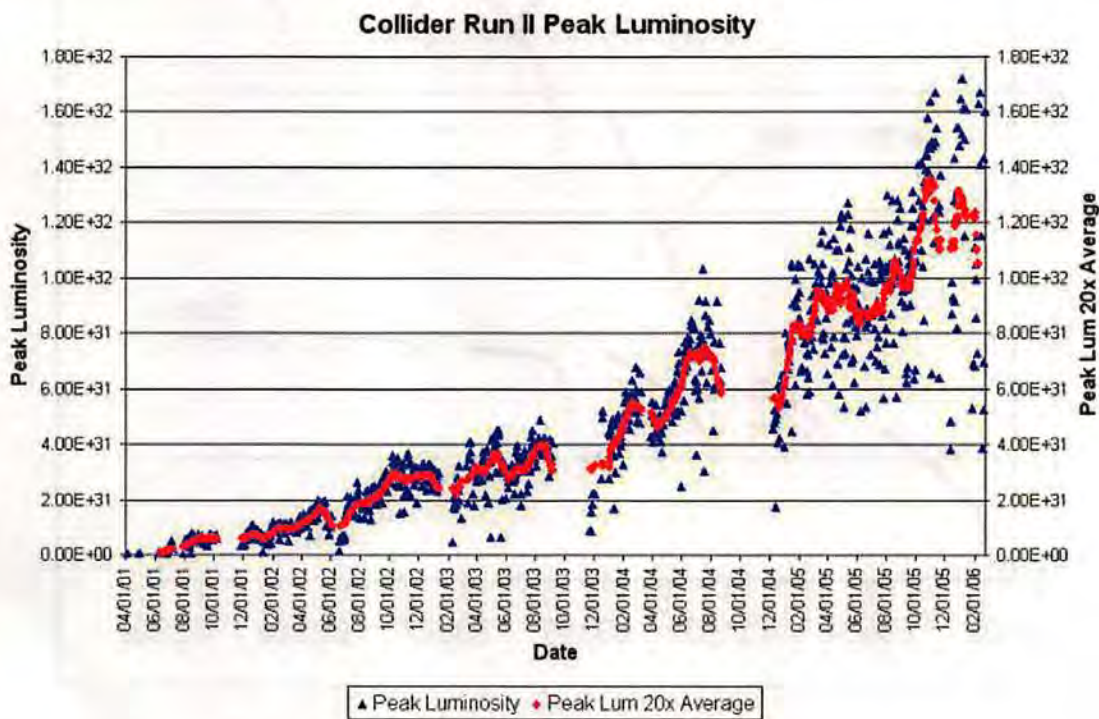


Figure 2. Peak luminosity of Tevatron runs from 2001 to 2006.

During 2006 a few crucial upgrades are being completed following the plan of increase of machine luminosity, whose critical ingredients are the efficient production, storage, and transfer of antiprotons. The two principal improvements are electron cooling of the antiproton beam and an increase of the stacktail bandwidth.

Electron cooling [1] has been recently demonstrated in the recycler ring by merging a 4.8 MeV beam of electrons with the 8.9 GeV beam of antiprotons. Because of the different masses, particles in the two beams move at the same speed; the electron current stabilizes the antiproton beam, reducing the longitudinal spread in antiproton velocities. An increase in the capability of antiproton stacking, through an upgrade of the accumulator stacktail cooling system, is expected to significantly improve the speed of antiproton collection and the resulting amount of available particles for Tevatron collisions.

If the described upgrades should not work as planned, the Tevatron will still be able to deliver a total of 4 fb^{-1} to each collider experiment by 2009 –what has been called *base plan*. But if the upgrades will produce the desired effect, the design luminosity of 8 fb^{-1} is likely to be collected

by that date (see Fig. 3). This latter *design plan* might change the perspective of Tevatron physics in Run II, giving CDF and DØ significant chances of a light Higgs boson discovery before or in coincidence with a LHC observation.

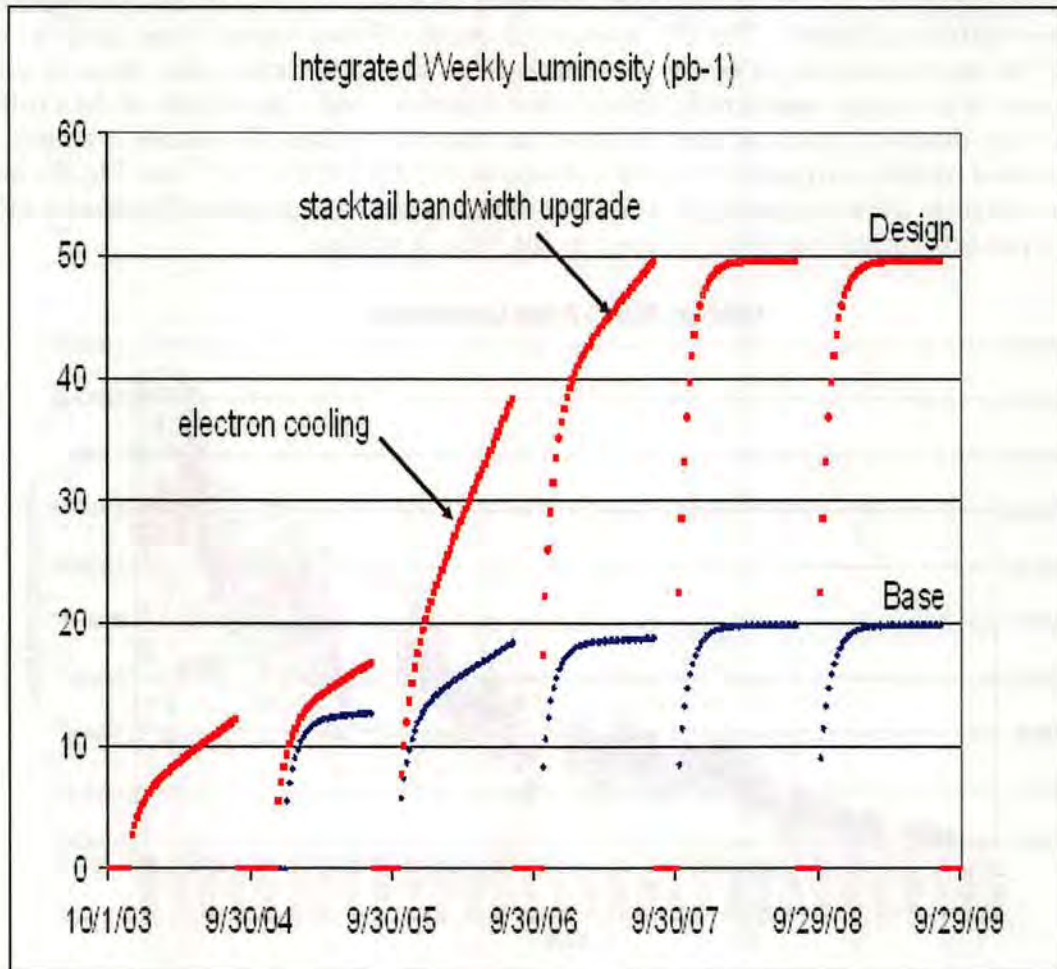


Figure 3. Predictions for weekly integrated luminosity delivered by the Tevatron accelerator. The design plan corresponds to a total integrated luminosity of 8fb^{-1} by the end of 2009, while the base plan corresponds to 4fb^{-1} .

1.2. The future

The Large Hadron Collider (LHC), the accelerating complex in construction at the CERN laboratory in Geneva, is a truly daring enterprise, attempting to scale the two significant machine design parameters –beam energy and luminosity– up by an order of magnitude from the previous records reached by its predecessor, the Tevatron collider of Fermilab.

From the 980 GeV beams of protons and antiprotons of the Tevatron to the 7000 GeV beams of protons of the LHC, the leap forwards is giant. It entails the construction of 1232 superconducting magnets to provide the necessary bending force in the CERN 26.7 km tunnel, which until 2002 hosted the LEP II accelerator. The total stored beam energy at the design luminosity of $10^{34}\text{cm}^{-2}\text{s}^{-1}$ equals the kinetic energy of a loaded Airbus A340-200 at landing speed.

Challenging is also the design and construction of a system capable of running with 2808 25 ns -spaced bunches of protons, achieving beam stability throughout the LHC tunnel, and squeezing the bunches transversely to a diameter of $\sim 34\mu m$ in the center of the experimental facilities.

Together with the technical challenges involved in the construction of the accelerating complex, the construction of the CMS and ATLAS experimental apparata are also quite demanding.

CMS and ATLAS were born originally different in a few key design features, but gradually became more similar as the first blueprints evolved into the commissioning phase, in a process of dynamical likening that was already observed between DØ and CDF a decade ago.

The focus of the experiments, it appears, has gradually shifted from a marked accent to muon detection –with the aim of observing the ultra-clean signature of Higgs boson decay to a pair of Z bosons, $p\bar{p} \rightarrow H \rightarrow ZZ \rightarrow \mu\mu\mu\mu$ – to a greater versatility. The motivation of that shift was the need to not only ensure detection of a Higgs boson whatever its mass, but also to do it with the smallest possible amount of data –*id est*, in the shortest possible time. Moreover, if the original motivation for building the experiments was principally the detection of the Higgs boson, maintaining a rich physics program and constant financing for many years is a more important item in the agenda once construction funds are secured: the Higgs discovery is by now practically given for granted, and the discovery of supersymmetry is the real goal for LHC.

As we approach the starting date of the first collisions, most of the construction problems are on the way of being successfully solved. The LHC must not fail: the high energy frontier will rely on that machine for the next ten years. Interestingly, a strong commitment to make the CMS and ATLAS experiments successful enterprises has been demonstrated recently also by the United States, where the active participation in the experiments has been dubbed "strategic" for the plan of bringing back the leadership in frontier particle physics to the american soil [2].

1.3. From the present to the future

For an experimentalist, the best way to exploit these few years that divide us from the time when the first data will be collected by the LHC is to prepare the ground for their successful exploitation, thinking in advance at what will be the dominant sources of uncertainty to the most intriguing measurements, and what solutions can be cooked up to reduce them.

A specific example of this preparatory action is the study of the effect of trigger selections to the calibration datasets which will be needed by many precision measurements. Take the top quark mass as a benchmark: in 2008 the relative uncertainty on this fundamental parameter of the Standard Model –after the combination of CDF and DØ results– will be likely smaller than 1.5 GeV, and quite possibly smaller than 1 GeV (see Fig. 4). If LHC experiments mean to improve still further the knowledge of that number, they will need a very careful planning of the reduction of systematic uncertainties from the jet energy scale and from all other sources. As far as the jet energy scale is concerned, the Tevatron experience shows that large samples of dijet production events are needed for an accurate modeling of detector effects, and as many photon-jet events as possible for checks of the systematic uncertainty. These "calibration samples" are taxing for the total data acquisition bandwidth, but they are really necessary. Jet energy scale systematics are discussed with some detail in Sec. 3.1.

1.4. Plan of the writeup

The present writeup will attempt at offering some insight on several important challenges in the use of Tevatron results, data, and experience to prepare the ground for the LHC.

Section 2 will provide a short overview of the CDF and DØ detectors. In Section 3 I will discuss some of the most important methods currently used to perform precise measurements of

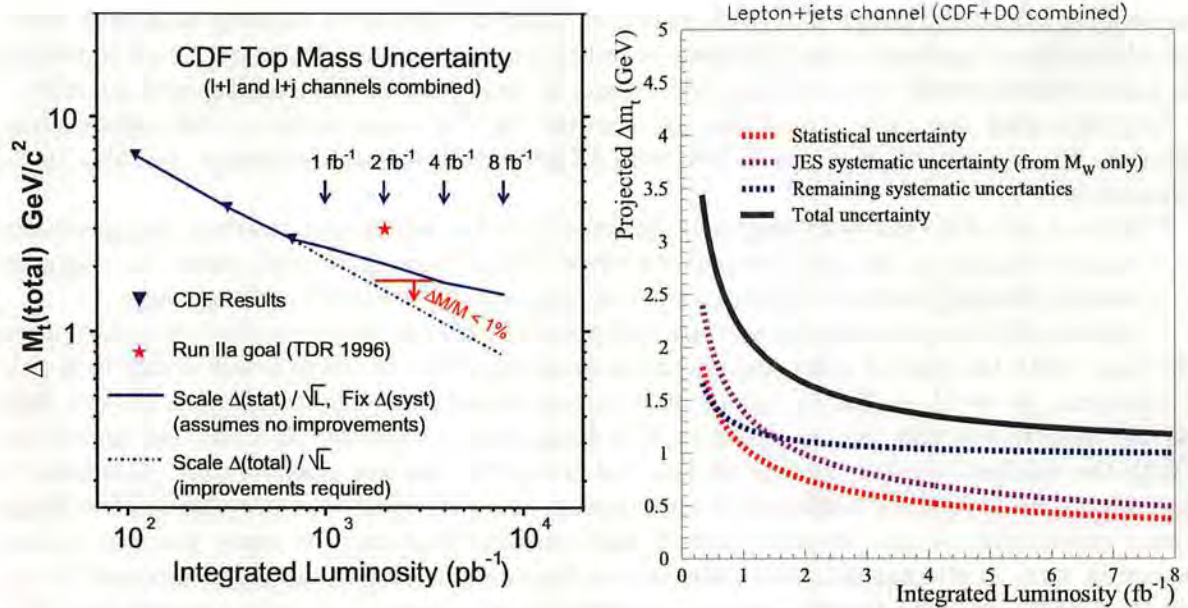


Figure 4. Left: expected top mass uncertainty from combined dilepton and single lepton CDF measurements, as a function of integrated luminosity in Run II. Right: expected top mass uncertainty from lepton plus jets events, CDF and DØ experimental results combined, as a function of integrated luminosity per experiment.

hadronic jets and efficient b -tagging, which are two critical ingredients to most of the high- P_T physics program of the Tevatron experiments.

In Section 4 the status of Higgs boson searches ongoing in CDF and DØ data will be discussed, along with some speculation on the possible scenarios that the LHC experiments will be dealing with. Section 5 will discuss a few selected issues in top quark physics, and the challenges posed by precision measurements of important quantities in the top sector.

Section 6 will deal with electroweak physics measurements that may not only help improve the picture of Standard Model physics before the LHC, but also provide some opportunities to reduce key systematic uncertainties on precision measurements by CMS and ATLAS.

A few concluding remarks are provided in Section 7.

2. Selected information on the Tevatron detectors

An overview of the CDF and DØ detectors for Run II at the Tevatron can be found in [3]. In what follows I will briefly mention some significant upgrades of benefit for the high- P_T physics program of the two experiments.

2.1. CDF

CDF (see Fig. 5) has been massively upgraded from Run I, to meet the more stringent requirements of Run II conditions, and to increase the discovery potential both in high- P_T and B -physics.

The smaller time interval between bunch crossings (which went from $3.5\mu\text{s}$ to 396ns , but was originally intended to reach 132ns) mandated the construction of a much faster drift chamber, the Central Outer Tracker (COT). The larger backgrounds and higher rates also dictated a

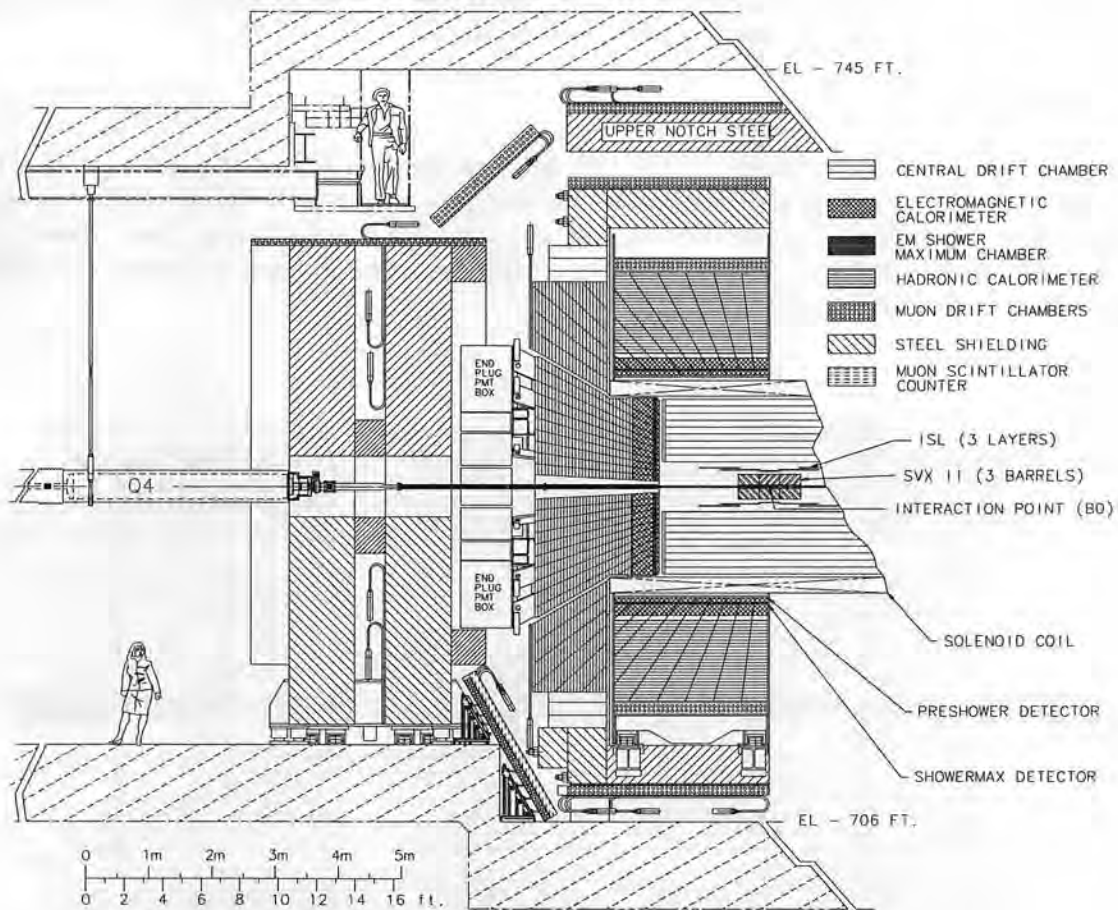


Figure 5. Cut-away view of the CDF detector.

replacement of forward calorimeters (which had gas as active medium in Run I) and a complete overhaul of data acquisition electronics.

A wider acceptance to electrons and muons, which is beneficial for the collection of top and Higgs decays, was achieved by the installation of new forward muon detectors and a more redundant and extended inner silicon tracking, now based on seven layers of strip sensors. CDF now measures W decays to rapidities in excess of $\eta = 2$ (see Sec. 6.1), with a significant acceptance increase for top quark decays and more power to constrain quark parton distribution functions from boson production asymmetries.

Of particular relevance for the present review is also the completely new device that was designed and built to achieve online silicon tracking at trigger level 2: the Silicon Vertex Tracker (SVT), capable of measuring track momentum, azimuth, and impact parameter with precision close to that attainable offline.

The SVT works by performing a linearized $R - \phi$ fit of track hits in four silicon layers together with a further “hit” at larger radius obtained from fast track reconstruction by the COT. Track candidates are identified by comparing hit patterns to a predetermined array of possible roads stored in associative memory banks. The 12-fold ϕ symmetry and six-fold z modularity allow for a natural parallelization of the task, and the parameters of central tracks are precisely obtained with 90% efficiency in about 10 microseconds. In particular, the impact parameter is determined with a $45\mu m$ resolution. The triggering capabilities of the SVT have enabled CDF to collect

huge samples of fully hadronic B hadron decays: the recent precise measurement of B_s mixing frequency achieved by CDF is almost entirely due to the SVT.

2.2. $D\emptyset$

The most substantial improvement of the $D\emptyset$ detector for Run II was the insertion of a two Tesla superconducting solenoidal magnet, which now provides it with charge and momentum measurement capabilities. Inside the magnet, $D\emptyset$ installed a scintillating fiber tracker (see Fig. 6), organized in eight concentric cylinders. Light from the fibers is transported to solid-state light detectors of very high gain.

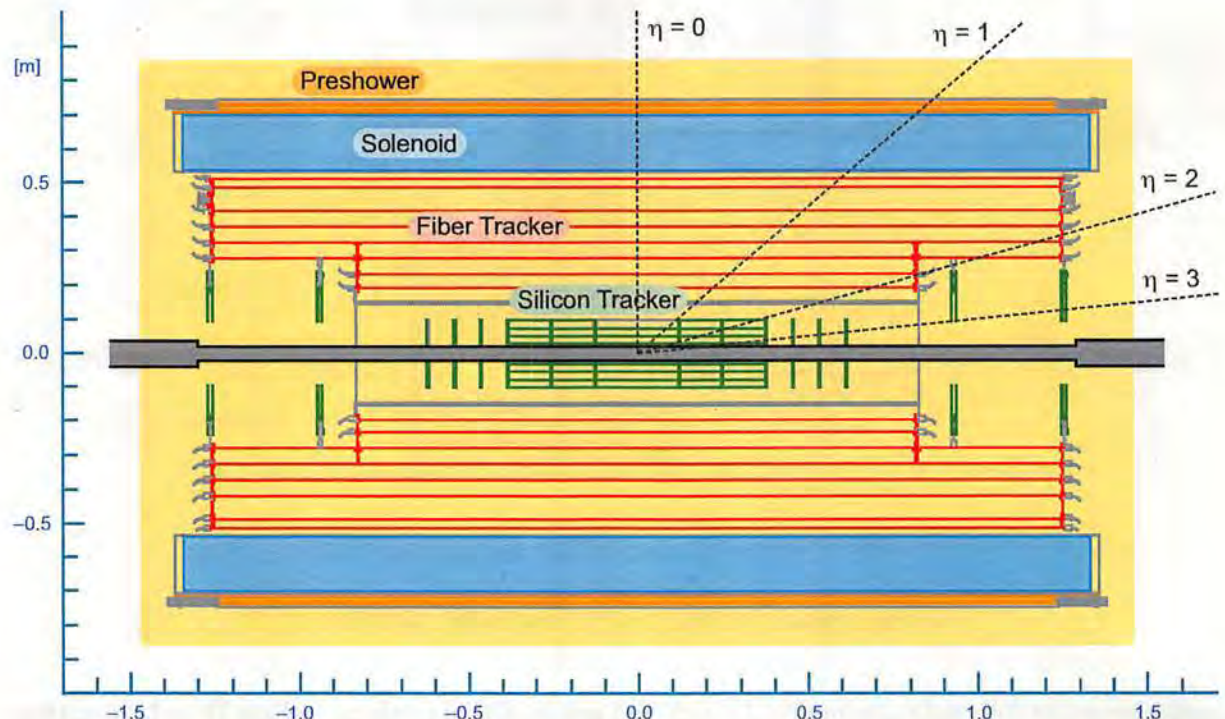


Figure 6. A view of the new tracking system of the $D\emptyset$ detector.

A redundant system of silicon microstrip detectors provides precise position measurement to enable a high-efficiency b -tagging of hadronic jets through the measurement of track impact parameter. Six barrels of silicon sensors organized in four concentrical layers provide coverage for central tracks, while a total of sixteen silicon disks allow reconstruction of large rapidity tracks.

The main addition to the calorimeter system of $D\emptyset$ was the installation of central and forward preshower detectors, whose purpose is to improve the trigger and offline purity of electrons and photons. The muon system was also upgraded to maintain an efficient operation in the higher fluxes of Run II. Mini-drift tubes composed of three planes, one in front and two in the back of the toroid magnets, were installed in the forward region.

3. Tools for precision high- P_T physics

3.1. Measuring hadronic jets

Hadronic jets are the most common and obvious phenomenon one can observe in high energy hadronic interactions; however, a precise definition of a jet that allows a unambiguous measurement of its properties is by no means trivial, and to some extent depends from the use one needs to make of the extracted measured quantities. If, for instance, one wishes to reconstruct the decay of a heavy object, one needs a jet identification algorithm which allows the best possible one-to-one matching with the quarks originated from the hard subprocess; other requirements in that case range from an optimization of the resulting signal to noise ratio, to an easy computation of systematic uncertainties affecting the energy measurement.

The choice resulting from the criteria mentioned above may be quite different from the ones which are most convenient for a differential cross section measurement of quantum chromodynamics, where the focus is primarily on the easiest, most accurate comparison to theory. Furthermore, a general requirement of jet identification algorithms is portability: the reproducible behavior of a procedure applied to data coming from different experiments is welcome when one wishes to combine results.

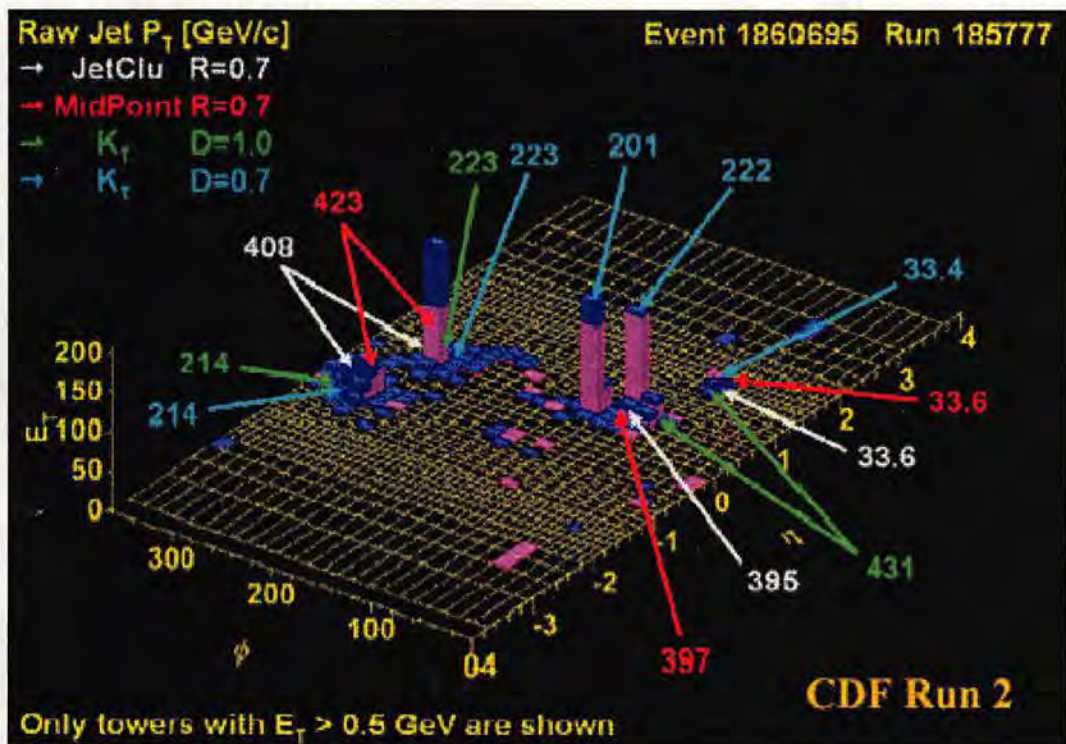


Figure 7. One event, three algorithms: the standard cone algorithm identifies four jets (white arrows) in this energetic multijet event collected by CDF. The same objects are reconstructed by the Midpoint algorithm, although measured energies differ. The K_T algorithm can correctly “split” the two narrow jets on the right, if ran with a suitable “cone” parameter.

The CDF and DØ experiments have implemented three different software algorithms for jet reconstruction: a standard iterative cone algorithm, a variant called *midpoint*, and a version of the K_T algorithm usable in hadronic environments. Fig. 7 shows the lego plot of calorimeter energy measured by CDF in a high- P_T multijet event, and the interpretation of energy deposits

as hadronic jets obtained by the use of these three different algorithms.

The cone algorithm is based on what is conventionally called the “Snowmass Accord” [4]. In CDF the list of all calorimeter cells above a fixed threshold in transverse energy, $E_T > 0.1$ GeV, is ordered by E_T , and a circle of predetermined radius is drawn in the $\eta - \phi$ space around the most energetic cell. The radius $R = 0.4$ is used for the reconstruction of the decay of heavy objects such as the top quark, $R = 0.7$ is a good compromise between a correct identification of the event topology and the measurement of soft gluon radiation off the final state partons, and $R = 1.0$ is only useful for dijet or photon-jet final states.

All cells within the circle are removed from the list, and a E_T baricenter is computed for the circle from the included cells. The highest- E_T cell remaining in the list constitutes the center of the next circle, and the clustering is repeated until no cells are left which have E_T above a “seed” threshold (typically equal to 1 GeV). The resulting circles are then redrawn around their own baricenter, sometimes including new cells or losing some; the procedure is repeated until the configuration is stable. A prescription for splitting or merging clusters takes care of cases when two circles partially overlap, and is based on the fraction of energy shared. From the final list of clusters the energy and direction of each jet is obtained.

A specialization of the cone algorithm described above is called *Midpoint*, and is the default choice in DØ. The midpoint algorithm adds seeds for the clustering at the middle point between the original clusters, thus avoiding the shortcomings of the splitting and merging prescription of the iterative cone procedure which make comparisons to theory difficult.

A different concept is the basis of the K_T algorithm, which uses energy along with spatial separation to define the distance between energy depositions, and allows more precise comparisons with analytical calculations, being unaffected by infrared and collinear singularities of soft parton emission. For that reason, the K_T algorithm is mainly of benefit to QCD cross section measurements.

When faced with the measurement of the kinematics of hard parton emissions based on a reconstruction algorithm such as the ones described above, one has to deal with two distinct issues: the precise determination of a energy scale, and the achievement of the best possible energy resolution.

Knowledge of the jet energy scale k of hadronic jets allows to calibrate the detector response such that a sample of partons of a given energy E_{true} will be reconstructed with that same energy, *on average*. A shift of the average \bar{E} from E_{true} signals a deviation of the scale from unity – and the need for a general correction $E' = kE$, with $k = E_{true}/\bar{E}$. It follows that the smaller the error on the value of k , the more precise will be any measurement of physical quantities derived from jet energies. In Sec. 5.3 a quantitative example of this correspondence will be given for the case of the top quark mass measurement by CDF.

A precise knowledge of k is not enough, however. While k determines the *collective* behavior of the energy measurement of jets we perform in our detector, the resolution σ – which can be defined as the width of a gaussian distribution of measured energy E from jets of the same true energy E_{true} – determines the typical deviation of the measured energy of *any given jet* from its expected value \bar{E} . A small value of jet resolution is a big asset for a high-energy experiment, since it improves any measurement affected by backgrounds, which become easier to handle. Typically, the signal of a jet-decaying resonance will increase its significance linearly with a decrease of σ : for Higgs boson searches at low mass, when the decay $H \rightarrow b\bar{b}$ is sought, the dijet mass resolution is one of the critical parameters. In Sec. 3.3 the matter is discussed in detail.

3.2. Jet calibration and determination of the energy scale

From an experimental standpoint, it is important to realize that the result of a jet measurement is affected by a multitude of effects of different origin. These effects need to be addressed separately,

to allow uniform definitions across different experiments and comparisons with theory.

The prime example of a detector-specific effect needing compensation is the non-uniformity of the detector response. Real detectors are always non-uniform in their mechanical construction, in the amount and location of dead channels, in the material budget as seen from the interaction region. Although a simulation of the apparatus may help us to understand the dominant non-uniformities, a detailed accounting of all effects requires the study of real data. With dijet events it is possible to use one jet to probe the detector response as a function of its relevant variables (such as rapidity and P_T), when the other jet (the one responsible for triggering the event) is constrained to be measured in a well-controlled region.

By computing the response function f , defined as

$$\langle f(\eta, P_T) \rangle = \frac{2}{N} \sum \frac{P_T^{\text{trigger}} - P_T^{\text{probe}}}{P_T^{\text{trigger}} + P_T^{\text{probe}}}$$

for a large set of jet pairs and with the probe jet spanning several bins in P_T and rapidity, one obtains a map of the detector output, which can be subsequently used to equalize the response. The P_T binning is necessary, since as their P_T grows jets become narrower, and they probe smaller scales of non-uniformity of the detector. A method roughly equivalent to the one discussed above involves the use of the fraction of missing transverse energy projected along a jet direction. Again, what one measures is a systematical bias of the response of different parts of the detector as a function of jet P_T and rapidity.

The CDF collaboration extracts their relative correction function using the dijet balancing technique, while DØ uses the missing E_T projection method. The relative response is shown for both detectors in Fig. 8.

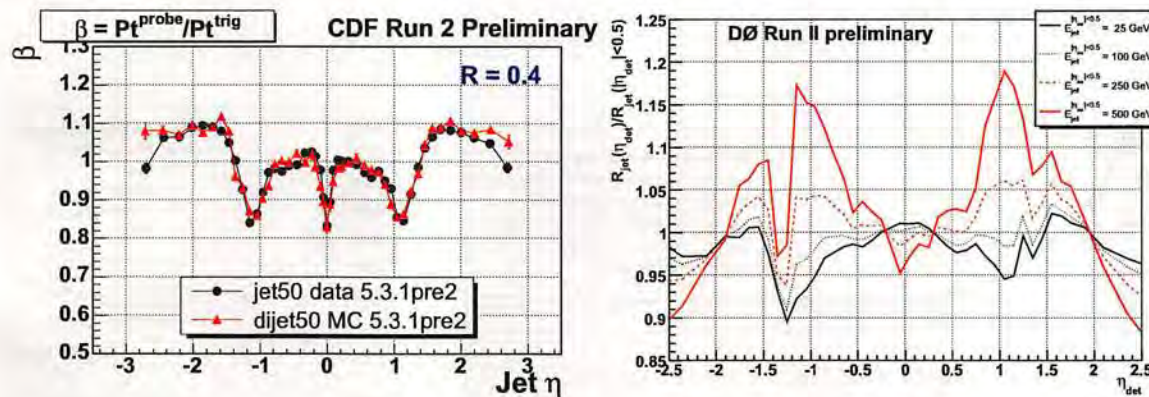


Figure 8. Left: a rapidity-dependent jet P_T correction factor extracted by CDF from dijet balancing studies. Right: a similar function obtained by DØ with the missing E_T projection method.

Another method must be devised to account for energy collected in the clustering cone from pile-up interactions occurring during the same bunch crossing. Pile-up energy is on average a linear function of instantaneous luminosity, but only through the number of pile-up interactions. It is therefore much better to correct jets on an event-by-event basis, by determining the average energy deposited in a random cone in the calorimeter (away from real jets) as a function of the number of primary interactions reconstructed through vertexed charged tracks.

A similar kind of random contribution to jet energy comes from a different origin: the same hard interaction that produces the jet activity may radiate additional energy through the so-called *underlying event*, which has to be understood as the combinative effect of proton remnants

• η -dep
(PC)
!!
correct by data

pile-up
!!
function of
primary vertex

UE (*parton recombination*
additional (semi)hard interaction)

recombination and additional hard or semi-hard interactions by the spectator partons. An average correction for this effect can be obtained by computing the energy deposit in cones in a region azimuthally orthogonal from the leading jets in generic QCD events.

Another small correction may be applied to account for energy flowing out of the clustering circle: this is called *out-of-cone correction* and is of course dependent on the choice made for the clustering radius R .

The most important effect for a calorimeter energy measurement is however the difference in response to particles creating electromagnetic showers in the first few radiation length of calorimeter material – essentially photons from π^0 decay, and electrons if there are any – and charged hadrons (mostly protons and light charged hadrons), which are measured predominantly in the hadron calorimeter. The energy of electron-like showers is determined with high precision in the electromagnetic section of the calorimeter, while hadronic showers generate nuclear interactions that cause substantial energy loss through a multitude of effects.

To determine the correction factor to apply to the measured energy and obtain the most probable value of the originating stream of *stable* particles (stable in the sense that their lifetime is long enough to allow detection before decay), a Monte Carlo simulation is used in CDF. The simulation is tuned with the known single-particle response functions determined from dedicated runs and test beam studies. With large samples of simulated jets a mapping function that relates the observed energy to the energy of the particle jet is extracted.

Once all correction factors and offsets are applied, the jet energy scale can be checked with events in experimental data where one jet recoils against an energetic photon (or leading neutral particle). The electromagnetic shower is well measured in the inner sections of the calorimeter, and the recoiling jet energy scale can be tested with good accuracy.

An uncertainty in the jet energy scale can then be determined by comparing the offset between data and Monte Carlo, if the Monte Carlo jets have been subjected to the same treatment as jets in experimental data.

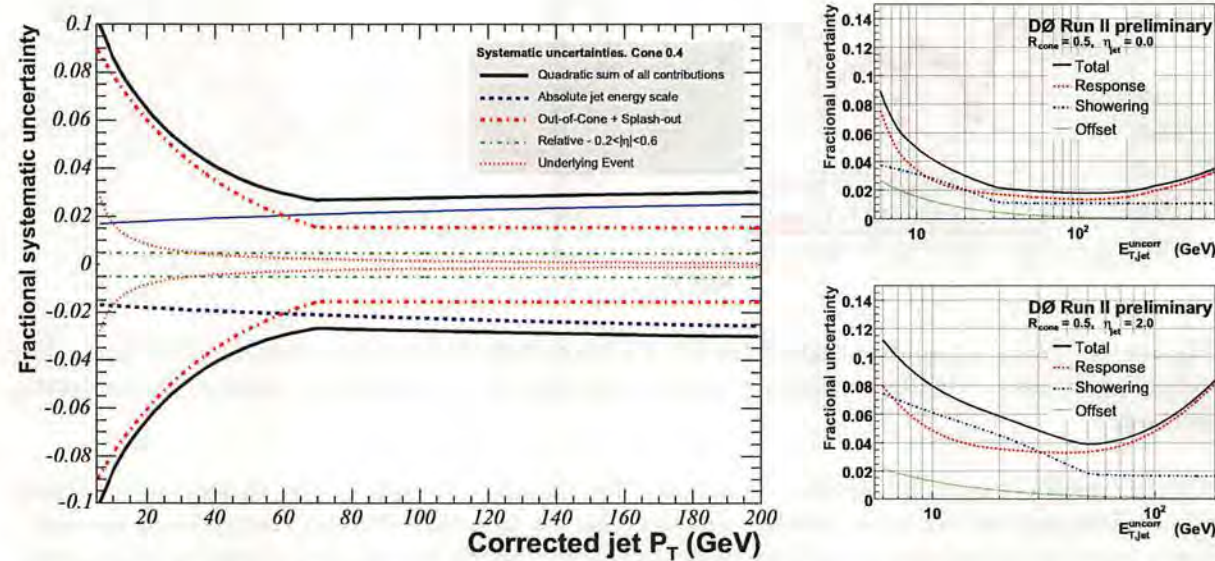


Figure 9. Left: total systematics on jet energy measurement as a function on jet P_T at CDF ($R = 0.4$, all jet rapidities). Right: total systematic uncertainty in DØ ($R = 0.5$, two different bins of jet rapidity).

The level of uncertainty in the determination of the jet energy scale at the Tevatron experiments

is below 3% for jet $P_T > 50$ GeV (Fig. 9), and is expected to decrease further as more data –particularly photon-jet events– are collected. The large samples of single lepton decay of $t\bar{t}$ pairs collected by the experiments have also allowed to cross-check the energy scale by using the $W \rightarrow jj$ resonance in top decay.

For a complete review of the determination of jet energy scale in CDF see [5]. The jet energy scale correction in DØ is described in [6].

3.3. Improvement of jet energy resolution

The resolution of jet energy measurement plays an increasingly important role as larger datasets of high P_T processes are collected at the Tevatron. It is of course a critical parameter in those searches for small cross section signals of hadronic resonances, such as a light Higgs boson; but it also affects significantly the accuracy of several precision measurements, and specifically wherever the kinematics of final state quarks requires to be pictured with accuracy. In particular, the precision of all jet-based top quark mass measurements also depends significantly on the accuracy with which final state partons are measured.

CDF and DØ have taken seriously the challenge to improve the jet energy resolution. The Higgs Sensitivity Working Group (HSWG), a joint CDF-DØ venture, spurred studies aimed at demonstrating that a 10% relative resolution on the dijet invariant mass for pairs of b -jets was achievable in both detectors [7]. The issue, however, does not involve only b -jets, which are less well measured but quite special in their characteristics –and therefore easier to improve.

A working group in CDF identified three main candidates for the improvement of the resolution on generic jets: the **H1 algorithm**, which uses the momentum of charged tracks instead of hadronic energy depositions in the calorimeter when possible; **JetCor2k**, an algorithm which attempts to perform a complete classification of energy deposits in calorimeter towers into photon-like, track-like, mixed, and unassigned, thereby correcting differently each of them; and the **Hyperball algorithm**, which attempts to use all jet observables –even ones which should have little information on the jet energy measurement error– to exploit the intercorrelation among these variables to determine the average P_T error of jets. A fourth candidate –and maybe the most obvious– has been under development by both DØ (for the HSWG) and later by CDF: a **Neural Network** classifier. Neural Networks are usually thought of as signal discrimination tools, but they are very flexible. In the case of jet energy correction, the network is trained to recognize jet energy given the input variables: it thus acts as a multi-dimensional non-parametric fit.

Here I will just describe with some detail the Hyperball algorithm, which I developed for the improvement of the Higgs mass resolution.

The Hyperball algorithm is nothing more than a fancy prescription for computing averages. Let us define a scalar function Δ as the average difference between the transverse momentum P_T^q of a final state quark and the measured P_T^{jet} of the resulting calorimeter cluster. $\Delta(\vec{x}) = P_t^q - P_T^{jet}(\vec{x})$ can be thought to be a continuous function of all measurable jet quantities \vec{x} our detector is capable of providing: for instance, $\Delta(\vec{x})$ is usually positive for jets showing a ratio between total track momentum and P_T^{jet} larger than unity, for in that case the calorimeter measurement is likely to be underestimated. Another example is the predictive power of a larger-than-average ratio between jet mass M^{jet} and P_T^{jet} , which can indicate either that the core of the jet has been undermeasured –for instance, due to the jet falling into a crack of the calorimeter– or that the energy far from the jet core has received extra energy, maybe from other jets or pile-up. Normally, one would be unable to decide which of the two causes is yielding a large M^{jet}/P_T^{jet} ratio, and a correction would be impossible; but in a multi-dimensional space, where the charged fraction is also considered, the two cases get easily separated.

It is obvious that a unlimited amount of simulated jets would allow $\Delta(\vec{x})$ to be known with

arbitrary accuracy: averaging $\Delta(\vec{x})$ for all jets with identical measured characteristics to the one under scrutiny enables one to compute an optimal corrected value $P'_T = P_T^{jet} + \Delta$. The Hyperball algorithm takes care of using to the fullest the limited statistics available of simulated jets. A generalized distance $R(\vec{x})$ in the multi-dimensional space spanned by all jet observables (\vec{x}) is defined such that those coordinates along which $\Delta(\vec{x})$ has the largest gradient weigh the most: for jets 1 and 2,

$$R(\vec{x}(1) - \vec{x}(2)) = \sqrt{\sum_i (\frac{\partial \Delta}{\partial x_i})^2 \times (x_i(1) - x_i(2))^2}.$$

With the above definition, one can then inflate a *hyperball* – a region of constant R – around the coordinates $\vec{x}(0)$ of the jet to be corrected, enclosing within it a suitable number N of simulated jets whose characteristics will be most similar to it, from the point of view of the value of Δ . Δ can then be computed as the average of the jet measurement error inside the hyperball, weighted with the inverse of R^2 .

Improvements of as much as 30% have been predicted on the resolution of b -quark jets in the range of interest for the search of top quarks and light Higgs bosons. The algorithm is currently under testing with the recently observed signal of $Z \rightarrow b\bar{b}$ decays in CDF data (see Sec. 4.1).

3.4. b -jet issues

Jets originated from b -quark fragmentation possess unique characteristics that constitute both a challenge and an opportunity for high- P_T physics at hadron colliders, regardless of the center-of-mass energy. Weak couplings make b -jet production rate in electroweak production processes larger, for any given Q^2 , than in QCD processes, so that their identification usually eases signal extraction.

An effective identification of b -jets from generic jets is actually made possible by the small value of the Cabibbo-Kobayashi-Maskawa (CKM) mixing matrix element V_{cb} and consequent long lifetime of B hadrons, which allows a reconstruction of the secondary decay vertex; and also by the large b -quark mass, which yields a significant fraction of semileptonic decays.

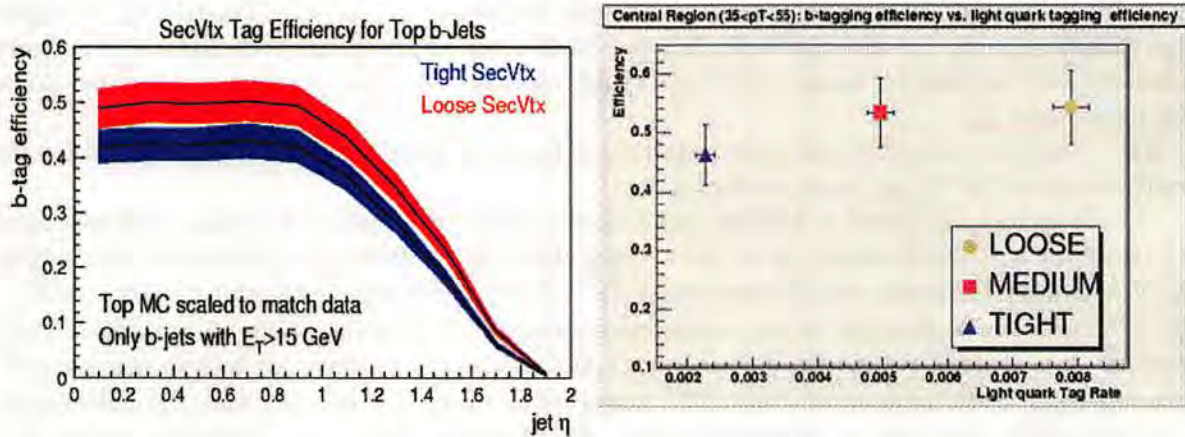


Figure 10. Left: efficiency of the loose and tight secondary vertex tagging algorithm by CDF as a function of jet rapidity. Right: the b -tagging efficiency of three versions of the vertex tagging algorithm developed by DØ are shown as a function of fake rate.

CDF and DØ have put a lot of effort into maximizing their b -tagging capabilities, developing several tagging strategies based on the main characteristics of b -quark decay. Performance of the

$$\begin{aligned} b \text{ tag: } & E_{\text{F}\ell} \quad 0.46 \sim 0.52 \\ & \text{false} \quad 0.002 \sim 0.008 \end{aligned}$$

secondary vertex tagging algorithms are similar in the two experiments, which developed both a *tight* and a *loose* version of the identification procedure; the *loose* version is typically used to retain high efficiency for double b -tag when reconstructing signals nominally yielding two b -jets, such as decay of $t\bar{t}$ pairs or light Higgs bosons. The efficiency to correctly identify a b -quark ranges from 40 to 50% for central jets, with fake rates of less than a percent (see Fig. 10); as jet rapidity increases, a deterioration of the efficiency is observed in both detectors, although the silicon disks of the DØ detector appear effective in keeping a reasonable efficiency out to $|\eta| < 2.0$.

As an alternative to fitting the tracks to a common secondary vertex, one can determine the global probability that those tracks all originate from the primary interaction vertex, by comparing track impact parameter d_0 with expected resolution functions; if properly computed, the probability P is flat for a sample of tracks originated from non-heavy flavor jets. P is a continuous variable which allows a dialing of the desired b -quark efficiency, by setting $P < P_{\max}$ (typically $P_{\max} = 0.01$), and the resulting fake rate (the fraction of tagged light flavor jets) which, to first order, is just $f = P_{\max}$. This algorithm, called **Jet Probability**, is interesting also for its ability to enrich the sample with charm-originated jets, if the probability cut is set at a larger value ($P_{\max} = 0.05$ is generally found as a good operating point for that purpose). A useful application of Jet Probability is discussed in Sec. 5.3.

Identification of soft leptons in b -jets provides an independent tool for b -tagging. However, the combined effect of leptonic branching ratio and sub-optimal identification efficiency of leptons inside hadronic jets make this tool a less powerful one than those based on track impact parameter.

Finally, a recent development has been the application of **Neural Networks** (one can hardly live without them these days!) to the discrimination of b -quark jets, based on the combined analysis of several variables sensitive to the flavor content of the jet. Once optimized, Neural Networks become the most effective tool for high-efficiency b -tagging.

b -jets also pose a challenge for their energy measurement, since some of their peculiarities are liable to affect the calorimeter determination of P_T . It was already noted above that this is a quite important issue for precise determinations of the top quark mass, which –to first order– is linearly correlated to the energy of the emitted b -jet in the rest frame of top decay. Moreover, the resolution of the b -jet energy has already been described above as a critical parameter in determining the Tevatron discovery reach for a light Higgs boson.

A distinguishing feature of jets originated from b -quarks is that they show a harder fragmentation than light-quark and gluon jets: this represents a source of bias in the energy measured in calorimeters whose e/π response (the ratio of response to electrons and charged pions of equal incident energy) is non-linear with momentum, as is often the case. A second issue is the copious amount of semileptonic decay of B hadrons, which causes a negative average offset in the response through energetic neutrinos escaping the detector unmeasured and muons behaving as minimum-ionizing particles: this causes a scale offset and a degradation in resolution. Third, b -jets produced by electroweak processes may be color-disconnected from the initial state (not so in top quark decay, but rather in Z or H decay), with a resulting difference in soft gluon radiation and in the resulting structure of out-of-cone energy, again affecting the energy scale, as well as the resolution if one applies a scale correction for the out-of-cone energy tuned on light quark or gluon jets.

The main difficulty in handling the peculiarities discussed above is the lack of suitable datasets where to measure biases, test corrections, and derive improvements. As we discussed above, the jet response in the calorimeter is equalized using large samples of dijet events, and tested with sizable amounts of gamma-jet events. Neither of these techniques are viable for b -jets, although CDF data collected with SVT triggers will eventually enable some statistics-limited checks.

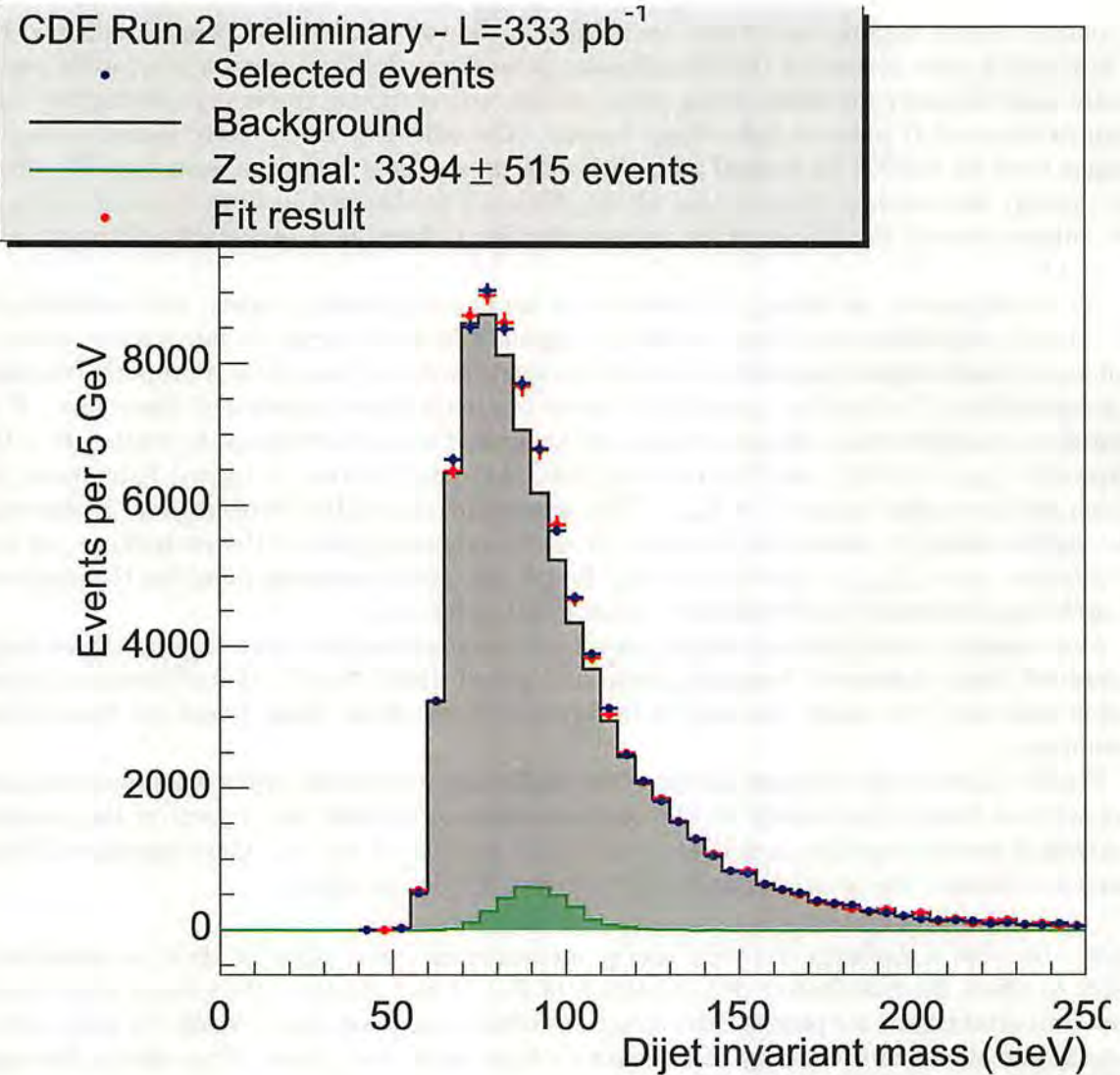


Figure 11. The signal of $Z \rightarrow b\bar{b}$ decays extracted from 333 pb^{-1} of CDF Run II data is visible as an excess of events in the dijet mass region around 90 GeV. The green histogram shows the fitted Z contribution.

The picture is not bleak, however, because the mentioned effects can be studied quite accurately with Monte Carlo simulations. The uncertainty in the b -quark fragmentation function is by now small enough that simulations should be able to determine the resulting bias in jet energy scale with satisfactory precision; the semileptonic decay is also well known; the details of color flow and soft gluon radiation are by now modeled well enough that a residual effect of their uncertainty on the jet energy scale should be minimal. All in all, these issues appear under control.

Furthermore, a large-statistics $Z \rightarrow b\bar{b}$ peak observed in CDF data collected by a dedicated SVT trigger can provide an independent sanity check and a reduction of systematic uncertainties on the b -jet energy scale. The signal has been extracted from 333 pb^{-1} of Run II data (see Fig. 11), and the goal is now to measure the scale with 1% accuracy using at least 1 fb^{-1} of data. Besides providing a precise measurement of the b -jet energy scale, the signal will also allow tests of algorithms devised to improve the b -jet energy resolution.

Another idea, recently investigated by DØ, is to determine the b -quark jet energy scale from photon-jet events where the heavy flavor content of the jet is enriched by b -tagging. Despite the small cross section of γb production, these events might allow to extract a meaningful measurement of the b -jet E_T scale by fitting the so-called missing- E_T projection fraction, defined by

$$MPF = 1 + \frac{\vec{E}_T^{miss} \cdot \vec{n}_T^\gamma}{E_T^\gamma},$$

where \vec{E}_T^{miss} is the missing transverse energy in the event, \vec{n}_T^γ is the versor of the photon in the transverse plane, and E_T^γ is the transverse energy of the photon. The method works well if the fraction f_b of fake vertex tags in the data is determined with precision. The extraction of f_b is performed by combined fits to the combined invariant mass of tracks coming from the secondary vertex and the transverse flight distance between primary and secondary vertex.

4. Searches for the Standard Model Higgs boson

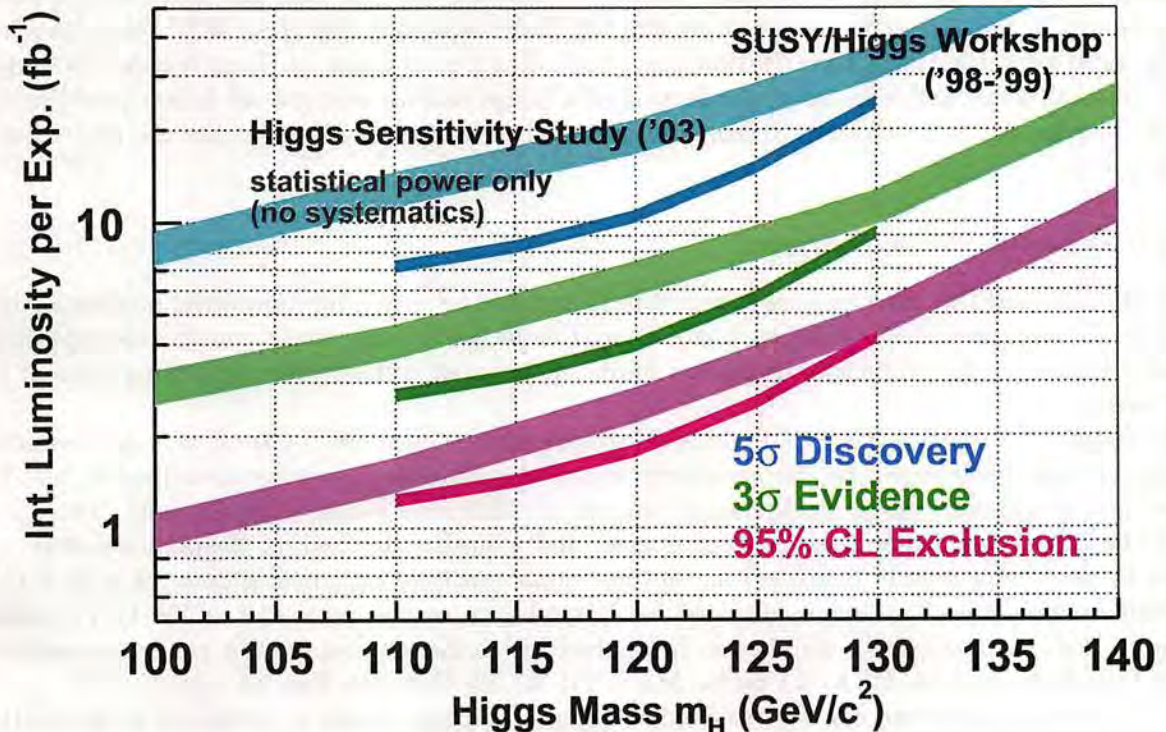


Figure 12. The three pairs of bands show the integrated luminosity per experiment needed for a 95% exclusion (purple), a 3 σ evidence (green), or a 5 σ discovery (blue) of the Higgs boson as a function of the particle mass, obtained by the 1998 and 2003 studies. The 2003 study shows slightly reduced luminosity thresholds for any given mass, but does not include systematic uncertainties.

The excellent agreement between experimental measurements of electroweak observables and Standard Model (SM) predictions constitute a strong motivation to search for the Higgs boson at the Tevatron [8]. The latest fits [9] –which indicate $M_H = 89_{-30}^{+42}$ GeV as the most likely value

for the Higgs mass— together with the direct lower limit $M_H > 114$ GeV obtained by the LEP II experiments [10], allow CDF and DØ to hope for a significant measurement before the next big players at the LHC start collecting data.

In 2003, prompted by the US Department of Energy, a joint committee of CDF and DØ members carried out a reassessment of the Tevatron reach in the search for the Higgs boson [7]. By using a more realistic model of the two detectors than the simplified one used in a study performed in 1998 [11], and using real data collected by the experiments in the first years of Run II, the committee determined that the earlier claims of sensitivity were not off the mark: by searching in all significant decay channels, and combining CDF and DØ measurements together, the extrapolations obtained in 1998 were nicely confirmed (see Fig. 12). In the meantime, the Tevatron has continued to improve its performance, recently surpassing the peak luminosity of $1.8 \times 10^{32} \text{ cm}^{-2} \text{ s}^{-1}$. The chances of the Tevatron delivering an integrated statistics of 8 fb^{-1} to each experiment by the end of 2009 appear now sizeable. Before the CMS and ATLAS collaborations start analyzing their first collisions, CDF and DØ might just be able to either discover a 115 GeV Higgs boson, or exclude it up to a mass of 135 GeV.

The search for the Higgs boson at the Tevatron is carried out by looking for two main decay channels, depending on the particle mass. For masses below 135 GeV, the dominant decay is $H \rightarrow b\bar{b}$, and the final state always includes the leptonic decay of an accompanying W or Z boson to allow triggering on the signal; the latest results from CDF and DØ in these final states are given in Sec. 4.1. For masses above the 135 GeV threshold, the $H \rightarrow WW$ decay provides the most promising signature. In that case, both direct production of Higgs bosons (yielding a WW final state) and associated production of a Higgs and an electroweak boson (yielding the spectacular signature of three vector bosons together) are considered; results are discussed in Sec. 4.2.

4.1. Light Higgs Boson Searches

Both CDF and DØ have analyzed their Run II datasets in search for associated production of a W or Z boson and a pair of b -quark jets from $H \rightarrow b\bar{b}$ decay, using the reconstructed dijet mass distribution as the prime tool to extract limits to the cross section times branching ratio of the process.

In 695 pb^{-1} of collider data CDF finds 29 events with a clean $W \rightarrow l\nu$ ($l = e, \mu$) candidate and two jets both tagged by the secondary vertex identification algorithm described in Sec. 3.4; estimated standard model backgrounds amount to 32.2 ± 6.2 events (Fig. 13, left). From a fit of the dijet mass distribution of these events, and a similar fit to an orthogonal set of $W + 2$ jet events which contain a single b -tag but are signal-enriched by a neural network, a 95% C.L. limit ranging from 4 to 2 pb is obtained for Higgs boson masses from 110 to 150 GeV. Similar limits are obtained by DØ who has so far analyzed a smaller dataset for this particular analysis. DØ limits range from 2.8 to 3.1 pb for $M_H = 115$ to 145 GeV (see Fig. 13, right).

A peculiar signature can be observed when a light Higgs boson is produced in association with a Z boson, and the latter decays to a pair of neutrinos. One may then observe a pair of b -jets with significant missing transverse energy. CDF has searched for this signature using data triggered by the requirement of SVT tracks with significant impact parameter and missing E_T . In 289 pb^{-1} of data they find 19 candidates, when 19.7 ± 3.5 are expected from background processes (Fig. 14).

The DØ collaboration also looks for the same signature in 261 pb^{-1} of data. They make separate searches for the Higgs boson in double b -tagged and single b -tagged data, by applying a search window in the dijet mass distribution, centered at the nominal value of M_H and with a width equal to three times the experimental dijet mass resolution. They always find good compatibility for the background-only hypothesis: for instance, for a $M_H = 115$ GeV search

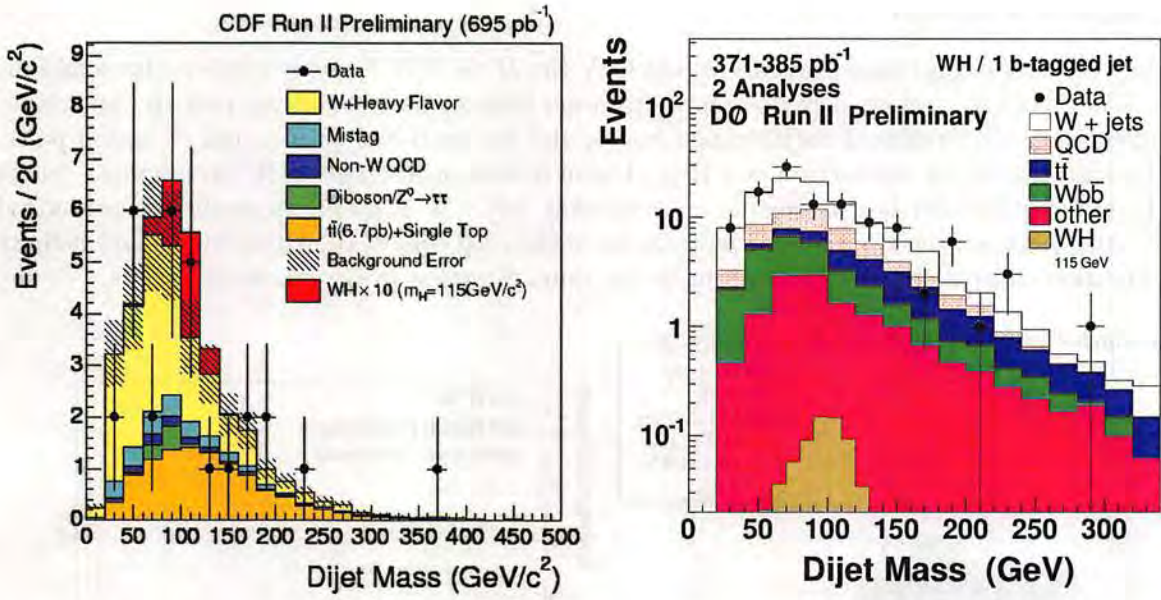


Figure 13. The dijet mass distribution of 29 $W + 2$ jet candidates (black points) is understood as a sum of several contributing SM backgrounds (left); a $H \rightarrow b\bar{b}$ signal 10 times larger than that expected by theoretical calculations is overlaid. Right: the dijet mass of doubly b -tagged $W + 2$ jet candidates found by $D\bar{\theta}$ is compared to the sum of expected backgrounds and to the expected signal contribution.

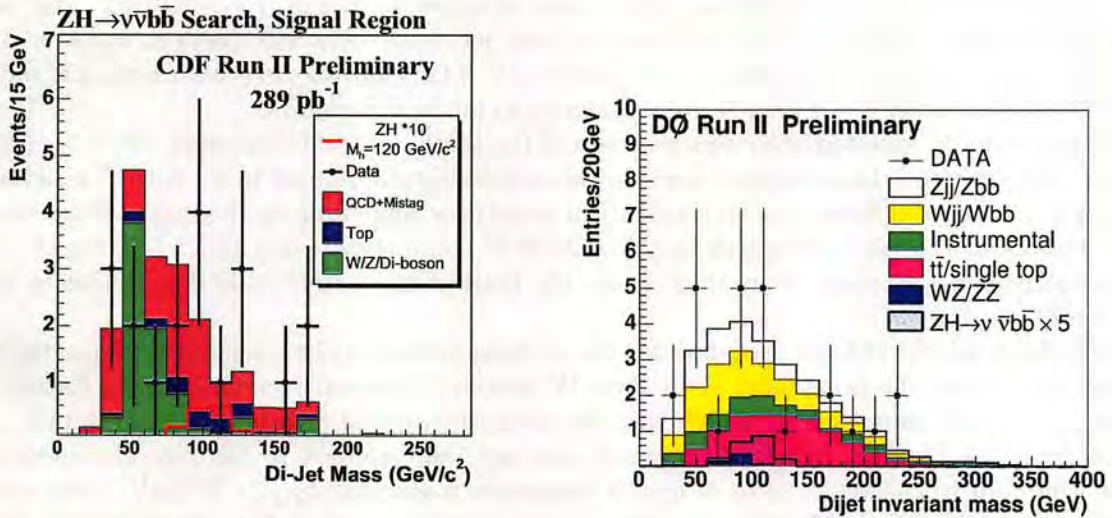


Figure 14. The dijet mass distribution of double b -tagged $ZH \rightarrow \nu\nu b\bar{b}$ candidates from CDF (left) and $D\bar{\theta}$ (right).

they find 11 candidates in the double b -tagged data, with 9.4 ± 1.8 expected from background sources; and 33 single b -tag candidates with 34 ± 6.1 expected from background sources. The event counts are finally used to set limits from this channel at 3.5 to 2.4 pb for M_H ranging from 105 to 135 GeV.

4.2. High Mass Searches

For any value of Higgs boson mass above 135 GeV the $H \rightarrow WW^{(*)}$ decay mode is the dominant one. When both W bosons decay to an electron-neutrino or muon-neutrino pair the final state is quite clean, with residual backgrounds mostly due to Drell-Yan production of lepton pairs. To discriminate direct production of a Higgs boson from non-resonant WW production - which in the standard model has a sizeable cross section [16] – it is useful to study the azimuthal angle $\Delta\Phi_{ll}$ between the two charged leptons, since the zero spin of the Higgs boson and helicity conservation conspire to produce leptons in the same direction in the transverse plane.

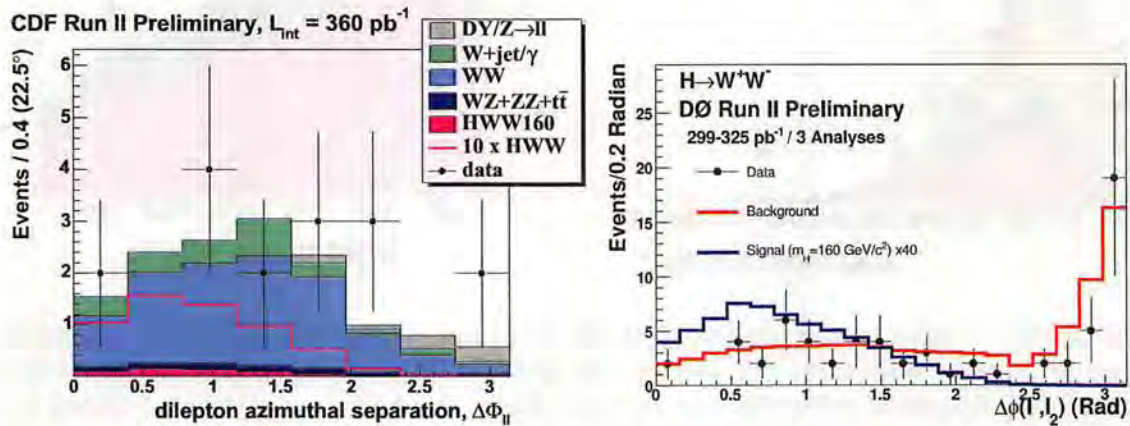


Figure 15. Azimuthal angle between the two charged lepton candidates in the CDF (left) and $D\bar{\phi}$ (right) $H \rightarrow WW$ analyses.

CDF selects WW pairs by identifying lepton pairs of opposite charge, $P_T > 20$ GeV, and then applying a missing E_T cut at 25 GeV and a tight jet veto. A small dilepton mass is then required: $M_{ll} < 55$ (80) GeV for $M_H = 140$ (180) GeV. The resulting $\Delta\Phi_{ll}$ distribution is shown in Fig. 15 for the 360pb^{-1} of Run II data analyzed so far in this channel.

$D\bar{\phi}$ has recently updated their own searches of the same final state by using 950pb^{-1} of Run II data. They require the azimuthal angle between the charged leptons to be $\Delta\Phi_{ll} < 2$ radians, and apply several additional cuts on kinematical quantities depending on the target Higgs boson mass. For the $M_H = 160$ GeV search they find 28 WW candidates, when 34.7 ± 1.7 are expected from non-Higgs SM sources. They thus obtain the limit of $\sigma_H \times B(H \rightarrow WW) < 2.2\text{pb}$ at 95% C.L. for $M_H = 160$ GeV.

CDF also searched 193.5pb^{-1} of data for the striking signature of associated WH production at high M_H , when the event may yield *three* W bosons. The search starts from a dataset of lepton pairs of the same charge, which is understood as a sum of fake lepton backgrounds and SM sources (see Fig. 15, right). Optimized cuts are then applied to the leptons transverse momentum and to the vector sum of lepton transverse momenta, $P_{T_{12}} > 35$ GeV. Zero events are observed, with 1.0 ± 0.6 expected from known sources. A 95% C.L. cross section times branching ratio limit of 8pb can thus be set for $M_H = 160$ GeV (see Fig. 16).

Figures 16 and 17 summarize the present status of Higgs boson searches at the Tevatron. It is necessary to note that most searches are still based on relatively small amounts of data; furthermore, CDF has not performed a combination of their results yet. The standard model prediction for Higgs production appears still far away: nevertheless, results are still roughly in line with those predicted by the 2003 Higgs sensitivity study, if one accounts for the statistics used by the analyses; moreover, several improvements in b -tagging efficiency and background rejection, as well as in the dijet mass resolution for pairs of b -jets, are under testing but still not used.

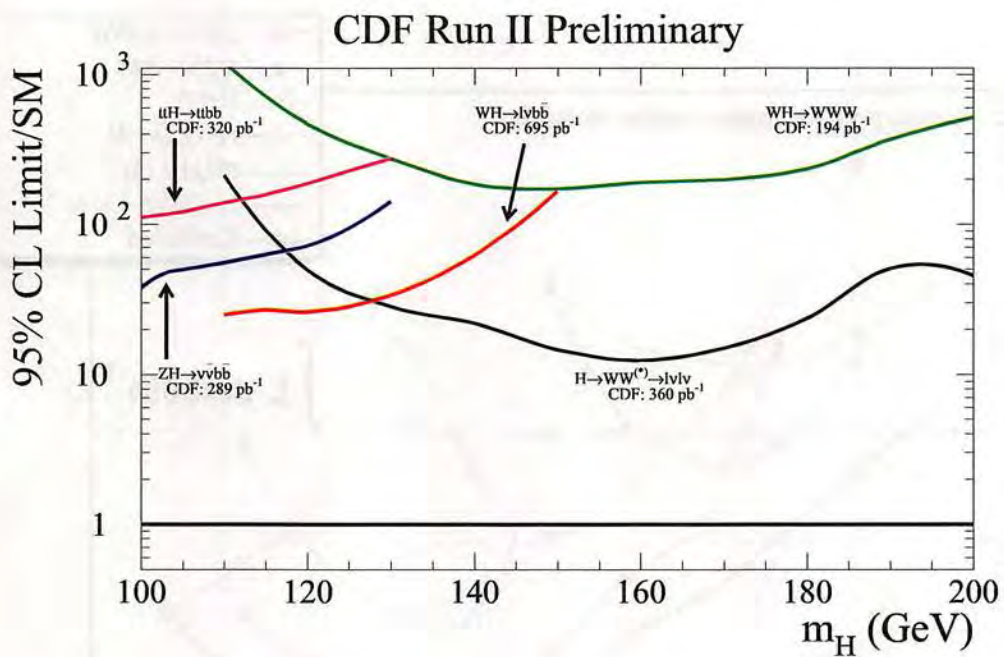


Figure 16. Summary of 95% C.L. limits for Higgs boson production obtained by CDF in several search channels.

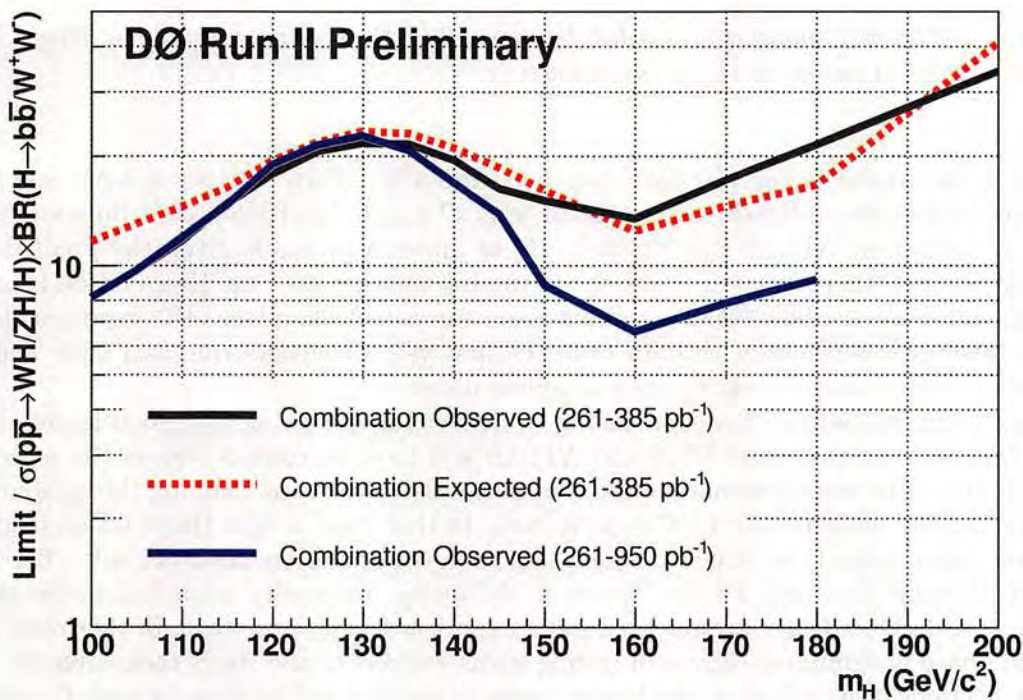


Figure 17. Summary of 95% C.L. limits obtained by DØ from Run II searches of the Higgs boson. The y axis shows the ratio between determined limit and standard model cross section.

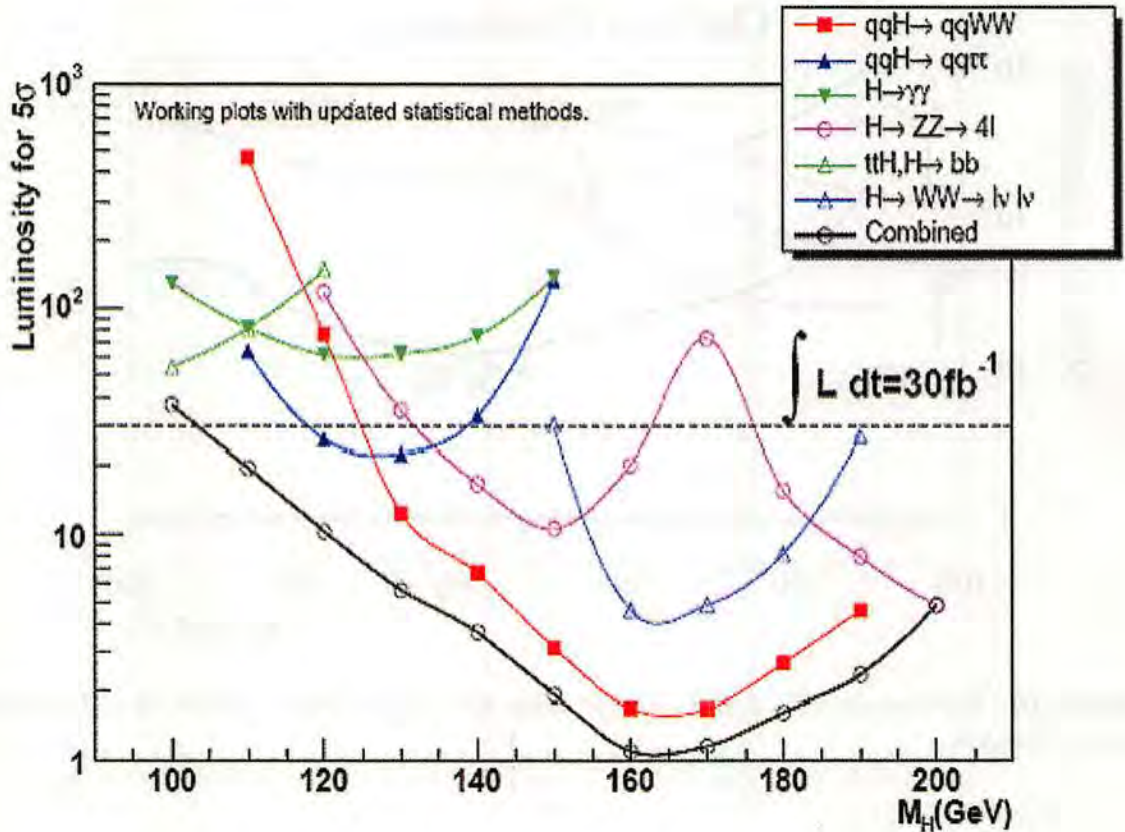


Figure 18. Expected luminosity needed by the ATLAS detector to observe Higgs boson production as a function of the Higgs boson mass.

The Higgs mass region below 130 GeV has been recently shown by the ATLAS and CMS experiments to be quite difficult to investigate with $\mathcal{O}(10\text{fb}^{-1})$ of integrated luminosity (see e.g. Fig. 18 for recent ATLAS predictions). If –as appears probable given the prediction of electroweak fits and the recent world average of the top quark mass– the Higgs boson is indeed lighter than 130 GeV, a whole set of scenarios opens for year 2009, when LHC experiments will try to produce physics results with data from the first year of physics run, and CDF and DØ will squeeze the most out of their then complete datasets.

The first scenario sees the Tevatron failing to deliver luminosity as described in the design plan (see Sec. 1.1): in that case, CMS and ATLAS will have no competitors in the search for the Higgs boson. The second scenario consist in a successful Tevatron running throughout year 2009, and a smooth start for the LHC experiments. In that case, a light Higgs boson might be observed on either side of the Atlantic ocean, and soon confirmed on the other side. The third scenario is the most favorable for the Tevatron, delivering luminosity according to the design plan while LHC further delays its startup date or experiences a bumpy start. In that case, CDF and DØ will have a significant chance of ending up as winners of the Higgs race, after all.

The forthcoming years will no doubt be extremely interesting and exciting for high P_T physics!

5. Top quark measurements

Ten years after the discovery of the top quark, the Tevatron experiments have started using $t\bar{t}$ events for precision measurements and as a laboratory for electroweak physics of quarks free from non-perturbative QCD effects.

The transition from the searches and then the first observations and measurements in Run I to the precision studies in Run II has been smooth, because the general strategy of the analyses has not changed: as more and more data is collected, cross section measurements are first performed; then determinations of the top mass follow, and studies of decay kinematics and searches for anomalies in production dynamics. Lastly, measurements of intrinsic physical properties are performed. The above *modus operandi* allows to optimize the output of physics results as analysis tools become more sophisticated and as the data are understood with increasing precision.

In the following is presented a summary of results on top cross section and top mass, and a mention of the most recent results of the search for single top production.

5.1. Brief introduction to top quark physics

At the Tevatron, production of $t\bar{t}$ pairs occurs by $q\bar{q}$ annihilation (85%) or gluon-gluon fusion (15%): proportions are exactly inverted from those that the LHC will provide. The next-to-next-to leading order prediction for top quark pair production cross section [15] is $6.1 pb$: one $t\bar{t}$ event is produced every ten billion inelastic collisions. That translates into a rate of about two top events per hour in the interaction regions.

Electroweak-mediated single top production is not irrelevant, being half as frequent; its signature, however, is way less characteristic, such that so far CDF and DØ have been able to only obtain upper limits to that process. In the remainder of this section, only pair production is discussed.

Since $V_{tb} \sim 1$ and $M_t > M_W + M_b$, the top quark almost exclusively decays to a W boson and a b quark. Final states of $t\bar{t}$ pairs are classified according to the decay of the two produced W bosons: when both decay to an electron-neutrino or muon-neutrino pair, the *dilepton* mode arises; when one of the two W 's decay to jet pairs and the other produces a $e\nu$ or $\mu\nu$ pair the final state is called *single lepton*; when both bosons decay to jet pairs, one has the *all-hadronic* final state. Decays to $\tau\nu$ pairs are excluded from this classification because of the less clear-cut signature of τ leptons, and because of the difficult identification of these particles: final states including τ leptons add a minor over-efficiency to analyses selecting the three final states mentioned above.

Top quark decays allow excellent studies of weak interactions of quarks, because of the large top quark mass. In fact, the top quark width –which is a cubic function of M_t – is computed to be $\Gamma_t \sim 1.5$ GeV, thus much larger than Λ_{QCD} . The top quark therefore is produced and decays free from non-perturbative QCD effects. Also, the top quark polarization can be measured in its decay, since the depolarization time $\tau_d = M_t/\Lambda_{QCD}^2$ is much longer than the decay time.

5.2. Production cross section measurements

The most precise $\sigma_{t\bar{t}}$ measurements come from the analysis of b -tagged single lepton decays, which represent a perfect compromise between signal to noise ratio and total yield.

The general recipe for selecting a signal-rich sample in the single lepton topology entails triggering on electrons or muons with $E_T > 15$ GeV or $P_T > 15$ GeV, respectively; offline, those thresholds are increased to 20 GeV, to which is added a requirement that the missing transverse energy E_T detected by the calorimeter be $E_T > 25$ GeV (at CDF) or 30 GeV (at DØ). To extract the top signal from backgrounds, principally due to $W +$ jets production, events with

a minimum of three hadronic jets are selected, and at least one jet is required to contain a secondary vertex b -tag.

Both CDF and DØ use Monte Carlo simulations to estimate physical backgrounds, while real data in suitable control regions depleted of $t\bar{t}$ contamination are employed to estimate the rate of false b -tags leaking in the signal samples. Events with only one or two jets besides the $W \rightarrow l\nu$ signature are used to verify sample composition and yield.

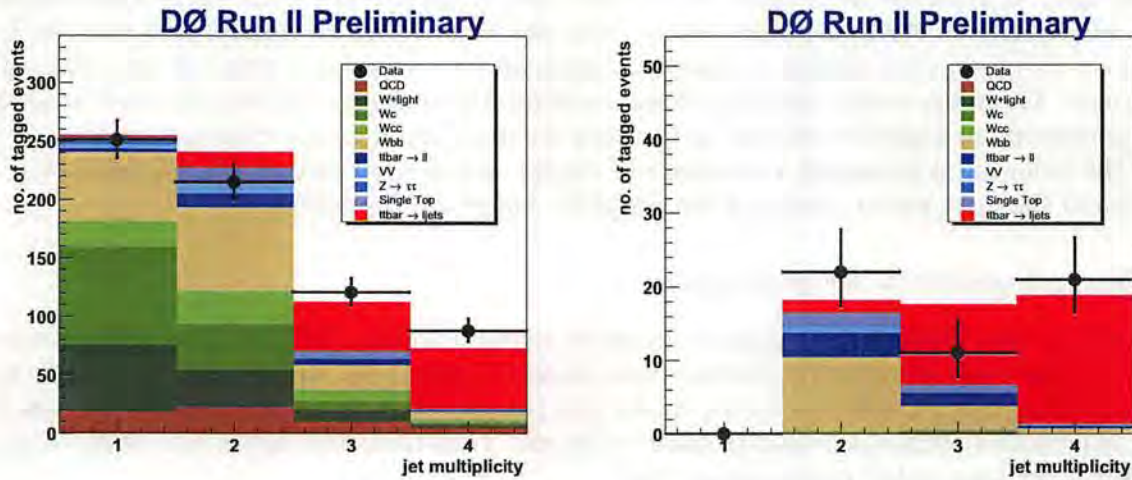


Figure 19. Distribution of the number of jets in selected $W +$ jet events by the DØ collaboration. Left: single b -tags; right: double b -tags.

As an example, the standard single lepton analysis in DØ uses events with a triggering electron or muon, missing $E_T > 30$ GeV, three or four jets with $E_T > 20$ GeV, and one or two secondary vertex b -tags. The selected data is then divided into eight separate categories depending on their characteristics (e or μ , three or four jets, one or two b -tags) and the eight independent determinations are combined in a likelihood fit. The result is $\sigma_{t\bar{t}} = 8.1^{+1.3}_{-1.2} \pm 0.5 \text{lumi pb}$. Figure 19 shows the selected data and its composition in terms of the contributing processes.

Each experiment has by now produced about a dozen different measurements of the $t\bar{t}$ cross section. The various CDF determinations have been combined by properly taking into account common sources of systematic uncertainties such as integrated luminosity and b -tagging efficiency. The obtained average value has a comparable precision to theoretical estimates. The base data and the average are shown in Fig. 20.

5.3. Top mass determinations

The Tevatron experiments have put a big effort to measure the top quark mass with the highest possible precision. The top mass is a fundamental parameter of the standard model, and its precise determination constitutes a very stringent test of consistency of the theory. This can be stated quantitatively by observing that a 1 GeV uncertainty in the top quark mass has the same constraining power on the unknown mass of the Higgs boson as a 6.1 MeV uncertainty on the W boson mass [17].

Another compelling reason to measure the top quark mass with the utmost precision is the intriguing fact that its Yukawa coupling appears to be “natural”: from the world average value of M_t one finds $y_t = \sqrt{2} \frac{M_t}{v} \sim 1.00$, with a precision of 1.3%. Many believe that the more we

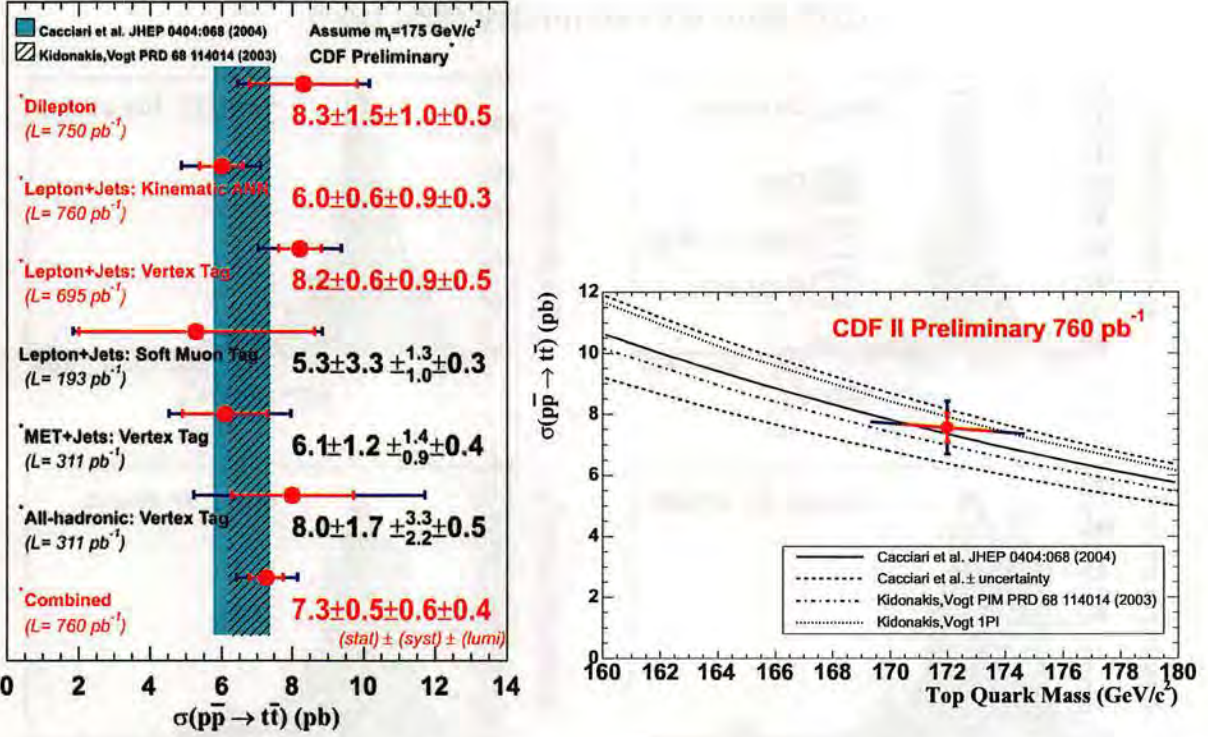


Figure 20. Left: summary of Run II measurements of the $t\bar{t}$ cross section by the CDF collaboration. Right: comparison of measured mass and top cross section with theoretical curves.

know about the top quark, the closest we will get to understanding the mechanism of electroweak symmetry breaking.

Several new methods have been devised to improve the precision of older measurements. In general, as collected statistics improves, the systematic uncertainty due to the knowledge of the jet energy scale (JES) becomes the target where to shoot all the bullets.

The jet energy scale has been determined with great precision by CDF using dijet events and gamma-jet events, as discussed in Sec. 3.1. However, the decay of top pairs offers an independent calibration point for jet energy through the knowledge of the W boson mass. The most precise single measurement of the top mass indeed comes from the use of that methodology. From a dataset of 680pb^{-1} of single lepton decays, with the selection of events containing four jets, a χ^2 technique finds the most probable value of the top mass by simultaneously fitting the JES from the $W \rightarrow q\bar{q}'$ portion of the hadronic decay. The result is $M_t = 173.4 \pm 1.7_{\text{stat}} \pm 1.8_{\text{JES}} \pm 1.3_{\text{syst}} \text{ GeV}$ (see Fig. 21). A measurement from DØ in the same channel, which also fits the jet energy scale together with the top quark mass, finds $M_t = 170.6 \pm 4.4_{\text{stat+JES}} \pm 1.7_{\text{syst}} \text{ GeV}$ in a smaller sample of 380pb^{-1} of Run II data.

Interestingly, new methods have allowed the dilepton and all-hadronic channels to provide determinations of the top quark mass which have remained competitive with the precise single lepton measurements. In the dilepton channel CDF uses a matrix element technique based on finding for each event the posterior probability for the top mass as a product of the differential cross section for leading order $t\bar{t}$ production. In 750pb^{-1} of data the result is $M_t = 164.5 \pm 4.5 \pm 3.1 \text{ GeV}$. In the all-hadronic final state a combination of matrix element and template fitting technique called *ideogram method* allows to extract $M_t = 177.1 \pm 4.9_{\text{stat}} \pm 4.7_{\text{syst}} \text{ GeV}$. The combined CDF average resulting from the above determinations is $M_t = 172.4 \pm 1.5_{\text{stat}} \pm 2.2_{\text{syst}}$.

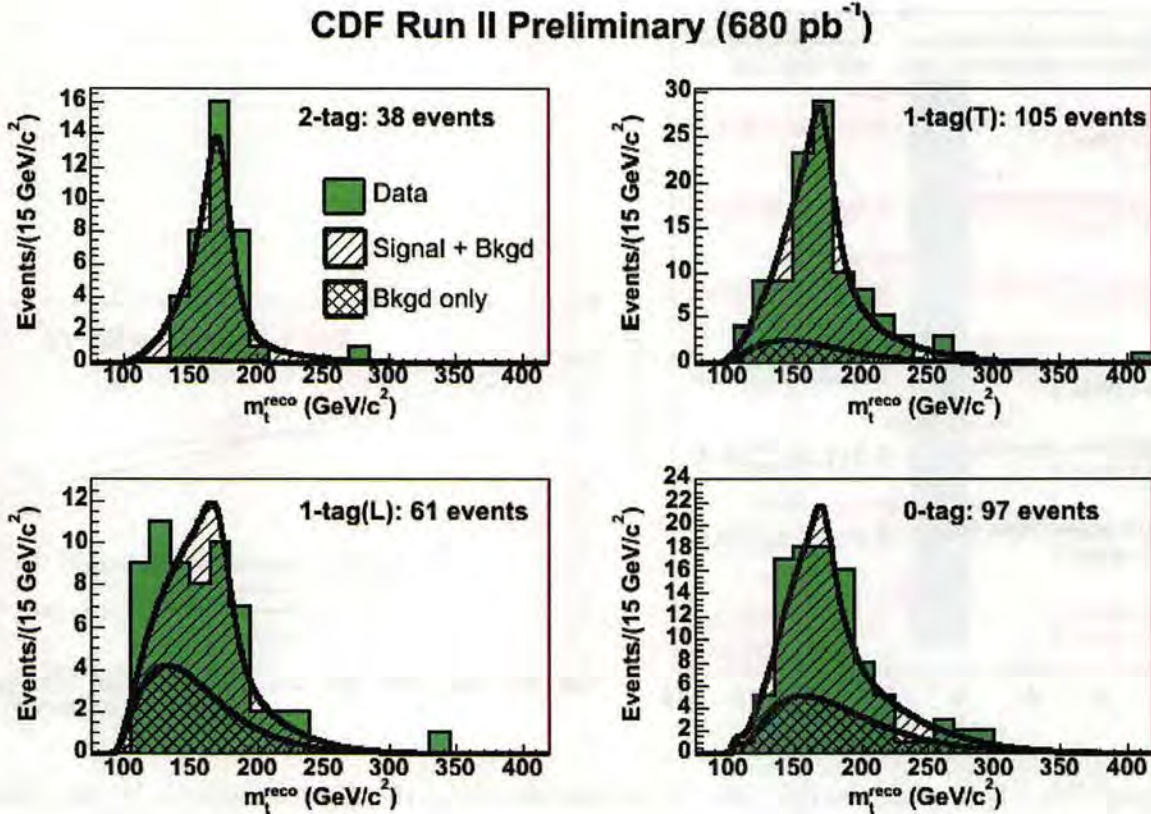


Figure 21. Reconstructed top mass from four independent subsets of single lepton $t\bar{t}$ candidates by CDF.

GeV.

Fig. 22 shows a summary of recent measurements of the top quark mass by CDF and D \emptyset . A new world average has been computed recently by the Tevatron electroweak working group [18]: $M_t = 172.5 \pm 1.3_{\text{stat}} \pm 1.9_{\text{syst}}$ GeV. The uncertainty is now at 1.3%: by 2009, the Tevatron might be able offer a top quark mass with 1.2 GeV precision.

LHC will certainly benefit from a precise measurement of the top mass in its first phase, when M_t can be used as a calibration point for a first jet energy scale determination. However, the indirect information on the mass of the standard model Higgs boson extracted from electroweak fits using the Tevatron measurements of M_W and M_t will still be insufficient to provide a target Higgs mass to aim at. Until we find it, the Higgs boson will require us to carry out searches in all measurable final states.

5.4. Electroweak production of single top quarks

The electroweak process of single top production has not been observed yet by the Tevatron experiments. However, the 95% confidence level limits are by now quite close to the standard model expectations for the two main production mechanisms, W -gluon fusion and t -channel production via a virtual W boson (see Fig. 23). Theoretical predictions for the cross section of the two processes are of 1.98 and 0.88 pb , respectively [19, 20].

The observation of single top production would provide the only tool for measuring the Cabibbo-Kobayashi-Maskawa mixing matrix element V_{tb} , which is closely tied to the number of

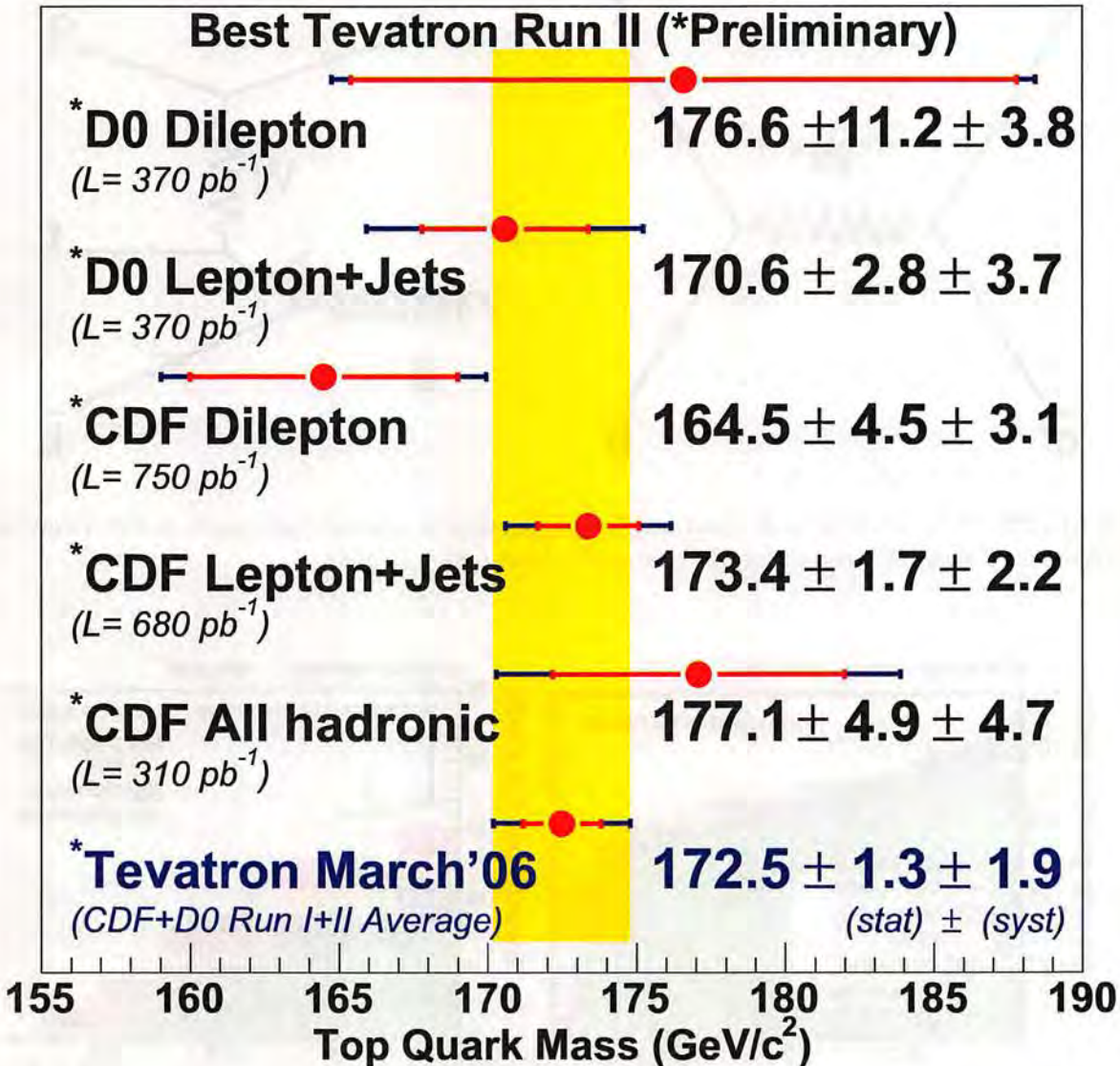


Figure 22. Summary of the best results on the top mass obtained in Run II by the CDF and DØ collaboration.

quark generations. Furthermore, the spin polarization of top quarks produced by the electroweak processes shown in Fig. 23 can be used to test the V-A structure of the weak charged current interaction. Of course, a precise measurement of these properties will only be accessible to the LHC experiments, and yet CDF and DØ have energetically attempted to find evidence for these processes in their Run II datasets, in the knowledge that measuring experimentally the production of single top at the Tevatron is important since it constitutes a background to light Higgs boson searches.

Currently, the best results come from CDF, who has recently completed the analysis of 700 pb^{-1} of data. The analysis is complex, and has been performed with two separate methods for the separation of signal and backgrounds based on the kinematical characteristics of the selected $W + 2$ jet data: a neural network (whose output is shown in Fig. 24) and a multivariate likelihood. The

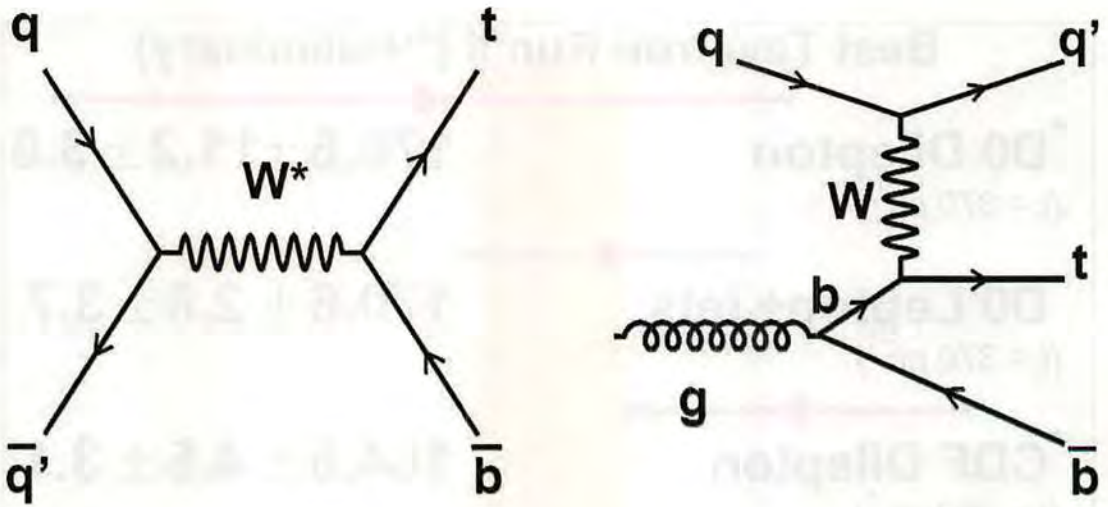


Figure 23. The two dominant diagrams for production of a single top quark at the Tevatron: s -channel off-shell W production (left) and W -gluon fusion (right).

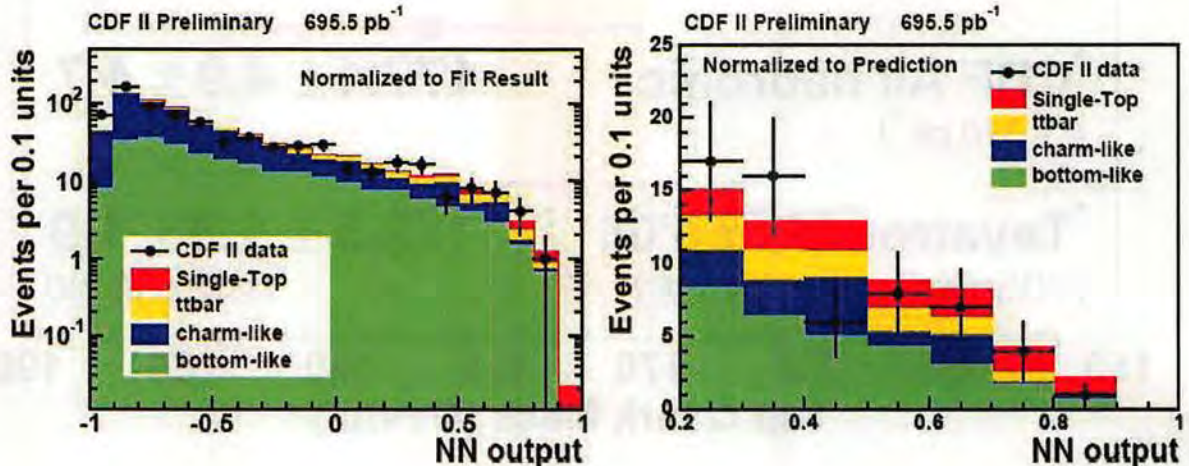


Figure 24. Results of the CDF search for single top production in 695 pb^{-1} of Run II data. On the left the entire output region of the neural network is shown, and the experimental data (black points) are compared to the sum of background processes and expected signal contribution (in red). On the right, a zoom into the signal region ($\text{NN output} > 0.2$) is shown.

limit for the two production processes together is set at 3.4 pb at 95% C.L. by the neural network method, but I believe it is better to quote the most probable value for the signal cross section borne by the data, extracted by the multivariate likelihood: $\sigma_{s+t} = 0.8^{+1.3}_{-0.8}(\text{stat})^{+0.2}_{-0.3}(\text{syst})\text{pb}$.

6. Precision electroweak physics at the Tevatron

6.1. Vector boson production

If the million-event datasets of Z boson production at LEP made the headlines in the 1990's, the W and Z boson datasets currently collected at the Tevatron in Run II are no less impressive by now. Using the decays collected with high- P_T lepton triggers a lot of precision electroweak physics measurements can be performed, besides the mandatory W mass measurement. Inclusive and differential cross sections, limits on anomalous couplings and rare decays, cross sections for associated boson pair production are all physical quantities whose measurements are starting to be systematics-dominated. Fig. 25 and 26 show a few recent results obtained with Run II boson samples.

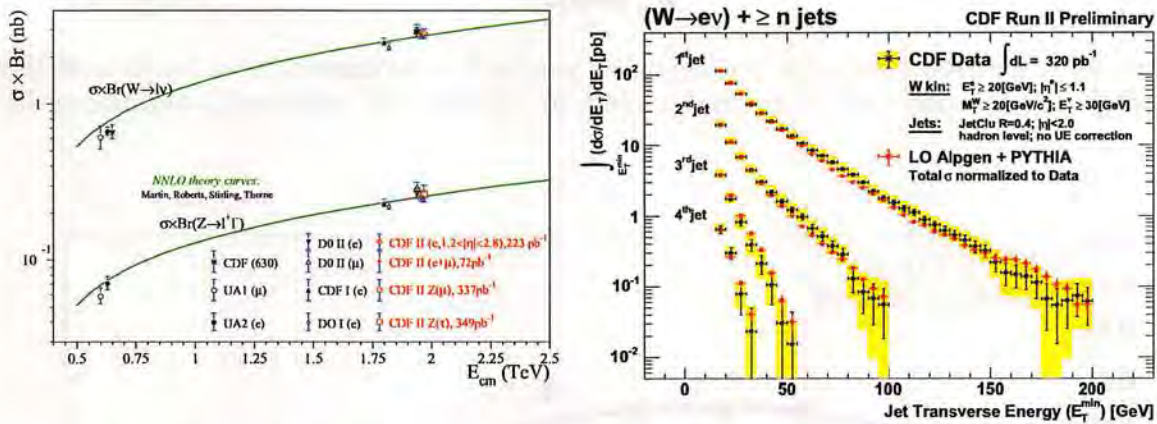


Figure 25. Left: summary of twenty years of W and Z boson cross section measurements at hadron colliders. Right: differential $W +$ jet cross section measurements by CDF as a function of jet E_t , for $N = 1, 2, 3, 4$ jets.

Here I will just mention the use of W decay to study the ratio of parton distribution functions $d(x)/u(x)$ in the proton, by measuring the charge asymmetry of the produced charged lepton. W bosons show in fact a production asymmetry at the Tevatron, due to the larger momentum carried by u quarks than d quarks in the proton. However, what is measurable is only the lepton rapidity, which obliges to $V - A$ coupling in W decay. It is worth noting here that at the LHC vector bosons will not exhibit any production asymmetry: this will prevent a *in situ* reduction of parton distribution functions (PDF) systematics in the measurement of the W mass.

CDF has pioneered the lepton charge asymmetry measurement in Run I, when the data helped constraining PDF fits at medium values of Bjorken's x , with the benefit of improving all subsequent W mass measurements by CDF and DØ. With Run II data, W decays are being studied in a wider rapidity range, thanks to the improved forward tracking of both detectors. Results (see Fig. 27) are putting the tightest constraints to the $d(x)$ and $u(x)$ distributions at medium values of x .

6.2. Parton Distribution Functions and cross section issues

An important contribution to LHC high- P_T physics measurements which the Tevatron experiments might offer is the improvement of the knowledge of proton PDF at very small values of x . Due to the very high center-of-mass energy, the precision of many cross section

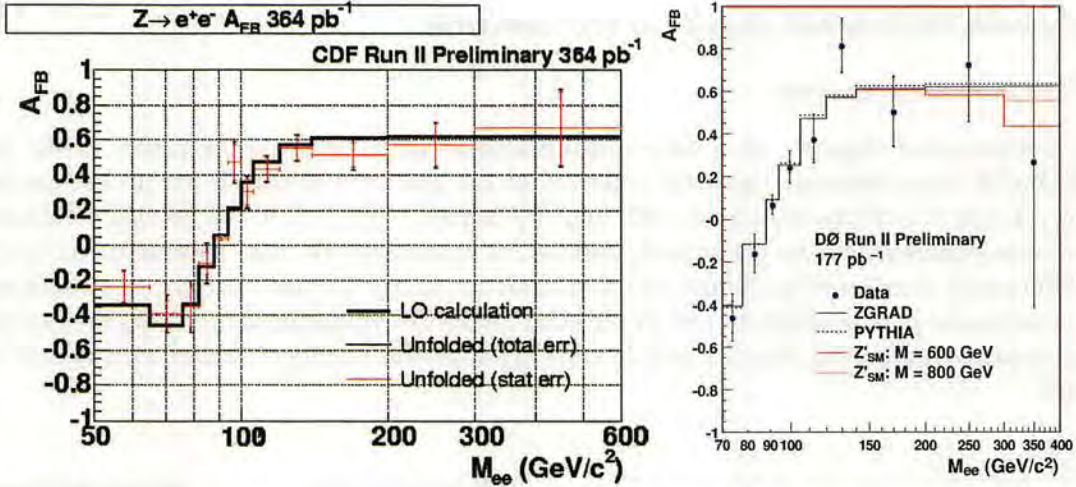


Figure 26. Tevatron results for the Drell-Yan production asymmetry as a function of the dilepton invariant mass. Left: The measurement by CDF. Right: measured Z asymmetry by DØ .

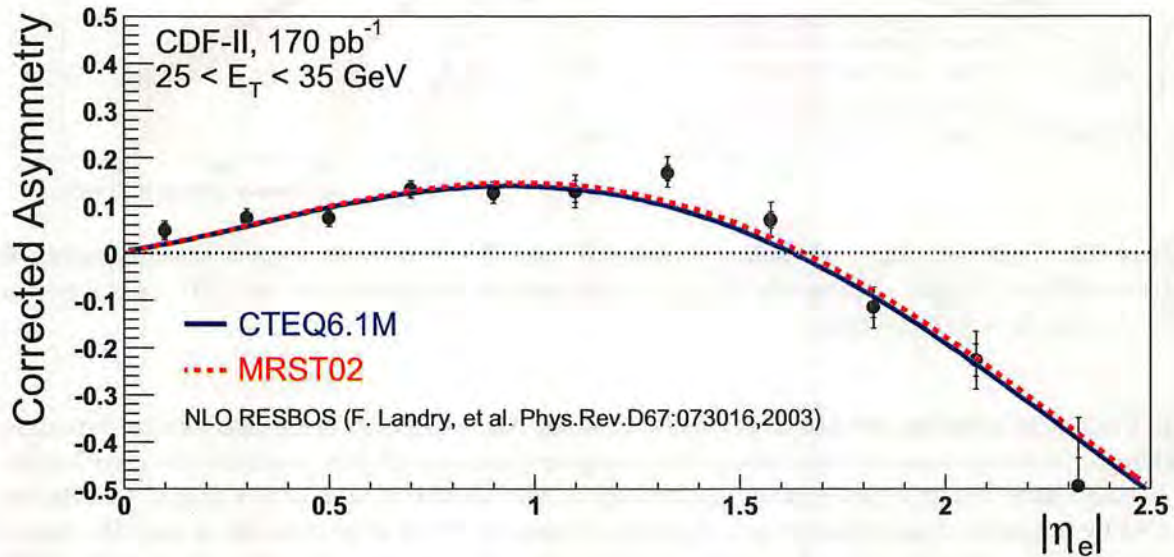


Figure 27. Lepton charge asymmetry in W decay measured by CDF as a function of lepton rapidity, for the bin of 25 to 35 GeV of lepton transverse energy. The data (points with error bars) are compared to two PDF sets.

measurements by the CMS and ATLAS collaborations will be limited by PDF systematics. The measurement of the W boson mass –for which the LHC goal is an accuracy of 15 MeV– will also strongly depend on the knowledge of production mechanisms for $x \simeq 5 \times 10^{-4} \div 10^{-2}$. Other LHC measurements which could be critically affected by limited precision on small- x PDF include the top quark mass, and any counting experiment attempting to put in evidence a small excess due to a new physics signal, since these would rely on accurate predictions for background rates.

In absence of improvements from the Tevatron, LHC will heavily rely on data from the HERA determinations. But CDF and DØ *can* help. Measuring small- x PDF at the Tevatron requires

the study of light things produced forwards. An attempt has already been done by D \emptyset who have measured high-rapidity quarkonium production. Their measurement is still affected by insufficient statistics to provide a real constraint, but it certainly goes in the right direction, and it can only be hoped that both CDF and D \emptyset will provide a precise determination with their full datasets in a few years.

Another interesting idea for the improvement of LHC cross section determinations has been supported by a recent paper [21]. All cross section measurements at the Tevatron – and the more so at the LHC – are affected by the knowledge of the inelastic cross section, which is known with a 4% precision. On the other hand, electroweak processes such as W production are now calculated to next-to-next-to leading order. One might then think of using the latter as a normalization point of integrated luminosity for a given dataset.

By examining existing data from CDF and D \emptyset one might draw the conclusion that it is indeed possible to measure $\sigma(W)$ to within 1–2% both at the Tevatron and at the LHC. Again, the knowledge of parton distribution functions at high rapidity is critical. Another difficult problem is the need to know the stability of data taking conditions very accurately, and to model with precision the collection efficiency for high- P_T leptons. This can be done with the data itself: Z bosons have provided measurements of lepton ID efficiencies during the last 20 years. However, at present this remains a clever but as of yet untested method.

7. Conclusions

The CMS and ATLAS experiments, currently in construction at the Large Hadron Collider, will start producing physics results in 2009. By that date, the CDF and D \emptyset experiments will be squeezing the most out of the several inverse femtobarns of proton-antiproton collisions collected since 2001: their analyses will represent both a challenge and a support to LHC precision measurements in the following years.

One challenge for LHC will be to improve measurements such as those of W and top quark masses, which will have reached already a high level of precision. A second challenge is of course constituted by the search for a light Higgs boson, where paradoxically 8fb^{-1} of pp collisions could prove insufficient for a discovery by CMS or ATLAS, whereas the same luminosity collected at a seven times smaller center-of-mass energy might be just enough for CDF and D \emptyset .

But the Tevatron data will be an asset as well. LHC cross section measurements might strongly benefit from improved precision in the knowledge of parton distribution functions at small x , which can and should be provided by specific measurements by CDF and D \emptyset . Further, the methodologies to improve the measurement of hadronic jets now under test at the Tevatron (in some instances –such is the case of the $Z \rightarrow b\bar{b}$ signal– on samples much harder to collect at 14 TeV) will be imported with confidence to the higher energy environment.

The perception in those sitting at the boundary between particle physics and funding agencies appears that CMS and ATLAS will only be successful if they discover new physics beyond the Standard Model. Some even believe that in the absence of anything new high energy physics might face the cancellation of all planned future projects [22]. I believe it is of paramount importance to demonstrate that LHC experiments can provide a huge advance in the knowledge of particle physics even if nothing is there to be found in going from 2 to 14 TeV besides a standard model Higgs boson: knowing with certainty that no new physics is manifest at the TeV scale is almost as much interesting, even if not as spectacular, as complex spectra of supersymmetric particles. That is the gamble that high-energy particle physics is facing in the next few years.

Acknowledgments

I wish to thank Riqie Arneberg for her editorial advice.

References

- [1] S.Nagaitsev *et al.*, Phys. Rev. Lett. **96**, 044801 (2006).
- [2] H.T.Shapiro *et al.*, *Revealing the Hidden Nature of Space and Time: Charting the Course for Elementary Particle Physics*, <http://www7.nationalacademies.org/bpa/EPP2010.html> .
- [3] T.LeCompte and H.T.Diehl, *The CDF and DØ upgrades for Run II*, Ann. Rev. Nucl. Part. Sci. 50 (2000), 71.
- [4] J.Huth *et al.*, *Research Directions for the decade*, Proceedings of the summer study on High energy Physics, Snowmass, Colorado, 1990, ed. E.L.Berger (World Scientific,1991).
- [5] A.Bhatti *et al.*, *Determination of the Jet Energy Scale at the collider detector at Fermilab*, hep-ex/0510047 (2005).
- [6] The jet energy correction method used by DØ in Run II has not been published yet. Details can be found in http://www-d0.fnal.gov/phys_id/jes/public/plots_v7.1/index.html .
- [7] CDF and DØ collaborations, *Results of the Tevatron Higgs Sensitivity Study*, FERMILAB-PUB-03/320-E.
- [8] J.Gunion *et al.*, *The Higgs Hunter's Guide*, Addison-Wesley, New York 1990.
- [9] The LEP Electroweak Working Group, <http://lepewwg.web.cern.ch/LEPWWG/>.
- [10] A.Heister *et al.*, Phys. Lett. B **565**, 61 (2003).
- [11] M.Carena *et al.*, *Higgs Working Group Report*, hep-ph/0010338.
- [12] D.Acosta *et al.*, Phys. Rev. Lett. **94**, 091803 (2005).
- [13] V.Abazov *et al.*, Phys. Rev. Lett. **94**, 151801 (2005).
- [14] A.Bardi *et al.*, Nucl. Instr. Meth. A **409**, 658 (1998).
- [15] N.Kidonakis and R.Vogt, Phys. Rev. **D68** (2003) 114014.
- [16] The latest measurement by CDF is $\sigma_{WW} = 13.6 \pm 2.8_{stat.} \pm 1.6_{syst.} \pm 1.2_{lum.}$, see hep-ex/0605066.
- [17] M.Beneke *et al.*, *Top Quark Physics*, hep-ph/0003033.
- [18] Tevatron Electroweak Working Group, *Combination of CDF and DØ Results on the Mass of the Top Quark*, hep-ex/0603039.
- [19] B.W.Harris *et al.*, Phys. Rev. **D66** (2002) 054024.
- [20] Z.Sullivan, Phys. Rev. **D70** (2004) 114012.
- [21] S.Frixione and M.Mangano, *How accurately can we measure the W cross section?*, hep-ph/0405130 (2004).
- [22] A discussion on this topic has been hosted in P.Woit's web-log *Not Even Wrong*, see <http://www.math.columbia.edu/~woit/wordpress/?p=399>.



Determination of the jet energy scale at the Collider Detector at Fermilab

A. Bhatti^s, F. Canelli^{b,*}, B. Heinemann^j, J. Adelman^d, D. Ambrose^p, J.-F. Arguin^m, A. Barbaro-Galtieriⁱ, H. Budd^r, Y.S. Chung^r, K. Chung^c, B. Cooper^k, C. Curratⁱ, M. D'Onofrio^h, T. Dorigoⁿ, R. Erbacher^e, R. Field^f, G. Flanagan^l, A. Gibsonⁱ, K. Hatakeyama^s, F. Happacher^g, D. Hoffman^d, G. Introzzi^o, S. Kuhlmann^a, S. Kwang^d, S. Jun^c, G. Latino^q, A. Malkus^d, M. Mattson^t, A. Mehta^j, P.A. Movilla-Fernandezⁱ, L. Nodulman^a, M. Paulini^c, J. Proudfoot^a, F. Ptakos^g, S. Sabik^m, W. Sakamoto^r, P. Savard^m, M. Shochet^d, P. Sinervo^m, V. Tiwari^c, A. Wicklund^a, G. Yun^r

^aArgonne National Laboratory, Argonne, IL 60439, USA

^bUniversity of California at Los Angeles, Los Angeles, CA 90024, USA

^cCarnegie Mellon University, Pittsburgh, PA 15213, USA

^dEnrico Fermi Institute, University of Chicago, Chicago, IL 60637, USA

^eFermi National Accelerator Laboratory, Batavia, IL 60510, USA

^fUniversity of Florida, Gainesville, FL 32611, USA

^gLaboratori Nazionali di Frascati, Istituto Nazionale di Fisica Nucleare, I-00044 Frascati, Italy

^hUniversity of Geneva, CH-1211 Geneva 4, Switzerland

ⁱErnest Orlando Lawrence Berkeley National Laboratory, Berkeley, CA 94720, USA

^jUniversity of Liverpool, Liverpool L69 7ZE, UK

^kUniversity College London, London WC1E 6BT, UK

^lMichigan State University, East Lansing, MI 48824, USA

^mUniversity of Toronto, Toronto, Canada M5S 1A7

ⁿUniversity of Padova, Istituto Nazionale di Fisica Nucleare, Sezione di Padova-Trento, I-35131 Padova, Italy

^oUniversity of Pavia, Istituto Nazionale di Fisica Nucleare, Sezione di Pavia, I-27100 Pavia, Italy

^pUniversity of Pennsylvania, Philadelphia, PA 19104, USA

^qIstituto Nazionale di Fisica Nucleare Pisa, University of Pisa, Siena and Scuola Normale Superiore di Pisa, I-56127 Pisa, Italy

^rUniversity of Rochester, Rochester, NY 14627, USA

^sThe Rockefeller University, New York, NY 10021, USA

^tWayne State University, Detroit, MI 48201, USA

Received 18 May 2006; received in revised form 23 May 2006; accepted 24 May 2006

Available online 10 July 2006

Abstract

A precise determination of the energy scale of jets at the Collider Detector at Fermilab at the Tevatron $p\bar{p}$ collider is described. Jets are used in many analyses to estimate the energies of partons resulting from the underlying physics process. Several correction factors are developed to estimate the original parton energy from the observed jet energy in the calorimeter. The jet energy response is compared between data and Monte Carlo simulation for various physics processes, and systematic uncertainties on the jet energy scale are determined. For jets with transverse momenta above 50 GeV the jet energy scale is determined with a 3% systematic uncertainty.

© 2006 Elsevier B.V. All rights reserved.

PACS: 14.65.—q; 14.65.Ha; 13.87.Fh; 07.20.Fw

Keywords: Jet energy scale; JES; Collider Detector at Fermilab; CDF; Fermilab; Particle physics; High-energy physics

*Corresponding author.

E-mail address: canelli@fnal.gov (F. Canelli).

1. Introduction

Measurements of hard scattering processes in $p\bar{p}$ collisions often depend on the determination of the four-momenta of quarks and gluons produced in the hard scatter. The measurement of these four-momenta relies on the reconstruction of hadronic jets, resulting from the quark or gluon fragmentation.

At the Collider Detector at Fermilab (CDF) jets are observed as clustered energy depositions in the calorimeters. In this article we describe how these jets are then corrected to correspond to the energy of the parent parton. The precision to which this can be achieved determines the precision of many measurements, e.g. a 1% uncertainty on the energy scale of jets results in an uncertainty of 10% on the cross-section for jet production at transverse momenta of $500 \text{ GeV}/c$ [1] and in a $1 \text{ GeV}/c^2$ uncertainty on the top quark mass [2].

The original parton transverse energy can be estimated by correcting the jet for instrumental effects and for radiation and fragmentation effects, such that

$$p_T^{\text{parton}} = (p_T^{\text{jet}} \times C_\eta - C_{\text{MI}}) \times C_{\text{Abs}} \\ - C_{\text{UE}} + C_{\text{OOC}} = p_T^{\text{particle}} - C_{\text{UE}} + C_{\text{OOC}} \quad (1)$$

where p_T^{parton} is the transverse momentum of the parent parton the procedure is aimed at, p_T^{jet} is the transverse momentum measured in the calorimeter jet, p_T^{particle} is the transverse momentum of the particle jet, that is, a jet corrected by all instrumental effects which corresponds to the sum of the momenta of the hadrons, leptons, and photons within the jet cone, and

- C_η , “ η -dependent” correction, ensures homogeneous response over the entire angular range;
- C_{MI} , “multiple interaction” correction, is the energy to subtract from the jet due to pile-up of multiple $p\bar{p}$ interactions in the same bunch crossing;
- C_{Abs} , “absolute” correction, is the correction of the calorimeter response to the momentum of the particle jet. Particle jets can be compared directly to data from other experiments or theoretical predictions which include parton radiation and hadronization.
- C_{UE} and C_{OOC} , the “underlying event” and “out-of-cone” corrections, correct for parton radiation and hadronization effects due to the finite size of the jet cone algorithm that is used. Note that these corrections are independent of the experimental setup, i.e. the CDF detector environment.

These corrections and their systematic uncertainties will be described below and in the following sections. All the correction factors are determined as a function of the jet transverse momentum but they apply to all components of the four-momentum of the jet.

The C_{Abs} correction is derived using a detailed Monte Carlo (MC) simulation of the physics processes and the

detector response. The corrections C_{UE} and C_{OOC} are determined using the PYTHIA MC generator. Thus, the major task is the tuning and validation of the detector simulation as well as of the physics modeling used in the simulation. The other corrections are mostly derived directly from data but are also compared to the simulation.

The following ingredients are necessary for deriving the corrections described above:

- The energy scale for the electromagnetic calorimeter is set using electrons from the decay $Z \rightarrow e^+e^-$. The energy scale for the hadronic calorimeter is set to the test-beam scale of $50 \text{ GeV}/c$ charged pions. Section 2 describes the CDF detector and the definition of the calorimeter energy scales.
- Jets are defined using a cone algorithm either on calorimeter towers, on stable particles, or on partons in the MC. Different cone sizes are studied and all the corrections are derived for the specific cone size. The details of the algorithm used for defining a jet are given in Section 3.
- Many data sets are used for either developing a correction procedure, or for validating or tuning the MC simulation. These are described in Section 4.
- Since the simulation is used to correlate a particle jet to a calorimeter jet a detailed understanding of the detector simulation is needed. Therefore, the simulation is tuned to model the response of the calorimeter to single particles by comparing the calorimeter energy measurement, E , to the particle momentum, p , measured in tracking detectors. Here, measurements based on both test beam and CDF data taken during Run II are used. The details of the simulation are given in Section 5.
- The calorimeter simulation is most reliable in the central part of the calorimeters since the tracking coverage in the forward regions is limited. Therefore, the forward calorimeter jet response is calibrated with respect to the central, to flatten out the jet response versus the jet polar angle. This procedure also corrects for the lower response in poorly instrumented regions of the calorimeter detectors. The η -dependent correction, C_η , is described in Section 6.
- After tuning the simulation to the individual particles response and achieving a jet response independent of the polar angle, calorimeter jets are corrected to a particle jet, i.e. they are corrected for the central calorimeter response. The absolute correction, C_{Abs} , is derived from the simulation and described in Section 7. Since the correction is derived from simulation, it is also important to ensure that the multiplicity and momentum spectrum of particles in the data is well reproduced by the simulation. This is also presented in Section 7.
- A further correction is made for pile-up of additional $p\bar{p}$ interactions. This pile-up can lead to an overestimate of the jet energy if particles produced in the additional interactions happen to overlap those produced in the

hard scattering process. A correction, C_{MI} , for this is derived from data and described in Section 8.

- The jet energy needs to be corrected for particles from the UE, i.e. interactions from spectator quarks and initial state QCD radiation, since the measurement aims at estimating the parton energy. This correction, C_{UE} , is described in Section 9.
- Since the jet cone is of finite size some particles originating from the initial parton may escape from the jet cone either in the fragmentation process or due to parton radiation. The OOC energy, C_{OOC} , is measured in MC simulated events and compared to the data. This correction is described in Section 9.
- Various cross-checks using different physics processes are presented to validate the universality of the procedure and verify the systematic uncertainties. These are presented in Section 10.
- A summary of the systematic uncertainties is given in Section 11. They take into account any differences observed between the data and the simulation and possible systematic biases in the procedure used to determine the corrections.

In Section 12 we present conclusions and an outlook of future possible improvements on this correction procedure and the systematic uncertainties.

2. CDF detector

The CDF Run II detector has been described in detail elsewhere [3]. In the following we use a cylindrical coordinate system with the origin at the center of the detector where the z-axis points along the beam pipe in which θ is the polar angle, ϕ is the azimuthal angle and $\eta = -\ln(\theta/2)$ is the pseudo-rapidity. The transverse energy, E_{T} , is defined as $E \sin \theta$ and the transverse momentum, p_{T} , as $p \sin \theta$, where E is the energy measured by the calorimeter and p the momentum measured in the tracking system. The imbalance in transverse energy, \vec{E}_{T} , is the magnitude of \vec{E}_{T} with $\vec{E}_{\text{T}} = -\sum_i E_{\text{T}}^i \vec{n}_i$, where \vec{n}_i is a unit vector that points from the interaction vertex to the i th calorimeter tower in the transverse plane.

Transverse momenta of charged particles (p_{T}) are measured by an eight-layer silicon strip detector [4] and a 96-layer drift chamber inside a 1.4 T magnetic field. The innermost layer of the silicon detector is located on the beam pipe at a radius of 1.5 cm, with the outermost layer located at 28 cm. The silicon detector provides tracking in the pseudo-rapidity region $|\eta| < 2$, with partial coverage up to $|\eta| < 2.8$. Outside of the silicon detector, the Central Outer Tracker (COT) [5] is a 3.1 m long, open-cell drift chamber with an active tracking region extending radially from 41 to 137 cm. The COT's 96 layers are divided into super-layers of 12 wires each that alternate between axial and stereo orientation. The COT provides coverage for $|\eta| \leq 1$. The efficiency for finding charged particle tracks is close to 100% for $|\eta| < 1$ and falls to about 40% for $|\eta| \approx 2$.

The momentum resolution is $\sigma(p_{\text{T}})/p_{\text{T}} = 0.15\% \times p_{\text{T}}$ for $|\eta| \leq 1.0$ and degrades with increasing $|\eta|$.

Located outside the solenoid, a segmented sampling calorimeter is installed for the measurement of the electromagnetic and the hadronic energy depositions, which is described in detail in Section 2.1. The central and forward part of the calorimeter have their own shower profile detector positioned at the expected maximum of the lateral shower profile, the Central Electromagnetic Showermax (CES [6]) and the Plug Electromagnetic Showermax (PES [7]) detectors. Located at the inner face of the central calorimeter, the Central Pre-Radiator (CPR [8]) chambers use the solenoid coil as a radiator to measure the shower development. These three detectors are mainly used for photon and electron identification. Drift chambers located outside the central calorimeters and detectors behind a 60 cm iron shield detect energy depositions from muons with $|\eta| < 0.6$ [9]. Additional drift chambers and scintillation counters detect muons in the region $0.6 < |\eta| < 1.0$. Luminosity monitoring is provided by the Cherenkov Luminosity Counter (CLC) [10].

2.1. Calorimeters

The CDF calorimeter is divided into a central and a forward section. A schematic view is shown in Fig. 1.

There are a total of five calorimeter compartments: the central electromagnetic CEM [11], and central hadronic CHA [12], the plug electromagnetic PEM [13], and plug hadronic PHA [13], and the wall hadronic WHA [12] in the region between the central and the forward calorimeter at $\theta \approx \pm 30^\circ$ (see Fig. 1).

The central calorimeter covers the region $|\eta| < 1.1$ and is divided in two halves at $|\eta| = 0$. It is segmented in towers of 15° in azimuth and 0.1 in η with lead-scintillator sampling for the electromagnetic measurements and steel-scintillator sampling for hadronic measurements. The material in the CEM has a depth of 18 radiation lengths. The energy resolution for high-energy electrons and photons is $\sigma(E_{\text{T}})/E_{\text{T}} = 13.5\%/\sqrt{E_{\text{T}}} \oplus 1.5\%$. The CHA and WHA are of similar construction, with alternating layers of steel and scintillator and are 4.7 interaction lengths deep. Three of the WHA towers are situated behind the CEM/CHA and three are behind the plug calorimeter. The energy resolution of the CHA is $\sigma(E_{\text{T}})/E_{\text{T}} = 50\%/\sqrt{E_{\text{T}}} \oplus 3\%$ and WHA is $\sigma(E_{\text{T}})/E_{\text{T}} = 75\%/\sqrt{E_{\text{T}}} \oplus 4\%$ for charged pions that do not interact in the CEM.

The forward “plug” calorimeters cover the angular range corresponding to $1.1 < |\eta| < 3.6$. They are segmented in 7.5° towers for $|\eta| < 2.11$ and 15° for $|\eta| > 2.11$. The PEM has a depth of 23.2 radiation lengths. The energy resolution for high-energy electrons and photons is $\sigma(E)/E = 16\%/\sqrt{E} \oplus 1\%$. The PHA has alternating layers of iron and scintillating tile, for a total of 6.8 interaction lengths. The energy resolution of the PHA is $\sigma(E)/E = 80\%/\sqrt{E} \oplus 5\%$ for charged pions that do not interact in the PEM.

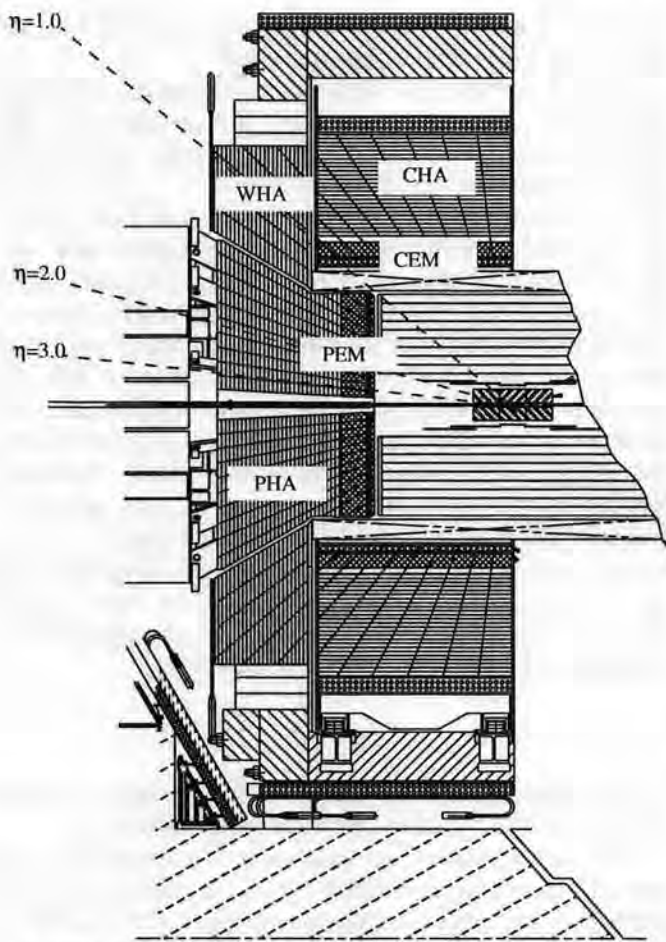


Fig. 1. Elevation view of one half of the CDF detector displaying the components of the CDF calorimeter: CEM, CHA, WHA, PEM, and PHA.

Each calorimeter tower is read out by two photomultipliers in the CEM, CHA, and WHA and by one photomultiplier in the PEM and PHA. The calorimeter readout electronics was upgraded for the Run II data taking period to accommodate the 396 ns beam bunch spacing as well as a possible upgrade to 132 ns. The ADC integration gate for the charge collection is 120 ns wide and collects 94–98% of the signal depending on the calorimeter type. During test beam and the previous Run I data taking period (1992–1996) the time between two bunches was 3.5 μ s and the integration time was 600 ns for all calorimeter compartments. The fractional energy loss due to the shorter ADC integration gate in Run II is measured in muon, electron, and jet data with an uncertainty of 1.5%.

2.2. Definition of the energy scale of calorimeter towers

The absolute energy scale of the CEM calorimeter is set such that for fully corrected electrons [14] the measured mass of the Z boson in the e^+e^- decay mode is consistent with the mass measured at LEP [15] taking into account

photon radiation. The ratio of the measured calorimeter energies and the track momenta for electron candidates, E/p , is used to apply additional relative calibrations for each tower to improve the resolution of the energy measurement. The PEM energy scale is set using $Z \rightarrow e^+e^-$ events with one electron in the CEM and one electron in the PEM.

For the hadronic calorimeters, CHA, WHA, and PHA, the initial energy scale is defined by their responses to a charged pion test beam of 50 GeV/c (see Section 4 and Refs. [16–18]) using pions with almost no interaction in the respective electromagnetic compartments CEM and PEM, respectively. The total raw energy deposited in a tower is given by the sum of CEM and CHA energies. For charged pions that interact in the CEM, the response is lower (see Sections 5 and 7).

2.3. Stability of the energy scale

The stability of the CDF calorimeter is monitored online using various calibration methods. The energy scale of both the electromagnetic and hadronic calorimeters in general decrease with time due to aging of both the scintillators and the photomultipliers. The online response is kept stable to better than 3%, while offline a stability better than 0.3–1.5% is achieved. The following methods are used to obtain this stability:

- In the CEM, E/p of electrons with transverse energies, $E_T > 8$ GeV, are used to monitor the time dependence. The energy scale decreases by 3% every 6 months, and is corrected accordingly.
- In the CHA and WHA the energy scale is monitored using three independent methods: a laser system [12], muons from $J/\psi \rightarrow \mu^+\mu^-$ decays and minimum bias data (these data sets are defined in Section 4). The test beam energy scale has been maintained since 1987 using Cs^{137} source calibration runs. The CHA response decreases by about 1% and the WHA response by about 3% per year which is corrected by adjusting the calibration.
- The PEM and PHA calorimeters are monitored using a laser system [3,19] and a radioactive source calibration using Co^{60} . The laser is only sensitive to aging of the photomultipliers while the source is sensitive to both the photomultiplier and scintillator aging. The plug calorimeter scale decreases by up to 2–10% per year, for $|\eta| = 1.2\text{--}3.6$. The largest decrease is observed in the region closest to the beam pipe, and is calibrated accordingly.

The calibration stability of the electromagnetic scales is verified using the time dependence of the reconstructed invariant Z boson mass. Fig. 2 shows the mean of the $Z \rightarrow e^+e^-$ mass distribution between 86 and 98 GeV/c² as a function of the run number. The range of run numbers corresponds to the data taking period from April 2002 until

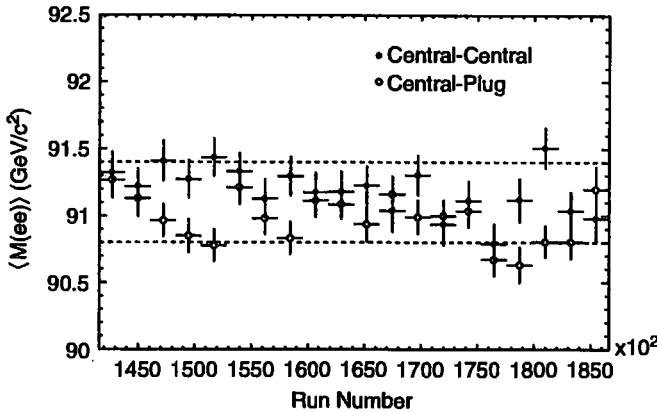


Fig. 2. Mean invariant mass of $Z \rightarrow e^+e^-$ candidates, $\langle M(ee) \rangle$, versus run number for events with $86 < M(ee) < 98 \text{ GeV}/c^2$. Shown are the values for events with both electrons in the central calorimeter (full circles) and for events with one electron in the central and one in the plug calorimeter (open circles). The dashed lines indicate a $\pm 0.3\%$ uncertainty around $91.1 \text{ GeV}/c^2$.

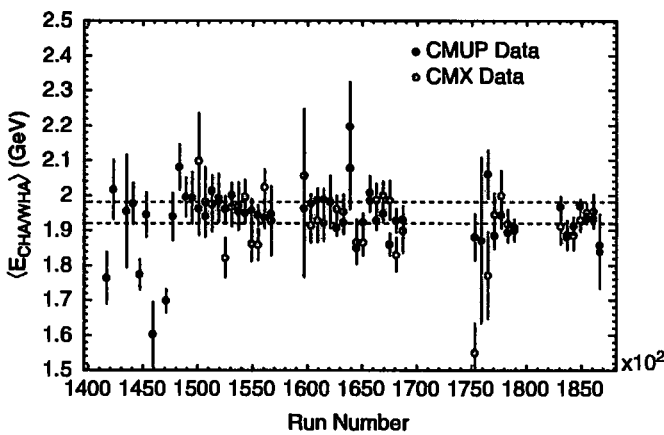


Fig. 3. Mean energy observed in the CHA/WHA for CMUP and CMX muons with $p_T > 20 \text{ GeV}/c$ from $W \rightarrow \mu\nu_\mu$ candidate events versus run number. The CMUP muons are confined to $|\eta| < 0.6$ and thus only sensitive to the central part of the CHA. The CMX muons cover the region $0.6 < |\eta| < 1.0$ and probe the outer part of the CHA plus the innermost part of the WHA. The dashed lines indicate a 1.5% uncertainty.

September 2004. The mean energy deposited by muons from $W \rightarrow \mu\nu_\mu$ candidate events is shown in Fig. 3 for muons with $|\eta| < 1$ to verify the stability of the CHA and WHA energy scales. For the PHA both muons and the jet response are used to verify the stability.

From Figs. 2 and 3 an uncertainty on the stability of the CEM of 0.3% and for the CHA of 1.5% is assigned. For a jet, which deposits typically 70% of the energy in the CEM and 30% in the CHA, the uncertainty is on order 0.5% .

3. Jet clustering algorithm

The energy of a jet is calculated from the energy deposited in the calorimeter towers using different types of clustering algorithms. For this study, jets are clustered

using a cone algorithm with a fixed cone size in which the center of the jet is defined as $(\eta^{\text{jet}}, \phi^{\text{jet}})$ and the size of the jet cone as $R = \sqrt{(\eta^{\text{lower}} - \eta^{\text{jet}})^2 + (\phi^{\text{lower}} - \phi^{\text{jet}})^2} = 0.4, 0.7,$ or 1.0 . The jet corrections and uncertainties are estimated for these three cone sizes.

3.1. Calorimeter jets

The jet clustering algorithm groups calorimeter towers with $E_{T,i} > 1 \text{ GeV}$ into jets. $E_{T,i} = E_i \sin \theta_i$ is the transverse energy of a tower with respect to the z-position of the $p\bar{p}$ interaction, and the energy E_i is the sum of the energies measured in the electromagnetic and hadronic compartments of that tower.

Firstly “seed towers” are defined in order of decreasing $E_{T,i}$. For each seed tower the towers within a radius of size R with respect to its position are used to build “clusters”. Once we have an initial list of clusters, the cluster transverse energy and the location of the cluster is calculated using the definitions:

$$E_T^{\text{jet}} = \sum E_{T,i} \quad (2)$$

$$\phi^{\text{jet}} = \sum \frac{E_{T,i} \phi_i}{E_T^{\text{jet}}} \quad (3)$$

$$\eta^{\text{jet}} = \sum \frac{E_{T,i} \eta_i}{E_T^{\text{jet}}} \quad (4)$$

where the sum is over the calorimeter towers inside the radius R with $E_T > 1 \text{ GeV}$.

This procedure is repeated iteratively, a new list of towers around the new center is determined. The jet E_T and direction are recalculated until the list of towers assigned to the clusters is stable, that is, when the geometrical center of the tower corresponds to the cluster centroid. Overlapping jets are merged if they overlap by more than 50% . If the overlap is smaller than 50% , each tower in the overlap region is assigned to the nearest jet.

The final jet energy and momentum coordinates are computed from the final list of towers:

$$E_{\text{jet}} = \sum_{i=0}^{N_{\text{low}}} E_i \quad (5)$$

$$p_x^{\text{jet}} = \sum_{i=0}^{N_{\text{low}}} E_i \sin(\theta_i) \cos(\phi_i) \quad (6)$$

$$p_y^{\text{jet}} = \sum_{i=0}^{N_{\text{low}}} E_i \sin(\theta_i) \sin(\phi_i) \quad (7)$$

$$p_z^{\text{jet}} = \sum_{i=0}^{N_{\text{low}}} E_i \cos(\theta_i) \quad (8)$$

$$p_T^{\text{jet}} = \sqrt{(p_x^{\text{jet}})^2 + (p_y^{\text{jet}})^2} \quad (9)$$

$$\phi_{\text{jet}} = \tan \frac{p_y^{\text{jet}}}{p_x^{\text{jet}}} \quad (10)$$

$$\sin \theta_{\text{jet}} = \frac{p_T^{\text{jet}}}{\sqrt{(p_x^{\text{jet}})^2 + (p_y^{\text{jet}})^2 + (p_z^{\text{jet}})^2}} \quad (11)$$

$$E_{T,\text{jet}} = E_{\text{jet}} \sin \theta_{\text{jet}}. \quad (12)$$

In general, jets with $E_T < 3 \text{ GeV}$ are not used in physics analyses at CDF.

3.2. Particle jets in MC

In MC simulation, particle jets are obtained using the same jet clustering algorithm on stable final state particles,¹ i.e. the sums in Eqs. (2)–(8) go over the stable particles instead of the towers. A particle jet includes any particles produced in the interaction, i.e. particles from the hard scattering process and also those from the underlying event (UE). Particles from additional overlapping interactions are not included.

4. Data and MC samples

In this section we describe the data and MC simulation samples used throughout this paper for studying and determining the jet response.

The following samples are used:

- **Test beam data:** The response of all calorimeters was first measured in a test beam. Test beam for the CEM, CHA, and WHA was taken in 1985 and 1988 [16,17] with a momentum range 5–180 GeV/c for electrons and 7–220 GeV/c for charged pions. The test beam for the plug calorimeters was taken in 1996 [18] with a momentum range 5.3–181 GeV/c for electrons and 8.6–231 GeV/c for charged pions.
- **Minimum bias:** This sample is collected requiring at least one $p\bar{p}$ interaction. It is triggered by activity in the luminosity counters, i.e. the trigger requires coincident hits in both the east and west CLC detectors. It is used for studying multiple interactions and the UE (see Sections 8 and 9). Tracks from this sample are also used for tuning the simulation (see Section 5).
- **Single track:** A special trigger was designed to take data with a high momentum track at p_T thresholds of 3, 7, and 10 GeV/c. These data are used to tune the central calorimeter response at larger p_T (see Section 5). The tracks in this data set are confined to the region in the COT where particles can traverse all available layers, that is $|\eta| < 1$.
- **Jet:** There are four samples triggered on at least one jet with transverse energy $E_T^{\text{jet}} > 20, 50, 70, \text{ and } 100 \text{ GeV}$ referred to as jet-20, jet-50, jet-70, and jet-100,

respectively. They are primarily used to calibrate the response as function of pseudo-rapidity (see Section 6). Apart from the jet-100 sample the data are taken with a fixed “prescale” depending on the p_T threshold. A prescale of e.g. 10 means that only 1 in 10 events passing the trigger requirements is recorded. There is another sample triggered on at least one trigger tower with $E_T > 5 \text{ GeV}$ referred to as single-tower-5.

- **γ -jet:** This sample is triggered on an isolated electromagnetic cluster with $E_T^{\gamma} > 25 \text{ GeV}$. It is used to cross-check many aspects of the calibration and to determine the systematic uncertainty on the OOC correction (see Section 9). The photon selection requirements are described in detail elsewhere [29].
- **$W \rightarrow e\nu_e$ and $W \rightarrow \mu\nu_\mu$:** These data are taken by an inclusive electron (e) or muon (μ) trigger with $E_T^e > 18 \text{ GeV}$ and $p_T^\mu > 18 \text{ GeV}/c$, respectively. The electron and muon identification is described in detail elsewhere [30]. The $W \rightarrow e\nu_e$ ($W \rightarrow \mu\nu_\mu$) sample is selected by requiring one electron (muon) with $E_T^e > 25 \text{ GeV}$ ($p_T^\mu > 25 \text{ GeV}/c$) and missing transverse energy $\cancel{E}_T > 25 \text{ GeV}$.
- **$Z \rightarrow e^+e^-$ and $Z \rightarrow \mu^+\mu^-$:** These data are taken with the same trigger to the previous W samples. They are selected by requiring two electrons (muons) with $E_T^e > 18 \text{ GeV}$ ($p_T^\mu > 20 \text{ GeV}/c$) and requiring the invariant mass of the electrons and muons to be between 76 and $106 \text{ GeV}/c^2$.
- **$J/\psi \rightarrow e^+e^-$ and $J/\psi \rightarrow \mu^+\mu^-$:** The $J/\psi \rightarrow e^+e^-$ data are taken with a dielectron trigger with $E_T^e > 2 \text{ GeV}$ for each electron. The $J/\psi \rightarrow \mu^+\mu^-$ data are taken with a dimuon trigger with $p_T^\mu > 1.5 \text{ GeV}/c$ for each muon. The dilepton invariant mass is required to be between 2.5 and $3.5 \text{ GeV}/c^2$ for the e^+e^- decay and between 3.0 and $3.2 \text{ GeV}/c^2$ for the $\mu^+\mu^-$ decay.

Corresponding MC samples are used for all processes. In all cases, MC samples are generated using both PYTHIA 6.216 [20] and HERWIG 6.505 [21] with CTEQ5L [23] parton distribution functions.

The following MC samples are generated:

- **Minimum bias and jet:** The inclusive $2 \rightarrow 2$ parton processes ($p\bar{p} \rightarrow q\bar{q} + X, p\bar{p} \rightarrow gq + X, p\bar{p} \rightarrow gg + X$) are generated at different thresholds for the transverse momentum of the outgoing partons, \hat{p}_T , greater than 0, 10, 18, 40, 60, 90, 150, 200, 300, 400, 500, 600 GeV/c. The sample with $\hat{p}_T > 0$ is referred to as minimum bias MC.
- **Single-particle:** Single charged particles are generated with a mixture of 60% π^\pm , 30% K^\pm and 10% p and \bar{p} .
- **γ -jet:** The processes $qg \rightarrow q\gamma + X$ and $q\bar{q} \rightarrow \gamma g + X$ are generated at different thresholds of the transverse momentum of the outgoing partons, $\hat{p}_T > 12, 20, \text{ and } 40 \text{ GeV}/c$.
- **W and Z:** W and Drell–Yan production is generated in both electron and muon decay channels as described in [30].

¹In PYTHIA and HERWIG, these are particles which have a lifetime long enough to not decay within the CDF detector volume.

- $J/\psi \rightarrow e^+e^-$ and $J/\psi \rightarrow \mu^+\mu^-$: This sample is generated using BGEM [25,26].
- $t\bar{t} \rightarrow WbWb$: Top pair production is generated using HERWIG. More details can be found in Ref. [39].
- $W+jets$: The ALPGEN 1.3 generator interfaced with HERWIG is used to simulate these type of events [39].

The matrix element of the hard scattering process, the UE, the higher order QCD correction (i.e. the parton showering process), and the fragmentation are all handled by PYTHIA and HERWIG. The matrix element is well known at leading order in QCD. However, the other three components are not fully calculable and thus modeled using an empirical approach. Note that PYTHIA and HERWIG use different models, which is helpful to study and understand the uncertainties associated with these effects. The modeling of the fragmentation and parton showering is mostly tuned to e^+e^- data. For modeling the underlying event we use a tuning optimized to describe CDF data from Run-I, which we refer to as “PYTHIA Tune A” [24]. For HERWIG the default parameters for the UE are used. The recent model for the UE, JIMMY [22], has not been used in this analysis.

After generation, the samples are processed through the CDF Run II detector simulation, which is described in detail in Section 5. They are then processed through the standard reconstruction program as the data. The details of particle and calorimeter jet reconstruction are in Section 3.

Throughout this article the data are primarily compared to PYTHIA MC samples but any differences between PYTHIA and HERWIG are discussed. Detailed comparisons between HERWIG and PYTHIA are presented in Section 10.

5. Calorimeter simulation

In this section we describe the simulation of the CDF calorimeter. A parameterized shower simulation is used with the simulation parameters tuned to describe the observed calorimeter response of single particles. The response of single isolated charged particles is measured using test beam data as well as minimum bias and single track trigger data from Run II. Similarly, the tuning of electromagnetic showers is based on electrons observed in $J/\psi \rightarrow e^+e^-$ and $Z \rightarrow e^+e^-$ decays. In the following, we first describe the shower parameterization, then the measurement of the calorimeter response is discussed, and finally the systematic uncertainty is assigned based on how well the MC simulation models the data.

5.1. Simulation of electromagnetic and hadronic showers

The CDF detector simulation uses GEANT [27] to track generated particles through the CDF detector and to simulate secondary physical processes such as energy loss, multiple scattering, and inelastic interactions. After the first inelastic interaction in the calorimeter, the particles are passed to the program GFLASH [28], a fast simulation of

electromagnetic and hadronic particle showers. GFLASH generates particle shower shapes within the calorimeter and computes the energy deposited in the calorimeter sensitive volumes, using parameterizations of the longitudinal and lateral shower profiles. The parameterizations of electromagnetic and hadronic showers are described in detail in Ref. [28] and are briefly outlined in this section.

5.1.1. Procedure

The simulation of electromagnetic and hadronic showers involves two steps. First, GFLASH calculates the spatial distribution of energy, E_{dp} , deposited by a shower within the calorimeter volume:

$$dE_{dp}(\vec{r}) = \frac{E_{dp}}{2\pi} L(z) T(r) dz dr \quad (13)$$

where $L(z)$ is the longitudinal energy profile which depends on the shower depth z , and $T(r)$ is the lateral shower profile which depends on the radial distance r from the trajectory of the particle. This parameterization takes into account the dependence on the incident particle energy and shower fluctuations, and further considers the repetitive sampling structure of the detector volume. Second, the fraction of the deposited energy which is visible to the active medium, $E_{vis}(\vec{r})$, is determined. $E_{vis}(\vec{r})$ is computed taking into account the relative sampling fractions of minimum ionizing particles, electromagnetically and hadronically showering particles. Two tunable parameters are the relative sampling fractions for electrons, S_e/S_{mip} , and for hadrons, S_{had}/S_{mip} , compared to the sampling fraction of a particle that does not interact inelastically in the calorimeter, S_{mip} .

5.1.2. Longitudinal shower profile

Electromagnetic showers. For the simulation of the longitudinal profile of electromagnetic showers, GFLASH assumes that they follow the Γ -distribution:

$$L_{em}(z) = \frac{x^{\alpha_{em}-1} e^{-x}}{\Gamma(\alpha_{em})}, \quad x = \beta_{em} z(X_0) \quad (14)$$

where z is the shower depth, measured in units of radiation lengths, X_0 . The parameters α_{em} and β_{em} are Gaussian distributed, and parameterized as a function of incident particle energy. The longitudinal profile of each shower is simulated by choosing an $(\alpha_{em}, \beta_{em})$ pair at random.

Hadronic showers. GFLASH distinguishes three classes of hadronic showers: purely hadronic showers (\mathcal{L}_h) whose propagation scales with the absorption length λ_0 , showers where a π^0 is produced in the first inelastic interaction (\mathcal{L}_f) and whose propagation scales with radiation length X_0 , and showers from π^0 which are produced at a later stage of the hadronic showering process (\mathcal{L}_l).

The hadronic showers in GFLASH are calculated as a superposition of the three shower classes:

$$\begin{aligned} dE_{dp} = & f_{dp} E_{inc} [c_h \mathcal{L}_h(x_h) dx_h \\ & + c_f \mathcal{L}_f(x_f) dx_f + c_l \mathcal{L}_l(x_l) dx_l] \end{aligned} \quad (15)$$

with

$$\mathcal{L}_h(x_h) = \frac{x_h^{\alpha_h-1} e^{-x_h}}{\Gamma(\alpha_h)}, \quad x_h = \beta_h z(\lambda_0) \quad (16)$$

$$\mathcal{L}_f(x_f) = \frac{x_f^{\alpha_f-1} e^{-x_f}}{\Gamma(\alpha_f)}, \quad x_f = \beta_f z(X_0) \quad (17)$$

$$\mathcal{L}_l(x_l) = \frac{x_l^{\alpha_l-1} e^{-x_l}}{\Gamma(\alpha_l)}, \quad x_l = \beta_l z(\lambda_0). \quad (18)$$

The coefficients c_h , c_f , and c_l are the fractions of the three contributions normalized such that $c_h + c_f + c_l = 1$. The factor f_{dp} is the fraction of deposited energy with respect to the energy of the incident particle, and takes the intrinsic losses during the hadronic shower development into account.

The probabilities of the three classes c_h , c_f , and c_l depend on the incident energy and are correlated through:

$$c_h(E) = 1 - f_{\pi^0}(E), \quad c_f(E) = f_{\pi^0}(E)(1 - f_{\pi^0}^l(E)), \\ c_l(E) = f_{\pi^0}(E)f_{\pi^0}^l(E) \quad (19)$$

where $f_{\pi^0}(E)$ is the probability that a hadronic shower contains any π^0 and $f_{\pi^0}^l(E)$ is the probability that a π^0 is produced “late”, i.e. not in the first interaction.

In total, the longitudinal hadronic shower development depends on 18 partially correlated parameters: the mean and σ values of the three different α - and β -values for each of the three shower types, and the fractions f_{dp} , f_{π^0} and $f_{\pi^0}^l$. For the electromagnetic shower development there are only four parameters: the mean and σ values of α_{em} and β_{em} .

5.1.3. Lateral shower profile

The parameterization for the lateral energy profile of electromagnetic and hadronic showers is taken to be

$$T(r) = \frac{2rR_{50}^2}{(r^2 + R_{50}^2)^2}. \quad (20)$$

R_{50} is given in the units of Molière radius R_M for electromagnetic showers, and absorption length, λ_0 , for hadronic showers. R_{50} is an approximate log-normal distribution, with a mean value $\langle R_{50}(E, z) \rangle$ and variance $\sigma_{R_{50}}$ parameterized as a function of the incident particle energy, E , and the shower depth, z ,

$$\langle R_{50}(E, z) \rangle = [R_1 + (R_2 - R_3 \log E)z]^n, \quad n = 1, 2 \quad (21)$$

$$\sigma_{R_{50}}(E, z) = [(S_1 + (S_2 - S_3 \log E)z)\langle R_0(E, z) \rangle]^2. \quad (22)$$

The z -evolution of the lateral spreading is linear for hadronic showers ($n = 1$) and quadratic for electromagnetic showers ($n = 2$). The electromagnetic and hadronic profiles are determined by their own set of adjustable R_i and S_i values, thus giving a total of 14 parameters.

5.1.4. Tuning to CDF data

The GFLASH longitudinal and lateral hadronic shower parameters were tuned using single, isolated tracks selected from minimum bias data ($0.5 < p < 2.5 \text{ GeV}/c$ in the central and $0.5 < p < 5 \text{ GeV}/c$ for the plug calorimeter) and test

beam data ($7 \leq p \leq 220 \text{ GeV}/c$). The electromagnetic shower parameters were tuned using test beam data and compared to data and simulation for $Z \rightarrow e^+e^-$ events. Further adjustments in addition to the above parameters are made to the energy deposited at the boundary between central and plug calorimeter.

Given the limited availability of CDF isolated single track and test beam data with current statistics, not all of the 34 parameters described above were tuned to CDF data. Furthermore, the current tuning of various parameters based on CDF data is restricted to relatively low particle momenta, below $2.5 \text{ GeV}/c$. Since GFLASH was originally developed for the H1 experiment at DESY, for the remaining parameters, we use their default setting [28]. At this stage, the parameters that are tuned to CDF data are α_h , α_l , β_f , f_{dp} , and f_{π^0} for both central and plug calorimeters, four of the parameters that characterize the lateral profile for the central calorimeter, R_1 , R_2 , S_1 , and S_2 , and the relative sampling fractions S_e/S_{mip} and $S_{\text{had}}/S_{\text{mip}}$ for the plug calorimeters.

Tuning these parameters gives a good description of the single track data as will be seen in the following sections. However, since the tuning was done on a limited data set there are some discrepancies with the latest single track data samples that extend up to momenta of $20 \text{ GeV}/c$. The newly collected data that are presented in the following sections will be used in the near future to further tune the simulation parameters. This is particularly important for the plug calorimeters.

5.2. Calorimeter response to hadronically showering particles

Stable charged and neutral hadrons carry approximately 70% of the jet energy and therefore a good description of their response is pivotal for a good simulation of the jet energy measurement. The hadronic shower development can best be studied using isolated charged particles.

In the rapidity range covered by the central calorimeters, CDF has an excellent tracking coverage and efficiency. The measurement of the response in the plug calorimeters is more difficult since there is no track trigger available and the tracking efficiency is limited.

5.2.1. Procedure

Reconstructed tracks are extrapolated to the impact point at the position of the CES or PES detectors, taking the magnetic field into account. If a track is extrapolated to a calorimeter tower, this tower is considered to be the target tower. Tracks are required to point to the inner 0.9×0.9 contour of the target tower to stay away from the tower edges, otherwise they are not considered.

From the eight towers surrounding the target tower, the measurement of the CEM energy uses a 2×2 subset containing the target tower and those three adjacent towers closest to the track impact point. For the CHA, the shower spread is typically larger and all eight adjacent towers are

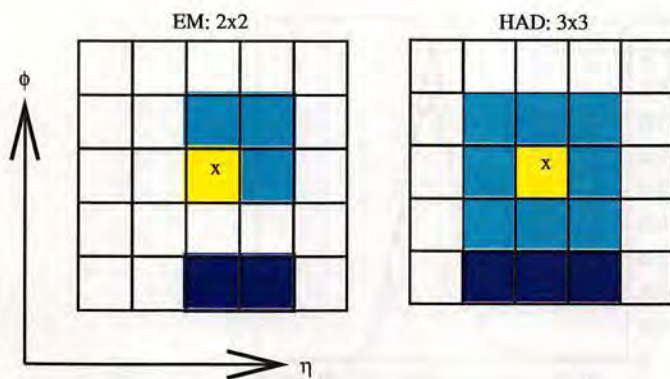


Fig. 4. Illustration of the target tower for the electromagnetic (EM) and the hadronic (HAD) sections used in the tuning of charged hadrons. The lightest shading region is the target tower. The “x” marks the impact point of the track. The light and medium shading region is the signal region and the darkest shading illustrates the background region. The horizontal axis represents the η direction and the vertical represents the ϕ direction.

considered in the signal energy definition. An illustration of the target tower and signal region definitions is shown in Fig. 4 for the CEM and the CHA.

The signal tower region may contain additional particles overlapping with the direction of the primary track that is being analyzed. This background is reduced by requiring no additional tracks within a 7×7 block of towers around the target tower. In addition, no energy depositions above 1 GeV in the CES detector are allowed within the 7×7 blocks of towers except within $\Delta R = \sqrt{(\eta_{\text{CES}} - \eta_{\text{track}})^2 + (\phi_{\text{CES}} - \phi_{\text{track}})^2} < 0.03$ around the extrapolated track position, where ϕ_{CES} (ϕ_{track}) and η_{CES} (η_{track}) denote the azimuthal angle and the pseudo-rapidity of the CES cluster (track). The first requirement removes charged particles and the second requirement mostly removes photons.

Even after these isolation requirements, some overlap background remains. The background is estimated using

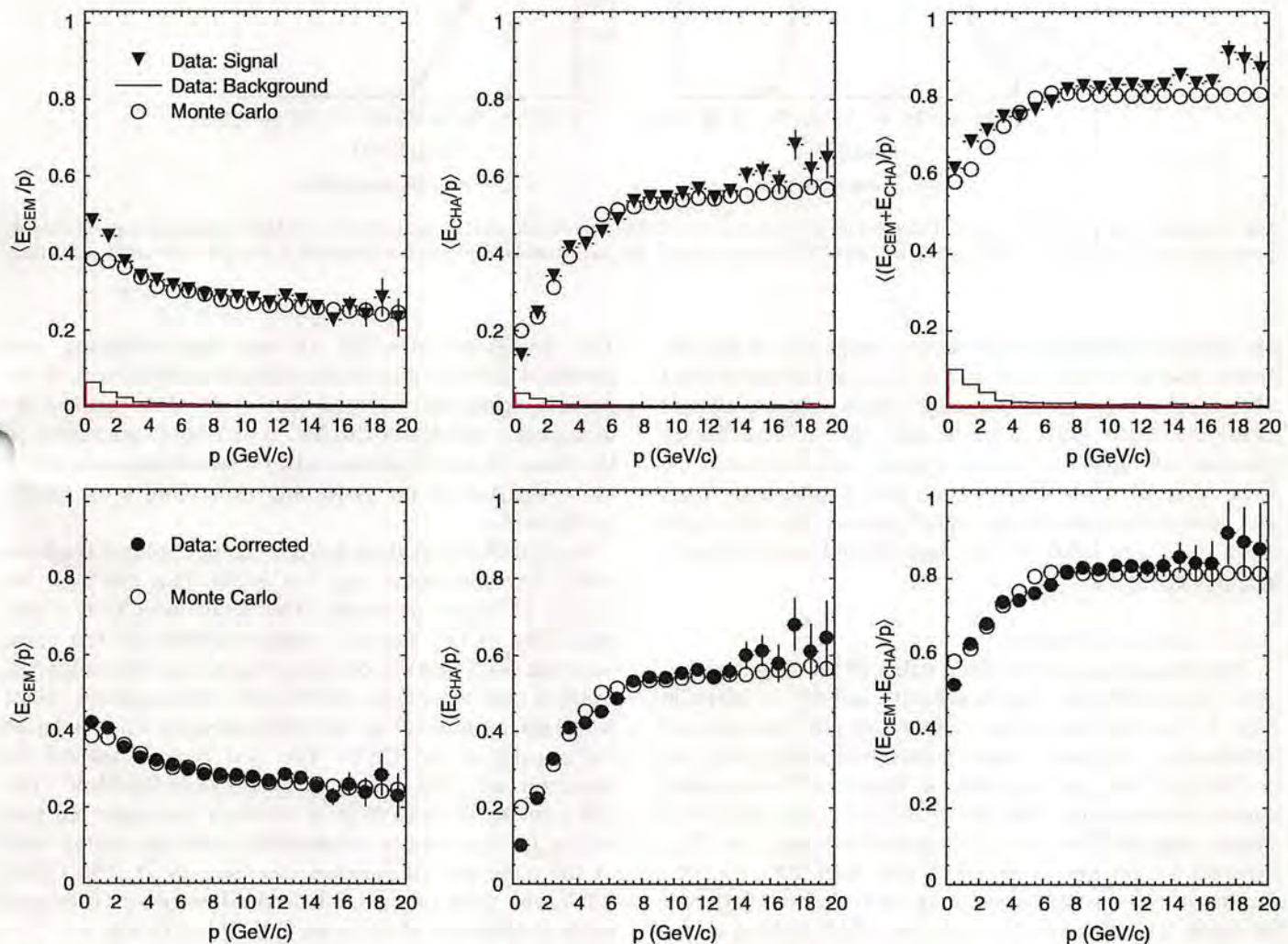


Fig. 5. Fractional energy observed in the central calorimeter as a function of incident particle momenta. The top row shows (E_{CEM}/p) , (E_{CHA}/p) and $((E_{\text{CEM}} + E_{\text{CHA}})/p)$ for data signal (triangles), background (histogram) and for single track MC simulation (open circles). The bottom row shows the same distributions for data after background subtraction (full circles) and MC simulation (open circles).

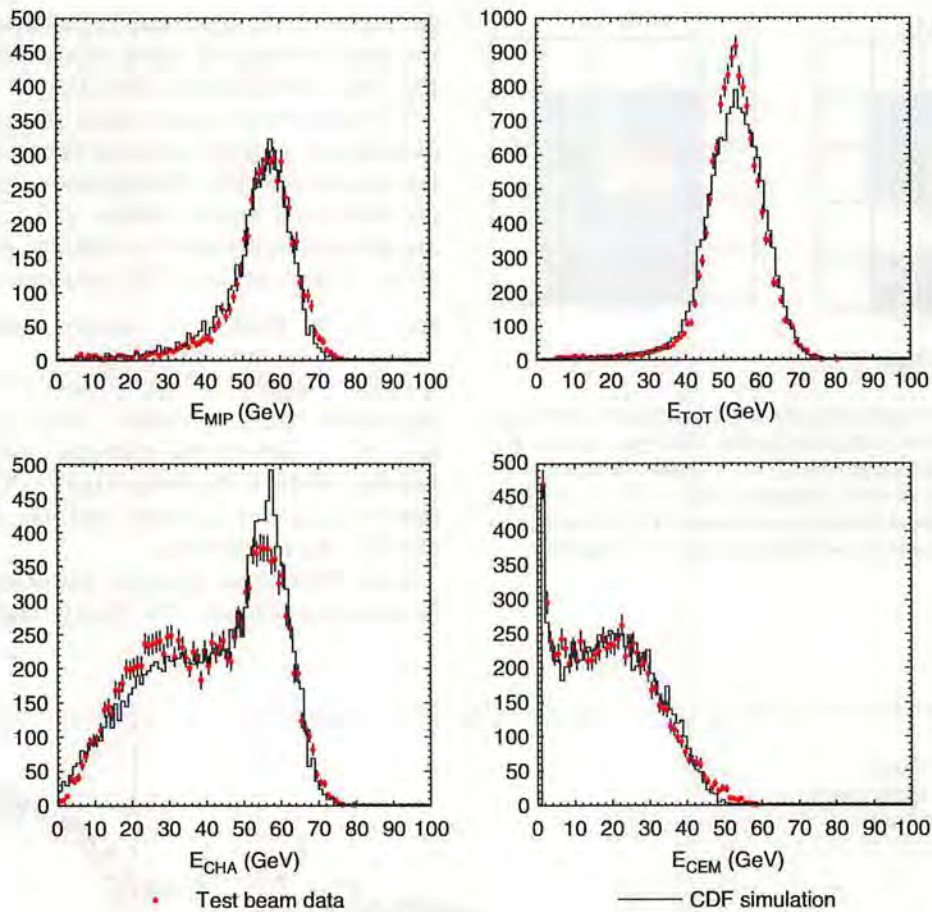


Fig. 6. Energy observed in CHA for particles that do not interact in the CEM (top left) and total energy in CHA + CEM (top right). Energy for charged pions with $p = 57 \text{ GeV}/c$ for CHA (bottom left) and CEM (bottom right). The test beam data (points) are compared to the CDF simulation (solid line).

the energy deposited in the same η range but within the towers along the edge in ϕ of a 5×5 tower group around the target tower, using the edge which is more distant from the track impact point, see Fig. 4. The energy measured in those background regions is then scaled to the area covered by the signal region and is subtracted from the energy measured in the signal regions. For the single track MC, the effect of the background subtraction is negligible.

5.2.2. Central calorimeter

The comparison of the mean value of the E/p distribution, $\langle E/p \rangle$, between single track data and MC is shown in Fig. 5. The data are shown before and after background subtraction. The background contributes significantly for $p < 3 \text{ GeV}/c$ but is negligible at higher p . For particle momenta increasing from 0.5 to $20 \text{ GeV}/c$, the fraction of energy deposited in the CEM drops from 40% to 25%, whereas the fraction in the CHA rises from 20% to 55%. In total, $\langle E/p \rangle$ rises from about 0.5 at $p = 0.5 \text{ GeV}/c$ to about 0.8 at $p \geq 5 \text{ GeV}/c$. For $p > 5 \text{ GeV}/c$ the response is almost independent of p . In general, the mean $\langle E/p \rangle$ agrees well between the data and the simulation separately for the CEM and the CHA energies and for their sum.

The deviations observed at very low momenta and around $4 \text{ GeV}/c$ are probably related to differences in the particle spectrum between data and MC caused by momentum cutoffs in the MC and trigger thresholds in the data. These differences will be taken into account in the evaluation of the systematic uncertainties on the jet energy scale.

Beyond $20 \text{ GeV}/c$ there are not enough isolated tracks to verify the simulation, and test beam data are used for studies of higher momenta. The simulated CEM, CHA, and CEM + CHA energy is compared with the test beam response for $57 \text{ GeV}/c$ pions in Fig. 6. For this study the charged pion sample is divided into two categories: pions which do not interact in the CEM and pions which interact inelastically in the CEM. The first type is selected by requiring the CEM energy to be less than 500 MeV .² The CHA energy of these pions is shown in the upper left plot in Fig. 6. This category is also used to set the energy scale of the hadronic calorimeters (see Section 7). The CEM, CHA, and total energy of the second category of charged pions is displayed in the other three plots in Fig. 6.

²The mean CEM response for non-interacting particles is about 300 MeV .

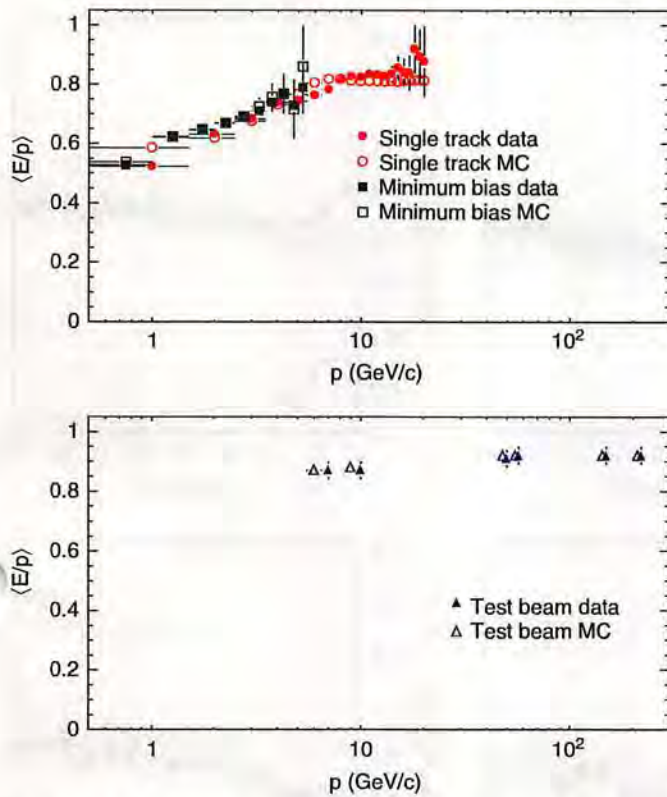


Fig. 7. $\langle E/p \rangle$ for the central calorimeter versus particle momentum p . The top plot shows the in situ minimum bias (circles) and single track data (squares) compared to the simulation (open symbols). The bottom plot compares the test beam data (closed triangles) to the simulation (open triangles). The error bars on the minimum bias and single track data are statistical. For the test beam data we display an uncertainty of 3.5% due to the systematic uncertainty on the test beam momentum scale which is correlated between all the data points. For the test beam comparison, the MC points have been shifted slightly in p -value to allow a better visual comparison.

The data are reasonably well described by the simulation and the differences between data and simulation will be taken as part of the systematic uncertainties.

Fig. 7 shows a summary plot of the response $\langle E/p \rangle$ for minimum bias, single track trigger, and test beam data together with the MC expectation.

Note, that in test beam the particles were aimed at the center of the tower while for the single track data the inner 81% of the towers are used. This difference in selection is estimated to cause about a 5% higher response for the test beam data. In addition, for the test beam, only one central calorimeter tower (covering the region $0.3 < |\eta| < 0.4$) was used. Therefore, the data cannot be compared directly between test beam and in situ measurements. However, in each case the results are consistent between data and simulation.

5.2.3. Plug calorimeter

In the plug calorimeter, the same procedure is used as in the central calorimeters. However, due to the smaller tower size, a larger fraction of the incident particle momentum is

measured by neighboring towers. Thus, for the $\langle E/p \rangle$ analysis, two adjacent towers in azimuth are treated as one target tower.

Some difficulties arise in the plug calorimeter which are not present in the central calorimeter:

- The tracking efficiency is rather low in the forward region of the detector, decreasing from 70% at $|\eta| \approx 1.2$ to 30% at $|\eta| = 2.2$. Thus, the background rejection is less efficient in the plug than in the central region where the efficiency is nearly 100%. Since the tracking efficiency in the very forward region $|\eta| > 2.2$ is even lower, this method cannot be used to evaluate the response.
- The triggers dedicated to collect high momentum tracks are limited to the COT coverage $|\eta| < 1.0$.
- The momentum resolution for tracks is poorer than in the central region because the track reconstruction is mostly based on the silicon vertex detector. This results in a less accurate determination of the reference momentum, particularly for high momentum. However, this problem can be minimized by using tracks with partial coverage by the COT. Tracks with combined COT and silicon hits are available up to $|\eta| < 1.8$.

A measurement of the single particle response in the plug calorimeter using combined COT and silicon tracks is shown in Fig. 8 for single track trigger data and simulation. The background is larger than in the central calorimeter as expected. After background subtraction the data and simulation agree well at low momenta but deviations of up to 13% are observed between 5 and 10 GeV/c. Note that, for the tuning relevant for this article, the data at the medium momentum range were not available. Using the data shown here the plug simulation will be improved in the near future.

Fig. 9 shows $\langle E/p \rangle$ versus p for the plug calorimeter for minimum bias data and test beam data compared with the corresponding simulations. At low momenta the response is about 60%, increasing to nearly 100% at high momenta.

Due to the discrepancies described above the plug calorimeter simulation is not used for determining the absolute jet energy scale. An additional calibration is made where the plug calorimeter response is calibrated with respect to the response of the central calorimeter using dijet events as will be described in Section 6. Therefore, no systematic uncertainty is associated directly with the $\langle E/p \rangle$ measurements for the plug calorimeter.

5.3. Calorimeter response to electromagnetically showering particles

On average, about 30% of the particles in a jet are neutral pions which mostly decay into two photons: $\pi^0 \rightarrow \gamma\gamma$. Therefore, a good understanding of the calorimeter response to electromagnetically showering particles is important. The electromagnetic single particle response

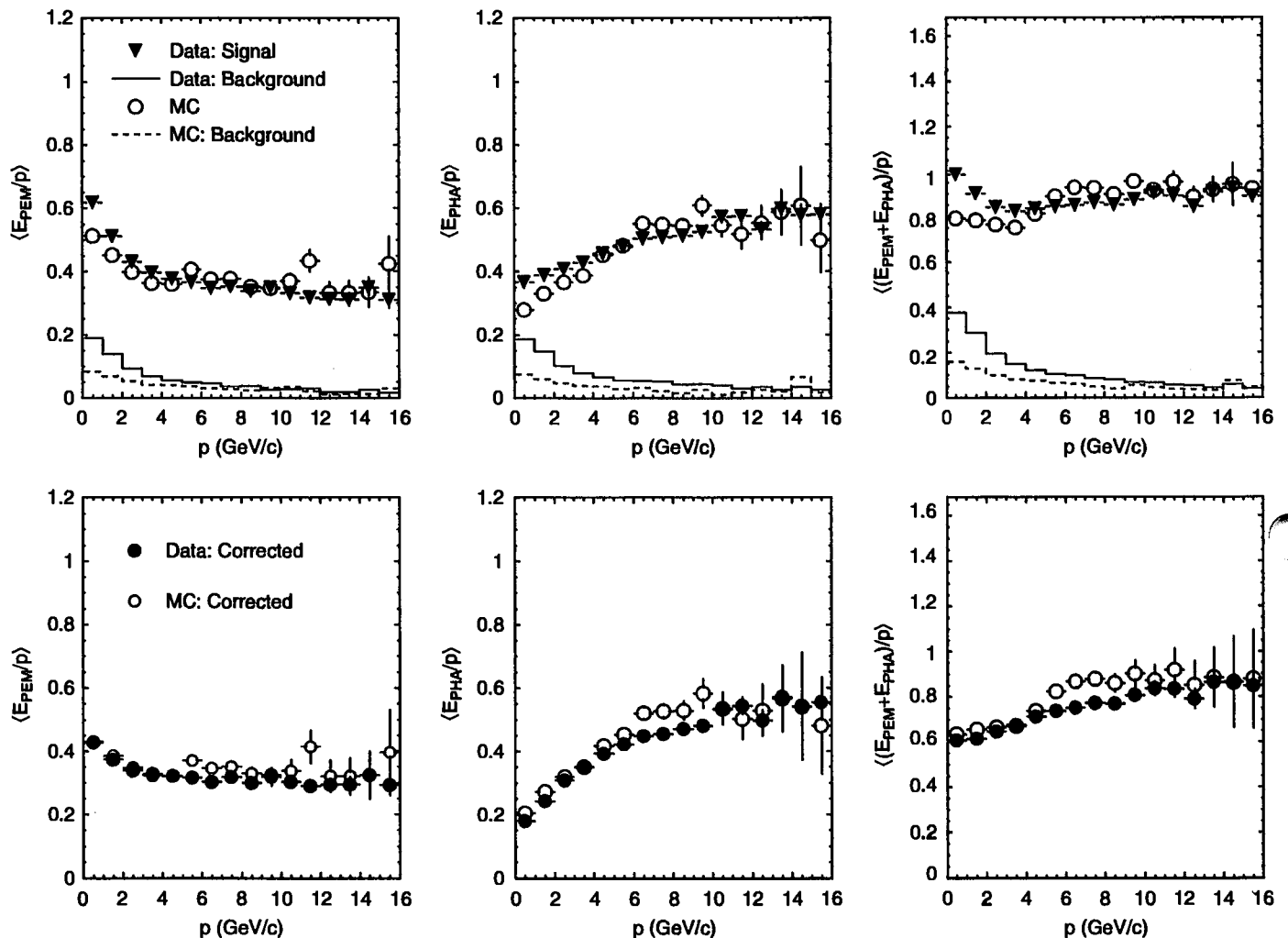


Fig. 8. $\langle E/p \rangle$ observed in the plug calorimeter as a function of incident particle momenta. The top rows shows E_{PEM}/p , E_{PHA}/p and $(E_{\text{PEM}} + E_{\text{PHA}})/p$ for data signal (closed triangles), background (solid line) and for MC simulation signal (open circles) and background (dashed line). The bottom row shows the same distributions for data after background subtraction (full circles) and MC simulation (open circles). The tuning of the calorimeter simulation used tracks up to momentum of 5 GeV/c.

is studied similarly to the hadronic response, using the track momentum as reference and EM energies measured in the target tower and the two towers adjacent in η around the track impact point.

A comparison of the $\langle E/p \rangle$ response for electrons and positrons is shown in Fig. 10 in $W \rightarrow e^\pm v_e$ and $J/\psi \rightarrow e^+e^-$ events. Overlaid is the simulated response from corresponding MC samples. A certain momentum dependence of $\langle E/p \rangle$ arises from the W and J/ψ selection cuts, due to final state radiation of photons. The simulation reproduces the data to better than 1% accuracy.

5.4. Systematic uncertainty

Fig. 11 shows the difference in the energy response between data and MC and is used to estimate the systematic uncertainty on the central calorimeter energy determined from the difference between data and simulation for charged hadrons.

We have derived the following momentum-dependent estimates for the average differences:

- 1.5% for $p < 12 \text{ GeV}/c$;
- 2.5% for $12 < p < 20 \text{ GeV}/c$;
- 3.5% for $p > 20 \text{ GeV}/c$.

The uncertainties at $p < 20 \text{ GeV}/c$ directly reflect the limited performance of the calorimeter simulation as well as limited available single isolated track statistics at medium momenta. The uncertainties at $p > 20 \text{ GeV}/c$ are due to uncertainties in the test beam momentum scale (2%) and the shorter integration time in the CDF detector readout compared to the test beam measurement (1.5%) (see Refs. [16,17] and Section 2). Adding those uncertainties linearly we obtain the systematic uncertainty for $p > 20 \text{ GeV}/c$ of 3.5%.

The $\langle E/p \rangle$ measurements presented so far are only sensitive to the inner 81% of the tower. The instrumentation

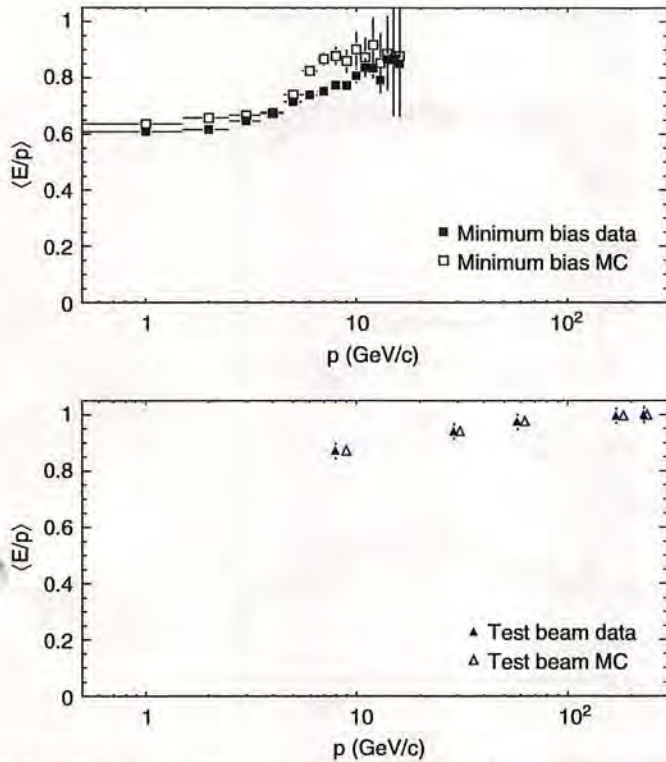


Fig. 9. $\langle E/p \rangle$ versus p for the plug calorimeters. The upper plot shows a comparison of single track and minimum bias data (closed squares) and MC (open squares). The bottom plot shows the comparison of test beam data (closed triangles) and single track MC (open triangles). The tuning of the calorimeter simulation used tracks up to momentum of $5 \text{ GeV}/c$. For the test beam comparison the MC points have been shifted slightly in p -value to allow a better visual comparison.

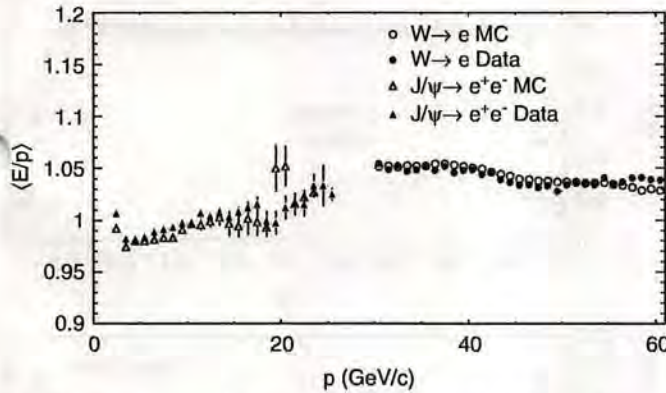


Fig. 10. $\langle E/p \rangle$ versus p for electrons and positrons from $J/\psi \rightarrow e^+e^-$ and $W \rightarrow e^\pm\nu_e$ data (closed triangles and circles) and MC samples (open triangles and circles) samples.

between the tower ϕ -boundaries is limited, and the exact modeling of this region in the simulation is difficult. Fig. 12 shows $\langle E/p \rangle$ versus relative ϕ (ϕ_{rel}), that is the azimuthal angle of the track impact point with respect to the target tower center. The normalization of ϕ_{rel} is chosen such that $\phi_{\text{rel}} = 0$ represents the tower center and $\phi_{\text{rel}} = \pm 1$ the tower boundaries. Shown are data and simulation for $p = 3\text{--}5$ and $12\text{--}16 \text{ GeV}/c$.

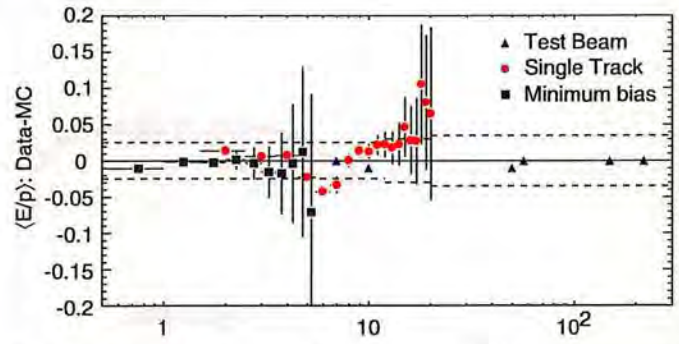


Fig. 11. Difference between $\langle E/p \rangle$ of data and MC versus particle momentum p . Shown is the difference for minimum bias data and MC (squares), single track data and MC (circles), and test beam data and MC (triangles). The dashed lines indicate the quoted systematic uncertainties. The error bars on the minimum bias and single track data are statistical. For the test beam data we do not display any uncertainty.

Data and MC differ by up to 10% near the ϕ -boundaries ($|\phi_{\text{rel}}| > 0.9$). Similar discrepancies are seen at the η boundaries of the towers. These 10% differences are taken as systematic uncertainty. Since these boundaries in η and ϕ correspond to 19% of the total tower area, the 10% uncertainty at the boundaries translates into a 1.9% systematic uncertainty on the overall particle response to charged hadrons.

Fig. 13 shows the difference in $\langle E/p \rangle$ between data and simulation for electrons. The data and the simulation agree to within 1% which is taken as the systematic uncertainty. This measurement only uses tracks pointing to the inner 84% of a tower in azimuth, ϕ_{rel} , as a consequence of the electron selection that involves a CES energy cluster fiducial cut.

The remaining 16% at the boundaries in ϕ are studied using $Z \rightarrow e^+e^-$ events where one electron is identified using the standard criteria [30] and the second electron is just taken to be the highest momentum track with $35 < p < 55 \text{ GeV}/c$ in the angular range covered by the central calorimeter. There is no requirement on the energy measured in the calorimeter and thus the measurement is unbiased toward the calorimeter response. The invariant mass between the electron and the candidate track is required to be within $10 \text{ GeV}/c^2$ of the Z boson mass. For these track-based electron candidates, $\langle E/p \rangle$ is shown in Fig. 14 as function of ϕ_{rel} .

Fig. 14 also shows the difference between data and simulation in $\langle E/p \rangle$ in $Z \rightarrow e^+e^-$ events as a function of relative ϕ . A discrepancy of about 10% is observed between data and simulation at $|\phi_{\text{rel}}| > 0.84$. This region corresponds to 16% of the tower area, thus causing an overall 1.6% difference between data and simulation for the response of electromagnetic particles.

A summary of the systematic uncertainties is given in Table 1. These uncertainties are uncorrelated and added in quadrature. The overall systematic uncertainty on the energy of charged hadrons is thus 2% for $p < 12 \text{ GeV}/c$,

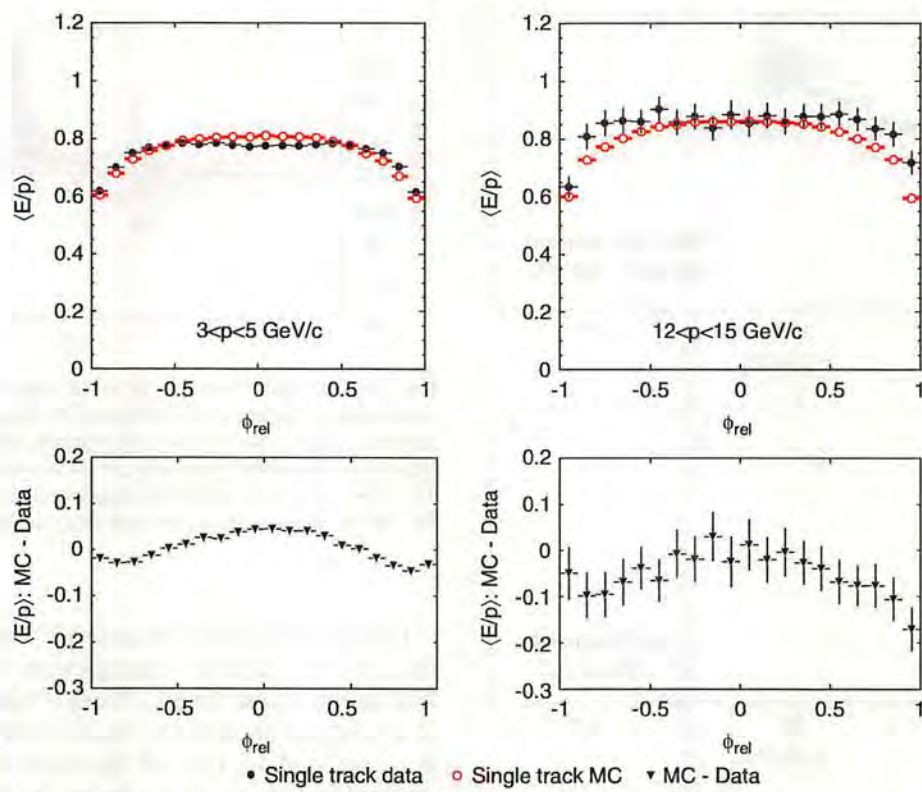


Fig. 12. $\langle E/p \rangle$ versus ϕ_{rel} for particles with momenta between 3 and 5 GeV/c (left) and for particles with momenta between 12 and 16 GeV/c (right). Top: data (closed circles) and MC (open circles). Bottom: difference between data and MC for the corresponding momentum ranges.

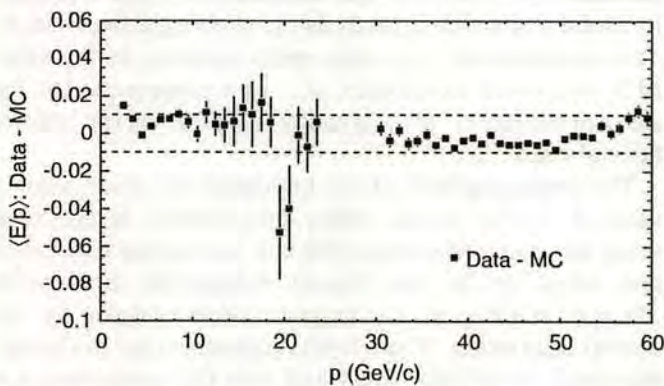


Fig. 13. Difference between $\langle E/p \rangle$ in data and simulation versus p for electrons from $J/\psi \rightarrow e^+e^-$ and $W \rightarrow e^\pm\nu_e$ (closed squares). The individual distributions for data and simulation are shown in Fig. 10. The dashed line indicates the systematic uncertainty on the electromagnetic energy scale.

3% for $12 < p < 20 \text{ GeV}/c$ and 4% for $p > 20 \text{ GeV}/c^2$. The total systematic uncertainty on the energy of electromagnetically showering particles is 1.7% independent of the momentum.

6. η -Dependent corrections

After the calorimeter energy calibrations described in Section 2, the response of the CDF calorimeter is not

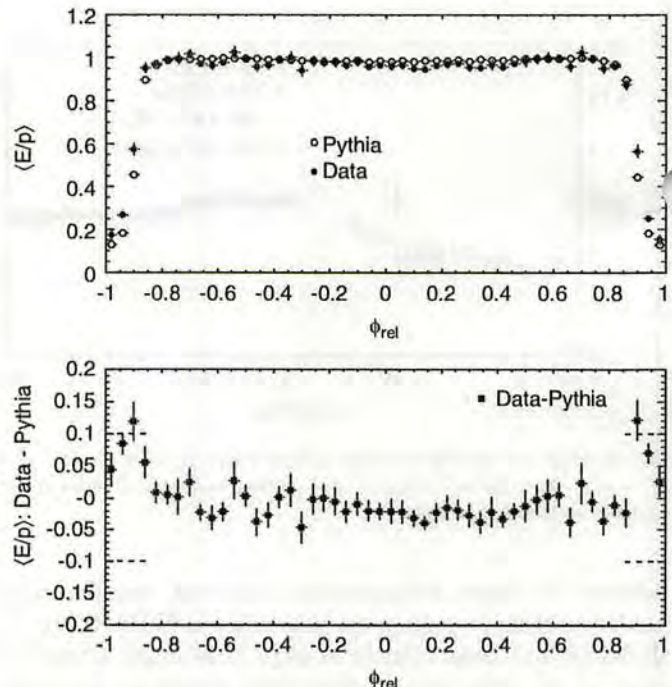


Fig. 14. Top: $\langle E/p \rangle$ versus ϕ_{rel} for electrons in $Z \rightarrow e^+e^-$ events. $\langle E/p \rangle$ is shown as a function of relative ϕ . Shown are data (closed circles) and simulation (open circles). Bottom: the difference in $\langle E/p \rangle$ between data and simulation for electrons.

uniform in pseudo-rapidity. The dependencies on η arise from the separation of calorimeter components at $\eta = 0$ where the two halves of the central calorimeter join and at $|\eta| \approx 1.1$ where the plug and central calorimeters join. The different responses of the plug and central calorimeters also cause a dependence on η . The η -dependent corrections are introduced to flatten the η dependence of the calorimeter response. The method implicitly also includes corrections for both the transverse spreading of calorimeter showers

Table 1

Summary of the relative uncertainties due to the modeling of the simulation of charged hadron showers and electromagnetic (EM) showers in the central calorimeter

| p (GeV/c) | 0–12 | 12–20 | >20 |
|--|------|-------|-----|
| $\langle E/p \rangle$ response to hadrons | | | |
| Total tower (%) | 1.5 | 2.5 | 3.5 |
| Near tower ϕ and η -boundaries (%) | 1.9 | 1.9 | 1.9 |
| Total for hadrons (%) | 2.5 | 3.0 | 4.0 |
| $\langle E/p \rangle$ response to EM particles | | | |
| Total tower (%) | 1.0 | 1.0 | 1.0 |
| Near tower ϕ -boundary (%) | 1.6 | 1.6 | 1.6 |
| Total for EM particles (%) | 1.7 | 1.7 | 1.7 |

All the uncertainties refer to the effect on the entire tower energy (see text). The total uncertainty is the quadratic sum of the individual uncertainties weighted with the area covered by the individual measurements.

outside the jet cone and any η dependence of gluon radiation and multiple parton interactions.

6.1. Correction procedure

The η -dependent corrections are obtained using the “dijet-balancing method”. They are determined based on the assumption that the two jets in dijet events should be balanced in p_T in the absence of hard QCD radiation. To determine the corrections, we define a jet with $0.2 < |\eta| < 0.6$ as a “trigger jet” and define the other jet as a “probe jet”. When both jets are in the region of $0.2 < |\eta_{\text{jet}}| < 0.6$, the trigger and probe jets are assigned randomly.

The p_T balancing fraction f_b is then formed:

$$f_b \equiv \frac{\Delta p_T}{p_T^{\text{ave}}} = \frac{p_T^{\text{probe}} - p_T^{\text{trigger}}}{(p_T^{\text{probe}} + p_T^{\text{trigger}})/2} \quad (23)$$

where p_T^{trigger} and p_T^{probe} are the transverse momenta of the trigger and probe jet, respectively. The correction factor required to correct the probe jet can then be inferred through

$$\beta_{\text{dijet}} \equiv \frac{2 + \langle f_b \rangle}{2 - \langle f_b \rangle}. \quad (24)$$

Note, that β_{dijet} is mathematically equal to $p_T^{\text{probe}}/p_T^{\text{trigger}}$. However, by inferring β_{dijet} from f_b we reduce the sensitivity of our measurement to non-Gaussian tails since

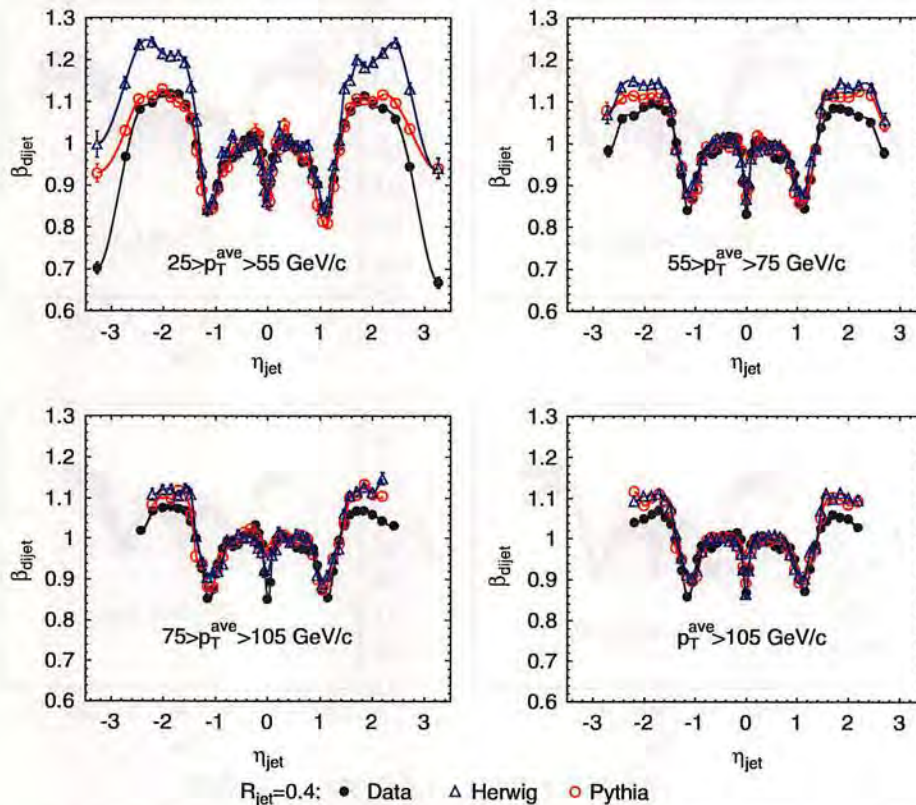


Fig. 15. Dijet balance, $\beta_{\text{dijet}} = p_T^{\text{probe}}/p_T^{\text{trigger}}$, as a function of η_{jet} in data, HERWIG, and PYTHIA MC samples for $R_{\text{jet}} = 0.4$ jets. Shown are the corrections for jet-20, jet-50, jet-70, and jet-100 jet samples, corresponding to $25 < p_T^{\text{ave}} < 55 \text{ GeV}/c$, $55 < p_T^{\text{ave}} < 75 \text{ GeV}/c$, $75 < p_T^{\text{ave}} < 105 \text{ GeV}/c$, and $p_T^{\text{ave}} > 105 \text{ GeV}/c$, respectively. The lines show the interpolation between the individual measurements used for correcting jets.

the f_b distribution is in good approximation a Gaussian distribution unlike the distribution of $p_T^{\text{probe}}/p_T^{\text{trigger}}$.

The η -dependent corrections are defined as $1/\beta_{\text{dijet}}$ and they are determined separately for data and MC and for different p_T^{jet} bins. For corrections obtained from data the samples single-tower-5, jet-20, jet-50, jet-70, and jet-100 are used. The corrections for the MC are obtained from the jet samples generated with the PYTHIA MC.

Several cuts are placed to reduce the effects of QCD radiation:

- The jets are required to be back to back in the $r-\phi$ plane, i.e. the difference of their azimuthal angle, $\Delta\phi(\text{jet}_{\text{probe}}, \text{jet}_{\text{trigger}})$, should be larger than 2.7 rad.
- If a third jet is present in the event, the p_T of this third jet should be less than 7 GeV/c for minimum bias data, less than 8 GeV/c for the samples triggered on 20 GeV or 50 GeV jets, and less than 10 GeV/c for the samples triggered on 70 GeV or 100 GeV jets.
- The average $p_T^{\text{ave}} = (p_T^{\text{jet}1} + p_T^{\text{jet}2})/2$ of the two jets is required to be 5 GeV/c higher than the trigger threshold of the respective sample.
- The significance of missing E_T is defined as $E_T/\sqrt{\sum_i E_{T,i}}$, where the sum extends to all the calorimeter towers. It is required to be less than

$$2\sqrt{\text{GeV}} + 0.018 \times p_T^{\text{leading-jet}}/\sqrt{\text{GeV}} \quad \text{for } p_T^{\text{leading-jet}} > 55 \text{ GeV}/c \text{ and less than } 3\sqrt{\text{GeV}} \text{ otherwise.}$$

In Fig. 15, the dijet balance β_{dijet} is shown for data, HERWIG, and PYTHIA MC samples for a jet cone size of $R_{\text{jet}} = 0.4$ and four transverse momentum regions $25 < p_T^{\text{ave}} < 55 \text{ GeV}/c$, $55 < p_T^{\text{ave}} < 75 \text{ GeV}/c$, $75 < p_T^{\text{ave}} < 105 \text{ GeV}/c$ and $p_T^{\text{ave}} > 105 \text{ GeV}/c$. Figs. 16 and 17 show the equivalent plots for $R_{\text{jet}} = 0.7$ and $R_{\text{jet}} = 1.0$, respectively. The lines in Figs. 15–17 show the interpolation between the individual measurements, and inverse of these functions is taken to be the η -dependent correction factor.

It is seen that $\beta_{\text{dijet}} \approx 1$ in the region where the trigger jet is selected, $0.2 < |\eta| < 0.6$, for both the data and the simulation. The dips at $|\eta| \approx 0$ and ± 1.1 are due to the gap between calorimeters in these regions, resulting in a lower average response. In the plug region, $|\eta| > 1.2$, the calorimeter response is higher than in the central region by about 10% at low p_T^{ave} and 5% at high p_T^{ave} .

Both PYTHIA and HERWIG reproduce the data well up to $|\eta| = 1.4$ at all p_T^{ave} . At larger $|\eta|$ and for $p_T^{\text{ave}} > 55 \text{ GeV}/c$ a difference of about 4% between data and simulation is observed. At $p_T^{\text{ave}} < 55 \text{ GeV}/c$ HERWIG differs significantly from the data and PYTHIA in the forward region. Due to

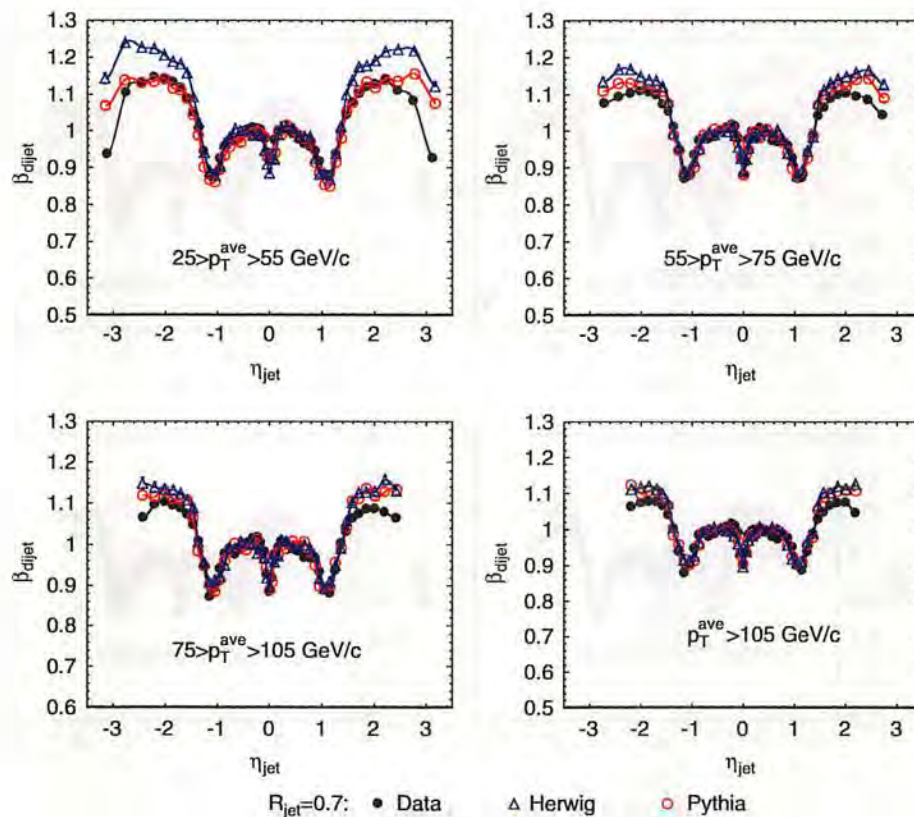


Fig. 16. Dijet balance, $\beta_{\text{dijet}} = p_T^{\text{probe}}/p_T^{\text{trigger}}$, as a function of η_{jet} in data, HERWIG, and PYTHIA MC samples for $R_{\text{jet}} = 0.7$ jets. Shown are the corrections for jet-20, jet-50, jet-70, and jet-100 jet samples, corresponding to $25 < p_T^{\text{ave}} < 55 \text{ GeV}/c$, $55 < p_T^{\text{ave}} < 75 \text{ GeV}/c$, $75 < p_T^{\text{ave}} < 105 \text{ GeV}/c$ and $p_T^{\text{ave}} > 105 \text{ GeV}/c$, respectively. The lines show the interpolation between the individual measurements used for correcting jets.

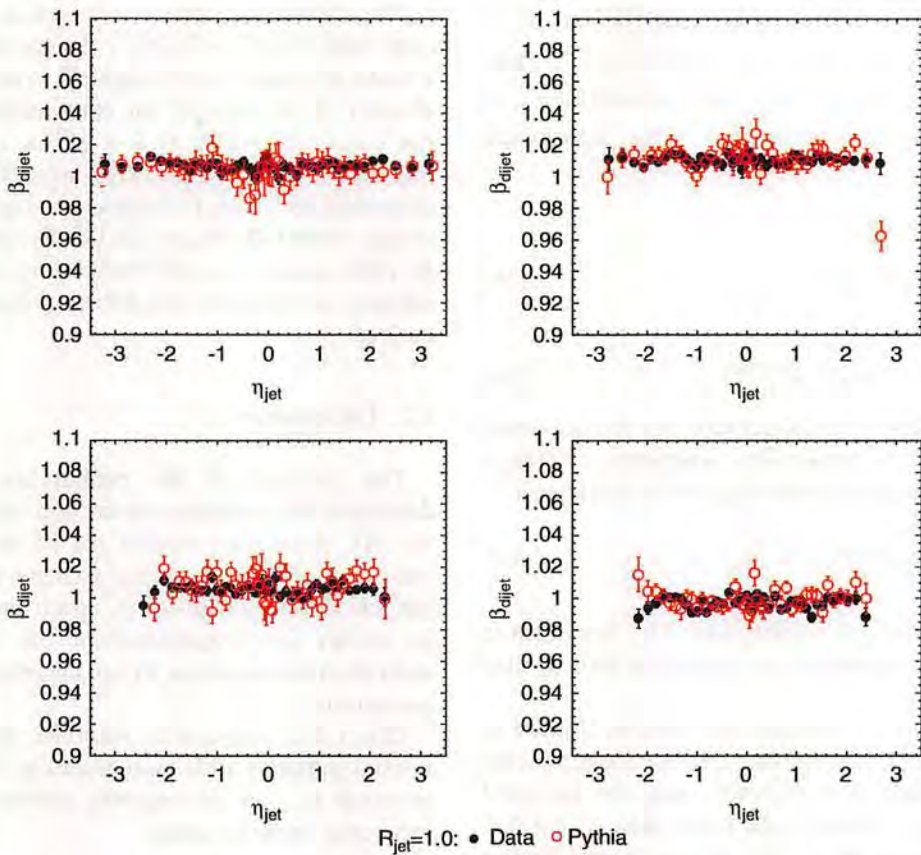


Fig. 20. Dijet balance, $\beta_{\text{dijet}} = p_T^{\text{probe}} / p_T^{\text{trigger}}$, as a function of η_{jet} in data and PYTHIA MC samples for cone size $R_{\text{jet}} = 1.0$ after applying the η -dependent corrections. Shown are the jet-20 (top left), jet-50 (top right), jet-70 (bottom left), and jet-100 (bottom right) jet samples, corresponding to $25 < p_T^{\text{ave}} < 55 \text{ GeV}/c$, $55 < p_T^{\text{ave}} < 75 \text{ GeV}/c$, $75 < p_T^{\text{ave}} < 105 \text{ GeV}/c$, and $p_T^{\text{ave}} > 105 \text{ GeV}/c$, respectively.

Table 2
Systematic uncertainties of the η -dependent corrections versus p_T^{jet} and $|\eta_{\text{jet}}|$

| $ \eta $ range | 0.0–0.2 | 0.2–0.6 | 0.6–0.9 | 0.9–1.4 | 1.4–2.0 | 2.0–2.6 | 2.6–3.6 |
|----------------------------------|---------|---------|---------|---------|---------|---------|---------|
| $\eta < 12 \text{ GeV}/c$ | 1.5% | 0.5% | 1.5% | 2.5% | 1.5% | 5.0% | 7.5% |
| $12 \leq p_T < 25 \text{ GeV}/c$ | 1.5% | 0.5% | 1.5% | 1.5% | 1.5% | 3.0% | 6% |
| $25 \leq p_T < 55 \text{ GeV}/c$ | 1.0% | 0.5% | 1.0% | 1.0% | 0.5% | 1.5% | 6% |
| $p_T \geq 55, \text{ GeV}/c$ | 0.5% | 0.5% | 0.5% | 0.5% | 0.5% | 1.5% | 6% |

7.1. Correction procedure

The absolute jet energy is defined as the most probable value for a jet transverse momentum, p_T^{jet} , given a particle jet with a fixed value of p_T^{particle} . The corresponding probability density function, dP , is parametrized as a function of $\Delta p_T = p_T^{\text{particle}} - p_T^{\text{jet}}$ according to

$$\begin{aligned} d\mathcal{P}(p_T^{\text{particle}}, p_T^{\text{jet}}) &= f(\Delta p_T) dp_T^{\text{particle}} dp_T^{\text{jet}} \\ f(\Delta p_T) &= \frac{1}{\sqrt{2\pi}(\sigma_1 + N_2\sigma_2)} \\ &\times [e^{-(1/2)((\Delta p_T - \mu_1)/\sigma_1)^2} \\ &+ N_2 e^{-(1/2)((\Delta p_T - \mu_2)/\sigma_2)^2}]. \end{aligned} \quad (25)$$

One Gaussian function describes the tails while the other one reproduces the core of the distribution. Their relative contributions are determined by the normalization of the second Gaussian, N_2 .

The parameters μ_1 , σ_1 , μ_2 , σ_2 , and N_2 depend on p_T^{particle} as shown by the different shapes of the histograms in Fig. 21. The dependence is modeled by a linear parameterization of the form:

$$\sigma_{1,2} = \sigma_{1,2}^a + \sigma_{1,2}^b p_T^{\text{particle}} \quad (26)$$

$$\mu_{1,2} = \mu_{1,2}^a + \mu_{1,2}^b p_T^{\text{particle}} \quad (27)$$

$$N_2 = N_2^a + N_2^b p_T^{\text{particle}} \quad (28)$$

using a total of 10 parameters.

The number of jets n with a p_T between p_T^{jet} and $p_T^{\text{jet}} + dp_T^{\text{jet}}$ and given particle jet with a p_T between p_T^{particle} and $p_T^{\text{particle}} + dp_T^{\text{particle}}$ is given by the convolution of $d\mathcal{P}(p_{T,i}^{\text{jet}}, p_{T,i}^{\text{particle}})$ with the p_T spectrum of the particle jets $d\mathcal{P}(p_{T,i}^{\text{particle}})$. That is,

$$\begin{aligned} n(p_T^{\text{jet}}, p_T^{\text{particle}}) & dp_T^{\text{jet}} dp_T^{\text{particle}} \\ = n(p_T^{\text{particle}}) & \times d\mathcal{P}(p_T^{\text{jet}}, p_T^{\text{particle}}). \end{aligned} \quad (29)$$

The likelihood has the form:

$$\mathcal{L} = \prod_i d\mathcal{P}(p_{T,i}^{\text{particle}}) \times d\mathcal{P}(p_{T,i}^{\text{jet}}, p_{T,i}^{\text{particle}}) \quad (30)$$

where the product goes over all particle jets. An unbinned likelihood fit is used to extract the parameters of $f(\Delta p_T)$ parameters, maximizing the logarithm of the likelihood

$$\log \mathcal{L} = \sum_{i=1}^N \log d\mathcal{P}(p_{T,i}^{\text{particle}}) + \sum_{i=1}^N \log f(\Delta p_{T,i}) \quad (31)$$

where N is the number of particle jets. The first term is independent of the parameters to determine and is thus ignored.

The dijet PYTHIA MC samples, described in Section 4, are used to calculate the likelihood. Jets are reconstructed at the calorimeter and particle level using the standard CDF jet clustering algorithm with cone radii of 0.4, 0.7, and 1.0. Jets are required to be in the central region ($0.2 < |\eta| < 0.6$) and to be one of the two leading jets. Each particle jet is required to match its closest calorimeter jet within $\Delta R = \sqrt{(\Delta\phi)^2 + (\Delta\eta)^2} < 0.1$. In total we selected about 50,000 particle jets matched to calorimeter jets, with p_T ranging from 0 to 600 GeV/c. The difference between the particle jet p_T and the calorimeter jet p_T is shown in Fig. 21 for four example p_T ranges. The distributions are not centered at zero as expected and have widths that change with p_T according to Eq. (25).

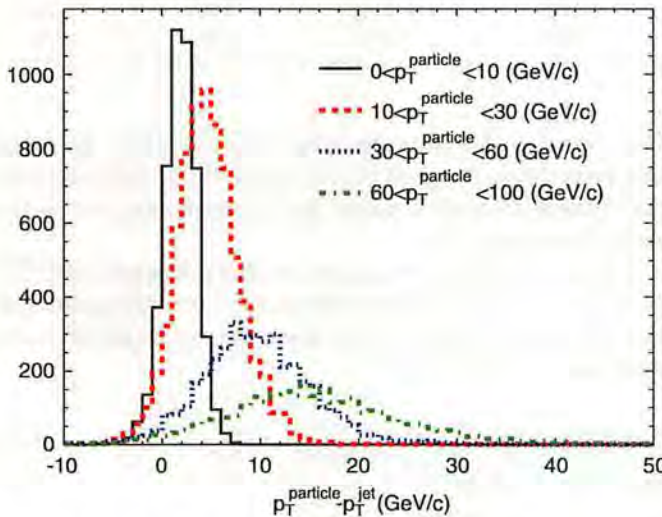


Fig. 21. $\Delta p_T = p_T^{\text{particle}} - p_T^{\text{jet}}$ for $R_{\text{jet}} = 0.4$ jets matched using $\Delta R < 0.1$ for different p_T^{particle} ranges.

The absolute correction is shown in Fig. 22 for the three cone radii. At $p_T^{\text{jet}} = 8$ GeV/c the correction factor is about 1.4 and decreases toward high p_T^{jet} to an asymptotic value of about 1.12. At high p_T^{jet} the corrections are independent of the cone size while at low p_T^{jet} a slight dependence is observed. For $p_T^{\text{jet}} < 8$ GeV/c, a large fraction of jets are not reconstructed since the observed single calorimeter tower energy often falls below the 1 GeV/c seed tower threshold. In these cases, it is not possible to establish a mapping between calorimeter and particle jets and no correction is derived.

7.2. Uncertainties

The validity of the probability function used to determine the absolute correction depends on how well the MC simulation models the jet response in data. The treatment of the jet response as a convolution of the single particle response with the p_T spectrum of the particles in a jet allows for propagation of the uncertainties of the individual components to an uncertainty of the absolute correction.

Given the calorimeter response $R(p)$ to charged and neutral particles with momentum p , the average expected response R_{ave} , or jet response, can be calculated from the generated particles using

$$R_{\text{ave}} = \frac{\sum_{i=1}^N p_i R(p_i)}{\sum_{i=1}^N p_i} \quad (32)$$

where N is the number of particles inside the jet cone with momenta p_i . The uncertainties on the absolute corrections are defined as the differences between data and simulation in the calorimeter response to single particles, $R(p)$, the differences in the momentum spectrum of the particles, p , and from the stability of the calorimeter calibrations in data. They are addressed in the following sections.

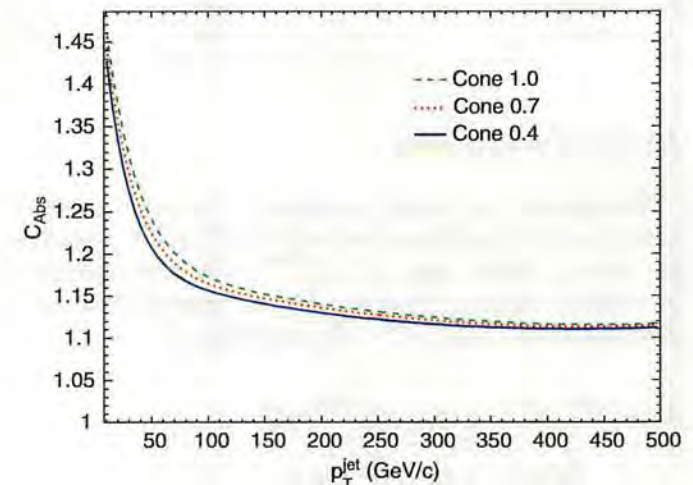


Fig. 22. Absolute corrections for different cone sizes as a function of calorimeter jet p_T . The solid line shows the corrections for $R_{\text{jet}} = 0.4$, the dashed line for $R_{\text{jet}} = 0.7$ and the dotted line for $R_{\text{jet}} = 1.0$.

7.2.1. Single particle response simulation

The measured calorimeter response $R(p) = \langle E/p \rangle$ (see Section 5) for hadrons is parameterized as follows:

$$\begin{aligned} p < 20 \text{ GeV}/c : \quad R(p) &= 0.70 \\ &+ 0.09 \tanh(2.13(\log(p) - 0.93)) \\ p > 20 \text{ GeV}/c : \quad R(p) &= 0.70 \\ &+ 0.14 \tanh(0.49(\log(p) - 1.15)) \end{aligned} \quad (33)$$

using the data in Fig. 7. For electromagnetic particles (electrons and photons) we set $R(p) = 1.0$.

The relative uncertainty on the jet energy scale response, $\Delta E/E$, is then

$$\begin{aligned} &= \left[\sum_{i=1}^N p_i R(p_i) - \sum_{i=1}^N p_i R(p_i)(1 \pm \Delta(E/p)) \right] / E \\ &= \mp \sum_{i=1}^N p_i R(p_i) \Delta(E/p) / E \end{aligned} \quad (34)$$

where $\Delta(E/p)$ is the uncertainty on $\langle E/p \rangle$ given in Table 1. For hadronic particles it is between 2.5% and 4%. However, since only 70% of the jet energy arises from hadronic particles the uncertainty on the jet energy is only 1.8–2.8%. The response function is then convoluted with the particle momentum spectra in jets to estimate the

systematic uncertainty as function of the jet energy. The uncertainty on the simulation of the response of electromagnetic particles is 1.7%. Since about 30% of the jet energy is due to electromagnetic particles, this results in a systematic uncertainty of 0.5% on jet energy scale, independent of jet p_T . The uncertainties are shown versus jet p_T in Fig. 25.

7.2.2. Fragmentation

Uncertainties related to the particle momentum spectrum in a jet originate from the modeling of hadronization effects using PYTHIA and HERWIG as well as from the estimate of track reconstruction efficiencies in data and detector simulation. The transverse momentum spectrum of tracks in data is corrected for inefficiencies as follows. The track reconstruction efficiency is measured by embedding simulated tracks inside jets in data events, after tuning the simulation of COT hits to distributions observed in data, and then parameterized versus jet p_T , track momentum and distance of track from the jet core. This parameterization is used to correct the data for any inefficiencies [31].

The average number of tracks is measured as a function of the track momentum for different values of p_T^{jet} . Only tracks that are within the jet cone are associated with the

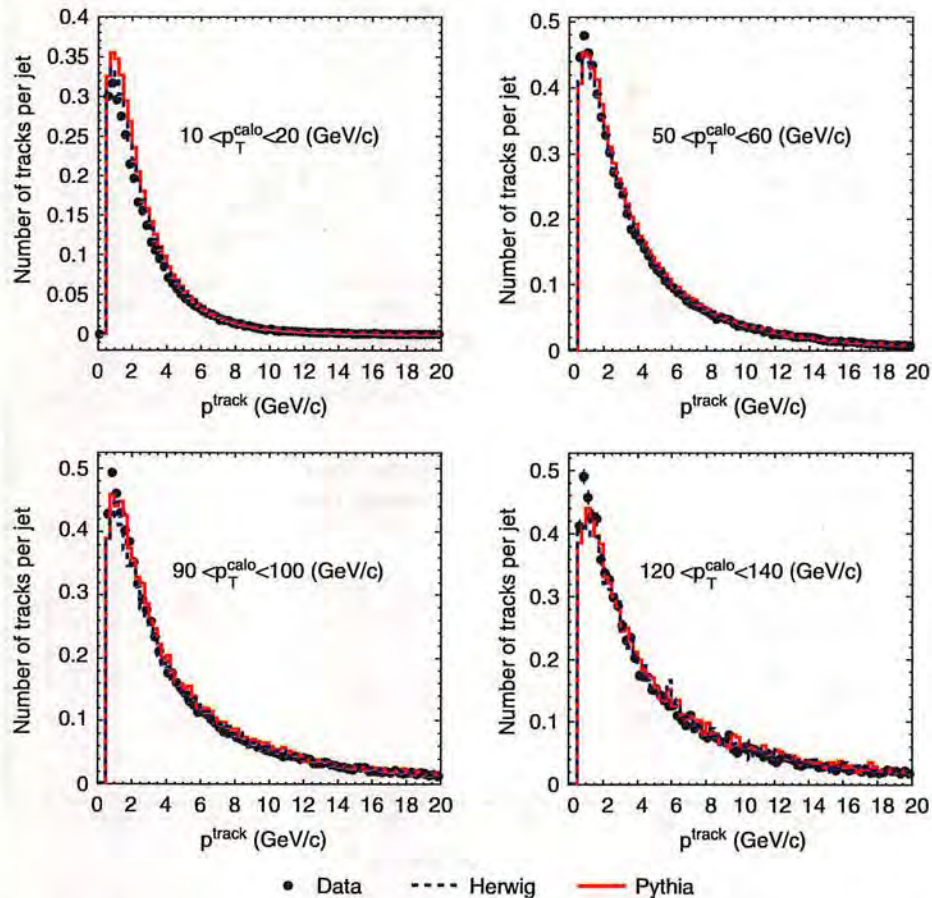


Fig. 23. Comparison of the particle momentum spectra in dijet events between data with PYTHIA and HERWIG. The CDF data have been corrected for track reconstruction efficiency.

jet. To account for UE contributions, tracks from the region transverse to the leading jet are subtracted event by event. Only events with exactly one reconstructed z-vertex are used to reject events with additional $p\bar{p}$ interactions. Fig. 23 shows a comparison of the track momentum spectra in data with PYTHIA and HERWIG simulation for four values of p_T^{jet} . The data are generally in good agreement with the MC, apart from some discrepancies at very low track momenta.

The systematic uncertainty on the jet p_T due to the particle multiplicity is calculated from the differences between the measured and simulated average calorimeter response, R_{ave} for a fixed single particle response $R(p)$. Fig. 24 shows the jet response for data, PYTHIA, and HERWIG. Note that this is an indirect measurement of the energy inferred from the track momenta. If the response of the calorimeter, $R(p)$, was one, as is the case of electromagnetic particles, this quantity would be unity. The deviation from one thus quantifies the fraction of the jet energy measured due to the low calorimeter response to charged hadrons. For a fixed $R(p)$ any difference between

data and simulation can only arise from a difference in the momentum spectrum.

The top plot of Fig. 24 shows R_{ave} versus p_T^{jet} for data taken with a trigger threshold of 20 GeV/c (see Section 4) compared to PYTHIA and HERWIG simulation. At $p_T^{\text{jet}} = 15$ GeV/c about 20% of the jet energy is not measured. The response improves with increasing p_T^{jet} as expected: e.g. for $p_T^{\text{jet}} = 120$ GeV/c only 14% is not measured. The data response is about 0.5% higher than that of the simulation. The bottom plot shows the difference between data and simulation. The largest observed difference of 1% is taken as a p_T independent systematic uncertainty on the jet energy scale due to differences in the particle momentum spectrum (see Fig. 25).

7.2.3. Stability of the calorimeter energy scale

The simulation is tuned using Run II data collected during a fixed period of time. The calorimeter calibration is kept constant to within 0.5% as described in Section 2.3. This value is taken to be an additional systematic uncertainty.

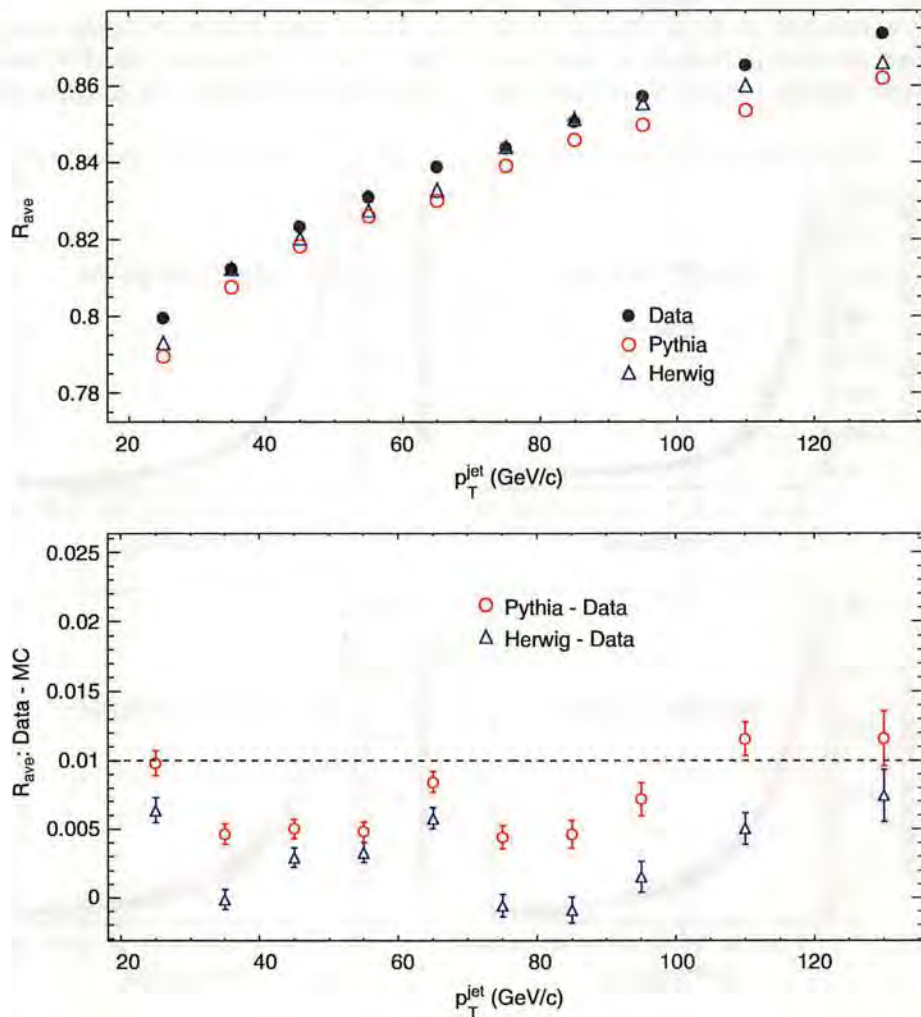


Fig. 24. Top: jet response R_{ave} for data (closed circles), PYTHIA (open circles), and HERWIG (open triangles) for $R_{\text{jet}} = 0.4$ jets as function of p_T^{jet} . Bottom: difference between data and PYTHIA (open circles) and data and HERWIG (open triangles).

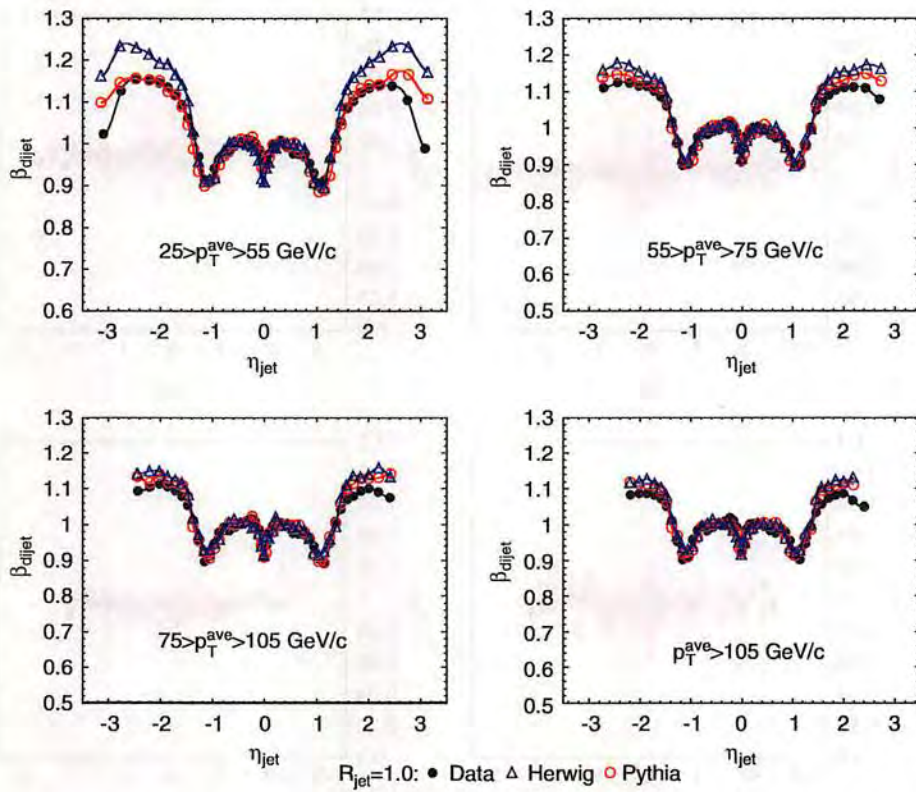


Fig. 17. Dijet balance, $\beta_{\text{dijet}} = p_{\text{T}}^{\text{probe}}/p_{\text{T}}^{\text{trigger}}$, as a function of η_{jet} in data, HERWIG, and PYTHIA MC samples for $R_{\text{jet}} = 1.0$ jets. Shown are the corrections for the jet-20, jet-50, jet-70, and jet-100 jet samples, corresponding to $25 < p_{\text{T}}^{\text{ave}} < 55 \text{ GeV}/c$, $55 < p_{\text{T}}^{\text{ave}} < 75 \text{ GeV}/c$, $75 < p_{\text{T}}^{\text{ave}} < 105 \text{ GeV}/c$ and $p_{\text{T}}^{\text{ave}} > 105 \text{ GeV}/c$, respectively. The lines show the interpolation between the individual measurements used for correcting jets.

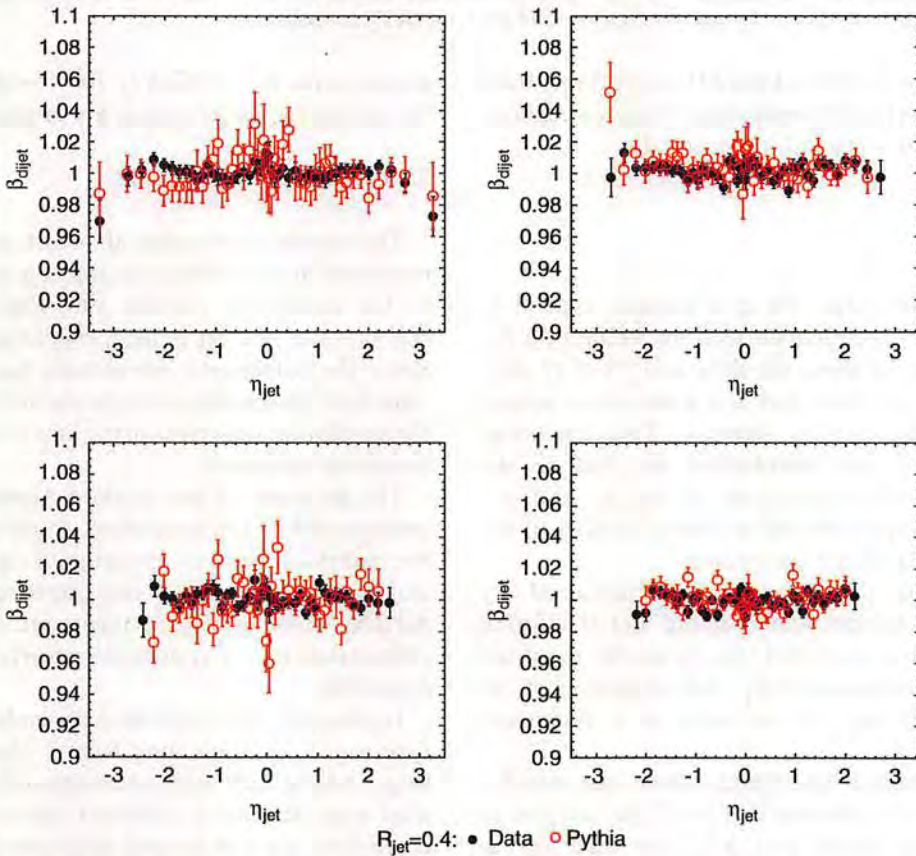


Fig. 18. Dijet balance, $\beta_{\text{dijet}} = p_{\text{T}}^{\text{probe}}/p_{\text{T}}^{\text{trigger}}$, as a function of η_{jet} in data and PYTHIA MC samples for cone size $R_{\text{jet}} = 0.4$ after applying the η -dependent corrections. Shown are the jet-20 (top left), jet-50 (top right), jet-70 (bottom left) and jet-100 (bottom right) jet samples, corresponding to $25 < p_{\text{T}}^{\text{ave}} < 55 \text{ GeV}/c$, $55 < p_{\text{T}}^{\text{ave}} < 75 \text{ GeV}/c$, $75 < p_{\text{T}}^{\text{ave}} < 105 \text{ GeV}/c$ and $p_{\text{T}}^{\text{ave}} > 105 \text{ GeV}/c$, respectively.

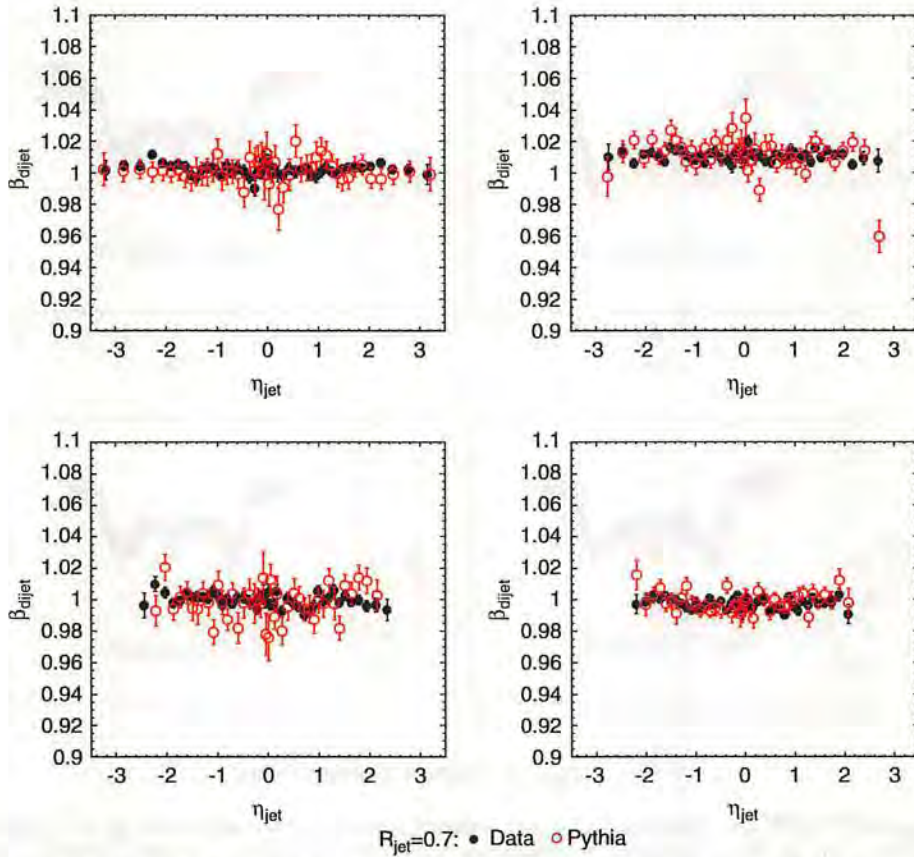


Fig. 19. Dijet balance, $\beta_{\text{dijet}} = p_{\text{T}}^{\text{probe}}/p_{\text{T}}^{\text{trigger}}$, as a function of η_{jet} in data and PYTHIA MC samples for cone size $R_{\text{jet}} = 0.7$ after applying the η -dependent corrections. Shown are the jet-20 (top left), jet-50 (top right), jet-70 (bottom left), and jet-100 (bottom right) jet samples, corresponding to $25 < p_{\text{T}}^{\text{ave}} < 55 \text{ GeV}/c$, $55 < p_{\text{T}}^{\text{ave}} < 75 \text{ GeV}/c$, $75 < p_{\text{T}}^{\text{ave}} < 105 \text{ GeV}/c$, and $p_{\text{T}}^{\text{ave}} > 105 \text{ GeV}/c$, respectively.

this large discrepancy we derived the MC corrections from the PYTHIA MC. Further discussions of these corrections and HERWIG MC can be found in Section 10.

6.2. Uncertainties

If this method was perfect the dijet balance applied to samples after these η -dependent corrections would be a flat line at one. Figs. 18–20 show the data and PYTHIA MC after corrections. It is seen that the corrections indeed flatten out the response as desired. The remaining discrepancies from a flat distribution are due to the limitations of the parameterization of the η - and p_{T} -dependence of the correction and are taken as part of the systematic uncertainty of the corrections.

Further systematic uncertainties are determined by varying the event selection requirements and the fitting procedure. Specifically, we varied the cut on the p_{T} of the third jet and the significance of E_{T} . Any deviation of the dijet balance β_{dijet} from unity is taken as a systematic uncertainty.

The overall systematic uncertainty from the sources described above are summarized in Table 2. In the low p_{T} region minimum bias data and MC are used up to $p_{\text{T}} < 15 \text{ GeV}/c$ and single-tower-5 data and the MC jet

sample with $\hat{p}_{\text{T}} > 10 \text{ GeV}/c$ for $15 < p_{\text{T}} < 25 \text{ GeV}/c$. Here, the systematic uncertainties are largest.

7. Absolute jet energy scale

The absolute correction aims to transform the jet energy measured in the calorimeter into the energy corresponding to the underlying particle jet. After this correction the energy scale of a jet is independent of the CDF detector. Since the calorimeter simulation has been optimized to reproduce the measured single particle response, we rely on the simulation to derive corrections over a large range of jet transverse momenta.

The accuracy of this method depends on how well jets are modeled by the simulation. In particular, it depends on the multiplicity and p_{T} spectrum of the particles inside a jet and on the response of the calorimeter to an individual particle. These two components are tested separately and propagated into a systematic uncertainty on the absolute correction.

In principle, this correction depends on the initial parton type, e.g. a jet originating from a gluon has on average a larger multiplicity than one originating from a quark and thus may require a different correction. However, the corrections are not derived separately for each parton type since the parton type in the data is a priori unknown.

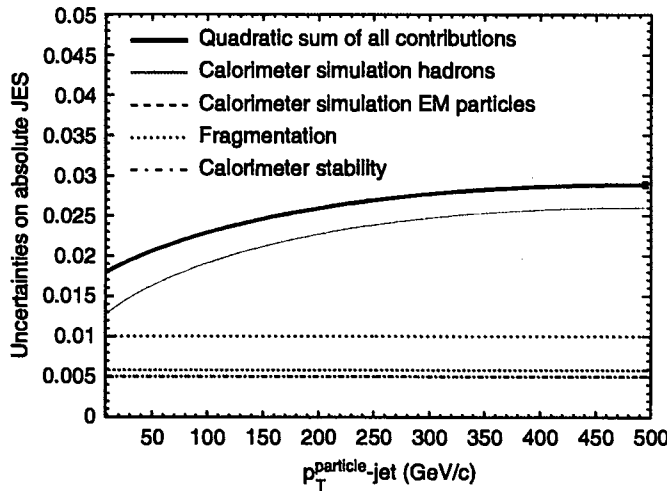


Fig. 25. Systematic uncertainty on the jet energy scale due to the calorimeter calibration and simulation. The solid line shows the total uncertainty and the other lines show individual contributions.

7.3. Summary

A summary of all the uncertainties is shown in Fig. 25. It rises from 2% at low p_T^{jet} to 3% at high p_T^{jet} . The dominant uncertainty arises from the uncertainty on the simulation of the calorimeter response to charged hadrons. The individual uncertainties are added in quadrature to give the total uncertainty. The uncertainties apply to all cone sizes. Further studies of the validity of the systematic uncertainties are presented in Section 10.

8. Multiple p \bar{p} interactions

At high instantaneous luminosities more than one p \bar{p} interaction occurs in the same bunch crossing at the Tevatron due to the large p \bar{p} cross-section. The number of p \bar{p} interactions per bunch crossing, N , follows a Poisson distribution with a mean $\langle N \rangle$ which depends linearly on the instantaneous luminosity. For the Run II configuration of the Tevatron, the average number of interactions is about one at $L = 0.4 \times 10^{32} \text{ cm}^{-2} \text{ s}^{-1}$ and increases to three at $L = 1.2 \times 10^{32} \text{ cm}^{-2} \text{ s}^{-1}$ and eight at $L = 3.2 \times 10^{32} \text{ cm}^{-2} \text{ s}^{-1}$. For the data taken up to September 2004, the instantaneous luminosity ranges between 0.1×10^{32} and $1 \times 10^{32} \text{ cm}^{-2} \text{ s}^{-1}$.

These extra p \bar{p} interactions give an apparent increase the energy of the jets from the hard scatter if their final state hadrons accidentally overlap with the jets. This extra energy therefore needs to be subtracted from the jet energy.

8.1. Correction procedure

The number of reconstructed z-vertices, N_{vtx} , is the best estimate of the number of interactions in a bunch crossing. Vertices are reconstructed using the intersections of the tracks with the beam line. Fig. 26 shows the number of

vertices as a function of the instantaneous luminosity in the first 350 pb^{-1} of CDF data in $W \rightarrow e\nu_e$ candidate events. The mean number of z-vertices, $\langle N_{\text{vtx}} \rangle$, is also shown. At low vertex multiplicity the expected linear correlation is observed.

The efficiency of the vertex finding algorithm depends on the track multiplicity. It is about 80% for minimum bias events, 98% for $W \rightarrow e\nu_e$ events and greater than 99.9% for $t\bar{t}$ events. These efficiencies have been determined in MC samples and verified by measuring the fraction of $W \rightarrow e\nu$ data events whose vertex is within 5 cm of the z-position of the electron track at the beam line.

The average transverse energy in a cone is measured using the minimum bias data sample. The cone is defined using a seed tower randomly selected in the central calorimeter region $0.2 < |\eta| < 0.6$. The transverse energy, E_T^R , in this cone is measured as a function of the number of vertices for three cone sizes. Fig. 27 shows E_T versus N_{vtx} . The data show the expected linear behavior.

The data are parameterized using a fitted straight line with coefficients given in Table 3. The slope parameters give the extra transverse energy per interaction as a function of N_{vtx} . Ideally, the intercept should be zero. The intercept values are in all cases close but are consistently larger than zero as a consequence of the imperfect vertex finding inefficiency. Note that the slope and intercept values measured for the three cone sizes are the same when taking into account the cone areas.

8.2. Uncertainty

The validity of this method depends on two aspects of the vertex finding algorithm:

- *Vertex reconstruction efficiency*: The efficiency of finding vertices from additional interactions may depend on the topology of the hard interaction. Any inefficiency will result in a steeper slope parameter and a larger intercept.
- *Vertex fake rate*: In events with high occupancy it may happen that fake vertices are found, i.e. vertices are reconstructed in z-positions where no interaction took place. This fake rate also depends on the event topology since the probability of confusion in both the tracking and the vertex finding increases with increasing number of tracks.

The impact of these effects is tested by repeating the multiple interaction measurement using several samples: $W \rightarrow e\nu_e$, minimum bias and a jet sample with E_T thresholds of 100 GeV. Fig. 28 shows no indication for any dependence on the instantaneous luminosity or on the topology of these samples. However, with the current statistical precision a 15% effect cannot be excluded, and it is taken as systematic uncertainty. This value of this uncertainty corresponds to 50 MeV for $R_{\text{jet}} = 0.4, 150 \text{ MeV}$ for $R_{\text{jet}} = 0.7$ and 300 MeV for $R_{\text{jet}} = 1.0$ per additional interaction.

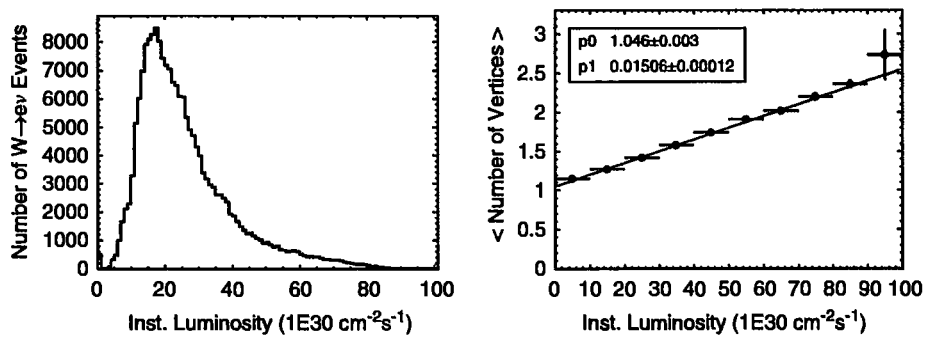


Fig. 26. Left: instantaneous luminosity for $W \rightarrow ev$ events measured up to September 2004. Right: mean number of reconstructed vertices in $W \rightarrow ev$ events versus the instantaneous luminosity. Also shown is a straight line fit.

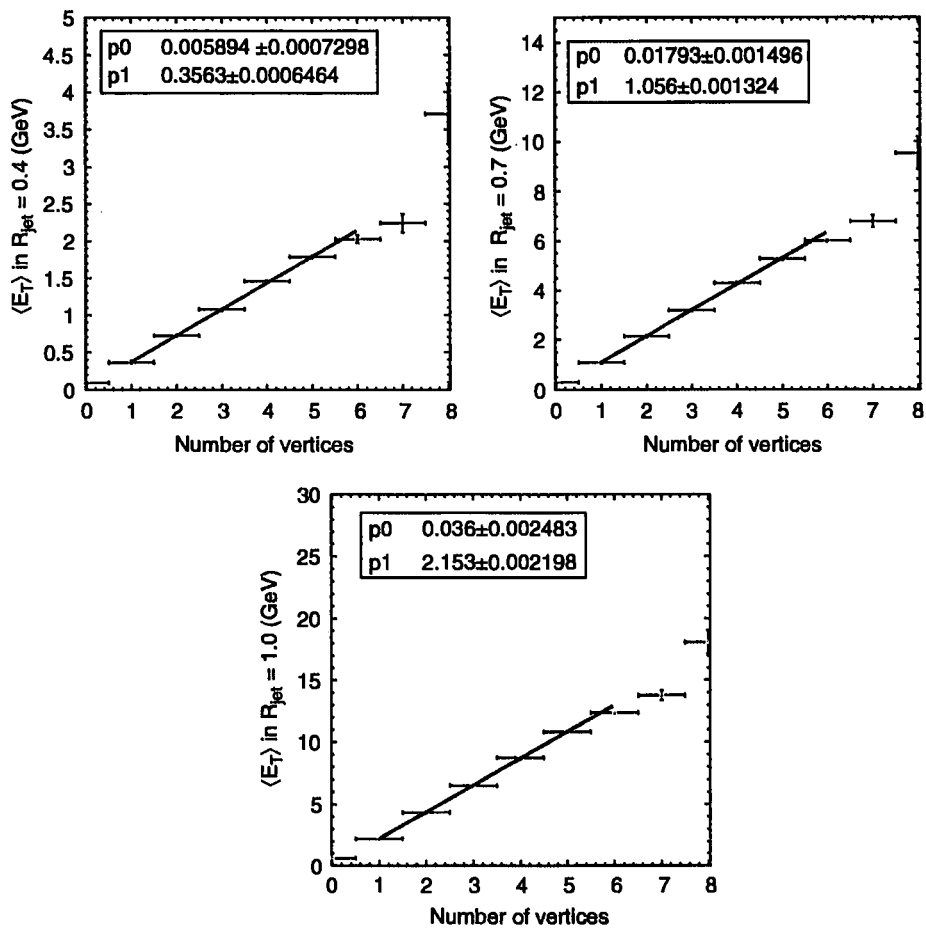


Fig. 27. $\langle E_T \rangle$ versus the number of z-vertices for $R_{\text{jet}} = 0.4$ (top left), $R_{\text{jet}} = 0.7$ (top right) and $R_{\text{jet}} = 1.0$ (bottom left). A linear fit is also shown.

Table 3

Intercepts and slopes of the multiple interaction correction for the three cone sizes

| Fit parameter | Cone 0.4 (GeV) | Cone 0.7 (GeV) | Cone 1.0 (GeV) |
|---------------|-------------------|-------------------|-------------------|
| Intercept | 0.006 ± 0.001 | 0.018 ± 0.002 | 0.036 ± 0.002 |
| Slope | 0.356 ± 0.001 | 1.056 ± 0.001 | 2.153 ± 0.002 |

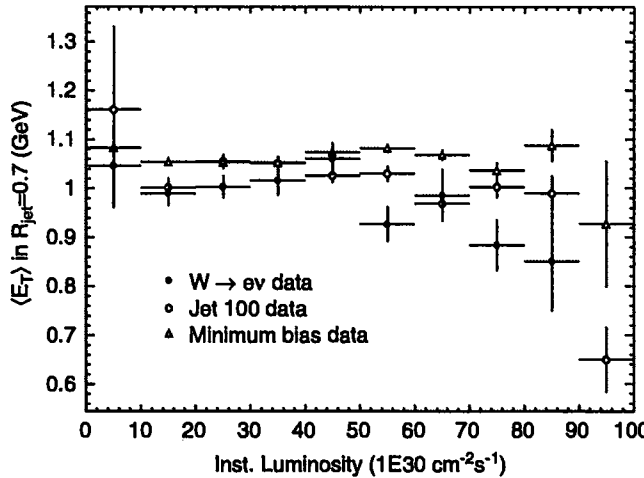


Fig. 28. Slope parameter of the multiple interaction correction for $R_{\text{jet}} = 0.7$ versus instantaneous luminosity in $W \rightarrow e\nu$ (closed circles), minimum bias (open triangles), as well as in a jet sample with E_T threshold of 100 GeV (open circles).

9. OOC energy and UE

It is often desirable to reconstruct the energy of the original parton rather than the energy of the jet, e.g. for the measurement of the top quark mass or the search for the Higgs boson, where parton energies are used to compute the invariant mass of the decay products.

The reconstruction of the parton energy from the particle jet energy is subject to several difficulties. A fraction of the parton energy can be lost from the jet cone due to final state gluon radiation (FSR) at large angles with respect to the parent parton or due to particles exiting the cone either in the fragmentation process or due to low p_T particles bending in the magnetic field. This energy is called OOC energy. On the other hand, the particle jet can also have contributions not related to the actual parent parton of the hard interaction of interest defining the jet, such as particles from the initial state gluon radiation (ISR), or particles from spectator partons with color connection to the other partons of the proton (“beam-beam-remnant”, BBR). These two contributions are called UE energy contributions.

Final state radiation and hadronization effects are correlated with the primary jet direction and the jet energy and are expected to decrease with increasing distance from the jet core. The UE is assumed to be uncorrelated with the direction of the outgoing parton and thus independent of the distance from the jet in η - ϕ space and almost independent of the jet energy.

In this section, we derive corrections for the OOC energy and the UE simultaneously using PYTHIA dijet MC samples. As in the case of the absolute corrections, the corrections are obtained using jets with $0.2 < |\eta_{\text{jet}}| < 0.6$ since any η -dependence of the OOC energy is taken into account by the relative corrections. The corrections are solely determined from MC simulation at particle gen-

erator level independent of the CDF detector. The systematic uncertainties of the OOC and UE corrections are derived from comparisons of the energy measured in calorimeter towers in certain annuli around the jet cone with the simulation based on PYTHIA and HERWIG.

9.1. Correction procedure

The OOC and UE corrections are obtained from PYTHIA dijet samples using particle jets which match a primary parton within $\Delta R < 0.4$. We parameterize the difference of the energy between the particle jet and the parton using the same method as for the absolute corrections (see Section 7.1). Fig. 29 shows $p_T^{\text{parton}} - p_T^{\text{particle}}$ for different parton momenta and $R_{\text{jet}} = 0.4, 0.7$, and 1.0. The energy outside the jet cone depends strongly on the cone size. The OOC corrections $p_T^{\text{parton}}/p_T^{\text{particle}}$ are shown in Fig. 30. For the smallest cone size, $R_{\text{jet}} = 0.4$, it is about +18% at $p_T^{\text{particle}} = 20 \text{ GeV}/c$. For the largest cone size, the correction is negative: -6% at $p_T^{\text{particle}} = 20 \text{ GeV}/c$, corresponding to 1.2 GeV/c. This shows that at small cone sizes the OOC losses dominate over the energy increase due to the UE, and at large cone sizes the extra energy from the UE is larger than the OOC losses. We have estimated that the UE transverse energy is about 0.4, 1.1 and 2.2 GeV for cone sizes of 0.4, 0.7, and 1.0, respectively (see Section 9.2.2).

9.2. Uncertainties

9.2.1. OOC energy

We determine the uncertainty on the OOC energy using $\gamma + \text{jets}$ samples. The reference energy scale is the photon p_T which serves as an estimator of the corrected jet p_T , i.e. $p_T^\gamma \equiv p_T^{\text{corr}}$.

The transverse energy around a jet of cone size R_{jet} is measured by adding the transverse energy in towers within the annulus defined by radii r_1 and r_2 around the jet axis, that is

$$p_T(r_1 - r_2) = \sqrt{\left(\sum_{i=1}^N E_x^i \right)^2 + \left(\sum_{i=1}^N E_y^i \right)^2} \quad (35)$$

where N is the number of towers for which $r_1 > \sqrt{(\eta_{\text{jet}} - \eta_i)^2 + (\phi_{\text{jet}} - \phi_i)^2} > r_2$. Fig. 31 shows $p_T(r_1 - r_2)$ in data, PYTHIA and HERWIG for different jet annuli. The shapes of the data and simulation distributions agree rather well, and in the following the mean value is used to quantify any disagreement between them.

Fig. 32 shows the difference between data and simulation for the mean values of $p_T(r_1 - r_2)$ as a function of p_T^{corr} . The largest difference is observed at low p_T^{corr} and is about 4%. The systematic uncertainty is defined as the largest difference between data and either PYTHIA or HERWIG, and is parameterized as a function of p_T^{corr} but independent of the jet cone size. Since this measurement is made at the

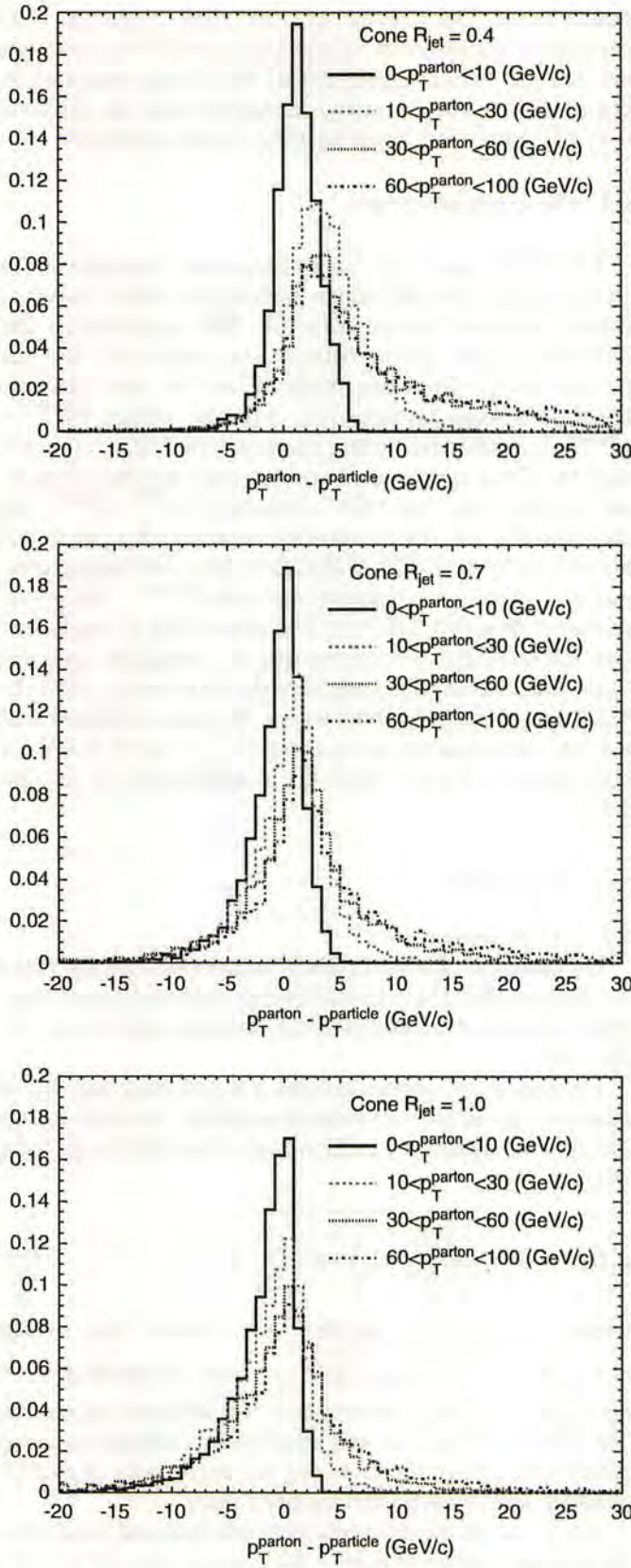


Fig. 29. Normalized distributions of $p_T^{\text{parton}} - p_T^{\text{particle}}$ for different p_T^{parton} for $R_{\text{jet}} = 0.4$ (top), $R_{\text{jet}} = 0.7$ (middle), and $R_{\text{jet}} = 1.0$ (bottom).

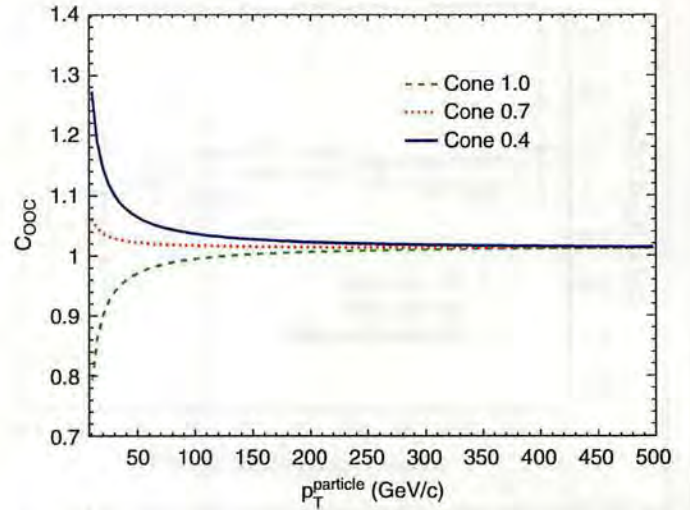


Fig. 30. OOC correction, C_{OOC} versus $p_T^{\text{parton}}/p_T^{\text{particle}}$, versus p_T^{particle} for cone sizes 0.4 (solid line), 0.7 (dashed line), and 1.0 (dotted line).

calorimeter tower level and we apply this correction to a jet after absolute correction, the uncertainties shown in Fig. 32 are multiplied by the factors 1.1, 1.35, and 1.6, for $R_{\text{jet}} = 0.4, 0.7$, and 1.0, respectively. These factors were determined from PYTHIA by comparing the particle and the calorimeter energy inside the annuli around the jet cone.

By considering alternative generators various modeling uncertainties contributing to the systematic error are taken into account. HERWIG and PYTHIA have very different BBR contributions. Furthermore, they differ in the modeling of QCD radiation and fragmentation.

9.2.2. Underlying event

Another source of systematic uncertainty comes from the varying UE in different physics processes. To first order these dependencies are taken into account by the MC generators, e.g. PYTHIA has been tuned to describe the UE in the data (PYTHIA Tune A, [24]). The UE uncertainties are derived from comparisons of the UE in data, PYTHIA Tune A and HERWIG [32]. This comparison is done using tracks with $p_T > 0.5 \text{ GeV}/c$ that are separated from the leading jet in azimuth by $60^\circ < \Delta\Phi(\text{jet}, \text{track}) < 120^\circ$, which is referred to as the “transverse region”. It is mostly sensitive to ISR and multiple parton interactions. Fig. 33 shows the average momenta of the tracks in the transverse region versus the leading jet p_T . The data agree well with PYTHIA but differ by up to 30% from HERWIG. This value is taken as the relative systematic uncertainty. As a further cross-check, Fig. 33 shows also the corresponding transverse momentum spectrum simulated by ISAJET [33] which has an alternate hadronization model. To get an estimate of the absolute UE uncertainty we use the energy measured in minimum bias data for $N_{\text{vtx}} = 1$ as shown in Fig. 27. The numbers are 0.4, 1.1, and 2.2 GeV for $R_{\text{jet}} = 0.4, 0.7$, and 1.0, respectively, which translate to UE uncertainties of 0.11, 0.32, and 0.66 GeV. We have also

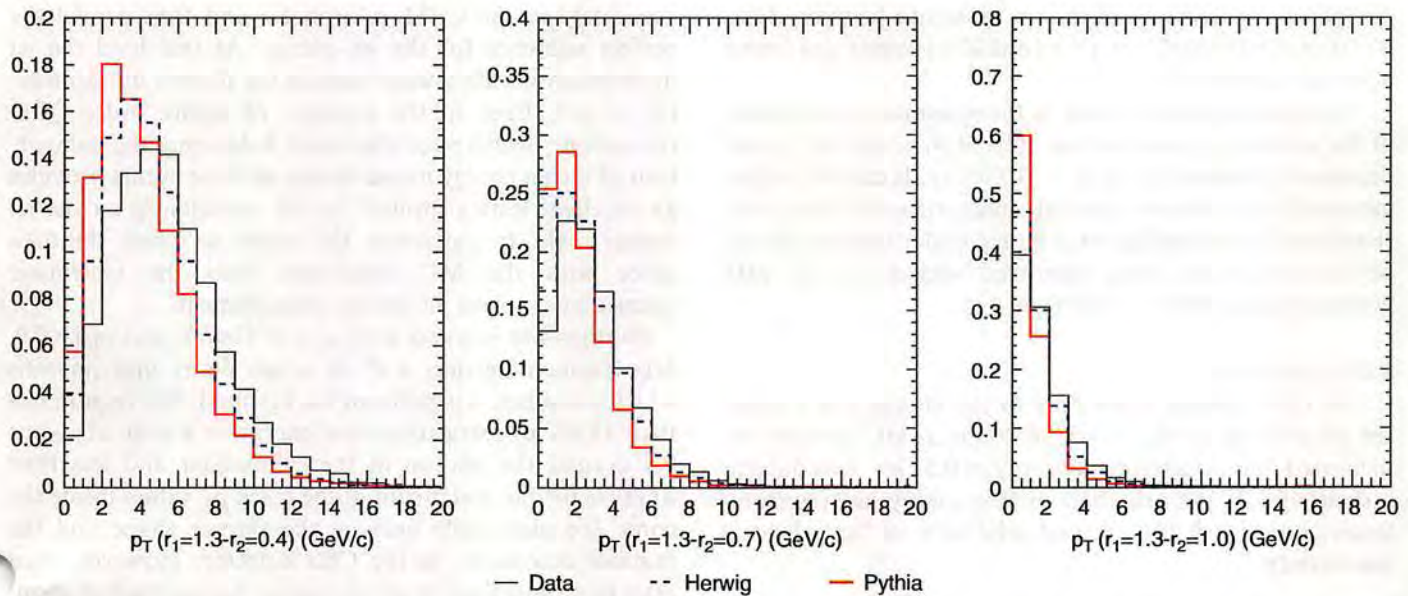


Fig. 31. Normalized distributions of the momentum in different annuli outside the jet cone for data, PYTHIA, and HERWIG $\gamma +$ jets events.

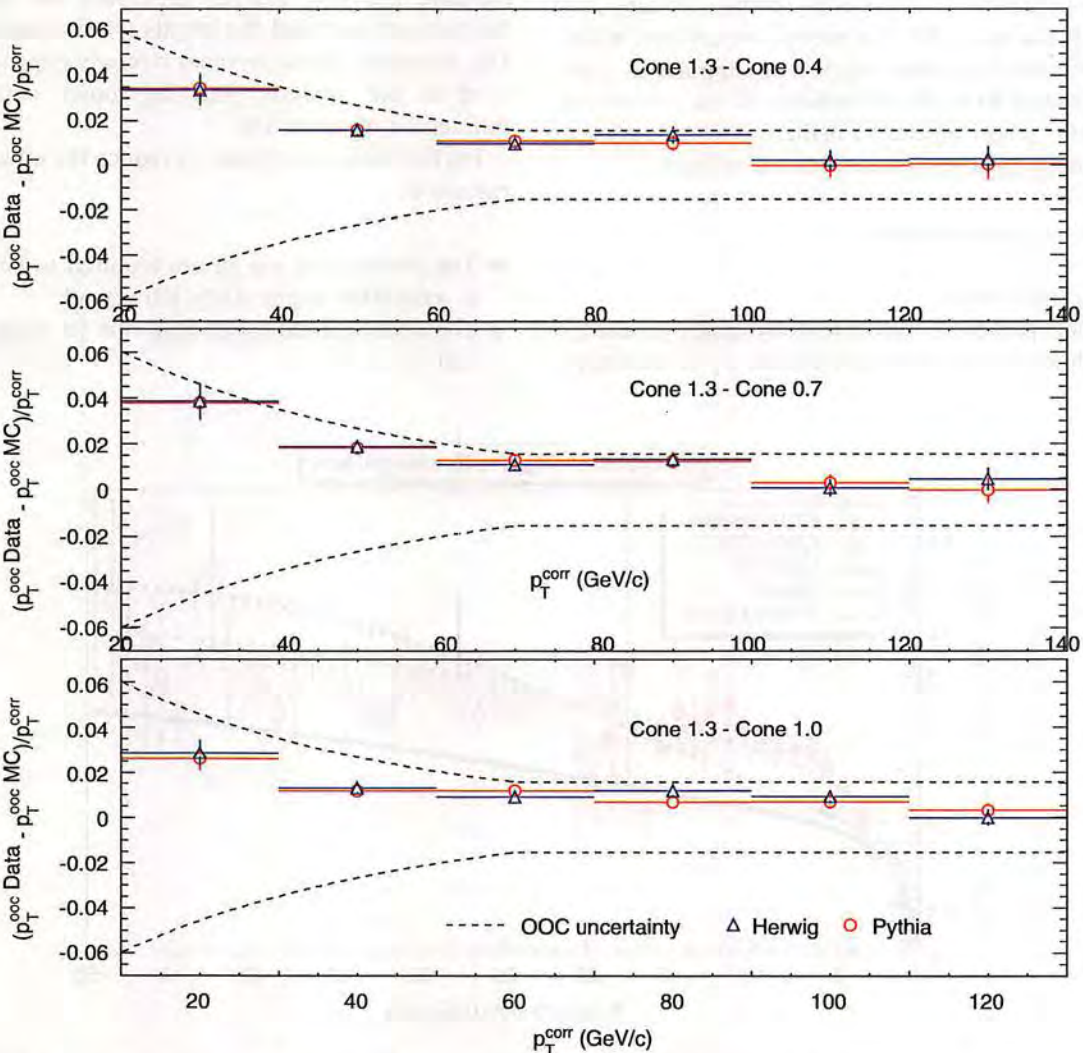


Fig. 32. Systematic uncertainty of OOC corrections for different cone sizes. The systematic uncertainty is taken as the largest difference between data and either PYTHIA or HERWIG and multiplied by the particle-jet/calorimeter-jet factors.

compared the average transverse momenta between data, PYTHIA, and HERWIG in γ -jet and Z-jet events and found a similar agreement.

The resulting contribution to the systematic uncertainty of the jet energy scale is about 10% at $p_T = 10 \text{ GeV}/c$ and decreases to about 2% at $p_T = 70 \text{ GeV}/c$. It can be further improved by a more detailed comparison of data and simulation, thus leading to a better understanding of the physics effects, or using improved versions of the MC generators as JIMMY or PYTHIA 6.3.

9.2.3. Splash-out

The OOC energy refers only to the energy lost outside the jet cone up to $R_{\text{jet}} = 1.3$. In PYTHIA MC samples we measured that an additional energy of 0.5 GeV falls outside a cone of 1.3. We take half of this energy as systematic uncertainty, i.e. 0.25 GeV, and refer to it as “splash-out” uncertainty.

10. Validation of the jet energy scale determination

Several consistency checks and further studies are presented in this section. The jet energy corrections, which are mostly derived from dijet samples are applied to γ -jet, Z-jet, and $t\bar{t}$ events to verify the validity of the corrections and systematic uncertainties. Furthermore, we present additional studies on the η -dependent corrections.

10.1. Test of the jet corrections

10.1.1. Using γ -jet events

The γ -jet data sample is ideal for studying the jet energy scale. The photon transverse momentum p_T^γ is measured

accurately in the CEM calorimeter and thus provides a perfect reference for the jet energy. At tree level the jet momentum should always balance the photon momentum: $p_T^{\text{jet}}/p_T^\gamma = 1$. Even in the presence of higher order QCD corrections, which spoil this exact balancing, the comparison of the jet energy measurement in these events provides an excellent testing ground for the uncertainty on the jet energy scale. In particular, the extent to which the data agree with the MC simulation tests the systematic uncertainties in the jet energy measurement.

Photons are selected with $p_T^\gamma > 27 \text{ GeV}/c$ and $|\eta^\gamma| < 0.9$. Jets fragmenting into a π^0 or η can decay into photons which constitute a significant background. We require less than 1 GeV of extra transverse energy in a cone of radius 0.4 around the photon in the calorimeter and less than 2 GeV/c for the scalar sum of the track p_T values inside the cone. We also apply cuts on the shower shape and the number of clusters in the CES detector. However, even after these cuts there is still a residual background of about 30% at $p_T^\gamma = 27 \text{ GeV}/c$. The background estimate is based on the number of hits in the CPR detector [29]. We estimate the γ -jet balance separately for the signal and background and find the results to be consistent to within 1%. However, the agreement strongly depends on the cuts used in the analysis, and for looser cuts we observe differences of up to 5%.

Further cuts are applied to reduce the effects from QCD radiation:

- The photon and the jet are required to be back to back in azimuthal angle: $\Delta\phi(\gamma, \text{jet}) > 3 \text{ rad}$.
- The event has no more than one jet with $p_T > 3 \text{ GeV}/c$ and $|\eta| < 2.4$.

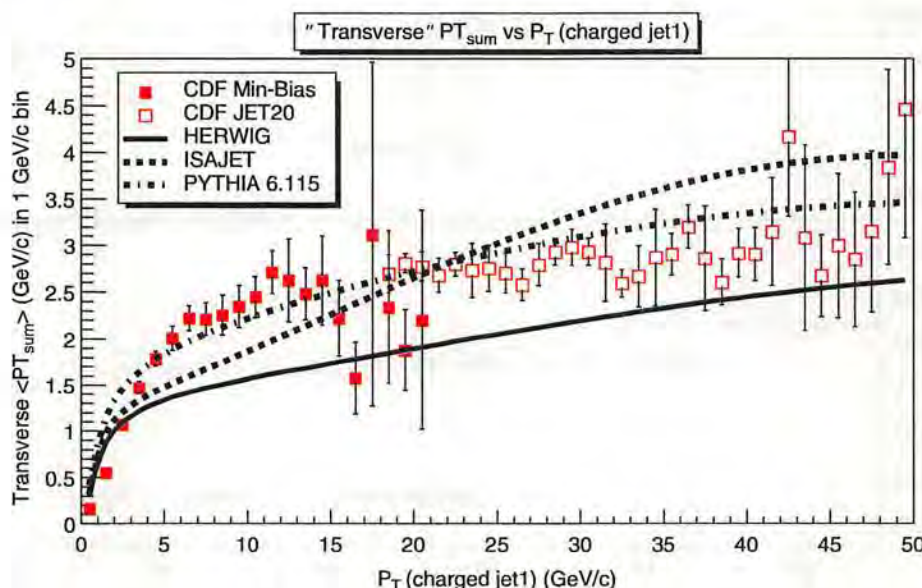


Fig. 33. The average transverse momentum of charged particles in the transverse region as described in the text versus leading jet p_T [32] calculated using tracks in $R_{\text{jet}} = 0.7$. The data are shown as points and are compared to the predictions from PYTHIA (dashed-dotted line), HERWIG (solid line), and ISAJET (dashed line).

Furthermore, only events with one reconstructed vertex are used, and thus no correction for multiple $p\bar{p}$ interactions is necessary.

The γ -jet balance is shown versus jet η after applying the η -dependent corrections in Fig. 34 for jet with $R_{\text{jet}} = 0.4$. The data, PYTHIA, and HERWIG show no residual dependence on η_{jet} as desired. Note that the p_T balance between the jet and the photon is not expected to be zero at this stage of the correction procedure. The overall scale difference between data, PYTHIA, and HERWIG will be discussed in Section 10.2.

Next, we apply also the absolute correction to the jet momenta making the jet p_T independent of the calorimeter response. Fig. 35 shows the resulting p_T balance for data, PYTHIA, and HERWIG for $R_{\text{jet}} = 0.4$. For comparison, the p_T balance calculated using particles at generator level without detector simulation is overlaid. Tables 4 and 5 summarize the mean and the width obtained from fits of Gaussians to these distributions within the range -0.4 to 0.4 for all jet cone sizes. For jets from data with $R_{\text{jet}} = 0.4$ the mean p_T balance is measured to be $p_T^{\text{jet}}/p_T^\gamma \approx 0.91$. Compared to the data, the mean found in PYTHIA is about 2% higher and for HERWIG it is 2% lower. Generally, the p_T of the jet is smaller than the p_T of the photon due to the energy lost outside the jet cone. In fact, one observes that for the larger cone sizes, in particular $R_{\text{jet}} = 1.0$, the mean is much closer to 0 since there is nearly no energy lost outside the cone. For particle jets, the mean values of PYTHIA and HERWIG agree with the respective calorimeter jets to within 1%, which proves the validity of the absolute correction procedure. The observed differences between the generators reflect the different modeling of the underlying physics process. This difference is largest for $R_{\text{jet}} = 0.4$. However, the data generally lie between PYTHIA and HERWIG and agree with both to within 2%.

From Table 5 we note that the data resolution is around 1–7% worse than HERWIG and 12% worse than PYTHIA.

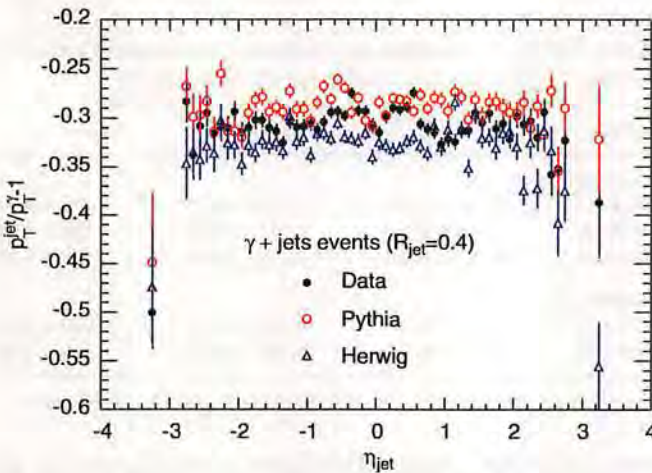


Fig. 34. p_T balance, $p_T^{\text{jet}}/p_T^\gamma - 1$, in data (full circles), PYTHIA (open circles) and HERWIG (open triangles) as function of η_{jet} for $R_{\text{jet}} = 0.4$.

We observe that HERWIG has a wider resolution than PYTHIA for both calorimeter and for particle jets.

After applying all corrections (η -dependent, absolute, OOC+UE) we obtain the γ -jet balance as shown in Fig. 36. Table 6 contains the corresponding mean values derived using a fit of a Gaussian to data and MC distributions for all three cone sizes. Data and MC agree with zero to within 2% except for HERWIG for a cone size of $R_{\text{jet}} = 0.4$. The differences between data and simulation are equal to those observed in Table 4, since the OOC and UE corrections were derived from PYTHIA and uniformly applied to all samples.

10.1.2. Using Z-jet events

Another excellent calibration sample is provided by $Z \rightarrow l^+l^-$ events where the p_T of the Z boson provides a reference scale for the jet. The advantage compared to the γ -jet sample is that it is nearly free from background contamination, at the expense of smaller statistics. For this study we require the jet and the Z boson to be back to back, $\Delta\phi(\text{jet}, Z) > 3$ rad, and no extra jets with $p_T > 3$ GeV/c and $|\eta| < 2.4$.

In Fig. 37 we compare the Z -jet balance, $p_T^{\text{jet}}/p_T^Z - 1$, in $Z \rightarrow e^+e^-$ and $Z \rightarrow \mu^+\mu^-$ events for data, PYTHIA, and HERWIG after all corrections. The mean values derived from fits of Gaussians to the Z -jet balance distributions between -0.3 and $+0.3$ are given in Table 7. They are reasonably close to zero for all cone sizes, and the data agree with the MC to within the statistical uncertainties of 1%.

10.1.3. Using dijet events

The η -dependent corrections have been obtained from the PYTHIA dijet and jet data samples. As explained in Section 6, the data and MC have different η -dependent corrections. This section describes the choice of the dijet-balancing technique as the η -dependent correction method and the use of only PYTHIA MC to correct all MC samples.

A different approach to address the η -dependence of jet response is the so-called “Missing E_T Projection Fraction” (MPF) method. This approach was used in Run I by the CDF [36] and DZero [40] experiments. The MPF is defined as

$$\text{MPF} = \frac{\vec{E}_T \cdot \vec{p}_T^{\text{probe}}}{(p_T^{\text{probe}} + p_T^{\text{trigger}})/2} \quad (36)$$

where the vector of the missing transverse energy, \vec{E}_T , is used to quantify the difference between p_T^{probe} and p_T^{trigger} rather than using $p_T^{\text{probe}} - p_T^{\text{trigger}}$ as is done in the dijet-balancing method (see Section 6). In an ideal dijet production process with no gluon radiation and fragmentation effects, the MPF and the dijet balance methods are equivalent. That is,

$$\beta(\text{MPF}) \equiv \frac{2 - \langle \text{MPF} \rangle}{2 + \langle \text{MPF} \rangle} = \frac{2 + \langle f_b \rangle}{2 - \langle f_b \rangle} \equiv \beta_{\text{dijet}}. \quad (37)$$

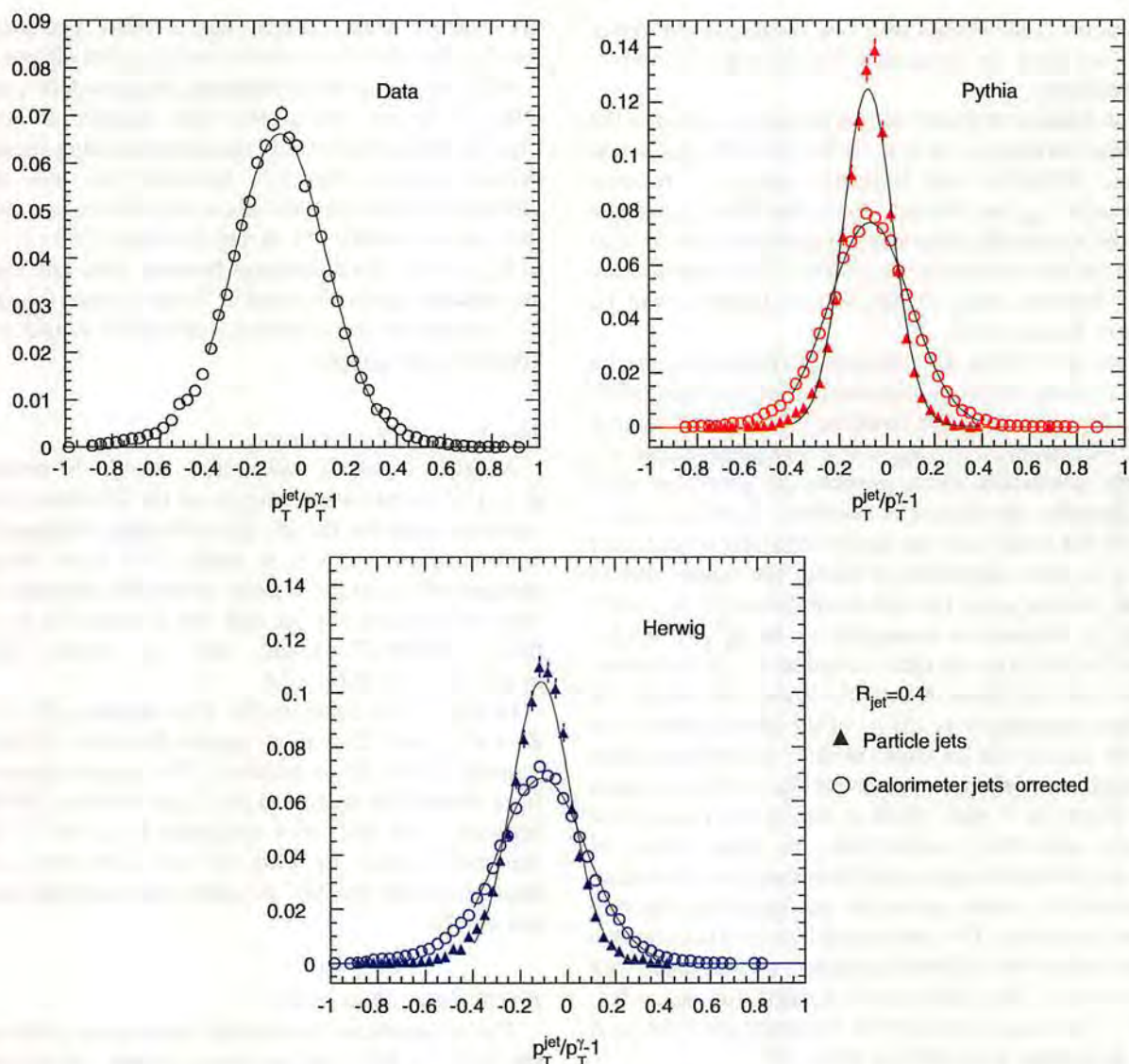


Fig. 35. γ -jet balance in data, PYTHIA, and HERWIG for $R_{\text{jet}} = 0.4$. Overlaid is the corresponding γ -jet balance on particle level jets (triangles) calculated using particles at generator level without detector simulation. The distributions are normalized to unit area.

Table 4

Mean value of $p_T^{\text{jet}}/p_T^{\gamma} - 1$ after η -dependent and absolute energy correction, for data, PYTHIA, and HERWIG for $R_{\text{jet}} = 0.4, 0.7$, and 1.0

| Sample | $R_{\text{jet}} = 0.4$ | $R_{\text{jet}} = 0.7$ | $R_{\text{jet}} = 1.0$ |
|-------------------------|------------------------|------------------------|------------------------|
| <i>Calorimeter jets</i> | | | |
| Data | -0.088 ± 0.001 | -0.016 ± 0.001 | 0.022 ± 0.001 |
| PYTHIA | -0.070 ± 0.001 | -0.015 ± 0.001 | -0.002 ± 0.001 |
| HERWIG | -0.108 ± 0.001 | -0.043 ± 0.001 | -0.024 ± 0.001 |
| <i>Particle jets</i> | | | |
| PYTHIA | -0.078 ± 0.001 | -0.037 ± 0.001 | -0.009 ± 0.001 |
| HERWIG | -0.113 ± 0.002 | -0.061 ± 0.002 | -0.019 ± 0.002 |

For PYTHIA and HERWIG, the values are given also for particle jets.

However, due to QCD radiation and OOC energy losses and UE contributions this does not exactly hold. In contrast to the dijet balancing method, the MPF method does not

Table 5

Width of $p_T^{\text{jet}}/p_T^{\gamma} - 1$ after the η -dependent and absolute energy correction, for data, PYTHIA, and HERWIG for $R_{\text{jet}} = 0.4, 0.7$, and 1.0

| Sample | $R_{\text{jet}} = 0.4$ | $R_{\text{jet}} = 0.7$ | $R_{\text{jet}} = 1.0$ |
|-------------------------|------------------------|------------------------|------------------------|
| <i>Calorimeter jets</i> | | | |
| Data | 0.199 ± 0.001 | 0.191 ± 0.001 | 0.191 ± 0.001 |
| PYTHIA | 0.176 ± 0.001 | 0.171 ± 0.001 | 0.169 ± 0.001 |
| HERWIG | 0.192 ± 0.001 | 0.181 ± 0.001 | 0.178 ± 0.001 |
| <i>Particle jets</i> | | | |
| PYTHIA | 0.105 ± 0.001 | 0.095 ± 0.001 | 0.090 ± 0.001 |
| HERWIG | 0.127 ± 0.002 | 0.116 ± 0.002 | 0.111 ± 0.002 |

For PYTHIA and HERWIG, the values are given also for particle jets.

correct for OOC energy. The reason is that E_T used in the MPF method is only affected by energy mismeasurement and has no sensitivity to the energy flow between the inside and

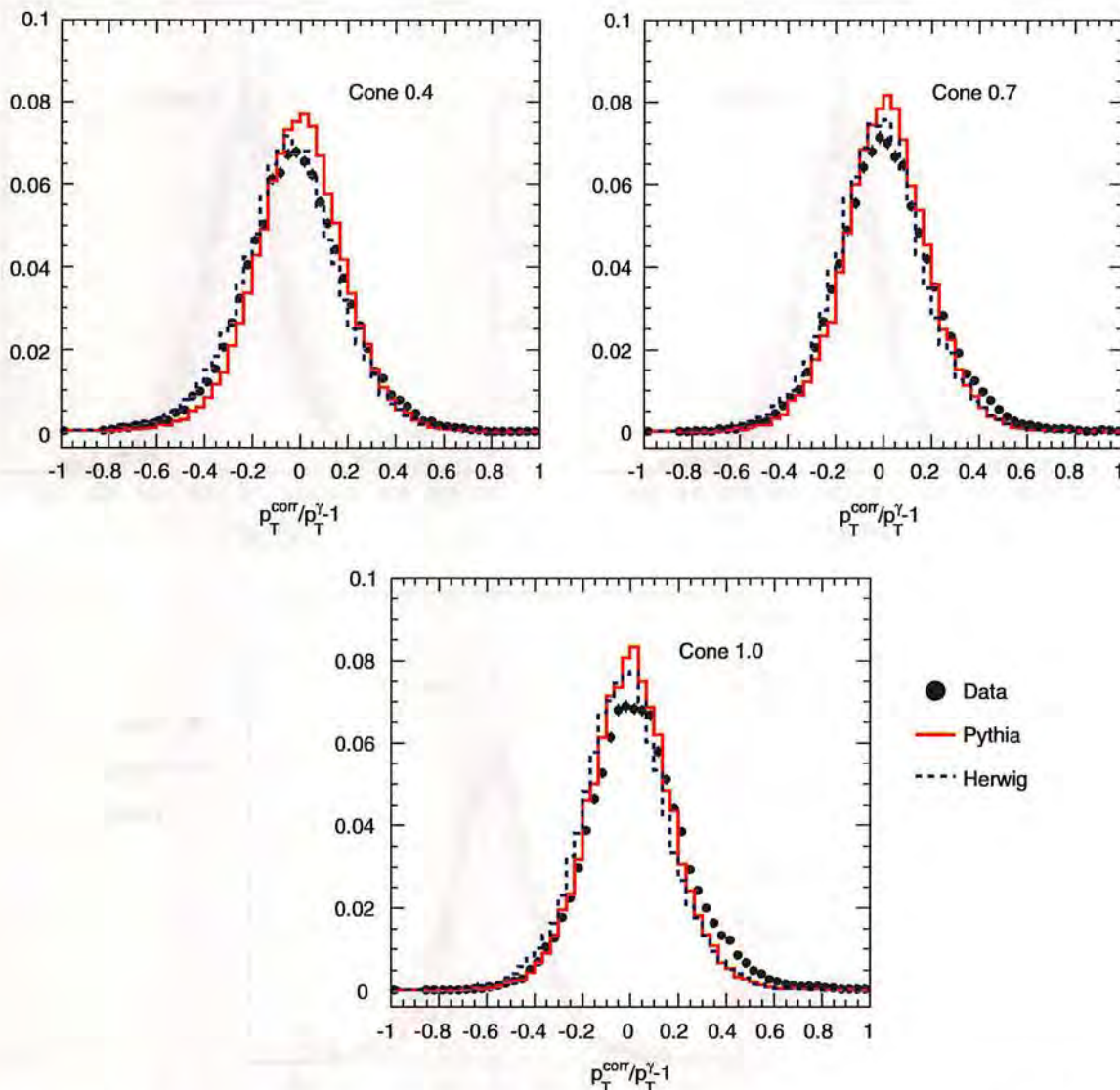


Fig. 36. γ -jet balance in data, PYTHIA, and HERWIG using $R_{\text{jet}} = 0.4, 0.7$, and 1.0 after η -dependent, absolute, and OOC + UE corrections.

Table 6

Mean value of $p_T^{\text{jet}}/p_T^\gamma - 1$ after all corrections, including the out-of-cone energy correction for data, PYTHIA, and HERWIG for jet cones of $R_{\text{jet}} = 0.4, 0.7$ and 1.0

| Sample | $R_{\text{jet}} = 0.4$ | $R_{\text{jet}} = 0.7$ | $R_{\text{jet}} = 1.0$ |
|--------|------------------------|------------------------|------------------------|
| Data | -0.019 ± 0.001 | 0.010 ± 0.001 | 0.024 ± 0.001 |
| PYTHIA | -0.001 ± 0.001 | 0.011 ± 0.001 | 0.000 ± 0.001 |
| HERWIG | -0.040 ± 0.001 | -0.018 ± 0.001 | -0.023 ± 0.001 |

the outside of the jet cone. On the other hand, the dijet-balancing method is sensitive to the energy inside the jet cone and will thus implicitly correct for an η -dependence of the OOC and UE effects. Since we estimate these corrections and systematic uncertainties only in the central region, we choose to use the dijet-balancing method as the primary correction method.

However, we use the MPF method to further investigate the discrepancy between PYTHIA and HERWIG in

Figs. 15–17 in Section 6. The HERWIG measurements are systematically higher than PYTHIA and data by about 10% for $25 < p_T^{\text{ave}} < 55 \text{ GeV}/c$ and $|\eta| > 0.6$ and agree very well at higher p_T^{ave} . The discrepancy is larger for $R_{\text{jet}} = 0.4$ jets than for $R_{\text{jet}} = 0.7$ and 1.0 . To shed more light on the origin of the discrepancy we compare the ratio $\beta(\text{MPF})/\beta_{\text{dijet}}$ as a function of η_{jet} for two different ranges of p_T^{ave} in Fig. 38. In the central region $\beta(\text{MPF})/\beta_{\text{dijet}}$ is consistent with unity for both ranges of p_T^{ave} . In the forward region $\beta(\text{MPF})$ increases with respect to β_{dijet} . For $25 < p_T^{\text{ave}} < 55 \text{ GeV}/c$ the data are well modeled by PYTHIA, but large discrepancies are observed in comparison to HERWIG. For $p_T^{\text{ave}} > 105 \text{ GeV}/c$, the data are in good agreement with both MC generators. Since the ratio $\beta(\text{MPF})/\beta_{\text{dijet}}$ is largely independent of the CDF jet energy scale, we conclude that the observed disagreement is not due to any residual problems of the CDF simulation but must originate from a difference in the underlying physics between HERWIG, PYTHIA, and data for low p_T dijet production.

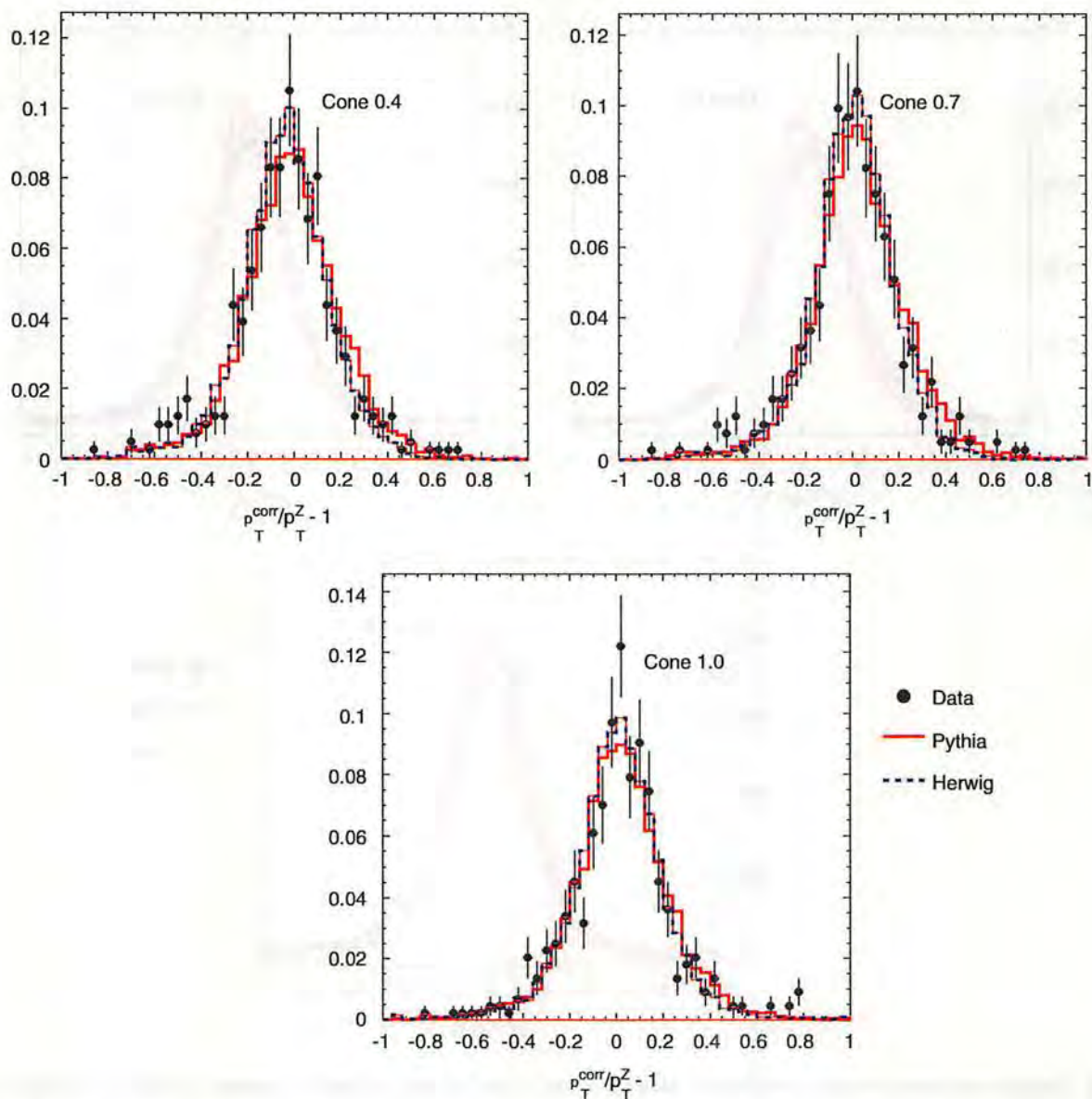


Fig. 37. Z-jet balance in data (closed black circles), PYTHIA (solid line), and HERWIG (dashed line) for $R_{\text{jet}} = 0.4$ (top left), $R_{\text{jet}} = 0.7$ (top right), and $R_{\text{jet}} = 1.0$ (bottom left) after all corrections.

Table 7

Measured mean value of $p_T^{\text{jet}}/p_T^Z - 1$ after all corrections, including the out-of-cone energy correction for data and PYTHIA calorimeter jets

| Sample | $R_{\text{jet}} = 0.4$ | $R_{\text{jet}} = 0.7$ | $R_{\text{jet}} = 1.0$ |
|--------|------------------------|------------------------|------------------------|
| Data | -0.026 ± 0.009 | 0.007 ± 0.009 | 0.013 ± 0.009 |
| PYTHIA | -0.016 ± 0.003 | 0.019 ± 0.003 | 0.015 ± 0.003 |
| HERWIG | -0.032 ± 0.003 | -0.011 ± 0.002 | -0.009 ± 0.003 |

The result is given for $R_{\text{jet}} = 0.4, 0.7$ and 1.0 .

We also compare the β_{dijet} for particle jets with $R_{\text{jet}} = 0.4$ between PYTHIA and HERWIG in Fig. 39 for $\hat{p}_T > 18 \text{ GeV}/c$ and find that for PYTHIA it is independent of η_{jet} while for HERWIG it rises with increasing η_{jet} . Since this behavior is

only found in the dijet samples, we do not consider HERWIG dijet samples for the determination of the η -dependent corrections or their systematic uncertainties. In γ -jet (see Fig. 34), Z-jet, or $t\bar{t}$ events no such problems are seen. At this moment we do not have any explanation for the differences. It could be due a number of effects such as modeling of initial or final state radiation or modeling of the UE, and it will be studied again in future versions of the generators.

10.1.4. Using $W \rightarrow jj$ decays in $t\bar{t}$ events

The jet energy scale can be studied using the hadronic decay of resonances with well-measured masses such as the W and Z bosons. Unfortunately, the decays of W and Z bosons to jets are swamped by multijet QCD backgrounds in hadron collider environments. One solution is to study

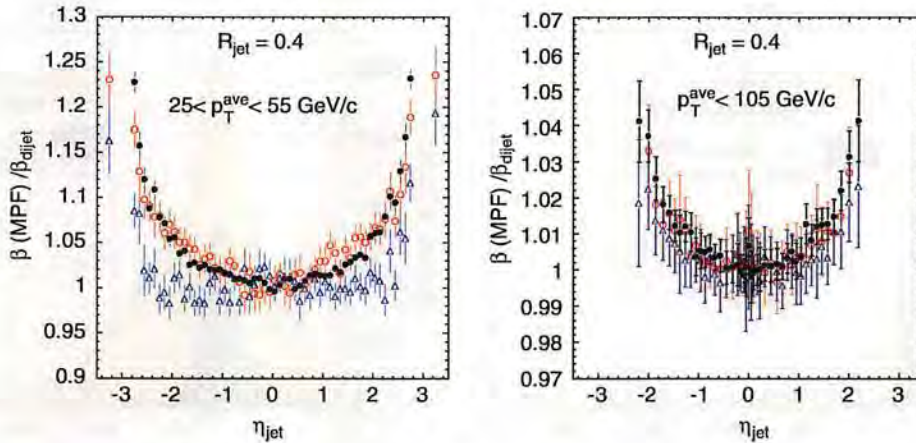


Fig. 38. $\beta(\text{MPF})/\beta_{\text{dijet}}$ as a function of η_{jet} for $R_{\text{jet}} = 0.4$ jets in data (circles), PYTHIA (open circles), and HERWIG (open triangles) for $25 < p_{\text{T}}^{\text{ave}} < 55 \text{ GeV}/c$ and $p_{\text{T}}^{\text{ave}} > 105 \text{ GeV}/c$.

hadronic W boson decays in $t\bar{t}$ events which have relatively small background contamination. This section summarizes the application of this technique. For complete details, see Ref. [37].

At the Tevatron, top quarks are produced primarily as top pairs and decay to W bosons and b quarks nearly 100% of the time. The W bosons in turn decay into lepton-neutrino (lν) or quark pairs (q q̄). This measurement uses the “lepton + jets” channel of $t\bar{t}$ candidates in which only one of two W bosons decays to lν while the other decays to quark pairs. The lepton + jets events are selected by requiring one well-identified electron or muon, large (E_T) due to the neutrino from the W decay, and at least four jets in the final state. The missing transverse energy \cancel{E}_T is measured by the imbalance in the calorimeter transverse energy and is required to be greater than 20 GeV. Jets are reconstructed with a radius $R_{\text{jet}} = 0.4$. The sample is divided into four subsamples with various sensitivities for better performance. First, the events are separated based on the number of jets that are b-tagged in the event. The SECVTX [38] algorithm based on the identification of secondary vertices inside jets is used to tag b-jets. Events with 2-, 1-, and 0-tag are considered separately. Furthermore, events with 1-tag are separated based on the fourth jet E_T threshold. Events in the 1-tag(T) category have four jets with $E_T > 15 \text{ GeV}$, while events in the 1-tag(L) category have three jets with $E_T > 15 \text{ GeV}$ and the fourth jet with $8 < E_T < 15 \text{ GeV}$.

Before reconstructing the invariant mass of hadronically decaying W bosons (m_{jj}), we apply the η -dependent and absolute corrections to jet energies. In addition, corrections specific to light quark jets from W boson decays in $t\bar{t}$ events are applied. To reconstruct m_{jj} , one has to know which of the jets in the final state comes from the W boson decay. This problem is dealt with by considering all the dijet combinations that can be made using the jets that are not b-tagged. Only the four highest E_T jets are considered. Consequently, there can be more than one mass per event that are considered. There are in fact 1, 3, and 6 m_{jj} per

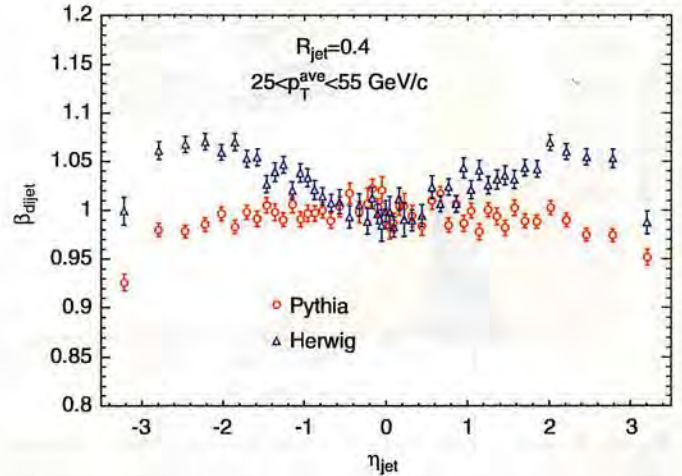


Fig. 39. β_{dijet} for particle jets as a function of jet η_{jet} for PYTHIA (open circles) and HERWIG (open triangles) for $\hat{p}_{\text{T}} > 18 \text{ GeV}/c$ and for $R_{\text{jet}} = 0.4$.

event for the 2-tag, 1-tag, and 0-tag subsamples, respectively. The distribution of m_{jj} for HERWIG $t\bar{t}$ events is shown in Fig. 40 for each event category (with a top quark mass (M_{top}) of $178 \text{ GeV}/c^2$). The mass resolution improves with the number of b-tagged jets present in the event.

Distributions of m_{jj} are constructed from HERWIG $t\bar{t}$ MC with $M_{\text{top}} = 178 \text{ GeV}/c^2$ (corresponding to the central value of the Tevatron Run I average) with jet energy scale values ranging from $-3\sigma_c$ to $+3\sigma_c$, where σ_c is the total jet energy scale uncertainty defined in Section 11 of this document. Smooth probability density functions are obtained by fitting the mass distributions as a function of M_{top} and jet energy scale using an analytical function. Fig. 41 shows the m_{jj} distribution for various jet energy scale values for the 2-tag subsample with the fitted templates overlaid. Templates for background events are obtained from W + jets, QCD multijets, and single-top MC events.

The fitted jet energy scale is obtained by comparing the reconstructed mass distributions obtained in the data with

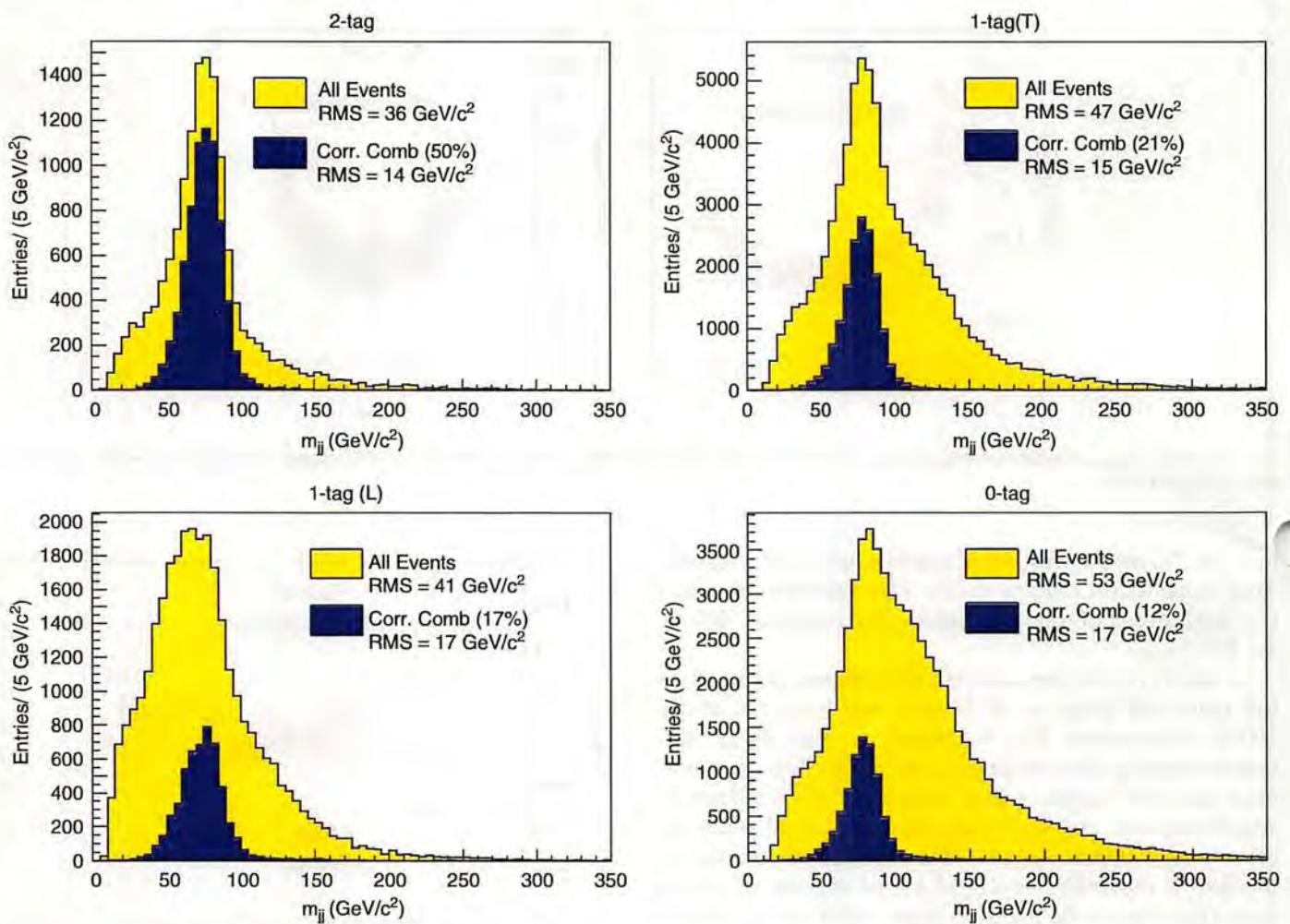


Fig. 40. Reconstructed hadronic W boson mass from HERWIG $t\bar{t}$ events with $M_{top} = 178 \text{ GeV}/c^2$ for 2-tag events (upper-left), 1-tag (T) events (upper-right), 1-tag(L) events (bottom-left), and 0-tag events (bottom-right). The outer histograms show the mass distributions for all combinations and the inner histograms show the distributions only for the correct jet-parton assignments.

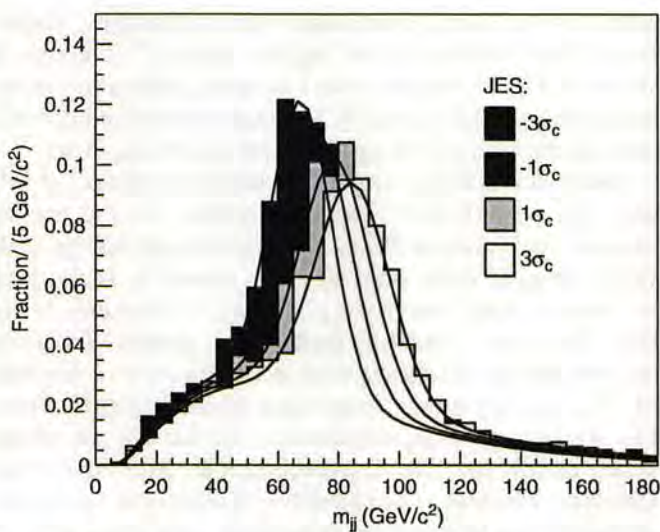


Fig. 41. Four m_W signal templates are shown for jet energy scale (JES) values ranging from $-3\sigma_c$ to $+3\sigma_c$. Overlaid are the fitted parameterizations at each value of jet energy scale.

the signal and background templates using an unbinned likelihood fit. The systematic uncertainties in this measurement arises from the MC modeling of signal and background events that we use to create the templates and thus extract the jet energy scale. We consider uncertainties in the top quark mass ($\pm 5 \text{ GeV}/c^2$), initial and final state radiation, parton distribution functions, background mass shape, and general MC modeling. The total systematic uncertainties correspond to $0.68\sigma_c$.

This measurement is performed using 318 pb^{-1} of data that results in a total of 165 events in the lepton+jets sample. The application of the likelihood fit to the data yields $-0.76 \pm 1.00 (\text{stat.})\sigma_c$. This means that the data and simulation of $t\bar{t}$ events is in agreement within one σ_c . By adding the systematic uncertainties, this result changes to $-0.76 \pm 1.27\sigma_c$. The m_W distributions reconstructed in the data are shown in Fig. 42. The shape of the signal and background MC templates corresponding to the best fit are overlaid on top of the histograms. We conclude that the average jet energy scale as determined by $W \rightarrow jj$ decays is

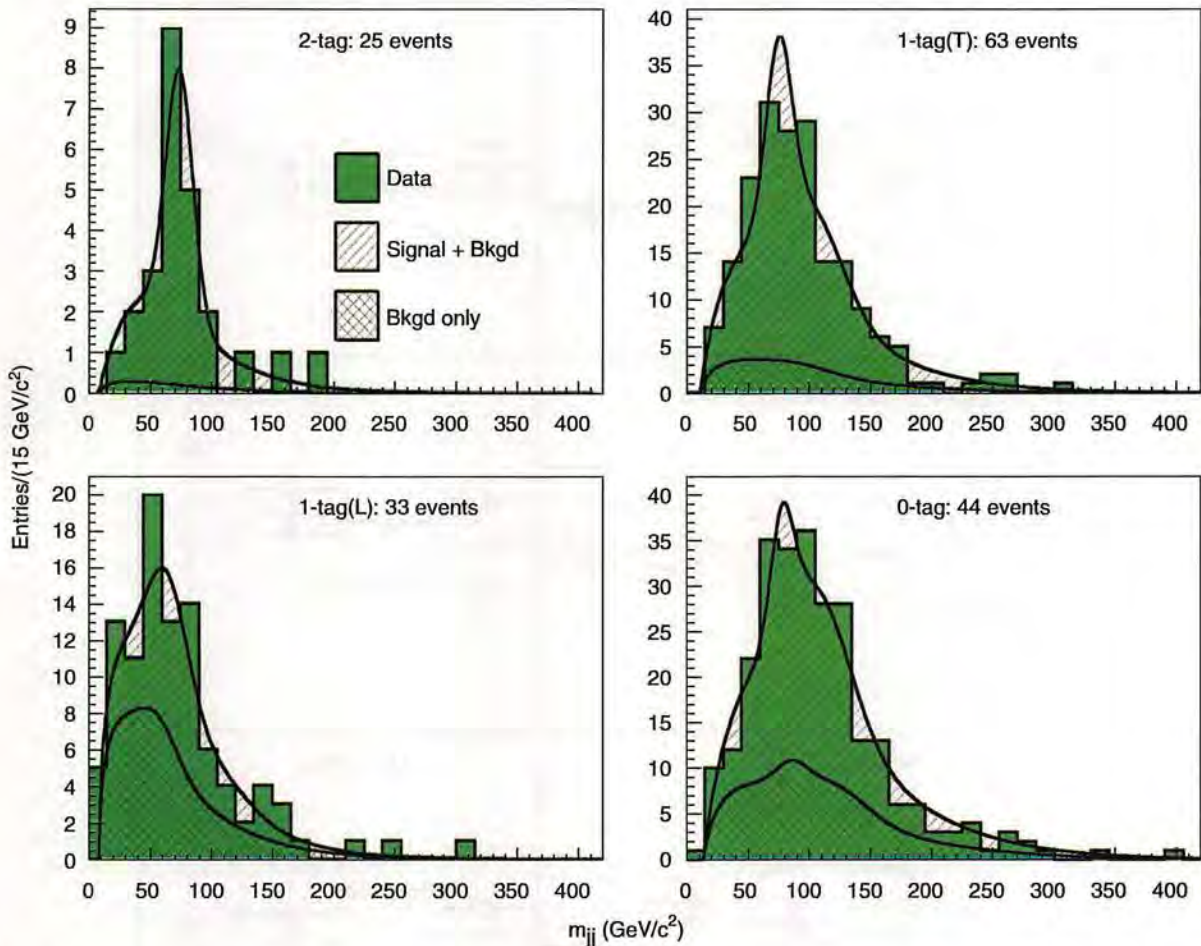


Fig. 42. Data m_{jj} distributions for the 2-tag (upper-left), 1-tag (T) (upper-right), 1-tag(L) (lower-left), and 0-tag (lower-right) subsamples. The signal and background template shapes corresponding to the best fit of the jet energy scale cross-check are overlaid on the histograms. The value of M_{top} has been constrained to be $178 \text{ GeV}/c^2$.

in good agreement with the nominal jet energy scale of the CDF MC simulation.

The calibration of the jet energy scale with $W \rightarrow jj$ decays has been used to measure precisely the top quark mass in Run II [39]. We note that jet energy scale uncertainties obtained from this technique are mostly statistical and will improve as more data are accumulated.

10.2. Test of the uncertainties

We test whether the agreement of data and MC is within the calculated uncertainties for all p_T and η bins. Fig. 43 shows the difference of the mean values of the γ -jet balance between data and PYTHIA as a function of p_T for six regions of pseudo-rapidity. Overlaid is the total systematic uncertainty on the jet energy scale. It is seen that the data are modeled well by the simulation at all η and p_T , and that any differences are covered by the quoted uncertainties. In Fig. 44, the same comparison has been made with HERWIG, leading to the same conclusion. The γ -jet balance for data, PYTHIA, and HERWIG is independent of p_T^γ and η_{jet} after applying all the corrections.

10.3. Summary

We have shown that the corrections and the systematic uncertainties are valid for several control samples. We have found that the transverse momentum of the jet, after all with corrections, is in balance the transverse momentum of the γ and the Z boson in both measured and simulated $\gamma + jets$ and $Z + jets$ samples, respectively. We also determined the average jet energy scale using $W \rightarrow jj$ decays in $t\bar{t}$ events and found good agreement between data and simulation.

We have also investigated differences between the PYTHIA and HERWIG MC generators. With the dijet-balancing technique we observe rather large differences in the plug calorimeter region, which are also seen for particle jets. For the dijet process, the data do not support the behavior of HERWIG. This problem is only observed in the dijet process, e.g. not in the γ -jet process.

11. Summary of systematic uncertainties

We have presented the systematic uncertainties associated with the jet energy response. The systematic

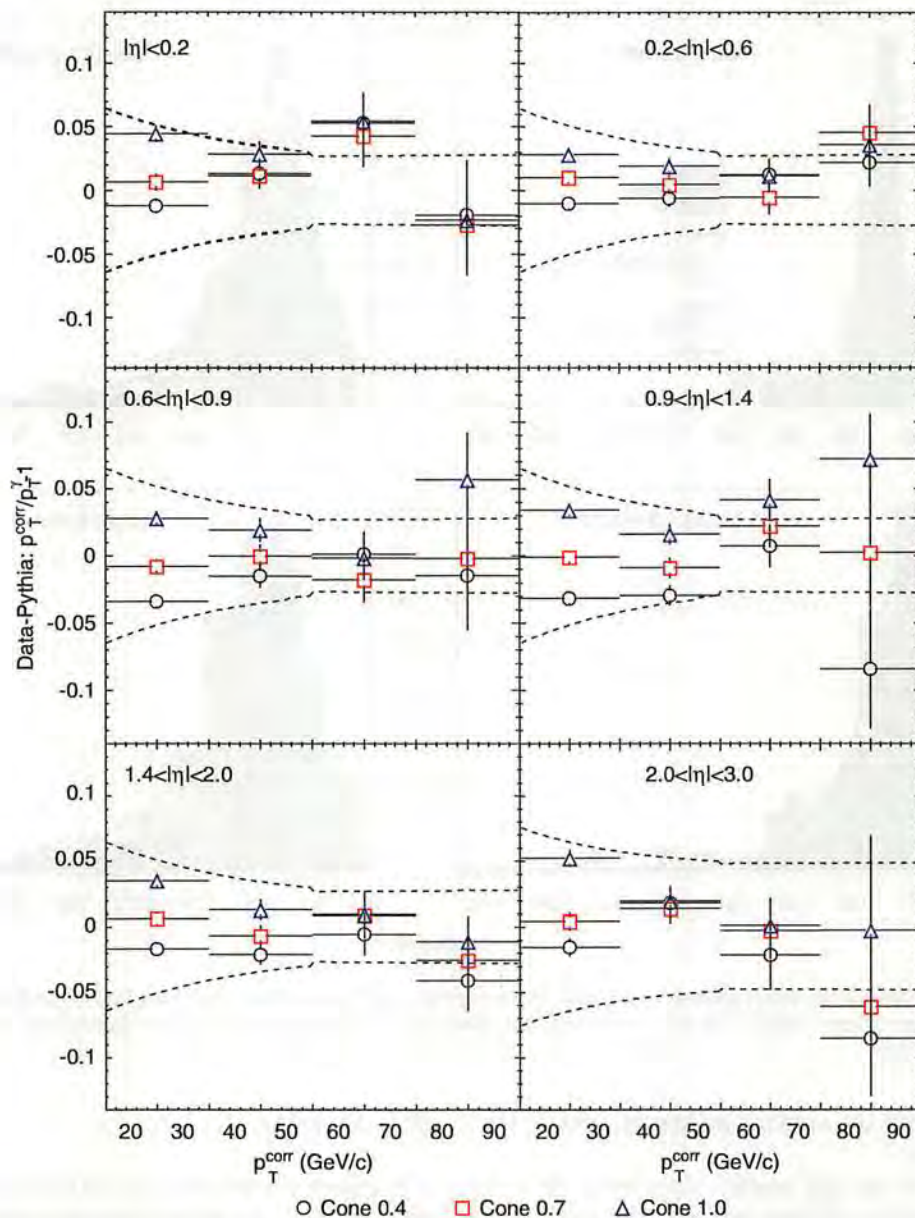


Fig. 43. Difference of the γ -jet balance between data and PYTHIA as a function of p_T^γ in six regions of η_{jet} . All three cone sizes are shown: 0.4 (open squares), 0.7 (open circles), and 1.0 (open triangles). The curves indicate the total systematic uncertainty in each η region.

uncertainties are largely independent of the corrections applied and mostly arise from the modeling of jets by MC simulation and from uncertainties in the calorimeter response to single particles.

Fig. 45 shows the individual systematic uncertainties as a function of jet p_T in the central region, of the calorimeter, $0.2 < |\eta| < 0.6$, of the calorimeter. They are independent and thus added in quadrature to derive the total uncertainty.

For $p_T > 60 \text{ GeV}/c$ the largest contribution arises from the absolute jet energy scale which is limited by the uncertainty of the calorimeter response to charged hadrons. A further reduction of the systematic uncertainties can be achieved by improving the tuning of the simulation, and by including in situ single track data which recently became available, replacing test beam data used so

far in the momentum region $7\text{--}20 \text{ GeV}/c$ and probably beyond.

At low p_T the largest uncertainty arises from the OOC energy which can be improved by further studying differences between the data and the predictions of PYTHIA and HERWIG, and by optimizing the fragmentation and UE model of both generators. Additional uncertainties arise from the fragmentation models, the stability of the calorimeter calibration and the underlying event modeling.

12. Conclusions

We have determined a set of corrections to estimate the parton energy from the jet energy measured in the CDF,

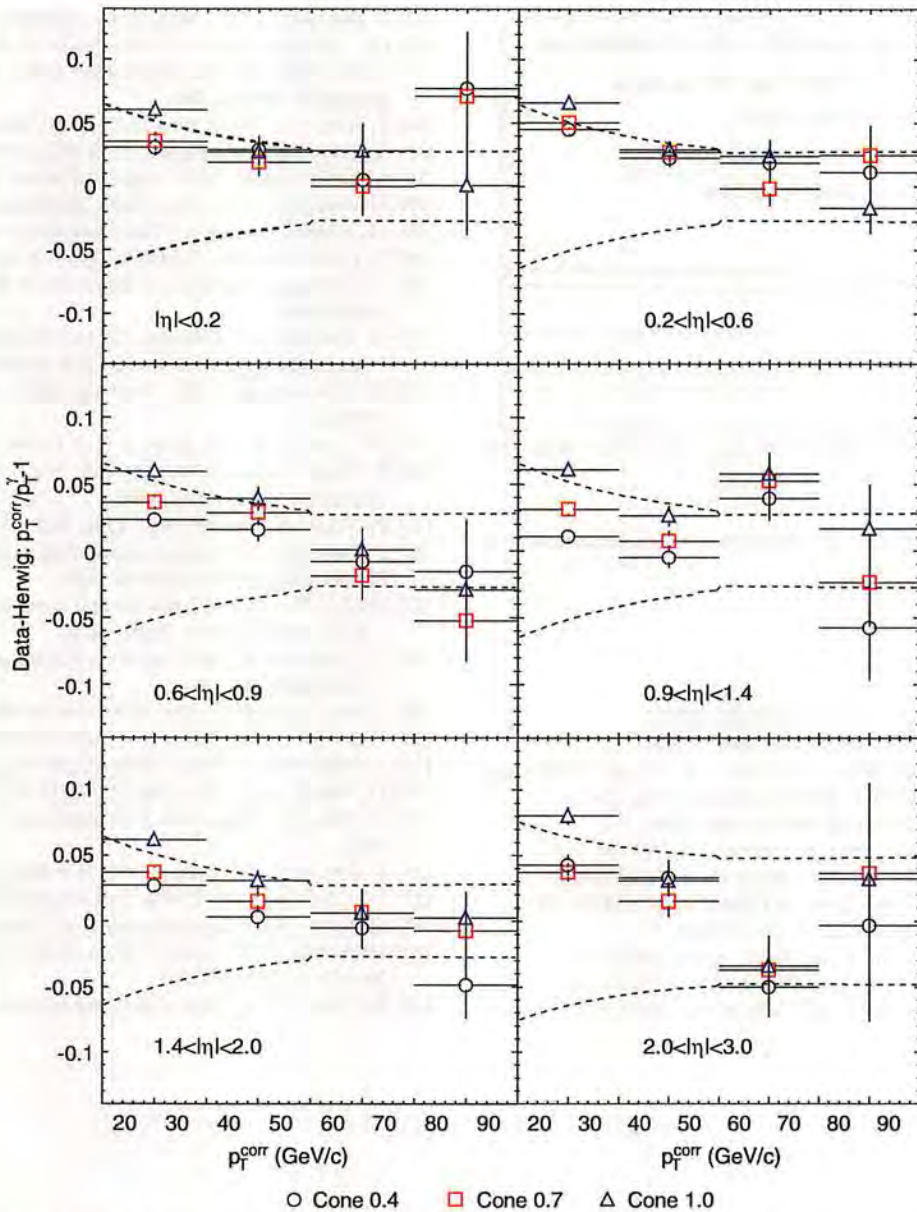


Fig. 44. Difference of the γ -jet balance between data and HERWIG as a function of p_T^γ in six regions of η_{jet} . All three cone sizes are shown: 0.4 (open squares), 0.7 (open circles), and 1.0 (open triangles). The curves indicate the total systematic uncertainty in each η region.

The corrections are based on data taken between 2001 and 2004 at the Tevatron $p\bar{p}$ collider, corresponding to an integrated luminosity of about 350 pb^{-1} , and on test beam data.

These corrections involve several steps, and for each step a systematic uncertainty is determined. Both the central and forward components of the calorimeter are calibrated using test beam and in situ data. The response of jets in the forward calorimeter is calibrated with respect to that of the central calorimeter. The shower simulation is tuned in detail to the data in the central rapidity region. Using several MC generators, it has been shown to provide a good description of the energy response of various physics processes. The MC simulation is used to derive a correction for the calorimeter jet energy response in the

central region. Further corrections are made for multiple $p\bar{p}$ interactions, the underlying event, and the fractional energy of the parton that is not contained within the jet cone. Finally, we have verified that the corrected jet energy is a good measure of the initial parton energy for prompt photon, Z events, and W boson samples, and we have shown that the various MC generators provide a good description of the data within the quoted systematic uncertainties.

The total systematic uncertainty on the jet energy scale varies between 8% at low jet p_T and 3% at high jet p_T . The dominant sources of systematic uncertainty are the uncertainty on the test beam measurements at high energy and the uncertainty in modeling the energy flow around the jet cone.

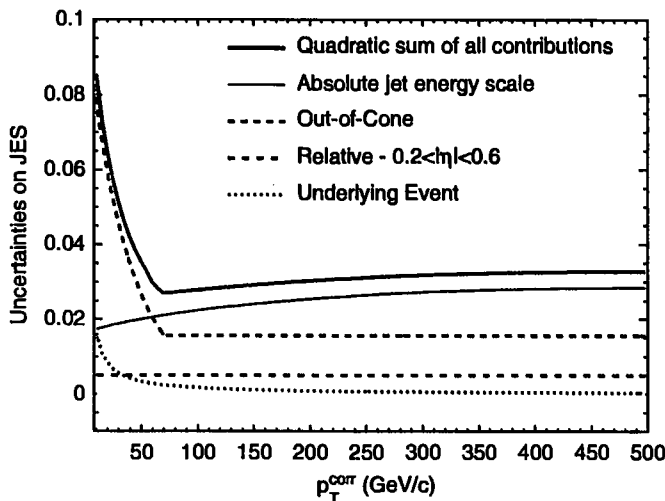


Fig. 45. Systematic uncertainties as a function of the corrected jet p_T in $0.2 < |\eta| < 0.6$.

References

- [1] T. Affolder, et al., Phys. Rev. D 64 (2001) 032001.
- [2] T. Affolder, et al., Phys. Rev. D 63 (2001) 032003.
- [3] F. Abe, et al., Nucl. Instr. and Meth. A 387–403 (1988) and FERMILAB-PUB-96-390-E, CDF-II Collaboration (1996).
- [4] A. Sill, et al., Nucl. Instr. and Meth. A 447 (2000) 1–8.
- [5] T. Affolder, et al., Nucl. Instr. and Meth. A 526 (2004) 249.
- [6] S. Kuhlmann, et al., Nucl. Instr. and Meth. A 518 (2004) 39.
- [7] G. Apollinari, et al., Nucl. Instr. and Meth. A 412 (1998) 515.
- [8] F. Abe, et al., Phys. Rev. Lett. 73 (1994) 2662.
- [9] G. Ascoli, et al., Nucl. Instr. and Meth. A 268 (1988) 33.
- [10] D. Acosta, et al., Nucl. Instr. and Meth. A 461 (2001) 540.
- [11] L. Balka, et al., Nucl. Instr. and Meth. A 267 (1988) 272.
- [12] S. Bertolucci, et al., Nucl. Instr. and Meth. A 301 (1988) 267.
- [13] G. Apollinari, et al., Proceedings of the Fourth International Conference on Calorimetry in High Energy Physics, World Scientific, Singapore, 1994, p. 200.
- [14] F. Abe, et al., Phys. Rev. D 52 (1995) 4784.
- [15] S. Eidelman, et al., Phys. Lett. B 592 (2004) 1.
- [16] S.R. Hahn, et al., Nucl. Instr. and Meth. A 267 (1988) 351.
- [17] S. Bertolucci, et al., Nucl. Instr. and Meth. A 267 (1988) 301.
- [18] M. Albrow, et al., Nucl. Instr. and Meth. A 480 (2002) 524.
- [19] D. Cauz, et al., Int. J. Modern Phys. A 16 (supp01c) (2001) 1126.
- [20] L. Lönnblad, S. Mrenna, T. Sjöstrand, P. Skands, LU-TP 01-21, hep-ph/0108264.
- [21] G. Corcella, I.G. Knowles, G. Marchesini, S. Moretti, K. Odagiri, P. Richardson, M.H. Seymour, B.R. Webber, JHEP 0101 (2001).
- [22] J.M. Butterworth, J.R. Forshaw, M.H. Seymour, Z. Phys. C 72 (1996) 637.
- [23] H.L. Lai, et al., Eur. Phys. J. C 12 (2000) 375.
- [24] R. Field, "HERWIG, JIMMY and PYTHIA Tune A", talk given at TeV4LHC at Fermilab, 2004.
- [25] P. Nason, S. Dawson, R.K. Ellis, Nucl. Phys. B 303 (1988) 607.
- [26] E. Gerchtein, M. Paulini, Computing in High Energy and Nuclear Physics 2003, physics/0306031, 2003.
- [27] GEANT, "Detector description and simulation tool", Cern Program Library Long Writeup W5013, 1993.
- [28] G. Grindhammer, M. Rudowicz, S. Petersen, Nucl. Instr. and Meth. A 290 (1990) 469.
- [29] F. Abe, et al., Phys. Rev. D 48 (1993) 2998.
- [30] T. Affolder, et al., Phys. Rev. Lett. 94 (2005) 091803.
- [31] S. Sabik, Ph.D. Thesis, University of Toronto, 2005.
- [32] D. Acosta, et al., Phys. Rev. D 70 (2004) 072002.
- [33] H. Baer, F.E. Paige, S.D. Protopescu, and X. Tata, hep-ph/0312045, 2003.
- [34] F. Abe, et al., Phys. Rev. Lett. 77 (1996) 438.
- [35] J.-F. Arguin, Ph.D. Thesis, University of Toronto, 2005.
- [36] D. Acosta, CDF Collaboration, et al., Phys. Rev. D 71 (2005) 052003.
- [37] D. Acosta, CDF Collaboration, et al., Phys. Rev. Lett. and Phys. Rev. D 72 (2006) 032003.
- [38] B. Abbott, et al., Nucl. Instr. and Meth. A 424 (1999) 352.

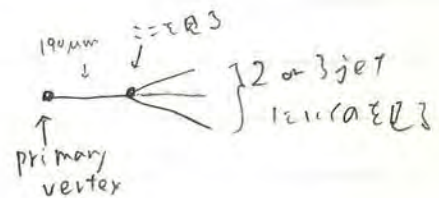
3

- CDF LJT 5.6 fb^{-1} (1010.4582)

Selection : 1 l 20

OR: $|e \text{ w. } E_T| > 20 \text{ & } |n| < 1.0$
 $|\mu \text{ w. } p_T| > 20 \text{ & } |\eta| < 1.0$
 $|\mu \text{ w. } p_T| > 20 \text{ & } |n| > 1.0 \text{ (trig. by } B_T)$

- MET20
 - $4^\circ < \Delta\eta < 2.0$
 - 1^+jet (SECVTX algorithm)



$$\begin{aligned}
 L(\mathcal{Y} | m_t, \Delta_{\text{JES}}) &= "(\text{M}_t, \Delta_{\text{JES}}) のときに \mathcal{Y} が検出される cross section" \\
 &= "\mathcal{Y} が検出されると \mathcal{X} の \text{尤度}" \\
 &= \int \frac{f(z_i) f(z_j)}{(\text{FF})} \underset{\substack{\text{PDF} \\ \text{CTE&SL}}}{\text{TF}}(\mathcal{Y} | \mathcal{X}, \Delta_{\text{JES}}) |\mathcal{M}(m_t, \mathcal{X})|^2 d\mathcal{X} \\
 &\quad \text{simulation} \quad \text{top} \xrightarrow{\text{LO}} \text{observed} \quad \text{MC} \\
 &\quad \text{top} \text{ が } m_t \text{ のとき } \\
 &\quad \{ \mathcal{X} \} \text{ の配位が } \text{あるところ}
 \end{aligned}$$

全 events が tE たりと仮定する。

$L_{tot}(\{\psi\} \mid m_t, \Delta_{JES}) := \prod L(\psi_i \mid m, \Delta)$ を最大化すればよ。

BGの寄与を除きたい。実は

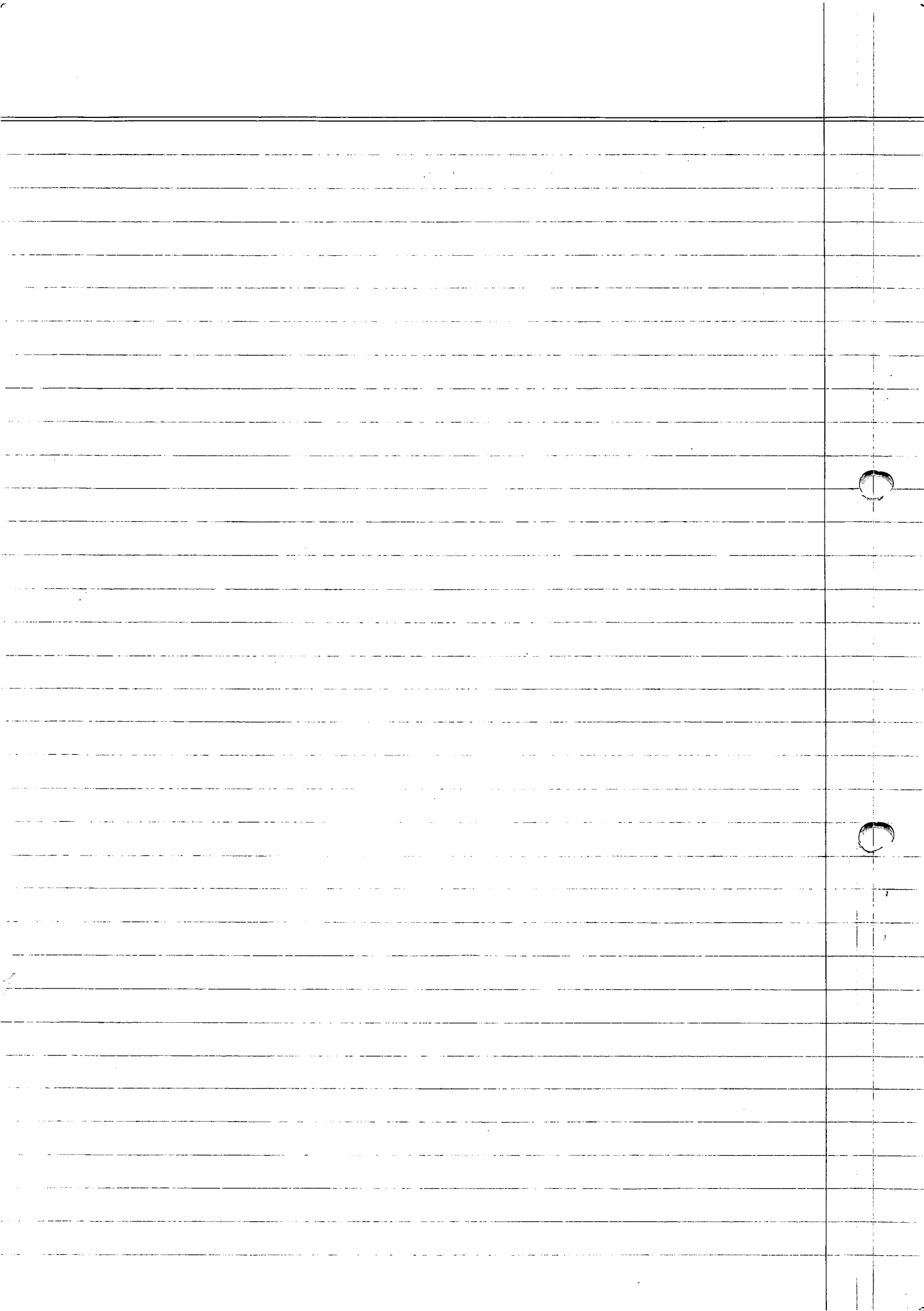
$$L_{tot} = \prod_{i \in sig} L_i \times \prod_{i \in BGS} L_i$$

102

$$\prod_{i \in \text{sig}} L = \frac{L_{\text{tot}}}{\prod_{i \in BG} L_i} \approx \frac{L_{\text{tot}}}{(L)^{n_{BG}}}$$

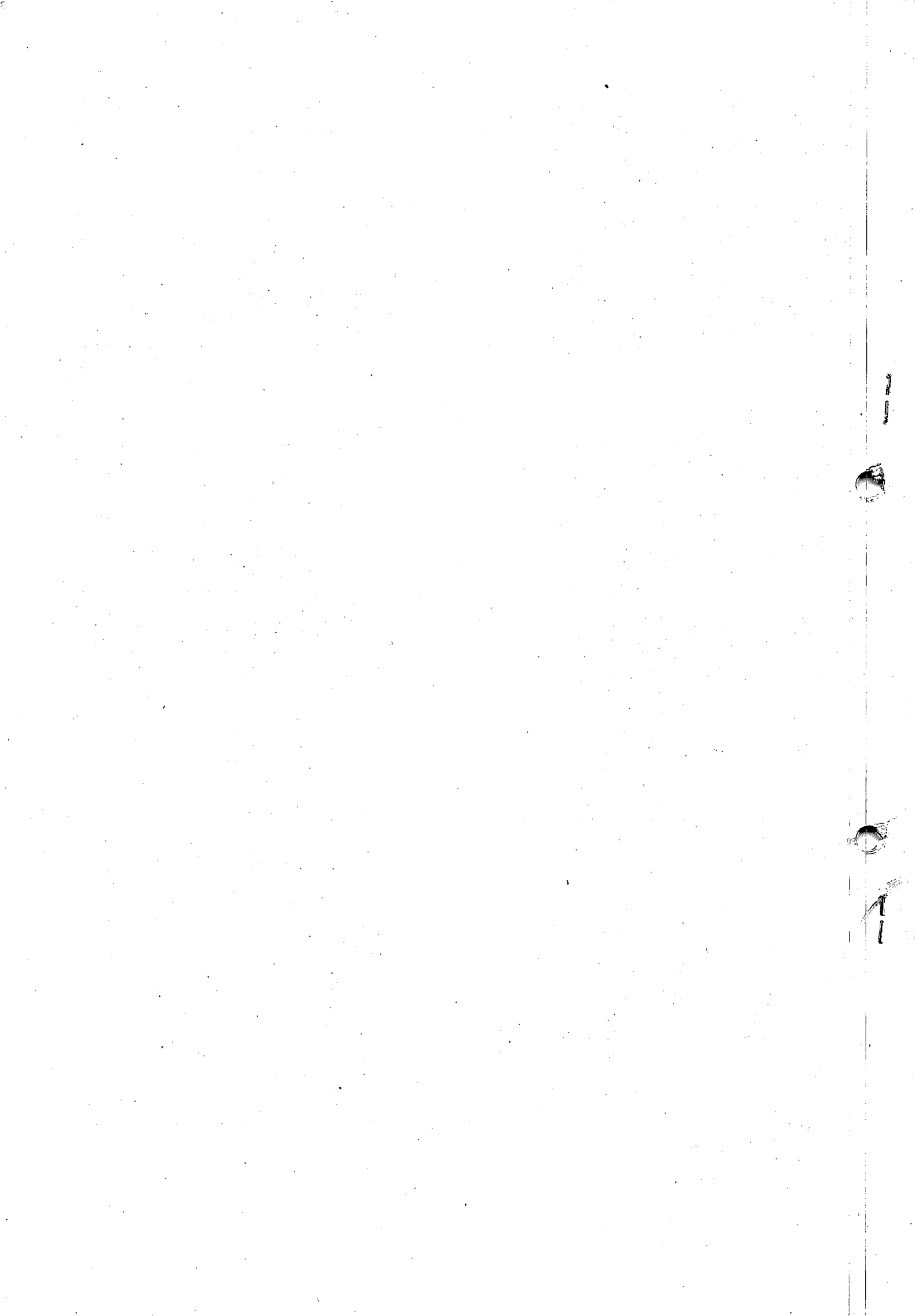
$$n_{BG} = \sum_{i \in T_{BG}} (\text{各 } i \text{ が } BG_i \text{ にある確率})$$

$\left\{ \begin{array}{l} W + (b|c) \times 2 \\ W + jj \\ QCD \\ diboson/Z + j \\ \text{Single top} \end{array} \right.$



Top Quark Mass Measurement in the lepton + jets Channel Using a Matrix Element Method and *in situ* Jet Energy Calibration

- T. Altonen,²¹ B. Álvarez González,^{9,w} S. Amerio,^{41a} D. Amidei,³² A. Anastassov,³⁶ A. Annovi,¹⁷ J. Antos,¹² G. Apollinari,¹⁵ J. A. Appel,¹⁵ A. Apresyan,⁴⁶ T. Arisawa,⁵⁷ A. Artikov,¹³ J. Asaadi,⁵¹ W. Ashmanskas,¹⁵ B. Auerbach,⁶⁰ A. Aurisano,⁵¹ F. Azfar,⁴⁰ W. Badgett,¹⁵ A. Barbaro-Galtieri,²⁶ V. E. Barnes,⁴⁶ B. A. Barnett,²³ P. Barria,^{44c,44a} P. Bartos,¹² M. Bause,^{41b,41a} G. Bauer,³⁰ F. Bedeschi,^{44a} D. Beecher,²⁸ S. Behari,²³ G. Bellettini,^{44b,44a} J. Bellinger,⁵⁹ D. Benjamin,¹⁴ A. Beretvas,¹⁵ A. Bhatti,⁴⁸ M. Binkley,^{15,a} D. Bisello,^{41b,41a} I. Bizjak,^{28,aa} K. R. Bland,⁵ B. Blumenfeld,²³ A. Bocci,¹⁴ A. Bodek,⁴⁷ D. Bortoletto,⁴⁶ J. Boudreau,⁴⁵ A. Boveia,¹¹ B. Brau,^{15,b} L. Brigliadori,^{6b,6a} A. Brisuda,¹² C. Bromberg,³³ E. Brucken,²¹ M. Bucciantonio,^{44b,44a} J. Budagov,¹³ H. S. Budd,⁴⁷ S. Budd,²² K. Burkett,¹⁵ G. Busetto,^{41b,41a} P. Bussey,¹⁹ A. Buzatu,³¹ C. Calancha,²⁹ S. Camarda,⁴ M. Campanelli,³³ M. Campbell,³² F. Canelli,^{12,15} A. Canepa,⁴³ B. Carls,²² D. Carlsmith,⁵⁹ R. Carosi,^{44a} S. Carrillo,^{16,l} S. Carron,¹⁵ B. Casal,⁹ M. Casarsa,¹⁵ A. Castro,^{6b,6a} P. Catastini,¹⁵ D. Cauz,^{53a} V. Cavaliere,^{44c,44a} M. Cavalli-Sforza,⁴ A. Cerri,^{26,g} L. Cerrito,^{28,r} Y. C. Chen,¹ M. Chertok,⁷ G. Chiarelli,^{44a} G. Chlachidze,¹⁵ F. Chlebana,¹⁵ K. Cho,²⁵ D. Chokheli,¹³ J. P. Chou,²⁰ W. H. Chung,⁵⁹ Y. S. Chung,⁴⁷ C. I. Ciobanu,⁴² M. A. Ciocci,^{44c,44a} A. Clark,¹⁸ G. Compostella,^{41b,41a} M. E. Convery,¹⁵ J. Conway,⁷ M. Corbo,⁴² M. Cordelli,¹⁷ C. A. Cox,⁷ D. J. Cox,⁷ F. Crescioli,^{44b,44a} C. Cuena Almenar,⁶⁰ J. Cuevas,^{9,w} R. Culbertson,¹⁵ D. Dagenhart,¹⁵ N. d'Ascenzo,^{42,u} M. Datta,¹⁵ P. de Barbaro,⁴⁷ S. De Cecco,^{49a} G. De Lorenzo,⁴ M. Dell'Orso,^{44b,44a} C. Deluca,⁴ L. Demortier,⁴⁸ J. Deng,^{14,d} M. Deninno,^{6a} F. Devoto,²¹ M. d'Errico,^{41b,41a} A. Di Canto,^{44b,44a} B. Di Ruzza,^{44a} J. R. Dittmann,⁵ M. D'Onofrio,²⁷ S. Donati,^{44b,44a} P. Dong,¹⁵ T. Dorigo,^{41a} K. Ebina,⁵⁷ A. Elagin,⁵¹ A. Eppig,³² R. Erbacher,⁷ D. Errede,²² S. Errede,²² N. Ershaidat,^{42,z} R. Eusebi,⁵¹ H. C. Fang,²⁶ S. Farrington,⁴⁰ M. Feindt,²⁴ J. P. Fernandez,²⁹ C. Ferrazza,^{44d,44a} R. Field,¹⁶ G. Flanagan,^{46,s} R. Forrest,⁷ M. J. Frank,⁵ M. Franklin,²⁰ J. C. Freeman,¹⁵ I. Furic,¹⁶ M. Gallinaro,⁴⁸ J. Galyardt,¹⁰ J. E. Garcia,¹⁸ A. F. Garfinkel,⁴⁶ P. Garosi,^{44c,44a} H. Gerberich,²² E. Gerchtein,¹⁵ S. Giagu,^{49b,49a} V. Giakoumopoulou,³ P. Giannetti,^{44a} K. Gibson,⁴² C. M. Ginsburg,¹⁵ N. Giokaris,³ P. Giromini,¹⁷ M. Giunta,^{44a} G. Giurgiu,²³ V. Glagolev,¹³ D. Glenzinski,¹⁵ M. Gold,³⁵ D. Goldin,⁵¹ N. Goldschmidt,¹⁶ A. Golossanov,¹⁵ G. Gomez,⁹ G. Gomez-Ceballos,³⁰ M. Goncharov,³⁰ O. González,²⁹ I. Gorelov,³⁵ A. T. Goshaw,¹⁴ K. Goulianos,⁴⁸ A. Gresele,^{41a} S. Grinstein,⁴ C. Grossi-Pilcher,¹¹ R. C. Group,⁵⁶ J. Guimaraes da Costa,²⁰ Z. Gunay-Unalan,³³ C. Haber,²⁶ S. R. Hahn,¹⁵ E. Halkiadakis,⁵⁰ A. Hamaguchi,³⁹ J. Y. Han,⁴⁷ F. Happacher,¹⁷ K. Hara,⁵⁴ D. Hare,⁵⁰ M. Hare,⁵⁵ R. F. Harr,⁵⁸ K. Hatakeyama,⁵ C. Hays,⁴⁰ M. Heck,²⁴ J. Heinrich,⁴³ M. Herndon,⁵⁹ S. Hewamanage,⁵ D. Hidas,⁵⁰ A. Hocker,¹⁵ W. Hopkins,^{15,b} D. Horn,²⁴ S. Hou,¹ R. E. Hughes,³⁷ M. Hurwitz,¹¹ U. Husemann,⁶⁰ N. Hussain,³¹ M. Hussein,³³ J. Huston,³³ G. Introzzi,^{44a} M. Iori,^{49b,49a} A. Ivanov,^{7,p} E. James,¹⁵ D. Jang,¹⁰ B. Jayatilaka,¹⁴ E. J. Jeon,²⁵ M. K. Jha,^{6b,6a} S. Jindariani,¹⁵ W. Johnson,⁷ M. Jones,⁴⁶ K. K. Joo,²⁵ S. Y. Jun,¹⁰ T. R. Junk,¹⁵ T. Kamon,⁵¹ P. E. Karchin,⁵⁸ Y. Kato,^{39,o} W. Ketchum,¹¹ J. Keung,⁴³ V. Khotilovich,⁵¹ B. Kilminster,¹⁵ D. H. Kim,²⁵ H. S. Kim,²⁵ H. W. Kim,²⁵ J. E. Kim,²⁵ M. J. Kim,²⁵ S. B. Kim,²⁵ S. H. Kim,²⁵ Y. K. Kim,¹¹ N. Kimura,⁵⁷ M. Kirby,¹⁵ S. Klimenko,¹⁶ K. Kondo,⁵⁷ D. J. Kong,²⁵ J. Konigsberg,¹⁶ A. V. Kotwal,¹⁴ M. Kreps,²⁴ J. Kroll,⁴³ D. Krop,¹¹ N. Krumnack,^{5,m} M. Kruse,¹⁴ V. Krutelyov,^{51,e} T. Kuhr,²⁴ M. Kurata,⁵⁴ S. Kwang,¹¹ A. T. Laasanen,⁴⁶ S. Lami,^{44a} S. Lammel,¹⁵ M. Lancaster,²⁸ R. L. Lander,⁷ K. Lannon,^{37,v} A. Lath,⁵⁰ G. Latino,^{44c,44a} I. Lazzizzera,^{41a} T. LeCompte,² E. Lee,⁵¹ H. S. Lee,¹¹ J. S. Lee,²⁵ S. W. Lee,^{51,x} S. Leo,^{44b,44c} S. Leone,^{44a} J. D. Lewis,¹⁵ C.-J. Lin,²⁶ J. Linacre,⁴⁰ M. Lindgren,¹⁵ E. Lipeles,⁴³ A. Lister,¹⁸ D. O. Litvinsev,¹⁵ C. Liu,⁴⁵ Q. Liu,⁴⁶ T. Liu,¹⁵ S. Lockwitz,⁶⁰ N. S. Lockyer,⁴³ A. Loginov,⁶⁰ D. Lucchesi,^{41b,41a} J. Lueck,²⁴ P. Lujan,²⁶ P. Lukens,¹⁵ G. Lungu,⁴⁸ J. Lys,²⁶ R. Lysak,¹² R. Madrak,¹⁵ K. Maeshima,¹⁵ K. Makhoul,³⁰ P. Maksimovic,²³ S. Malik,⁴⁸ G. Manca,^{27,c} A. Manousakis-Katsikakis,³ F. Margaroli,⁴⁶ C. Marino,²⁴ M. Martínez,⁴ R. Martínez-Ballarín,²⁹ P. Mastrandrea,^{49a} M. Mathis,²³ M. E. Mattson,⁵⁸ P. Mazzanti,^{6b,6a} K. S. McFarland,⁴⁷ P. McIntyre,⁵¹ R. McNulty,^{27,j} A. Mehta,²⁷ P. Mehtala,²¹ A. Menzione,^{44a} C. Mesropian,⁴⁸ T. Miao,¹⁵ D. Mietlicki,³² A. Mitra,¹ H. Miyake,⁵⁴ S. Moed,²⁰ N. Moggi,^{6b,6a} M. N. Mondragon,^{15,l} C. S. Moon,²⁵ R. Moore,¹⁵ M. J. Morello,¹⁵ J. Morlock,²⁴ P. Movilla Fernandez,¹⁵ A. Mukherjee,¹⁵ Th. Muller,²⁴ P. Murat,¹⁵ M. Mussini,^{6b,6a} J. Nachtman,^{15,n} Y. Nagai,⁵⁴ J. Naganoma,⁵⁷ I. Nakano,³⁸ A. Napier,⁵⁵ J. Nett,⁵⁹ C. Neu,⁵⁶ M. S. Neubauer,²² J. Nielsen,^{26,f} L. Nodulman,² O. Norniella,²² E. Nurse,²⁸ L. Oakes,⁴⁰ S. H. Oh,¹⁴ Y. D. Oh,²⁵ I. Oksuzian,⁵⁶ T. Okusawa,³⁹ R. Orava,²¹ L. Ortolan,⁴ S. Pagan Griso,^{41b,41a} C. Pagliarone,^{53a} E. Palencia,^{9,g} V. Papadimitriou,¹⁵ A. A. Paramonov,² J. Patrick,¹⁵ G. Pauleta,^{53b,53a} M. Paulini,¹⁰ C. Paus,³⁰ D. E. Pellett,⁷ A. Penzo,^{53a} T. J. Phillips,¹⁴ G. Piacentino,^{44a} E. Pianori,⁴³ J. Pilot,³⁷ K. Pitts,²² C. Plager,⁸ L. Pondrom,⁵⁹ K. Potamianos,⁴⁶ O. Poukhov,^{13,a} F. Prokoshin,^{13,y} A. Pronko,¹⁵ F. Ptohos,^{17,i} E. Pueschel,¹⁰ G. Punzi,^{44b,44a} J. Pursley,⁵⁹ A. Rahaman,⁴⁵ V. Ramakrishnan,⁵⁹ N. Ranjan,⁴⁶ I. Redondo,²⁹



(4)

- 各 event が BG である確率を求める。

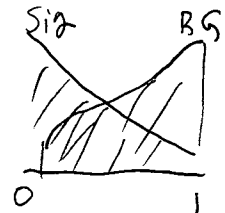
- Y の "BG, はい" を与える NN $\nu(Y)$ を構築する

- MC を使、2. event をつくる $\nu(Y)$ (both sig. & BG.)

\Rightarrow "BG, はい" に対する MC の結果を plot する

\Rightarrow "Y" が BG である確率 $\approx f = \nu(Y)$ が BG であるか

$$= \frac{BG(E)}{Sig(E) + BG(E)}$$



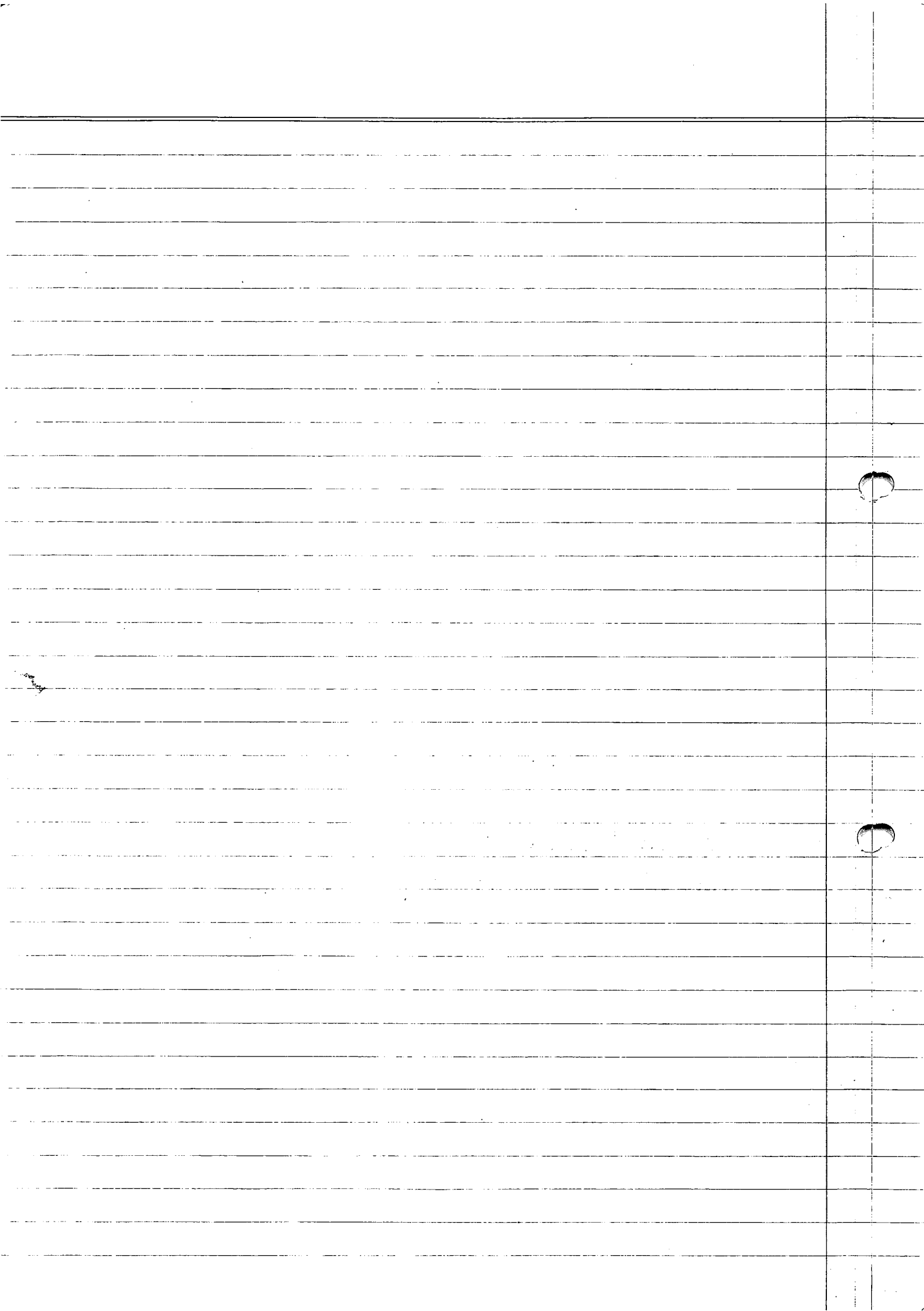
$$L_{adj} = \prod_{sig} L_i = \frac{L_{tot}}{\langle L \rangle_{tot}^{S_i}}$$

$$\log L_{adj} = \sum_{tot} \log L_i - \sum_{tot} f_i \log \bar{L}_{sig}$$

$$\Rightarrow m_t = 173.0 \pm 0.7 \text{ stat} \pm 0.6 \text{ JES} \pm 0.9 \text{ syst} \text{ GeV}$$

$$\Delta_{JES} = 0.15 \pm 0.1$$

- Matrix Element Method
- in-situ jet calibration



• CDF HAD [CDF 10456 ; PRD 81, 052011] 5.85b⁻

Selection

- 6 to 8 jets, $| \eta | < 2$, $\text{sep} \Delta R > 0.5$ (trig)
- No MET ($E_T / \sqrt{\sum E_T} < 3 \text{ GeV}$)
- $O \ell 20$
- primary vtx detected w. $|z| < 60 \text{ cm}$
- 1 b or $2^+ b$ among 6 leading jets. secvtx

- + Neural Network \rightsquigarrow 3 層 perceptron で MC 教師あり training
- + χ^2 - test × 2 Input: P_T , E. jet shape etc..

$$\left[\begin{array}{l} \text{trig} \\ \text{L1: } 1E_{\text{flow}}/10 \\ \text{L2: } \sum E_{\text{flow}} > 175 \\ \quad \& \\ \quad 4^+ E_T^{\text{clus}} > 15 \\ \text{L3: } 4^+ E_T > 10 \end{array} \right]$$



* BG: Data driven

◎ b-tag probability $P(E_T; N_{\text{trk}}^{\text{jet}}, N_{\text{vertex}})$

5-jet sample (BG dominated) を用いて求める

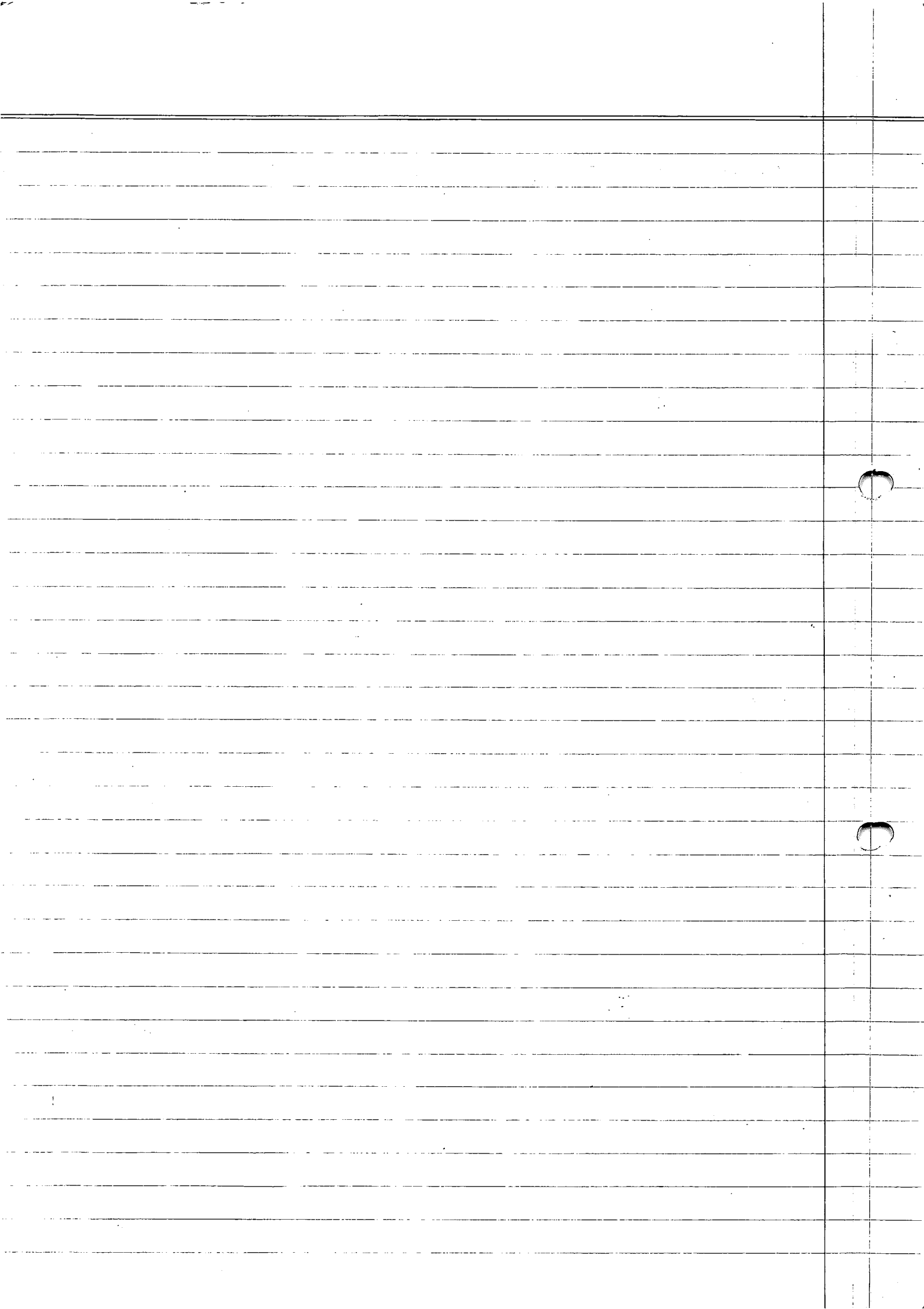
$$P = \frac{\# \text{tagged jets}}{\# \text{fiducial jets}} = \frac{P_{\text{true}} \# \text{sid b} + P_{\text{fake}} \# \text{fid b}}{\# \text{fiducial}}$$

↑ its track reconstructed in
silicon vtx det.

found in silicon
vtx detector

P_{fake} の求め方 より詳しく見て求める

($N_{\text{out}} < 0.25$ の 6~8jet sample を用いて)



• Analysis (parton to W/t building)

- consider only 6 leading jets

\Rightarrow 1-tagged: ${}_5C_2 \times {}_3C_2 = 30$ permutation

2⁺-tagged: $2 \Rightarrow {}_4C_2 = 6$

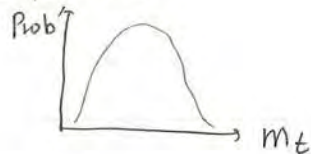
$3 \Rightarrow {}_4C_2 \times 3 = 18$

$$\chi^2_t = \sum_{1,2} \left[\frac{(m_{jj} - m_w)^2}{P_{W \rightarrow 2.1 \text{ GeV}}^2} + \frac{(m_{bjj} - m_t)^2}{P_t^2 \rightarrow 1.5 \text{ GeV}} \right] + \sum_{i=0}^6 \frac{(P_{T,i}^{\text{fit}} - P_{T,i})^2}{\sigma_{i \rightarrow \text{known}}^2}$$

$t, \{m_t, P_{T,i}^{\text{fit}}; \text{PERMUTATION}\}$ に關する最適化

\Rightarrow minimized $m_t \in \text{template} = d^3$

" m_t -template"



• 同じく $\{m_w, m_t, P_{T,i}^{\text{fit}}; \text{PER}\}$ に χ^2_w を d^3

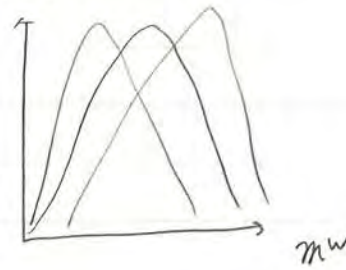
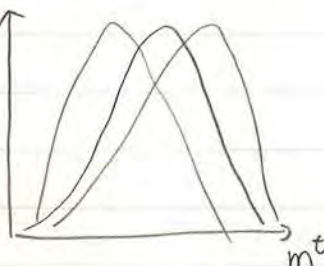
χ^2_w の最小化 \Rightarrow minimized $m_w \in \text{template} = d^3$

accept 33% of π_{fit}

$\chi^2 = M_t - m_t + \Delta \text{JES}$

$\Delta \text{JES} \sim \chi^2$

(Ncut, χ^2_t , χ^2_w)



確率分布関数 $f(m_t | M_t^{\text{input}}, \Delta \text{JES})$ $\in \text{MC} = d^3$ まで

$f(m_w |)$

実験 data の $f(m_t)$, $f(m_w)$ を求める

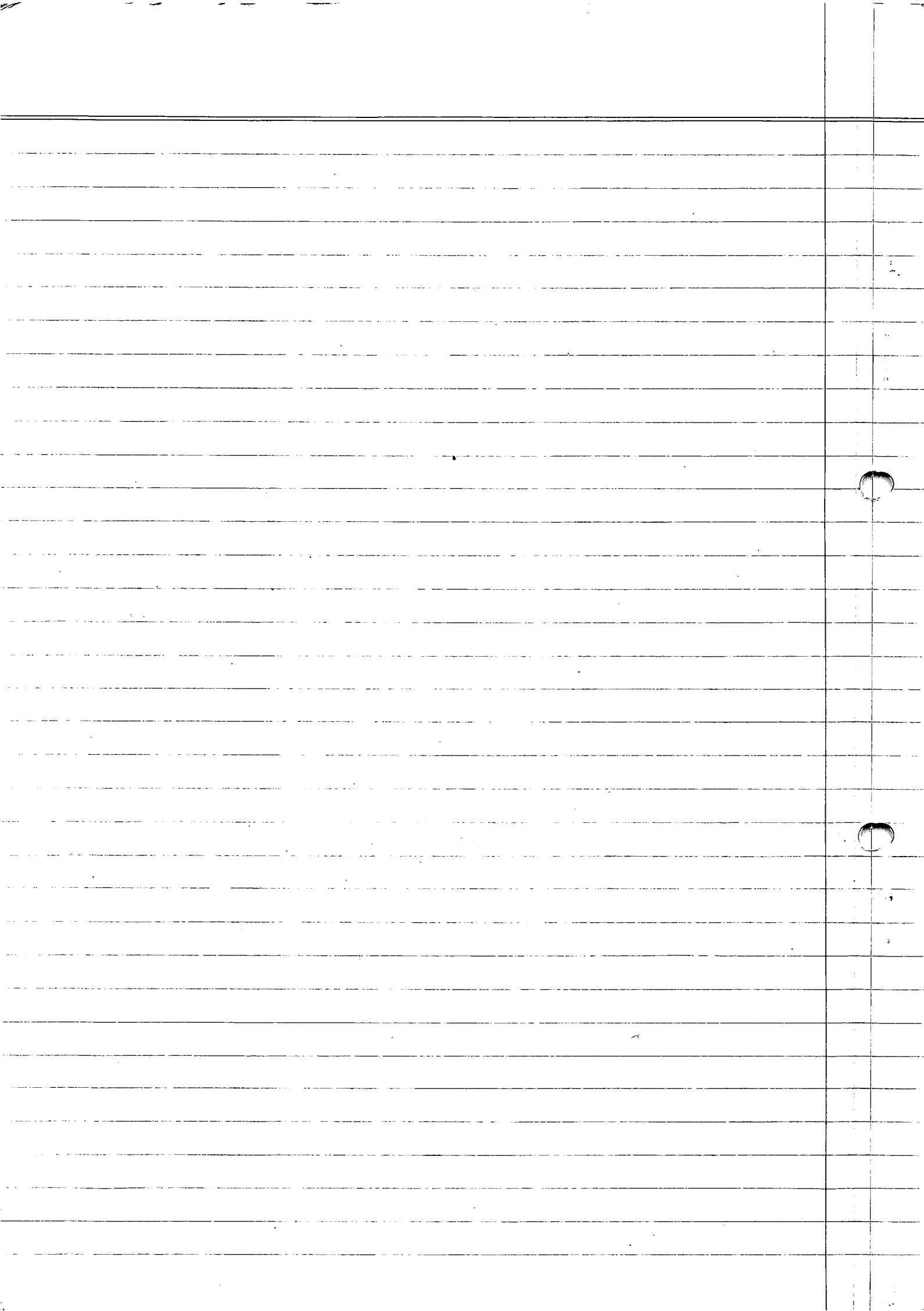
$\otimes f(m_w) \rightarrow M_t^{\text{input}}$ は ΔJES に insensitive である

ΔJES の calibration は $\rightarrow \chi^2$

• BG からの template $f_{bg}(m_t | \Delta \text{JES})$, $t > 3$

$\otimes m_w \sim s$

$M_{\text{top}} = 172.5 \pm 1.4 \pm 1.0 \pm 1.2 \quad , \quad \Delta \text{JES} = (0.10 \pm 0.3 \pm 0.4)^\circ$



- DØ Lepton+Jets [2.6+1.0 fb⁻¹, 1105.6287]

- Object ID

- e : ◦ Calolimeter → narrow deposit ($R < 0.2$)

- Track → match

↓ Loose

- Likelihood (cal; trk)

- Neural Network

↓ tight

- μ : ◦ Muon system → hit

- Trk → match

- $\Delta R > 0.5$ separation from $P_T > 15$ jets ↓ loose isolated

- E_T^{miss} energy $\pm 10\%$ in 2 fm

↓ veto
tight

- j : ◦ midpoint cone $R = 0.5$

- $P_T > 8 GeV$

- $E_{EM}/E_{T\text{tot}} < 0.95$ LF (to reject e)

- < 0.05 HF (to reject noise)

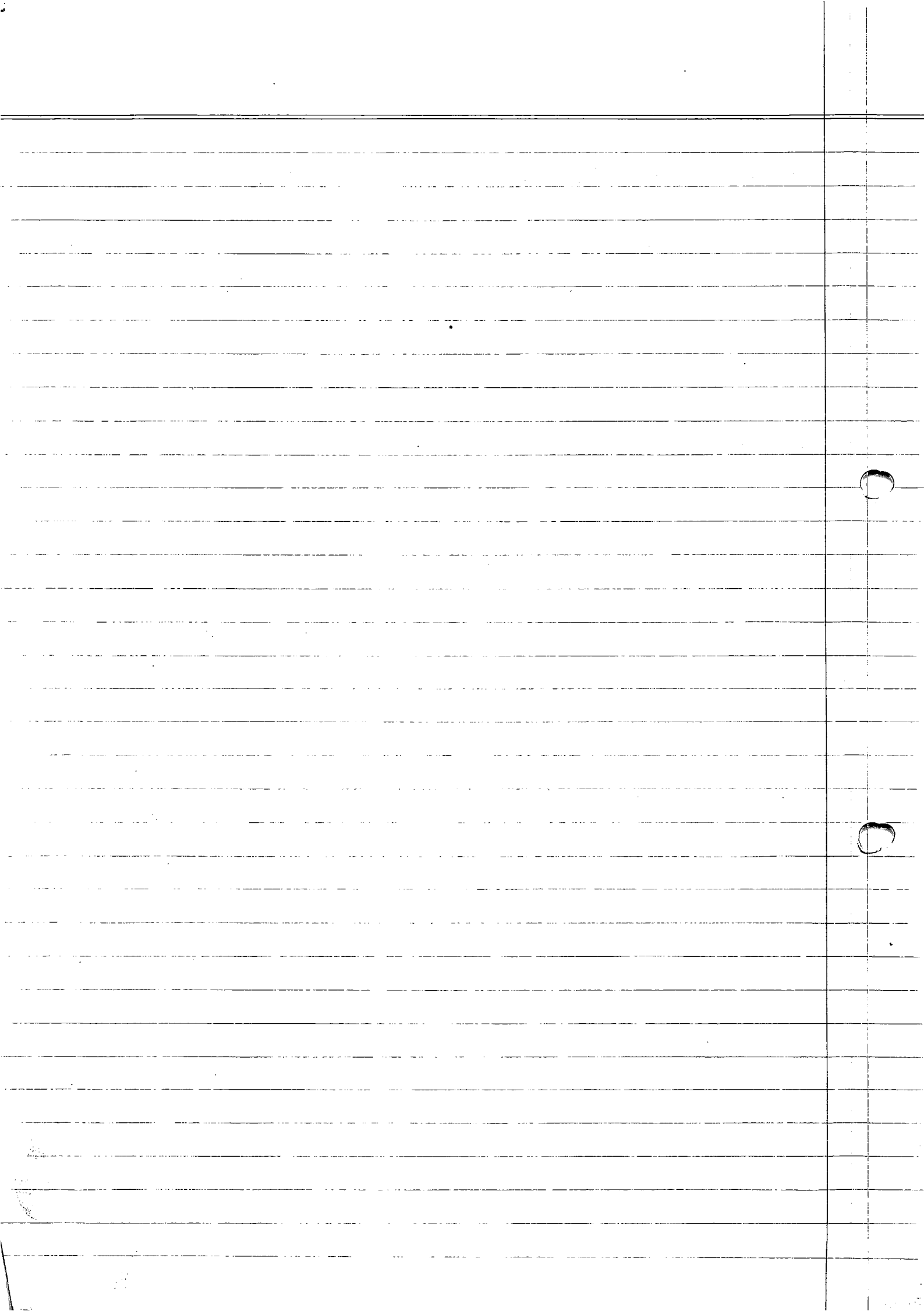
- $P_T > 20$ or $\Delta R > 0.5$ for $\eta > 2.4$

- ⊕ Correction

- b : NN tag & fit (displaced vtx, displaced trk)

rate: 65%

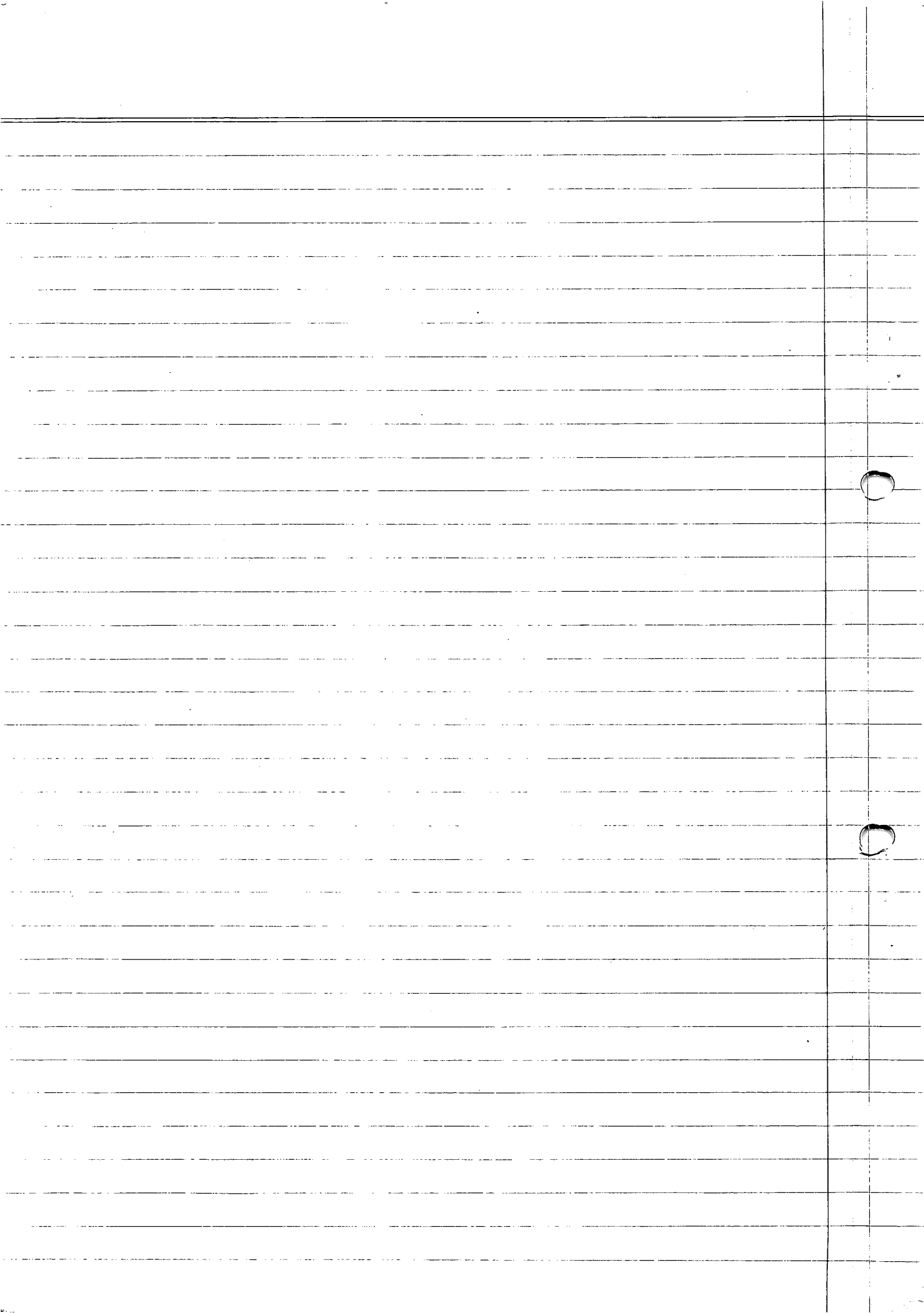
fake: 3%



◦ Selection

triggered jet & lepton Z
 $\bar{t} + t \rightarrow$

- $4^{\circ} j 40, 20^3$ in $|\eta| < 2.5$ AND 1+ b jet
 - Primary Vtx w. 2+ trk in fiducial region of SMT
 - OR $\begin{cases} 1^{\circ} e \text{ (tight)} 20 & \text{in } |\eta| < 1.1 \\ 1^{\circ} \mu \text{ (tight)} 20 & \text{in } |\eta| < 2 \end{cases}$
 * 2つ以上 e, μ [e: 15, $|\eta| < 2.5$] がある reject
 $\begin{matrix} \text{tight} \\ \text{tight} \end{matrix}$ $\begin{matrix} \text{loose} \\ \text{loose} \end{matrix}$
 - MET 20/25 for e/μ
 - $\Delta\phi(e_{\mu}, p_T) > 2.1 - 0.035 p_T$
 to reduce QCD w. $j \rightarrow l$ misid
 - 2 μ loose w. $p_T > 15$ or τ^{\pm}
 $\eta_0 < m_{\mu\mu} < 110$ ε reject (to reduce $Z \rightarrow \mu\mu b\bar{b}$)
- ⇒ $\begin{cases} 312 \text{ ej} \\ 303 \text{ μj} \end{cases}$ samples



Precise measurement of the top-quark mass from lepton+jets events at D0

- V.M. Abazov,³⁵ B. Abbott,⁷³ B.S. Acharya,²⁹ M. Adams,⁴⁹ T. Adams,⁴⁷ G.D. Alexeev,³⁵ G. Alkhazov,³⁹
 A. Alton^a,⁶¹ G. Alverson,⁶⁰ G.A. Alves,² L.S. Ancu,³⁴ M. Aoki,⁴⁸ M. Arov,⁵⁸ A. Askew,⁴⁷ B. Åsman,⁴¹
 O. Atramentov,⁶⁵ C. Avila,⁸ J. BackusMayes,⁸⁰ F. Badaud,¹³ L. Bagby,⁴⁸ B. Baldin,⁴⁸ D.V. Bandurin,⁴⁷
 S. Banerjee,²⁹ E. Barberis,⁶⁰ P. Baringer,⁵⁶ J. Barreto,³ J.F. Bartlett,⁴⁸ U. Bassler,¹⁸ V. Bazterra,⁴⁹ S. Beale,⁶
 A. Bean,⁵⁶ M. Begalli,³ M. Begel,⁷¹ C. Belanger-Champagne,⁴¹ L. Bellantoni,⁴⁸ S.B. Beri,²⁷ G. Bernardi,¹⁷
 R. Bernhard,²² I. Bertram,⁴² M. Besançon,¹⁸ R. Beuselinck,⁴³ V.A. Bezzubov,³⁸ P.C. Bhat,⁴⁸ V. Bhatnagar,²⁷
 G. Blazey,⁵⁰ S. Blessing,⁴⁷ K. Bloom,⁶⁴ A. Boehlein,⁴⁸ D. Boline,⁷⁰ E.E. Boos,³⁷ G. Borissov,⁴² T. Bose,⁵⁹
 A. Brandt,⁷⁶ O. Brandt,²³ R. Brock,⁶² G. Brooijmans,⁶⁸ A. Bross,⁴⁸ D. Brown,¹⁷ J. Brown,¹⁷ X.B. Bu,⁴⁸
 M. Buehler,⁷⁹ V. Buescher,²⁴ V. Bunichev,³⁷ S. Burdin^b,⁴² T.H. Burnett,⁸⁰ C.P. Buszello,⁴¹ B. Calpas,¹⁵
 E. Camacho-Pérez,³² M.A. Carrasco-Lizarraga,⁵⁶ B.C.K. Casey,⁴⁸ H. Castilla-Valdez,³² S. Chakrabarti,⁷⁰
 D. Chakraborty,⁵⁰ K.M. Chan,⁵⁴ A. Chandra,⁷⁸ G. Chen,⁵⁶ S. Chevalier-Théry,¹⁸ D.K. Cho,⁷⁵ S.W. Cho,³¹
 S. Choi,³¹ B. Choudhary,²⁸ S. Cihangir,⁴⁸ D. Claes,⁶⁴ J. Clutter,⁵⁶ M. Cooke,⁴⁸ W.E. Cooper,⁴⁸ M. Corcoran,⁷⁸
 F. Couderc,¹⁸ M.-C. Cousinou,¹⁵ A. Croc,¹⁸ D. Cutts,⁷⁵ A. Das,⁴⁵ G. Davies,⁴³ K. De,⁷⁶ S.J. de Jong,³⁴
 E. De La Cruz-Burelo,³² F. Déliot,¹⁸ M. Demarteau,⁴⁸ R. Demina,⁶⁹ D. Denisov,⁴⁸ S.P. Denisov,³⁸ S. Desai,⁴⁸
 C. Deterre,¹⁸ K. DeVaughan,⁶⁴ H.T. Diehl,⁴⁸ M. Diesburg,⁴⁸ A. Dominguez,⁶⁴ T. Dorland,⁸⁰ A. Dubey,²⁸
 L.V. Dudko,³⁷ D. Duggan,⁶⁵ A. Duperrin,¹⁵ S. Dutt,²⁷ A. Dyshkant,⁵⁰ M. Eads,⁶⁴ D. Edmunds,⁶² J. Ellison,⁴⁶
 V.D. Elvira,⁴⁸ Y. Enari,¹⁷ H. Evans,⁵² A. Evdokimov,⁷¹ V.N. Evdokimov,³⁸ G. Facini,⁶⁰ T. Ferbel,⁶⁹ F. Fiedler,²⁴
 F. Filthaut,³⁴ W. Fisher,⁶² H.E. Fisk,⁴⁸ M. Fortner,⁵⁰ H. Fox,⁴² S. Fuess,⁴⁸ A. Garcia-Bellido,⁶⁹ V. Gavrilov,³⁶
 P. Gay,¹³ W. Geng,^{15,62} D. Gerbaudo,⁶⁶ C.E. Gerber,⁴⁹ Y. Gershtein,⁶⁵ G. Ginther,^{48,69} G. Golovanov,³⁵
 A. Goussiou,⁸⁰ P.D. Grannis,⁷⁰ S. Greder,¹⁹ H. Greenlee,⁴⁸ Z.D. Greenwood,⁵⁸ E.M. Gregores,⁴ G. Grenier,²⁰
 Ph. Gris,¹³ J.-F. Grivaz,¹⁶ A. Grohsjean,¹⁸ S. Grünendahl,⁴⁸ M.W. Grünewald,³⁰ T. Guillemin,¹⁶ F. Guo,⁷⁰
 G. Gutierrez,⁴⁸ P. Gutierrez,⁷³ A. Haas^c,⁶⁸ S. Hagopian,⁴⁷ J. Haley,⁶⁰ L. Han,⁷ K. Harder,⁴⁴ A. Harel,⁶⁹
 J.M. Hauptman,⁵⁵ J. Hays,⁴³ T. Head,⁴⁴ T. Hebbeker,²¹ D. Hedin,⁵⁰ H. Hegab,⁷⁴ A.P. Heinson,⁴⁶ U. Heintz,⁷⁵
 C. Hensel,²³ I. Heredia-De La Cruz,³² K. Herner,⁶¹ G. Hesketh^d,⁴⁴ M.D. Hildreth,⁵⁴ R. Hirosky,⁷⁹ T. Hoang,⁴⁷
 J.D. Hobbs,⁷⁰ B. Hoeneisen,¹² M. Hohlfeld,²⁴ Z. Hubacek,^{10,18} N. Huske,¹⁷ V. Hynek,¹⁰ I. Iashvili,⁶⁷
 R. Illingworth,⁴⁸ A.S. Ito,⁴⁸ S. Jabeen,⁷⁵ M. Jaffré,¹⁶ D. Jamin,¹⁵ A. Jayasinghe,⁷³ R. Jesik,⁴³ K. Johns,⁴⁵
 M. Johnson,⁴⁸ D. Johnston,⁶⁴ A. Jonckheere,⁴⁸ P. Jonsson,⁴³ J. Joshi,²⁷ A.W. Jung,⁴⁸ A. Juste,⁴⁰
 K. Kaadze,⁵⁷ E. Kajfasz,¹⁵ D. Karmanov,³⁷ P.A. Kasper,⁴⁸ I. Katsanos,⁶⁴ R. Kehoe,⁷⁷ S. Kermiche,¹⁵
 N. Khalatyan,⁴⁸ A. Khanov,⁷⁴ A. Kharchilava,⁶⁷ Y.N. Kharzeev,³⁵ D. Khatidze,⁷⁵ M.H. Kirby,⁵¹ J.M. Kohli,²⁷
 A.V. Kozelov,³⁸ J. Kraus,⁶² S. Kulikov,³⁸ A. Kumar,⁶⁷ A. Kupco,¹¹ T. Kurča,²⁰ V.A. Kuzmin,³⁷ J. Kvita,⁹
 S. Lammers,⁵² G. Landsberg,⁷⁵ P. Lebrun,²⁰ H.S. Lee,³¹ S.W. Lee,⁵⁵ W.M. Lee,⁴⁸ J. Lellouch,¹⁷ L. Li,⁴⁶
 Q.Z. Li,⁴⁸ S.M. Lietti,⁵ J.K. Lim,³¹ D. Lincoln,⁴⁸ J. Linnemann,⁶² V.V. Lipaev,³⁸ R. Lipton,⁴⁸ Y. Liu,⁷
 Z. Liu,⁶ A. Lobodenko,³⁹ M. Lokajicek,¹¹ R. Lopes de Sa,⁷⁰ H.J. Lubatti,⁸⁰ R. Luna-Garcia^e,³² A.L. Lyon,⁴⁸
 A.K.A. Maciel,² D. Mackin,⁷⁸ R. Madar,¹⁸ R. Magaña-Villalba,³² S. Malik,⁶⁴ V.L. Malyshev,³⁵ Y. Maravin,⁵⁷
 J. Martínez-Ortega,³² R. McCarthy,⁷⁰ C.L. McGivern,⁵⁶ M.M. Meijer,³⁴ A. Melnitchouk,⁶³ D. Menezes,⁵⁰
 P.G. Mercadante,⁴ M. Merkin,³⁷ A. Meyer,²¹ J. Meyer,²³ F. Miconi,¹⁹ N.K. Mondal,²⁹ G.S. Muanza,¹⁵
 M. Mulhearn,⁷⁹ E. Nagy,¹⁵ M. Naimuddin,²⁸ M. Narain,⁷⁵ R. Nayyar,²⁸ H.A. Neal,⁶¹ J.P. Negret,⁸ P. Neustroev,³⁹
 S.F. Novaes,⁵ T. Nunnemann,²⁵ G. Obrant,³⁹ J. Orduna,⁷⁸ N. Osman,¹⁵ J. Osta,⁵⁴ G.J. Otero y Garzón,¹
 M. Padilla,⁴⁶ A. Pal,⁷⁶ N. Parashar,⁵³ V. Parihar,⁷⁵ S.K. Park,³¹ J. Parsons,⁶⁸ R. Partridge^c,⁷⁵ N. Parua,⁵²
 A. Patwa,⁷¹ B. Penning,⁴⁸ M. Perfilov,³⁷ K. Peters,⁴⁴ Y. Peters,⁴⁴ K. Petridis,⁴⁴ G. Petrillo,⁶⁹ P. Pétroff,¹⁶
 R. Piegaia,¹ J. Piper,⁶² M.-A. Pleier,⁷¹ P.L.M. Podesta-Lerma^f,³² V.M. Podstavkov,⁴⁸ P. Polozov,³⁶ A.V. Popov,³⁸
 M. Prewitt,⁷⁸ D. Price,⁵² N. Prokopenko,³⁸ S. Protopopescu,⁷¹ J. Qian,⁶¹ A. Quadt,²³ B. Quinn,⁶³ M.S. Rangel,²
 K. Ranjan,²⁸ P.N. Ratoff,⁴² I. Razumov,³⁸ P. Renkel,⁷⁷ M. Rijssenbeek,⁷⁰ I. Ripp-Baudot,¹⁹ F. Rizatdinova,⁷⁴
 M. Rominsky,⁴⁸ A. Ross,⁴² C. Royon,¹⁸ P. Rubinov,⁴⁸ R. Ruchti,⁵⁴ G. Safronov,³⁶ G. Sajot,¹⁴ P. Salcido,⁵⁰
 A. Sánchez-Hernández,³² M.P. Sanders,²⁵ B. Sanghi,⁴⁸ A.S. Santos,⁵ G. Savage,⁴⁸ L. Sawyer,⁵⁸ T. Scanlon,⁴³
 R.D. Schamberger,⁷⁰ Y. Scheglov,³⁹ H. Schellman,⁵¹ T. Schliephake,²⁶ S. Schlobohm,⁸⁰ C. Schwanenberger,⁴⁴
 R. Schwienhorst,⁶² J. Sekaric,⁵⁶ H. Severini,⁷³ E. Shabalina,²³ V. Shary,¹⁸ A.A. Shchukin,³⁸ R.K. Shivpuri,²⁸
 V. Simak,¹⁰ V. Sirotenko,⁴⁸ P. Skubic,⁷³ P. Slattery,⁶⁹ D. Smirnov,⁵⁴ K.J. Smith,⁶⁷ G.R. Snow,⁶⁴ J. Snow,⁷²

S. Snyder,⁷¹ S. Söldner-Rembold,⁴⁴ L. Sonnenschein,²¹ K. Soustruznik,⁹ J. Stark,¹⁴ V. Stolin,³⁶ D.A. Stoyanova,³⁸
 M. Strauss,⁷³ D. Strom,⁴⁹ L. Stutte,⁴⁸ L. Suter,⁴⁴ P. Svoisky,⁷³ M. Takahashi,⁴⁴ A. Tanasijczuk,¹ W. Taylor,⁶
 M. Titov,¹⁸ V.V. Tokmenin,³⁵ Y.-T. Tsai,⁶⁹ D. Tsybychev,⁷⁰ B. Tuchming,¹⁸ C. Tully,⁶⁶ L. Uvarov,³⁹ S. Uvarov,³⁹
 S. Uzunyan,⁵⁰ R. Van Kooten,⁵² W.M. van Leeuwen,³³ N. Varelas,⁴⁹ E.W. Varnes,⁴⁵ I.A. Vasilyev,³⁸
 P. Verdier,²⁰ L.S. Vertogradov,³⁵ M. Verzocchi,⁴⁸ M. Vesterinen,⁴⁴ D. Vilanova,¹⁸ P. Vokac,¹⁰ H.D. Wahl,⁴⁷
 M.H.L.S. Wang,⁶⁹ J. Warchol,⁵⁴ G. Watts,⁸⁰ M. Wayne,⁵⁴ M. Weber⁹,⁴⁸ L. Welty-Rieger,⁵¹ A. White,⁷⁶
 D. Wicke,²⁶ M.R.J. Williams,⁴² G.W. Wilson,⁵⁶ M. Wobisch,⁵⁸ D.R. Wood,⁶⁰ T.R. Wyatt,⁴⁴ Y. Xie,⁴⁸ C. Xu,⁶¹
 S. Yacoob,⁵¹ R. Yamada,⁴⁸ W.-C. Yang,⁴⁴ T. Yasuda,⁴⁸ Y.A. Yatsunenko,³⁵ Z. Ye,⁴⁸ H. Yin,⁴⁸ K. Yip,⁷¹
 S.W. Youn,⁴⁸ J. Yu,⁷⁶ S. Zelitch,⁷⁹ T. Zhao,⁸⁰ B. Zhou,⁶¹ J. Zhu,⁶¹ M. Zielinski,⁶⁹ D. Ziemska,⁵² and L. Zivkovic⁷⁵

(The D0 Collaboration)

¹Universidad de Buenos Aires, Buenos Aires, Argentina

²LAFEX, Centro Brasileiro de Pesquisas Físicas, Rio de Janeiro, Brazil

³Universidade do Estado do Rio de Janeiro, Rio de Janeiro, Brazil

⁴Universidade Federal do ABC, Santo André, Brazil

⁵Instituto de Física Teórica, Universidade Estadual Paulista, São Paulo, Brazil

⁶Simon Fraser University, Vancouver, British Columbia, and York University, Toronto, Ontario, Canada

⁷University of Science and Technology of China, Hefei, People's Republic of China

⁸Universidad de los Andes, Bogotá, Colombia

⁹Charles University, Faculty of Mathematics and Physics,

Center for Particle Physics, Prague, Czech Republic

¹⁰Czech Technical University in Prague, Prague, Czech Republic

¹¹Center for Particle Physics, Institute of Physics,

Academy of Sciences of the Czech Republic, Prague, Czech Republic

¹²Universidad San Francisco de Quito, Quito, Ecuador

¹³LPC, Université Blaise Pascal, CNRS/IN2P3, Clermont, France

¹⁴LPSC, Université Joseph Fourier 1, CNRS/IN2P3,

Institut National Polytechnique de Grenoble, Grenoble, France

¹⁵CPPM, Aix-Marseille Université, CNRS/IN2P3, Marseille, France

¹⁶LAL, Université Paris-Sud, CNRS/IN2P3, Orsay, France

¹⁷LPNHE, Universités Paris VI and VII, CNRS/IN2P3, Paris, France

¹⁸CEA, Irfu, SPP, Saclay, France

¹⁹IPHC, Université de Strasbourg, CNRS/IN2P3, Strasbourg, France

²⁰IPNL, Université Lyon 1, CNRS/IN2P3, Villeurbanne, France and Université de Lyon, Lyon, France

²¹III. Physikalisches Institut A, RWTH Aachen University, Aachen, Germany

²²Physikalisches Institut, Universität Freiburg, Freiburg, Germany

²³II. Physikalisches Institut, Georg-August-Universität Göttingen, Göttingen, Germany

²⁴Institut für Physik, Universität Mainz, Mainz, Germany

²⁵Ludwig-Maximilians-Universität München, München, Germany

²⁶Fachbereich Physik, Bergische Universität Wuppertal, Wuppertal, Germany

²⁷Panjab University, Chandigarh, India

²⁸Delhi University, Delhi, India

²⁹Tata Institute of Fundamental Research, Mumbai, India

³⁰University College Dublin, Dublin, Ireland

³¹Korea Detector Laboratory, Korea University, Seoul, Korea

³²CINVESTAV, Mexico City, Mexico

³³FOM-Institute NIKHEF and University of Amsterdam/NIKHEF, Amsterdam, The Netherlands

³⁴Radboud University Nijmegen/NIKHEF, Nijmegen, The Netherlands

³⁵Joint Institute for Nuclear Research, Dubna, Russia

³⁶Institute for Theoretical and Experimental Physics, Moscow, Russia

³⁷Moscow State University, Moscow, Russia

³⁸Institute for High Energy Physics, Protvino, Russia

³⁹Petersburg Nuclear Physics Institute, St. Petersburg, Russia

⁴⁰Institució Catalana de Recerca i Estudis Avançats (ICREA) and Institut de Física d'Altes Energies (IFAE), Barcelona, Spain

⁴¹Stockholm University, Stockholm and Uppsala University, Uppsala, Sweden

⁴²Lancaster University, Lancaster LA1 4YB, United Kingdom

⁴³Imperial College London, London SW7 2AZ, United Kingdom

⁴⁴The University of Manchester, Manchester M13 9PL, United Kingdom

⁴⁵University of Arizona, Tucson, Arizona 85721, USA

⁴⁶University of California Riverside, Riverside, California 92521, USA

⁴⁷Florida State University, Tallahassee, Florida 32306, USA

⁴⁸Fermi National Accelerator Laboratory, Batavia, Illinois 60510, USA

- ⁴⁹ University of Illinois at Chicago, Chicago, Illinois 60607, USA
⁵⁰ Northern Illinois University, DeKalb, Illinois 60115, USA
⁵¹ Northwestern University, Evanston, Illinois 60208, USA
⁵² Indiana University, Bloomington, Indiana 47405, USA
⁵³ Purdue University Calumet, Hammond, Indiana 46329, USA
⁵⁴ University of Notre Dame, Notre Dame, Indiana 46556, USA
⁵⁵ Iowa State University, Ames, Iowa 50011, USA
⁵⁶ University of Kansas, Lawrence, Kansas 66045, USA
⁵⁷ Kansas State University, Manhattan, Kansas 66506, USA
⁵⁸ Louisiana Tech University, Ruston, Louisiana 71272, USA
⁵⁹ Boston University, Boston, Massachusetts 02215, USA
⁶⁰ Northeastern University, Boston, Massachusetts 02115, USA
⁶¹ University of Michigan, Ann Arbor, Michigan 48109, USA
⁶² Michigan State University, East Lansing, Michigan 48824, USA
⁶³ University of Mississippi, University, Mississippi 38677, USA
⁶⁴ University of Nebraska, Lincoln, Nebraska 68588, USA
⁶⁵ Rutgers University, Piscataway, New Jersey 08855, USA
⁶⁶ Princeton University, Princeton, New Jersey 08544, USA
⁶⁷ State University of New York, Buffalo, New York 14260, USA
⁶⁸ Columbia University, New York, New York 10027, USA
⁶⁹ University of Rochester, Rochester, New York 14627, USA
⁷⁰ State University of New York, Stony Brook, New York 11794, USA
⁷¹ Brookhaven National Laboratory, Upton, New York 11973, USA
⁷² Langston University, Langston, Oklahoma 73050, USA
⁷³ University of Oklahoma, Norman, Oklahoma 73019, USA
⁷⁴ Oklahoma State University, Stillwater, Oklahoma 74078, USA
⁷⁵ Brown University, Providence, Rhode Island 02912, USA
⁷⁶ University of Texas, Arlington, Texas 76019, USA
⁷⁷ Southern Methodist University, Dallas, Texas 75275, USA
⁷⁸ Rice University, Houston, Texas 77005, USA
⁷⁹ University of Virginia, Charlottesville, Virginia 22901, USA
⁸⁰ University of Washington, Seattle, Washington 98195, USA

(Dated: May 30, 2011)

We report a measurement of the mass of the top quark in lepton+jets final states of $p\bar{p} \rightarrow t\bar{t}$ data corresponding to 2.6 fb^{-1} of integrated luminosity collected at the D0 experiment at the Fermilab Tevatron Collider. Using a matrix element method, we combine an *in situ* jet energy calibration with the standard jet energy scale derived in studies of γ +jet and dijet events and employ a novel flavor-dependent jet response correction to measure a top-quark mass of $m_t = 176.01 \pm 1.64 \text{ GeV}$. Combining this result with a previous result obtained on an independent data set, we measure a top-quark mass of $m_t = 174.94 \pm 1.49 \text{ GeV}$ for a total integrated luminosity of 3.6 fb^{-1} .

PACS numbers: 14.65.Ha

I. INTRODUCTION

The observation of the top quark in 1995 [1, 2] confirmed the existence of the six quarks in three generations of fermions expected in the standard model (SM) of particle interactions. Because of its mass, the lifetime of the top quark is much shorter than the time-scale for QCD interactions, making it the only quark whose characteristics can be studied in an isolated quark system. The large mass of the top quark (m_t), corresponding to a Yukawa coupling to the Higgs boson equal to 1 within the current uncertainties, suggests a special role for the top quark in the breaking of electroweak symmetry. It is therefore not surprising that the precise determination of the mass of the top quark has received great attention. The interest in the top-quark mass also arises from the constraint imposed on the mass of the Higgs boson,

m_H , from the relationship among the values of m_t , m_H , and the SM radiative corrections to the mass of the W boson [3]. A precise measurement of m_t also provides a useful constraint on contributions from physics beyond the standard model [4].

The statistical uncertainty on the world average value of m_t is 0.3%, and the accuracy of the measurement of m_t is now dominated by systematic uncertainties [5]. The main systematic contributions arise from uncertainties on the jet energy calibration and on the Monte Carlo (MC) simulation of $t\bar{t}$ events.

We present a new measurement of the mass of the top quark based on 2.6 fb^{-1} of integrated luminosity from $p\bar{p}$ collisions at $\sqrt{s} = 1.96 \text{ TeV}$, collected with the D0 detector at the Fermilab Tevatron Collider. The analysis focuses on $t\bar{t}$ events identified in lepton+jets (ℓ +jets) final states (with ℓ representing either an electron or a muon) [6], in which the top and antitop quark are as-

sumed to decay into a W boson and b quark [7], with one of the W bosons in the $W^+W^-b\bar{b}$ final system decaying via $W \rightarrow \ell\nu$ into a lepton and neutrino and the other via $W \rightarrow q\bar{q}'$ into two quarks, and all four quarks ($q\bar{q}'b\bar{b}$) hadronizing into jets. Such events are characterized by an isolated electron or muon with large transverse momentum (p_T), an undetected neutrino that causes a large imbalance in transverse momentum, and four high- p_T jets. In selecting candidate events, we exploit this distinct signature, which helps distinguish these events from background.

Compared to the previous measurement based on data corresponding to 1 fb^{-1} of integrated luminosity [8], we use a larger data set and an improved evaluation of systematic uncertainties. The analysis uses the same ~~matrix element (ME)~~ analysis technique, with an *in situ* jet energy calibration based on constraining the invariant mass of the two jets from the decay of the W boson to the world average value of $M_W = 80.4 \text{ GeV}$ [9]. As in the previous measurement, the standard jet energy scale (JES), derived from $\gamma + \text{jet}$ and dijet data samples, is used as an additional constraint, and implemented through a Gaussian prior on its absolute value and uncertainty. A major improvement in this new measurement is the significant reduction of the uncertainty associated with the modeling of differences in the calorimeter response to b -quark and light-quark jets originating from the introduction of a new flavor-dependent jet energy response correction.

This measurement, like all direct measurements of m_t , relies on MC $t\bar{t}$ events for absolute calibration. It is therefore important to understand the precise definition of the input mass m_t^{gen} in MC $t\bar{t}$ event generators, such as ALPGEN [10] and PYTHIA [11], used to calibrate the direct measurements. Although m_t^{gen} is not well defined in leading order (LO) generators that use parton showers to model higher-order effects and hadronization, it has been argued that m_t^{gen} should be viewed as being close to the pole mass [12]. In Ref. [13], the D0 Collaboration has extracted m_t from a comparison of the measured $t\bar{t}$ production cross section with predictions from higher-order quantum chromodynamics (QCD), by equating m_t^{gen} both with the pole mass (m_t^{pole}) and with the $\overline{\text{MS}}$ mass ($m_t^{\overline{\text{MS}}}$). The extracted m_t , under the assumption $m_t^{\text{gen}} \equiv m_t^{\text{pole}}$, is found to agree with the average value of m_t from the Tevatron, while the m_t extracted assuming $m_t^{\text{gen}} \equiv m_t^{\overline{\text{MS}}}$ is found to be different from the average value of m_t . These results favor the pole mass interpretation of m_t^{gen} .

This paper is arranged as follows. A brief description of the D0 detector is given in Sec. II, which is followed by a discussion of the selection and reconstruction of the physical objects in this analysis in Sec. III. Section IV summarizes the MC samples used to simulate the events of interest, and Sec. V discusses the technique used to extract the value of m_t . This is followed by a description of the calibration of the response of the analysis method in Sec. VI and a discussion of the flavor-dependent jet

response correction used to bring the simulation of the calorimeter response to jets into agreement with data in Sec. VII. The result of the calibration is applied to the data in Sec. VIII, where the measured value of m_t and its statistical uncertainty are also presented. Section IX describes the evaluation of systematic uncertainties and the final result is given in Sec. X. We combine this new measurement in Sec. XI with an updated version of that from Ref. [8] in which the flavor-dependent jet response correction mentioned above has been applied and the systematic uncertainties have been updated.

II. THE D0 DETECTOR

The D0 detector consists primarily of a magnetic central tracking system, calorimetry, and a muon system. The central tracking system comprises a silicon microstrip tracker (SMT) and a central fiber tracker (CFT), both located within a 1.9 T superconducting solenoidal magnet [14]. The SMT [15] has $\approx 800,000$ individual strips, with typical pitch of $50 - 80 \mu\text{m}$, and a design optimized for track and vertex finding at $|\eta| < 2.5$, where the pseudorapidity $\eta = -\ln[\tan(\theta/2)]$, and θ is the polar angle with respect to the proton beam direction relative to the center of the detector. The system has a six-barrel longitudinal structure, each with a set of four layers arranged axially around the beam pipe, and interspersed with 16 radial disks. In 2006, a fifth layer, referred to as *Layer 0*, was installed close to the beam pipe [16, 17]. The CFT has eight thin coaxial barrels, each supporting two doublets of overlapping scintillating fibers of 0.835 mm diameter, one doublet being parallel to the collision axis, and the other alternating by $\pm 3^\circ$ relative to the axis. Light signals are transferred via clear fibers to solid-state photon counters (VLPCs) that have $\approx 80\%$ quantum efficiency.

Central and forward preshower detectors, located just outside of the superconducting coil (in front of the calorimetry), are constructed of several layers of extruded triangular scintillator strips that are read out using wavelength-shifting fibers and the VLPC. These detectors provide initial sampling of electromagnetic showers, and thereby help distinguish incident photons from electrons. The next layer of detection involves three liquid-argon/uranium calorimeters: a central section (CC) covering $|\eta|$ up to ≈ 1.1 , and two end calorimeters (EC) that extend coverage to $|\eta| \approx 4.2$, all housed in separate cryostats. The electromagnetic (EM) section of the calorimeter is segmented into four layers, with transverse segmentation of the cells in pseudorapidity and azimuth of $\Delta\eta \times \Delta\phi = 0.1 \times 0.1$, except for the third layer, where the segmentation is 0.05×0.05 . The hadronic portion of the calorimeter is located after the EM sections, and consists of fine hadron-sampling layers, followed by more coarse hadronic layers. In addition, scintillators between the CC and EC cryostats provide sampling of developing showers for $1.1 < |\eta| < 1.4$.

A muon system [18] is located beyond the calorimetry, and consists of a layer of tracking detectors and scintillation trigger counters before 1.9 T toroids, followed by two similar layers after the toroids. Tracking for $|\eta| < 1$ relies on 10 cm wide drift tubes, while 1 cm mini-drift tubes are used for $1 < |\eta| < 2$.

Luminosity is measured using plastic scintillator arrays located in front of the EC cryostats, covering $2.7 < |\eta| < 4.4$. The trigger and data acquisition systems are designed to accommodate the high instantaneous luminosities of the Tevatron [14, 19]. Based on preliminary information from tracking, calorimetry, and muon systems, the output of the first level of the trigger is used to limit the rate for accepted events to ≈ 2 kHz. At the next trigger stage, with more refined information, the rate is reduced further to ≈ 1 kHz. These first two levels of triggering rely mainly on hardware and firmware. The third and final level of the trigger, with access to all of the event information, uses software algorithms and a computing farm, and reduces the output rate to ≈ 100 Hz, which is written to tape.

III. OBJECT RECONSTRUCTION AND EVENT SELECTION

In the following sections, we summarize how the physical objects in data and MC events are reconstructed from information in the detector and the criteria applied to these objects to select the $\ell + \text{jets } t\bar{t}$ candidate events.

A. Object Reconstruction

This section describes the reconstruction of electrons, muons, missing transverse momentum, and jets, and the identification of b jets.

1. Identification of Electrons

Electron candidates are defined by narrow clusters of energy deposited in towers of the electromagnetic calorimeter located within a cone of radius $\mathcal{R} = \sqrt{(\Delta\eta)^2 + (\Delta\phi)^2} = 0.2$, where $\Delta\eta$ is the pseudorapidity, and $\Delta\phi$ is the azimuthal angle of each cluster relative to the seed cluster. At least 90% of the total energy measured within this cone is required to be located within the electromagnetic section to be consistent with expectations for electromagnetic showers. Isolation from energy deposited by hadrons is imposed by requiring $(E_{\text{tot}} - E_{\text{EM}})/E_{\text{EM}} < 0.15$, where E_{tot} (E_{EM}) is the total (electromagnetic) energy in a cone of radius $\mathcal{R} = 0.4$ ($\mathcal{R} = 0.2$). Candidate electrons are required to have longitudinal and transverse shower profiles compatible with those of electromagnetic showers and to be spatially matched to a track reconstructed in the central

tracking system. Electron candidates meeting these criteria are referred to as *loose* electrons. Finally, (i) the value of a multivariable likelihood discriminant based on tracking system and calorimeter information is required to be consistent with that for an electron, and (ii) a neural network, trained using information from the tracking system, calorimeter, and central preshower detector is used to further reject background from jets misidentified as electrons. Electron candidates meeting these criteria are referred to as *tight* electrons, and are those used to obtain the final selection.

2. Identification of Muons

Muons are identified by requiring a minimum number of wire and scintillator hits on both sides of the toroidal magnets in the muon detector [18]. Cosmic ray background is rejected by requiring scintillator signals consistent in time with muons originating from the $p\bar{p}$ collision. Tracks in the muon system are required to match a reconstructed track in the central tracker having a small impact parameter with respect to the $p\bar{p}$ interaction vertex (PV) to reject muons from cosmic rays and decays in flight of kaons and pions. Muon candidates must also be isolated from jets with $p_T > 15$ GeV by requiring a separation in $\eta - \phi$ space between the muon and jet of $\Delta\mathcal{R}(\mu, \text{jet}) > 0.5$ [20]. Candidates satisfying these requirements are referred to as *loosely isolated* muons. The following two variables are used to impose additional isolation requirements: $E_{\text{halo}}^{\text{scaled}}$ is defined as the ratio of calorimeter energy within an annulus of $0.1 < \mathcal{R} < 0.4$ around the muon direction to the p_T of the muon; $p_{T,\text{cone}}^{\text{scaled}}$ is defined as the ratio of the total p_T of all tracks within a cone of $\mathcal{R} = 0.5$, excluding the muon, to the p_T of the muon. Muon candidates meeting all the requirements above that satisfy $E_{\text{halo}}^{\text{scaled}} < 0.12$ and $p_{T,\text{cone}}^{\text{scaled}} < 0.12$ are referred to as *veto* muons. Further tightening these requirements to $E_{\text{halo}}^{\text{scaled}} < 0.08$ and $p_{T,\text{cone}}^{\text{scaled}} < 0.06$ selects candidates referred to as *tightly isolated* muons.

3. Measurement of the Imbalance in Transverse Momentum

We use the conservation of momentum to measure the momentum imbalance in the transverse plane (\not{p}_T). From that, we infer the presence of the neutrino. The \not{p}_T is determined from the vector sum of the energies of all cells in the electromagnetic and hadronic calorimeters. Subsequent energy corrections applied to reconstructed objects such as jets and muons are also propagated to the missing transverse momentum.

4. Identification of Jets

Jet candidates are reconstructed using the iterative midpoint cone algorithm with a cone radius of $\mathcal{R} =$

0.5 [21]. Only calorimeter cells with energies that are 2.5 standard deviations above the mean of the noise distribution are considered in the reconstruction. Isolated cells with energies less than 4 standard deviations above the mean of the noise distribution are also discarded. Among the jet candidates with $p_T > 8$ GeV, the following selection criteria are imposed. The electromagnetic fraction of the jet energy is required to be below 0.95 to reject electrons and above 0.05 to suppress jets dominated by noise from the hadronic part of the calorimeter. Jets with a large fraction of their energy deposited in the coarse hadronic layers of the calorimeter are rejected to suppress jets dominated by noise typical for those layers. To minimize background from jet candidates arising from noise in the precision readout of the calorimeter, confirmation from the readout system of the first level trigger is required for reconstructed jets. Jets matched to loose electrons with $p_T > 20$ GeV and $\Delta R(e, \text{jet}) < 0.5$ [20] are also rejected. Energies of jets containing muons are corrected with the measured muon momentum after accounting for the typical energy deposited by a minimum ionizing particle.

The energy of a reconstructed jet is corrected, on average, to that of a *particle jet* [22] containing the final-state particles within a cone of radius $\mathcal{R} = 0.5$ corresponding to the reconstructed jet. The first step involves the subtraction of the offset energy due to calorimeter noise and contributions from previous and following beam crossings and multiple interactions within the same beam crossing. This is followed by an absolute response correction determined from γ -jet events and a relative η -dependent correction based on γ -jet and dijet events. Finally, a showering correction is applied to account for the lateral leakage of energy across the jet cone boundary.

5. Identification of b jets

The lifetime of the b quark, unlike that of the top quark, is far longer than the time scale for strong interactions. This means that, during QCD evolution, the b quark can form short lived b hadrons that travel $\gtrsim 1$ mm before decaying through the weak interaction. We identify the b jets among the candidates satisfying the jet selection criteria described in the previous section by using a neural network (NN) b -tagging algorithm that selects jets with displaced vertices and tracks relative to the PV [23]. The NN tagger is based on nine input variables that can be separated into two categories. The first category is related to the reconstructed secondary vertex and includes the vertex quality, the number of associated tracks, the invariant mass of the vertex, the number of secondary vertices reconstructed within the jet, the spatial separation between the jet axis and the position vector of the secondary vertex relative to the PV, and the length of the flight path projected on the transverse plane divided by its uncertainty (which provides a measure of the decay length significance in terms

of standard deviations). The second category relies only on the characteristics of the tracks within the jets such as impact parameters, transverse momentum, and track quality. The b -jet candidates are also required to have at least two good quality tracks originating from the PV. The tagging efficiency for b jets is $\approx 65\%$ for a misidentification rate of $\approx 3\%$ for u , d , s quark, or gluon jets [24].

B. Event Selection

The data sample used in this analysis was collected with the D0 detector at the Tevatron between June 2006 and June 2008, and corresponds to an integrated luminosity of 2.6 fb^{-1} . The selected events must satisfy a single-lepton trigger, requiring a high p_T electron or muon, or a lepton+jets trigger, requiring a lower- p_T electron or muon accompanied by a jet. Events are required to have at least one PV with > 2 tracks reconstructed within the fiducial region of the SMT. We require exactly four jets with $|\eta| < 2.5$, with the leading (highest p_T) jet having $p_T > 40$ GeV, and the other jets $p_T > 20$ GeV. Leptons are required to originate from within 1 cm of the PV in the coordinate along the beam line. Exactly one tight electron (or tightly isolated muon) with $p_T > 20$ GeV and $|\eta| < 1.1$ ($|\eta| < 2$) is also required. Electron+jets events containing a second tight electron with $p_T > 15$ GeV and $|\eta| < 2.5$ or a veto muon with $p_T > 15$ GeV and $|\eta| < 2$ are rejected. Muon+jets events containing a second muon that is a veto muon with $p_T > 15$ GeV and $|\eta| < 2$ or a tight electron with $p_T > 15$ GeV and $|\eta| < 2.5$ are rejected. The missing transverse momentum is required to satisfy $\cancel{p}_T > 20$ GeV ($\cancel{p}_T > 25$ GeV) for e +jets (μ +jets) events. Multijet background, typically arising from mismeasurement of lepton or jet energies, is suppressed by requiring a minimal azimuthal separation between the lepton direction and the \cancel{p}_T vector with $\Delta\phi(e, \cancel{p}_T) > 0.7\pi - 0.045 \cdot \cancel{p}_T$ for electrons and $\Delta\phi(\mu, \cancel{p}_T) > 2.1 - 0.035 \cdot \cancel{p}_T$ for muons, with \cancel{p}_T in GeV and $\Delta\phi(l, \cancel{p}_T) = |\phi_l - \phi_{\cancel{p}_T}|$. Any μ +jets events with an invariant mass, $m_{\mu\mu}$, of the isolated muon and a second muon (with $p_T > 15$ GeV and even lower quality requirements than a loosely isolated muon) of $70 < m_{\mu\mu} < 110$ GeV are rejected in order to suppress $Z(\rightarrow \mu\mu)$ +jets events. The data sample satisfying the above criteria consists of 825 e +jets and 737 μ +jets events. We further require at least one jet to be identified as a b jet, which yields the final data samples of 312 e +jets and 303 μ +jets events.

IV. MONTE CARLO SAMPLES

The MC events used to model the $t\bar{t}$ signal and the W +jets background needed for the calibration of the measurement (described in Sec. VI) are generated using ALPGEN [10] to simulate the hard-scattering process and PYTHIA [11] to simulate hadronization and shower evo-

lution. The MLM matching scheme [25] is employed to avoid overlaps between components of the event belonging to the hard process, implemented through a matrix element, and parton evolution (showering) into jets. The W +jets background samples are divided into two categories: (i) $W + lp$ and (ii) $W + (c\bar{c}, b\bar{b})$ and $W + (bb, lp)$, where lp (light partons) denotes u , d , s -quarks, or gluons. Although the individual processes are produced with ALPGEN which is a LO generator, the relative contributions between the two categories are determined using next-to-leading order (NLO) calculations, with next-to-leading logarithmic (NLL) corrections based on the MCFM MC generator [26]. The MC samples used to derive jet transfer functions that correlate jet energies with those of partons in the $t\bar{t}$ events (described in Sec. V B 1) are generated using PYTHIA to simulate both the hard-scattering process and the subsequent hadronization and shower evolution for the events. All MC samples are generated with CTEQ6L1 parton distribution functions (PDFs) [27], and passed through a full GEANT3-based [28] simulation of the D0 detector. To simulate the effects from additional $p\bar{p}$ interactions, events with no trigger requirements selected from random $p\bar{p}$ crossings in the collider data having the same instantaneous luminosity profile as the data are overlayed on the fully simulated MC events. This is then followed by the same reconstruction and analysis chain as applied to data.

V. METHOD OF ANALYSIS

The top-quark mass is measured using all kinematic information with a likelihood technique based on probability densities (PDs) constructed, for each individual event, from matrix elements of the processes contributing to the observed final state. This analysis technique, referred to as the matrix element (ME) method [29], is described below.

A. Matrix Element Method

If the processes contributing to an observed event do not interfere, the total PD for observing a given event is the sum of all contributing probabilities for that specific final state. Assuming that $t\bar{t}$ and W +jets production are the only two contributions, the PD for observing each event is given in terms of the top-quark mass m_t , the jet energy scale factor k_{JES} dividing the energies of all jets, and the fractions of $t\bar{t}$ signal (f) and of W +jets

background ($1 - f$) in the data by:

$$P_{\text{evt}} = A(x)[f P_{\text{sig}}(x; m_t, k_{\text{JES}}) + (1 - f) P_{\text{bkg}}(x; k_{\text{JES}})], \quad (1)$$

where x represents the measured jet and lepton energies and angles; $A(x)$, which depends only on x , accounts for the geometrical acceptance and efficiencies; and P_{sig} and P_{bkg} are the PDs for $t\bar{t}$ and W +jets production, respectively. For events satisfying $P_{\text{bkg}} \gg P_{\text{sig}}$, the relative contribution of P_{sig} to P_{evt} is negligible and has minimal influence on the determination of m_t . Multijet events satisfy this condition and can therefore be represented by P_{bkg} , as the event kinematics are far closer to W +jets than to $t\bar{t}$ production.

Due to the finite detector resolution and the hadronization process, the measured set x for the observed events will not, in general, be identical to the corresponding set y of the original final-state partons and the relationship between x and y is described by a transfer function. In addition, the initial partons carry momenta q_1 and q_2 in the colliding p and \bar{p} . To account for this complication, P_{sig} and P_{bkg} must be integrated over all parton states contributing to the observed set x . This involves a convolution of the partonic differential cross section $d\sigma(y)$ with the PDFs and a transfer function $W(x, y; k_{\text{JES}})$ that relates x and y :

$$P(x, \alpha) = \frac{1}{\sigma(\alpha)} \int \sum_{\text{flavors}} d\sigma(y, \alpha) dq_1 dq_2 f(q_1) f(q_2) \times W(x, y; k_{\text{JES}}), \quad (2)$$

where α represents the parameters to be determined in the analysis, the sum runs over all possible initial-state parton flavors, and $f(q_i)$ are CTEQ6L1 PDFs for finding a parton of a given flavor and longitudinal momentum fraction q_i in the p or \bar{p} . Detector resolution is taken into account in $W(x, y; k_{\text{JES}})$, representing the probability density for the measured set x to have arisen from the partonic set y . Dividing by the total observed cross section for the process, $\sigma(\alpha)$, ensures $P(x; \alpha)$ is normalized to unity.

The differential cross section term for P_{sig} is calculated using the LO ME of the quark-antiquark annihilation process ($\mathcal{M}_{t\bar{t}}$). A total of 24 integration variables are associated with the two initial state partons and the six particles in the final state. Since the angles for the four jets and the charged lepton are sufficiently well measured, the angular resolution terms in $W(x, y; k_{\text{JES}})$ can be approximated by Dirac δ -functions. Integrating over these and four more δ -functions that impose energy-momentum conservation leaves 10 integrals to evaluate the probability density that represents the $t\bar{t}$ production probability for a given m_t and k_{JES} [30]:

$$P_{\text{sig}} = \frac{1}{\sigma_{\text{obs}}^{t\bar{t}}} \sum_{i=1}^{24} w_i \int d\rho dm_1^2 dM_1^2 dm_2^2 dM_2^2 d\rho_\ell dq_1^x dq_1^y dq_2^x dq_2^y$$

$$\sum_{\text{flavors}, \nu} |\mathcal{M}_{t\bar{t}}|^2 \frac{f'(q_1)f'(q_2)}{\sqrt{(\eta_{\alpha\beta} q_1^\alpha q_2^\beta)^2 - m_{q_1}^2 m_{q_2}^2}} \Phi_6 W(x, y; k_{\text{JES}}), \quad (3)$$

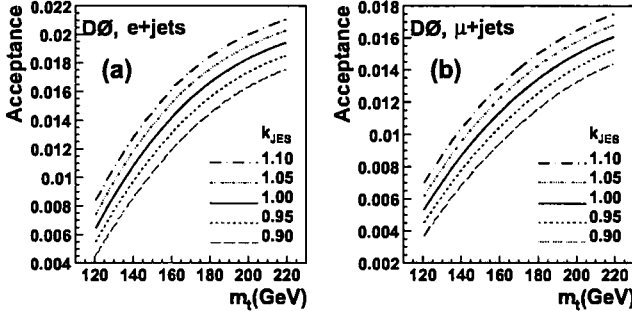


Figure 1. (color online) The mean acceptance as a function of m_t and k_{JES} for the (a) $e+\text{jets}$ and (b) $\mu+\text{jets}$ channels.

where, in addition to the CTEQ6L1 PDF given by $f(q_i)$, the $f'(q_i)$ also include parameterizations of the probability distributions for the transverse momenta $q_i^{x,y}$ of the initial-state partons in PYTHIA [11]. The masses of the initial-state partons are given by m_{q_i} , and Φ_6 includes the 6-body phase-space factor and other constants. The first sum is over all 24 jet permutations, each carrying a weight w_i , which is the product of four jet weights. The weight for a b -tagged jet with a given p_T and η is the average tagging efficiency $\epsilon_\alpha(p_T, \eta)$ for a given parton hypothesis α ($= b, c, \text{light } q, \text{ or gluon}$). The weight for a jet that is not b -tagged is $1 - \epsilon_\alpha(p_T, \eta)$. The second sum includes up to eight solutions for neutrino kinematics, and conservation of transverse momentum used to calculate the transverse momentum of the neutrino. The parameter ρ represents the fraction of the energy carried by one of the quarks from the $W \rightarrow q\bar{q}'$ decay. The masses of the two W bosons (M_1, M_2) and of the pair of top quarks (m_1, m_2) are chosen as integration variables because of computational efficiency related to the four Breit-Wigner mass terms that make the ME negligible everywhere except at the mass peaks. The energy (the curvature $1/p_T$) of the electron (muon) is defined by ρ_ℓ . The integration over q_i involves only transverse components. $W(x, y; k_{\text{JES}})$ is the product of five terms for the four jets and one charged lepton, described below. The normalization $\sigma_{\text{obs}}^{t\bar{t}} = \int A(x) P_{\text{sig}} dx = \sigma^{t\bar{t}}(m_t) \times \langle A(m_t, k_{\text{JES}}) \rangle$ is calculated from the product of the total cross section corresponding to the ME used and the mean acceptance for events whose dependencies on m_t and k_{JES} are determined from MC events. The mean acceptance is shown in Fig. 1 as a function of m_t for different values of k_{JES} .

The differential cross section in P_{bkg} is calculated using the $W+4$ jets matrix elements from the VECBOS [31] MC program. The initial-state partons are assumed to have no transverse momenta. The integration is performed over the W boson mass, the energy ($1/p_T$) of the electron

(muon), and the energies of the four partons producing the jets, summing over the 24 jet permutations and all neutrino solutions.

The top-quark mass is extracted from n events with a measured set of variables $\tilde{x} = (x_1, x_2, \dots, x_n)$ through a likelihood function for individual event probabilities P_{evt} according to

$$L(\tilde{x}; m_t, k_{\text{JES}}, f) = \prod_{i=1}^n P_{\text{evt}}(x_i; m_t, k_{\text{JES}}, f). \quad (4)$$

For every assumed pair of (m_t, k_{JES}) values, the value of f^{best} that maximizes the likelihood is determined. To obtain the best estimate of m_t and k_{JES} , the two-dimensional likelihood:

$$L(\tilde{x}; m_t, k_{\text{JES}}) = L[\tilde{x}; m_t, k_{\text{JES}}, f^{\text{best}}(m_t, k_{\text{JES}})] \quad (5)$$

is projected onto the m_t and k_{JES} axes according to

$$L(\tilde{x}; m_t) = \int L(\tilde{x}; m_t, k_{\text{JES}}) G(k_{\text{JES}}) dk_{\text{JES}} \quad (6)$$

and

$$L(\tilde{x}; k_{\text{JES}}) = \int L(\tilde{x}; m_t, k_{\text{JES}}) dm_t, \quad (7)$$

using Simpson's rule [32], where the prior probability distribution $G(k_{\text{JES}})$ is a Gaussian function centered at $k_{\text{JES}} = 1$ with standard deviation (sd) 0.02 determined from the mean of the fractional uncertainty of the standard jet energy scale corrections applied to all jets in the MC samples used in this analysis. The best estimates and the uncertainties on the mass of the top quark and the jet energy scale are then extracted using the mean and the RMS of $L(\tilde{x}; m_t)$ and $L(\tilde{x}; k_{\text{JES}})$, respectively. The mean is calculated from $\bar{\alpha} = \int \alpha L(\tilde{x}; \alpha) d\alpha / \int L(\tilde{x}; \alpha) d\alpha$ and the RMS from $\sigma^2(\alpha) = \int (\alpha - \bar{\alpha})^2 L(\tilde{x}; \alpha) d\alpha / \int L(\tilde{x}; \alpha) d\alpha$, where α corresponds to m_t or k_{JES} , also using Simpson's rule.

The fit parameter k_{JES} , associated with the *in situ* jet energy calibration, has the effect of rescaling the energies of all the jets, and thereby the 2-jet invariant mass of the hadronically decaying W boson, with the jet energy scale factor k_{JES} . The presence of the Breit-Wigner mass term associated with the hadronically decaying W boson in the ME of Eq. (3) maximizes the likelihood in Eq. (4) when the 2-jet invariant mass coincides with the Breit-Wigner pole fixed at the world average of $M_W = 80.4$ GeV [9]. The additional constraint to the standard scale derived from $\gamma+\text{jet}$ and dijet samples is applied through the prior probability distribution $G(k_{\text{JES}})$ in Eq. (6).

Table I. Transfer function parameters for light quarks (a_i in GeV).

| Par. | Light-quark jets | | | | |
|-------|------------------------|------------------------|------------------------|------------------------|--|
| | $ \eta < 0.5$ | $0.5 < \eta < 1$ | $1 < \eta < 1.5$ | $1.5 < \eta < 2.5$ | |
| a_1 | -2.74×10^0 | -8.02×10^{-1} | 1.69×10^{-1} | 1.52×10^1 | |
| b_1 | 1.67×10^{-2} | -3.59×10^{-3} | 1.32×10^1 | -2.17×10^{-1} | |
| a_2 | 5.44×10^0 | 5.40×10^0 | -3.26×10^{-1} | 3.34×10^0 | |
| b_2 | 6.29×10^{-2} | 8.46×10^{-2} | 6.97×10^0 | 1.45×10^{-1} | |
| b_3 | 4.30×10^{-4} | 4.80×10^{-4} | 2.52×10^{-2} | 4.06×10^{-3} | |
| a_4 | 1.54×10^1 | 2.00×10^1 | 4.71×10^0 | 1.72×10^1 | |
| b_4 | -2.12×10^{-1} | -2.38×10^{-1} | -8.37×10^{-3} | -3.69×10^{-2} | |
| a_5 | 1.77×10^1 | -2.38×10^{-1} | 1.03×10^1 | 1.75×10^1 | |
| b_5 | 1.96×10^{-1} | 1.89×10^1 | 6.42×10^{-2} | 5.34×10^{-2} | |

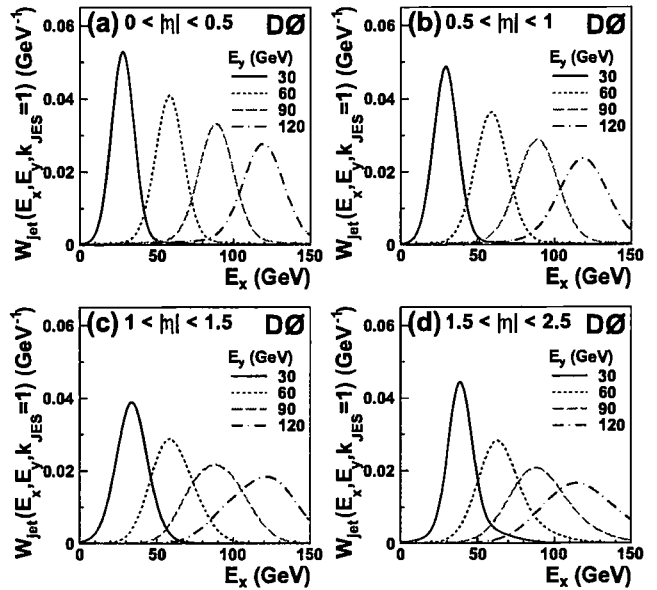


Figure 2. (color online) Transfer functions for $k_{\text{JES}} = 1$ light-quark jets as a function of measured jet energy for different parton energies in η regions: (a) $|\eta| < 0.5$, (b) $0.5 < |\eta| < 1.0$, (c) $1.0 < |\eta| < 1.5$, and (d) $1.5 < |\eta| < 2.5$.

B. Detector Resolution

In this section, we describe the parameterizations for the jet and electron energy and muon p_T resolutions used in the transfer function $W(x, y; k_{\text{JES}})$ which is the product of four jet transfer functions for a given jet permutation and an electron or muon transfer function.

1. Parameterization of Jet Energy Resolution

The transfer function for jets, $W_{\text{jet}}(E_x, E_y; k_{\text{JES}})$, represents the probability that a measured jet energy E_x in the detector corresponds to a parent quark of energy E_y . It is parameterized in terms of a double Gaussian function whose means and widths are dependent on E_y . For the case $k_{\text{JES}} = 1$, it is given by

$$W_{\text{jet}}(E_x, E_y; k_{\text{JES}} = 1) = \frac{1}{\sqrt{2\pi}(p_2 + p_3 p_5)} \times \left[e^{-\frac{[(E_x - E_y) - p_1]^2}{2p_2^2}} + p_3 e^{-\frac{[(E_x - E_y) - p_4]^2}{2p_5^2}} \right], \quad (8)$$

where the p_i are functions of the quark energy for quark i and are parameterized as linear functions of the E_y :

$$p_i = a_i + E_y \cdot b_i. \quad (9)$$

The parameters a_i and b_i are determined from fully simulated $t\bar{t}$ events, following all jet energy corrections and smearing to match resolutions in data. These events are generated with PYTHIA at nine values of the top-quark mass ranging from 155 to 195 GeV in 5 GeV intervals. The parton and jet energies are used in an unbinned likelihood fit that minimizes the product of the W_{jet} terms

for each event with respect to a_i and b_i . A different set of parameters is derived (i) for three varieties of quarks: light quarks (u, d, s, c), b quarks with a soft muon tag in the jet [33], and all other b quarks, and (ii) for four η regions: $|\eta| < 0.5$, $0.5 < |\eta| < 1.0$, $1.0 < |\eta| < 1.5$, and $1.5 < |\eta| < 2.5$, to minimize possible effects due to non-uniform calorimeter response. The values for these parameters are shown in Tables I and II for light-quark and b -quark jets, respectively. Figure 2 illustrates the transfer functions for light-quark jets as a function of E_x for different values of E_y . In Fig. 3, we compare the 2-jet and 3-jet invariant mass distributions for two types of PYTHIA $t\bar{t} \ell + \text{jets}$ events: (i) parton level events with jet energies smeared using the transfer functions and (ii) fully simulated events where all four reconstructed jets are matched to partons with $\Delta\mathcal{R}(\text{parton}, \text{jet}) < 0.5$. The 2-jet (3-jet) invariant masses are calculated using the two light-quark jets (all three jets) from the hadronic branch of the $t\bar{t} \ell + \text{jets}$ events and correspond to the W boson (top-quark) mass. The overlaid distributions in Fig. 3 indicate that the jet transfer functions describe the jet resolutions well.

For $k_{\text{JES}} \neq 1$, the jet transfer function is changed to

$$W_{\text{jet}}(E_x, E_y; k_{\text{JES}}) = \frac{W_{\text{jet}}\left(\frac{E_x}{k_{\text{JES}}}, E_y; 1\right)}{k_{\text{JES}}}, \quad (10)$$

where the k_{JES} factor in the denominator preserves the normalization $\int W_{\text{jet}}(E_x, E_y; k_{\text{JES}}) dE_x = 1$.

Table II. Transfer function parameters for b -quark jets without and with a muon within the jet cone (a_i in GeV).

| b -quark jets without a muon within the jet cone | | | | | b -quark jets with a muon within the jet cone | | | | |
|--|------------------------|------------------------|------------------------|------------------------|---|------------------------|------------------------|------------------------|------------------------|
| Par. | $ \eta < 0.5$ | $0.5 < \eta < 1$ | $1 < \eta < 1.5$ | $1.5 < \eta < 2.5$ | Par. | $ \eta < 0.5$ | $0.5 < \eta < 1$ | $1 < \eta < 1.5$ | $1.5 < \eta < 2.5$ |
| a_1 | 3.30×10^0 | 5.38×10^0 | 2.85×10^0 | 1.38×10^1 | a_1 | 6.37×10^0 | 6.31×10^0 | 8.00×10^0 | 1.65×10^1 |
| b_1 | -2.13×10^{-1} | -2.26×10^{-1} | -1.85×10^{-1} | -2.90×10^{-1} | b_1 | -1.46×10^{-1} | -1.40×10^{-1} | -1.39×10^{-1} | -1.91×10^{-1} |
| a_2 | 5.02×10^0 | 5.08×10^0 | 9.78×10^{-1} | 3.86×10^0 | a_2 | 2.53×10^0 | 3.89×10^0 | 8.54×10^0 | 4.88×10^0 |
| b_2 | 1.73×10^{-1} | 1.77×10^{-1} | 1.83×10^{-1} | 1.36×10^{-1} | b_2 | 1.43×10^{-1} | 1.37×10^{-1} | 1.28×10^{-1} | 1.43×10^{-1} |
| b_3 | 3.48×10^{-2} | 2.49×10^{-2} | 6.69×10^{-3} | 7.52×10^{-3} | b_3 | 3.90×10^{-4} | 3.40×10^{-4} | 1.90×10^{-4} | 1.20×10^{-4} |
| a_4 | -6.68×10^0 | -6.56×10^0 | 8.54×10^{-1} | 5.59×10^0 | a_4 | 2.80×10^1 | 1.52×10^1 | 7.89×10^1 | 4.73×10^1 |
| b_4 | 2.38×10^{-2} | 1.91×10^{-2} | -2.83×10^{-2} | -4.54×10^{-2} | b_4 | -3.87×10^{-1} | -9.74×10^{-2} | 2.22×10^{-1} | 5.21×10^{-2} |
| a_5 | 5.06×10^0 | 4.36×10^0 | 1.38×10^1 | 1.50×10^1 | a_5 | 1.80×10^1 | 2.32×10^1 | 2.80×10^1 | 2.83×10^1 |
| b_5 | 4.71×10^{-2} | 6.99×10^{-2} | 6.04×10^{-2} | 7.60×10^{-2} | b_5 | 1.30×10^{-1} | 2.91×10^{-2} | -2.87×10^{-1} | -8.55×10^{-2} |

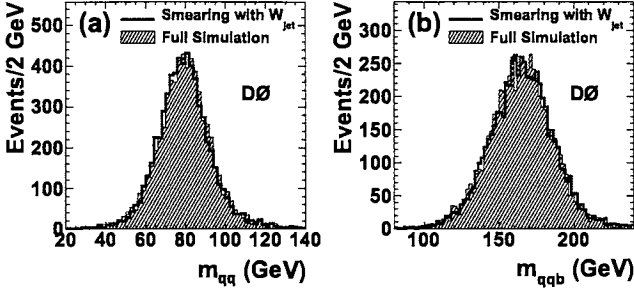


Figure 3. (color online) Comparison of (a) 2-jet and (b) 3-jet invariant mass distributions for parton-level $t\bar{t}$ MC events with energies smeared using the transfer functions (open histogram) and fully simulated $t\bar{t}$ MC events with all four jets spatially matched to partons (filled histogram).

2. Parameterization of Energy Resolution for Electrons

The electron energy resolution is parameterized by the transfer function

$$W_e(E_x, E_y) = \frac{1}{\sqrt{2\pi}\sigma} \exp \left[-\frac{1}{2} \left(\frac{E_x - E'_y}{\sigma} \right)^2 \right], \quad (11)$$

where E_x is the reconstructed electron energy,

$$E'_y = 1.000 \cdot E_y + 0.324 \text{ GeV}, \quad (12)$$

$$\sigma = \sqrt{(0.028 \cdot E'_y)^2 + (S \cdot E'_y)^2 + (0.4 \text{ GeV})^2}, \quad (13)$$

$$S = \frac{0.164 \text{ GeV}^{1/2}}{\sqrt{E'_y}} + \frac{0.122 \text{ GeV}^{1/2}}{E'_y} e^{C/\sin \theta_e} - C, \quad (14)$$

$$C = 1.3519 - \frac{2.0956 \text{ GeV}}{E'_y} - \frac{6.9858 \text{ GeV}}{E'^2_y}, \quad (15)$$

E_y is the energy of the original electron, and θ_e is the polar angle of the electron with respect to the proton beam direction. The parameters above are derived from the detailed modeling of electron energy response and resolution used in Ref. [34].

3. Parameterization of Momentum Resolution for Muons

We describe the resolution of the central tracker through the uncertainty on the signed curvature of a track, the ratio of the electric charge and of the transverse momentum of a particle, parameterized as a function of pseudorapidity. The muon transfer function is parameterized as

$$W_\mu(\kappa_x, \kappa_y) = \frac{1}{\sqrt{2\pi}\sigma} \exp \left[-\frac{1}{2} \left(\frac{\kappa_x - \kappa_y}{\sigma} \right)^2 \right], \quad (16)$$

where $\kappa_x = (q/p_T)_x$ and $\kappa_y = (q/p_T)_y$, with the charge q and transverse momentum p_T of the original muon (y) or its reconstructed track (x). The resolution

$$\sigma = \begin{cases} \tilde{\sigma} & \text{for } |\eta| \leq 1.4 \\ \sqrt{\tilde{\sigma}^2 + \{c \cdot (|\eta| - 1.4)\}^2} & \text{for } |\eta| > 1.4 \end{cases} \quad (17)$$

is obtained from muon tracks in simulated events where the $\tilde{\sigma}$ and c parameters are linear functions of $1/p_T$:

$$\tilde{\sigma} = \tilde{\sigma}_0 + \tilde{\sigma}_1 \cdot 1/p_T, \quad (18)$$

$$c = c_0 + c_1 \cdot 1/p_T. \quad (19)$$

The values of the coefficients are given in Table III for muon tracks with associated and no associated hits in the silicon tracker. This simplified parameterization of the momentum resolution is valid at high transverse momenta ($p_T > 20$ GeV) where the limitations in coordinate resolution dominate over the effects of multiple scattering.

VI. CALIBRATION OF THE MEASUREMENT

The fully simulated MC samples described in Sec. IV are used in ensemble studies to calibrate the result from the ME method by determining and correcting for biases

Table III. Parameters for muon transfer functions for muon tracks with and without hits in the SMT.

| Parameter | With hits in the SMT | No hits in the SMT |
|-----------------------------------|-------------------------|------------------------|
| $\tilde{\sigma}_0$ (GeV $^{-1}$) | 2.082×10^{-3} | 3.620×10^{-3} |
| $\tilde{\sigma}_1$ | 1.125×10^{-2} | 1.388×10^{-2} |
| c_0 (GeV $^{-1}$) | 7.668×10^{-3} | 2.070×10^{-2} |
| c_1 | 7.851×10^{-2} | 7.042×10^{-2} |

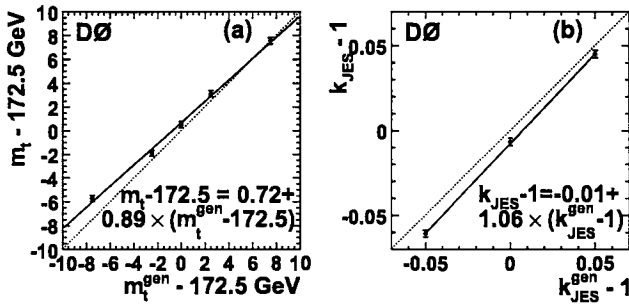


Figure 4. Mean values of (a) m_t and (b) k_{JES} extracted from ensemble studies, as a function of the input values fitted to straight lines. Dashed lines represent 1:1 correlations of extracted and input values.

in the extracted parameters and their estimated uncertainties. Such biases can be due, for example, to limitations in the LO ME used in Eq. (3) or to the imperfect description of detector resolution using transfer functions with a limited number of parameters. Five $t\bar{t}$ MC samples are generated for $m_t^{\text{gen}} = 165, 170, 172.5, 175$, and 180 GeV, with two more produced from the 172.5 GeV sample by re-scaling all jet energies by $\pm 5\%$. P_{sig} and P_{bkg} are calculated for these samples and for the $W+\text{jets}$ MC samples. Events are drawn randomly from a $t\bar{t}$ sample with a particular mass and the $W+\text{jets}$ sample to form pseudoexperiments, each with a number of events equal to the one observed in data (before requiring ≥ 1 b -tagged jets), with the signal fraction fluctuated according to a binomial distribution relative to that determined from

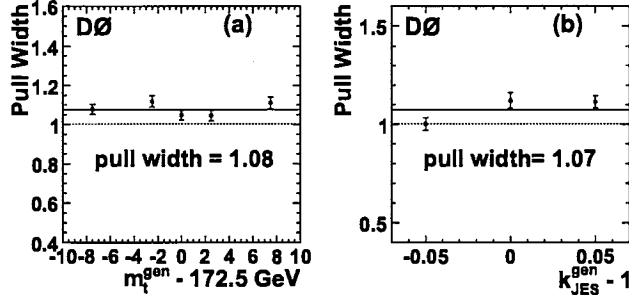


Figure 5. Widths of the pull distributions for (a) m_t and (b) k_{JES} from ensemble studies as a function of the input values.

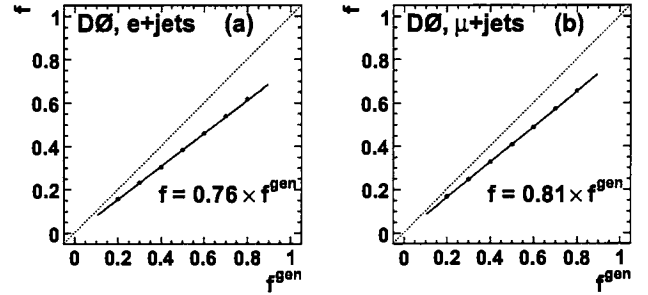


Figure 6. Extracted signal fractions from ensemble studies as a function of the input values for the (a) $e+\text{jets}$ and (b) $\mu+\text{jets}$ channels.

data. The values of m_t and k_{JES} are extracted for each pseudoexperiment according to the procedure described in Sec. V A using only events with at least one b -tagged jet. A thousand pseudoexperiments are performed for each of the $7 t\bar{t}$ samples. The means (and their uncertainties) of all 1000 measured values of m_t and k_{JES} in each sample are determined from Gaussian fits to their distributions and plotted versus the input $m_t^{\text{gen}} - 172.5$ GeV and $k_{\text{JES}} - 1$, respectively. A straight line is fitted to the plotted points, representing the response function used to correct the measurement from data (Fig. 4). For each pseudoexperiment, we also calculate the pulls, defined as $(m_t - \langle m_t \rangle)/\sigma(m_t)$ and $(k_{\text{JES}} - \langle k_{\text{JES}} \rangle)/\sigma(k_{\text{JES}})$, where $\langle m_t \rangle$ and $\langle k_{\text{JES}} \rangle$ are the mean measured m_t and k_{JES} , respectively, for all pseudoexperiments, and $\sigma(m_t)$ and $\sigma(k_{\text{JES}})$ are the RMS of m_t and k_{JES} , respectively, for the given pseudoexperiment. The width of the pull distributions for m_t and k_{JES} are shown as a function of m_t^{gen} and $k_{\text{JES}}^{\text{gen}}$ in Fig. 5. The average widths of the m_t and k_{JES} pull distributions are 1.08 and 1.07, respectively.

The signal fraction for the ensemble studies is determined from the selected data sample using the method described in Sec. V A. To correct for biases in the determination of this fraction, a calibration is done using the $W+\text{jets}$ and 172.5 GeV $t\bar{t}$ MC samples, wherein 1000 pseudoexperiments are performed using the same procedure as described in the previous paragraph, but with signal fractions set to a different value in each test. The extracted signal fractions as a function of their input values are shown in Figs. 6(a) and 6(b) for the $e+\text{jets}$ and $\mu+\text{jets}$ channels, respectively. Straight lines are fitted to the points in plots representing the response functions used to correct the fractions determined from the selected data sample. The calibration of the signal fraction is performed separately for the $e+\text{jets}$ and $\mu+\text{jets}$ channels. The corrected fractions are 0.35 ± 0.05 and 0.41 ± 0.06 for the $e+\text{jets}$ and $\mu+\text{jets}$ channels, respectively, prior to requiring at least one b -tagged jet. These fractions are 0.71 ± 0.05 and 0.75 ± 0.04 for the $e+\text{jets}$ and $\mu+\text{jets}$ channels, respectively, after requiring at least one b -tagged jet.

VII. FLAVOR-DEPENDENT JET RESPONSE CORRECTION FOR MC EVENTS

The validity of the calibration procedure described in the previous section is based on the assumption of a perfect MC simulation of the events and of the detector. Uncertainties in this assumption are discussed in the section on systematic uncertainties (Sec. IX). The *in situ* jet energy scale employed in this analysis can account for a global scale discrepancy between data and MC jet energy scales (see Sec. IX B 1) by rescaling the energies of the two light jets from the $W \rightarrow q\bar{q}'$ decay of $t\bar{t}$ events to the world average mass of the W boson [9]. This same rescaling is also applied to the two b jets in the event. However, jets originating from different partons have different kinematic characteristics and particle compositions. In particular, b and light jets with different electromagnetic fractions can lead to different responses in a non-compensating calorimeter. Such features, if not properly simulated, can result in a systematic shift in the determination of the top-quark mass. In fact, the largest contribution to the total systematic uncertainty of our previous analysis in Ref. [8] is the b /light-quark response ratio which was an estimate of the effect of such a discrepancy.

To bring the simulation of the calorimeter response to jets into agreement with data, and thereby reduce the systematic uncertainty associated with a jet response difference in data and MC, we determine a flavor-dependent correction factor as follows. We note a discrepancy in the predicted energy deposition in the calorimeter between data and MC when we apply the single-particle responses from data and MC to the individual particles within MC jets that are spatially matched to reconstructed jets [35]:

$$\mathcal{D} = \frac{\sum E_i \cdot R_i^{\text{Data}}}{\sum E_i \cdot R_i^{\text{MC}}}, \quad (20)$$

where the sums run over each particle i in the MC particle jet, E_i is the true energy of particle i , and R_i^{Data} and R_i^{MC} are the single-particle responses in data and MC, respectively. We define a correction factor for a jet of flavor β (= light quark, gluon, or b quark) as the ratio of the discrepancy for jets of flavor β to the flavor-averaged discrepancy for jets in γ -jet events, $F_{\text{corr}}^\beta = \mathcal{D}^\beta / \langle \mathcal{D}^{\gamma+\text{jet}} \rangle$. Defining the correction this way preserves the standard MC jet energy scale that is, strictly speaking, only appropriate for the γ -jet events from which it is derived. At the same time, it brings the relative response difference between jets of flavor β and jets in γ -jet events in MC into agreement with that in data. The quantity $F_{\text{corr}}^\beta - 1$ is shown in Fig. 7 as a function of jet p_T and η for light-quark, gluon, and b jets. The shaded band at $F_{\text{corr}}^\beta - 1 = 0$ in each plot corresponds to the correction for jets in γ -jet events. We apply these correction factors to the light-quark jets and b jets in a $t\bar{t}$ MC sample generated with $m_t^{\text{gen}} = 172.5$ GeV, extract m_t and k_{JES} using our analysis technique, and compare them with the

values extracted from the same set of events without using this correction. We find shifts of $\Delta m_t = 1.26$ GeV and $\Delta k_{\text{JES}} = -0.005$ relative to the uncorrected sample. Repeating this study on a $t\bar{t}$ MC sample appropriate for the previous analysis [8] yields shifts of $\Delta m_t = 1.28$ GeV and $\Delta k_{\text{JES}} = -0.005$.

VIII. MEASUREMENT OF THE TOP-QUARK MASS

The likelihoods $L(\tilde{x}; m_t)$ and $L(\tilde{x}; k_{\text{JES}})$ for the selected data, calculated according to Eq. (6) and Eq. (7), respectively, are calibrated by replacing m_t and k_{JES} by parameters fitted to the response plots of Sec. VI:

$$m_t^{\text{calib}} = \frac{(m_t - 172.5 \text{ GeV}) - p_0^{m_t}}{p_1^{m_t}} + 172.5 \text{ GeV}, \quad (21)$$

$$k_{\text{JES}}^{\text{calib}} = \frac{(k_{\text{JES}} - 1) - p_0^{k_{\text{JES}}}}{p_1^{k_{\text{JES}}}} + 1, \quad (22)$$

where $p_i^{m_t}$ and $p_i^{k_{\text{JES}}}$ are the parameters of the m_t and k_{JES} response functions shown in Fig. 4(a) and Fig. 4(b), respectively, and m_t and k_{JES} and their uncertainties are extracted from the mean and RMS values of the calibrated likelihoods shown in Figs. 8(a) and 8(b). The extracted uncertainties are also corrected for the deviation of the average pull width from unity (see Sec. VI). Figure 9 shows the fitted Gaussian contours of equal probability for the two-dimensional likelihoods as a function of m_t and k_{JES} . We find $m_t = 174.75 \pm 1.28(\text{stat} + \text{JES})$ GeV and $k_{\text{JES}} = 1.013 \pm 0.008(\text{stat})$. Applying the shifts of $\Delta m_t = 1.26$ GeV and $\Delta k_{\text{JES}} = -0.005$ described in Sec. VII yields a measured top-quark mass and jet energy scale factor of

$$m_t = 176.01 \pm 1.01(\text{stat}) \pm 0.79(\text{JES}) \text{ GeV}, \\ k_{\text{JES}} = 1.013 \pm 0.008(\text{stat}).$$

Distributions in expected uncertainties determined from 1000 pseudoexperiments performed on the MC $t\bar{t}$ sample for $m_t^{\text{gen}} = 172.5$ GeV are shown in Figs. 10(a) and 10(b) for m_t and k_{JES} , respectively. The measured uncertainties, indicated by the arrows, are within the expected range observed in MC.

IX. SYSTEMATIC UNCERTAINTIES

We evaluate systematic uncertainties for three categories. The first category, *modeling of production*, addresses uncertainties in the MC modeling of $t\bar{t}$ and $W+\text{jets}$ production. The second category, *modeling of detector*, deals with the uncertainties in jet energy and lepton momentum scales and the simulation of detector response and any associated efficiencies. The third category involves uncertainties in the calibration of both m_t and the signal fraction f , and a possible bias from the

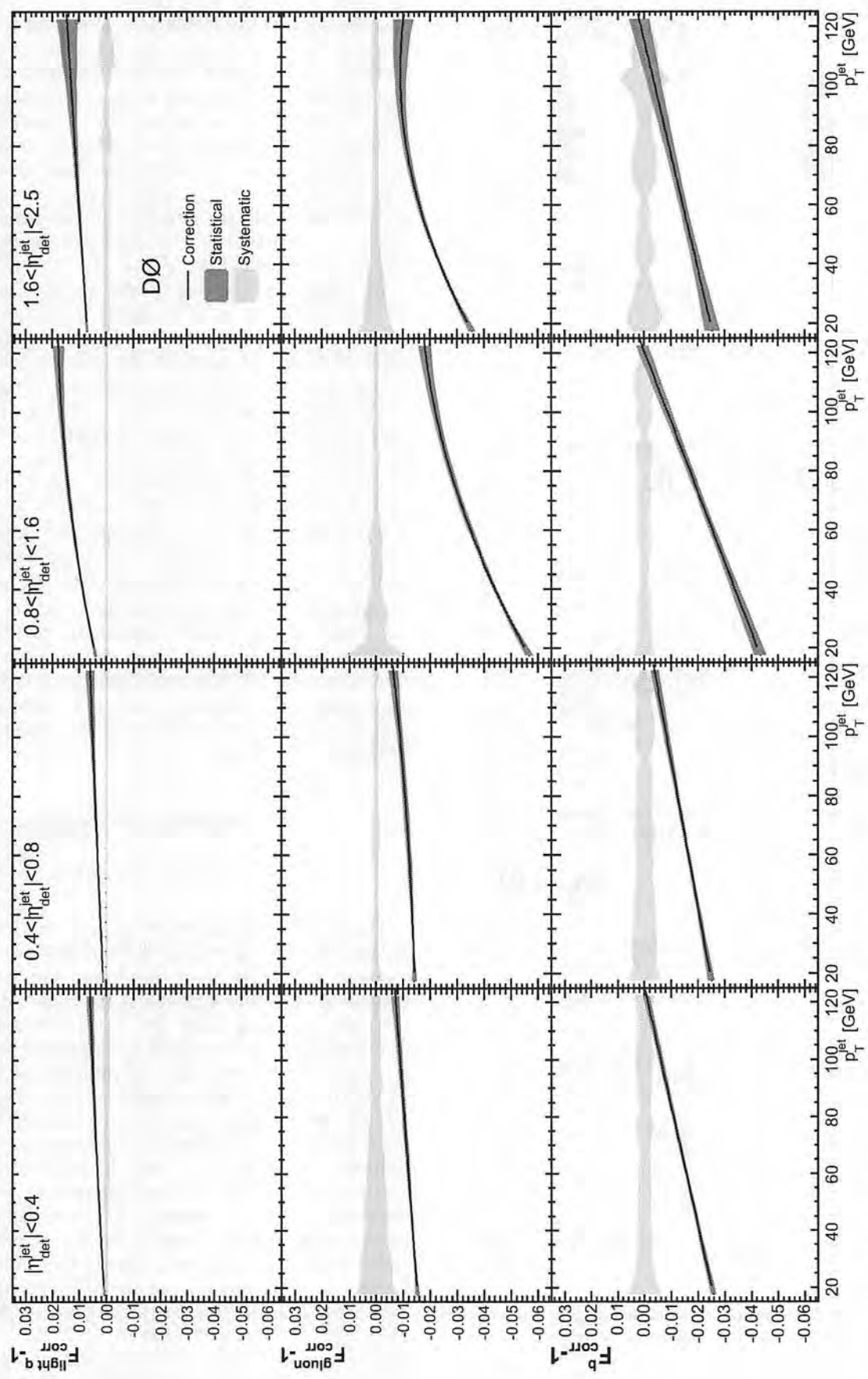


Figure 7. (color online) Correction factors for data-MC jet response difference for light-quark, gluon, and b jets as a function of jet p_T and η . Light shaded bands represent statistical uncertainties and dark shaded bands represent systematic uncertainties

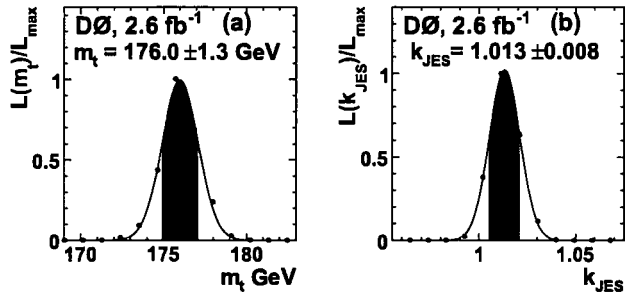


Figure 8. Calibrated projections of the data likelihoods onto the (a) m_t and (b) k_{JES} axes with 68% confidence level regions indicated by the shaded areas. The values of m_t and k_{JES} shown in the figures are after applying the corrections described in Sec. VII and Sec. VIII.

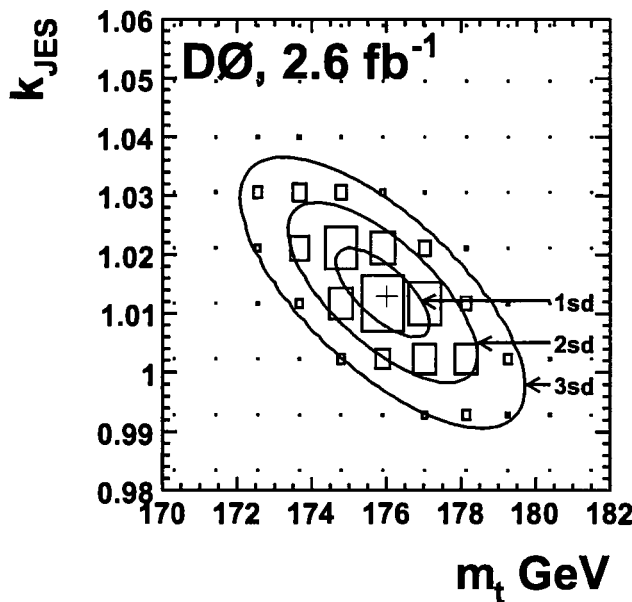


Figure 9. (color online) Fitted contours of equal probability for the two-dimensional likelihood $L(\tilde{x}; m_t, k_{\text{JES}})$.

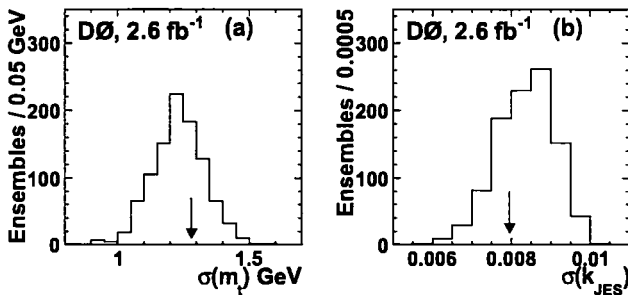


Figure 10. Expected uncertainty distributions for (a) m_t and (b) k_{JES} with the measured uncertainties indicated by the arrows.

exclusion of multijet events in MC ensemble studies. The contributions to the systematic uncertainty are summarized in Table IV. In the first three sections below, we describe the evaluation of each of these contributions in more detail. In the fourth section, we discuss how systematic uncertainties from the previous analysis of 1 fb^{-1} of integrated luminosity [8] are updated to facilitate the combination of the two results presented in Sec. XI. Except for the *Data-MC jet response difference* described in Sec. IX.B 2, all of the systematic uncertainties described below are calculated prior to the flavor-dependent jet response corrections of Sec. VII.

We adopt the following convention for systematic uncertainties δm_t in m_t , and classify them into two types. The first type, referred to as the *Type I* uncertainty, is the effect of the $\pm 1 \text{ sd}$ variation of a relevant quantity. The second type, referred to as the *Type II* uncertainty, is due to the difference between models. For Type I uncertainties, we refer to the central or default value of the measurement as m_t^0 and to the measurement corresponding to the 1 sd (-1 sd) variation as $m_t^+ (m_t^-)$. We compute Type I uncertainties according to $\delta m_t = |m_t^+ - m_t^-|/2$ if $m_t^- < m_t^0 < m_t^+$ or $m_t^+ < m_t^0 < m_t^-$ and according to $\delta m_t = \max(|m_t^+ - m_t^0|/2, |m_t^- - m_t^0|/2)$ if $m_t^+ - m_t^0$ and $m_t^- - m_t^0$ have the same sign. We compute Type II uncertainties by taking the maximal difference between the models as the + and - systematic variations.

Many of our systematic uncertainties are evaluated by comparing two MC $t\bar{t}$ samples generated with the same input mass m_t^{gen} . For these studies, we use samples with a value of m_t^{gen} close to the world average of m_t such as 172.5 GeV or 170 GeV .

A. Modeling of Production

1. Higher-Order Effects

The MC $t\bar{t}$ samples used to calibrate our measurement are generated using ALPGEN for the hard-scattering process and PYTHIA for shower evolution and hadronization (Sec. IV). We compare the LO generator ALPGEN with the next-to-leading order MC generator MC@NLO [36], in order to evaluate possible contributions from higher-order effects such as additional radiation of hard jets or gg contributions. We compare ALPGEN and MC@NLO MC $t\bar{t}$ samples with identical values of m_t^{gen} that both use HERWIG [37] for shower evolution and hadronization. HERWIG is used in both cases for consistency because MC@NLO can only be used with HERWIG (ALPGEN can be used with PYTHIA or HERWIG) and we are not interested in comparing different models for shower evolution and hadronization in this study. Ensemble studies are performed on both samples and the difference in the mean extracted m_t from ensembles for the two samples is found to be $m_t^{\text{MC@NLO}} - m_t^{\text{ALPGEN}} = 0.10 \pm 0.25 \text{ GeV}$. Here, as in all the other systematic sources described below, when a shift in the value of the estimated parameter is statisti-

Table IV. Summary of systematic uncertainties.

| Source | Uncertainty (GeV) |
|------------------------------------|-------------------|
| <i>Modeling of production:</i> | |
| <i>Modeling of signal:</i> | |
| Higher-order effects | ± 0.25 |
| ISR/FSR | ± 0.26 |
| Hadronization and UE | ± 0.58 |
| Color reconnection | ± 0.28 |
| Multiple $p\bar{p}$ interactions | ± 0.07 |
| Modeling of background | ± 0.16 |
| $W+jets$ heavy-flavor scale factor | ± 0.07 |
| Modeling of b jets | ± 0.09 |
| Choice of PDF | ± 0.24 |
| <i>Modeling of detector:</i> | |
| Residual jet energy scale | ± 0.21 |
| Data-MC jet response difference | ± 0.28 |
| b -tagging efficiency | ± 0.08 |
| Trigger efficiency | ± 0.01 |
| Lepton momentum scale | ± 0.17 |
| Jet energy resolution | ± 0.32 |
| Jet ID efficiency | ± 0.26 |
| <i>Method:</i> | |
| Multijet contamination | ± 0.14 |
| Signal fraction | ± 0.10 |
| MC calibration | ± 0.20 |
| Total | ± 1.02 |

cially dominated, we replace the shift with its statistical uncertainty for the estimate of uncertainty. We, therefore, assign an uncertainty of ± 0.25 GeV as the contribution from this source.

2. ISR/FSR

The uncertainties from this source are in the modeling of additional jets due to initial and final-state radiation (ISR/FSR). To evaluate this contribution, we compare three PYTHIA samples having identical values of m_t^{gen} , with input parameters taken from a CDF ISR/FSR study based on the Drell-Yan process [38]. The three sets of parameters correspond to a fit to data and ± 1 sd excursions. Half of the difference between the two excursions corresponds to a change in m_t of 0.26 ± 0.19 GeV.

3. Hadronization and Underlying Event

In simulating parton evolution and hadronization, PYTHIA and HERWIG model the parton showering, hadronization, and underlying event (UE) differently. To estimate the impact of this difference, we compare

two MC $t\bar{t}$ samples with identical values of m_t^{gen} , using ALPGEN for the hard-scattering process, but one sample using PYTHIA and the other using HERWIG for parton showering and hadronization. Ensemble studies indicate a difference in the means of the extracted m_t to be $m_t^{\text{PYTHIA}} - m_t^{\text{HERWIG}} = 0.58 \pm 0.25$ GeV.

4. Color Reconnection

The MC samples used in this analysis do not simulate color reconnection for the final-state particles [39]. To evaluate the possible effect of color reconnection on the determination of m_t , we compare two MC $t\bar{t}$ samples with identical values of m_t^{gen} , using PYTHIA 6.4 tunes Apro and ACRpro, which are identical except for the inclusion of color reconnection in ACRpro. Ensemble studies of $t\bar{t}$ events performed on both samples yield a difference in the means of the extracted m_t of $m_t^{\text{Apro}} - m_t^{\text{ACRpro}} = 0.26 \pm 0.28$ GeV. We take the uncertainty on this difference and assign ± 0.28 GeV as the contribution from this source.

5. Modeling of Jet Mass

Unlike the jet algorithm used in Run I of Tevatron, the iterative midpoint cone algorithm used for Run II defines jets of intrinsic mass [21]. The effect of inaccuracies in the simulation of jet masses on the top-quark mass measurement is found to be negligible and is presently ignored.

6. Multiple $p\bar{p}$ Interactions

Effects from additional $p\bar{p}$ interactions are simulated by overlaying on MC events unbiased triggers from random $p\bar{p}$ crossings. These overlaid events are then reweighted according to the number of interaction vertices to assure that the simulation reflects the instantaneous luminosity profile of the data. To evaluate the contribution from the uncertainty associated with the reweighting procedure, we repeat the ensemble studies used to derive the m_t calibration, but without the reweighting. The rederived calibration is applied to $L(\tilde{x}; m_t)$ for the selected data sample, m_t is extracted and compared with the value from the default calibration, and found to shift by -0.07 GeV. This extreme check of the size of this contribution to the uncertainty shows that our result is not affected significantly by variations in luminosity.

7. Modeling of Background

This systematic uncertainty receives contributions from two sources, one based on the data-MC discrepancy in background-dominated distributions, and a second from uncertainty in the renormalization scale used to generate the $W+jets$ samples. For the first source, we

identify distributions in which there is poor agreement between data and MC in the modeling of background. Specifically, in both channels, we examine lepton p_T and the η of the jet of lowest p_T in the 3-jet multiplicity bin. Ensemble studies are performed on a sample of MC $t\bar{t}$ events using background events reweighted to match the distributions in data. The mean of the extracted m_t for this sample is found to shift by -0.03 GeV relative to that of the same MC $t\bar{t}$ events using the default background events.

The W +jets MC samples used in this analysis (Sec. IV) are generated using identical renormalization and factorization scales of $\mu = M_W^2 + \sum p_T^2$ where the sum is over the jets in an event. To evaluate the effect of the uncertainty in this scale, we generate two more W +jets MC samples with modified renormalization and factorization scales of $\mu/2$ and 2μ . We perform ensemble studies on a $t\bar{t}$ MC sample using these modified W +jets samples, and find that the means of the extracted m_t shift by 0.13 GeV ($\mu/2$) and 0.32 GeV (2μ) relative to the studies using the default W +jets sample. We take half of the larger excursion and assign ± 0.16 GeV as the contribution from this source.

The contributions from the above data-MC discrepancy for the background and from the uncertainty on the scales are combined in quadrature for a total of systematic uncertainty of ± 0.16 GeV.

8. W +jets Heavy-Flavor Scale Factor

The default heavy-flavor content in LO ALPGEN MC W +jets (Sec. IV) is increased by a factor of 1.47 for the $Wc\bar{c}$ +jets and $Wb\bar{b}$ +jets contributions to achieve agreement with NLO calculations of cross sections that include NLL corrections based on the MCFM MC generator [26]. To evaluate the uncertainty from this source, we shift this factor up to 1.97 and down to 0.97 and, for each variation, repeat the ensemble studies described in Sec. VI for the calibration of m_t , apply this to $L(\tilde{x}; m_t)$ in data, and re-extract m_t . The shifts in m_t relative to the default value are found to be -0.07 GeV and 0.02 GeV when the scale factors are shifted up and down, respectively. We assign ± 0.07 GeV as the contribution from this source to the uncertainty of m_t .

9. Modeling of b jets

Possible effects in modeling b -quark fragmentation are studied by reweighting the simulated $t\bar{t}$ events used in the calibration of the measurement to simulate other choices of b -quark fragmentation models for the b jets. All the default MC samples used in this analysis consist of events that are reweighted from the default PYTHIA b -quark fragmentation function (based on the Bowler model [40]) to a Bowler scheme with parameters tuned to data collected at the LEP e^+e^- collider [41]. To evaluate the

systematic uncertainty, these events are reweighted again to account for differences between LEP and SLAC e^+e^- data [41]. The ensemble studies of m_t are repeated using these reweighted events, the new calibration applied to $L(\tilde{x}; m_t)$ for data, and m_t extracted. m_t is found to shift by 0.08 GeV relative to the default value.

Additional differences in the response of b jets can be expected in the presence of semileptonic decays of b or c -quarks. The incorrect simulation of semileptonic b and c -quark decay branching fractions can therefore lead to a systematic shift in the extracted value of m_t . We take an uncertainty of ± 0.05 GeV determined in Ref. [42] as the contribution from this source.

Combining the two above uncertainties in quadrature gives ± 0.09 GeV, which we assign as the systematic uncertainty for the modeling of b jets.

10. Choice of PDF

We evaluate this systematic uncertainty using a PYTHIA MC $t\bar{t}$ sample that is reweighted to match possible excursions in the PDF parameters represented by the 20 CTEQ6M uncertainty PDFs [27]. Ensemble studies are repeated for each of these variants for only $t\bar{t}$ events, and the uncertainty evaluated using the following formula [27]:

$$\delta m_t^{\text{PDF}} = \frac{1}{2} \left(\sum_{i=1}^{20} [\Delta M(S_i^+) - \Delta M(S_i^-)]^2 \right)^{1/2} \quad (23)$$

where the sum runs over PDF excursions in the positive (S_i^+) and negative (S_i^-) directions. δm_t^{PDF} is found to be 0.24 GeV.

B. Modeling of Detector

1. Residual JES Uncertainty

The *in situ* jet energy calibration employed in this analysis addresses a possible global scale difference in JES between data and MC. Any other discrepancy, such as a dependence on p_T and η , can have a systematic effect on the determination of m_t . To estimate this, the fractional uncertainty associated with the standard jet energy correction, derived using the γ +jet and dijet samples, is parameterized as a function of p_T and η . This uncertainty includes statistical and systematic contributions from both data and MC added in quadrature. All jet energies in a $t\bar{t}$ MC sample are then scaled up by the parameterized uncertainty as a function of p_T and η . The parameters are then shifted in such a way that the average scale shift applied to all jets vanishes. Ensemble studies are performed on the default and scaled samples, and the extracted m_t found to shift by 0.21 GeV relative to the default sample.

2. Data-MC Jet Response Difference

The uncertainties in the flavor-dependent jet response correction for MC events (described in Sec. VII), used to bring the simulation of calorimeter response into agreement with that observed in the data, are associated with uncertainties in single-particle responses in data and MC. To evaluate the effect of these uncertainties on the value of m_t , we change the correction factors by ± 1 sd and apply them to the light jets and b jets in a $t\bar{t}$ MC sample. The value of m_t is extracted and the mean is found to shift by ± 0.28 GeV relative to the sample corrected using the central values.

3. b -Tagging Efficiency

Discrepancies in the b -tagging efficiency between data and MC can lead to a systematic shift in the extracted m_t . To evaluate the effect of possible discrepancies, the tag rate functions for b and c quarks and the mistag rate function for light quarks are changed by 5% [23] and 20%, respectively, corresponding to the uncertainties on these functions. Ensemble studies for all $t\bar{t}$ MC samples are then repeated and the m_t calibration rederived and applied to data to extract m_t . The result is compared with that from the default calibration and found to shift by -0.08 GeV.

4. Trigger Efficiency

The MC events used in this analysis have associated weights to simulate the effect of trigger efficiencies. To evaluate the effect of the uncertainties in these weights on the top-quark mass, we repeat the ensemble studies on all $t\bar{t}$ MC samples with the weights set to unity, rederive the m_t calibration, and apply it to the data to extract m_t . The result is found to shift by -0.01 GeV.

5. Lepton Momentum Scale

A relative difference in the lepton momentum scale between data and MC can have a systematic effect on m_t . To evaluate this, we first determine the size of the discrepancy and correct the scale of one $t\bar{t}$ MC sample. Ensemble studies are repeated on the corrected sample and the mean of the extracted m_t is found to shift by 0.17 GeV relative to the default sample.

6. Jet Energy Resolution

Since the jet transfer functions used are derived from MC samples, improper simulation of jet energy resolution can result in a bias in the extracted m_t . To evaluate a

possible bias, ensemble studies are performed using a $t\bar{t}$ MC sample with jet energy resolutions degraded by 1 sd. The mean of the extracted m_t in this sample is found to shift by 0.32 GeV [44].

7. Jet ID Efficiency

The uncertainties associated with the scale factors used to achieve data-MC agreement in jet ID efficiencies are propagated to the measurement of m_t by decreasing the jet ID efficiencies in a $t\bar{t}$ MC sample according to these uncertainties. We can only simulate a decrease and not an increase, as reconstructed jets can be dropped but not created. Ensemble studies indicate that the mean of the extracted m_t shifts by 0.26 GeV relative to that of the default sample [44, 45].

C. Method

1. Multijet Contamination

The multijet background is not included in the ensemble studies used to derive the calibrations described in Sec. VI as we have assumed that $P_{\text{bkg}} \gg P_{\text{sig}}$ for such events (see Sec. V A), resulting in a negligible influence on the determination of m_t . To evaluate possible systematic effects due to this assumption, we select a multijet-enriched sample of events from data by inverting the lepton isolation criterion in the event selections. We repeat the ensemble studies to derive the m_t calibration using the multijet-enriched sample in the sample composition. The rederived calibration is applied to data and the extracted m_t is found to shift by 0.14 GeV relative to the default calibration [45].

2. Signal Fraction

The signal fractions determined from data and used in the ensemble studies have associated statistical uncertainties. These signal fractions are varied by their uncertainties, independently for each decay channel, and the ensemble studies repeated for all MC samples to rederive the m_t calibration shown in Fig. 4(a). The new calibrations are then applied to the data and results compared with those obtained using the default calibration. The resulting uncertainties in m_t evaluated by changing the signal fractions in each decay channel are then added in quadrature and divided by two to obtain a total of ± 0.10 GeV.

3. MC Calibration

We estimate the effect of the statistical uncertainties associated with the offset and slope parameters deter-

mined from the fit to the response plot shown in Fig. 4(a). To estimate this uncertainty, we change these two parameters, one at a time, by their uncertainties, and apply the modified calibration to the data to extract m_t , and calculate the difference relative to the m_t extracted using the default calibration. We combine, in quadrature, the differences in m_t resulting from such changes in each parameter, and find an uncertainty of ± 0.20 GeV.

D. Treatment of Systematic Uncertainties in Previous Analysis

To facilitate the combination of the new measurement with the previous one, we have updated the systematic uncertainties presented in Table I of Ref. [8]. All of the uncertainties in this table are unchanged, except for the uncertainties in the modeling of signal and the relative b /light-quark response ratio. The uncertainty for the modeling of signal in the previous analysis is replaced with one from the current analysis, which includes contributions from uncertainties in the modeling of higher-order effects, ISR/FSR, hadronization and underlying event, color reconnection, and multiple hadron interactions. The uncertainty on b /light-quark response is replaced with that associated with differences in jet response in data and MC for the current analysis (see also Sec. VII). The uncertainty in the modeling of background in Table I of Ref. [8] is the sum in quadrature of (i) the uncertainty in the heavy-flavor scale factor, and (ii) the uncertainty associated with discrepancies between data and MC background distributions. Since the uncertainty on the renormalization and factorization scale was not evaluated in the previous analysis, we include the additional contribution described in the second part of Sec. IX A 7. We also evaluate the uncertainty associated with the flavor-dependent jet-response correction factors appropriate for the previous analysis, using the procedure described in Sec. IX B 2. We find the mean of the extracted m_t shifts by 0.13 GeV (-0.22 GeV) relative to the sample corrected with the central values when we change the correction factors by 1 sd (-1 sd). We assign ± 0.22 GeV as the contribution from this source. Adding the contributions from all sources in quadrature gives a total of ± 0.97 GeV.

X. RESULT OF THE CURRENT MEASUREMENT

We measure the mass of the top quark in $t\bar{t}$ lepton+jets events using a matrix element method that combines an

in situ jet energy calibration with additional information from the standard jet energy scale derived from γ +jet and dijets samples. Using data corresponding to 2.6 fb^{-1} of integrated luminosity collected by the D0 experiment from Run II of the Tevatron collider, we extract the value:

$$m_t = 176.01 \pm 1.01(\text{stat}) \pm 0.79(\text{JES}) \pm 1.02(\text{syst}) \text{ GeV}, \text{ or } m_t = 176.01 \pm 1.64 \text{ GeV}.$$

XI. COMBINATION WITH THE PREVIOUS MEASUREMENT

Our result from a previous measurement using the same analysis technique, and based on earlier data corresponding to 1 fb^{-1} of integrated luminosity, is $m_t = 171.5 \pm 1.76(\text{stat} + \text{JES}) \pm 1.1(\text{syst}) \text{ GeV}$ [8]. Applying the shift of $\Delta m_t = 1.28$ GeV described in Sec. VII, and using updated systematic uncertainties described in Sec. IX D, yields

$$m_t = 172.74 \pm 1.44(\text{stat}) \pm 1.05(\text{JES}) \pm 0.97(\text{syst}) \text{ GeV},$$

$$\text{or } m_t = 172.74 \pm 2.03 \text{ GeV}.$$

We combine the two measurements using the BLUE method [46, 47] to get a result equivalent to 3.6 fb^{-1} of integrated luminosity. The combined value of the mass is

$$m_t = 174.94 \pm 0.83(\text{stat}) \pm 0.78(\text{JES}) \pm 0.96(\text{syst}) \text{ GeV},$$

or $m_t = 174.94 \pm 1.49$ GeV. The procedure we follow uses the same method and classes of uncertainty as used by the Tevatron Electroweak Working Group [5] in combining individual measurements for Tevatron averages of the top-quark mass.

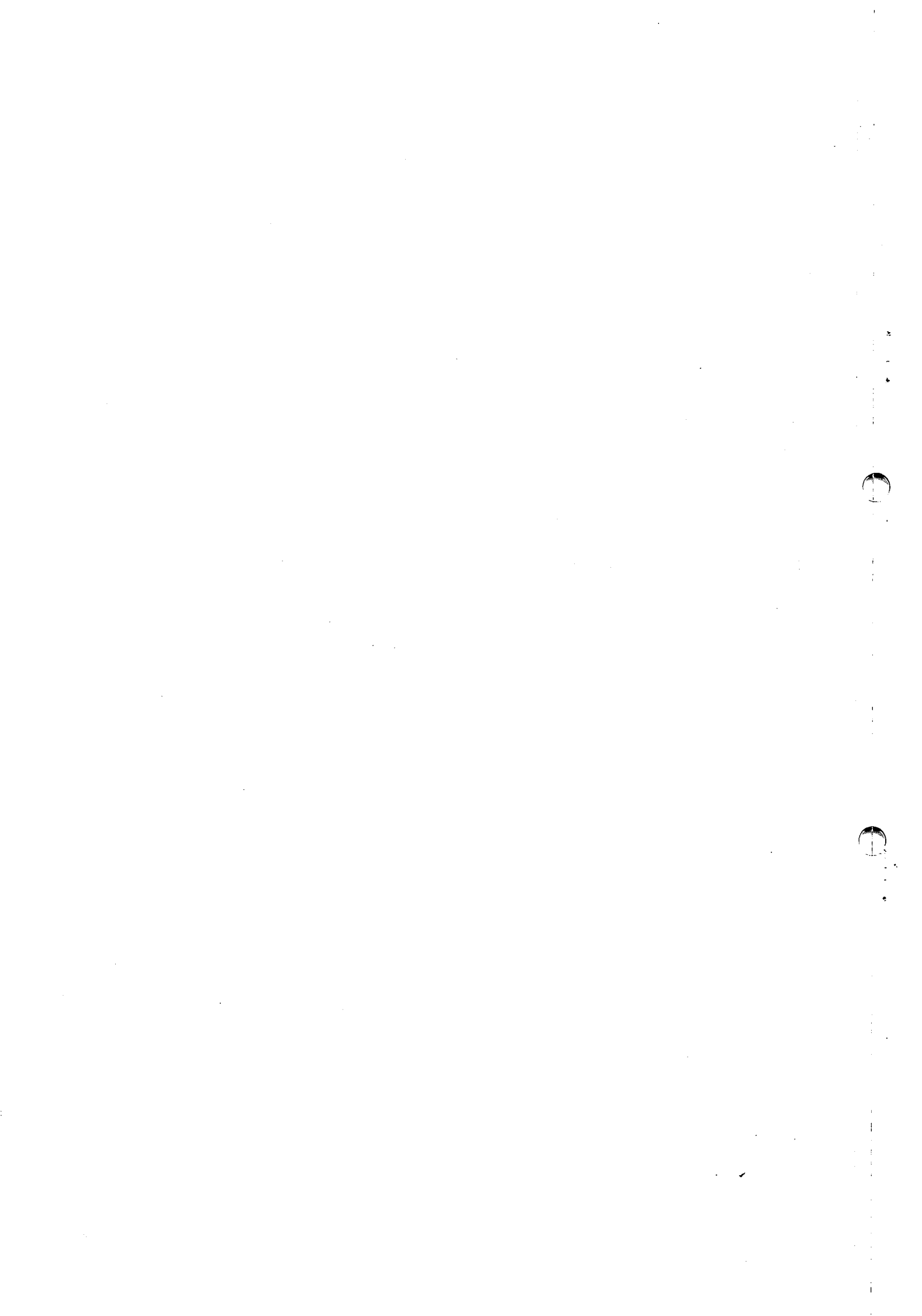
ACKNOWLEDGEMENTS

We thank the staffs at Fermilab and collaborating institutions, and acknowledge support from the DOE and NSF (USA); CEA and CNRS/IN2P3 (France); FASI, Rosatom and RFBR (Russia); CNPq, FAPERJ, FAPESP and FUNDUNESP (Brazil); DAE and DST (India); Colciencias (Colombia); CONACyT (Mexico); KRF and KOSEF (Korea); CONICET and UBACyT (Argentina); FOM (The Netherlands); STFC and the Royal Society (United Kingdom); MSMT and GACR (Czech Republic); CRC Program and NSERC (Canada); BMBF and DFG (Germany); SFI (Ireland); The Swedish Research Council (Sweden); and CAS and CNSF (China).

[1] S. Abachi *et al.* (D0 Collaboration), Phys. Rev. Lett. **74**, 2632 (1995).

[2] F. Abe *et al.* (CDF Collaboration), Phys. Rev. Lett. **74**, 2626 (1995).

- [3] The ALEPH, CDF, D0, DELPHI, L3, OPAL, SLC Collaborations, the LEP Electroweak Working Group, the Tevatron Electroweak Working Group, and the SLD electroweak and heavy flavour groups, arXiv:hep-ex/1012.2367v2, (2011); LEP Electroweak Working Group, <http://lepewwg.web.cern.ch/LEPEWWG/>.
- [4] S. Heinemeyer *et al.*, J. High Energy Phys. **09**, 075 (2003).
- [5] The Tevatron Electroweak Working Group, arXiv:hep-ex/1007.3178v1, (2010); Tevatron Electroweak Working Group, <http://tevewwg.fnal.gov>.
- [6] Events with $W \rightarrow \tau\nu$ decays can pass our selection criteria when the τ decays leptonically. This is accounted for by including the simulation of $W \rightarrow \tau\nu$ decays in the MC samples used to calibrate the measurement.
- [7] In the SM, the top-quark decays via $t \rightarrow Wb$ 100% of the time.
- [8] V. M. Abazov *et al.* (D0 Collaboration), Phys. Rev. Lett. **101**, 182001 (2008).
- [9] K. Nakamura *et al.* (Particle Data Group), J. Phys. G **37**, 075021 (2010)
- [10] M. L. Mangano *et al.*, J. High Energy Phys. **07**, 001 (2003).
- [11] T. Sjöstrand *et al.*, Comp. Phys. Commun. **135**, 238 (2001); T. Sjöstrand, S. Mrenna, and P. Skands, J. High Energy Phys. **05**, 026 (2006).
- [12] A. Buckley *et al.*, arXiv:hep-ph/1101.2500, (2011).
- [13] V. M. Abazov *et al.*, arXiv:hep-ex/1104.2887, (2011).
- [14] V. M. Abazov *et al.* (D0 Collaboration), Nucl. Instrum. Methods Phys. Res. Sec. A **565**, 463 (2006).
- [15] S. N. Ahmed *et al.*, Nucl. Instrum. Methods Phys. Res. Sec. A **634**, 8 (2011).
- [16] The previous measurement in Ref. [8] is based on data corresponding to 1 fb^{-1} of integrated luminosity recorded before the installation of Layer 0 while the new measurement presented here is based on data corresponding to 2.6 fb^{-1} of integrated luminosity recorded after this installation.
- [17] R. Angstadt *et al.*, Nucl. Instrum. Methods Phys. Res. Sec. A **622**, 298 (2010).
- [18] V. M. Abazov *et al.*, Nucl. Instrum. Methods Phys. Res. Sec. A **552**, 372 (2005).
- [19] M. Abolins *et al.*, Nucl. Instrum. Methods Phys. Res. Sec. A **584**, 75 (2008).
- [20] The separation in $\eta - \phi$ space between objects a and b is defined as $\Delta\mathcal{R} = \sqrt{(\eta_a - \eta_b)^2 + (\phi_a - \phi_b)^2}$.
- [21] G. C. Blazey *et al.*, arXiv:hep-ex/0005012, (2000).
- [22] Particle jets are defined as the objects, consisting of stable final-state particles originating from the hard-scattering process or the underlying event, found by applying the jet reconstruction algorithm on these particles instead of the calorimeter cell towers.
- [23] V. M. Abazov *et al.* (D0 Collaboration), Nucl. Instrum. Meth. Res. Sec. A **620**, 490 (2010).
- [24] These values are valid for the specific settings of the NN b -tagging algorithm chosen in this analysis.
- [25] M. L. Mangano *et al.*, J. High Energy Phys. **01**, 013 (2007).
- [26] J. M. Campbell and R. K. Ellis, Nucl. Phys. Proc. Suppl. **205**, 10 (2010).
- [27] J. Pumpin *et al.*, J. High Energy Phys. **07**, 012 (2002).
- [28] CERN Application Software Group, CERN Program Library Long Writeup W5013, CERN, Geneva (1993).
- [29] V. M. Abazov *et al.* (D0 Collaboration), Nature **429**, 638 (2004).
- [30] The 24 independent variables are associated with the vector momenta of the two initial-state and six final-state particles, whose masses are assumed known. Ten constraints are imposed if the direction vectors of the lepton and four final-state quarks are known precisely. This leaves 14 variables involving the vector momenta of the two initial state particles and the ν and the magnitude of the momenta of the four quarks and the ℓ . Conservation of energy and momentum imposes four additional constraints, eliminating the longitudinal components of the two initial state particles and the transverse components of the ν , leaving ten variables. For reasons indicated subsequently in the text, we replace these ten variables with the magnitudes of the momenta of the ℓ and of one of the light q from the W boson, the four transverse components of the two initial-state partons, the masses of the two W bosons and of the top quarks.
- [31] F.A. Berends *et al.*, Nucl. Phys. B **357**, 32 (1991).
- [32] S. Koonin and D. Meredith, *Computational Physics* (Addison-Wesley Publishing Company, Reading, MA, 1990).
- [33] Soft muon tagging refers to the identification of b -jet candidates by searching within jets for the presence of relatively low momentum muons originating from semimuonic b decays.
- [34] V. M. Abazov *et al.* (D0 Collaboration), Phys. Rev. Lett. **103**, 141801 (2009).
- [35] We apply separate single-particle responses for the following particles: γ , e^\pm , μ^\pm , π^\pm , K^\pm , K_S^0 , K_L^0 , p/\bar{p} , n/\bar{n} , and $\Lambda^0/\bar{\Lambda}^0$.
- [36] S. Frixione and B. R. Webber, J. High Energy Phys. **06**, 029 (2002).
- [37] G. Corcella *et al.*, J. High Energy Phys. **01**, 010 (2001).
- [38] Private communication with CDF collaboration; A. Abulencia *et al.* (CDF Collaboration), Phys. Rev. D **73**, 032003 (2006).
- [39] D. Wicke and P. Z. Skands, Nuovo Cim. B **123**, S1 (2008) S1.
- [40] M. G. Bowler, Z. Phys C **11**, 169 (1981).
- [41] Y. Peters, K. Hamacher, and D. Wicke, Fermilab-TM-2425-E (2006).
- [42] V. M. Abazov *et al.* (D0 Collaboration), Phys. Rev. D **74**, 092005 (2006).
- [43] A. D. Martin *et al.*, Phys. Lett. B **531**, 216 (2002).
- [44] Although this is a Type I uncertainty described in the introduction of Sec. IX, we do not take half of this value as the change is only evaluated in one direction.
- [45] These systematic uncertainties are taken from Ref. [8].
- [46] L. Lyons, D. Gilbaut, and P. Clifford, Nucl. Instrum. Meth. Phys. Res. Sec. A **270**, 110 (1988)
- [47] A. Valassi, Nucl. Instrum. Meth. Phys. Res. Sec. A **500**, 391 (2003).





Determination of the pole and $\overline{\text{MS}}$ masses of the top quark from the $t\bar{t}$ cross section

- V.M. Abazov,³⁵ B. Abbott,⁷³ B.S. Acharya,²⁹ M. Adams,⁴⁹ T. Adams,⁴⁷ G.D. Alexeev,³⁵ G. Alkhazov,³⁹ A. Alton^a,⁶¹ G. Alverson,⁶⁰ G.A. Alves,² L.S. Ancu,³⁴ M. Aoki,⁴⁸ M. Arov,⁵⁸ A. Askew,⁴⁷ B. Åsman,⁴¹ O. Atramentov,⁶⁵ C. Avila,⁸ J. BackusMayes,⁸⁰ F. Badaud,¹³ L. Bagby,⁴⁸ B. Baldin,⁴⁸ D.V. Bandurin,⁴⁷ S. Banerjee,²⁹ E. Barberis,⁶⁰ P. Baringer,⁵⁶ J. Barreto,³ J.F. Bartlett,⁴⁸ U. Bassler,¹⁸ V. Bazterra,⁴⁹ S. Beale,⁶ A. Bean,⁵⁶ M. Begalli,³ M. Begel,⁷¹ C. Belanger-Champagne,⁴¹ L. Bellantoni,⁴⁸ S.B. Beri,²⁷ G. Bernardi,¹⁷ R. Bernhard,²² I. Bertram,⁴² M. Besançon,¹⁸ R. Beuselinck,⁴³ V.A. Bezzubov,³⁸ P.C. Bhat,⁴⁸ V. Bhatnagar,²⁷ G. Blazey,⁵⁰ S. Blessing,⁴⁷ K. Bloom,⁶⁴ A. Boehlein,⁴⁸ D. Boline,⁷⁰ E.E. Boos,³⁷ G. Borissov,⁴² T. Bose,⁵⁹ A. Brandt,⁷⁶ O. Brandt,²³ R. Brock,⁶² G. Brooijmans,⁶⁸ A. Bross,⁴⁸ D. Brown,¹⁷ J. Brown,¹⁷ X.B. Bu,⁴⁸ M. Buehler,⁷⁹ V. Buescher,²⁴ V. Bunichev,³⁷ S. Burdin^b,⁴² T.H. Burnett,⁸⁰ C.P. Buszello,⁴¹ B. Calpas,¹⁵ E. Camacho-Pérez,³² M.A. Carrasco-Lizarraga,⁵⁶ B.C.K. Casey,⁴⁸ H. Castilla-Valdez,³² S. Chakrabarti,⁷⁰ D. Chakraborty,⁵⁰ K.M. Chan,⁵⁴ A. Chandra,⁷⁸ G. Chen,⁵⁶ S. Chevalier-Théry,¹⁸ D.K. Cho,⁷⁵ S.W. Cho,³¹ S. Choi,³¹ B. Choudhary,²⁸ S. Cihangir,⁴⁸ D. Claes,⁶⁴ J. Clutter,⁵⁶ M. Cooke,⁴⁸ W.E. Cooper,⁴⁸ M. Corcoran,⁷⁸ F. Couderc,¹⁸ M.-C. Cousinou,¹⁵ A. Croc,¹⁸ D. Cutts,⁷⁵ A. Das,⁴⁵ G. Davies,⁴³ K. De,⁷⁶ S.J. de Jong,³⁴ E. De La Cruz-Burelo,³² F. Déliot,¹⁸ M. Demarteau,⁴⁸ R. Demina,⁶⁹ D. Denisov,⁴⁸ S.P. Denisov,³⁸ S. Desai,⁴⁸ C. Deterre,¹⁸ K. DeVaughan,⁶⁴ H.T. Diehl,⁴⁸ M. Diesburg,⁴⁸ A. Dominguez,⁶⁴ T. Dorland,⁸⁰ A. Dubey,²⁸ L.V. Dudko,³⁷ D. Duggan,⁶⁵ A. Duperrin,¹⁵ S. Dutt,²⁷ A. Dyshkant,⁵⁰ M. Eads,⁶⁴ D. Edmunds,⁶² J. Ellison,⁴⁶ V.D. Elvira,⁴⁸ Y. Enari,¹⁷ H. Evans,⁵² A. Evdokimov,⁷¹ V.N. Evdokimov,³⁸ G. Facini,⁶⁰ T. Ferbel,⁶⁹ F. Fiedler,²⁴ F. Filthaut,³⁴ W. Fisher,⁶² H.E. Fisk,⁴⁸ M. Fortner,⁵⁰ H. Fox,⁴² S. Fuess,⁴⁸ A. Garcia-Bellido,⁶⁹ V. Gavrilov,³⁶ P. Gay,¹³ W. Geng,^{15,62} D. Gerbaudo,⁶⁶ C.E. Gerber,⁴⁹ Y. Gershtein,⁶⁵ G. Ginther,^{48,69} G. Golovanov,³⁵ A. Goussiou,⁸⁰ P.D. Grannis,⁷⁰ S. Greder,¹⁹ H. Greenlee,⁴⁸ Z.D. Greenwood,⁵⁸ E.M. Gregores,⁴ G. Grenier,²⁰ Ph. Gris,¹³ J.-F. Grivaz,¹⁶ A. Grohsjean,¹⁸ S. Grünendahl,⁴⁸ M.W. Grünewald,³⁰ T. Guillemin,¹⁶ F. Guo,⁷⁰ G. Gutierrez,⁴⁸ P. Gutierrez,⁷³ A. Haas^c,⁶⁸ S. Hagopian,⁴⁷ J. Haley,⁶⁰ L. Han,⁷ K. Harder,⁴⁴ A. Harel,⁶⁹ J.M. Hauptman,⁵⁵ J. Hays,⁴³ T. Head,⁴⁴ T. Hebbeker,²¹ D. Hedin,⁵⁰ H. Hegab,⁷⁴ A.P. Heinson,⁴⁶ U. Heintz,⁷⁵ C. Hensel,²³ I. Heredia-De La Cruz,³² K. Herner,⁶¹ G. Hesketh^d,⁴⁴ M.D. Hildreth,⁵⁴ R. Hirosky,⁷⁹ T. Hoang,⁴⁷ J.D. Hobbs,⁷⁰ B. Hoeneisen,¹² M. Hohlfeld,²⁴ Z. Hubacek,^{10,18} N. Huske,¹⁷ V. Hynek,¹⁰ I. Iashvili,⁶⁷ R. Illingworth,⁴⁸ A.S. Ito,⁴⁸ S. Jabeen,⁷⁵ M. Jaffré,¹⁶ D. Jamin,¹⁵ A. Jayasinghe,⁷³ R. Jesik,⁴³ K. Johns,⁴⁵ M. Johnson,⁴⁸ D. Johnston,⁶⁴ A. Jonckheere,⁴⁸ P. Jonsson,⁴³ J. Joshi,²⁷ A.W. Jung,⁴⁸ A. Juste,⁴⁰ K. Kaadze,⁵⁷ E. Kajfasz,¹⁵ D. Karmanov,³⁷ P.A. Kasper,⁴⁸ I. Katsanos,⁶⁴ R. Kehoe,⁷⁷ S. Kermiche,¹⁵ N. Khalatyan,⁴⁸ A. Khanov,⁷⁴ A. Kharchilava,⁶⁷ Y.N. Kharzeev,³⁵ D. Khatidze,⁷⁵ M.H. Kirby,⁵¹ J.M. Kohli,²⁷ A.V. Kozelov,³⁸ J. Kraus,⁶² S. Kulikov,³⁸ A. Kumar,⁶⁷ A. Kupco,¹¹ T. Kurča,²⁰ V.A. Kuzmin,³⁷ J. Kvita,⁹ S. Lammers,⁵² G. Landsberg,⁷⁵ P. Lebrun,²⁰ H.S. Lee,³¹ S.W. Lee,⁵⁵ W.M. Lee,⁴⁸ J. Lelloouch,¹⁷ L. Li,⁴⁶ Q.Z. Li,⁴⁸ S.M. Lietti,⁵ J.K. Lim,³¹ D. Lincoln,⁴⁸ J. Linnemann,⁶² V.V. Lipaev,³⁸ R. Lipton,⁴⁸ Y. Liu,⁷ Z. Liu,⁶ A. Lobodenko,³⁹ M. Lokajicek,¹¹ R. Lopes de Sa,⁷⁰ H.J. Lubatti,⁸⁰ R. Luna-Garcia^e,³² A.L. Lyon,⁴⁸ A.K.A. Maciel,² D. Mackin,⁷⁸ R. Madar,¹⁸ R. Magaña-Villalba,³² S. Malik,⁶⁴ V.L. Malyshev,³⁵ Y. Maravin,⁵⁷ J. Martínez-Ortega,³² R. McCarthy,⁷⁰ C.L. McGivern,⁵⁶ M.M. Meijer,³⁴ A. Melnitchouk,⁶³ D. Menezes,⁵⁰ P.G. Mercadante,⁴ M. Merkin,³⁷ A. Meyer,²¹ J. Meyer,²³ F. Miconi,¹⁹ N.K. Mondal,²⁹ G.S. Muanza,¹⁵ M. Mulhearn,⁷⁹ E. Nagy,¹⁵ M. Naimuddin,²⁸ M. Narain,⁷⁵ R. Nayyar,²⁸ H.A. Neal,⁶¹ J.P. Negret,⁸ P. Neustroev,³⁹ S.F. Novaes,⁵ T. Nunnemann,²⁵ G. Obrant,³⁹ J. Orduna,⁷⁸ N. Osman,¹⁵ J. Osta,⁵⁴ G.J. Otero y Garzón,¹ M. Padilla,⁴⁶ A. Pal,⁷⁶ N. Parashar,⁵³ V. Parihar,⁷⁵ S.K. Park,³¹ J. Parsons,⁶⁸ R. Partridge^c,⁷⁵ N. Parua,⁵² A. Patwa,⁷¹ B. Penning,⁴⁸ M. Perfilov,³⁷ K. Peters,⁴⁴ Y. Peters,⁴⁴ K. Petridis,⁴⁴ G. Petrillo,⁶⁹ P. Pétroff,¹⁶ R. Piegaia,¹ J. Piper,⁶² M.-A. Pleier,⁷¹ P.L.M. Podesta-Lerma^f,³² V.M. Podstavkov,⁴⁸ P. Polozov,³⁶ A.V. Popov,³⁸ M. Prewitt,⁷⁸ D. Price,⁵² N. Prokopenko,³⁸ S. Protopopescu,⁷¹ J. Qian,⁶¹ A. Quadt,²³ B. Quinn,⁶³ M.S. Rangel,² K. Ranjan,²⁸ P.N. Ratoff,⁴² I. Razumov,³⁸ P. Renkel,⁷⁷ M. Rijssenbeek,⁷⁰ I. Ripp-Baudot,¹⁹ F. Rizatdinova,⁷⁴ M. Rominsky,⁴⁸ A. Ross,⁴² C. Royon,¹⁸ P. Rubinov,⁴⁸ R. Ruchti,⁵⁴ G. Safronov,³⁶ G. Sajot,¹⁴ P. Salcido,⁵⁰ A. Sánchez-Hernández,³² M.P. Sanders,²⁵ B. Sanghi,⁴⁸ A.S. Santos,⁵ G. Savage,⁴⁸ L. Sawyer,⁵⁸ T. Scanlon,⁴³ R.D. Schamberger,⁷⁰ Y. Scheglov,³⁹ H. Schellman,⁵¹ T. Schliephake,²⁶ S. Schlobohm,⁸⁰ C. Schwanenberger,⁴⁴ R. Schwienhorst,⁶² J. Sekaric,⁵⁶ H. Severini,⁷³ E. Shabalina,²³ V. Shary,¹⁸ A.A. Shchukin,³⁸ R.K. Shivpuri,²⁸ V. Simak,¹⁰ V. Sirotenko,⁴⁸ P. Skubic,⁷³ P. Slattery,⁶⁹ D. Smirnov,⁵⁴ K.J. Smith,⁶⁷ G.R. Snow,⁶⁴ J. Snow,⁷² S. Snyder,⁷¹ S. Söldner-Rembold,⁴⁴ L. Sonnenschein,²¹ K. Soustruznik,⁹ J. Stark,¹⁴ V. Stolin,³⁶ D.A. Stoyanova,³⁸

M. Strauss,⁷³ D. Strom,⁴⁹ L. Stutte,⁴⁸ L. Suter,⁴⁴ P. Svoisky,⁷³ M. Takahashi,⁴⁴ A. Tanasijczuk,¹ W. Taylor,⁶
M. Titov,¹⁸ V.V. Tokmenin,³⁵ Y.-T. Tsai,⁶⁹ D. Tsybychev,⁷⁰ B. Tuchming,¹⁸ C. Tully,⁶⁶ L. Uvarov,³⁹ S. Uvarov,³⁹
S. Uzunyan,⁵⁰ R. Van Kooten,⁵² W.M. van Leeuwen,³³ N. Varelas,⁴⁹ E.W. Varnes,⁴⁵ I.A. Vasilyev,³⁸ P. Verdier,²⁰
L.S. Vertogradov,³⁵ M. Verzocchi,⁴⁸ M. Vesterinen,⁴⁴ D. Vilanova,¹⁸ P. Vokac,¹⁰ H.D. Wahl,⁴⁷ M.H.L.S. Wang,⁶⁹
J. Warchol,⁵⁴ G. Watts,⁸⁰ M. Wayne,⁵⁴ M. Weber^g,⁴⁸ L. Welty-Rieger,⁵¹ A. White,⁷⁶ D. Wicke,²⁶
M.R.J. Williams,⁴² G.W. Wilson,⁵⁶ M. Wobisch,⁵⁸ D.R. Wood,⁶⁰ T.R. Wyatt,⁴⁴ Y. Xie,⁴⁸ C. Xu,⁶¹ S. Yacoob,⁵¹
R. Yamada,⁴⁸ W.-C. Yang,⁴⁴ T. Yasuda,⁴⁸ Y.A. Yatsunenko,³⁵ Z. Ye,⁴⁸ H. Yin,⁴⁸ K. Yip,⁷¹ S.W. Youn,⁴⁸
J. Yu,⁷⁶ S. Zelitch,⁷⁹ T. Zhao,⁸⁰ B. Zhou,⁶¹ J. Zhu,⁶¹ M. Zielinski,⁶⁹ D. Ziemska,⁵² and L. Zivkovic⁷⁵

(The D0 Collaboration*)

¹Universidad de Buenos Aires, Buenos Aires, Argentina

²LAFEX, Centro Brasileiro de Pesquisas Físicas, Rio de Janeiro, Brazil

³Universidade do Estado do Rio de Janeiro, Rio de Janeiro, Brazil

⁴Universidade Federal do ABC, Santo André, Brazil

⁵Instituto de Física Teórica, Universidade Estadual Paulista, São Paulo, Brazil

⁶Simon Fraser University, Vancouver, British Columbia, and York University, Toronto, Ontario, Canada

⁷University of Science and Technology of China, Hefei, People's Republic of China

⁸Universidad de los Andes, Bogotá, Colombia

⁹Charles University, Faculty of Mathematics and Physics,
Center for Particle Physics, Prague, Czech Republic

¹⁰Czech Technical University in Prague, Prague, Czech Republic

¹¹Center for Particle Physics, Institute of Physics,
Academy of Sciences of the Czech Republic, Prague, Czech Republic

¹²Universidad San Francisco de Quito, Quito, Ecuador

¹³LPC, Université Blaise Pascal, CNRS/IN2P3, Clermont, France

¹⁴LPSC, Université Joseph Fourier Grenoble 1, CNRS/IN2P3,
Institut National Polytechnique de Grenoble, Grenoble, France

¹⁵CPPM, Aix-Marseille Université, CNRS/IN2P3, Marseille, France

¹⁶LAL, Université Paris-Sud, CNRS/IN2P3, Orsay, France

¹⁷LPNHE, Universités Paris VI and VII, CNRS/IN2P3, Paris, France

¹⁸CEA, Irfu, SPP, Saclay, France

¹⁹IPHC, Université de Strasbourg, CNRS/IN2P3, Strasbourg, France

²⁰IPNL, Université Lyon 1, CNRS/IN2P3, Villeurbanne, France and Université de Lyon, Lyon, France

²¹III. Physikalisches Institut A, RWTH Aachen University, Aachen, Germany

²²Physikalisches Institut, Universität Freiburg, Freiburg, Germany

²³II. Physikalisches Institut, Georg-August-Universität Göttingen, Göttingen, Germany

²⁴Institut für Physik, Universität Mainz, Mainz, Germany

²⁵Ludwig-Maximilians-Universität München, München, Germany

²⁶Fachbereich Physik, Bergische Universität Wuppertal, Wuppertal, Germany

²⁷Panjab University, Chandigarh, India

²⁸Delhi University, Delhi, India

²⁹Tata Institute of Fundamental Research, Mumbai, India

³⁰University College Dublin, Dublin, Ireland

³¹Korea Detector Laboratory, Korea University, Seoul, Korea

³²CINVESTAV, Mexico City, Mexico

³³FOM-Institute NIKHEF and University of Amsterdam/NIKHEF, Amsterdam, The Netherlands

³⁴Radboud University Nijmegen/NIKHEF, Nijmegen, The Netherlands

³⁵Joint Institute for Nuclear Research, Dubna, Russia

³⁶Institute for Theoretical and Experimental Physics, Moscow, Russia

³⁷Moscow State University, Moscow, Russia

³⁸Institute for High Energy Physics, Protvino, Russia

³⁹Petersburg Nuclear Physics Institute, St. Petersburg, Russia

⁴⁰Institució Catalana de Recerca i Estudis Avançats (ICREA) and Institut de Física d'Altes Energies (IFAE), Barcelona, Spain

⁴¹Stockholm University, Stockholm and Uppsala University, Uppsala, Sweden

⁴²Lancaster University, Lancaster LA1 4YB, United Kingdom

⁴³Imperial College London, London SW7 2AZ, United Kingdom

⁴⁴The University of Manchester, Manchester M13 9PL, United Kingdom

⁴⁵University of Arizona, Tucson, Arizona 85721, USA

⁴⁶University of California Riverside, Riverside, California 92521, USA

⁴⁷Florida State University, Tallahassee, Florida 32306, USA

⁴⁸Fermi National Accelerator Laboratory, Batavia, Illinois 60510, USA

⁴⁹University of Illinois at Chicago, Chicago, Illinois 60607, USA

⁵⁰Northern Illinois University, DeKalb, Illinois 60115, USA

- ⁵¹*Northwestern University, Evanston, Illinois 60208, USA*
⁵²*Indiana University, Bloomington, Indiana 47405, USA*
⁵³*Purdue University Calumet, Hammond, Indiana 46323, USA*
⁵⁴*University of Notre Dame, Notre Dame, Indiana 46556, USA*
⁵⁵*Iowa State University, Ames, Iowa 50011, USA*
⁵⁶*University of Kansas, Lawrence, Kansas 66045, USA*
⁵⁷*Kansas State University, Manhattan, Kansas 66506, USA*
⁵⁸*Louisiana Tech University, Ruston, Louisiana 71272, USA*
⁵⁹*Boston University, Boston, Massachusetts 02215, USA*
⁶⁰*Northeastern University, Boston, Massachusetts 02115, USA*
⁶¹*University of Michigan, Ann Arbor, Michigan 48109, USA*
⁶²*Michigan State University, East Lansing, Michigan 48824, USA*
⁶³*University of Mississippi, University, Mississippi 38677, USA*
⁶⁴*University of Nebraska, Lincoln, Nebraska 68588, USA*
⁶⁵*Rutgers University, Piscataway, New Jersey 08855, USA*
⁶⁶*Princeton University, Princeton, New Jersey 08544, USA*
⁶⁷*State University of New York, Buffalo, New York 14260, USA*
⁶⁸*Columbia University, New York, New York 10027, USA*
⁶⁹*University of Rochester, Rochester, New York 14627, USA*
⁷⁰*State University of New York, Stony Brook, New York 11794, USA*
⁷¹*Brookhaven National Laboratory, Upton, New York 11973, USA*
⁷²*Langston University, Langston, Oklahoma 73050, USA*
⁷³*University of Oklahoma, Norman, Oklahoma 73019, USA*
⁷⁴*Oklahoma State University, Stillwater, Oklahoma 74078, USA*
⁷⁵*Brown University, Providence, Rhode Island 02912, USA*
⁷⁶*University of Texas, Arlington, Texas 76019, USA*
⁷⁷*Southern Methodist University, Dallas, Texas 75275, USA*
⁷⁸*Rice University, Houston, Texas 77005, USA*
⁷⁹*University of Virginia, Charlottesville, Virginia 22901, USA*
⁸⁰*University of Washington, Seattle, Washington 98195, USA*

(Dated: April 14, 2011)

We use higher-order quantum chromodynamics calculations to extract the mass of the top quark from the $t\bar{t}$ cross section measured in the lepton+jets channel in $p\bar{p}$ collisions at $\sqrt{s} = 1.96$ TeV using 5.3 fb^{-1} of integrated luminosity collected by the D0 experiment at the Fermilab Tevatron Collider. The extracted top quark pole mass and $\overline{\text{MS}}$ mass are compared to the current Tevatron average top quark mass obtained from direct measurements.

PACS numbers: 14.65.Ha, 12.38.Bx

The mass of the top quark (m_t) has been measured with a precision of 0.6%, and its current Tevatron average value is $m_t = 173.3 \pm 1.1$ GeV [1]. Beyond leading-order quantum chromodynamics (LO QCD), the mass of the top quark is a convention-dependent parameter. Therefore, it is important to know how to interpret this experimental result in terms of renormalization conventions [2] if the value is to be used as an input to higher-order QCD calculations or in fits of electroweak precision observables and the resulting indirect Higgs boson mass bounds [3]. The definition of mass in field theory can be divided into two categories [4]: (i) driven by long-distance behavior, which corresponds to the pole-mass scheme, and (ii)

driven by short-distance behavior, which, for example, is represented by the $\overline{\text{MS}}$ mass scheme. The difference between the masses in different schemes can be calculated as a perturbative series in α_s . However, the concept of the pole mass is ill-defined, since there is no pole in the quark propagator in a confining theory such as QCD [5].

There are two approaches to directly measure m_t from the reconstruction of the final states in decays of top-antitop ($t\bar{t}$) pairs. One is based on a comparison of Monte Carlo (MC) templates for different assumed values of m_t with distributions of kinematic quantities measured in data. In the second approach, m_t is extracted from the reconstruction of the final states in data using a calibration curve obtained from MC simulation. In both cases the quantity measured in data therefore corresponds to the top quark mass scheme used in the MC simulation, which we refer to as m_t^{MC} .

Current MC simulations are performed in LO QCD, and higher order effects are simulated through parton showers at modified leading logarithms (LL) level. In principle, it is not possible to establish a direct connec-

*with visitors from ^aAugustana College, Sioux Falls, SD, USA,

^bThe University of Liverpool, Liverpool, UK, ^cSLAC, Menlo Park, CA, USA, ^dUniversity College London, London, UK, ^eCentro de Investigacion en Computacion - IPN, Mexico City, Mexico,

^fECFM, Universidad Autonoma de Sinaloa, Culiacán, Mexico, and

^gUniversität Bern, Bern, Switzerland.

tion between m_t^{MC} and any other mass scheme, such as the pole or $\overline{\text{MS}}$ mass scheme, without calculating the parton showers to at least next-to-leading logarithms (NLL) accuracy. However, it has been argued that m_t^{MC} should be close to the pole mass [6, 7]. The relation between m_t^{MC} and the top quark pole mass (m_t^{pole}) or $\overline{\text{MS}}$ mass ($m_t^{\overline{\text{MS}}}$) is still under theoretical investigation. In calculations such as in Ref. [3] it is assumed that m_t^{MC} measured at the Tevatron is equal to m_t^{pole} .

In this Letter, we extract the pole mass at the scale of the pole mass, $m_t^{\text{pole}}(m_t^{\text{pole}})$, and the $\overline{\text{MS}}$ mass at the scale of the $\overline{\text{MS}}$ mass, $m_t^{\overline{\text{MS}}}(m_t^{\overline{\text{MS}}})$, comparing the measured inclusive $t\bar{t}$ production cross section $\sigma_{t\bar{t}}$ with fully inclusive calculations at higher-order QCD that involve an unambiguous definition of m_t and compare our results to m_t^{MC} . This extraction provides an important test of the mass scheme as applied in MC simulations and gives complementary information, with different sensitivity to theoretical and experimental uncertainties than the direct measurements of m_t^{MC} that rely on kinematic details of the mass reconstruction.

We use the measurement of $\sigma_{t\bar{t}}$ in the lepton+jets channel in $p\bar{p}$ collisions at $\sqrt{s} = 1.96$ TeV using 5.3 fb^{-1} of integrated luminosity collected by the D0 experiment [8]. We calculate likelihoods for $\sigma_{t\bar{t}}$ as a function of m_t , and use higher-order QCD predictions based on the pole-mass or the $\overline{\text{MS}}$ -mass conventions to extract m_t^{pole} or $m_t^{\overline{\text{MS}}}$, respectively.

The criteria applied to select the sample of $t\bar{t}$ candidates used in the cross section measurement introduce a dependence of the signal acceptance, and therefore of the measured value of $\sigma_{t\bar{t}}$, on the assumed value of m_t^{MC} . This dependence is studied using MC samples of $t\bar{t}$ events generated at different values of m_t^{MC} in intervals of at least 5 GeV and is found to be much weaker than the dependence of the theoretical calculation of $\sigma_{t\bar{t}}$ on m_t . The $t\bar{t}$ signal is simulated with the ALPGEN event generator [9], and parton evolution is simulated with PYTHIA [10]. Jet-parton matching is applied to avoid double-counting of partonic event configurations [11]. The resulting measurement of $\sigma_{t\bar{t}}$ can be described by

$$\begin{aligned} \sigma_{t\bar{t}}(m_t^{\text{MC}}) &= \frac{1}{(m_t^{\text{MC}})^4} [a + b(m_t^{\text{MC}} - m_0) \\ &\quad + c(m_t^{\text{MC}} - m_0)^2 + d(m_t^{\text{MC}} - m_0)^3], \end{aligned} \quad (1)$$

where $\sigma_{t\bar{t}}$ and m_t^{MC} are in pb and GeV, respectively, $m_0 = 170$ GeV, and a, b, c, d are free parameters. For the mass extraction, we consider the experimental $t\bar{t}$ cross section measured using the b -jet identification technique [8]. This $\sigma_{t\bar{t}}$ determination provides the weakest dependence on m_t^{MC} of the results presented in Ref. [8], which leads to a smaller uncertainty on the extracted m_t , and thereby reduces the ambiguity of whichever convention (here pole or $\overline{\text{MS}}$) best reflects m_t^{MC} . When using b -tagging, the data sample is split into events with 0, 1 or > 1 b -tagged jets, and the numbers of events in each of

the three categories, corrected for mass-dependent acceptance, yield the measurement of $\sigma_{t\bar{t}}$. The other methods used in Ref. [8] rely on additional topological information that introduces a stronger dependence of the measured $\sigma_{t\bar{t}}$ on m_t^{MC} . They are therefore not used in this analysis. The parameters derived from a fit of $\sigma_{t\bar{t}}$ to Eq. (1) are: $a = 6.95 \times 10^9 \text{ pb GeV}^4$, $b = 1.25 \times 10^8 \text{ pb GeV}^3$, $c = 1.16 \times 10^6 \text{ pb GeV}^2$, and $d = -2.55 \times 10^3 \text{ pb GeV}$. Possible fit shape changes due to the uncertainties on these parameters are small compared to the experimental uncertainties on the $\sigma_{t\bar{t}}$ measurement which are almost fully correlated between different m_t . For $m_t^{\text{MC}} = 172.5$ GeV, we measure $\sigma_{t\bar{t}} = 8.13^{+1.02}_{-0.90} \text{ pb}$ [8].

We compare the obtained parameterization to a pure next-to-leading-order (NLO) QCD [12] calculation, to a calculation including NLO QCD and all higher-order soft-gluon resummations in NLL [13], to a calculation including also all higher-order soft-gluon resummations in next-to-next-to-leading logarithms (NNLL) [14] and to two approximations of the next-to-next-to-leading-order (NNLO) QCD cross section that include next-to-next-to-leading logarithms (NNLL) relevant in NNLO QCD [15, 16]. The computations in Ref. [15] were obtained using the program documented in Ref. [17].

Following the method of Refs. [18, 19], we extract the most probable m_t values and their 68% C.L. bands for the pole-mass and $\overline{\text{MS}}$ -mass conventions by computing the most probable value of a normalized joint-likelihood function:

$$L(m_t) = \int f_{\text{exp}}(\sigma|m_t) [f_{\text{scale}}(\sigma|m_t) \otimes f_{\text{PDF}}(\sigma|m_t)] d\sigma. \quad (2)$$

The first term f_{exp} corresponds to a function for the measurement constructed from a Gaussian function with mean value given by Eq. (1) and with standard deviation (sd) equal to the total experimental uncertainty which is described in detail in Ref. [8]. The second term f_{scale} in Eq. (2) is a theoretical likelihood formed from the uncertainties on the renormalization and factorization scales of QCD, which are taken to be equal, and varied up and down by a factor of two from the default value. Within this range, f_{scale} is taken to be constant [12–16]. It is convoluted with a term that represents the uncertainty of parton density functions (PDFs), taken to be a Gaussian function, with rms equal to the uncertainty determined in Refs. [12–16]. Table I summarizes the theoretical predictions from different calculations for $m_t^{\text{pole}} = 175$ GeV used as an input to the likelihood fit.

In Refs. [12–16] $\sigma_{t\bar{t}}$ is calculated as a function of m_t^{pole} and, consequently, comparing the measured $\sigma_{t\bar{t}}(m_t^{\text{MC}})$ to these theoretical predictions provides a value of m_t^{pole} . Therefore, we extract m_t^{pole} (i) assuming that the definition of m_t^{MC} is equivalent to m_t^{pole} , and (ii) taking m_t^{MC} to be equal to $m_t^{\overline{\text{MS}}}$ to estimate the effect of interpreting m_t^{MC} as any other mass definition. For case (i), Fig. 1 shows the parameterization of the measured and the predicted $\sigma_{t\bar{t}}(m_t^{\text{pole}})$ [14–16]. The results for the de-

TABLE I: Theoretical predictions for $\sigma_{t\bar{t}}$ with uncertainties $\Delta\sigma$ due to scale dependence and PDFs at the Tevatron for $m_t^{\text{pole}}=175$ GeV from different theoretical calculations used as input to the mass extraction. Note that Refs. [12] and [13] use the CTEQ6.6 PDF set [20] while Refs. [14], [15], and [16] use the MSTW08 PDF set [21].

| Theoretical prediction | $\sigma_{t\bar{t}}$ (pb) | $\Delta\sigma_{\text{scale}}$ (pb) | $\Delta\sigma_{\text{PDF}}$ (pb) |
|------------------------|--------------------------|------------------------------------|----------------------------------|
| NLO [12] | 6.39 | +0.33 -0.70 | +0.35 -0.35 |
| NLO+NLL [13] | 6.61 | +0.26 -0.46 | +0.44 -0.34 |
| NLO+NNLL [14] | 5.93 | +0.18 -0.17 | +0.30 -0.22 |
| Approximate NNLO [15] | 6.71 | +0.28 -0.37 | +0.17 -0.12 |
| Approximate NNLO [16] | 6.66 | +0.11 -0.06 | +0.42 -0.35 |

TABLE II: Values of m_t^{pole} , with their 68% C.L. uncertainties, extracted for different predictions of $\sigma_{t\bar{t}}$. The results assume that $m_t^{\text{MC}} = m_t^{\text{pole}}$ (left column). The right column shows the change Δm_t^{pole} between these results if it is assumed that $m_t^{\text{MC}} = m_t^{\overline{\text{MS}}}$. The combined experimental and theoretical uncertainties are shown.

| Theoretical prediction | m_t^{pole} (GeV) | Δm_t^{pole} (GeV) |
|---------------------------------------|--|----------------------------------|
| MC mass assumption | | |
| $m_t^{\text{MC}} = m_t^{\text{pole}}$ | $m_t^{\text{MC}} = m_t^{\overline{\text{MS}}}$ | |
| NLO [12] | $164.8^{+5.7}_{-5.4}$ | -3.0 |
| NLO+NLL [13] | $166.5^{+5.5}_{-4.8}$ | -2.7 |
| NLO+NNLL [14] | $163.0^{+5.1}_{-4.6}$ | -3.3 |
| Approximate NNLO [15] | $167.5^{+5.2}_{-4.7}$ | -2.7 |
| Approximate NNLO [16] | $166.7^{+5.2}_{-4.5}$ | -2.8 |

termination of m_t^{pole} are given in Table II. In case (ii) the cross section predictions use the pole-mass convention, and the value of $m_t^{\text{MC}} = m_t^{\overline{\text{MS}}}$ is converted to m_t^{pole} using the relationship at the three-loop level [5, 22]:

$$m_t^{\text{pole}} = m_t^{\overline{\text{MS}}}(m_t^{\overline{\text{MS}}}) \left[1 + \frac{4}{3} \frac{\overline{\alpha}_s(m_t^{\overline{\text{MS}}})}{\pi} \right. \\ + (-1.0414N_L + 13.4434) \left(\frac{\overline{\alpha}_s(m_t^{\overline{\text{MS}}})}{\pi} \right)^2 \\ \left. + (0.6527N_L^2 - 26.655N_L + 190.595) \left(\frac{\overline{\alpha}_s(m_t^{\overline{\text{MS}}})}{\pi} \right)^3 \right], \quad (3)$$

where $\overline{\alpha}_s$ is the strong coupling in the $\overline{\text{MS}}$ scheme, and $N_L = 5$ is the number of light quark flavors. The strong coupling $\overline{\alpha}_s(m_t^{\text{pole}})$ is taken at the three-loop level from Ref. [23]. By iteratively rederiving the $\overline{\text{MS}}$ mass using Eq. (3) $\overline{\alpha}_s(m_t^{\text{pole}})$ is transformed into $\overline{\alpha}_s(m_t^{\overline{\text{MS}}})$ leading to a difference of only 0.1 GeV to the final extraction of $m_t^{\overline{\text{MS}}}$. For $m_t^{\text{pole}} = 173.3$ GeV, the $\overline{\text{MS}}$ mass $m_t^{\overline{\text{MS}}}(m_t^{\overline{\text{MS}}})$ is lower by 9.8 GeV. With this change of

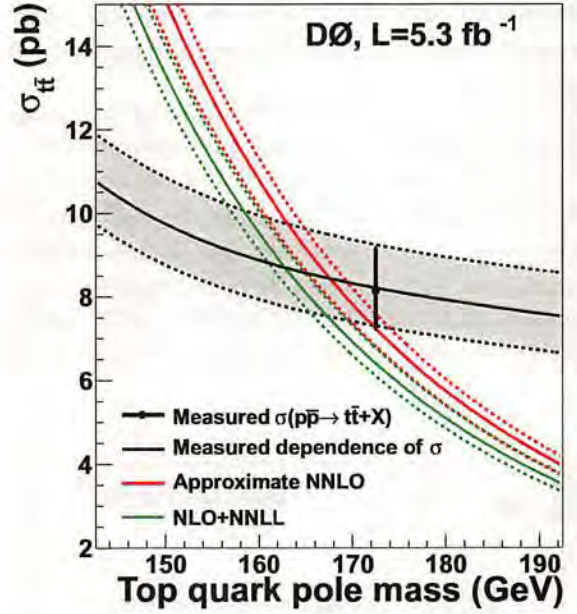


FIG. 1: (Color online) Measured $\sigma_{t\bar{t}}$ and theoretical NLO+NNLL [14] and approximate NNLO [15] calculations of $\sigma_{t\bar{t}}$ as a function of m_t^{pole} , assuming that $m_t^{\text{MC}} = m_t^{\text{pole}}$. The colored dashed lines represent the uncertainties for the two theoretical calculations from the choice of the PDF and the renormalization and factorization scales (added quadratically). The theoretical calculation of Ref. [16] (not displayed) agrees with Ref. [15] within 1% both in mean value and uncertainty. The point shows the measured $\sigma_{t\bar{t}}$ for $m_t^{\text{MC}} = 172.5$ GeV, the black curve is the fit to Eq. (1), and the gray band corresponds to the total experimental uncertainty.

the m_t^{MC} interpretation in Eq. (1), we form a new likelihood $f_{\text{exp}}(\sigma|m_t)$ and extract m_t^{pole} using Eq. (2). The difference Δm_t^{pole} between assuming $m_t^{\text{MC}} = m_t^{\text{pole}}$ and $m_t^{\text{MC}} = m_t^{\overline{\text{MS}}}$ is given in Table II. Given the uncertainties, interpreting m_t^{MC} as either m_t^{pole} or as $m_t^{\overline{\text{MS}}}$ has no significant bearing on the value of the extracted m_t . We include half of this difference symmetrically in the systematic uncertainties. As a result we extract $m_t^{\text{pole}} = 163.0^{+5.4}_{-4.9}$ GeV using the NLO+NNLL calculation of Ref. [14] and $m_t^{\text{pole}} = 167.5^{+5.4}_{-4.9}$ GeV using the approximate NNLO calculation of Ref. [15]. Our measurement of m_t^{pole} based on the approximate NNLO cross section calculation is consistent within 1 sd with the Tevatron measurement of m_t from direct reconstruction of top quark decay products, $m_t = 173.3 \pm 1.1$ GeV [1]. The result based on the NLO+NNLL calculation is consistent within 2 sd.

Calculations of the $t\bar{t}$ cross section [14, 15] have also

been performed as a function of $m_t^{\overline{\text{MS}}}$. Comparing the dependence of the measured $\sigma_{t\bar{t}}$ to theory as a function of m_t provides an estimate of $m_t^{\overline{\text{MS}}}$. We note that a previous extraction of $m_t^{\overline{\text{MS}}}$ [15] ignored the m_t dependence of the measured $\sigma_{t\bar{t}}$.

We extract the value of $m_t^{\overline{\text{MS}}}$, again, for two cases: (i) assuming that the definition of m_t implemented in the MC simulation is equal to m_t^{pole} , and (ii) assuming that m_t^{MC} corresponds to $m_t^{\overline{\text{MS}}}$. For case (i), m_t^{pole} must first be converted to $m_t^{\overline{\text{MS}}}$ using Eq. (3). Figure 2 shows the measured $\sigma_{t\bar{t}}$ as a function of $m_t^{\overline{\text{MS}}}$, together with the calculation that includes NLO+NNLL QCD resummation [14] and the approximate NNLO calculation [15].

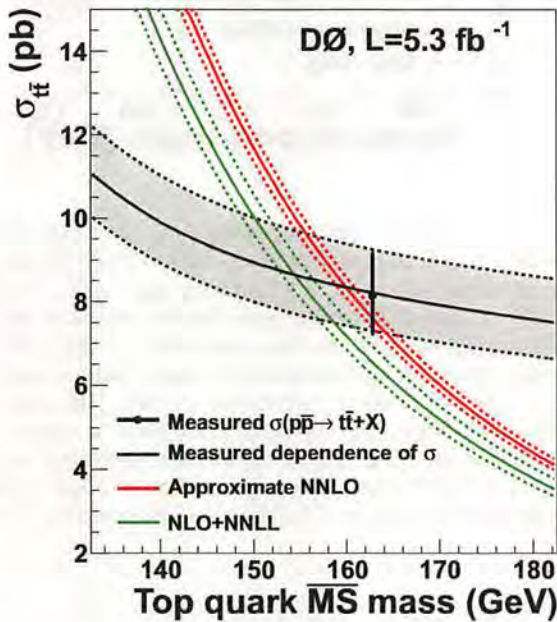


FIG. 2: (Color online) Measured $\sigma_{t\bar{t}}$ and theoretical NLO+NNLL [14] and approximate NNLO [15] calculations of $\sigma_{t\bar{t}}$ as a function of $m_t^{\overline{\text{MS}}}$, assuming that $m_t^{\text{MC}} = m_t^{\text{pole}}$. The colored dashed lines represent the uncertainties for the two theoretical calculations from the choice of the PDF and the renormalization and factorization scales (added quadratically). The point shows the measured $\sigma_{t\bar{t}}$ for $m_t^{\text{MC}} = 172.5$ GeV, the black curve is the fit to Eq. (1), and the gray band corresponds to the total experimental uncertainty.

The results for the extracted values of $m_t^{\overline{\text{MS}}}$ are given in Table III.

In case (ii), we assume that the mass definition in the MC simulation corresponds to the $\overline{\text{MS}}$ mass. We set $m_t^{\text{MC}} = m_t^{\overline{\text{MS}}}$ in Eq. (2), form a new likelihood $f_{\text{exp}}(\sigma | m_t)$ and extract $m_t^{\overline{\text{MS}}}$ using Eq. (2) for the two calculations of Fig. 2. The difference $\Delta m_t^{\overline{\text{MS}}}$ between assuming that $m_t^{\text{MC}} = m_t^{\text{pole}}$ and assuming $m_t^{\text{MC}} = m_t^{\overline{\text{MS}}}$ is given in

TABLE III: Values of $m_t^{\overline{\text{MS}}}$, with their 68% C.L. uncertainties, extracted for different theoretical predictions of $\sigma_{t\bar{t}}$. The results assume that m_t^{MC} corresponds to m_t^{pole} (left column). The right column shows the change $\Delta m_t^{\overline{\text{MS}}}$ between these results if it is assumed that $m_t^{\text{MC}} = m_t^{\overline{\text{MS}}}$. The combined experimental and theoretical uncertainties are shown.

| Theoretical prediction | $m_t^{\overline{\text{MS}}} \text{ (GeV)}$ | $\Delta m_t^{\overline{\text{MS}}} \text{ (GeV)}$ |
|------------------------|--|---|
| MC mass assumption | $m_t^{\text{MC}} = m_t^{\text{pole}}$ | $m_t^{\text{MC}} = m_t^{\overline{\text{MS}}}$ |
| NLO+NNLL [14] | $154.5^{+5.0}_{-4.3}$ | -2.9 |
| Approximate NNLO [15] | $160.0^{+4.8}_{-4.3}$ | -2.6 |

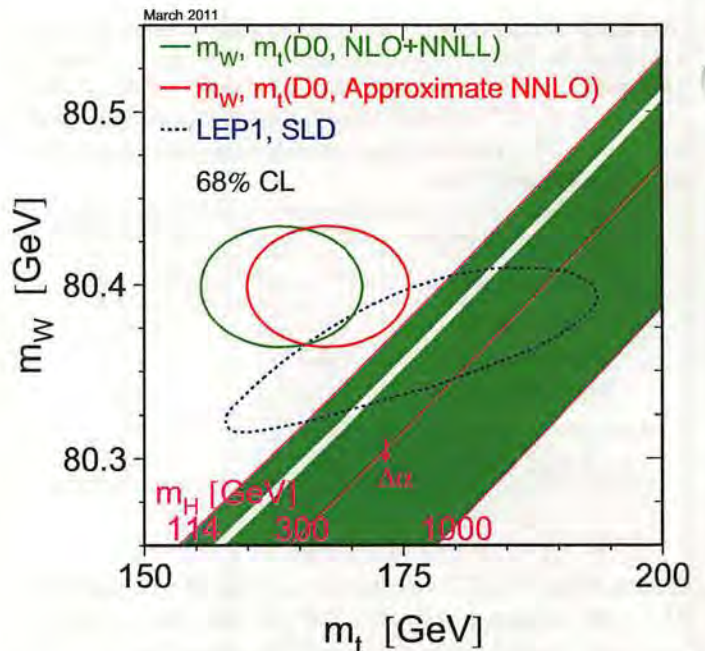


FIG. 3: (Color online) Constraints on the W boson mass from the LEP-II/Tevatron experiments and the top quark pole mass extracted from the $t\bar{t}$ cross section in NLO+NNLL [14] (green contour) and approximate NNLO [15] (red contour). This is compared to the indirect constraints on the W boson mass and the top quark mass based on LEP-I/SLD data (dashed contour). In both cases the 68% CL contours are given. Also shown is the SM relationship for the masses as a function of the Higgs mass in the region favoured by theory (< 1000 GeV) and not excluded by direct searches (114 GeV to 158 GeV and > 173 GeV). The arrow labelled $\Delta\alpha$ shows the variation of this relation if $\alpha(m_Z^2)$ is varied between -1 and +1 sd. This variation gives an additional uncertainty to the SM band shown in the figure.

Table III. We include half of this difference symmetrically in the systematic uncertainties and derive a value of $m_t^{\overline{\text{MS}}} = 154.5^{+5.2}_{-4.5} \text{ GeV}$ using the calculation of Ref. [14] and $m_t^{\overline{\text{MS}}} = 160.0^{+5.1}_{-4.5} \text{ GeV}$ using Ref. [15].

To summarize, we extract the pole mass (Table II) and the $\overline{\text{MS}}$ mass (Table III) for the top quark by comparing the measured $\sigma_{t\bar{t}}$ with different higher-order perturbative QCD calculations. The Tevatron direct measurements of m_t are consistent with both m_t^{pole} measurements within 2 sd, but they are different by more than 2 sd from the extracted $m_t^{\overline{\text{MS}}}$. The results on m_t^{pole} and their interplay with other electroweak results within the SM are displayed in Fig. 3, which is based on Ref. [3].

For the first time, $m_t^{\overline{\text{MS}}}$ is extracted with the m_t dependence of the measured $\sigma_{t\bar{t}}$ taken into account. Our measurements favor the interpretation that the Tevatron m_t measurements based on reconstructing top quark decay products is closer to the pole than to the $\overline{\text{MS}}$ top quark mass.

Acknowledgments

We wish to thank M. Cacciari, S. Moch, M. Neubert, M. Seymour, and P. Uwer for fruitful discussions regarding this analysis. We would also like to thank M. Cacciari, N. Kidonakis, and L. L. Yang for providing us with their latest theoretical computations.

We thank the staffs at Fermilab and collaborating institutions, and acknowledge support from the DOE and NSF (USA); CEA and CNRS/IN2P3 (France); FASI, Rosatom and RFBR (Russia); CNPq, FAPERJ, FAPESP and FUNDUNESP (Brazil); DAE and DST (India); Colciencias (Colombia); CONACyT (Mexico); KRF and KOSEF (Korea); CONICET and UBACyT (Argentina); FOM (The Netherlands); STFC and the Royal Society (United Kingdom); MSMT and GACR (Czech Republic); CRC Program and NSERC (Canada); BMBF and DFG (Germany); SFI (Ireland); The Swedish Research Council (Sweden); and CAS and CNSF (China).

-
- [1] CDF and D0 Collaborations, arXiv:1007.3178 [hep-ex].
 - [2] A. H. Hoang, A. Jain, I. Scimemi and I. W. Stewart, Phys. Rev. Lett. **101**, 151602 (2008).
 - [3] ALEPH, CDF, D0, DELPHI, L3, OPAL, and SLD Collaborations, LEP Electroweak Working Group, Tevatron Electroweak Working Group, SLD Electroweak Working Group, and SLD Heavy Flavour Group, arXiv:1012.2367 [hep-ex].
 - [4] A. H. Hoang and I. W. Stewart, Nucl. Phys. Proc. Suppl. **185**, 220 (2008); A. Buckley *et al.*, arXiv:1101.2599 [hep-ph].
 - [5] M. C. Smith and S. S. Willenbrock, Phys. Rev. Lett. **79**, 3825 (1997).
 - [6] S. Fleming, A. H. Hoang, S. Mantry and I. W. Stewart, Phys. Rev. D **77**, 074010 (2008).
 - [7] An estimate for the mass parameter that appears in parton shower algorithms can be obtained by speculating how an ideal all-order algorithm would work [4] using the approach developed in Ref. [6]. Comparing parton shower results with an all-order calculation, a relation between m_t^{pole} and m_t can be derived. Hence, the pole mass of the top quark could be about 1 GeV higher than m_t from direct Tevatron measurements.
 - [8] V. M. Abazov *et al.* [D0 Collaboration], arXiv:1101.0124 [hep-ex], submitted to Phys. Rev. D.
 - [9] M. L. Mangano, M. Moretti, F. Piccinini, R. Pittau, and A. D. Polosa, J. High Energy Phys. **0307**, 001 (2003).
 - [10] T. Sjostrand, S. Mrenna, and P. Z. Skands, J. High Energy Phys. **0605**, 026 (2006).
 - [11] M. L. Mangano, M. Moretti, F. Piccinini, and M. Treccani, J. High Energy Phys. **0701**, 013 (2007).
 - [12] P. M. Nadolsky *et al.*, Phys. Rev. D **78**, 013004 (2008); W. Beenakker, H. Kuijf, W. L. van Neerven and J. Smith, Phys. Rev. D **40**, 54 (1989).
 - [13] M. Cacciari, S. Frixione, M. L. Mangano, P. Nason, and G. Ridolfi, J. High Energy Phys. **0404**, 068 (2004).
 - [14] V. Ahrens, A. Ferroglio, M. Neubert, B. D. Pecjak, and L. L. Yang, J. High Energy Phys. **1009**, 097 (2010); V. Ahrens, A. Ferroglio, M. Neubert, B. D. Pecjak, and L. L. Yang, Nucl. Phys. Proc. Suppl. **205–206**, 48 (2010).
 - [15] S. Moch and P. Uwer, Phys. Rev. D **78**, 034003 (2008); U. Langenfeld, S. Moch, and P. Uwer, Phys. Rev. D **80**, 054009 (2009).
 - [16] N. Kidonakis and R. Vogt, Phys. Rev. D **68**, 114014 (2003); N. Kidonakis, Phys. Rev. D **82**, 114030 (2010).
 - [17] M. Aliev, H. Lacker, U. Langenfeld *et al.*, Comput. Phys. Commun. **182**, 1034 (2011).
 - [18] V. M. Abazov *et al.* [D0 Collaboration], Phys. Rev. Lett. **100**, 192004 (2008).
 - [19] V. M. Abazov *et al.* [D0 Collaboration], Phys. Lett. B **679**, 177 (2009).
 - [20] P. M. Nadolsky *et al.*, Phys. Rev. D **78**, 013004 (2008).
 - [21] A. D. Martin, W. J. Stirling, R. S. Thorne, and G. Watt, Eur. Phys. J. C **63**, 189 (2009).
 - [22] N. Gray, D. J. Broadhurst, W. Grafe, and K. Schilcher, Z. Phys. C **48**, 673 (1990); K. Melnikov and T. v. Ritbergen, Phys. Lett. B **482**, 99 (2000).
 - [23] S. Bethke, Eur. Phys. J. C **64**, 689 (2009).





Measurement of Top Quark and Anti-top quark mass difference in the Lepton+jets channel

The CDF Collaboration

URL <http://www-cdf.fnal.gov>

(Dated: June 7, 2010)

We report a measurement of the mass difference between top quark and anti-top quark (ΔM_{top}) in the Lepton+Jets channel using $p\bar{p}$ collisions at $\sqrt{s} = 1.96$ TeV from 5.6 fb^{-1} of data collected with the CDF detector at the Fermilab Tevatron. A top quark mass difference (Δm_{reco}) is reconstructed for every event by minimizing a χ^2 -like function to the overconstrained kinematics of the $t\bar{t}$ system with assumption of averaged top quark mass (M_{top}) equal to $172.5 \text{ GeV}/c^2$. To use more information of mass difference, we include a reconstructed mass difference from 2nd best χ^2 fit ($\Delta m_{reco}^{(2)}$). The values of Δm_{reco} and $\Delta m_{reco}^{(2)}$ for 2294 Lepton+Jets candidate events including both zero b -tagging and b -tagged events are compared to two-dimensional probability density function derived by applying kernel density estimation to fully simulated MC events with different values of the mass difference in the detector. We measure $\Delta M_{top} = -3.3 \pm 1.4 \text{ (stat.)} \pm 1.0 \text{ (syst.) } \text{GeV}/c^2$.

Preliminary Results of ΔM_{top} using 5.6 fb^{-1}

$$\mathcal{L}_k = \exp\left(-\frac{(n_b - n_b^0)^2}{2\sigma_{n_b}^2}\right) \times \prod_{i=1}^N \frac{n_s P_{sig}(\Delta m_{reco}, \Delta m_{reco}^{(2)}; \Delta M_{top}) + n_b P_{bg}(\Delta m_{reco}, \Delta m_{reco}^{(2)})}{n_s + n_b}. \quad (\text{VI.1})$$

The overall likelihood is a product over the six individual subsample likelihoods:

$$\mathcal{L} = \mathcal{L}_{0\text{-tag}}, (+) \text{ lepton} \times \mathcal{L}_{0\text{-tag}}, (-) \text{ lepton} \times \mathcal{L}_{1\text{-tag}}, (+) \text{ lepton} \times \mathcal{L}_{1\text{-tag}}, (-) \text{ lepton} \times \mathcal{L}_{2\text{-tag}}, (+) \text{ lepton} \times \mathcal{L}_{2\text{-tag}}, (-) \text{ lepton}. \quad (\text{VI.2})$$

The above gives values of $-\ln \mathcal{L}$ only for points in the ΔM_{top} grid corresponding to generated MC points, and not as

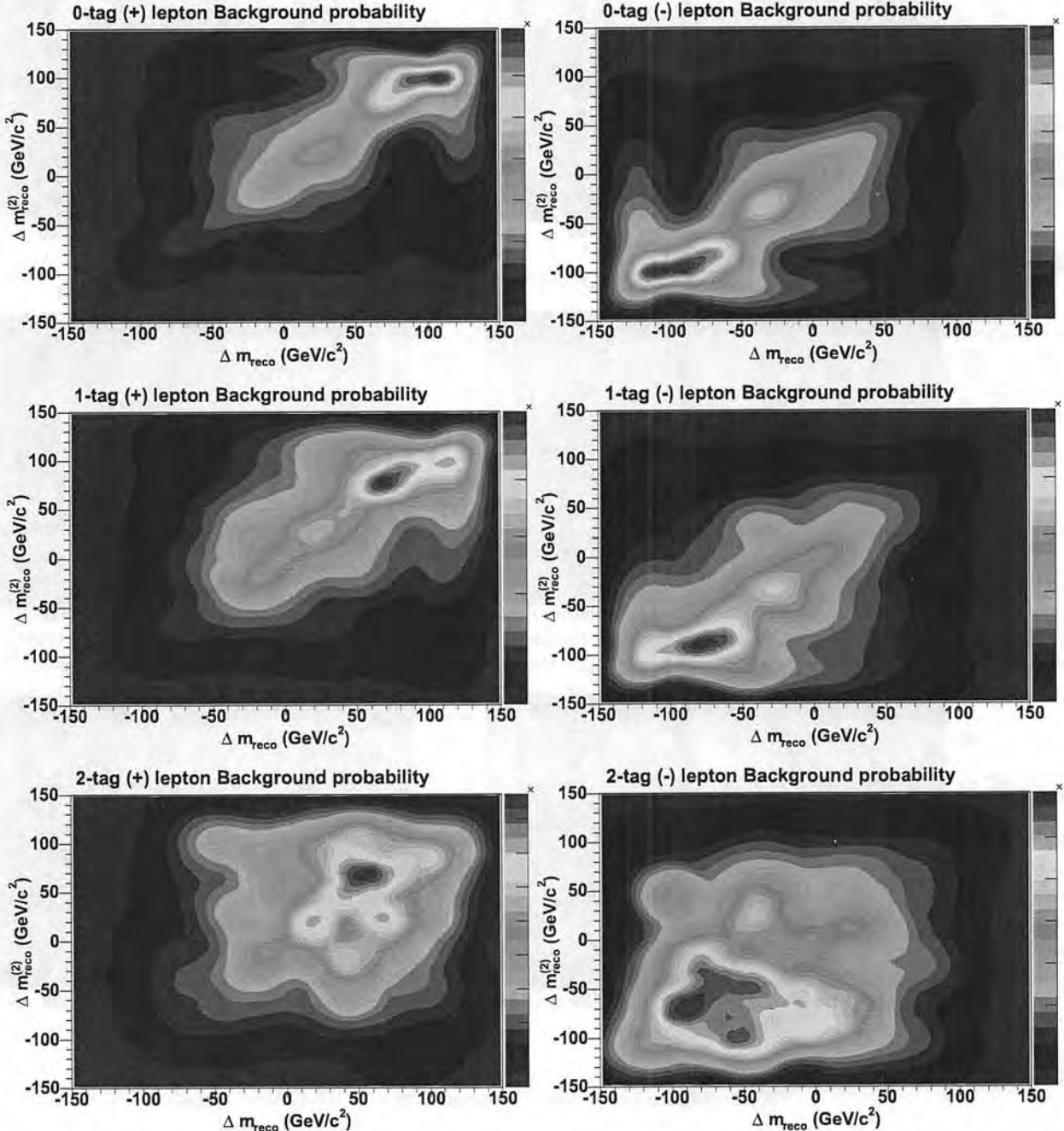


FIG. 2: 2d density estimates for backgrounds

a continuous function. To obtain density estimates for an arbitrary point in the ΔM_{top} grid, we use local polynomial smoothing [12] on a per-event basis. This allows for a smooth likelihood that can be minimized. The measured uncertainty on ΔM_{top} comes from the largest possible shift in ΔM_{top} on the $\Delta \ln \mathcal{L} = 0.5$.

VII. METHOD CHECK

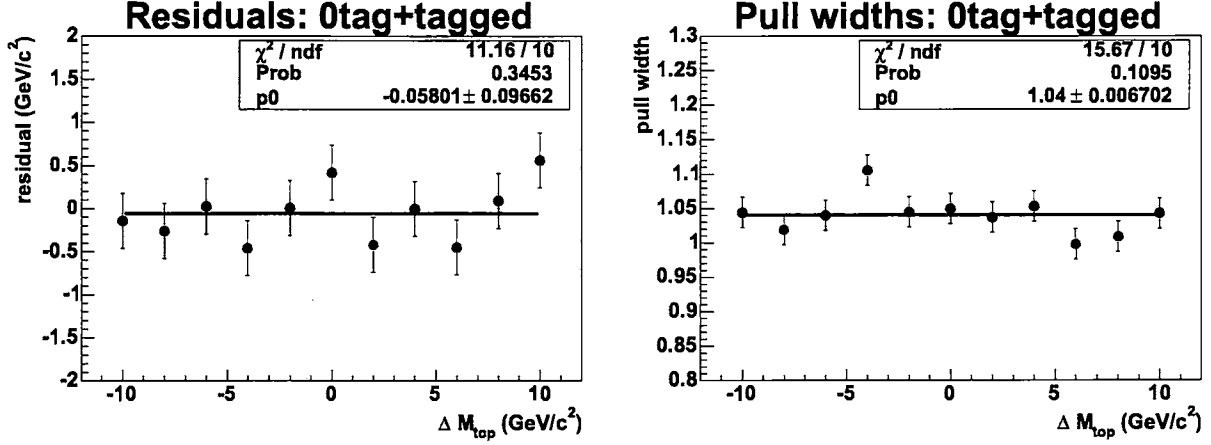


FIG. 3: Residual shift of mass difference (left) and pull widths (right) as a function of input ΔM_{top} from pseudoexperiments.

We test our machinery by running pseudoexperiments with varying values of ΔM_{top} from $-10 \text{ GeV}/c^2$ to $10 \text{ GeV}/c^2$. Figure 3 (left) shows the ΔM_{top} residuals as a function of true ΔM_{top} . We can see that there is no bias on our measurement. Right plot shows pull width of our measurement. We need to increase our measured uncertainty by 4.0% which is applied to all of systematic studies and data fits.

VIII. RESULTS

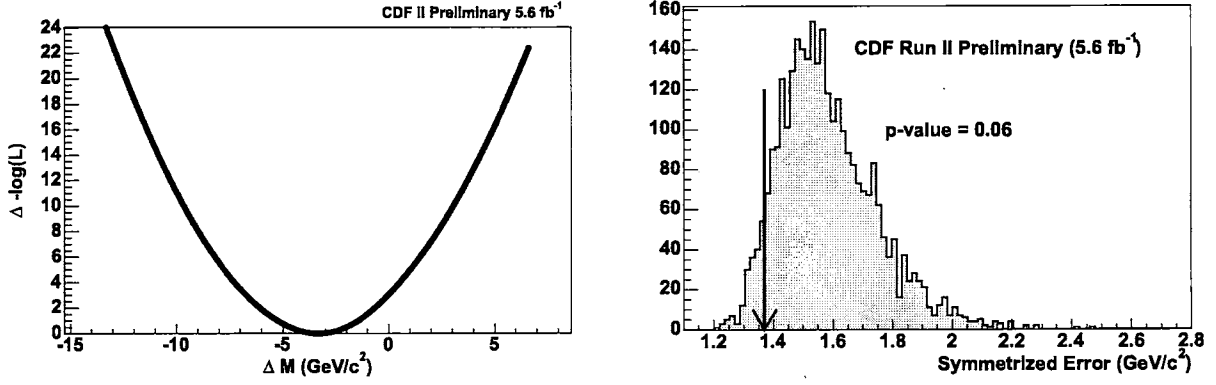


FIG. 4: (Left) Negative log-likelihood of data fit. (Right) P-value plot of measured uncertainty with expectation from pseudo-experiments.

The likelihood procedure when applied to the data yields $\Delta M_{\text{top}} = -3.3 \pm 1.4 \text{ GeV}/c^2$. The 1d $\Delta \text{log-likelihood}$ is shown in Figure 4 left. As shown in Figure 4 right, only 6% of pseudoexperiments have a smaller error than the value measured in data.

TABLE III: Summary of systematics. All numbers have units of GeV/c^2 .

| CDF II Preliminary 5.6 fb^{-1} | |
|--|-----------------------------|
| Systematic | Result (GeV/c^2) |
| Signal Modeling | 0.7 |
| JES | 0.2 |
| PDFs | 0.1 |
| b jet energy | 0.1 |
| b/\bar{b} asymmetry | 0.3 |
| Background shape | 0.2 |
| gg fraction | 0.1 |
| Radiation | 0.1 |
| MC statistics | 0.1 |
| Lepton energy | 0.1 |
| MHI | 0.4 |
| Color Reconnection | 0.2 |
| Total systematic | 1.0 |

IX. SYSTEMATIC UNCERTAINTIES

We examine a variety of effects that could systematically shift our measurement. Dominant systematic uncertainty is signal modeling. Comparing pseudoexperiments generated with MADGRAPH and PYTHIA gives an estimate of one part of the signal modeling. We also take different parton showering from HERWIG [18] compared with nominal PYTHIA parton showering as another part of signal modeling. We apply variations within uncertainties of Jet Energy Scale (JES) calibrations [19] in both signal and background pseudodata and measure resulting shifts in ΔM_{top} from pseudoexperiments, giving a JES uncertainty. We also vary the energy of b jets, which have different fragmentation than light quarks jets, as well as semi-leptonic decays and different color flow, resulting in a b -JES systematic. Effects due to uncertain modeling of radiation including initial-state radiation (ISR) and final-state radiation (FSR) are studied by extrapolating uncertainties in the p_T of Drell-Yan events to the $t\bar{t}$ mass region, resulting in a radiation systematics. A systematic on different parton distribution functions is obtained by varying the independent eigenvector of the CTEQ6M set, comparing parton distribution functions with different values of Λ_{QCD} , and comparing CTEQ5L with MRST72. We also test the effect of reweighting MC to increase the fraction of $t\bar{t}$ events initiated by gg (vs qq) from the 6% in the leading order MC to 20%. Systematics due to lepton energy scales are estimated by propagating 1% shifts on electron and muon energies scales. Background composition systematics are obtained by varying the fraction of the different types of backgrounds in pseudoexperiments and the normalization of total backgrounds. We also vary the uncertain Q^2 of background events in a background shape systematic. It has been suggested that color reconnection effects could cause a bias in the top quark mass measurement [20]. We account Color Reconnection [20] systematics by generating MCs with and without CR and taking the difference as systematics. Because we are measuring mass difference, we investigate possible systematics from different response of b quark and \bar{b} quark. We measure p_T balance of b and \bar{b} quarks using dijet sample by SECVTX b -tagging both jets with identifying the flavor using soft muon of leptonic decay of b . We measured p_T balance difference between MC and data and propagate to b/\bar{b} asymmetry systematics. We also investigate the effect of faking lepton charge by 1% added in lepton p_T systematics.

The total systematic error is $1.0 \text{ GeV}/c^2$. The systematics are summarized in Table III.

X. CONCLUSIONS

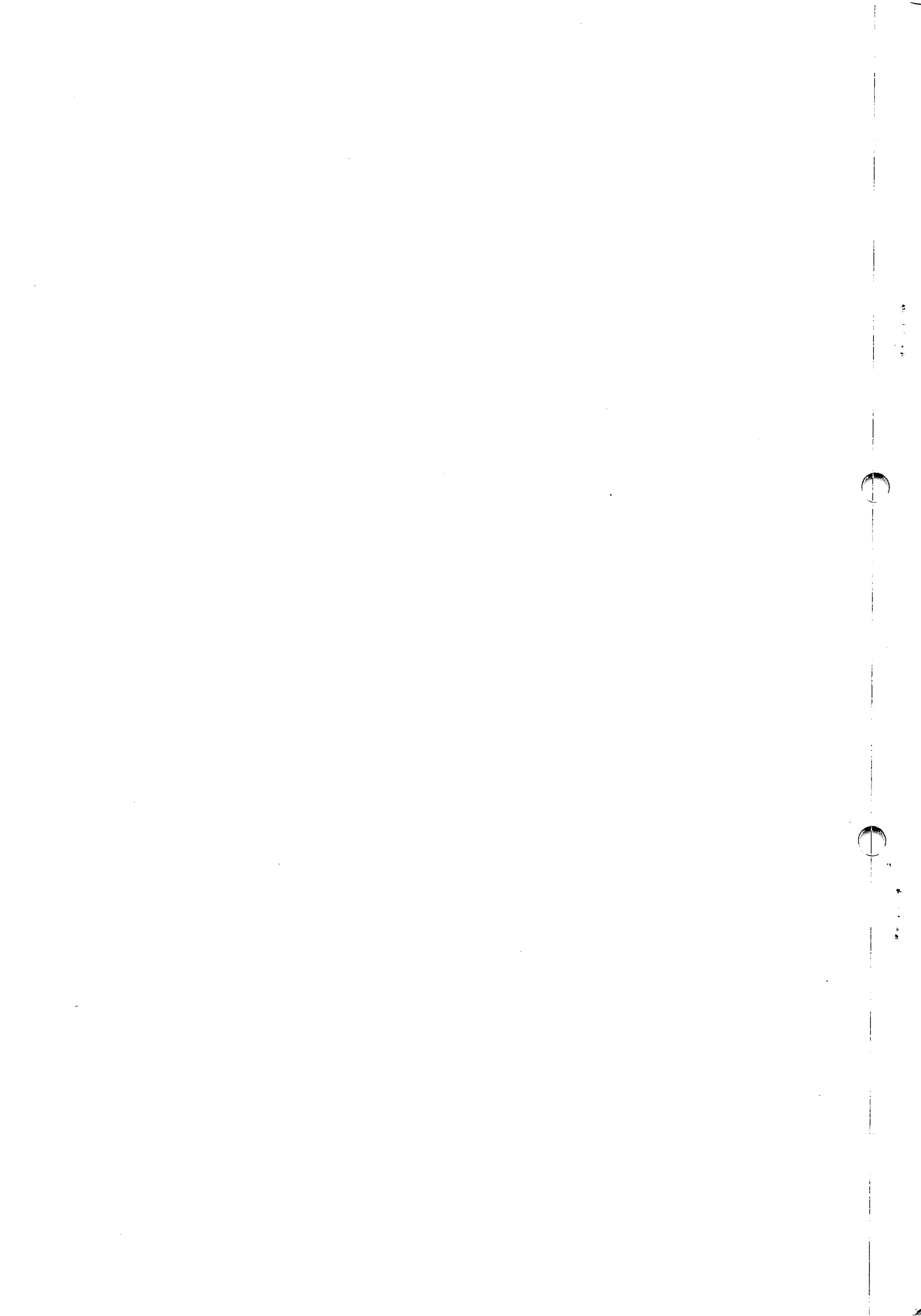
We present a measurement of the mass difference between top quark and anti-top quark in the Lepton+Jets channel using a template-based technique. Using 2d templates derived from Kernel Density Estimation and 5.6 fb^{-1} of data collected by the Tevatron, we measure

$$\Delta M_{\text{top}} = -3.3 \pm 1.4 \text{ (stat.)} \pm 1.0 \text{ (syst.) } \text{GeV}/c^2 = -3.3 \pm 1.7 \text{ GeV}/c^2$$

Acknowledgments

We thank the Fermilab staff and the technical staffs of the participating institutions for their vital contributions. This work was supported by the U.S. Department of Energy and National Science Foundation; the Italian Istituto Nazionale di Fisica Nucleare; the Ministry of Education, Culture, Sports, Science and Technology of Japan; the Natural Sciences and Engineering Research Council of Canada; the National Science Council of the Republic of China; the Swiss National Science Foundation; the A.P. Sloan Foundation; the Bundesministerium für Bildung und Forschung, Germany; the Korean Science and Engineering Foundation and the Korean Research Foundation; the Science and Technology Facilities Council and the Royal Society, UK; the Institut National de Physique Nucléaire et Physique des Particules/CNRS; the Russian Foundation for Basic Research; the Ministerio de Ciencia e Innovación, and Programa Consolider-Ingenio 2010, Spain; the Slovak R&D Agency; and the Academy of Finland.

- [1] CDF and D0 Collaborations, FERMILAB-TM-2427-E (2009), arXiv:0903.2503v1.
- [2] J.A.R. Cembranos, A. Rajaraman, and F. Takayama, *Europhys. Lett.* **82** (2008) 21001.
- [3] D. Colladay and V. A. Kostelecky, *Phys. Rev. D* **55** (1997) 6760; J. P. Hsu and M. Hongoh, *Phys. Rev. D* **6** (1972) 256; C. Ragiadakos and C. Zenses, *Phys. Lett B* **76** (1978); G. Barenboim and J. Lykken, *Phys. Lett. B* **554** (2003) 73; Y. A. Sitenko and K. Y. Rulik, *Eur. Phys. J. C* **28** (2003) 405; R. S. Raghavan, *JCAP* **0308** (2003) 002; H. Belich *et al.*, *Phys. Rev. D* **68** (2003) 065030.
- [4] V. M. Abazov, *et al.*, *Phys. Rev. Lett.* **103**, 132001 (2009).
- [5] F. Abe, *et al.*, *Nucl. Instrum. Methods Phys. Res. A* **271**, 387 (1988).
- [6] T. Aaltonen, *et al.*, *Phys. Rev. D* **79**, 092005 (2009).
- [7] A. Abulencı, *et al.*, *Phys. Rev. D* **73**, 032003 (2006).
- [8] A. Abulencı *et al.*, *Phys. Rev. Lett.* **96**, 022004 (2006).
- [9] J. Alwall, *et al.*, *J. High Energy Phys.* **0709**, 028 (2007).
- [10] T. Sjostrand, S. Mrenna, and P. Skands, *J. High Energy Phys.* **0605**, 026 (2006).
- [11] K. S. Cranmer, *Comput. Phys. Commun.* **136**, 198 (2001).
- [12] C. Loader, *Local Regression and Likelihood*, New York, USA, (Springer, 1999).
- [13] T. Aaltonen, *et al.*, *Phys. Rev. D* **81**, 031102 (2010).
- [14] F. Abe, *et al.*, *Phys. Rev. D* **45**, 1448 (1992).
- [15] T. Affolder, *et al.*, *Phys. Rev. D* **64**, 032002 (2001).
- [16] M. L. Mangano, *et al.*, *J. High Energy Phys.* **0307**, 001 (2003).
- [17] T. Aaltonen, *et al.*, arXiv:1004.3224v1 (2010).
- [18] G. Corcella, *et al.*, *J. High Energy Phys.* **0101**, 010 (2001).
- [19] A. Bhatti, *et al.*, *Nucl. Instrum. Methods Phys. Res. A* **566**, 375 (2006).
- [20] P. Z. Skands, D. Wicke, *Eur. Phys. J. C* **52**, 133 (2007).



Direct measurement of the mass difference between top and antitop quarks

V.M. Abazov,³⁵ B. Abbott,⁷³ B.S. Acharya,²⁹ M. Adams,⁴⁹ T. Adams,⁴⁷ G.D. Alexeev,³⁵ G. Alkhazov,³⁹ A. Alton^{a,61}
 G. Alverson,⁶⁰ G.A. Alves,² M. Aoki,⁴⁸ M. Arov,⁵⁸ A. Askew,⁴⁷ B. Åsman,⁴¹ O. Atramentov,⁶⁵ C. Avila,⁸ J. BackusMayes,⁸⁰
 F. Badaud,¹³ L. Bagby,⁴⁸ B. Baldin,⁴⁸ D.V. Bandurin,⁴⁷ S. Banerjee,²⁹ E. Barberis,⁶⁰ P. Baringer,⁵⁶ J. Barreto,³ J.F. Bartlett,⁴⁸
 U. Bassler,¹⁸ V. Bazterra,⁴⁹ S. Beale,⁶ A. Bean,⁵⁶ M. Begalli,³ M. Begel,⁷¹ C. Belanger-Champagne,⁴¹ L. Bellantoni,⁴⁸
 S.B. Beri,²⁷ G. Bernardi,¹⁷ R. Bernhard,²² I. Bertram,⁴² M. Besançon,¹⁸ R. Beuselinck,⁴³ V.A. Bezzubov,³⁸ P.C. Bhat,⁴⁸
 V. Bhatnagar,²⁷ G. Blazey,⁵⁰ S. Blessing,⁴⁷ K. Bloom,⁶⁴ A. Boehlein,⁴⁸ D. Boline,⁷⁰ E.E. Boos,³⁷ G. Borissov,⁴²
 T. Bose,⁵⁹ A. Brandt,⁷⁶ O. Brandt,²³ R. Brock,⁶² G. Brooijmans,⁶⁸ A. Bross,⁴⁸ D. Brown,¹⁷ J. Brown,¹⁷ X.B. Bu,⁴⁸
 M. Buehler,⁷⁹ V. Buescher,²⁴ V. Bunichev,³⁷ S. Burdin^{b,42} T.H. Burnett,⁸⁰ C.P. Buszello,⁴¹ B. Calpas,¹⁵ E. Camacho-Pérez,³²
 M.A. Carrasco-Lizarraga,⁵⁶ B.C.K. Casey,⁴⁸ H. Castilla-Valdez,³² S. Chakrabarti,⁷⁰ D. Chakraborty,⁵⁰ K.M. Chan,⁵⁴
 A. Chandra,⁷⁸ G. Chen,⁵⁶ S. Chevalier-Théry,¹⁸ D.K. Cho,⁷⁵ S.W. Cho,³¹ S. Choi,³¹ B. Choudhary,²⁸ S. Cihangir,⁴⁸ D. Claes,⁶⁴
 J. Clutter,⁵⁶ M. Cooke,⁴⁸ W.E. Cooper,⁴⁸ M. Corcoran,⁷⁸ F. Couderc,¹⁸ M.-C. Cousinou,¹⁵ A. Croc,¹⁸ D. Cutts,⁷⁵ A. Das,⁴⁵
 G. Davies,⁴³ K. De,⁷⁶ S.J. de Jong,³⁴ E. De La Cruz-Burelo,³² F. Déliot,¹⁸ M. Demarteau,⁴⁸ R. Demina,⁶⁹ D. Denisov,⁴⁸
 S.P. Denisov,³⁸ S. Desai,⁴⁸ C. Deterre,¹⁸ K. DeVaughan,⁶⁴ H.T. Diehl,⁴⁸ M. Diesburg,⁴⁸ P.F. Ding,⁴⁴ A. Dominguez,⁶⁴
 T. Dorland,⁸⁰ A. Dubey,²⁸ L.V. Dudko,³⁷ D. Duggan,⁶⁵ A. Duperrin,¹⁵ S. Dutt,²⁷ A. Dyshkant,⁵⁰ M. Eads,⁶⁴ D. Edmunds,⁶²
 J. Ellison,⁴⁶ V.D. Elvira,⁴⁸ Y. Enari,¹⁷ H. Evans,⁵² A. Evdokimov,⁷¹ V.N. Evdokimov,³⁸ G. Facini,⁶⁰ T. Ferbel,⁶⁹ F. Fiedler,²⁴
 F. Filthaut,³⁴ W. Fisher,⁶² H.E. Fisk,⁴⁸ M. Fortner,⁵⁰ H. Fox,⁴² S. Fuess,⁴⁸ A. Garcia-Bellido,⁶⁹ V. Gavrilov,³⁶ P. Gay,¹³
 W. Geng,^{15,62} D. Gerbaudo,⁶⁶ C.E. Gerber,⁴⁹ Y. Gershtein,⁶⁵ G. Ginther,^{48,69} G. Golovanov,³⁵ A. Goussiou,⁸⁰ P.D. Grannis,⁷⁰
 S. Greder,¹⁹ H. Greenlee,⁴⁸ Z.D. Greenwood,⁵⁸ E.M. Gregores,⁴ G. Grenier,²⁰ Ph. Gris,¹³ J.-F. Grivaz,¹⁶ A. Grohsjean,¹⁸
 S. Grünendahl,⁴⁸ M.W. Grünewald,³⁰ T. Guillemin,¹⁶ F. Guo,⁷⁰ G. Gutierrez,⁴⁸ P. Gutierrez,⁷³ A. Haasc,⁶⁸ S. Hagopian,⁴⁷
 J. Haley,⁶⁰ L. Han,⁷ K. Harder,⁴⁴ A. Harel,⁶⁹ J.M. Hauptman,⁵⁵ J. Hays,⁴³ T. Head,⁴⁴ T. Hebbeker,²¹ D. Hedin,⁵⁰ H. Hegab,⁷⁴
 A.P. Heinson,⁴⁶ U. Heintz,⁷⁵ C. Hensel,²³ I. Heredia-De La Cruz,³² K. Herner,⁶¹ G. Hesketh^{d,44} M.D. Hildreth,⁵⁴ R. Hirosky,⁷⁹
 T. Hoang,⁴⁷ J.D. Hobbs,⁷⁰ B. Hoeneisen,¹² M. Hohlfeld,²⁴ Z. Hubacek,^{10,18} N. Huske,¹⁷ V. Hynek,¹⁰ I. Iashvili,⁶⁷
 Y. Ilchenko,⁷⁷ R. Illingworth,⁴⁸ A.S. Ito,⁴⁸ S. Jabeen,⁷⁵ M. Jaffré,¹⁶ D. Jamin,¹⁵ A. Jayasinghe,⁷³ R. Jesik,⁴³ K. Johns,⁴⁵
 M. Johnson,⁴⁸ D. Johnston,⁶⁴ A. Jonckheere,⁴⁸ P. Jonsson,⁴³ J. Joshi,²⁷ A.W. Jung,⁴⁸ A. Juste,⁴⁰ K. Kaadze,⁵⁷ E. Kajfasz,¹⁵
 D. Karmanov,³⁷ P.A. Kasper,⁴⁸ I. Katsanos,⁶⁴ R. Kehoe,⁷⁷ S. Kermiche,¹⁵ N. Khalatyan,⁴⁸ A. Khanov,⁷⁴ A. Kharchilava,⁶⁷
 Y.N. Kharzeev,³⁵ M.H. Kirby,⁵¹ J.M. Kohli,²⁷ A.V. Kozelov,³⁸ J. Kraus,⁶² S. Kulikov,³⁸ A. Kumar,⁶⁷ A. Kupco,¹¹ T. Kurča,²⁰
 V.A. Kuzmin,³⁷ J. Kvita,⁹ S. Lammers,⁵² G. Landsberg,⁷⁵ P. Lebrun,²⁰ H.S. Lee,³¹ S.W. Lee,⁵⁵ W.M. Lee,⁴⁸ J. Lellouch,¹⁷
 L. Li,⁴⁶ Q.Z. Li,⁴⁸ S.M. Lietti,⁵ J.K. Lim,³¹ D. Lincoln,⁴⁸ J. Linnemann,⁶² V.V. Lipaev,³⁸ R. Lipton,⁴⁸ Y. Liu,⁷ Z. Liu,⁶
 A. Lobodenko,³⁹ M. Lokajicek,¹¹ R. Lopes de Sa,⁷⁰ H.J. Lubatti,⁸⁰ R. Luna-Garcia^{e,32} A.L. Lyon,⁴⁸ A.K.A. Maciel,²
 D. Mackin,⁷⁸ R. Madar,¹⁸ R. Magaña-Villalba,³² S. Malik,⁶⁴ V.L. Malyshev,³⁵ Y. Maravin,⁵⁷ J. Martínez-Ortega,³²
 R. McCarthy,⁷⁰ C.L. McGivern,⁵⁶ M.M. Meijer,³⁴ A. Melnitchouk,⁶³ D. Menezes,⁵⁰ P.G. Mercadante,⁴ M. Merkin,³⁷
 A. Meyer,²¹ J. Meyer,²³ F. Miconi,¹⁹ N.K. Mondal,²⁹ G.S. Muanza,¹⁵ M. Mulhearn,⁷⁹ E. Nagy,¹⁵ M. Naimuddin,²⁸
 M. Narain,⁷⁵ R. Nayyar,²⁸ H.A. Neal,⁶¹ J.P. Negret,⁸ P. Neustroev,³⁹ S.F. Novaes,⁵ T. Nunnemann,²⁵ G. Obrant^{f,39}
 J. Orduna,⁷⁸ N. Osman,¹⁵ J. Osta,⁵⁴ G.J. Otero y Garzón,¹ M. Padilla,⁴⁶ A. Pal,⁷⁶ N. Parashar,⁵³ V. Parihar,⁷⁵ S.K. Park,³¹
 J. Parsons,⁶⁸ R. Partridge^{c,75} N. Parua,⁵² A. Patwa,⁷¹ B. Penning,⁴⁸ M. Perfilov,³⁷ K. Peters,⁴⁴ Y. Peters,⁴⁴ K. Petridis,⁴⁴
 G. Petrillo,⁶⁹ P. Pétroff,¹⁶ R. Piegaia,¹ M.-A. Pleier,⁷¹ P.L.M. Podesta-Lerma^{f,32} V.M. Podstavkov,⁴⁸ P. Polozov,³⁶
 A.V. Popov,³⁸ M. Prewitt,⁷⁸ D. Price,⁵² N. Prokopenko,³⁸ S. Protopopescu,⁷¹ J. Qian,⁶¹ A. Quadt,²³ B. Quinn,⁶³ M.S. Rangel,²
 K. Ranjan,²⁸ P.N. Ratoff,⁴² I. Razumov,³⁸ P. Renkel,⁷⁷ M. Rijssenbeek,⁷⁰ I. Ripp-Baudot,¹⁹ F. Rizatdinova,⁷⁴ M. Rominsky,⁴⁸
 A. Ross,⁴² C. Royon,¹⁸ P. Rubinov,⁴⁸ R. Ruchti,⁵⁴ G. Safronov,³⁶ G. Sajot,¹⁴ P. Salcido,⁵⁰ A. Sánchez-Hernández,³²
 M.P. Sanders,²⁵ B. Sanghi,⁴⁸ A.S. Santos,⁵ G. Savage,⁴⁸ L. Sawyer,⁵⁸ T. Scanlon,⁴³ R.D. Schamberger,⁷⁰ Y. Scheglov,³⁹
 H. Schellman,⁵¹ T. Schliephake,²⁶ S. Schlobohm,⁸⁰ C. Schwanenberger,⁴⁴ R. Schwienhorst,⁶² J. Sekaric,⁵⁶ H. Severini,⁷³
 E. Shabalina,²³ V. Shary,¹⁸ A.A. Shchukin,³⁸ R.K. Shivpuri,²⁸ V. Simak,¹⁰ V. Sirotenko,⁴⁸ P. Skubic,⁷³ P. Slattery,⁶⁹
 D. Smirnov,⁵⁴ K.J. Smith,⁶⁷ G.R. Snow,⁶⁴ J. Snow,⁷² S. Snyder,⁷¹ S. Söldner-Rembold,⁴⁴ L. Sonnenschein,²¹
 K. Soustruznik,⁹ J. Stark,¹⁴ V. Stolin,³⁶ D.A. Stoyanova,³⁸ M. Strauss,⁷³ D. Strom,⁴⁹ L. Stutte,⁴⁸ L. Suter,⁴⁴
 P. Svoisky,⁷³ M. Takahashi,⁴⁴ A. Tanasijczuk,¹ W. Taylor,⁶ M. Titov,¹⁸ V.V. Tokmenin,³⁵ Y.-T. Tsai,⁶⁹ D. Tsybychev,⁷⁰
 B. Tuchming,¹⁸ C. Tully,⁶⁶ L. Uvarov,³⁹ S. Uvarov,³⁹ S. Uzunyan,⁵⁰ R. Van Kooten,⁵² W.M. van Leeuwen,³³ N. Varelas,⁴⁹
 E.W. Varnes,⁴⁵ I.A. Vasilyev,³⁸ P. Verdier,²⁰ L.S. Vertogradov,³⁵ M. Verzocchi,⁴⁸ M. Vesterinen,⁴⁴ D. Vilanova,¹⁸
 P. Vokac,¹⁰ H.D. Wahl,⁴⁷ M.H.L.S. Wang,⁴⁸ J. Warchol,⁵⁴ G. Watts,⁸⁰ M. Wayne,⁵⁴ M. Weber^{g,48} L. Welty-Rieger,⁵¹
 A. White,⁷⁶ D. Wicke,²⁶ M.R.J. Williams,⁴² G.W. Wilson,⁵⁶ M. Wobisch,⁵⁸ D.R. Wood,⁶⁰ T.R. Wyatt,⁴⁴ Y. Xie,⁴⁸

C. Xu,⁶¹ S. Yacoob,⁵¹ R. Yamada,⁴⁸ W.-C. Yang,⁴⁴ T. Yasuda,⁴⁸ Y.A. Yatsunenko,³⁵ Z. Ye,⁴⁸ H. Yin,⁴⁸ K. Yip,⁷¹ S.W. Youn,⁴⁸ J. Yu,⁷⁶ S. Zelitch,⁷⁹ T. Zhao,⁸⁰ B. Zhou,⁶¹ J. Zhu,⁶¹ M. Zielinski,⁶⁹ D. Ziemska,⁵² and L. Zivkovic⁷⁵

(The D0 Collaboration*)

¹Universidad de Buenos Aires, Buenos Aires, Argentina

²LAFEX, Centro Brasileiro de Pesquisas Físicas, Rio de Janeiro, Brazil

³Universidade do Estado do Rio de Janeiro, Rio de Janeiro, Brazil

⁴Universidade Federal do ABC, Santo André, Brazil

⁵Instituto de Física Teórica, Universidade Estadual Paulista, São Paulo, Brazil

⁶Simon Fraser University, Vancouver, British Columbia, and York University, Toronto, Ontario, Canada

⁷University of Science and Technology of China, Hefei, People's Republic of China

⁸Universidad de los Andes, Bogotá, Colombia

⁹Charles University, Faculty of Mathematics and Physics, Center for Particle Physics, Prague, Czech Republic

¹⁰Czech Technical University in Prague, Prague, Czech Republic

¹¹Center for Particle Physics, Institute of Physics, Academy of Sciences of the Czech Republic, Prague, Czech Republic

¹²Universidad San Francisco de Quito, Quito, Ecuador

¹³LPC, Université Blaise Pascal, CNRS/IN2P3, Clermont, France

¹⁴LPSC, Université Joseph Fourier Grenoble 1, CNRS/IN2P3,

Institut National Polytechnique de Grenoble, Grenoble, France

¹⁵CPPM, Aix-Marseille Université, CNRS/IN2P3, Marseille, France

¹⁶LAL, Université Paris-Sud, CNRS/IN2P3, Orsay, France

¹⁷LPNHE, Universités Paris VI and VII, CNRS/IN2P3, Paris, France

¹⁸CEA, Irfu, SPP, Saclay, France

¹⁹IPHC, Université de Strasbourg, CNRS/IN2P3, Strasbourg, France

²⁰IPNL, Université Lyon 1, CNRS/IN2P3, Villeurbanne, France and Université de Lyon, Lyon, France

²¹III. Physikalisches Institut A, RWTH Aachen University, Aachen, Germany

²²Physikalisches Institut, Universität Freiburg, Freiburg, Germany

²³II. Physikalisches Institut, Georg-August-Universität Göttingen, Göttingen, Germany

²⁴Institut für Physik, Universität Mainz, Mainz, Germany

²⁵Ludwig-Maximilians-Universität München, München, Germany

²⁶Fachbereich Physik, Bergische Universität Wuppertal, Wuppertal, Germany

²⁷Panjab University, Chandigarh, India

²⁸Delhi University, Delhi, India

²⁹Tata Institute of Fundamental Research, Mumbai, India

³⁰University College Dublin, Dublin, Ireland

³¹Korea Detector Laboratory, Korea University, Seoul, Korea

³²CINVESTAV, Mexico City, Mexico

³³Nikhef, Science Park, Amsterdam, the Netherlands

³⁴Radboud University Nijmegen, Nijmegen, the Netherlands and Nikhef, Science Park, Amsterdam, the Netherlands

³⁵Joint Institute for Nuclear Research, Dubna, Russia

³⁶Institute for Theoretical and Experimental Physics, Moscow, Russia

³⁷Moscow State University, Moscow, Russia

³⁸Institute for High Energy Physics, Protvino, Russia

³⁹Petersburg Nuclear Physics Institute, St. Petersburg, Russia

⁴⁰Institució Catalana de Recerca i Estudis Avançats (ICREA) and Institut de Física d'Altes Energies (IFAE), Barcelona, Spain

⁴¹Stockholm University, Stockholm and Uppsala University, Uppsala, Sweden

⁴²Lancaster University, Lancaster LA1 4YB, United Kingdom

⁴³Imperial College London, London SW7 2AZ, United Kingdom

⁴⁴The University of Manchester, Manchester M13 9PL, United Kingdom

⁴⁵University of Arizona, Tucson, Arizona 85721, USA

⁴⁶University of California Riverside, Riverside, California 92521, USA

⁴⁷Florida State University, Tallahassee, Florida 32306, USA

⁴⁸Fermi National Accelerator Laboratory, Batavia, Illinois 60510, USA

⁴⁹University of Illinois at Chicago, Chicago, Illinois 60607, USA

⁵⁰Northern Illinois University, DeKalb, Illinois 60115, USA

⁵¹Northwestern University, Evanston, Illinois 60208, USA

⁵²Indiana University, Bloomington, Indiana 47405, USA

⁵³Purdue University Calumet, Hammond, Indiana 46323, USA

⁵⁴University of Notre Dame, Notre Dame, Indiana 46556, USA

⁵⁵Iowa State University, Ames, Iowa 50011, USA

⁵⁶University of Kansas, Lawrence, Kansas 66045, USA

⁵⁷Kansas State University, Manhattan, Kansas 66506, USA

⁵⁸Louisiana Tech University, Ruston, Louisiana 71272, USA

⁵⁹Boston University, Boston, Massachusetts 02215, USA

- ⁶⁰*Northeastern University, Boston, Massachusetts 02115, USA*
⁶¹*University of Michigan, Ann Arbor, Michigan 48109, USA*
⁶²*Michigan State University, East Lansing, Michigan 48824, USA*
⁶³*University of Mississippi, University, Mississippi 38677, USA*
⁶⁴*University of Nebraska, Lincoln, Nebraska 68588, USA*
⁶⁵*Rutgers University, Piscataway, New Jersey 08855, USA*
⁶⁶*Princeton University, Princeton, New Jersey 08544, USA*
⁶⁷*State University of New York, Buffalo, New York 14260, USA*
⁶⁸*Columbia University, New York, New York 10027, USA*
⁶⁹*University of Rochester, Rochester, New York 14627, USA*
⁷⁰*State University of New York, Stony Brook, New York 11794, USA*
⁷¹*Brookhaven National Laboratory, Upton, New York 11973, USA*
⁷²*Langston University, Langston, Oklahoma 73050, USA*
⁷³*University of Oklahoma, Norman, Oklahoma 73019, USA*
⁷⁴*Oklahoma State University, Stillwater, Oklahoma 74078, USA*
⁷⁵*Brown University, Providence, Rhode Island 02912, USA*
⁷⁶*University of Texas, Arlington, Texas 76019, USA*
⁷⁷*Southern Methodist University, Dallas, Texas 75275, USA*
⁷⁸*Rice University, Houston, Texas 77005, USA*
⁷⁹*University of Virginia, Charlottesville, Virginia 22901, USA*
⁸⁰*University of Washington, Seattle, Washington 98195, USA*

(Dated: June 10, 2011)

We present a direct measurement of the mass difference between top and antitop quarks (Δm) in lepton+jets $t\bar{t}$ final states using the “matrix element” method. The purity of the lepton+jets sample is enhanced for $t\bar{t}$ events by identifying at least one of the jet as originating from a b quark. The analyzed data correspond to 3.6 fb^{-1} of $p\bar{p}$ collisions at $\sqrt{s} = 1.96 \text{ TeV}$ acquired by D0 in Run II of the Fermilab Tevatron Collider. The combination of the $e+\text{jets}$ and $\mu+\text{jets}$ channels yields $\Delta m = 0.8 \pm 1.8 \text{ (stat)} \pm 0.5 \text{ (syst) GeV}$, which is in agreement with the standard model expectation of no mass difference.

PACS numbers: 14.65.Ha

I. INTRODUCTION

The standard model (SM) is a local gauge-invariant quantum field theory (QFT), with invariance under charge, parity, and time reversal (*CPT*) providing one of its most fundamental principles [1–4], which also constrains the SM [5]. In fact, any Lorentz-invariant local QFT must conserve *CPT* [6]. A difference in the mass of a particle and its antiparticle would constitute a violation of *CPT* invariance. This issue has been tested extensively for many elementary particles of the SM [7]. Quarks, however, carry color charge, and therefore are not observed directly, but must first hadronize via quantum chromodynamic (QCD) processes into jets of colorless particles. These hadronization products reflect properties of the initially produced quarks, such as their masses, electric charges, and spin states. Except for the top quark, the time scale for hadronization of quarks is orders of magnitude less than for electroweak decay, thereby favoring the formation of QCD-bound hadronic states before decay. This introduces a significant dependence of the mass of a quark on the model of QCD binding and evolution. In contrast to other quarks, no bound states are formed before decay of produced top quarks, thereby providing a unique opportunity to measure directly the mass difference between a quark and its antiquark [8].

In proton-antiproton collisions at the Fermilab Tevatron Collider, top quarks are produced in $t\bar{t}$ pairs via the strong interaction, or singly via the electroweak interaction. In the SM, the top quark decays almost exclusively into a W boson

and a b quark. The topology of a $t\bar{t}$ event is therefore determined by the subsequent decays of the W bosons. The world’s most precise top quark mass measurements are performed in the lepton+jets ($\ell+\text{jets}$) channels, which are characterized by the presence of one isolated energetic electron or muon from one $W \rightarrow \ell\nu$ decay, an imbalance in transverse momentum relative to the beam axis from the escaping neutrino, and four or more jets from the evolution of the two b quarks and the two quarks from the second $W \rightarrow q\bar{q}$ decay.

The top quark was discovered [9, 10] in proton-antiproton collision data at a center of mass energy of $\sqrt{s} = 1.8 \text{ TeV}$ in Run I of the Tevatron. After an upgrade to a higher center of mass energy of $\sqrt{s} = 1.96 \text{ TeV}$ and higher luminosities, Run II of the Tevatron commenced in 2001. Since then, a large sample of $t\bar{t}$ events has been collected, yielding precision measurements of various SM parameters such as the mass of the top quark, which has been determined to an accuracy of about 0.6% or $m_{\text{top}} \equiv \frac{1}{2}(m_t + m_{\bar{t}}) = 173.3 \pm 1.1 \text{ GeV}$ [11], where m_t ($m_{\bar{t}}$) is the mass of the top (antitop) quark.

The D0 Collaboration published the first measurement of the top-antitop quark mass difference, $\Delta m \equiv m_t - m_{\bar{t}}$, using 1 fb^{-1} of Run II integrated luminosity [12]. Our new measurement, presented here, employs the same matrix element (ME) technique [13, 14], suggested initially by Kondo *et al.* [15–17], and developed to its current form by D0 [18]. Our previous study measured a mass difference

$$\Delta m = 3.8 \pm 3.4 \text{ (stat.)} \pm 1.2 \text{ (syst.) GeV.}$$

Recently, CDF has also measured Δm [19] based on 5.6 fb^{-1}

*with visitors from ^aAugustana College, Sioux Falls, SD, USA, ^bThe University of Liverpool, Liverpool, UK, ^cSLAC, Menlo Park, CA, USA, ^dUniversity College London, London, UK, ^eCentro de Investigacion en Computacion - IPN, Mexico City, Mexico, ^fECFM, Universidad Autonoma de Sinaloa, Cu-

55 of Run II data, using a template technique, and found

105

$$\Delta m = -3.3 \pm 1.4 \text{ (stat.)} \pm 1.0 \text{ (syst.) GeV.}$$

106

107

56 In this paper, we extend our first measurement of Δm using an additional 2.6 fb^{-1} of Run II integrated luminosity, and combining our two results. We also re-examine the uncertainties from the modeling of signal processes and of the response of the detector. Moreover, we consider additional systematic uncertainties from modeling the response of the detector. Most important is a possible presence of asymmetries in the calorimeter response to b and \bar{b} -quark jets, which we evaluate using a purely data-driven method. We also consider for the first time a bias from asymmetries in response to c and \bar{c} -quark jets.

118

67 This paper is arranged as follows: after a brief description of the D0 detector in Sec. II, we review the event selection and reconstruction in Sec. III. In Sec. IV, we define the samples of Monte Carlo (MC) events used in the analysis. The extraction of the top-antitop quark mass difference using the ME technique is then briefly reviewed in Sec. V. The calibration of this technique, based on MC events, and the measurement of the mass difference in 2.6 fb^{-1} of Run II integrated luminosity are presented in Sec. VI. The evaluation of systematic uncertainties and cross checks are discussed in Sec. VII and VII C, respectively. Finally, the combination of the measurements for the 2.6 fb^{-1} and 1 fb^{-1} data samples is presented in Sec. VIII.

130

131

132

133

134

135

136

137

138

139

140

141

142

143

144

145

146

147

148

149

150

151

152

153

154

155

156

157

158

159

160

161

162

163

164

165

166

167

168

169

170

171

172

173

174

175

176

177

178

179

II. THE D0 DETECTOR

80 The D0 detector has a central-tracking system, calorimetry, and a muon system. The central-tracking system consists of a silicon microstrip tracker (SMT) and a central fiber tracker (CFT), both located within a 1.9 T superconducting solenoidal magnet [20–22], with designs optimized for tracking and vertexing at pseudorapidities $|\eta| < 3$ [23]. The SMT can reconstruct the $p\bar{p}$ interaction vertex (PV) with a precision of about 40 μm in the plane transverse to the beam direction and determine the impact parameter of any track relative to the PV [24] with a precision between 20 and 50 μm , depending on the number of hits in the SMT. These are the key elements to lifetime-based b -quark jet tagging. The liquid-argon and uranium sampling calorimeter has a central section (CC) covering pseudorapidities $|\eta| \lesssim 1.1$ and two end calorimeters (EC) that extend coverage to $|\eta| \approx 4.2$, with all three housed in separate cryostats [20, 25]. Central and forward preshower detectors are positioned just before the CC and EC. An outer muon system, at $|\eta| < 2$, consists of a layer of tracking detectors and scintillation trigger counters in front of 1.8 T toroids, followed by two similar layers after the toroids [26]. The luminosity is calculated from the rate of $p\bar{p}$ inelastic collisions measured with plastic scintillator arrays, which are located in front of the EC cryostats. The trigger and data acquisition systems are designed to accommodate the high instantaneous luminosities of Run II [27].

III. EVENT SELECTION

In this new measurement of Δm , we analyze data corresponding to an integrated luminosity of about 2.6 fb^{-1} for both the e +jets and μ +jets channels.

Candidate $t\bar{t}$ events are required to pass an isolated energetic lepton trigger or a lepton+jet(s) trigger. These events are enriched in $t\bar{t}$ content by requiring exactly four jets reconstructed using the Run II cone algorithm [28] with cone radius $\Delta R \equiv \sqrt{(\Delta\eta)^2 + (\Delta\phi)^2} = 0.5$, transverse momenta $p_T > 20 \text{ GeV}$, and pseudorapidities $|\eta| < 2.5$. The jet of highest transverse momentum in a given event must have $p_T > 40 \text{ GeV}$. Furthermore, we require exactly one isolated electron with $p_T > 20 \text{ GeV}$ and $|\eta| < 1.1$, or exactly one isolated muon with $p_T > 20 \text{ GeV}$ and $|\eta| < 2.0$. The leptons must originate within 1 cm of the PV in the coordinate along the beamline. Events containing an additional isolated lepton (either e or μ) with $p_T > 15 \text{ GeV}$ are rejected. Lepton isolation criteria are based on calorimetric and tracking information along with object identification criteria, as described in Ref. [29]. The positively (negatively) charged leptons are used to tag the top (antitop) quark in a given event. To reduce instrumental effects that can cause charge-dependent asymmetries in the lepton momentum scale, the polarity of the solenoidal magnetic field is routinely reversed, splitting the total data into two samples of approximately equal size. The PV must have at least three associated tracks and lie within the fiducial region of the SMT. At least one neutrino is expected in the ℓ +jets final state; hence, an imbalance in transverse momentum (defined as the opposite of the vector sum of the transverse energies in each calorimeter cell, corrected for the energy carried by identified muons and energy added or subtracted due to the jet energy scale calibration described below) of $p_T > 20 \text{ GeV}$ (25 GeV) must be present in the e +jets (μ +jets) channel. These kinematic selections are summarized in Table 1.

To reduce the contribution of multijet production (MJ) in the e +jets channel, $\Delta\phi(e, p_T) > 2.2 - p_T \times 0.045 \text{ GeV}^{-1}$ is required for the azimuthal difference $\Delta\phi(e, p_T) = |\phi_e - \phi_{p_T}|$ between the electron and the direction of p_T . Likewise, $\Delta\phi(\mu, p_T) > 2.1 - p_T \times 0.035 \text{ GeV}^{-1}$ is required in the μ +jets channel. Jets from b quarks are identified by a neural-network-based b -tagging algorithm [30], which combines variables that characterize properties of secondary vertices and tracks within the jet that have large impact parameters relative to the PV. Typically, its efficiency for b -quark jets is about 65%, while the probability for misidentifying u , d , s -quark and gluon jets as b jets is about 3%. To increase $t\bar{t}$ purity, and to reduce the number of combinatoric possibilities for assigning jets to $t\bar{t}$ decay products, we require at least one b -tagged jet to be present in the events used to measure Δm .

After all acceptance requirements, a data sample of 312 (303) events is selected in the e +jets (μ +jets) channel. As discussed above, each of those samples is split according to lepton charge. In the e +jets channel, 174 (138) events have a positive (negative) lepton in the final state. Likewise, the μ +jets sample is split to subsets of 145 and 158 events.

TABLE 1: A summary of kinematic event selections applied.

| | | | |
|----------------------------------|---------------------------------|-----------------------|-----|
| Exactly 1 charged lepton | $p_T > 20 \text{ GeV}$ | $ \eta < 1.1 (e)$ | 207 |
| | $p_T > 20 \text{ GeV}$ | $ \eta < 2.0 (\mu)$ | 208 |
| Exactly 4 jets | $p_T > 20 \text{ GeV}$ | $ \eta < 2.5$ | |
| Jet of highest p_T | $p_T > 40 \text{ GeV}$ | $ \eta < 2.5$ | |
| Imbalance in transverse momentum | $\cancel{p}_T > 20 \text{ GeV}$ | ($e+\text{jets}$) | |
| | $\cancel{p}_T > 25 \text{ GeV}$ | ($\mu+\text{jets}$) | |

(180 GeV, 180 GeV), excluding the two extreme points at (165 GeV, 180 GeV) and (180 GeV, 165 GeV). The four points with $m_t = m_{\bar{t}}$ are generated with the standard PYTHIA, whereas all others use our modified version of the generator.

209

B. Monte Carlo and other simulations of background

IV. MONTE CARLO SIMULATION

Large samples of simulated MC events are used to determine the resolution of the detector and to calibrate the Δm measurement as well as the statistical sensitivity of the method. After simulation of the hard scattering part of the interaction and parton shower corrections, MC events are passed through a detailed detector simulation based on GEANT [31], overlaid with data collected from a random subsample of beam crossings to model the effects of noise and multiple interactions, and reconstructed using the same algorithms that are used for data. Although the fraction of signal events, f , is fitted in the analysis, we also cross check that the entire data sample is described adequately by the simulations.

A. Monte Carlo samples for signal

Simulated $t\bar{t}$ events with different m_t and $m_{\bar{t}}$ are required to calibrate the Δm measurement. We use the PYTHIA generator [32], version 6.413, to model the $t\bar{t}$ signal. This generator models the Breit-Wigner shape of the invariant mass distribution of t and \bar{t} quarks, whose correct description is important for the Δm measurement.

In the standard PYTHIA, it is not possible to generate $t\bar{t}$ events with different masses m_t and $m_{\bar{t}}$. Therefore, we modify the PYTHIA program to provide signal events with $m_t \neq m_{\bar{t}}$. In applying these modifications, we adjust the description of all quantities that depend on the two masses, for example, the respective decay widths Γ_t and $\Gamma_{\bar{t}}$. Technical details of this implementation can be found in Appendix I.

We generate $t\bar{t}$ events using the CTEQ6L1 parton distribution function set (PDF) [33] at the momentum transfer scale $Q^2 = (p_T^{\text{scat}})^2 + \frac{1}{2} \{P_1^2 + P_2^2 + m_t^2 + m_{\bar{t}}^2\}$, where p_T^{scat} is the transverse momentum for the hard scattering process, and P_i is the four-momentum of the incoming parton i . For $m_t = m_{\bar{t}}$, the expression used for Q^2 is identical to that in the standard PYTHIA. All other steps in the event simulation process aside from the generation of the hard-scattering process, e.g., the modeling of the detector response, are unchanged from the standard PYTHIA.

We check our modified PYTHIA version against the original by comparing large samples of simulated $t\bar{t}$ events for $(m_t, m_{\bar{t}}) = (170 \text{ GeV}, 170 \text{ GeV})$, at both the parton and reconstruction levels, and find full consistency.

The $t\bar{t}$ samples are generated at fourteen combinations of top and antitop quark masses $(m_t, m_{\bar{t}})$, which form a grid spaced at 5 GeV intervals between (165 GeV, 165 GeV) and

The dominant background to $t\bar{t}$ decays into $\ell+\text{jets}$ final states is from the electroweak production of a W boson in association with jets from gluon radiation. We simulate the hard scattering part of this process using the ALPGEN MC program [34], which is capable of simulating up to five additional particles in the final state at leading order (LO) in α_s . ALPGEN is coupled to PYTHIA, which is used to model the hadronization of the partons and the evolution of the shower. The MLM matching scheme is applied to avoid double-counting of partonic event configurations [35]. The $W+\text{jets}$ contribution is divided into two categories according to parton flavor: (i) $W+b\bar{b}+\text{jets}$ and $W+c\bar{c}+\text{jets}$, and (ii) $W+\text{jets}$, where “jets” generically denotes jets from u , d , s -quarks or gluons. While the individual processes are generated with ALPGEN, the relative contributions of the two categories are determined using next-to-LO (NLO) calculations, with next-to-leading logarithmic (NLL) corrections based on the MCFM MC generator [36]. This increases the contribution of (i) by a factor of 1.47 ± 0.22 . We rely on theoretical calculations only for determining the relative contributions of (i) and (ii) to $W+\text{jets}$ production and use this to improve the descriptions of kinematic distributions from this background. No theoretical predictions for the absolute contribution of $W+\text{jets}$ production are used (Sec. V).

Additional background contributions arise from WW , WZ , ZZ , single top quark electroweak production, $Z \rightarrow \tau\tau$, and $Z \rightarrow ee$ ($Z \rightarrow \mu\mu$) production in the $e+\text{jets}$ ($\mu+\text{jets}$) channel. The predictions for these backgrounds are taken from MC simulations, and, with the exception of single top quark electroweak production, their production cross sections are normalized to NLO+NLL calculations with MCFM. Diboson processes are simulated with PYTHIA. The hard-scattering part of single top quark production is simulated with COMPHEP [37], while ALPGEN is used for $Z+\text{jets}$ boson production. For both backgrounds, PYTHIA is employed to model hadronization and shower evolution. The CTEQ6L1 PDFs are used in the generation of all the background MC samples.

Events from MJ production can pass our selection criteria, which typically happens when a jets mimics an electron, or a muon that arises from a semileptonic decay of a b or c quark appears to be isolated. The kinematic distributions of the MJ background are modeled using events in data that fail only the electron identification (muon isolation) criteria, but pass loosened versions of these criteria. The absolute contribution of this background to each of the channels is estimated using the method described in Ref. [38].

C. Event yields

We split the selected ℓ +jets events into subsamples according to lepton flavor (e or μ), jet multiplicity, and the number of b -tagged jets in the event to verify an adequate description of the data with our signal and background model. In general, we observe good agreement between data and simulations, and systematic uncertainties on the final result explicitly account for moderate agreement observed in some kinematic distributions (cf. Sec. VII).

The numbers of events surviving the final stage of selection with at least one b -tag are summarized in Table 2. Here, for ease of comparison, the contributions from $t\bar{t}$ events are scaled to $7.45^{+0.5}_{-0.7}$ pb, the NLO cross section including NNLO approximations [39]. The total W +jets cross section is adjusted to bring the absolute yield from our signal and background model into agreement with the number of events selected in data before applying b -jet identification criteria. The distributions in the transverse mass of the W boson, M_T^W [40], and in p_T are shown in Fig. 1 for data with at least one b -tag, together with the predictions from our signal and background models.

TABLE 2: Numbers of events selected in data, compared to yield predictions for individual processes using simulations, in the e +jets and μ +jets channels with exactly 4 jets and at least one b -tagged jet, split according to b -tag multiplicity. Uncertainties are purely statistical. See text for details.

| | 1 b -tag | >1 b -tags |
|-------------|-----------------|-----------------|
| e +jets | | |
| $t\bar{t}$ | 139.2 ± 3.0 | 91.8 ± 2.5 |
| W +jets | 39.9 ± 1.2 | 4.7 ± 0.3 |
| MJ | 23.5 ± 2.1 | 5.7 ± 1.0 |
| Z+jets | 7.6 ± 0.7 | 0.9 ± 0.1 |
| Other | 6.6 ± 0.4 | 1.9 ± 0.1 |
| Total | 216.7 ± 3.9 | 105.1 ± 2.7 |
| Observed | 223 | 89 |
| μ +jets | | |
| $t\bar{t}$ | 105.9 ± 2.4 | 70.9 ± 2.0 |
| W +jets | 59.9 ± 1.8 | 7.2 ± 0.5 |
| MJ | 5.2 ± 0.9 | 2.0 ± 0.6 |
| Z+jets | 5.3 ± 0.5 | 1.2 ± 0.2 |
| Other | 5.0 ± 0.3 | 1.3 ± 0.1 |
| Total | 181.3 ± 3.2 | 82.6 ± 2.2 |
| Observed | 191 | 112 |

V. GENERAL DESCRIPTION OF THE METHOD

In this section, we describe the measurement of Δm using the ME method. The procedure is similar to the one used in Ref. [13, 41] to measure the average top quark mass m_{top} , but instead of simultaneously determining m_{top} and the jet energy scale (JES), here we measure directly the masses of the top and antitop quarks, m_t and $m_{\bar{t}}$, which provides Δm and m_{top} . We review the ME approach in Sec. VA, the calculation of signal and background event probabilities in Secs. VB A-D.

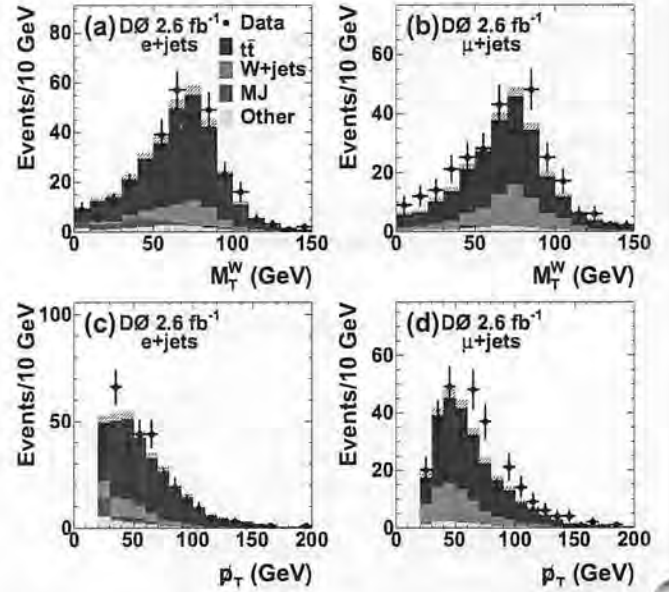


FIG. 1: The transverse mass of the W boson M_T^W for events with at least one b -tag is shown for the (a) e +jets and (b) μ +jets channels. Similarly, p_T is shown for the (c) e +jets and (d) μ +jets channels. The statistical uncertainties on the prediction from the $t\bar{t}$ signal and background models are indicated by the hatched area.

and VC, respectively, as well as the parametrization of the detector response and the use of b -tagging information in Sec. VD.

A. Probability densities for events

To optimize the use of kinematic and topological information, each event is assigned a probability P_{evt} to observe it as a function of the assumed top and antitop quark masses: $P_{\text{evt}} = P_{\text{evt}}(m_t, m_{\bar{t}})$. The individual probabilities for all events in a given sample are combined to form a likelihood, from which the Δm and m_{top} parameters are extracted. Simplifying assumptions are made in the expression of the likelihood about, e.g., detector response or the sample composition, are made to render the problem numerically solvable. It is therefore necessary to calibrate the method using fully simulated MC events, as detailed in Sec. VI B. Systematic uncertainties are estimated to account for possible effects of these assumptions on the extracted value of Δm .

Assuming that the signal and background physics processes do not interfere, the contribution to the overall probability from a single event can be formulated as

$$P_{\text{evt}}(x; m_t, m_{\bar{t}}, f) = A(x) \{ f \cdot P_{\text{sig}}(x; m_t, m_{\bar{t}}) + (1 - f) \cdot P_{\text{bkg}}(x) \}, \quad (1)$$

where x denotes the set of measured kinematic variables for the event observed in the detector, f is the fraction of signal events in the sample, $A(x)$ reflects the detector acceptance and efficiencies for a given x , and P_{sig} and P_{bkg} are the probabilities for the event to arise from $t\bar{t}$ or W +jets production,

311 respectively. The production of W bosons in association with₃₅₅
 312 jets is the dominant background, and we neglect all other con-₃₅₆
 313 tributions to P_{bkg} . Kinematically similar contributions from₃₅₇
 314 other background processes like MJ production are accounted
 315 for in the analysis implicitly (cf. Sec. VII).

316 Both signal and background probabilities depend on the
 317 JES, which is defined as the ratio of the calibrated energy of a
 318 jet over its uncalibrated energy. The standard calibration of jet
 319 energies accounts for the energy response of the calorimeters,₃₅₈
 320 the energy that crosses the cone boundary due to the transverse₃₅₉
 321 shower size, and the additional energy from pileup of events₃₆₀
 322 and from multiple $p\bar{p}$ interactions in a single beam crossing.₃₆₁
 323 Although the Δm observable is not expected to show a strong₃₆₂
 324 dependence on JES by construction, we apply an additional₃₆₃
 325 absolute calibration to the JES using a matrix element which₃₆₄
 326 is a function of m_{top} and JES from Refs. [13, 41]. The poten-₃₆₅
 327 tial systematic bias on Δm from the uncertainty on the absolute
 328 value of the JES is estimated in Sec. VII.

329 To extract the masses m_t and $m_{\bar{t}}$ from a set of n selected
 330 events, with sets of measured kinematic quantities x_1, \dots, x_n , a
 331 likelihood function is defined from the individual event prob-₃₆₆
 332 abilities according to Eq. (1):₃₆₇

$$L(x_1, \dots, x_n; m_t, m_{\bar{t}}, f) = \prod_{i=1}^n P_{\text{evt}}(x_i; m_t, m_{\bar{t}}, f). \quad (2)$$

333 For every assumed $(m_t, m_{\bar{t}})$ pair, we first determine the value
 334 of $f \equiv f^{\text{best}}$ that maximizes this likelihood.

B. Calculation of signal probability P_{sig}

335 The probability density for the signal to yield a given set of
 336 partonic final state four-momenta y in $p\bar{p}$ collisions is propor-₃₇₀
 337 tional to the differential cross section $d\sigma$ for $t\bar{t}$ production:₃₇₁

$$d\sigma(p\bar{p} \rightarrow t\bar{t} \rightarrow y; m_t, m_{\bar{t}}) = \int \sum_{q_1, q_2 \text{ quark flavors}} dq_1 dq_2 f(q_1) f(q_2) \times \frac{(2\pi)^4 |\mathcal{M}(q\bar{q} \rightarrow t\bar{t} \rightarrow y)|^2}{2q_1 q_2 s} d\Phi_6, \quad (3)$$

339 where \mathcal{M} denotes the matrix element for the $q\bar{q} \rightarrow t\bar{t} \rightarrow$
 340 $b(l\nu)\bar{b}(q\bar{q})$ process, s is the square of the center-of-mass en-₃₇₂
 341 ergy, q_i is the momentum fraction of the colliding parton i (as-₃₇₃
 342 sumed to be massless), and $d\Phi_6$ is an infinitesimal element of₃₇₄
 343 six-body phase space. The $f(q_i)$ denote the probability densi-₃₇₅
 344 ties for finding a parton of given flavor and momentum frac-₃₇₆
 345 tion q_i in the proton or antiproton, and the sum runs over all₃₇₇
 346 possible flavor configurations of the colliding quark and an-₃₇₈
 347 tiquark. In our definition of \mathcal{M} , and therefore the $t\bar{t}$ signal₃₇₉
 348 probability, only quark-antiquark annihilation at LO is taken₃₈₀
 349 into account; in this sense, Eq. (3) does not represent the full₃₈₁
 350 differential cross section for $t\bar{t}$ production in $p\bar{p}$ collisions.₃₈₂
 351 Effects from gluon-gluon and quark-gluon induced $t\bar{t}$ produc-₃₈₃
 352 tion are accounted for in the calibration procedure described₃₈₄
 353 in Sec. VI B. We further test for an effect on Δm from from₃₈₅
 354 higher-order corrections in Sec. VII C.

The differential cross section for observing a $t\bar{t}$ event with a set of kinematic quantities x measured in the detector can be written as

$$\begin{aligned} d\sigma(p\bar{p} \rightarrow t\bar{t} \rightarrow x; m_t, m_{\bar{t}}, k_{\text{JES}}) \\ = A(x) \int_y dy d\sigma(p\bar{p} \rightarrow t\bar{t} \rightarrow y; m_t, m_{\bar{t}}) W(x, y; k_{\text{JES}}), \end{aligned} \quad (4)$$

where finite detector resolution and offline selections are taken explicitly into account through the convolution over a transfer function $W(x, y; k_{\text{JES}})$ that defines the probability for a partonic final state y to appear as x in the detector given an absolute JES correction k_{JES} .

With the above definitions, the differential probability to observe a $t\bar{t}$ event with a set of kinematic quantities x measured in the detector is given by

$$P_{\text{sig}}(x; m_t, m_{\bar{t}}, k_{\text{JES}}) = \frac{d\sigma(p\bar{p} \rightarrow t\bar{t} \rightarrow x; m_t, m_{\bar{t}}, k_{\text{JES}})}{\sigma_{\text{obs}}(p\bar{p} \rightarrow t\bar{t}; m_t, m_{\bar{t}}, k_{\text{JES}})}, \quad (5)$$

where σ_{obs} is the cross section for observing $t\bar{t}$ events in the detector for the specific ME \mathcal{M} defined in Eq. (3):

$$\begin{aligned} \sigma_{\text{obs}}(p\bar{p} \rightarrow t\bar{t}; m_t, m_{\bar{t}}, k_{\text{JES}}) \\ = \int_{x,y} dx dy d\sigma(p\bar{p} \rightarrow t\bar{t} \rightarrow y; m_t, m_{\bar{t}}) W(x, y; k_{\text{JES}}) A(x) \\ = \int_y dy d\sigma(p\bar{p} \rightarrow t\bar{t} \rightarrow y; m_t, m_{\bar{t}}) \int_x W(x, y; k_{\text{JES}}) A(x). \end{aligned}$$

The normalization factor σ_{obs} is calculated using MC integration techniques:

$$\sigma_{\text{obs}}(p\bar{p} \rightarrow t\bar{t}; m_t, m_{\bar{t}}, k_{\text{JES}}) \simeq \sigma_{\text{tot}}(m_t, m_{\bar{t}}) \times \langle A | m_t, m_{\bar{t}} \rangle, \quad (6)$$

where

$$\sigma_{\text{tot}}(m_t, m_{\bar{t}}) = \int_y dy d\sigma(p\bar{p} \rightarrow t\bar{t} \rightarrow y; m_t, m_{\bar{t}}), \quad (7)$$

and

$$\langle A | m_t, m_{\bar{t}} \rangle \equiv \frac{1}{N_{\text{gen acc}}} \sum \omega. \quad (8)$$

To calculate the $\langle A | m_t, m_{\bar{t}} \rangle$ term, events are generated according to $d\sigma(p\bar{p} \rightarrow t\bar{t}; m_t, m_{\bar{t}})$ using PYTHIA and passed through the full simulation of the detector. Here, N_{gen} is the total number of generated events, ω are the MC event weights that account for trigger and identification efficiencies, and the sum runs over all accepted events.

The formulae used to calculate the total cross section σ_{tot} and the matrix element \mathcal{M} are described below in Secs. V B 1 and V B 2. In all other respects, the calculation of the signal probability proceeds identically to that in Refs. [13, 41], with the following exceptions: (i) CTEQ6L1 PDFs are used throughout, and (ii) the event probabilities are calculated on a grid in m_t and $m_{\bar{t}}$ spaced at 1 GeV intervals along each axis. As described in Sec. VI A, a transformation of variables to Δm and m_{top} is performed when defining the likelihood.

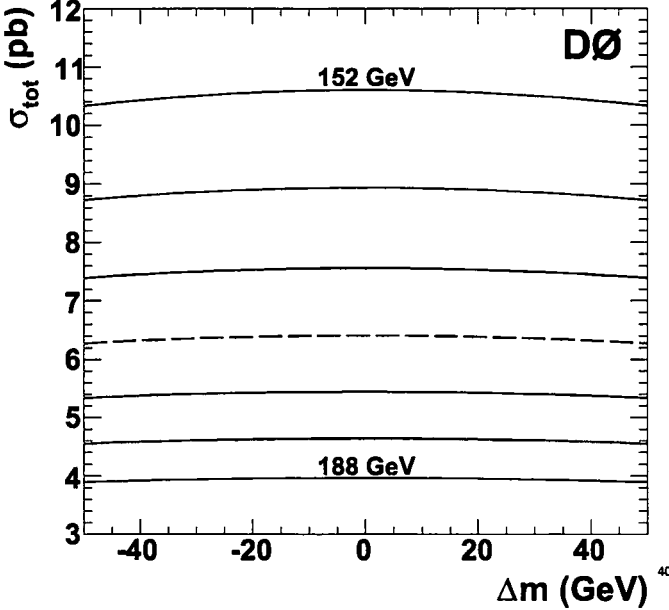


FIG. 2: The total $p\bar{p} \rightarrow t\bar{t}$ production cross section σ_{tot} defined in Eq. (7) as a function of Δm and m_{top} . Each line shows σ_{tot} as a function of Δm for a given value of m_{top} displayed above the curve. The range from 152 GeV to 188 GeV is shown in 6 GeV increments, the broken line corresponds to 170 GeV.

387

1. Calculation of the total cross section σ_{tot}

Without the assumption of equal top and antitop quark masses, the total LO cross section for the $q\bar{q} \rightarrow t\bar{t}$ process in the center of mass frame is given by

$$\sigma = \frac{16\pi\alpha_s^2}{27s^{\frac{5}{2}}} |\vec{p}| [3E_t E_{\bar{t}} + |\vec{p}|^2 + 3m_t m_{\bar{t}}], \quad (9)$$

where E_t ($E_{\bar{t}}$) are the energies of the top and antitop quark, and \vec{p} is the three-momentum of the top quark. This reduces to the familiar form for $m_t = m_{\bar{t}}$.

$$\sigma = \frac{4\pi\alpha_s^2}{9s} \beta \left(1 - \frac{\beta^2}{3}\right),$$

where $\beta = |\vec{p}_t|/E_t = |\vec{p}_{\bar{t}}|/E_{\bar{t}}$ represents the velocity of the t (or \bar{t}) quark in the $q\bar{q}$ rest frame.

Integrating Eq. (9) over all incoming $q\bar{q}$ momenta and using the appropriate PDF yields $\sigma_{\text{tot}}(p\bar{p} \rightarrow t\bar{t}; m_t, m_{\bar{t}})$, as defined for any values of m_t and $m_{\bar{t}}$ in Eq. (7). Figure 2 displays the dependence of σ_{tot} on Δm for a given m_{top} . The corresponding average acceptance term $\langle A|m_t, m_{\bar{t}} \rangle$, as defined in the same equation, is shown in Fig. (3) for the $e+\text{jets}$ and $\mu+\text{jets}$ chan-

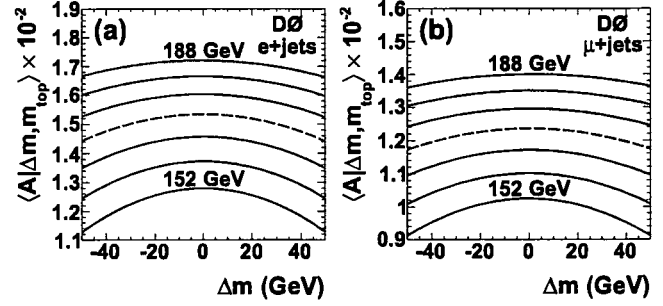


FIG. 3: The dependence of the overall average acceptance $\langle A|m_t, m_{\bar{t}} \rangle$ on Δm and m_{top} , as defined in Eq. (8), for the (a) $e+\text{jets}$ and (b) $\mu+\text{jets}$ signal MC samples. Each line shows $\langle A|m_t, m_{\bar{t}} \rangle$ as a function of Δm for a given value of m_{top} displayed above the curve. The range from 152 GeV to 188 GeV is shown in 6 GeV increments, the broken lines correspond to 170 GeV.

2. Calculation of the matrix element \mathcal{M}

The LO matrix element for the $q\bar{q} \rightarrow t\bar{t}$ process we use in our analysis is

$$|\mathcal{M}|^2 = \frac{g_s^4}{9} F\bar{F} \cdot \frac{2}{s} \times \{(E_t - |\vec{p}_t|c_{qt})^2 + (E_{\bar{t}} + |\vec{p}_{\bar{t}}|c_{q\bar{t}})^2 + 2m_t m_{\bar{t}}\}. \quad (10)$$

The form factors $F\bar{F}$ are identical to those given in Eqs. (24) and (25) of Ref. [13]. For the special case of $m_t = m_{\bar{t}}$, the expression in Eq. (10) reduces to

$$|\mathcal{M}|^2 = \frac{g_s^4}{9} F\bar{F} \cdot (2 - \beta^2 s_{qt}^2),$$

which is identical to Refs. [13, 42], where s_{qt} is the sine of the angle between the incoming parton and the outgoing top quark in the $q\bar{q}$ rest frame.

C. Calculation of the background probability P_{bkg}

The expression for the background probability P_{bkg} is similar to that for P_{sig} in Eq. (5), except that the ME $\mathcal{M}_{W+\text{jets}}$ is for $W+\text{jets}$ production, and all jets are assumed to be light quark or gluon jets. Clearly, $\mathcal{M}_{W+\text{jets}}$ does not depend on m_t or $m_{\bar{t}}$, and P_{bkg} is therefore independent of either. We use a LO parameterization of \mathcal{M} from the VECBOS [43] program. More details on the calculation of the background probability can be found in Ref. [13].

D. Description of detector response

The transfer function $W(x, y, k_{\text{JES}})$, which relates the set of variables x characterizing the reconstructed final-state objects to their partonic quantities y , is crucial for the calculation of the signal probability according to Eq. (5), and the corresponding expression for P_{bkg} . A full simulation of the detector would not be feasible for calculating event probabilities

because of the overwhelming requirements for computing re-⁴⁷⁵
sources. Therefore, we parametrize the detector response and⁴⁷⁶
resolution through a transfer function.

In constructing the transfer function, we assume that the⁴⁷⁷
functions for individual final-state particles are not correlated.
We therefore factorize the transfer function into contributions⁴⁷⁸
from each measured final-state object used in calculating P_{sig} ,⁴⁷⁹
that is the isolated lepton and four jets. The poorly measured⁴⁸⁰
imbalance in transverse momentum \cancel{p}_T , and consequently the⁴⁸¹
transverse momentum of the neutrino, is not used in defining⁴⁸²
event probabilities. We assume that the directions of e , μ ,⁴⁸³
and jets in (η, ϕ) space are well-measured, and therefore define
the transfer functions for these quantities as δ functions:
 $\delta^2(\eta, \phi) \equiv \delta(\eta_y - \eta_x)\delta(\phi_y - \phi_x)$. This reduces the number of
integrations over the 6-particle phase space $d\Phi_6$ by $5 \times 2 = 10$
dimensions. The magnitudes of particle momenta $|\vec{p}|$ display⁴⁸⁴
significant variations in resolution for leptons and jets and are⁴⁸⁵
therefore parameterized by their corresponding resolutions.⁴⁸⁶

There is an inherent ambiguity in assigning jets reconstructed in the detector to specific partons from $t\bar{t}$ decay. Consequently, all 24 permutations of jet-quark assignments are⁴⁸⁷
considered in the analysis. The inclusion of b -tagging information provides improved identification of the correct permutation.⁴⁸⁸ This additional information enters the probability calculation through a weight w_i on a given permutation i of⁴⁸⁹
jet-parton assignments. The w_i are larger for those permutations that assign the b -tagged jets to b quarks and untagged jets to light quarks. The sum of weights is normalized to unity:⁴⁹⁰
 $\sum_{i=1}^{24} w_i = 1$.

Based on the above, we define the transfer function as

$$W(x, y; k_{\text{JES}}) = W_\ell(E_x, E_y) \delta_\ell^2(\eta, \phi) \\ \times \sum_{i=1}^{24} w_i \left\{ \prod_{j=1}^4 \delta_{ij}^2(\eta, \phi) W_{\text{jet}}(E_x^i, E_y^j; k_{\text{JES}}) \right\}, \quad (11)$$

where ℓ denotes the lepton flavor, with a term W_e describing the energy resolution for electrons and W_μ the resolution in the transverse momentum for muons. Similarly, W_{jet} describes the energy resolution for jets. The sum in i is taken over the 24 possible permutations of assigning jets to quarks in a given event. More details on W_ℓ and W_{jet} can be found in Ref. [41].

The weight w_i for a given permutation i is defined by⁵¹¹
a product of individual weights w_j^i for each jet j . For b -tagged jets, w_j^i is equal to the per-jet tagging efficiency⁵¹²
 $\epsilon_{\text{tag}}(\alpha_k; E_T^j, \eta^j)$, where α_k labels the three possible parton-flavor assignments of the jet: (i) b quark, (ii) c quark, and (iii) light (u, d, s) quark or gluon. For untagged jets, the w_j^i factors are equal to $1 - \epsilon_{\text{tag}}(\alpha_k; E_T^j, \eta^j)$.

Because the contributions to $W+\text{jets}$ are parameterized by⁵¹⁶
 $M_{W+\text{jets}}$ without regard to heavy-flavor content, the weights⁵¹⁷
 w_i for each permutation in the background probability are all⁵¹⁸
set equal.

VI. MEASUREMENT OF THE TOP-ANTITOP QUARK MASS DIFFERENCE

A. Fit to the top-antitop quark mass difference

For the set of selected events, the likelihood $L(m_t, m_{\bar{t}})$ is calculated from Eq. (2) (Sec. V A). The signal fraction f^{best} that maximizes the likelihood is determined at each $(m_t, m_{\bar{t}})$ point for grid spacings of 1 GeV. Subsequently, a transformation is made to the more appropriate set of variables $(\Delta m, m_{\text{top}})$:

$$L(x_1, \dots, x_n; \Delta m, m_{\text{top}}) \\ = L[x_1, \dots, x_n; \Delta m, m_{\text{top}}, f^{\text{best}}(\Delta m, m_{\text{top}})]. \quad (12)$$

To obtain the best estimate of Δm in data, the two-dimensional likelihood in Eq. (12) is projected onto the Δm axis, and the mean value $\langle \Delta m \rangle$, that maximizes it, as well as the uncertainty $\delta_{\Delta m}$ on $\langle \Delta m \rangle$ are calculated. This procedure accounts for any correlations between Δm and m_{top} . As a consistency check, we simultaneously extract the average mass m_{top} by exchanging $\Delta m \leftrightarrow m_{\text{top}}$ above.

B. Calibration of the method

We calibrate the ME method by performing 1000 MC pseudo-experiments at each input point $(m_t, m_{\bar{t}})$. These are used to correlate the fitted parameters with their true input values and to assure the correctness of the estimated uncertainties. Each pseudo-experiment is formed by drawing N_{sig} signal and N_{bkg} background events from a large pool of fully simulated $t\bar{t}$ and $W+\text{jets}$ MC events. We assume that $W+\text{jets}$ events also represent the kinematic distributions expected from MJ production and other background processes with smaller contributions, and evaluate a systematic uncertainty from this assumption. Events are drawn randomly and can be used more than once, and an “oversampling” correction [44] is applied. The size of each pseudo-experiment, $N = N_{\text{sig}} + N_{\text{bkg}}$, is fixed by the total number of events observed in the data, i.e., $N = 312$ (303) events for the $e+\text{jets}$ ($\mu+\text{jets}$) channel. The fraction of signal events is allowed to fluctuate relative to the signal fraction f determined from data (Sec. VII B 1), assuming binomial statistics. The same $W+\text{jets}$ background sample is used to form pseudo-experiments for each $(m_t, m_{\bar{t}})$ mass point.

1. Determining the signal fraction in data

The signal fraction f is determined independently for the $e+\text{jets}$ and $\mu+\text{jets}$ channels directly from the selected data sample. The likelihood depends explicitly on three parameters: Δm , m_{top} , and f , as defined in Eq. (12). The uncalibrated signal fraction f^{uncal} is calculated in data as an average of f^{best} determined at each point in the $(m_t, m_{\bar{t}})$ grid and weighted by the value of the likelihood at that point. To calibrate f^{uncal} ,

we form 1000 pseudo-experiments for each input signal fraction f^{true} in the interval $[0, 1]$ in increments of 0.1, and extract f^{uncal} for each one, following the same procedure as in data. Signal MC events with $m_t = m_{\bar{t}} = 172.5 \text{ GeV}$ are used for this calibration. A linear dependence is observed between f^{extr} and f^{true} , where f^{extr} is the average of f^{uncal} values extracted in 1000 pseudo-experiments for a given f^{true} . We use the results of a linear fit of f^{extr} to f^{true} to calibrate the fraction of signal events in data. The results are summarized in Table 3. Possible systematic biases on the measured value of Δm from the uncertainty on f are discussed in Sec. VII.

TABLE 3: Signal fractions determined from data for the assumption that $m_t = m_{\bar{t}} = 172.5 \text{ GeV}$. The uncertainties are statistical only.

| Channel | Measured signal fraction |
|-------------------|--------------------------|
| $e+\text{jets}$ | 0.71 ± 0.05 |
| $\mu+\text{jets}$ | 0.75 ± 0.04 |

TABLE 4: Fit parameters for the calibration of Δm and m_{top} , defined by Eq. (13), and average pull-widths $\langle \omega_{\pi} \rangle$ for pulls in Δm and m_{top} , defined in Eq. (14).

| Channel | $\xi_0 \text{ (GeV)}$ | ξ_1 | $\langle \omega_{\pi} \rangle$ |
|------------------|-----------------------|------------------|--------------------------------|
| Δm | $e+\text{jets}$ | 0.28 ± 0.14 | 1.10 ± 0.02 |
| | $\mu+\text{jets}$ | -0.08 ± 0.13 | 0.99 ± 0.02 |
| m_{top} | $e+\text{jets}$ | 0.53 ± 0.08 | 0.99 ± 0.02 |
| | $\mu+\text{jets}$ | 0.24 ± 0.07 | 1.02 ± 0.02 |

and (d) of the same figure. The corresponding fit parameters and average pull widths are also summarized in Table 4.

C. Results

With the calibration of Δm and m_{top} , we proceed to extract Δm and, as a cross check, m_{top} , from the data, as described in Sec. V. As indicated previously, the probabilities for the selected events are calculated using the ME method, and the likelihoods in Δm and m_{top} are constructed independently for the $e+\text{jets}$ and $\mu+\text{jets}$ channels.

The calibration of data involves a linear transformation of the uncalibrated axes of the likelihoods in Δm and m_{top} to their corrected values, which we denote as Δm^{cal} and $m_{\text{top}}^{\text{cal}}$, accord-

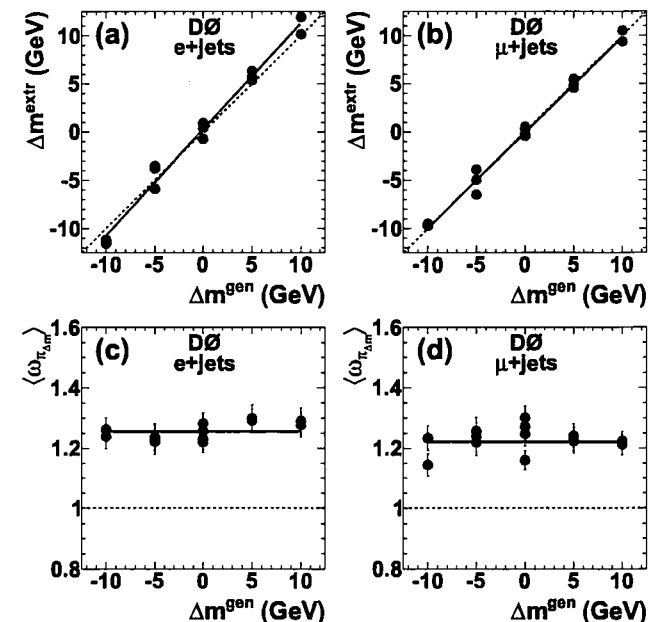


FIG. 4: The calibration of the extracted Δm value as a function of generated Δm is shown for the (a) $e+\text{jets}$ and (b) $\mu+\text{jets}$ channels. The points are fitted to a linear function. Each point represents a set of 1000 pseudo-experiments for one of the fourteen $(m_t, m_{\bar{t}})$ combinations. Similarly, the pull widths, as defined in the text, are given for the (c) $e+\text{jets}$ and (d) $\mu+\text{jets}$ channels.

3. Calibration of m_{top}

Results from an analogous calibration of m_{top} are displayed in Fig. 5 (a) and (b) for the $e+\text{jets}$ and $\mu+\text{jets}$ channel, respectively. The distributions in pull widths are given in parts (c)

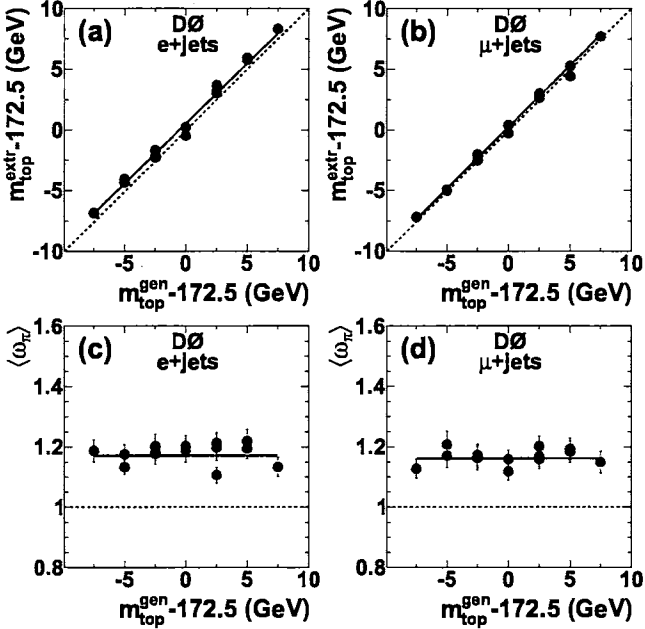


FIG. 5: The calibration of the extracted m_{top} value as a function of generated m_{top} is shown for the (a) $e + \text{jets}$ and (b) $\mu + \text{jets}$ channels. The dependence is fitted to a linear function. Each point represents a set of 1000 pseudo-experiments for one of the fourteen ($m_t, m_{\bar{t}}$) combinations. Similarly, the pull widths, as defined in the text, are given for the (c) $e + \text{jets}$ and (d) $\mu + \text{jets}$ channels.

ing to:

$$\Delta m^{\text{cal}} = \frac{\Delta m - \xi_0^{\Delta m}}{\xi_1^{\Delta m}}, \quad (15)$$

$$m_{\text{top}}^{\text{cal}} = \frac{m_{\text{top}} - 172.5 \text{ GeV} - \xi_0^{m_{\text{top}}}}{\xi_1^{m_{\text{top}}}} + 172.5 \text{ GeV}, \quad (16)$$

where the ξ_i are summarized in Table 4. The resulting likelihoods for data, as a function of Δm and m_{top} are shown in Figs. 6 and 7, respectively.

After calibration, $\langle \Delta m \rangle$ and $\langle m_{\text{top}} \rangle$ with their respective uncertainties $\delta_{\Delta m}$ and $\delta_{m_{\text{top}}}$, are extracted from the likelihoods as described in Sec. VI A. The uncertainties are scaled up by the average pull widths given in Table 4. The resulting distributions in expected uncertainties $\delta_{\Delta m}^{\text{cal}}$ are also shown in Fig. 6.

The final measured results for Δm and m_{top} are summarized below according to channel, as well as combined:

$$\begin{aligned} e + \text{jets}, 2.6 \text{ fb}^{-1}: & \Delta m = 0.1 \pm 3.1 \text{ GeV} \\ & m_{\text{top}} = 173.9 \pm 1.6 \text{ GeV} \\ \mu + \text{jets}, 2.6 \text{ fb}^{-1}: & \Delta m = -0.5 \pm 2.9 \text{ GeV} \\ & m_{\text{top}} = 175.3 \pm 1.3 \text{ GeV} \\ \ell + \text{jets}, 2.6 \text{ fb}^{-1}: & \Delta m = -0.2 \pm 2.1 \text{ GeV} \\ & m_{\text{top}} = 174.7 \pm 1.0 \text{ GeV}. \end{aligned} \quad (17)$$

The uncertainties given thus far are purely statistical. The combined $\ell + \text{jets}$ results are obtained by using the canonical weighted average formulae assuming Gaussian uncertainties.

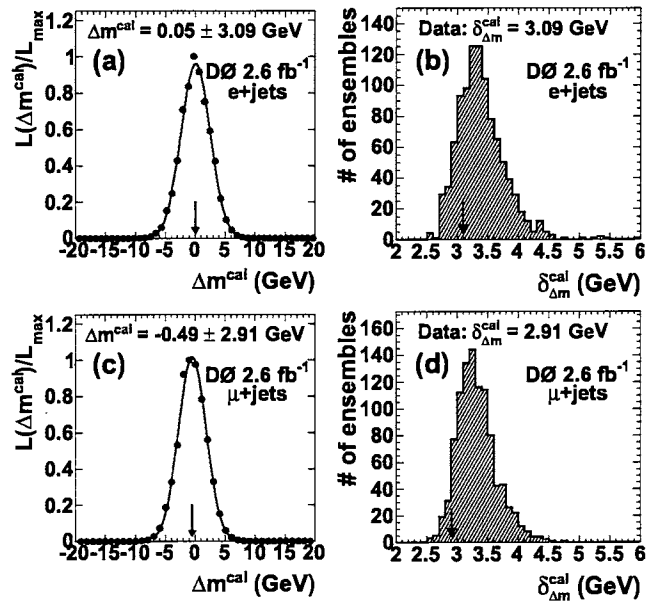


FIG. 6: The normalized likelihood in Δm^{cal} after calibration via Eq. (15), together with a Gaussian fit, is shown for the (a) $e + \text{jets}$ and (c) $\mu + \text{jets}$ events in data. The extracted Δm^{cal} values are indicated by arrows. The distributions in expected uncertainties $\delta_{\Delta m}^{\text{cal}}$ after calibration via Eq. (15) and correction for the pull width, obtained from ensemble studies using simulated MC events, is displayed for the (b) $e + \text{jets}$ and (d) $\mu + \text{jets}$ channel. The observed $\delta_{\Delta m}^{\text{cal}}$ values are indicated by arrows.

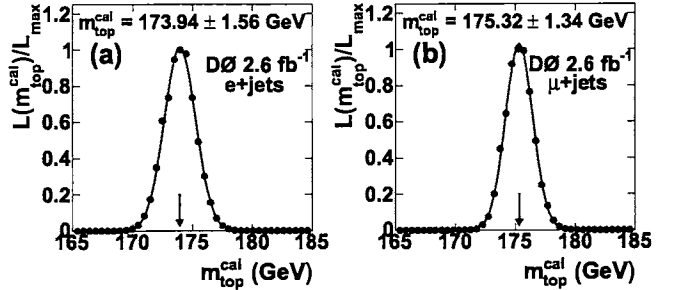


FIG. 7: The normalized likelihood in $m_{\text{top}}^{\text{cal}}$ after calibration via Eq. (16) together with a Gaussian fit for the (a) $e + \text{jets}$ and (b) $\mu + \text{jets}$ channel. Arrows indicate the extracted $m_{\text{top}}^{\text{cal}}$ values.

We cross check the above values for m_{top} with those obtained from the absolute top quark mass analysis [41, 45] and find them to be consistent.

As an additional cross check, we independently extract the masses of the top and antitop quarks from the same data sample. The two-dimensional likelihood densities, as functions of m_t and $m_{\bar{t}}$, are displayed in Fig. 8. Also shown are contours of equal probability for two-dimensional Gaussian fits to the likelihood densities, where the Gaussian functions are of the form

$$P(x, y) = \frac{A}{2\pi\sigma_x\sigma_y} \frac{1}{\sqrt{1-\rho^2}}$$

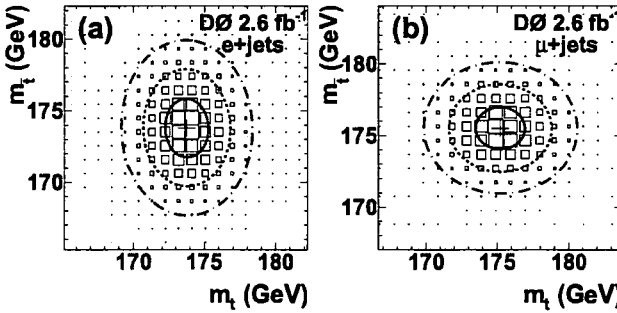


FIG. 8: Two-dimensional likelihood densities in m_t and \bar{m}_t for the (a) $e + \text{jets}$ and (b) $\mu + \text{jets}$ channels. The bin contents are proportional to the area of the boxes. The solid, dashed, and dash-dotted lines represent the 1, 2, and 3 SD contours of two-dimensional Gaussian fits (corresponding to approximately 40%, 90% and 99% confidence level, respectively) to the distributions defined in Eq. (18), respectively.

$$\times \exp \left\{ -\frac{1}{2} \frac{1}{1-\rho^2} \left[\frac{(x-\bar{x})^2}{\sigma_x^2} + \frac{(y-\bar{y})^2}{\sigma_y^2} + \frac{2\rho(x-\bar{x})(y-\bar{y})}{\sigma_x\sigma_y} \right] \right\}, \quad (18)$$

with $x \equiv m_t$ and $y \equiv \bar{m}_t$. The fits to data yield

$$\begin{aligned} \text{e+jets, } 2.6 \text{ fb}^{-1}: \quad & m_t = 173.8 \pm 1.5 \text{ GeV} \\ & \bar{m}_t = 173.8 \pm 2.0 \text{ GeV} \\ & \rho = -0.02 \\ & m_t = 175.2 \pm 1.8 \text{ GeV} \\ \text{mu+jets, } 2.6 \text{ fb}^{-1}: \quad & \bar{m}_t = 175.5 \pm 1.5 \text{ GeV} \\ & \rho = -0.01. \end{aligned} \quad (19)$$

The above uncertainties are again purely statistical; however, in contrast to Eq. (17), they are not corrected for pull widths in m_t and \bar{m}_t . The correlation coefficients ρ are consistent with the absence of correlations.

In Sec. VIII, we will combine the results for Δm summarized in Eq. (17) with the previous measurement using 1 fb^{-1} of integrated luminosity [12].

VII. SYSTEMATIC UNCERTAINTIES

For the measurement of m_{top} we typically consider three main types of sources of systematic uncertainties [41]: (i) modeling of $t\bar{t}$ production and background processes, (ii) modeling of detector response, and (iii) limitations inherent in the measurement method. However, in the context of a Δm measurement, many systematic uncertainties are reduced because of correlations between the measured properties of top and antitop quarks, such as, the uncertainty from the absolute JES calibration. Given the small value of the upper limit of $O(5\%)$ already observed for $|\Delta m|/m_{\text{top}}$, several other sources of systematic uncertainties relevant in the measurement of m_{top} , such as modeling of hadronization, are not expected to contribute to Δm because they would affect t and \bar{t} in a similar manner. Following [46], we check for any effects

TABLE 5: Summary of systematic uncertainties on Δm .

| Source | Uncertainty on Δm (GeV) |
|--------------------------------------|---------------------------------|
| Modeling of detector: | |
| Jet energy scale | 0.15 |
| Remaining jet energy scale | 0.05 |
| Response to b and light quarks | 0.09 |
| Response to b and \bar{b} quarks | 0.23 |
| Response to c and \bar{c} quarks | 0.11 |
| Jet identification efficiency | 0.03 |
| Jet energy resolution | 0.30 |
| Determination of lepton charge | 0.01 |
| ME method: | |
| Signal fraction | 0.04 |
| Background from multijet events | 0.04 |
| Calibration of the ME method | 0.18 |
| Total | 0.47 |

on Δm that might arise from sources in the latter category in Sec. VII C, and find them consistent with having no significant impact. We therefore do not consider them further in the context of this measurement. On the other hand, we estimate systematic uncertainties from additional sources which are not considered in the m_{top} measurement, for example from the asymmetry in calorimeter response to b and \bar{b} quark jets.

Typically, to propagate a systematic uncertainty on some parameter to the final result, that parameter is changed in the simulation used to calibrate the ME method, and the Δm result is re-derived. If the change in a parameter can be taken into account through a reweighting of events, a new calibration is determined using those weights and applied directly to data. When this procedure is not possible, a re-evaluation of event probabilities is performed for one sample of $t\bar{t}$ MC events corresponding to a particular choice of m_t and \bar{m}_t closest to the most likely value according to our measurement, i.e. $m_t = \bar{m}_t = 175$ GeV, or, when no such sample of MC events with a changed parameter is available, $m_t = \bar{m}_t = 172.5$ GeV. Consequently, the results of ensemble studies are compared to those found for the default sample for the same values of m_t and \bar{m}_t .

The systematic uncertainties are described below and summarized in Table 5. The total systematic uncertainty is obtained by adding all contributions in quadrature.

A. Modeling of detector

- (i) *Jet energy scale:* As indicated in Sec. VI C, we use the absolute JES calibration of $k_{\text{JES}} = 1.018 \pm 0.008$ determined from data. To propagate this uncertainty to Δm , we scale the jet energies in the selected data sample by $k_{\text{JES}} \pm 1\text{SD}$.
- (ii) *Remaining jet energy scale:* The systematic uncertainty on the absolute JES discussed above does not account for possible effects from uncertainties on jet energy corrections that depend on E_{jet} and η_{jet} . To estimate this effect on Δm , we rescale the energies of jets

in the default $t\bar{t}$ MC sample by a differential scale factor $S(E_{jet}, \eta_{jet})$ that is a function of the JES uncertainties, but conserves the magnitude of the absolute JES correction.

(iii) *Response to b and light quarks:* The difference in the hadronic/electromagnetic response of the calorimeter leads to differences in the response to b and light quarks between data and simulation. This uncertainty is evaluated by re-scaling the energies of jets matched to b quarks in the default $t\bar{t}$ MC sample.

(iv) *Response to b and \bar{b} quarks:* The measurement of Δm can be affected by differences in the reconstruction of the transverse momenta of particles and antiparticles. A difference could in principle be caused by different p_T scales for μ^+ and μ^- . However, the data consist of an almost equal mix of events with opposite net polarities, thereby minimizing such biases. We do not observe any difference in calorimeter response to e^+ and e^- .

A systematic bias to Δm can also be caused by differences in calorimeter response to quarks and anti-quarks. In the case of $t\bar{t}$ events, this bias could arise especially from a different response to b and \bar{b} -quarks. Several mechanisms could contribute to this, most notably a different content of K^+/K^- mesons, which have different interaction cross sections. In our evaluation of this systematic uncertainty, we assume that, although differences in response to b/ \bar{b} quarks are present in data, they are not modeled in MC events. We measure the difference of the calorimeter response to b quarks to that of \bar{b} quarks, $\mathcal{R}_{b,\bar{b}} \equiv \mathcal{R}_b - \mathcal{R}_{\bar{b}}$, using a “tag-and-probe” method in data. Namely, we select back-to-back dijet events, and enhance the $b\bar{b}$ content by requiring b -tags for both jets. The tag jet is defined by the presence of a muon within the jet cone, whose charge serves as an indication whether the probe jet is more likely to be a b or a \bar{b} -quark jet. By evaluating the $|\vec{p}_T|$ imbalance between tag and probe jets for positively and negatively charged muon tags, we find an upper bound $|\mathcal{R}_{b,\bar{b}}| < 0.0042$. Based on this result, we modify the default $t\bar{t}$ MC sample by re-scaling the momenta $|\vec{p}|$ of b (\bar{b})-quark jets by $1 \pm \frac{1}{2} \cdot \mathcal{R}_{b,\bar{b}} = 0.9979$ (1.0021), and adjusting their 4-vectors accordingly. We repeat the ensemble studies after recalculating the probabilities for the modified sample and quote the difference relative to the default sample as a systematic uncertainty.

(v) *Response to c and \bar{c} quarks:* A difference in calorimeter response to c and \bar{c} quarks can potentially bias Δm since c quarks appear in decays of W^+ bosons from t quark decays, and vice versa for \bar{c} and \bar{t} . It is experimentally difficult to isolate a sufficiently clean sample of $c\bar{c}$ dijet events, since it will suffer from considerable contributions from bb dijet events. However, the major underlying mechanisms that could cause a response asymmetry, like, e.g., the different content of K^+/K^- mesons, are the same, but of roughly opposite magni-

tude between c and b quark jets, which would result in an anticorrelation. Based on the above, we assume the same upper bound $|\mathcal{R}_{c,\bar{c}}| \leq \mathcal{R}_{b,\bar{b}} < 0.0042$, and treat $\mathcal{R}_{c,\bar{c}}$ and $\mathcal{R}_{b,\bar{b}}$ as uncorrelated. To propagate the systematic uncertainty from $\mathcal{R}_{c,\bar{c}}$ to Δm , we apply a similar technique to that for the estimation of the systematic uncertainty due to different response to b and \bar{b} quarks.

(vi) *Jet identification efficiency:* D0 uses scale factors to achieve data/MC agreement in jet identification efficiencies. To propagate to the Δm measurement the effect of uncertainties on these scale factors, we decrease the jet identification efficiencies in the default $t\bar{t}$ sample according to their uncertainties.

(vii) *Jet energy resolution:* To evaluate any effect from data/MC disagreement in jet energy resolutions on Δm , we modify the default $t\bar{t}$ MC sample by varying the jet energy resolution within its uncertainty.

(viii) *Determination of lepton charge:* This analysis uses the charge of the lepton in $t\bar{t}$ candidate events to distinguish the top quark from the antitop quark. Incorrectly reconstructed lepton charges can result in a systematic shift in the measurement. The charge misidentification rate is found to be less than 1% in studies of $Z \rightarrow ee$ data events. To estimate the contribution of this uncertainty, we assume a charge misidentification rate of 1% for both $e+jets$ and $\mu+jets$ final states and evaluate the effects on Δm resulting from a change in the mean values of the extracted m_t^{cal} and $m_{\bar{t}}^{\text{cal}}$.

B. ME method

(i) *Signal fraction:* The signal fractions f presented in Table 3 are changed by their respective uncertainties for each decay channel, and ensemble studies are repeated for all MC samples to re-derive the calibration for Δm . The new calibrations are applied to data and the results compared with those obtained using the default calibration.

(ii) *Background from multijet events:* In the calibration of this analysis, the background contribution to pseudo-experiments is formed using only $W+jets$ events, as they are also assumed to model the small MJ background from QCD processes and smaller contributions from other background processes present in the data. To estimate the systematic uncertainty from this assumption, we define a dedicated MJ-enriched sample of events from data. The calibration is re-derived with this background sample included in forming pseudo-experiments.

(iii) *Calibration of the ME method:* The statistical uncertainties associated with the offset (ξ_0) and slope (ξ_1) parameters that define the mass calibration in Sec. VI B contribute to the uncertainty on Δm . To quantify this,

TABLE 6: Summary of additional checks for a possible bias on Δm .
 None of those show any significant bias on Δm . Note that the numbers shown reflect an upper limit on a possible bias. This limitation is of statistical origin and due to the number of available simulated MC events.

| Source | Change in Δm (GeV) |
|--|-------------------------------|
| Modeling of physical processes: | |
| Higher-order corrections | 0.26 |
| ISR/FSR | 0.21 |
| Hadronization and underlying event | 0.23 |
| Color reconnection | 0.27 |
| <i>b</i> -fragmentation | 0.03 |
| PDF uncertainty | 0.10 |
| Multiple hadron interactions | 0.06 |
| Modeling of background | 0.07 |
| Heavy-flavor scale factor | 0.02 |
| Modeling of detector: | |
| Trigger selection | 0.07 |
| <i>b</i> -tagging efficiency | 0.25 |
| Momentum scale for e | 0.05 |
| Momentum scale for μ | 0.06 |

we calculate the uncertainty $\delta_{\Delta m}$ due to δ_{ξ_0} and δ_{ξ_1} for each channel according to the error propagation formula

$$\delta_{\Delta m} = \left\{ \left(\frac{\Delta m - \xi_0}{\xi_1^2} \cdot \delta_{\xi_1} \right)^2 + \left(\frac{\delta_{\xi_0}}{\xi_1} \right)^2 \right\}^{-\frac{1}{2}}$$

and then combine the resulting uncertainties for the e +jets and μ +jets channels in quadrature.

C. Additional checks

We check for effects on Δm from sources of systematic uncertainties considered in the m_{top} measurement [41] which are not expected to contribute any bias in the context of the measurement of Δm . For this, we follow the same approach as outlined at the beginning of this Section. We find the results of our checks to be indeed consistent with no bias on Δm .

The additional checks are described below and summarized in Table 6. Note that the numbers quoted merely reflect an upper bound on a possible bias, rather than any true effect. This limitation is statistical in nature and due to the number of available simulated MC events. Furthermore, if the difference between the central result and the one obtained for a check is smaller than the statistical uncertainty on this difference, we quote the latter.

1. Modeling of physical processes

- (i) *Higher-order corrections:* To check the effect of higher-order corrections on Δm , we perform ensemble studies using $t\bar{t}$ events generated with (i) the NLO MC

generator MC@NLO [47], and (ii) the LO MC generator ALPGEN, with HERWIG [48] for hadronization and shower evolution.

- (ii) *Initial and final-state radiation:* The modeling of extra jets from ISR/FSR is checked by comparing PYTHIA samples with modified input parameters, such as the ± 1 SD changes, found in a study of Drell-Yan processes [49].
 - (iii) *Hadronization and underlying event:* To check a possible effect of Δm from the underlying event as well as the hadronization models, we compare samples hadronized using PYTHIA with those hadronized using HERWIG.
 - (iv) *Color reconnection:* The default PYTHIA tune used at D0 (tune A), does not include explicit color reconnection. For our check, we quantify the difference between Δm values found in ensemble studies for $t\bar{t}$ MC samples generated using tunes Apro and ACRpro, where the latter includes an explicit model of color reconnection [50, 51].
 - (v) **b*-fragmentation:* Uncertainties in the simulation of *b*-quark fragmentation can affect the measurement of m_{top} in several phases of the analysis, such as in *b*-tagging and in the *b*-quark transfer functions used in the ME calculations. Such effects are studied in the context of Δm by reweighting the simulated $t\bar{t}$ events used in the calibration of the method from the default Bowler scheme [52], which is tuned to LEP (ALEPH, OPAL, and DELPHI) data, to a tune that accounts for differences between SLD and LEP data [53].
 - (vi) *Uncertainty on PDF:* The CTEQ6M [33] PDFs provide a set of possible excursions in parameters from their central values. To check the effect on Δm from PDFs, we change the default $t\bar{t}$ MC sample (generated using CTEQ6L1) by reweighting it to CTEQ6M, repeat the ensemble studies for each of the parameter variations, and evaluate the uncertainty using the prescribed formula [33]:
- $$\delta_{\Delta m, \text{PDF}} = \frac{1}{2} \left\{ \sum_{i=1}^{20} [\Delta m(S_i^+) - \Delta m(S_i^-)]^2 \right\}^{\frac{1}{2}},$$
- where the sum runs over PDF uncertainties for positive (S_i^+) and negative (S_i^-) excursions.
- (vii) *Multiple hadron interactions:* When calibrating the ME method, we reweight the luminosity profiles of our MC samples to the instantaneous luminosity profile for that data-taking period. For our check, we re-derive the calibration ignoring luminosity-dependent weights.
 - (viii) *Modeling of background:* We check the effect of inadequate modeling of background processes on our Δm measurement by identifying distributions in the background-dominated $\ell + 3$ jets events that display only limited agreement between data and predictions from the sum of our signal and background models, as

determined through a Kolmogorov-Smirnov test [54].⁸⁸³ The calibration of the method is then re-done using⁸⁸⁴ $W+jets$ events that are reweighted to bring the identified⁸⁸⁵ distributions of predicted signal and background⁸⁸⁶ events into better agreement with data.⁸⁸⁷

- (ix) *Heavy-flavor scale-factor:* As discussed in Sec. IV, a heavy-flavor scale-factor of 1.47 ± 0.22 is applied to the $W+bb+jets$ and $W+c\bar{c}+jets$ production cross sections⁸⁸⁶ to increase the heavy-flavor content in the ALPGEN⁸⁸⁷ $W+jets$ MC samples. Moreover, a scale factor of⁸⁸⁸ 1.27 ± 0.15 for the $W+c+jets$ production cross section⁸⁸⁹ is obtained using MCFM. We re-derive the calibration⁸⁹⁰ with the heavy-flavor scale-factor changed by $\pm 30\%$ to⁸⁹¹ check the magnitude of the effect on Δm .⁸⁹²

2. Modeling of detector

- (i) *Trigger selection:* To check the magnitude the effect from differential trigger efficiencies on Δm , we re-derive a new Δm calibration ignoring the trigger weights.⁸⁹⁷
- (ii) *b-tagging efficiency:* We check the possibility of a bias in our Δm measurement from discrepancies in the b -tagging efficiency between data and MC events by using absolute uncertainties on the b -tagging efficiencies,⁹⁰² and account independently for possible discrepancies that are differential in η and p_T of the jet by reweighting the b -tagging rate in simulated $t\bar{t}$ MC events to that observed in data. The total magnitude of a possible effect is determined by combining in quadrature excursions of Δm values obtained with the modified calibrations for both absolute and differential changes.⁹¹³
- (iii) *Momentum scale for electrons:* D0 calibrates the energy of electrons based on studies of the $Z \rightarrow ee$ mass for data and MC events. We rescale the electron energies in the default signal MC sample according to the uncertainties on the electron energy calibration to check⁹¹⁵ the magnitude of the effect in the context of Δm .⁹¹⁶
- (iv) *Momentum scale for muons:* The absolute momentum scale for muons is obtained from $J/\psi \rightarrow \mu\mu$ and⁹¹⁹ $Z \rightarrow \mu\mu$ data. However, both linear and quadratic interpolation between these two points can be employed for the calibration. We check the effect of each extrapolation on Δm by applying the respective corrections to simulated $t\bar{t}$ MC events in the default sample, and find⁹²² a larger shift in Δm for the linear parametrization.⁹²³

VIII. COMBINING THE 2.6 fb^{-1} AND 1 fb^{-1} ANALYSES

We use the BLUE method [55, 56] to combine our new measurement (Eq. 17) with the result of the analysis performed on data corresponding to 1 fb^{-1} [12]. The BLUE

method assumes Gaussian uncertainties and accounts for correlations among measurements.

For reference, we summarize the results obtained for 1 fb^{-1} :

$$\begin{aligned} e+jets, 1 \text{ fb}^{-1} : \quad \Delta m &= 0.3 \pm 5.0 \text{ (stat) GeV}, \\ \mu+jets, 1 \text{ fb}^{-1} : \quad \Delta m &= 6.7 \pm 4.7 \text{ (stat) GeV}, \\ \ell+jets, 1 \text{ fb}^{-1} : \quad \Delta m &= 3.8 \pm 3.4 \text{ (stat) GeV}. \end{aligned}$$

The 1 fb^{-1} analysis used a data-driven method to estimate systematic uncertainties from modeling of signal processes. This method did not distinguish between different sources of systematic uncertainties such as: (i) higher-order corrections, (ii) initial and final state radiation, (iii) hadronization and the underlying event, and (iv) color reconnection. The above sources are studied in the context of the m_{top} measurement [41], but are not expected to contribute any bias to the measurement of Δm . We cross-check their impact on Δm in Sec. VII C, and find them consistent with no bias. Based on our findings, we do not consider any systematic uncertainties from modeling of signal and background processes.

Two sources of systematic uncertainties from modeling of detector performance (Table 5) are taken to be uncorrelated between the two measurements: JES and remaining JES. The rest are taken to be fully correlated.

In the 1 fb^{-1} analysis, a systematic uncertainty of 0.4 GeV from the difference in calorimeter response to b and \bar{b} quarks was estimated using MC studies and checks in data. This systematic uncertainty has been re-evaluated using an entirely data-driven approach (item (iv) in Sec. VII A), and we therefore use this new result for the analysis of the 1 fb^{-1} data. Furthermore, we now evaluated a systematic uncertainty from the difference in calorimeter response to c and \bar{c} quarks, and propagate our findings to the 1 fb^{-1} analysis.

All other systematic uncertainties not explicitly mentioned above are taken as uncorrelated.

The combined result for Δm corresponding to 3.6 fb^{-1} of data is

$$\Delta m = 0.84 \pm 1.81 \text{ (stat.)} \pm 0.48 \text{ (syst.) GeV}. \quad (20)$$

In this combination, BLUE determines a relative weight of 72.8% (27.2%) for the 2.6 fb^{-1} (1 fb^{-1}) measurement. The χ^2/N_{dof} of the combination is 0.96. The combined likelihood densities for the two analyses are presented in Fig. 9 as functions of m_t and $m_{\bar{t}}$, separately for the $e+jets$ and $\mu+jets$ channels.

IX. CONCLUSION

We have applied the matrix element method to the measurement of the mass difference Δm between top and antitop quarks using $t\bar{t}$ candidate events in the lepton+jets channel in data corresponding to an integrated luminosity of about 3.6 fb^{-1} . We find

$$\Delta m = 0.8 \pm 1.8 \text{ (stat.)} \pm 0.5 \text{ (syst.) GeV},$$

which is compatible with no mass difference at the level of $\approx 1\%$ of the mass of the top quark.

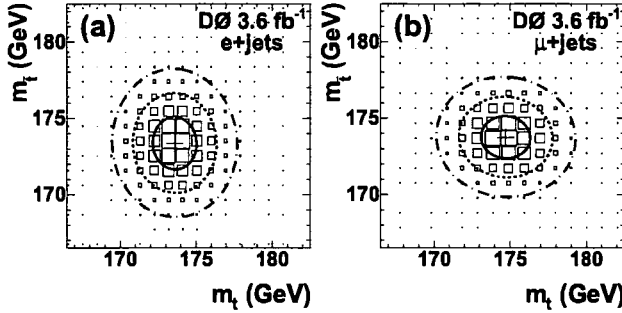


FIG. 9: Combined likelihoods of the 2.6 fb^{-1} and 1 fb^{-1} measurements as functions of m_t and $m_{\bar{t}}$ in data for the (a) $e + \text{jets}$ and (b) $\mu + \text{jets}$ channel. The bin contents are proportional to the area of the boxes. The solid, dashed, and dash-dotted lines represent the 1, 2, and 3 SD contours of two-dimensional Gaussian fits defined in Eq. (18) (corresponding to approximately 40%, 90% and 99% confidence level, respectively) to the distributions, respectively. No pull corrections have been applied, and therefore the figures are for illustrative purposes only.

I. APPENDIX: GENERATION OF $t\bar{t}$ EVENTS WITH $M_t \neq M_{\bar{t}}$

We briefly describe below the modifications to the standard PYTHIA [32] code which were necessary to generate $t\bar{t}$ events with $M_t \neq M_{\bar{t}}$. A new entry in the KF particle table is

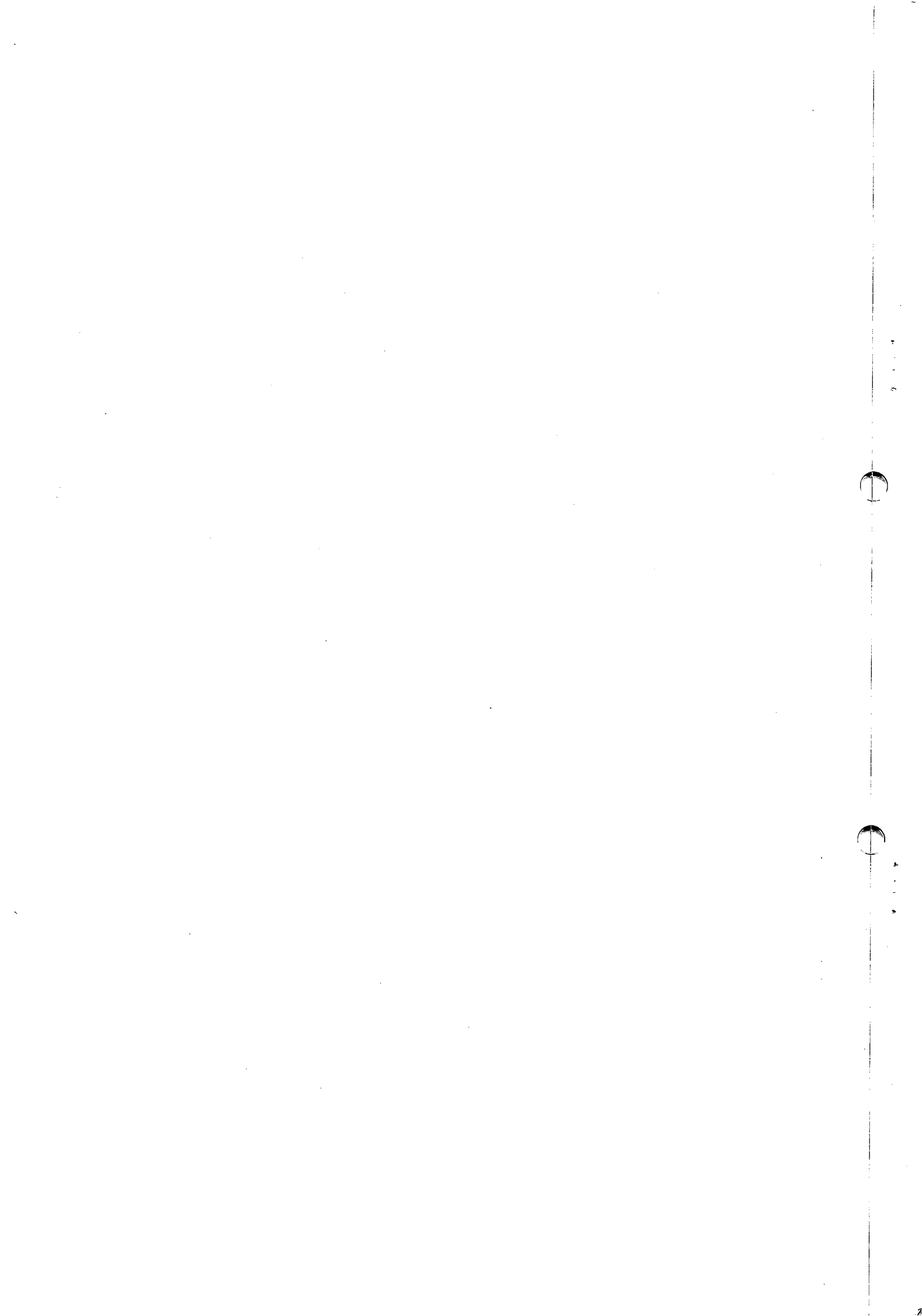
created for the \bar{t} quark. The PYINPR subroutine is modified for use cases in which one of the $t\bar{t}$ production subprocesses (ISUB = 81, 82, 84, 85) is called. The \bar{t} quark is assigned as the second final-state particle whenever a t quark is selected as the first final-state particle. Furthermore, the ordering of the first and second final-state particles are swapped, as needed, in the subroutine PYSCAT. Additional changes are made in the subroutines PYMAXI, PYRAND, and PYRESID to set the lower limit on the combined masses of the W^+ (W^-) boson and b (\bar{b}) quark to the t (\bar{t}) quark mass. Finally, the subroutine PYWIDT is modified to adjust the resonance widths Γ_t and $\Gamma_{\bar{t}}$ as functions of m_t and $m_{\bar{t}}$.

Acknowledgments

We thank the staffs at Fermilab and collaborating institutions, and acknowledge support from the DOE and NSF (USA); CEA and CNRS/IN2P3 (France); FASI, Rosatom and RFBR (Russia); CNPq, FAPERJ, FAPESP and FUNDUNESP (Brazil); DAE and DST (India); Colciencias (Colombia); CONACyT (Mexico); KRF and KOSEF (Korea); CONICET and UBACyT (Argentina); FOM (The Netherlands); STFC and the Royal Society (United Kingdom); MSMT and GACR (Czech Republic); CRC Program and NSERC (Canada); BMBF and DFG (Germany); SFI (Ireland); The Swedish Research Council (Sweden); and CAS and CNSF (China).

-
- [1] J. Schwinger, Phys. Rev. **82**, 914 (1951).
[2] G. Luders, K. Dan. Vidensk. Selsk. Mat. Fys. Medd. **28**, 5 (1954).
[3] *Niels Bohr and the Development of Physics*, ed. W. Pauli (McGraw-Hill, New York, 1955), p30.
[4] J. S. Bell, Proc. R. Soc. A **231**, 479 (1955).
[5] D. Colladay and V. A. Kostelecky, Phys. Rev. D **55**, 6760 (1997).
[6] O. W. Greenberg, Phys. Rev. Lett. **89**, 231602 (2002).
[7] K. Nakamura *et al.* (Particle Data Group), J. Phys. G **37**, 075021 (2010).
[8] J. A. R. Cembranos, A. Rajaraman, and F. Takayama, Europhys. Lett. **82**, 21001 (2008).
[9] F. Abe *et al.* (CDF Collaboration), Phys. Rev. Lett. **74**, 2626 (1995).
[10] S. Abachi *et al.* (D0 Collaboration), Phys. Rev. Lett. **74**, 2632 (1995).
[11] Tevatron Electroweak Working Group, arXiv:1007.3178 [hep-ex] (2010).
[12] V. M. Abazov *et al.* (D0 Collaboration), Phys. Rev. Lett. **103**, 132001 (2009).
[13] V. M. Abazov *et al.* (D0 Collaboration), Phys. Rev. D **74**, 092005 (2006).
[14] V. M. Abazov *et al.* (D0 Collaboration), Phys. Rev. Lett. **101**, 182001 (2008).
[15] K. Kondo, J. Phys. Soc. Jpn. **57**, 4126 (1988).
[16] R. H. Dalitz, G. R. Goldstein, and K. Sliwa, Phys. Rev. D **47**, 967 (1993).
[17] R. H. Dalitz and G. R. Goldstein, Proc. Royal Soc. London A **445**, 2803 (1999).
[18] V. M. Abazov *et al.* (D0 Collaboration), Nature **429**, 638 (2004).
[19] T. Aaltonen *et al.* (CDF Collaboration), Phys. Rev. Lett. **106**, 152001 (2011).
[20] V. M. Abazov *et al.* (D0 Collaboration), Nucl. Instrum. Meth. Phys. Res. A **565**, 463 (2006).
[21] R. Angstadt *et al.*, Nucl. Instrum. Methods Phys. Res. Sec. A **622**, 298 (2010).
[22] The previous measurement in Ref. [12] is based on data corresponding to 1 fb^{-1} of integrated luminosity recorded before the installation of Layer 0, while the new measurement presented here is based on data corresponding to 2.6 fb^{-1} of integrated luminosity recorded after this installation.
[23] D0 uses a cylindrical coordinate system with the z axis running along the proton beam axis. The angles θ and ϕ are the polar and azimuthal angles, respectively. Rapidity y and pseudorapidity η are defined as functions of the polar angle θ and parameter β as $y(\theta, \beta) \equiv \frac{1}{2} \ln[(1 + \beta \cos \theta)/(1 - \beta \cos \theta)]$ and $\eta(\theta) \equiv y(\theta, 1)$, where β is the ratio of a particle's momentum to its energy. Throughout, we define η with respect to the center of the detector.
[24] The transverse impact parameter is defined as the distance of closest approach (dca) of the track to the PV in the plane transverse to the beamline. Its significance is defined as $dca/\delta dca$, where δdca is the uncertainty on dca.
[25] S. Abachi *et al.* (D0 Collaboration), Nucl. Instrum. Meth. Phys. Res. A **338**, 185 (1994).
[26] V. M. Abazov *et al.* (D0 Collaboration), Nucl. Instrum. Meth.

- 1016 Phys. Res. A **552**, 372 (2005).
 1017 [27] M. Abolins *et al.*, Nucl. Instrum. Meth. Phys. Res. A **584**, 75047
 1018 (2008).
 1019 [28] G. C. Blazey *et al.*, in *Proceedings of the Workshop: “QCD and 1048
 1020 Weak Boson Physics in Run II,”* edited by U. Baur, R. K. Ellis, 1050
 1021 and D. Zeppenfeld (Fermilab, Batavia, IL, 2000), p. 47; see 1051
 1022 Sec. 3.5 for details, arXiv:hep-ex/0005012.
 1023 [29] V. M. Abazov *et al.* (D0 Collaboration), Phys. Rev. D **76**, 092007 1052
 1024 (2007).
 1025 [30] V. M. Abazov *et al.* (D0 Collaboration), Nucl. Instrum. Meth. Phys. Res. A **620**, 490 (2010).
 1026 [31] R. Brun and F. Carminati, CERN Program Library Long 1057
 1027 Writeup W5013, CERN, Geneva (1993).
 1028 [32] T. Sjöstrand *et al.*, J. High Energy Phys. **05**, 026 (2006).
 1029 [33] J. Pumplin *et al.*, J. High Energy Phys. **07**, 012 (2002);
 1030 D. Stump *et al.*, J. High Energy Phys. **10**, 046 (2003).
 1031 [34] M. L. Mangano, M. Moretti, F. Piccinini, R. Pittau, and 1058
 1032 A. D. Polosa, J. High Energy Phys. **07**, 001 (2003).
 1033 [35] M. L. Mangano, M. Moretti, F. Piccinini, and M. Treccani, J. 1064
 1034 High Energy Phys. **01**, 013 (2007).
 1035 [36] J. M. Campbell and R. K. Ellis, arXiv:1007.3492 [hep-ex] 1066
 1036 (2007).
 1037 [37] E. Boos *et al.* (CompHEP Collaboration), Nucl. Instrum. Meth. 1068
 1038 Phys. Res. A **534**, 250 (2004).
 1039 [38] V. M. Abazov *et al.* (D0 Collaboration), Phys. Rev. D **76**, 092007 1070
 1040 (2007).
 1041 [39] S. Moch and P. Uwer, Phys. Rev. D **78**, 034003 (2008).
 1042 [40] J. Smith, W. L. van Neerven, and J. A. M. Vermaasen, Phys. Rev. Lett. **50**, 1738 (1983).
 1043 [41] V. M. Abazov *et al.* (D0 Collaboration), submitted to PRD,
 1044
 1045 arXiv:1105.6287 [hep-ex] (2011).
 [42] G. Mahlon and S. J. Parke, Phys. Lett. B **411**, 173 (1997).
 [43] F. A. Berends *et al.*, Nucl. Phys. **B357**, 32 (1991).
 [44] R. Barlow, MAN/HEP/99/4 preprint (2000).
 [45] To check the consistency, our measured value of m_{top} is to be compared with that found in Ref. [41], but before applying the sample-dependent corrections described in Sec. VII of Ref. [41]. These corrections produce shifts of $\Delta m_{\text{top}} = 1.26 \text{ GeV}$ and $\Delta k_{\text{JES}} = -0.005$. Hence, the values of m_{top} from our analysis serve only as cross-checks, whereas the final result in Ref. [41] includes all the relevant corrections.
 [46] R. Barlow, arXiv:hep-ex/0207026 (2002).
 [47] S. Frixione and B. R. Webber, J. High Energy Phys. **06**, 029 (2002).
 [48] G. Corcella *et al.*, J. High Energy Phys. **01**, 010 (2001); G. Corcella *et al.*, arXiv:hep-ph/0210213 (2002).
 [49] A. Abulencia *et al.* (CDF Collaboration), Phys. Rev. D **73**, 032003 (2006).
 [50] P. Z. Skands and D. Wicke, Eur. Phys. J. C **52**, 133 (2007).
 [51] A. Buckley *et al.*, Eur. Phys. J. C **65**, 331 (2010).
 [52] M. G. Bowler, Z. Phys. C **11**, 169 (1981).
 [53] Y. Peters, K. Hamacher, and D. Wicke, FERMILAB-TM-2425-E (2009).
 [54] A. Kolmogorov, G. Inst. Ital. Attuari **4**, 83 (1933); N. V. Smirnov, Ann. Math. Statist. **19**, 279 (1948).
 [55] L. Lyons, D. Giabut and P. Cliffort, Nucl. Instrum. Meth. Phys. Res. A **270**, 110 (1988).
 [56] A. Valassi, Nucl. Instrum. Meth. Phys. Res. A **500**, 391 (2003).





Measurement of the top quark mass with *in situ* jet energy scale calibration in the all-hadronic channel using the Template Method with 5.8 fb^{-1}

The CDF Collaboration
URL <http://www-cdf.fnal.gov>
(Dated: March 28, 2011)

We present here the measurement of the top quark mass with simultaneous (*in situ*) calibration of the Jet Energy Scale (JES), by the Template Method in the all-hadronic channel, i.e. where both W 's decay into $q\bar{q}'$ pairs. The measurement discussed here is performed using about 5.8 fb^{-1} of $p\bar{p}$ collisions collected with a multijet trigger at $\sqrt{s} = 1.96 \text{ TeV}$ with the Collider Detector at Fermilab (CDF). The method relies on the comparison, for events selected by a Neural Network, of the reconstructed top quark and W boson masses distributions in the data to expectation from signal Monte Carlo and data-driven background events, to extract the top mass and the JES through an unbinned likelihood technique. The measurement gives a top quark mass $M_{top} = [172.5 \pm 1.4(\text{stat}) \pm 1.5(\text{syst})] \text{ GeV}/c^2$.

Preliminary Results for Winter 2011 Conferences

I. INTRODUCTION

At Fermilab, top quarks are mainly pair produced in $p\bar{p}$ collisions via $q\bar{q}$ annihilation (85%) and gluon-gluon fusion (15%). According to the Standard Model, the top quarks decay into W bosons and b quarks with a branching ratio (BR) about equal to 1. In this analysis we search for events in which both W bosons decay into quark pairs, leading to an all-hadronic final state. This channel has the advantage of the largest BR , about 44%, and of the fully reconstructed kinematics. The major downside is the huge background from QCD multijet production which dominates the signal by three orders of magnitude even after the application of the specific top multijet trigger. A sophisticated event selection based on kinematical and topological variables, followed by the request of identified b -jets, is thus needed in order to further improve the signal to background ratio (S/B).

We present here a measurement of the top quark mass performed using about 5.8 fb^{-1} of data. Distributions (templates) of variables sensitive to the main observables we want to measure, i.e. the top mass (M_{top}) and the jet energy scale (JES), are built and used to discriminate the possible values of these variables. At the same time, the differences between signal and background distributions allow to estimate the respective average contributions to the observed events, so that the measurement can be obtained by maximizing a likelihood fit of the data to the signal and background templates. As we use templates to measure, above all, two quantities simultaneously, i.e. M_{top} and JES, the technique is referred to as TMT2D (Top Mass Templates 2-Dimensional measurement). The reliability of the method, its expected performance and the main sources of systematic uncertainties have been evaluated by large sets of simulated experiments (*pseudo-experiments*) before the actual measurement on the data.

II. EVENT SELECTION

All data and simulated Monte Carlo events, previously selected by a multijet trigger, have to pass some prerequisites which require a well centered primary vertex and no lepton with high transverse momentum (p_T) identified in the event. The events satisfying this first selection are then required to have a number of detected “tight” jets (i.e. jets with $E_T \geq 15 \text{ GeV}$, $|\eta| \leq 2.0$) between 6 and 8 with a minimum distance between each pair of jets in the (η, ϕ) plane (ΔR_{min}) larger than 0.5, and no significant missing transverse energy. A number of kinematic variables are then reconstructed using tight jets and serve as inputs to a neural network with 13 input variables, one hidden layer and one output layer. As described in [1], the 13 inputs include both variables depending on energy and direction of jets, and also on their shape. The latter are very effective in distinguishing jets produced by light flavor quark (present in signal events) from the wider jets initiated by gluons, in principle typical of background events only.

Events are selected if the output value from the neural network, N_{out} , exceeds a given threshold. Finally we require the presence of jets tagged as b -jets among the six leading jets, and subdivide our sample in events with exactly one tagged jet (1-tag sample) and two or three tagged jets (≥ 2 -tags sample). A jet is tagged if some of its tracks form a secondary vertex significantly displaced from the interaction point. Different values of the N_{out} threshold are chosen for the two categories of tagged events, in such a way to maximize the statistical significance of the mass measurement, as described in section VI.

On signal Monte Carlo samples, generated with values of M_{top} in the range between 160 and $185 \text{ GeV}/c^2$, the event selection is repeated changing the value of the JES from $-2\sigma_{\text{JES}}$ to $+2\sigma_{\text{JES}}$, in steps of $0.5\sigma_{\text{JES}}$, with respect to its central value as measured in [2], where σ_{JES} is the uncertainty on that value itself. In the following we then evaluate the JES in terms of its displacement, Δ_{JES} , from the nominal value (corresponding therefore to $\Delta_{\text{JES}} = 0\sigma_{\text{JES}}$) and using σ_{JES} as the unit.

III. BACKGROUND MODELING

The background consists mainly of QCD production of light and heavy flavor quarks. Its modeling and estimate are data-driven and based on a tag rate parametrization derived in a sample of events with exactly 5 jets and therefore dominated by the background. The probability to tag a jet is ~~parametrized according to the jet- E_T , jet track multiplicity, and number of well-defined vertices in the event~~, and can then be applied to taggable jets (i.e. jets accepted by the b -tagging algorithm) identified in events selected by the kinematic requirements, to evaluate the inclusive number of tagged jets originating from background events. Direct exploitation of the tag rate matrix to predict the number of background events with a given number of tags would give incorrect numbers because the matrix, by construction, refers to an inclusive tagging probability and does not consider that in QCD background real heavy flavour quarks come in pairs and have therefore an enhanced double-tagging probability, so that the probability to tag a pair of jets in the same event is not simply equal to the product of the tag rates of single jets.

$$P(E_T; \underset{\text{jet}}{\text{mult}}, \underset{\text{vertex}}{\text{#}})$$

To account for this we introduce correction factors to obtain a better estimate for the number of 1-tag and ≥ 2 -tags events. These factors are derived in a control sample dominated by the background (events with 6-8 jets and $N_{out} \leq 0.25$, where the signal contribution is negligible) and represent average corrections to the probability for a possible “tag configuration”, that is for the assumption that given taggable jets in an event in the pretag sample are the only tagged jets in the same event after b -tagging.

The data-driven background prediction must be performed starting from events in the pretag sample, but, as this contains also events from $t\bar{t}$ signal, the raw prediction must be corrected to take these into account.

IV. BUILDING TEMPLATES

The $t\bar{t}$ events under study in this work are characterized by the nominal presence of 6 quarks in the final states, two of which are b -quarks. Therefore, the signal signature would ideally consist of 6 reconstructed jets in the detector, with some being tagged as b -jets. We want to fully reconstruct the kinematics of events passing the kinematical selection, partially described in section II, and exploit the presence of the W and top quark to constrain the event topology. In order to do so we consider only the 6 leading (in E_T) jets in the event to limit the number of ways in which we can combine the jets to reconstruct the events. There are 90 possible permutations of jet-to-parton association with two jet doublets giving a W and two jet triplets giving the top quarks. Since we consider only events with tagged jets, we further reduce the number of permutations by requiring the association of the b -tagged jets to a b quark; we are therefore left with 30 possible parton-jet assignment in 1-tag sample, and 6 or 18 in the ≥ 2 -tags sample[12].

A. m_t^{rec} templates

We reconstruct the kinematic of the event by a fit based on the following χ^2 -like quantity:

$$\chi^2 = \frac{(m_{jj}^{(1)} - M_W)^2}{\Gamma_W^2} + \frac{(m_{jj}^{(2)} - M_W)^2}{\Gamma_W^2} + \frac{(m_{jjb}^{(1)} - m_t^{rec})^2}{\Gamma_t^2} + \frac{(m_{jjb}^{(2)} - m_t^{rec})^2}{\Gamma_t^2} + \sum_{i=1}^6 \frac{(p_{T,i}^{fit} - p_{T,i}^{meas})^2}{\sigma_i^2}$$

where $m_{jj}^{(1,2)}$ are the invariant masses of the dijet systems assigned to light flavor quarks, $m_{jjb}^{(1,2)}$ are the invariant masses of the trijet systems including one b -quark, $M_W = 80.4 \text{ GeV}/c^2$ and $\Gamma_W = 2.1 \text{ GeV}/c^2$ are the measured mass and natural width of the W boson [4], and $\Gamma_t = 1.5 \text{ GeV}/c^2$, is the assumed natural width of the top quark. The measured jet transverse momenta, $p_{T,i}^{meas}$ are free to vary within their known resolution, σ_i . The measured jet transverse momenta can vary, but are constrained to the measured value, $p_{T,i}^{meas}$, within their known resolution, σ_i .

For each permutation of the jet-to-parton assignments in the event, the χ^2 is minimized with respect to 7 free parameters, i.e. the reconstructed top quark mass, m_t^{rec} , and the 6 jets transverse momenta $p_{T,i}^{fit}$ and the combination which gives the lowest χ^2 value is selected. The m_t^{rec} value corresponding to this permutation enters an invariant mass distribution, i.e. the template which will serve as a reference for the M_{top} measurement. This procedure is repeated on selected signal Monte Carlo events with all the different input values of M_{top} and ΔJES and, to parametrize the dependence of the m_t^{rec} templates on these variables, we perform a fit of the distributions to functional forms which vary smoothly with respect to these variables. So, we obtain probability density functions (p.d.f.’s) which we will use to form an unbinned likelihood for the final measurement. The signal p.d.f., $P_s^{m_t^{rec}}(m_t|M_{top}, \Delta\text{JES})$, represents the probability to obtain a value m_t for m_t^{rec} , given a true top quark mass M_{top} and a true value ΔJES of the displacement of the jet energy scale, in a $t\bar{t}$ event.

B. m_W^{rec} templates

Reconstructing the mass of W bosons by dijet systems represents a possibility to obtain a variable in principle insensitive to M_{top} which allows, therefore, a determination of JES not dependent on M_{top} itself.

To build the m_W^{rec} templates we use the same procedure and χ^2 expression considered for m_t^{rec} templates, but now also the W mass is left as a free parameter in the fit (i.e. M_W becomes m_W^{rec}). Again, for each event, the value of m_W^{rec} corresponding to the permutation of the jet-to-parton assignments with the lowest χ^2 enters the template, and this procedure is repeated on selected signal Monte Carlo events with all the different input values of M_{top} and ΔJES . Like for m_t^{rec} , also the m_W^{rec} templates need to be parametrized by functions depending on M_{top} and ΔJES . The m_W^{rec} p.d.f., $P_s^{m_W^{rec}}(m_W|M_{top}, \Delta\text{JES})$, represents the probability to obtain a value m_W for m_W^{rec} , given true inputs M_{top} and ΔJES , in a $t\bar{t}$ event.

C. Background m_t^{rec} and m_W^{rec} templates

As in the case of background normalization, we must build background m_t^{rec} and m_W^{rec} templates considering events and taggable jets (instead of tagged ones) in the pretag sample. In particular all the possible combinations where 1, 2, or 3 taggable jets among the 6 leading jets are *assumed* as tagged must be considered, and, for each combination, the same procedures described in sections IV A and IV B must then be repeated to extract corresponding values of m_t^{rec} and m_W^{rec} . These values then enter the templates weighted by the *corrected* probability (see section III) that the jets assumed as tagged in the combination are effectively the tagged ones in the event after b -tagging. Corrections for the presence of signal events in the pretag sample must be taken into account, and the corresponding contribution to the shape subtracted. No dependence on M_{top} and JES is considered for the background templates, but effects of differences due to corrections performed by signal events corresponding to different values of these variables are taken into account by the calibration procedure (section VIII B). The background p.d.f.'s, $P_b^{m_t^{rec}}(m_t)$ and $P_b^{m_W^{rec}}(m_W)$, represent the probabilities to obtain values m_t for m_t^{rec} and m_W for m_W^{rec} respectively, in a background event.

V. BACKGROUND VALIDATION

In order to check how properly our modeling describes the background, we consider events in control regions defined by the N_{out} value, in ranges where the signal presence after tagging is still very low. In these regions the templates, i.e. the distributions which are essential to our measurement, are reconstructed by the procedure described in the previous sections both for the signal and the background. As the final selections of the data samples include cuts on the N_{out} value and on the χ^2 of the fits used to build the m_W^{rec} and m_t^{rec} templates (denoted in the following by $\chi^2(m_W^{rec})$ and $\chi^2(m_t^{rec})$ respectively), as it will be described in section VI, also these distributions are really important. Obviously, as it concerns the background, they must be evaluated by the same procedure of weighting each assumed possible configuration with 1, 2 or 3 tagged jets described in section IV C for the templates.

The agreement between expected and observed distributions is rather good in all the control regions, and this confirms the reliability of the background model. In Fig. 1 the output of the neural network over the whole range of values $N_{out} > 0.5$ is shown, while Figs 2 and 3 show distributions of $\chi^2(m_W^{rec})$, $\chi^2(m_t^{rec})$, m_W^{rec} and m_t^{rec} in one of the control regions both for 1-tag and ≥ 2 -tags events, where the sum of signal and background is compared to the same distributions reconstructed in the data. In these plots the signal distributions corresponding to $M_{top} = 172.5 \text{ GeV}/c^2$ and $\Delta\text{JES} = 0 \sigma_{\text{JES}}$ have been normalized assuming $\sigma_{t\bar{t}} = 7.45 \text{ pb}$ [3], while the amount of background events corresponds to the difference between the number of observed events and the expected signal.

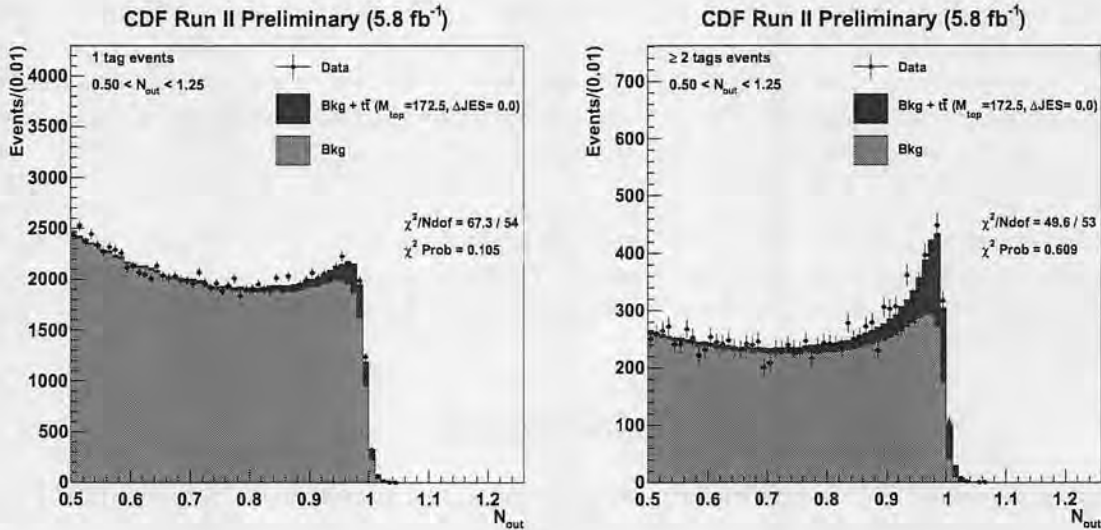


FIG. 1: Distributions of the output from the Neural Net, N_{out} , for 1-tag events, left plot, and ≥ 2 -tags events, right plot, are shown in the whole region defined by $N_{out} > 0.5$. Along with the data are plotted the corrected expected background and the signal contribution. We see that the agreement is generally good. The value of the purely statistical χ^2 probability is also reported on each plot.

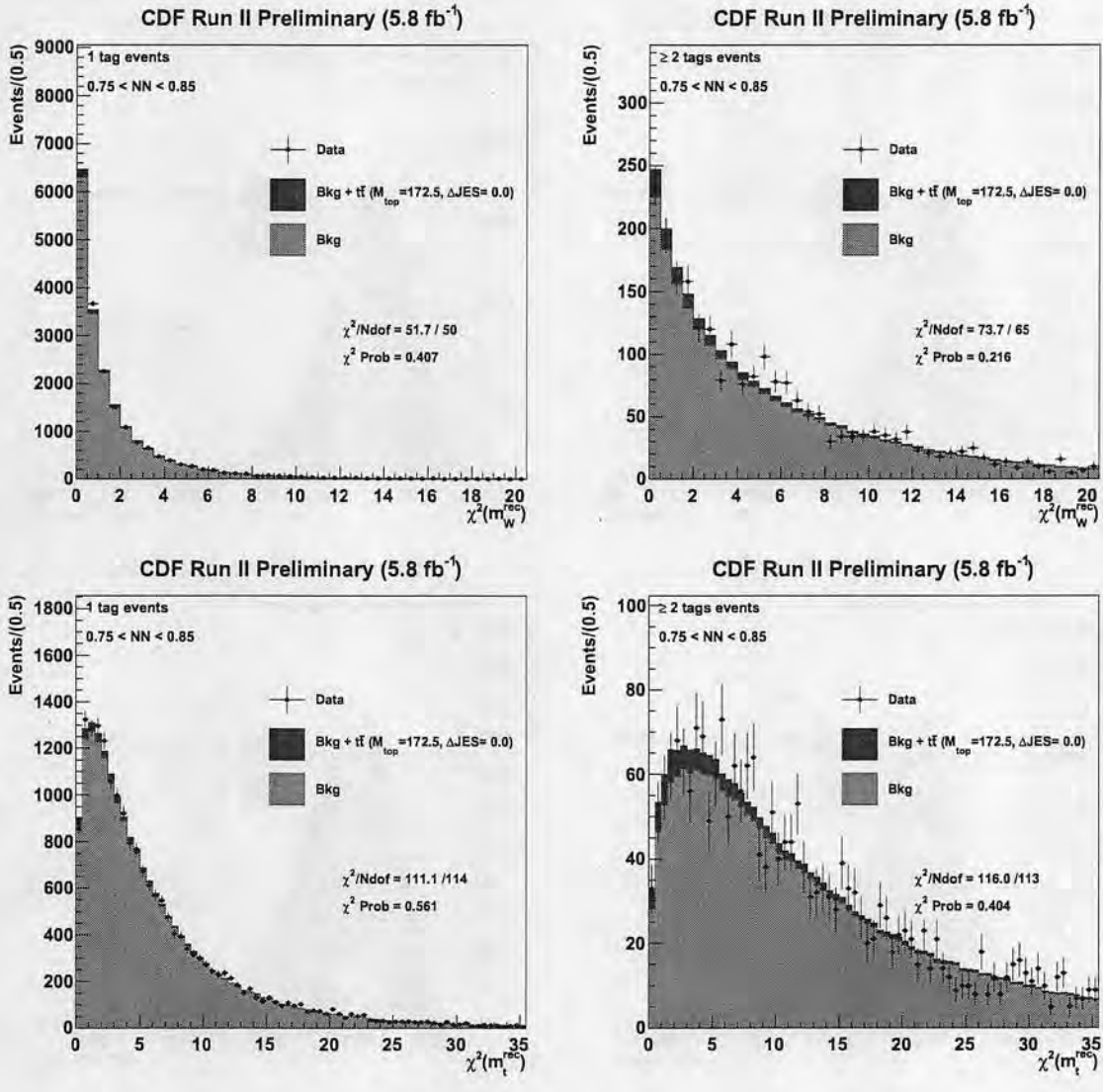


FIG. 2: Distributions of the χ^2 of the fit used to build the m_W^{rec} (upper plots) and m_t^{rec} (lower plots) templates, are shown in a control region defined by $0.75 \leq N_{out} < 0.85$ both for 1-tag events, left plots and ≥ 2 -tags events, right plots. Along with the data are plotted the corrected expected background and the signal contribution. We see that the agreement is generally good. The value of the purely statistical χ^2 probability is also reported on each plot.

VI. EVENTS SAMPLES

In order to obtain the best performance from our method, we performed sets of pseudo-experiments (PEs) to find the requirements on the values of N_{out} , $\chi^2(m_W^{rec})$, and $\chi^2(m_t^{rec})$ which minimize the statistical uncertainty on the top mass measurement.

Two different samples of events, denoted by S_{JES} and $S_{M_{top}}$, are defined and used to build the m_W^{rec} and m_t^{rec} templates respectively. The set S_{JES} is selected by requirements on N_{out} and $\chi^2(m_W^{rec})$, while $S_{M_{top}}$ by a further requirement on $\chi^2(m_t^{rec})$, so that $S_{M_{top}} \subseteq S_{JES}$. As S_{JES} is somehow used to calibrate the JES, while $S_{M_{top}}$ is more strictly related to the top quark mass measurement, we also refer to S_{JES} and $S_{M_{top}}$ as “JES-sample” and “ M_{top} -sample” respectively.

The procedure used in PEs to obtain the cuts optimization is totally similar, being a simplified version, to the one described in section VIII A exploiting a binned version of the same likelihood function. It is applied separately to 1-tag and ≥ 2 -tags samples and considers many different combinations $\{N_{out}, \chi^2(m_W^{rec}), \chi^2(m_t^{rec})\}$ of cuts. The smallest values of uncertainties are obtained using $\{N_{out} \geq 0.97, \chi^2(m_W^{rec}) \leq 2, \chi^2(m_t^{rec}) \leq 3\}$ in the 1-tag sample

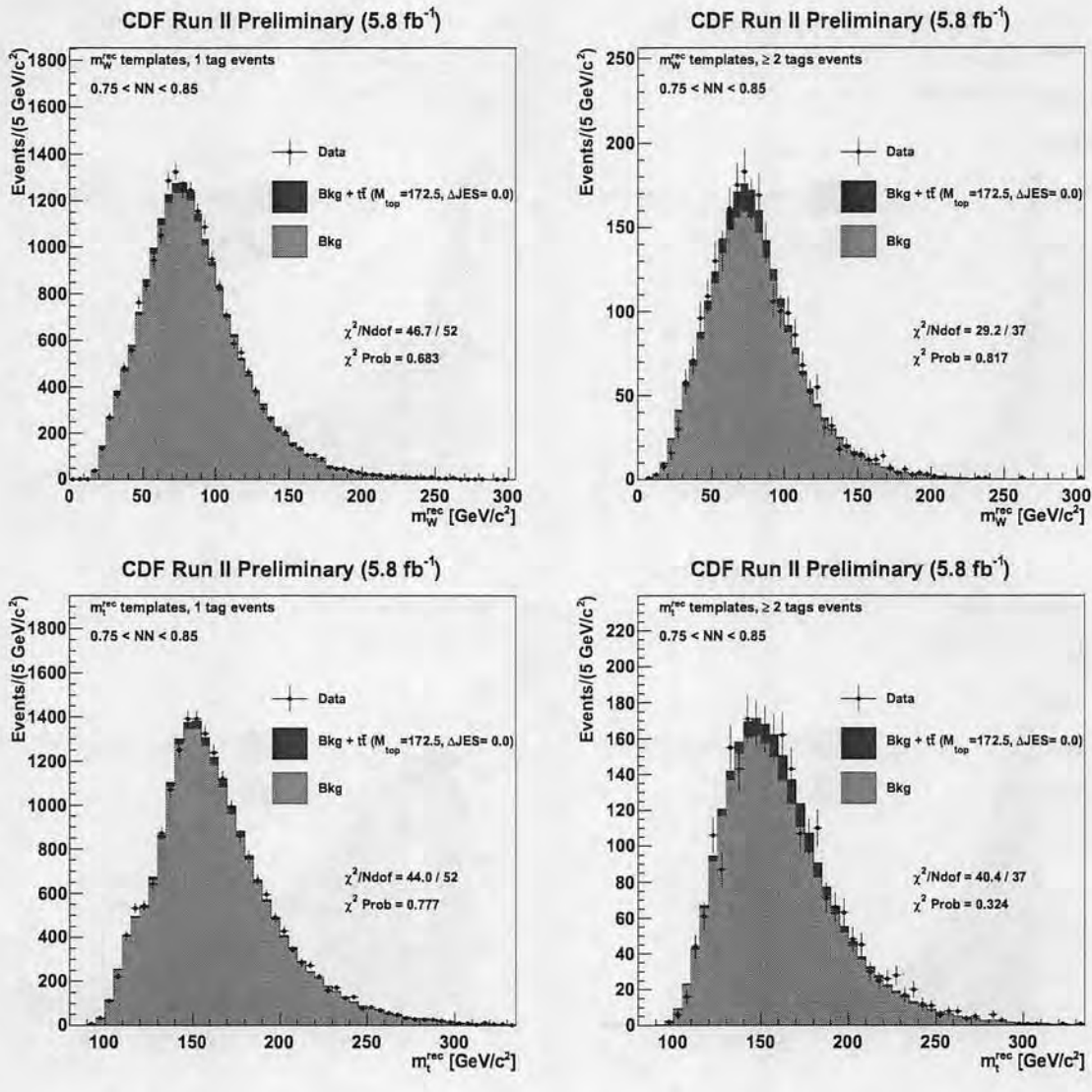


FIG. 3: Templates of the reconstructed W mass, m_W^{rec} (upper plots), and top quark mass, m_t^{rec} (lower plots), are shown in a control region defined by $0.75 \leq N_{\text{out}} < 0.85$ both for 1-tag events, left plots, and ≥ 2 -tags events, right plots. Along with the data are plotted the corrected expected background and the signal contribution. We see that the agreement is generally good. The value of the purely statistical χ^2 probability is also reported on each plot.

and $\{N_{\text{out}} \geq 0.94, \chi^2(m_W^{\text{rec}}) \leq 3, \chi^2(m_t^{\text{rec}}) \leq 4\}$ in the ≥ 2 -tags sample.

We therefore finally set, besides the prerequisites described in section II:

- 1-tag events :
 - S_{JES} sample: $N_{\text{out}} \geq 0.97, \chi^2(m_W^{\text{rec}}) \leq 2$ and 1 tagged jet;
 - $S_{M_{\text{top}}}$ sample: $N_{\text{out}} \geq 0.97, \chi^2(m_W^{\text{rec}}) \leq 2, \chi^2(m_t^{\text{rec}}) \leq 3$ and 1 tagged jet;
- ≥ 2 -tags events :
 - S_{JES} sample: $N_{\text{out}} \geq 0.94, \chi^2(m_W^{\text{rec}}) \leq 3$ and 2 or 3 tagged jets;
 - $S_{M_{\text{top}}}$ sample: $N_{\text{out}} \geq 0.94, \chi^2(m_W^{\text{rec}}) \leq 3, \chi^2(m_t^{\text{rec}}) \leq 4$ and 2 or 3 tagged jets;

as the requirements and the samples to be used in our analysis.

For $t\bar{t}$ events corresponding to $M_{top} = 172.5 \text{ GeV}/c^2$ and $\Delta\text{JES} = 0 \sigma_{\text{JES}}$, the values of the efficiencies of the JES-sample selections are 2.1% and 1.1% for 1-tag and ≥ 2 -tags respectively, while for the corresponding M_{top} -samples we obtain 1.4% and 0.7%. For the same M_{top} and ΔJES , the fraction of events of the JES-sample selected by the requirements on $\chi^2(m_t^{\text{rec}})$ only, and therefore belonging to the M_{top} -sample, are 68.5% and 67.6%, as can be inferred by the ratios of the absolute efficiencies. These latter acceptances will be denoted by \mathcal{A}_s in the following and their values generally depend on M_{top} and ΔJES .

A. Expected background

Given the final requirements we can evaluate, as described in section III, the average amounts of background events expected in the selected samples. As already mentioned, the raw prediction obtained applying the corrected tag rate on jets and events of the pretag data sample, must be corrected for the presence of $t\bar{t}$ events. The correction to obtain central values is performed assuming $M_{top} = 172.5 \text{ GeV}/c^2$, $\Delta\text{JES} = 0 \sigma_{\text{JES}}$ and the theoretical signal cross section as calculated in [3]. Uncertainties due to these assumptions are taken into account, together with the discrepancy between the observed number of events in the data and the sum of the predicted background and the expected contribution from the signal.

The numbers of expected background events are summarized in Tab. I, together with the observed data and expected signal selected for this analysis.

| Sample | N_{obs} | Exp Bkg (B) | Exp $t\bar{t}$ (S) ($M_{top} = 172.5$, $\Delta\text{JES} = 0$) | S/B |
|----------------|---------------|-----------------|--|--------------|
| 1-tag | S_{JES} | 4368 | 3652 ± 181 | 881 ± 73 |
| | $S_{M_{top}}$ | 2256 | 1712 ± 77 | 604 ± 50 |
| ≥ 2 -tags | S_{JES} | 1196 | 718 ± 14 | 468 ± 38 |
| | $S_{M_{top}}$ | 600 | 305 ± 22 | 316 ± 26 |

TABLE I: Numbers of observed data (N_{obs}) and expected amount of background and signal events in the samples selected for this analysis. The signal-to-background ratios (S/B) are also shown.

From these values we can derive also for the background the values of the acceptances \mathcal{A}_b , given by the ratios of the number of events expected in the M_{top} and JES samples. Taking into account the correlations among the uncertainties we obtain $\mathcal{A}_b = (46.9 \pm 0.7)\%$ for 1-tag events and $\mathcal{A}_b = (42.5 \pm 3.6)\%$ for ≥ 2 -tags events.

B. Parametrizations

Having defined the best requirements for this analysis, we can proceed to build the signal and background templates from events in the selected samples and, for the signal, to parametrize their dependence on M_{top} and ΔJES into smooth probability density functions. The method have been already described in section IV. Figures 4 and 5 show the fitted p.d.f.'s superimposed to the m_t^{rec} and m_W^{rec} signal templates respectively for different M_{top} and ΔJES values.

The background m_t^{rec} and m_W^{rec} templates and the corresponding fitted parametrized p.d.f.'s for the signal region are shown in Figure 6 both for 1-tag and ≥ 2 -tags events.

For signal events, also the acceptances \mathcal{A}_s defined in section VI depend on M_{top} and ΔJES , with values in the range between 60% and 70% in the ranges $160 \leq M_{top} \leq 185$ and $-2 \leq \Delta\text{JES} \leq +2$. Therefore, as they appear in the likelihood function described in section VII, also their values must be parametrized and this is done by polynomial functions.

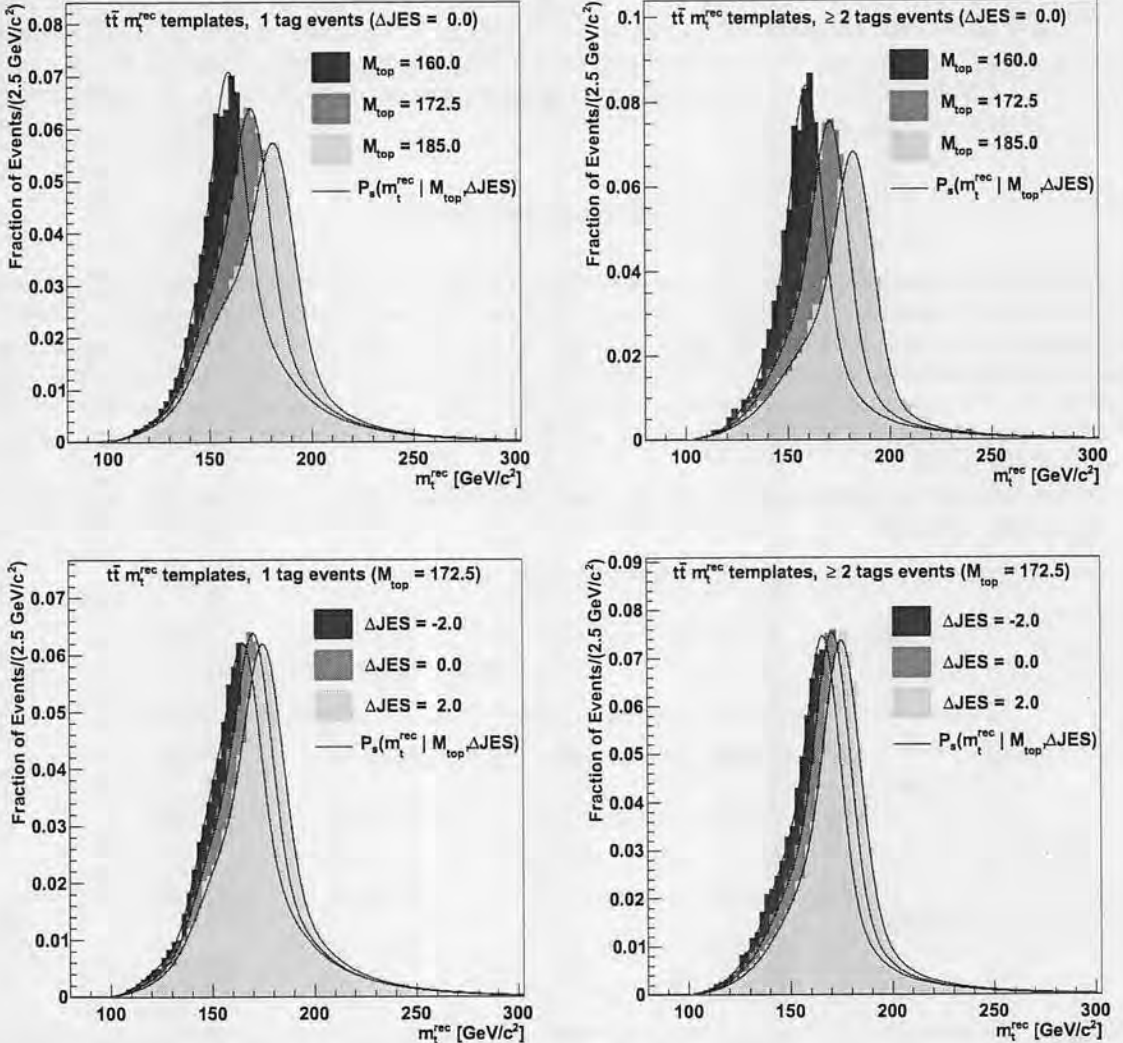


FIG. 4: Probability density functions for the signal m_t^{rec} templates for 1-tag (left plots), and ≥ 2 -tags events (right plots) for a constant ΔJES value ($0 \sigma_{JES}$), but varying the input top quark mass (upper plots) and for a constant M_{top} value ($172.5 \text{ GeV}/c^2$), but varying the input jet energy scale (lower plots).

VII. LIKELIHOOD

The simultaneous measurement of the top quark mass and the jet energy scale by the template method (TMT2D) consists in finding the values of M_{top} , JES, and the number of signal (n_s) and background (n_b) events for each tagging category which best reproduce the observed distributions of m_t^{rec} and m_W^{rec} , as reconstructed in the selected data samples, given the p.d.f.'s expected for signal and background.

This is done by performing a fit where a likelihood function is maximized, or, equivalently, its negative logarithm is minimized. This function is divided into 3 main parts: the first two terms are the ones strictly needed for the M_{top} and the JES *in situ* measurements, where the probability for the observed distributions are calculated as a function of the free parameters (M_{top} , ΔJES , n_s^{1tag} , n_b^{1tag} , $n_s^{\geq 2tags}$ and $n_b^{\geq 2tags}$) for the two tagging categories, taking also into account the *a priori* expectation for the background normalizations and their errors, while the third one constrains the JES parameter to the *a priori* independent measurement [2] (i.e. $\Delta JES = 0 \sigma_{JES}$ in our notation) to reduce the uncertainty on this variable.

Namely the likelihood, \mathcal{L} , is written as:

$$\mathcal{L} = \mathcal{L}_{1tag} \times \mathcal{L}_{\geq 2tags} \times \mathcal{L}_{\Delta JES_{constr}}$$

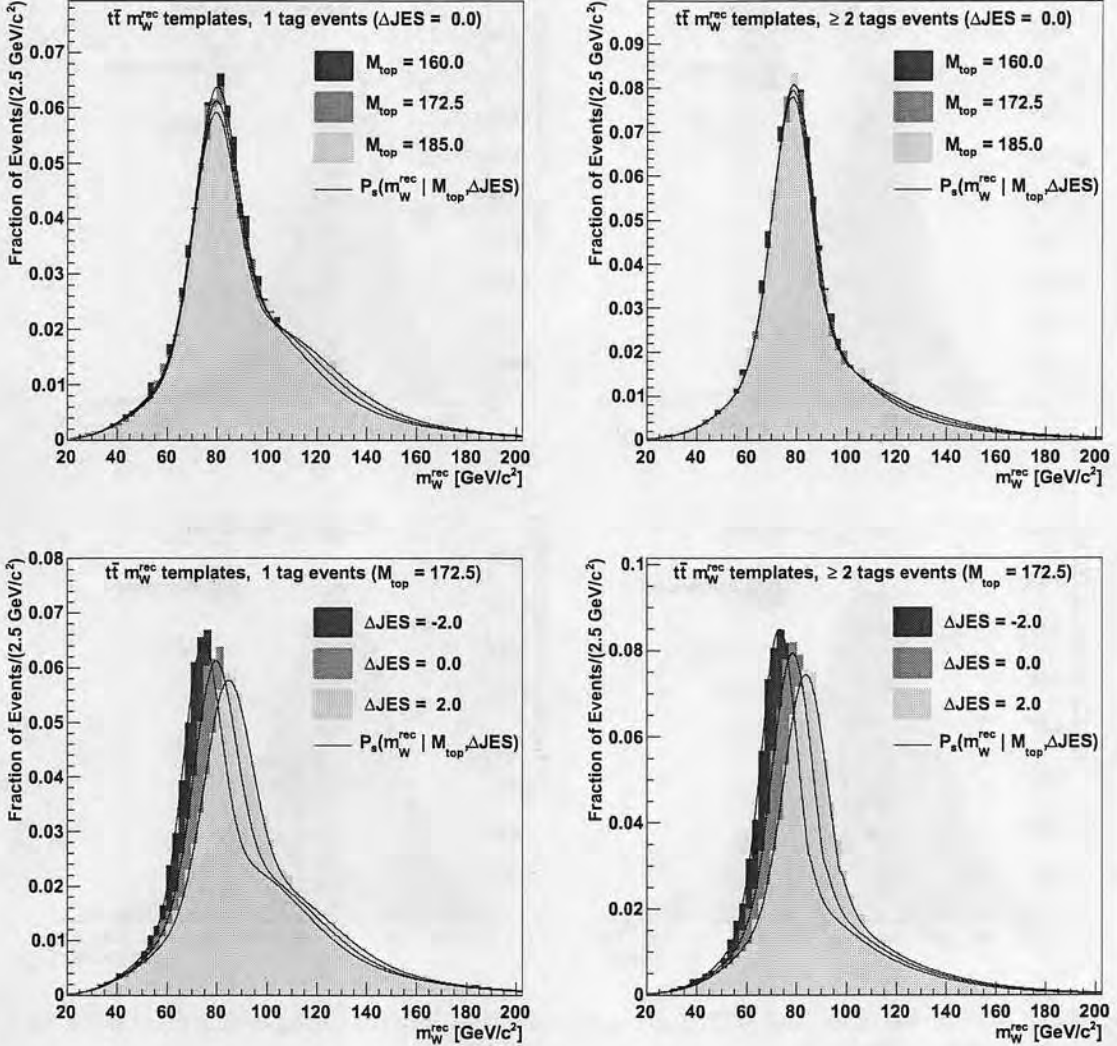


FIG. 5: Probability density functions for the signal m_W^{rec} templates for 1-tag (left plots), and ≥ 2 -tags events (right plots) for a constant ΔJES value ($0 \sigma_{\text{JES}}$), but varying the input top quark mass (upper plots) and for a constant M_{top} value ($172.5 \text{ GeV}/c^2$), but varying the input jet energy scale (lower plots).

The $\mathcal{L}_{1,\geq 2 \text{ tags}}$ terms further consist of other factors:

$$\mathcal{L}_{1,\geq 2 \text{ tags}} = \mathcal{L}_{\Delta \text{JES}} \times \mathcal{L}_{M_{top}} \times \mathcal{L}_{\text{evts}} \times \mathcal{L}_{N_{\text{constr}}^{\text{bkg}}}$$

where the four terms assume the following form (the superscripts referring to the tag sample are omitted):

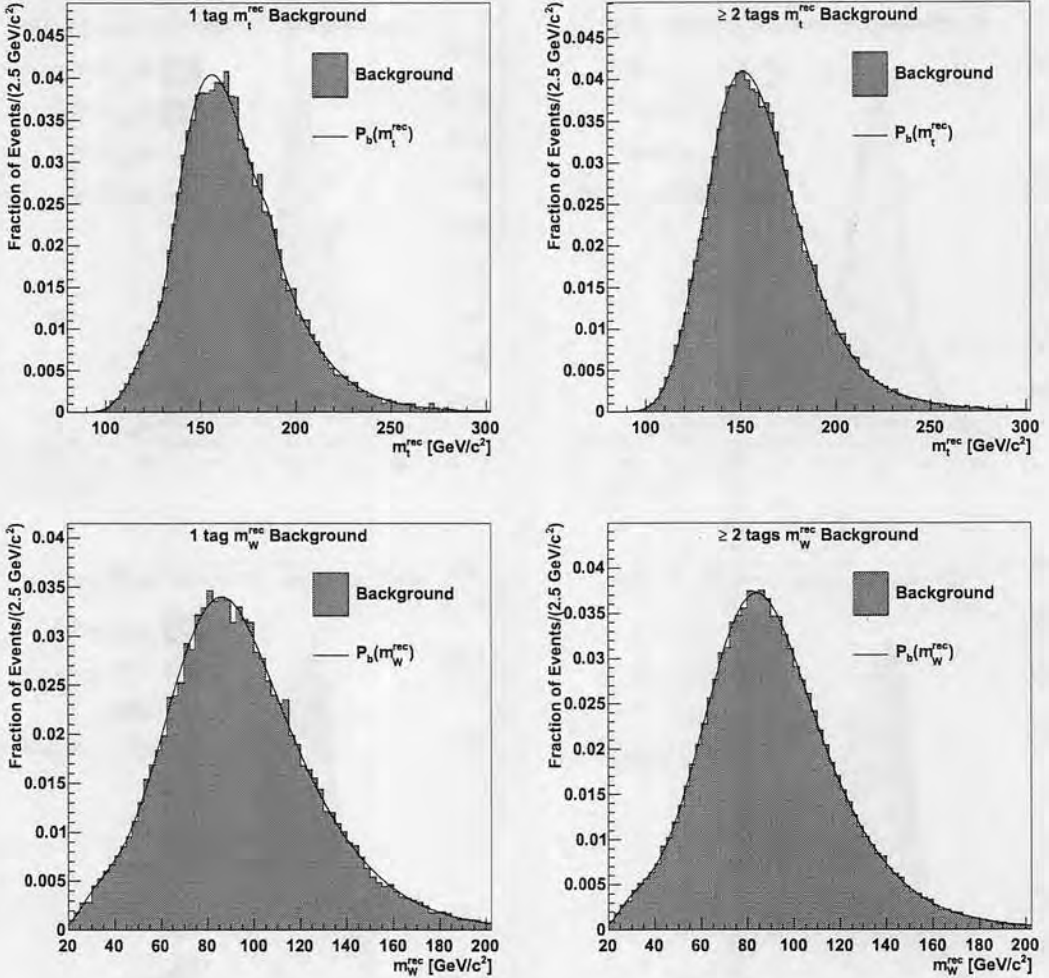


FIG. 6: Background m_t^{rec} (upper plots) and m_W^{rec} (lower plots) templates with the corresponding fitted p.d.f. for 1-tag events, left plots, and ≥ 2 -tags events, right plots.

$$\begin{aligned}
 \mathcal{L}_{\Delta JES} &= \prod_{i=1}^{N_{obs}^{S_{JES}}} \frac{n_s \cdot P_s^{m_W^{rec}}(m_{W,i} | M_{top}, \Delta JES) + n_b \cdot P_b^{m_W^{rec}}(m_{W,i})}{n_s + n_b} \\
 \mathcal{L}_{M_{top}} &= \prod_{i=1}^{N_{obs}^{S_{M_{top}}}} \frac{\mathcal{A}_s(M_{top}, \Delta JES) \cdot n_s \cdot P_s^{m_t^{rec}}(m_{t,i} | M_{top}, \Delta JES) + \mathcal{A}_b \cdot n_b \cdot P_b^{m_t^{rec}}(m_{t,i})}{\mathcal{A}_s(M_{top}, \Delta JES) \cdot n_s + \mathcal{A}_b \cdot n_b} \\
 \mathcal{L}_{events} &= \sum_{r_s+r_b=N_{obs}^{S_{JES}}} P(r_s, n_s) \cdot P(r_b, n_b) \cdot \left[\sum_{\substack{t_s \leq r_s, t_b \leq r_b \\ t_s+t_b=N_{obs}^{S_{M_{top}}}}} B(t_s, r_s, \mathcal{A}_s) \cdot B(t_b, r_b, \mathcal{A}_b) \right] \\
 \mathcal{L}_{N_{constr}^{bkg}} &= e^{-\frac{(n_b - n_{(b, exp)})^2}{2\sigma_{n_{(b, exp)}}^2}}
 \end{aligned}$$

In the first term the probability to observe the set $m_{W,i}$, ($i = 1, \dots, N_{obs}^{S_{JES}}$) of m_W^{rec} values reconstructed in the data JES-sample is calculated by the signal and background p.d.f.'s, $P_s^{m_W^{rec}}$ and $P_b^{m_W^{rec}}$ respectively, as a function of the free

parameters of the fit. In the second the same is done for the distributions of the observed reconstructed top masses in the M_{top} -sample $m_{t,i}$, ($i = 1, \dots, N_{obs}^{S_{M_{top}}}$), and the m_t^{rec} p.d.f.'s. The third term, \mathcal{L}_{evts} , gives the probability to observe simultaneously the number of events selected in the data for the JES-sample and the M_{top} -sample, given the assumed values for the average number of signal (n_s) and background (n_b) events to be expected in S_{JES} and the acceptances $\mathcal{A}_s(M_{top}, \Delta JES)$ and \mathcal{A}_b . It depends on the Poisson (P) and Binomial (B) probabilities

$$P(r, n) = \frac{e^{-n} \cdot n^r}{r!}$$

$$B(t, r, \mathcal{A}) = \binom{r}{t} \cdot \mathcal{A}^t \cdot (1 - \mathcal{A})^{r-t}$$

In the last term, $\mathcal{L}_{N_{constr}^{bg}}$, the parameter n_b is constrained by a Gaussian to the *a priori* background estimate given in section VI A, i.e. $n_{(b, exp)} = 3652 \pm 181$ for 1-tag events and $n_{(b, exp)} = 718 \pm 14$ for ≥ 2 -tags events.

Finally, $\mathcal{L}_{\Delta JES_{constr}}$ is a Gaussian term constraining the parameter JES to the value measured and reported in [2], which is equivalent, in our notation, to constrain the parameter ΔJES to 0:

$$\begin{aligned} \mathcal{L}_{\Delta JES_{constr}} &= e^{-\frac{(\text{JES} - \text{JES}_{constr})^2}{2\sigma_{\text{JES}}^2}} \\ &= e^{-\frac{[(\text{JES}_{constr} + \Delta \text{JES} \cdot \sigma_{\text{JES}}) - \text{JES}_{constr}]^2}{2\sigma_{\text{JES}}^2}} \\ &= e^{-\frac{[\Delta \text{JES}]^2}{2}} \\ &= e^{-\frac{[\Delta \text{JES} - \Delta \text{JES}_{constr}]^2}{2}} \end{aligned}$$

where, generally, $\Delta \text{JES}_{constr} = 0$.

In order to facilitate the computation, we minimize the negative logarithm of the likelihood using MINUIT. The uncertainties on the parameters are given by MINOS taking positive and negative statistical error as the difference between the observable (O) central value and the values O^+ and O^- for which stands the relation $-\ln L(O^\pm) + \ln L(O) = -1/2$. Following [5] we then take as unique, symmetric errors the average between O^+ and O^- for each parameter. By construction, the MINOS uncertainties take into account the correlations among all the parameters, so that the error on each fitted variable includes both the statistical contribution and the systematic one due to the uncertainties on the other parameters.

VIII. SANITY CHECKS AND EXPECTED PERFORMANCE

We want to investigate the possible presence of biases in the top mass and jet energy scale measurements introduced by our method, as well as to have an estimate of the TMT2D method statistical power before performing the measurement on the actual data sample. To do so, we run realistic pseudo-experiments where “pseudo-data” are extracted from simulated signal and data-driven background templates corresponding to known values of M_{top} and ΔJES (M_{top}^{in} , ΔJES^{in}) and used as inputs to the likelihood fit to perform the measurement. Also the other parameters of the fit, i.e. the average numbers of input signal and background events, are modified. The results obtained from the fit can then be compared to the true values of the input parameters to study the behavior of the machinery.

A. Pseudo-experiments setup

Sets of about 2000 PEs have been performed at many “points” in the six-dimensional space of the fit parameters. Actually, given the practical impossibility to consider all the possible simultaneous variations of the parameters, we vary pairs of variables, grouping together the two with the largest mutual correlation, while the remaining ones are kept constant to their central values. In particular sets of PEs have been performed with variations of the pairs $\{M_{top}^{in}, \Delta JES^{in}\}$, $\{n_s^{1\text{ tag}, in}, n_b^{1\text{ tag}, in}\}$, and $\{n_s^{\geq 2\text{ tags}, in}, n_b^{\geq 2\text{ tags}, in}\}$.

The procedure is the same for each PE of any set:

1. For each tagging category we generate the actual number $N_{(s, obs)}^{S_{JES}}$ of signal events in the JES-sample by a Poisson distribution with mean n_s^{in} , i.e. the n_s input value; the same is repeated for the actual number of background events $N_{(b, obs)}^{S_{JES}}$, by using a Poisson with mean n_b^{in} .

2. The number of signal events in the M_{top} -sample, $N_{(s, obs)}^{S_{M_{top}}}$, is generated by a Binomial distribution, given $N_{(s, obs)}^{S_{JES}}$ and the acceptance \mathcal{A}_s corresponding to the input values M_{top}^{in} and ΔJES^{in} . Again, the same procedure is repeated for the background, to obtain $N_{(b, obs)}^{S_{M_{top}}}$, obviously using $N_{(b, obs)}^{S_{JES}}$ and \mathcal{A}_b .
3. The generated number of signal events must correspond to the same numbers of reconstructed masses, with average distributions given by the signal templates. In particular we have one m_W^{rec} value for each event in S_{JES} and one m_t^{rec} value for each event in $S_{M_{top}}$. More precisely, as being $S_{M_{top}} \subseteq S_{JES}$, values of both m_W^{rec} and m_t^{rec} exist for each event in the M_{top} -sample, while for events belonging to S_{JES} but *NOT* to $S_{M_{top}}$ one has a value of m_W^{rec} only.

Then, to take into account correlations between m_t^{rec} and m_W^{rec} in the same event, $N_{(s, obs)}^{S_{M_{top}}}$ m_W^{rec} and m_t^{rec} values are both drawn from signal two-dimensional histograms where m_W^{rec} vs m_t^{rec} are plotted for each event in $S_{M_{top}}$. Finally, the missing $N_{(s, obs)}^{S_{JES}} - N_{(s, obs)}^{S_{M_{top}}}$ values of m_W^{rec} are drawn from distributions of m_W^{rec} obtained from events belonging to S_{JES} but *NOT* to $S_{M_{top}}$ (this set is simply denoted by $S_{JES} - S_{M_{top}}$ in the following). Obviously all the histograms used here correspond to the input values $\{M_{top}^{in}, \Delta JES^{in}\}$.

4. The same procedure just outlined for the signal events is repeated to generate the $N_{(b, obs)}^{S_{JES}}$ and $N_{(b, obs)}^{S_{M_{top}}}$ m_W^{rec} and m_t^{rec} values respectively by the background templates. We remind here that the raw shapes must be corrected by the presence of signal in the pretag sample, like mentioned in section IV C. In performing PEs the corrections is done coherently to the input values of the parameters, so that effects due to possible variations of the corrected background templates can be calibrated.
5. The actual values of $n_{(b, exp)}$ to be used in $\mathcal{L}_{N_{constr}^{bkg}}$ are generated from a Gaussian distribution of mean $n_{(b, exp)}$ and width $\sigma_{n_{(b, exp)}}$ both for 1-tag sample and ≥ 2 -tags sample. $n_{(b, exp)}$ is the true input value n_b^{in} and $\sigma_{n_{(b, exp)}}$ is the uncertainty evaluated on central values $\sigma_{n_{(b, exp)}} = 181$ for 1-tag and $\sigma_{n_{(b, exp)}} = 14$ for ≥ 2 -tags.
6. The actual value of ΔJES_{constr} to be used in the term $\mathcal{L}_{\Delta JES_{constr}}$ is extracted from a Gaussian of mean ΔJES^{in} and width 1;
7. $-\log \mathcal{L}$ is simultaneously minimized with respect to the 6 free parameters, M_{top} , ΔJES , $n_s^{1\text{tag}}$, $n_b^{1\text{tag}}$, $n_s^{\geq 2\text{tags}}$, and $n_b^{\geq 2\text{tags}}$.

Histograms are filled by outputs from each PE and then used to study the average behavior of the measurement machinery with respect to the true input quantities. Uncertainties on variables extracted from these histograms and related to the limited statistic of the samples used to build the templates[13], are evaluated by a *bootstrap* procedure [6, 7], that is fluctuating the contents of each bin in the templates by its statistical uncertainty and performing PEs extracting data from the set of “fluctuated” templates. This is repeated 200 times, and the RMS of variables extracted from histograms are taken as the statistical uncertainties.

B. Calibration

There are many factors which may introduce a bias using the TMT2D method and, given our machinery, the most likely is an unappropriate parametrizations of the templates by smooth p.d.f.’s. We take advantage of the PE procedure to find calibration functions to be applied to the outputs of a measurement to obtain, on the average, more reliable estimates of the true input values of the fitted parameters. As it concerns in particular M_{top} and ΔJES , the calibrated values will be denoted by M_{top}^{corr} and ΔJES^{corr} respectively. Obviously, also the uncertainties from the likelihood fit have to be propagated through the calibration. To test the goodness of the calibration we performed a complete set of PEs where it is applied PE by PE. In Fig. 7 we show examples of the residuals of M_{top} and ΔJES after the calibration. These plots show how the applied corrections get rid of most of the average biases.

To check that the calibrated uncertainties are unbiased we consider the width of M_{top}^{corr} and ΔJES^{corr} pull distributions. Fig. 8 shows examples of the values of the M_{top} and ΔJES pull widths as a function of the input top mass, M_{top}^{in} and of the input ΔJES , ΔJES^{in} , after the calibration. To derive a correction we average the pull widths over all the M_{top}^{in} and ΔJES^{in} values, setting to 1 possible values smaller than 1. This procedure leads to multiplicative correction factors equal to 1.06 for δM_{top}^{corr} and to 1.07 for $\delta \Delta JES^{corr}$.

Figures 9 shows examples of the expected uncertainties after both the calibration and the pull width correction have been applied. The values of these average expected uncertainty on the measured top quark mass and jet energy scale displacement for true M_{top} and ΔJES around $172.5 \text{ GeV}/c^2$ and $0 \sigma_{JES}$, are:

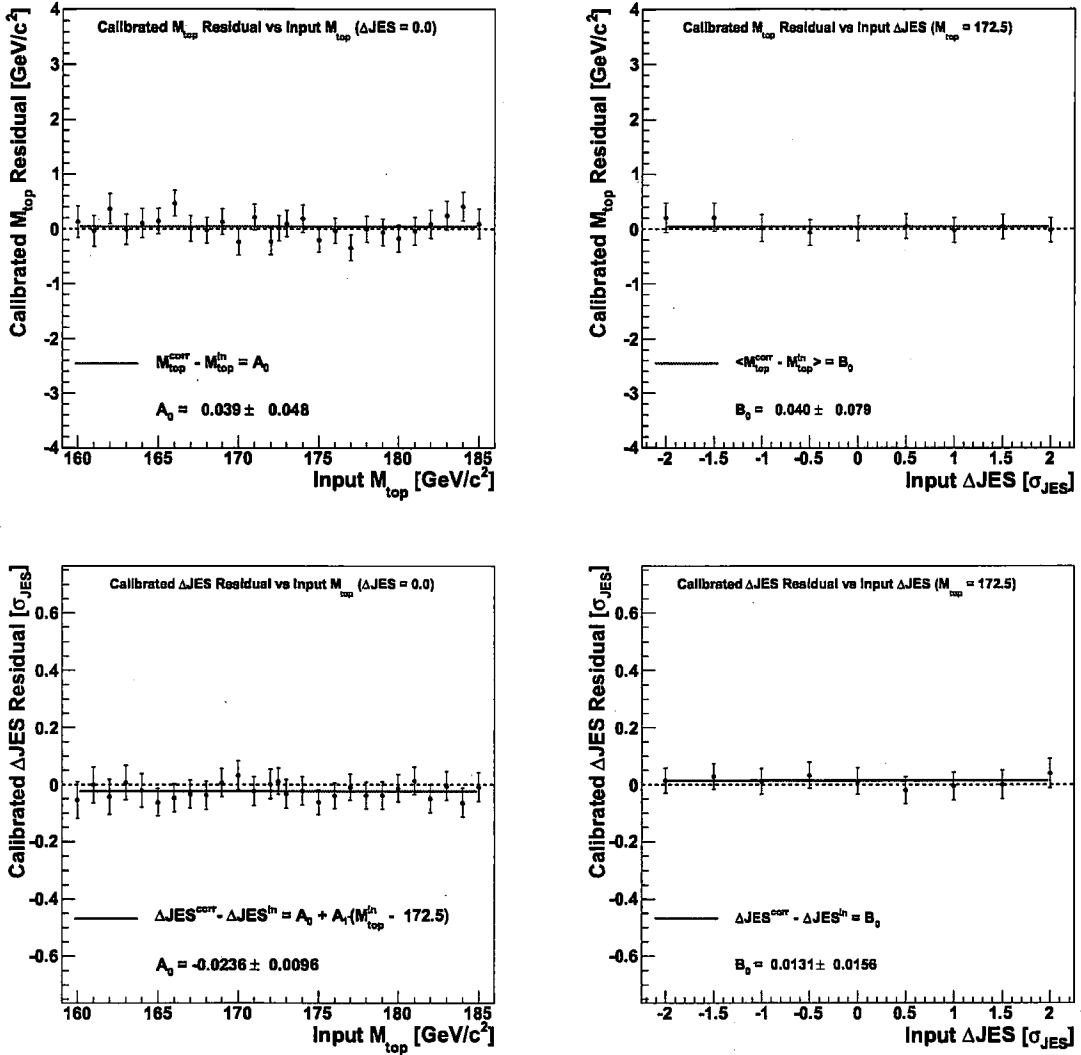


FIG. 7: Examples of residuals of the calibrated top quark mass ($M_{top}^{corr} - M_{top}^{in}$, upper plots) and jet energy scale displacement ($\Delta JES^{corr} - \Delta JES^{in}$, lower plots) as a function of the input M_{top} (left plots), and of input ΔJES (right plots). The results of fits by a straight line are superimposed.

$$\begin{aligned}\delta M_{top}^{corr} (\text{stat + JES}) &\simeq 1.5 \text{ GeV}/c^2 \\ \delta \Delta JES^{corr} (\text{stat + } M_{top}) &\simeq 0.34 \sigma_{JES}\end{aligned}$$

These uncertainties actually include the systematic contributions due to all the parameters of the fit, but the contributions from the n_s and n_b parameters are negligible with respect to the one coming from JES for M_{top}^{corr} and from M_{top} for ΔJES^{corr} .

IX. SYSTEMATIC UNCERTAINTIES ON THE TOP QUARK MASS AND THE JET ENERGY SCALE

Various sources of systematic uncertainties might affect the top quark mass and the jet energy scale measurements. The main possible effect have been studied and are summarized in this section. These arise mostly from the measurement technique itself, from uncertainties in the simulation of the $t\bar{t}$ events, from mismodeling in the simulation of the

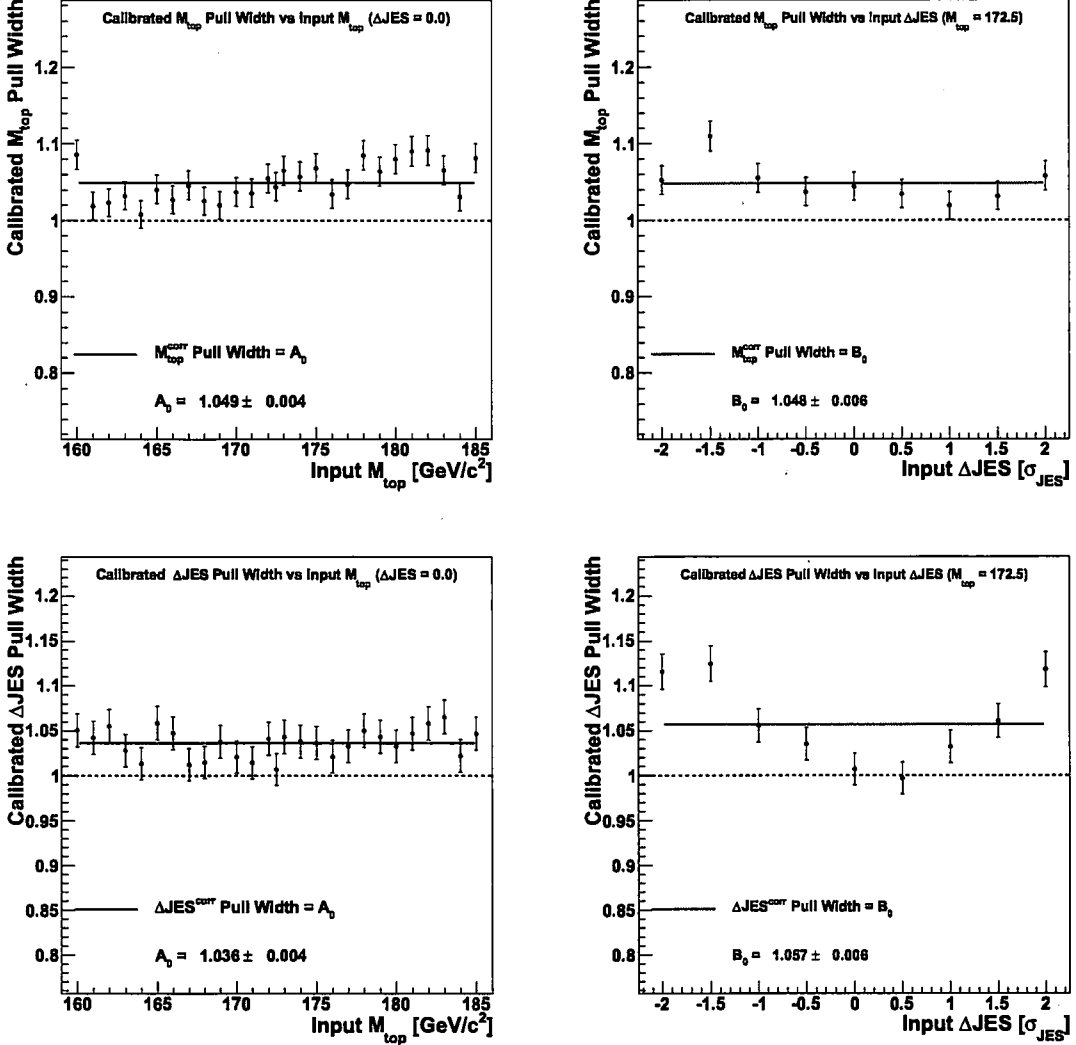


FIG. 8: Widths of the pull distributions for M_{top}^{corr} (upper plots) and ΔJES^{corr} (lower plots) as a function of the input M_{top} at constant $\Delta JES = 0 \sigma_{JES}$ (left plots) and of the input ΔJES for $M_{top}^{in} = 172.5 \text{ GeV}/c^2$ (right plots). The straight lines denote the fit by a constant function.

detector response and from uncertainty on the shapes of signal and background templates used to derive the p.d.f.'s and to calibrate the measurement.

They are usually evaluated by performing PEs extracting pseudo-data from templates built using signal samples where the possible systematic effects have been considered and included. Corresponding corrections to the shape of raw background templates, are performed to obtain also the corrected background templates in agreement with the effect one wants to study. On the contrary, nothing is changed in the measurement machinery, i.e. in the elements of the likelihood fit, because it is this machinery that we want to apply to the data and that, therefore, we have to test in front of possible mismodeling of the data themselves.

The results from these PEs are then compared to the ones obtained by using default templates, and the shifts in the average M_{top}^{corr} and ΔJES^{corr} values are taken as the estimate of the systematic uncertainty. In some cases the statistical uncertainty on the shifts may be larger than the shifts themselves and therefore we use conservatively the former as systematic uncertainty.

a. Residual bias The calibration gets rid of the *average* biases, related especially to the templates parametrization by smooth probability density functions. Anyway, as can be observed in Fig. 7, residual biases usually exist at single $\{M_{top}^{in}, \Delta JES^{in}\}$ points, and have to be taken into account. Similarly to what done to define a correction for

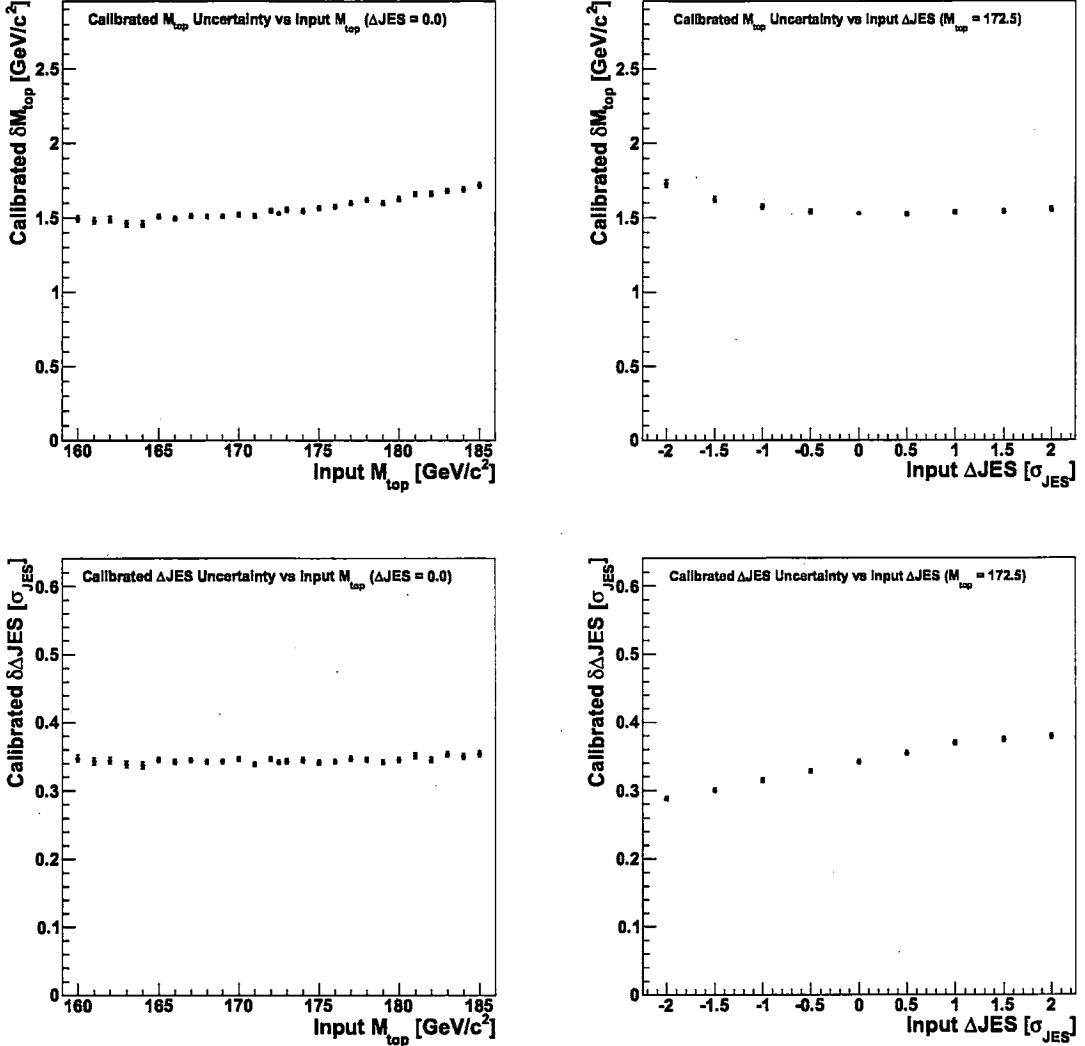


FIG. 9: The expected uncertainties on the top mass (δM_{top} (stat+JES)) and on the jet energy scale displacement ($\delta \Delta JES$ (stat+ M_{top})) are shown as a function of M_{top}^{in} (at constant $\Delta JES = 0$, left) and of ΔJES^{in} for $M_{top}^{in} = 172.5 \text{ GeV}/c^2$ (right), after both the calibration and the pull width corrections have been applied.

the calibrated uncertainties in section VIII B, to evaluate the residual bias we consider the *mean* of pull distributions at all different $\{M_{top}^{in}, \Delta JES^{in}\}$ points. Examples of pull means are shown in figure 10.

To consider properly the local biases, we perform separate averages of positive and negative pull means. This leads to

$$\begin{aligned} \delta M_{top}^{syst} (\text{Res. Bias}) &\simeq (+0.10) \cdot \delta M_{top}^{corr} (\text{stat + JES}) \\ \delta \Delta JES^{syst} (\text{Res. Bias}) &\simeq (+0.12) \cdot \delta \Delta JES^{corr} (\text{stat + } M_{top}) \end{aligned}$$

This means that, at central points like $\{M_{top}^{in} = 172.5 \text{ GeV}/c^2, \Delta JES^{in} = 0 \sigma_{\text{JES}}\}$, systematic “residual bias” uncertainties of about $(+0.15) \text{ GeV}/c^2$ for M_{top} and $(+0.040) \sigma_{\text{JES}}$ for ΔJES may be expected.

b. Calibration The uncertainties on the parameters of the calibration give a small uncertainty on the corrected values M_{top}^{corr} and ΔJES^{corr} . This can be calculated in each single measurement. At $M_{top}^{in} = 172.5 \text{ GeV}/c^2$ and $\Delta JES^{in} = 0 \sigma_{\text{JES}}$ we obtain on average $\delta M_{top}^{syst} (\text{Calib}) \simeq 0.18 \text{ GeV}/c^2$ and $\delta \Delta JES^{syst} (\text{Calib}) \simeq 0.020 \sigma_{\text{JES}}$ by this source of uncertainty.

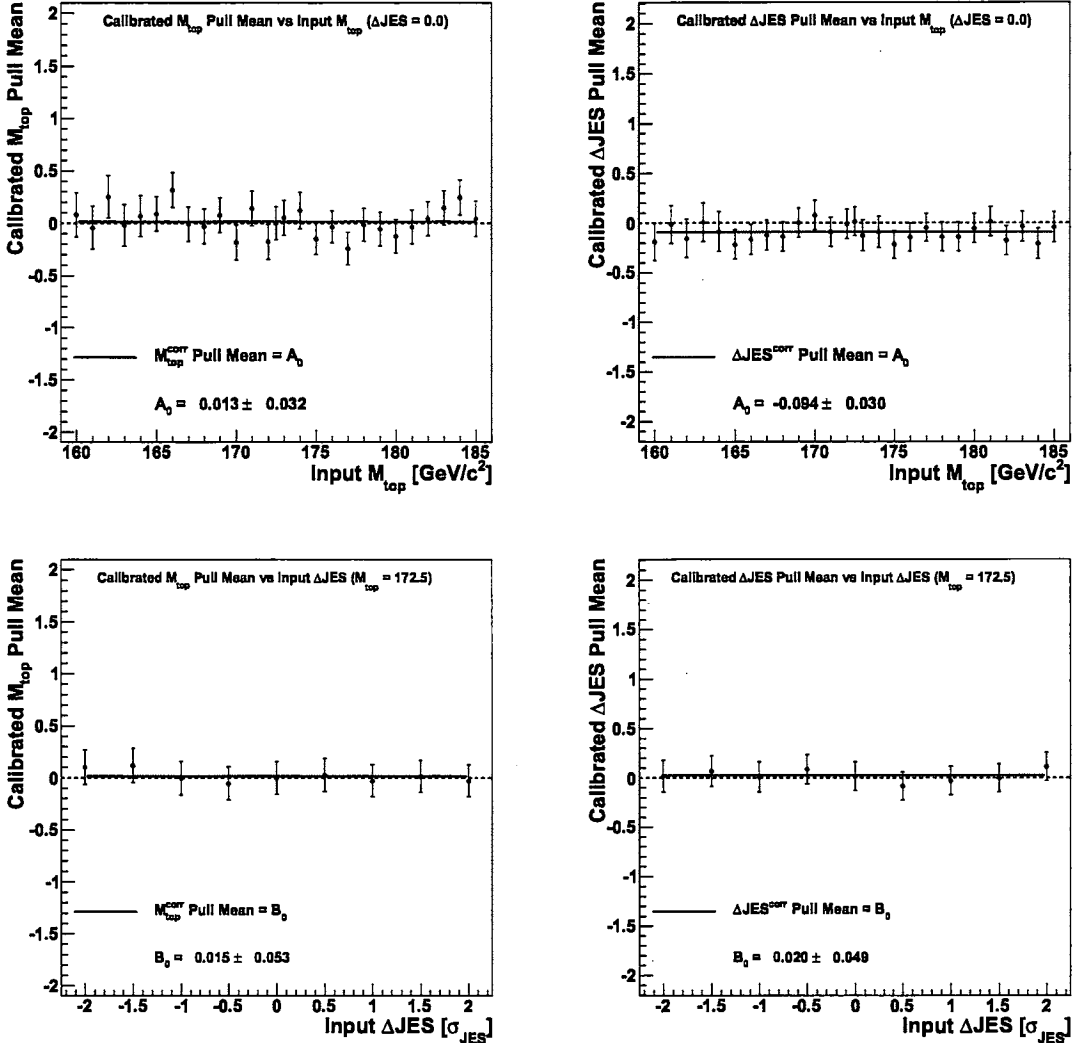


FIG. 10: M_{top} (on the left) and ΔJES (on the right) pull means as a function of M_{top}^{in} at constant $\Delta JES = 0 \sigma_{JES}$ (upper plots) and as a function of ΔJES^{in} for $M_{top}^{in} = 172.5$ GeV/c² (lower plots). The straight lines denote the fit by a constant function.

c. Generator Many sources of systematic effects arise from uncertainty in the Monte Carlo modeling of the hard interaction. PYTHIA and HERWIG generators differ in their hadronization schemes and in their description of the underlying event and multiple interactions. The default signal Monte Carlo samples have been generated by PYTHIA. Templates are built for events generated by HERWIG (at $M_{top}^{in} = 172.5$ GeV/c², $\Delta JES^{in} = 0 \sigma_{JES}$) and PEs are performed drawing pseudo-data from these distributions. By considering the shift with respect to the default, the estimated systematic uncertainties due to this source are δM_{top}^{syst} (Generator) $\simeq 0.48$ GeV/c² and $\delta \Delta JES^{syst}$ (Generator) $\simeq 0.211 \sigma_{JES}$.

d. Initial and final state radiation (ISR) Additional jets coming from possible emission of hard gluons might fall among the six leading jets and populate the tails in the top quark invariant mass distribution. The amount of radiation from partons in the initial (ISR) or final (FSR) state is set by parameters of the PYTHIA generator used to simulate signal events. To study these effects, templates are built using samples where the values of the parameters have been changed with respect to the default, to increase or to decrease the amount of radiation. Again, PEs are performed where pseudo-data are drawn from these modified templates and the results compared to the default. The resulting uncertainties are δM_{top}^{syst} (ISR/FSR) $\simeq 0.10$ GeV/c² and $\delta \Delta JES^{syst}$ (ISR/FSR) $\simeq 0.040 \sigma_{JES}$.

e. **b -jets energy scale** Since the default jet energy corrections are derived on data samples deprived of heavy flavors, an additional uncertainty comes from considering the different properties of b quarks. We account for the uncertainties due to the b -quark semileptonic branching ratios, the fragmentation modeling, and the response of the calorimeters to b and c hadrons. Templates are built varying the default assumption for the three mentioned sources, and PEs are performed drawing pseudo-data from these modified distributions. The comparison to the default results gives systematic uncertainties δM_{top}^{syst} (b -jets) $\simeq 0.15 \text{ GeV}/c^2$ and $\delta \Delta\text{JES}^{syst}$ (b -jets) $\simeq 0.050 \sigma_{\text{JES}}$.

f. **b -tagging efficiency** The different efficiency of the b -tagging algorithm on data and Monte Carlo simulated events is usually considered a constant Scale Factor (b -tag SF). However this value might have a dependence on the transverse energy of jets, leading to possible variations in the shapes of m_t^{rec} and m_W^{rec} templates. Since the background estimate is data-driven, the analysis is sensitive to an overall uncertainty in the b -tagging scale factor only through signal shapes. Signal templates are built taking into account the possible dependence of the SF on the jet E_T and then used in PEs. The corresponding systematic effects have been evaluated to be δM_{top}^{syst} (b -tag SF) $\simeq 0.09 \text{ GeV}/c^2$ and $\delta \Delta\text{JES}^{syst}$ (b -tag SF) $\simeq 0.007 \sigma_{\text{JES}}$.

g. **Residual JES** Our templates are built displacing the value of the jet energy scale by fractions of its uncertainty σ_{JES} , as estimated in [2]. However σ_{JES} results from many independent effects with different behavior with respect to properties of jets like E_T and η , and represents therefore a leading order estimate. So, second order effects can arise from uncertainties on single levels of correction of the jet energies. To evaluate these possible effects, we build signal templates by varying separately by $\pm 1\sigma$ the single corrections and PEs were then performed by using these templates and not applying the constraint $\mathcal{L}_{\Delta\text{JES},\text{constr}}$ in the likelihood fit. The resulting uncertainties have been added in quadrature to obtain a “Residual JES” uncertainty on the top mass: δM_{top}^{syst} (Res. JES) $\simeq 0.45 \text{ GeV}/c^2$

h. **Parton distribution functions** The choice of parton distribution functions (PDF) inside the proton can affect the kinematics of $t\bar{t}$ events and thus the top quark mass measurement. We estimate the uncertainty resulting from the possible PDF models by using our standard signal Monte Carlo samples and reweighting the events by their probability to occur according many different PDF’s. Templates are built by weighted events, PEs are performed by extracting pseudo-data from these modified distributions and the shifts in the average M_{top}^{corr} and ΔJES^{corr} values are taken as systematic uncertainties. We considered four sources of uncertainties:

1. The difference arising from the use of the default CTEQ5L [9] PDF and the one calculated from the MRST group, MRST72 [10].
2. The uncertainty depending on the value of α_s . This is evaluated by the difference between the use of MRST72 and MRST75 PDF’s.
3. The uncertainty depending on the differences between the leading order (LO) and next-to-leading order (NLO) calculations of PDF, evaluated by the difference between using default CTEQ5L (LO) and CTEQ6M (NLO) PDF.
4. The uncertainties on PDF deriving from experimental data uncertainties. These are encoded by 20 pairs of values, where each pair corresponds to variations of $\pm 1\sigma$ of the experimental uncertainties on CTEQ6M PDF.

The resulting total uncertainties due to parton distributions are δM_{top}^{syst} (PDF) $\simeq (+0.23, -0.16) \text{ GeV}/c^2$ and $\delta \Delta\text{JES}^{syst}$ (PDF) $\simeq (+0.026, -0.051) \sigma_{\text{JES}}$.

i. **Multiple Hadron Interactions** The probability to have multiple $p\bar{p}$ interactions during the same bunch-crossing is a function of the instantaneous luminosity. We account for the fact that our nominal MC for the signal description does not model the actual luminosity profile of the data, and that there is a residual dependence in the jet energy response in the MC as a function of the reconstructed number of primary vertices, even after specific corrections. The systematic due to the above effects is estimated to be δM_{top}^{syst} (MHI) $\simeq 0.08 \text{ GeV}/c^2$ and $\delta \Delta\text{JES}^{syst}$ (MHI) $\simeq 0.036 \sigma_{\text{JES}}$.

j. **Color Reconnections** Uncertainties from modeling of color reconnections effects [11] are estimated by comparing the results of two sets of PEs performed drawing pseudo-data from templates built by Monte Carlo samples where different tunes of parameters have been set, corresponding to different models of color reconnections. This gives δM_{top}^{syst} (Color Reconn.) $\simeq 0.32 \text{ GeV}/c^2$ and $\delta \Delta\text{JES}^{syst}$ (Color Reconn.) $\simeq 0.116 \sigma_{\text{JES}}$ for this source of uncertainties.

k. Templates statistics As mentioned in section VIII A, the shapes of signal and background templates are affected by uncertainties due to the limited statistics of the Monte Carlo (for the signal) and data (for the background) samples used to build them. These uncertainties affect the results of a measurement, which is performed by an unbinned likelihood where parametrized p.d.f.'s, fitted to default templates, are evaluated. We address this effect obtaining 200 sets of templates by statistical fluctuations of default ones, and performing pseudo-experiments drawing data from each of these sets separately. The spread in the average values of M_{top}^{corr} and ΔJES^{corr} distributions is taken as systematic uncertainty. This was repeated at many (M_{top}^{in} , ΔJES^{in}) points and an average gives δM_{top}^{syst} (Templ. Stat.) $\simeq 0.27 \text{ GeV}/c^2$ and $\delta\Delta\text{JES}^{syst}$ (Templ. Stat.) $\simeq 0.052 \sigma_{\text{JES}}$.

l. Background acceptances In the likelihood function (section VII) the signal and background acceptances, A_s and A_b , appear. The meaning of these variables are explained in sections VI and VIA. For the background the values of A_b have rather large uncertainty, but in the likelihood fit, as well as during the default PEs procedure, the values of $A_b^{1\text{ tag}}$ and $A_b^{\geq 2\text{ tags}}$ are kept constant to their central values, i.e. 46.9% and 42.5% respectively, section VIA. We perform PEs changing the input values of A_b by $\pm 1\sigma$ and consider the shifts of M_{top}^{corr} and ΔJES^{corr} with respect to the default to obtain δM_{top}^{syst} (Acceptances A_b) $\simeq 0.55 \text{ GeV}/c^2$ and $\delta\Delta\text{JES}^{syst}$ (Acceptances A_b) $\simeq 0.112 \sigma_{\text{JES}}$.

m. Background shape Apart from uncertainties related to the limited statistics of the samples we use to build the templates, we must consider also possible systematic mismodelings of the data-driven background distributions. To take this possibility into account we perform, for each template, a bin-by-bin comparison of the total expected number of events (i.e. the sum of the expected signal and the background) to the observed data. The background templates are modified in such a way to obtain an a priori agreement between the expectation and the data. PEs are then performed extracting pseudo-data from default signal templates and the new systematic background templates and results are compared to what obtained in the default PEs. Taking the shift as the uncertainty we obtain δM_{top}^{syst} (Bkg Shape) $\simeq 0.51 \text{ GeV}/c^2$ and $\delta\Delta\text{JES}^{syst}$ (Bkg Shape) $\simeq 0.175 \sigma_{\text{JES}}$.

n. Trigger The multijet trigger, used for the first online selection of $t\bar{t}$ candidate events in the data, is simulated on signal Monte Carlo events. Uncertainties on this simulation, possibly related to mismodeling of the energy deposition in the calorimeters and/or changes of the trigger algorithms and requirements not faithfully reproduced in the default Monte Carlo samples, are taken into account. Templates are built by events where the trigger simulation has been modified and PEs performed drawing pseudo-data from them. Comparison to the default PEs leads to uncertainties δM_{top}^{syst} (Trigger) $\simeq 0.20 \text{ GeV}/c^2$ and $\delta\Delta\text{JES}^{syst}$ (Trigger) $\simeq 0.042 \sigma_{\text{JES}}$.

A. Total systematic uncertainty

Table II shows a summary of all the systematic uncertainties and their quadrature sum, which gives a total systematic uncertainty of $1.2 \text{ GeV}/c^2$ for the M_{top} measurement and $0.3 \sigma_{\text{JES}}$ for the ΔJES , where the “residual bias” uncertainty, depending on the statistical errors, is already evaluated at the values given by the measurement on the data, described in section X.

X. THE TOP QUARK MASS MEASUREMENT

After the kinematic selections with $N_{out} \geq 0.97$ ($N_{out} \geq 0.94$), $\chi^2(m_W^{rec}) \leq 2.0$ ($\chi^2(m_W^{rec}) \leq 3.0$) and $\chi^2(m_t^{rec}) \leq 3.0$ ($\chi^2(m_t^{rec}) \leq 4.0$) for events with 1 tag (≥ 2 tags), we are left with 4368 and 2256 events in the JES-sample and M_{top} -sample with 1 tag respectively, and 1196 and 600 events in the corresponding samples with ≥ 2 tags. The expected background, corrected for the contribution due to $t\bar{t}$ events amounts to 3652 ± 181 (1-tag JES-sample), 1712 ± 77 (1-tag M_{top} -sample), 718 ± 14 (≥ 2 -tag JES-sample), and 305 ± 22 (≥ 2 -tag M_{top} -sample) events. The likelihood fit described in Sec. VII has been applied to the data samples to derive the best top quark mass and jet energy scale displacement from the default value to be

$$M_{top}^{fit} = 172.45 \pm 1.48 (\text{stat + JES}) \text{ GeV}/c^2$$

$$\Delta\text{JES}^{fit} = -0.038 \pm 0.285 (\text{stat + } M_{top}) \sigma_{\text{JES}}$$

Figure 11 shows the behavior of the likelihood as a function of the M_{top} and ΔJES parameters and the contours corresponding to variations of one, two and three standard deviations of the same parameters with respect to the values maximizing the likelihood itself (before the calibration).

| Source | δM_{top}^{syst} (GeV/c^2) | $\delta \Delta\text{JES}^{syst}$ (σ_{JES}) |
|------------------------------|--|--|
| Residual bias | 0.2 | 0.03 |
| Calibration | 0.1 | 0.01 |
| Generator | 0.5 | 0.21 |
| ISR/FSR | 0.1 | 0.04 |
| b -jets energy scale | 0.2 | 0.05 |
| SF E_T dependence | 0.1 | 0.01 |
| Residual JES | 0.4 | -- |
| PDF | 0.2 | 0.04 |
| Multiple Hadron Interactions | 0.1 | 0.04 |
| Color Reconnections | 0.3 | 0.12 |
| Templates Statistics | 0.3 | 0.05 |
| Background Acceptances | 0.6 | 0.11 |
| Background Shape | 0.5 | 0.18 |
| Trigger | 0.2 | 0.04 |
| Total | 1.2 | 0.34 |

TABLE II: Breakdown of *observed* systematic uncertainties from different sources and their respective amount. The contribution depending on the statistical errors (i.e. the “residual bias”) has been calculated here by the values observed in the measurement on data. The total uncertainty is obtained by the quadrature sum of single contributions.

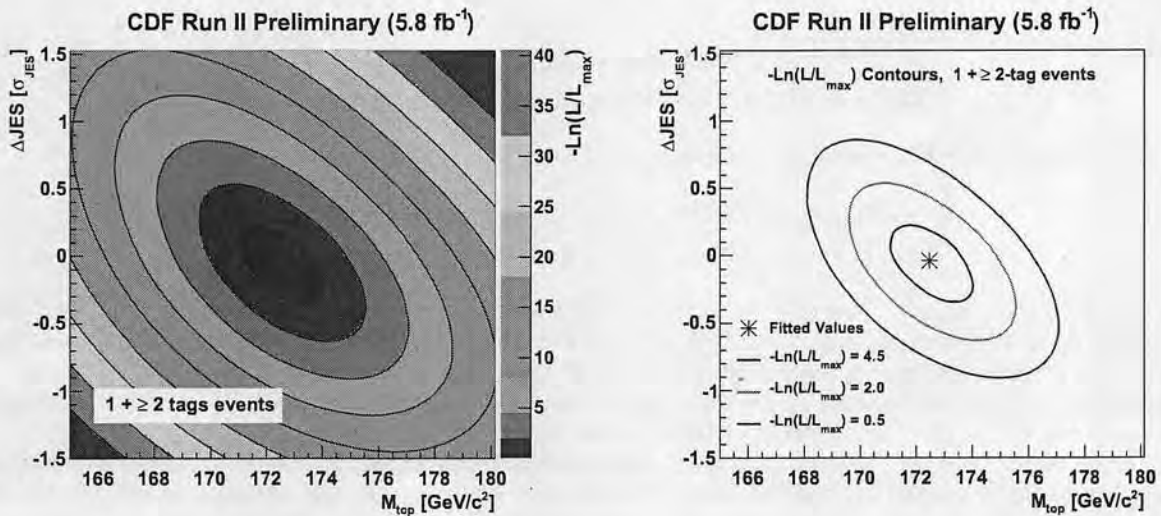


FIG. 11: Measured likelihood as a function of the M_{top} and ΔJES parameters (left) and contours corresponding to variations of the same parameters of one, two and three standard deviations as given by MINOS (right). The fitted central values, corresponding to the maximum likelihood (or minimum $-\ln \mathcal{L}$), are also shown.

These values have to be calibrated and the uncertainties have then also to be corrected by multiplicative factors 1.06 and 1.07 for M_{top} and ΔJES respectively, as mentioned in section VIII B, so that we finally obtain :

$$M_{top}^{corr} = 172.47 \pm 1.72 (\text{stat} + \text{JES}) \text{ GeV}/c^2$$

$$\Delta\text{JES}^{corr} = -0.105 \pm 0.331 (\text{stat} + M_{top}) \sigma_{\text{JES}}$$

The purely statistical part of the uncertainty can be isolated and the results written as :

$$M_{top}^{corr} = 172.47 \pm 1.43 (stat) \pm 0.96 (\text{JES}) \text{ GeV}/c^2$$

$$\Delta\text{JES}^{corr} = -0.105 \pm 0.276 (stat) \pm 0.183 (M_{top}) \sigma_{\text{JES}}$$

The whole set of parameters, as measured in the data by the likelihood fit, is summarized in Table III together with the corrected values.

| Variable | Fitted value | Calibrated value |
|----------------------|-------------------|-------------------|
| M_{top} | 172.46 ± 1.48 | 172.47 ± 1.72 |
| ΔJES | -0.04 ± 0.285 | -0.10 ± 0.33 |
| $n_s^{1\,tag}$ | 925 ± 86 | 904 ± 97 |
| $n_b^{1\,tag}$ | 3463 ± 92 | 3482 ± 102 |
| $n_s^{\geq 2\,tags}$ | 449 ± 31 | 446 ± 32 |
| $n_b^{\geq 2\,tags}$ | 724 ± 13 | 725 ± 14 |

TABLE III: The values of free parameters and their uncertainties as fitted by MINUIT in the data by the likelihood fit, and their values after the calibration. For δM_{top}^{corr} and $\delta\Delta\text{JES}^{corr}$ also the multiplicative correction factors evaluated by the pull widths have been applied.

Summarizing, including the systematic uncertainties, the measured values for the top quark mass and the jet energy scale are:

$$M_{top} = 172.5 \pm 1.7 (\text{stat} + \text{JES}) \pm 1.2 (\text{syst}) \text{ GeV}/c^2$$

$$\Delta\text{JES} = -0.10 \pm 0.3 (\text{stat} + M_{top}) \pm 0.3 (\text{syst}) \sigma_{\text{JES}}$$

or, dividing completely the statistical and systematic contributions

$$M_{top} = 172.5 \pm 1.4 (\text{stat}) \pm 1.5 (\text{syst}) \text{ GeV}/c^2$$

$$\Delta\text{JES} = -0.10 \pm 0.3 (\text{stat}) \pm 0.4 (\text{syst}) \sigma_{\text{JES}}$$

The plots in Fig. 12 show the m_t^{rec} and m_W^{rec} distributions for the data compared to the probability density functions corresponding to the fitted values of M_{top} and ΔJES , while in Fig. 13 the N_{out} distributions are shown for a top quark mass of $172.5 \text{ GeV}/c^2$ and a jet energy scale displacement of $0 \sigma_{\text{JES}}$, that is the values of simulated M_{top} and ΔJES as close as possible to the measurements in the data. In all these plots the signal and background contributions are normalized to the respective number of events as fitted in the data.

The plots in Fig. 14 compare the observed calibrated uncertainties, to the expected distribution from default pseudo-experiments using as input mass $M_{top} = 172.5 \text{ GeV}/c^2$ and $\Delta\text{JES} = 0 \sigma_{\text{JES}}$, i.e. the available templates with input top quark mass and ΔJES as close as possible to the values measured in the data. We find that the probability of achieving a better sensitivity is 89.2% for M_{top} and 35.3% for ΔJES .

XI. CONCLUSIONS

We described in this note the Template Method technique with *in situ* calibration used to measure the top quark mass on the latest available data sample, corresponding to an integrated luminosity of 5.8 fb^{-1} . The method has been studied and calibrated through thousands of pseudo-experiments and the systematic uncertainties estimated by the same procedure. We then applied the technique to the data to measure a top quark mass of $[172.5 \pm 1.4 (\text{stat}) \pm 1.5 (\text{syst})] \text{ GeV}/c^2$ and a displacement of the jet energy scale from the value measured in [2] of $[-0.1 \pm 0.3 (\text{stat}) \pm 0.4 (\text{syst})] \sigma_{\text{JES}}$, in units of the uncertainty on that value itself.

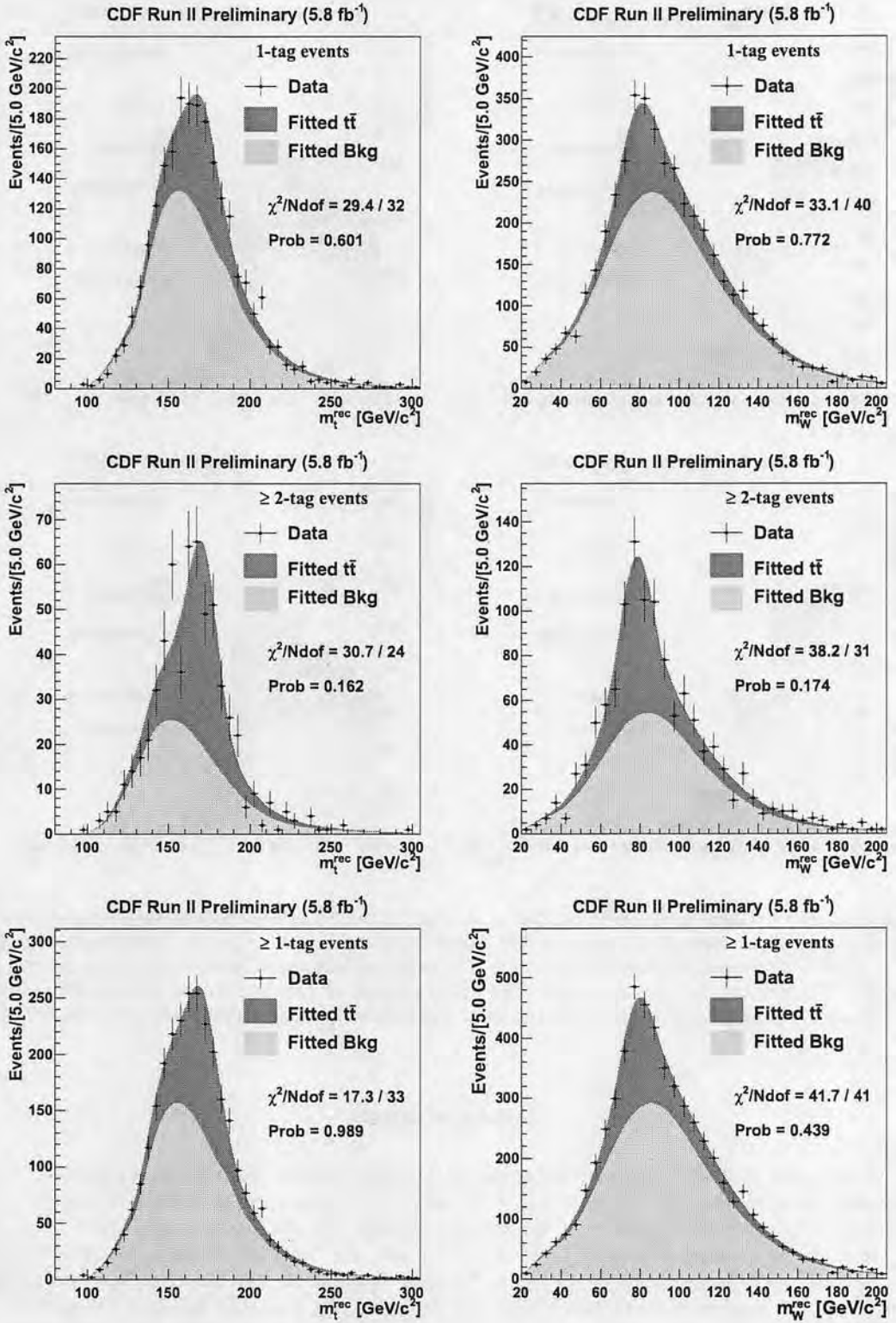


FIG. 12: Distributions of m_t^{rec} (left plots) and m_W^{rec} (right plots) as obtained in the data (black points) are compared to the probability density functions from signal and background corresponding, both in shape and normalization, to the likelihood fit parameters measured in the data. The upper and middle plots show distributions for the 1-tag and $\geq 2\text{-tags}$ samples respectively, while the lower plots are their sum.

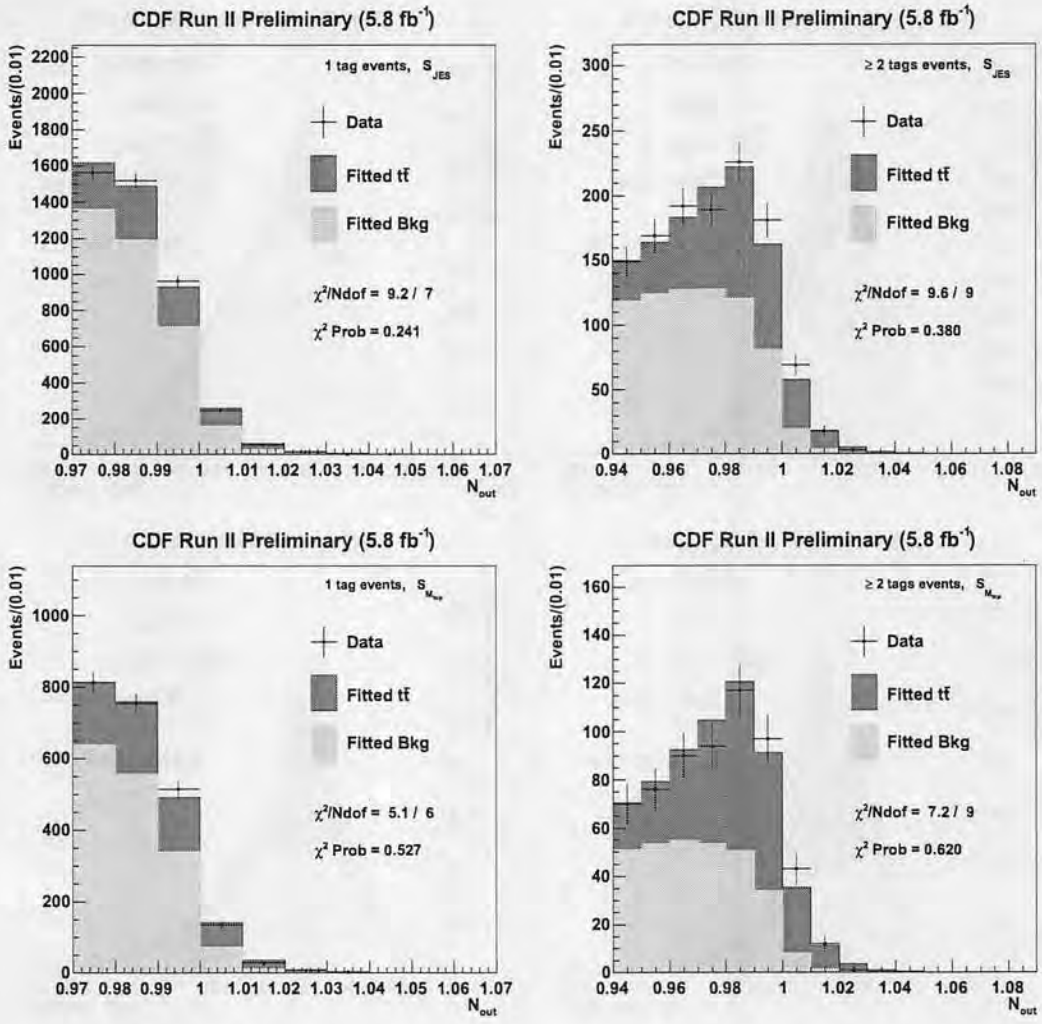


FIG. 13: Distributions of the output from the Neural Net as obtained in the data (black points) are compared to the distributions from signal and background corresponding to $M_{top} = 172.5 \text{ GeV}/c^2$ and $\Delta \text{JES} = 0 \sigma_{\text{JES}}$, i.e. the values of simulated M_{top} and ΔJES as close as possible to the measurements in the data. The expected histograms are normalized to the measured values for the average number of signal and background events. The upper plots show the distributions in the JES-sample for the 1-tag (left) and ≥ 2 -tags events (right) respectively, while the lower plots show the same distributions for events in the M_{top} -sample.

Acknowledgments

We thank the Fermilab staff and the technical staffs of the participating institutions for their vital contributions. This work was supported by the U.S. Department of Energy and National Science Foundation; the Italian Istituto Nazionale di Fisica Nucleare; the Ministry of Education, Culture, Sports, Science and Technology of Japan; the Natural Sciences and Engineering Research Council of Canada; the National Science Council of the Republic of China; the Swiss National Science Foundation; the A.P. Sloan Foundation; the Bundesministerium für Bildung und Forschung, Germany; the Korean World Class University Program, the National Research Foundation of Korea; the Science and Technology Facilities Council and the Royal Society, UK; the Institut National de Physique Nucléaire et Physique des Particules/CNRS; the Russian Foundation for Basic Research; the Ministerio de Ciencia e Innovación, and Programa Consolider-Ingenio 2010, Spain; the Slovak R&D Agency; the Academy of Finland; and the Australian

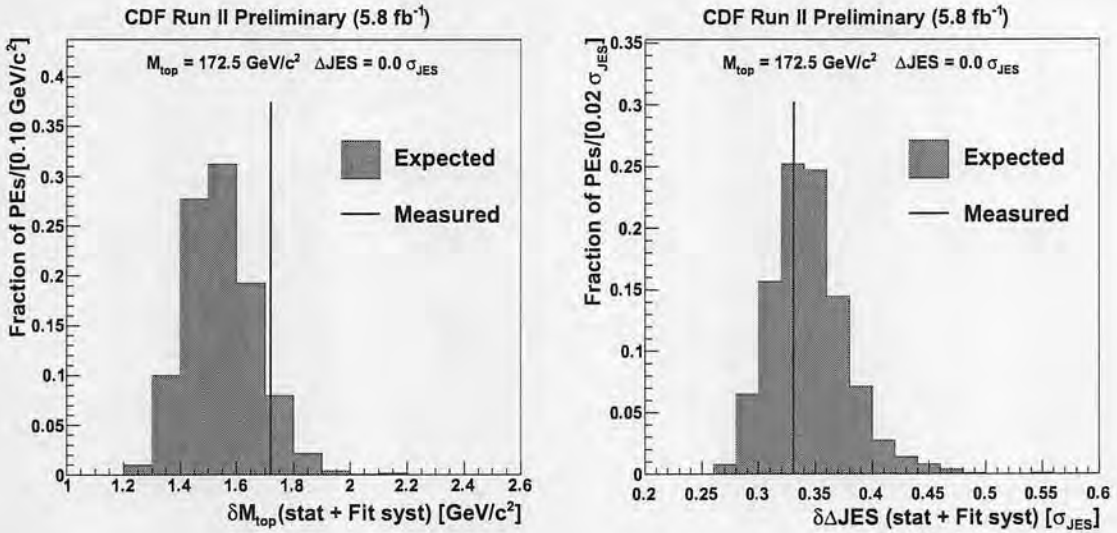
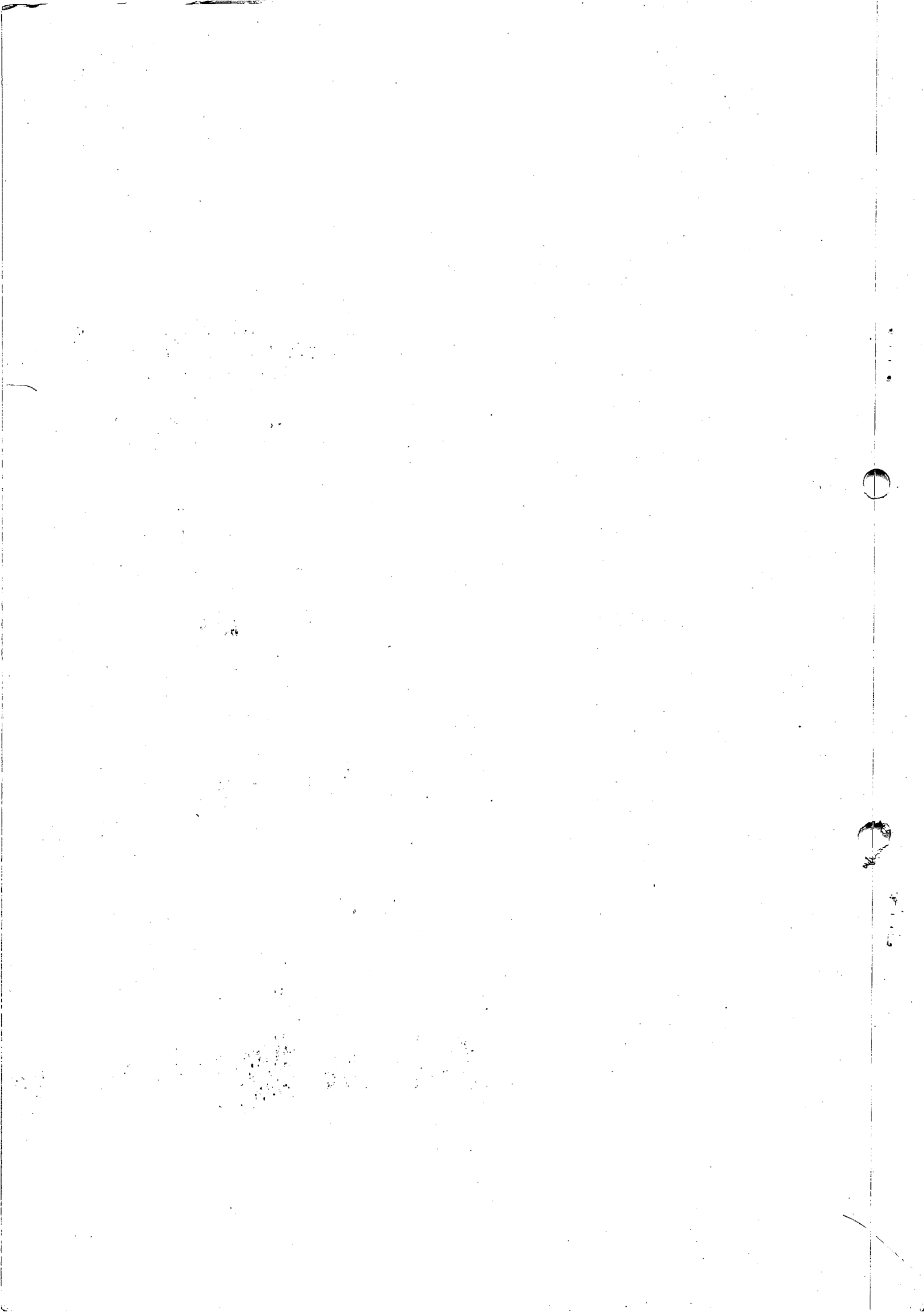


FIG. 14: Uncertainties on the top quark mass (left) and the jet energy scale displacement (right) as measured in default PEs performed at $M_{top}^{in} = 172.5 \text{ GeV}/c^2$ and JES = $0 \sigma_{\text{JES}}$, i.e. using the available set of PEs with input top quark mass and ΔJES as close as possible to the values measured in the data. The red lines indicate the uncertainties obtained in the data.

Research Council (ARC).

- [1] T. Aaltonen *et al.* [CDF Collaboration], Phys. Rev. D **81**, 052011 (2010);
L. Brigliadori, A. Castro, F. Margaroli; *Measurement of the Top Mass with in-situ jet energy scale calibration in the All-Hadronic channel using the Template Method with 2.9 fb⁻¹*, CDF public Note 9694, February 2009.
- [2] A. Bhatti *et al.*, Nucl. Instrum. Meth. A **566**, 375 (2006).
- [3] U. Langenfeld, S. Moch and P. Uwer, *Measuring the running top-quark mass*, arXiv:0906.5273 (2009).
- [4] K. Nakamura *et al.* (Particle Data Group), J. Phys. G **37**, 075021 (2010).
- [5] G. D'Agostini, *Asymmetric uncertainties: sources, treatment and potential dangers*, arXiv:physics/0403086 (2004).
- [6] B. Efron, Ann. Stat. 7(1) 1–26, 1979.
- [7] B. Efron and R. Tibshirani, *An Introduction to the Bootstrap* Chapman & Hall/CRC, 1994.
- [8] G. Marchesini *et al.*, Comput. Phys. Commun. **67**, 465 (1992);
G. Corcella *et al.*, J. High Energy Phys. **0101**, 010 (2001).
- [9] H. L. Lai *et al.* Eur. Phys. J. C **12**, 375 (2000).
- [10] A.D. Martin, R.G. Roberts, W.J. Stirling and R.S Thorne, Eur. Phys. J. C **4**, 463 (1998).
- [11] P. Skands, D. Wicke, *Non-perturbative QCD effects and the Top Mass at the Tevatron*, arXiv:0807.3248 [hep-ph].
- [12] The ≥ 2 -tags sample actually consists of events with 2 or 3 tagged jets. When 3 tags are present, the 3 different possible assignments of two out of three jets to b quarks are also tested, with the remaining tagged jet considered as a light quark
- [13] Given the large number of pseudo-experiments, fluctuations due to the PEs statistic are negligible



Measurement of the top quark mass and $p\bar{p} \rightarrow t\bar{t}$ cross section in the all-hadronic mode with the CDF II detector

- T. Aaltonen,²⁴ J. Adelman,¹⁴ B. Álvarez González,^{12,x} S. Amerio,^{44b,44a} D. Amidei,³⁵ A. Anastassov,³⁹ A. Annovi,²⁰ J. Antos,¹⁵ G. Apollinari,¹⁸ J. Appel,¹⁸ A. Apresyan,⁴⁹ T. Arisawa,⁵⁸ A. Artikov,¹⁶ J. Asaadi,⁵⁴ W. Ashmanskas,¹⁸ A. Attal,⁴ A. Aurisano,⁵⁴ F. Azfar,⁴³ W. Badgett,¹⁸ A. Barbaro-Galtieri,^{a29} V. E. Barnes,⁴⁹ B. A. Barnett,²⁶ P. Barria,^{47c,47a} P. Bartos,¹⁵ G. Bauer,³³ P.-H. Beauchemin,³⁴ F. Bedeschi,^{47a} D. Beecher,³¹ S. Behari,²⁶ G. Bellettini,^{47b,47a} J. Bellinger,⁶⁰ D. Benjamin,¹⁷ A. Beretvas,¹⁸ A. Bhatti,⁵¹ M. Binkley,¹⁸ D. Bisello,^{44b,44a} I. Bizjak,^{31,ee} R. E. Blair,² C. Blocker,⁷ B. Blumenfeld,²⁶ A. Bocci,¹⁷ A. Bodek,⁵⁰ V. Boisvert,⁵⁰ D. Bortoletto,⁴⁹ J. Boudreau,⁴⁸ A. Boveia,¹¹ B. Brau,^{11,b} A. Bridgeman,²⁵ L. Brigliadori,^{6b,6a} C. Bromberg,³⁶ E. Brubaker,¹⁴ J. Budagov,¹⁶ H. S. Budd,⁵⁰ S. Budd,²⁵ K. Burkett,¹⁸ G. Busetto,^{44b,44a} P. Bussey,²² A. Buzatu,³⁴ K. L. Byrum,² S. Cabrera,^{17,z} C. Calancha,³² S. Camarda,⁴ M. Campanelli,³¹ M. Campbell,³⁵ F. Canelli,^{14,18} A. Canepa,⁴⁶ B. Carls,²⁵ D. Carlsmith,⁶⁰ R. Carosi,^{47a} S. Carrillo,^{19,o} S. Carron,¹⁸ B. Casal,¹² M. Casarsa,¹⁸ A. Castro,^{6b,6a} P. Catastini,^{47c,47a} D. Cauz,^{55a} V. Cavaliere,^{47c,47a} M. Cavalli-Sforza,⁴ A. Cerri,^{a29} L. Cerrito,^{31,r} S. H. Chang,²⁸ Y. C. Chen,¹ M. Chertok,⁸ G. Chiarelli,^{47a} G. Chlachidze,¹⁸ F. Chlebana,¹⁸ K. Cho,²⁸ D. Chokheli,¹⁶ J. P. Chou,²³ K. Chung,^{18,p} W. H. Chung,⁶⁰ Y. S. Chung,⁵⁰ T. Chwalek,²⁷ C. I. Ciobanu,⁴⁵ M. A. Ciocci,^{47c,47a} A. Clark,²¹ D. Clark,⁷ G. Compostella,^{44a} M. E. Convery,¹⁸ J. Conway,⁸ M. Corbo,⁴⁵ M. Cordelli,²⁰ C. A. Cox,⁸ D. J. Cox,⁸ F. Crescioli,^{47b,47a} C. Cuena Almenar,⁶¹ J. Cuevas,^{12,x} R. Culbertson,¹⁸ J. C. Cully,³⁵ D. Dagenhart,¹⁸ N. d'Ascenzo,^{45,w} M. Datta,¹⁸ T. Davies,²² P. de Barbaro,⁵⁰ S. De Cecco,^{52a} A. Deisher,^{a29} G. De Lorenzo,⁴ M. Dell'Orso,^{47b,47a} C. Deluca,⁴ L. Demortier,⁵¹ J. Deng,^{17,g} M. Deninno,^{6a} M. d'Errico,^{44b,44a} A. Di Canto,^{47b,47a} B. Di Ruza,^{47a} J. R. Dittmann,⁵ M. D'Onofrio,⁴ S. Donati,^{47b,47a} P. Dong,¹⁸ T. Dorigo,^{44a} S. Dube,⁵³ K. Ebina,⁵⁸ A. Elagin,⁵⁴ R. Erbacher,⁸ D. Errede,²⁵ S. Errede,²⁵ N. Ershaidat,^{45,dd} R. Eusebi,⁵⁴ H. C. Fang,^{a29} S. Farrington,⁴³ W. T. Fedorko,¹⁴ R. G. Feild,⁶¹ M. Feindt,²⁷ J. P. Fernandez,³² C. Ferrazza,^{47d,47a} R. Field,¹⁹ G. Flanagan,^{49,i} R. Forrest,⁸ M. J. Frank,⁵ M. Franklin,²³ J. C. Freeman,¹⁸ I. Furic,¹⁹ M. Gallinaro,⁵¹ J. Galyardt,¹³ F. Garberson,¹¹ J. E. Garcia,²¹ A. F. Garfinkel,⁴⁹ P. Garosi,^{47c,47a} H. Gerberich,²⁵ D. Gerdes,³⁵ A. Gessler,²⁷ S. Giagu,^{52b,52a} V. Giakoumopoulou,³ P. Giannetti,^{47a} K. Gibson,⁴⁸ J. L. Gimmell,⁵⁰ C. M. Ginsburg,¹⁸ N. Giokaris,³ M. Giordani,^{55b,55a} P. Giromini,²⁰ M. Giunta,^{47a} G. Giurgiu,²⁶ V. Glagolev,¹⁶ D. Glenzinski,¹⁸ M. Gold,³⁸ N. Goldschmidt,¹⁹ A. Golossanov,¹⁸ G. Gomez,¹² G. Gomez-Ceballos,³³ M. Goncharov,³³ O. Gonzalez,³² I. Gorelov,³⁸ A. T. Goshaw,¹⁷ K. Goulianatos,⁵¹ A. Gresele,^{44b,44a} S. Grinstein,⁴ C. Grossi-Pilcher,¹⁴ R. C. Group,¹⁸ U. Grundler,²⁵ J. Guimaraes da Costa,²³ Z. Gunay-Unalan,³⁶ C. Haber,^{a29} S. R. Hahn,¹⁸ E. Halkiadakis,⁵³ B.-Y. Han,⁵⁰ J. Y. Han,⁵⁰ F. Happacher,²⁰ K. Hara,⁵⁶ D. Hare,⁵³ M. Hare,⁵⁷ R. F. Harr,⁵⁹ M. Hartz,⁴⁸ K. Hatakeyama,⁵ C. Hays,⁴³ M. Heck,²⁷ J. Heinrich,⁴⁶ M. Herndon,⁶⁰ J. Heuser,²⁷ S. Hewamanage,⁵ D. Hidas,⁵³ C. S. Hill,^{11,d} D. Hirschbuehl,²⁷ A. Hocker,¹⁸ S. Hou,¹ M. Houlden,³⁰ S.-C. Hsu,^{a29} R. E. Hughes,⁴⁰ M. Hurwitz,¹⁴ U. Husemann,⁶¹ M. Hussein,³⁶ J. Huston,³⁶ J. Incandela,¹¹ G. Introzzi,^{47a} M. Iori,^{52b,52a} A. Ivanov,^{8,q} E. James,¹⁸ D. Jang,¹³ B. Jayatilaka,¹⁷ E. J. Jeon,²⁸ M. K. Jha,^{6a} S. Jindariani,¹⁸ W. Johnson,⁸ M. Jones,⁴⁹ K. K. Joo,²⁸ S. Y. Jun,¹³ J. E. Jung,²⁸ T. R. Junk,¹⁸ T. Kamon,⁵⁴ D. Kar,¹⁹ P. E. Karchin,⁵⁹ Y. Kato,^{42,n} R. Kephart,¹⁸ W. Ketchum,¹⁴ J. Keung,⁴⁶ V. Khotilovich,⁵⁴ B. Kilminster,¹⁸ D. H. Kim,²⁸ H. S. Kim,²⁸ H. W. Kim,²⁸ J. E. Kim,²⁸ M. J. Kim,²⁰ S. B. Kim,²⁸ S. H. Kim,⁵⁶ Y. K. Kim,¹⁴ N. Kimura,⁵⁸ L. Kirsch,⁷ S. Klimentko,¹⁹ K. Kondo,⁵⁸ D. J. Kong,²⁸ J. Konigsberg,¹⁹ A. Korytov,¹⁹ A. V. Kotwal,¹⁷ M. Kreps,²⁷ J. Kroll,⁴⁶ D. Krop,¹⁴ N. Krumnack,⁵ M. Kruse,¹⁷ V. Krutelyov,¹¹ T. Kuhr,²⁷ N. P. Kulkarni,⁵⁹ M. Kurata,⁵⁶ S. Kwang,¹⁴ A. T. Laasanen,⁴⁹ S. Lami,^{47a} S. Lammel,¹⁸ M. Lancaster,³¹ R. L. Lander,⁸ K. Lannon,^{40,v} A. Lath,⁵³ G. Latino,^{47c,47a} I. Lazzizzera,^{44b,44a} T. LeCompte,² E. Lee,⁵⁴ H. S. Lee,¹⁴ J. S. Lee,²⁸ S. W. Lee,^{54,y} S. Leone,^{47a} J. D. Lewis,¹⁸ C.-J. Lin,^{a29} J. Linacre,⁴³ M. Lindgren,¹⁸ E. Lipeles,⁴⁶ A. Lister,²¹ D. O. Litvintsev,¹⁸ C. Liu,⁴⁸ T. Liu,¹⁸ N. S. Lockyer,⁴⁶ A. Loginov,⁶¹ L. Lovas,¹⁵ D. Lucchesi,^{44b,44a} J. Lueck,²⁷ P. Lujan,^{a29} P. Lukens,¹⁸ G. Lungu,⁵¹ J. Lys,^{a29} R. Lysak,¹⁵ D. MacQueen,³⁴ R. Madrak,¹⁸ K. Maeshima,¹⁸ K. Makhoul,³³ P. Maksimovic,²⁶ S. Malde,⁴³ S. Malik,³¹ G. Manca,^{30,f} A. Manousakis-Katsikakis,³ F. Margaroli,⁴⁹ C. Marino,²⁷ C. P. Marino,²⁵ A. Martin,⁶¹ V. Martin,^{22,l} M. Martínez,⁴ R. Martínez-Ballarín,³² P. Mastrandrea,^{52a} M. Mathis,²⁶ M. E. Mattson,⁵⁹ P. Mazzanti,^{6a} K. S. McFarland,⁵⁰ P. McIntyre,⁵⁴ R. McNulty,^{30,k} A. Mehta,³⁰ P. Mehtala,²⁴ A. Menzione,^{47a} C. Mesropian,⁵¹ T. Miao,¹⁸ D. Mietlicki,³⁵ N. Miladinovic,⁷ R. Miller,³⁶ C. Mills,²³ M. Milnik,²⁷ A. Mitra,¹ G. Mitselmakher,¹⁹ H. Miyake,⁵⁶ S. Moed,²³ N. Moggi,^{6a} M. N. Mondragon,^{18,o} C. S. Moon,²⁸ R. Moore,¹⁸ M. J. Morello,^{47a} J. Morlock,²⁷ P. Movilla Fernandez,¹⁸ J. Müllenstädt,^{a29} A. Mukherjee,¹⁸ Th. Muller,²⁷ P. Murat,¹⁸ M. Mussini,^{6b,6a} J. Nachtman,^{18,p} Y. Nagai,⁵⁶ J. Naganoma,⁵⁶ K. Nakamura,⁵⁶ I. Nakano,⁴¹ A. Napier,⁵⁷ J. Nett,⁶⁰ C. Neu,^{46,bb} M. S. Neubauer,²⁵ S. Neubauer,²⁷ J. Nielsen,^{a29,h} L. Nodulman,² M. Norman,¹⁰ O. Norniella,²⁵ E. Nurse,³¹ L. Oakes,⁴³ S. H. Oh,¹⁷ Y. D. Oh,²⁸ I. Oksuzian,¹⁹ T. Okusawa,⁴² R. Orava,²⁴ K. Osterberg,²⁴ S. Pagan Griso,^{44b,44a}

C. Pagliarone,^{55a} E. Palencia,¹⁸ V. Papadimitriou,¹⁸ A. Papaikonomou,²⁷ A. A. Paramanov,² B. Parks,⁴⁰ S. Pashapour,³⁴ J. Patrick,¹⁸ G. Pauletta,^{55b,55a} M. Paulini,¹³ C. Paus,³³ T. Peiffer,²⁷ D. E. Pellett,⁸ A. Penzo,^{55a} T. J. Phillips,¹⁷ G. Piacentino,^{47a} E. Pianori,⁴⁶ L. Pinera,¹⁹ K. Pitts,²⁵ C. Plager,⁹ L. Pondrom,⁶⁰ K. Potamianos,⁴⁹ O. Poukhov,^{16,a} F. Prokoshin,^{16,aa} A. Pronko,¹⁸ F. Ptahos,^{18,j} E. Pueschel,¹³ G. Punzi,^{47b,47a} J. Pursley,⁶⁰ J. Rademacker,^{43,d} A. Rahaman,⁴⁸ V. Ramakrishnan,⁶⁰ N. Ranjan,⁴⁹ I. Redondo,³² P. Renton,⁴³ M. Renz,²⁷ M. Rescigno,^{52a} S. Richter,²⁷ F. Rimondi,^{6b,6a} L. Ristori,^{47a} A. Robson,²² T. Rodrigo,¹² T. Rodriguez,⁴⁶ E. Rogers,²⁵ S. Rolli,⁵⁷ R. Roser,¹⁸ M. Rossi,^{55a} R. Rossin,¹¹ P. Roy,³⁴ A. Ruiz,¹² J. Russ,¹³ V. Rusu,¹⁸ B. Rutherford,¹⁸ H. Saarikko,²⁴ A. Safonov,⁵⁴ W. K. Sakamoto,⁵⁰ L. Santi,^{55b,55a} L. Sartori,^{47a} K. Sato,⁵⁶ V. Saveliev,^{45,w} A. Savoy-Navarro,⁴⁵ P. Schlabach,¹⁸ A. Schmidt,²⁷ E. E. Schmidt,¹⁸ M. A. Schmidt,¹⁴ M. P. Schmidt,^{61,a} M. Schmitt,³⁹ T. Schwarz,⁸ L. Scodellaro,¹² A. Scribano,^{47c,47a} F. Scuri,^{47a} A. Sedov,⁴⁹ S. Seidel,³⁸ Y. Seiya,⁴² A. Semenov,¹⁶ L. Sexton-Kennedy,¹⁸ F. Sforza,^{47b,47a} A. Sfyrla,²⁵ S. Z. Shalhout,⁵⁹ T. Shears,³⁰ P. F. Shepard,⁴⁸ M. Shimojima,^{56,u} S. Shiraishi,¹⁴ M. Shochet,¹⁴ Y. Shon,⁶⁰ I. Shreyber,³⁷ A. Simonenko,¹⁶ P. Sinervo,³⁴ A. Sisakyan,¹⁶ A. J. Slaughter,¹⁸ J. Slaunwhite,⁴⁰ K. Sliwa,⁵⁷ J. R. Smith,⁸ F. D. Snider,¹⁸ R. Snihur,³⁴ A. Soha,¹⁸ S. Somalwar,⁵³ V. Sorin,⁴ P. Squillacioti,^{47c,47a} M. Stanitzki,⁶¹ R. St. Denis,²² B. Stelzer,³⁴ O. Stelzer-Chilton,³⁴ D. Stentz,³⁹ J. Strologas,³⁸ G. L. Strycker,³⁵ J. S. Suh,²⁸ A. Sukhanov,¹⁹ I. Suslov,¹⁶ A. Taffard,^{25,g} R. Takashima,⁴¹ Y. Takeuchi,⁵⁶ R. Tanaka,⁴¹ J. Tang,¹⁴ M. Tecchio,³⁵ P. K. Teng,¹ J. Thom,^{18,i} J. Thome,¹³ G. A. Thompson,²⁵ E. Thomson,⁴⁶ P. Tipton,⁶¹ P. Tito-Guzmán,³² S. Tkaczyk,¹⁸ D. Toback,⁵⁴ S. Tokar,¹⁵ K. Tollefson,³⁶ T. Tomura,⁵⁶ D. Tonelli,¹⁸ S. Torre,²⁰ D. Torretta,¹⁸ P. Totaro,^{55b,55a} M. Trovato,^{47d,47a} S.-Y. Tsai,¹ Y. Tu,⁴⁶ N. Turini,^{47c,47a} F. Ukegawa,⁵⁶ S. Uozumi,²⁸ N. van Remortel,^{24,c} A. Varganov,³⁵ E. Vataga,^{47d,47a} F. Vázquez,^{19,o} G. Velev,¹⁸ C. Vellidis,³ M. Vidal,³² I. Vila,¹² R. Vilar,¹² M. Vogel,³⁸ I. Volobouev,^{a29,y} G. Volpi,^{47a,47a} P. Wagner,⁴⁶ R. G. Wagner,² R. L. Wagner,¹⁸ W. Wagner,^{27,cc} J. Wagner-Kuhr,²⁷ T. Wakisaka,⁴² R. Wallny,⁹ S. M. Wang,¹ A. Warburton,³⁴ D. Waters,³¹ M. Weinberger,⁵⁴ J. Weinelt,²⁷ W. C. Wester III,¹⁸ B. Whitehouse,⁵⁷ D. Whiteson,^{46,g} A. B. Wicklund,² E. Wicklund,¹⁸ S. Wilbur,¹⁴ G. Williams,³⁴ H. H. Williams,⁴⁶ P. Wilson,¹⁸ B. L. Winer,⁴⁰ P. Wittich,^{18,i} S. Wolbers,¹⁸ C. Wolfe,¹⁴ H. Wolfe,⁴⁰ T. Wright,³⁵ X. Wu,²¹ F. Würthwein,¹⁰ A. Yagil,¹⁰ K. Yamamoto,⁴² J. Yamaoka,¹⁷ U. K. Yang,^{14,s} Y. C. Yang,²⁸ W. M. Yao,^{a29} G. P. Yeh,¹⁸ K. Yi,^{18,p} J. Yoh,¹⁸ K. Yorita,⁵⁸ T. Yoshida,^{42,m} G. B. Yu,¹⁷ I. Yu,²⁸ S. S. Yu,¹⁸ J. C. Yun,¹⁸ A. Zanetti,^{55a} Y. Zeng,¹⁷ X. Zhang,²⁵ Y. Zheng,^{9,e} and S. Zucchelli^{6b,6a}

(CDF Collaboration)

¹Institute of Physics, Academia Sinica, Taipei, Taiwan 11529, Republic of China²Argonne National Laboratory, Argonne, Illinois 60439, USA³University of Athens, 157 71 Athens, Greece⁴Institut de Fisica d'Altes Energies, Universitat Autònoma de Barcelona, E-08193, Bellaterra (Barcelona), Spain⁵Baylor University, Waco, Texas 76798, USA^{6a}Istituto Nazionale di Fisica Nucleare Bologna, I-40127 Bologna, Italy^{6b}University of Bologna, I-40127 Bologna, Italy⁷Brandeis University, Waltham, Massachusetts 02254, USA⁸University of California, Davis, Davis, California 95616, USA⁹University of California, Los Angeles, Los Angeles, California 90024, USA¹⁰University of California, San Diego, La Jolla, California 92093, USA¹¹University of California, Santa Barbara, Santa Barbara, California 93106, USA¹²Instituto de Fisica de Cantabria, CSIC-University of Cantabria, 39005 Santander, Spain¹³Carnegie Mellon University, Pittsburgh, Pennsylvania 15213, USA¹⁴Enrico Fermi Institute, University of Chicago, Chicago, Illinois 60637, USA¹⁵Comenius University, 842 48 Bratislava, Slovakia;

Institute of Experimental Physics, 040 01 Kosice, Slovakia

¹⁶Joint Institute for Nuclear Research, RU-141980 Dubna, Russia¹⁷Duke University, Durham, North Carolina 27708, USA¹⁸Fermi National Accelerator Laboratory, Batavia, Illinois 60510¹⁹University of Florida, Gainesville, Florida 32611, USA²⁰Laboratori Nazionali di Frascati, Istituto Nazionale di Fisica Nucleare, I-00044 Frascati, Italy²¹University of Geneva, CH-1211 Geneva 4, Switzerland²²Glasgow University, Glasgow G12 8QQ, United Kingdom²³Harvard University, Cambridge, Massachusetts 02138, USA²⁴Division of High Energy Physics, Department of Physics, University of Helsinki and Helsinki Institute of Physics, FIN-00014, Helsinki, Finland

- ²⁵*University of Illinois, Urbana, Illinois 61801, USA*
²⁶*The Johns Hopkins University, Baltimore, Maryland 21218, USA*
²⁷*Institut für Experimentelle Kernphysik, Karlsruhe Institute of Technology, D-76131 Karlsruhe, Germany*
²⁸*Center for High Energy Physics: Kyungpook National University, Daegu 702-701, Korea;
Seoul National University, Seoul 151-742, Korea;
Sungkyunkwan University, Suwon 440-746, Korea;*
*Korea Institute of Science and Technology Information, Daejeon 305-806, Korea;
Chonnam National University, Gwangju 500-757, Korea;
Chonbuk National University, Jeonju 561-756, Korea*
- ^{a29}*Ernest Orlando Lawrence Berkeley National Laboratory, Berkeley, California 94720, USA*
³⁰*University of Liverpool, Liverpool L69 7ZE, United Kingdom*
³¹*University College London, London WC1E 6BT, United Kingdom*
- ³²*Centro de Investigaciones Energeticas Medioambientales y Tecnologicas, E-28040 Madrid, Spain*
³³*Massachusetts Institute of Technology, Cambridge, Massachusetts 02139, USA*
³⁴*Institute of Particle Physics: McGill University, Montréal, Québec, Canada H3A 2T8;
Simon Fraser University, Burnaby, British Columbia, Canada V5A 1S6;
University of Toronto, Toronto, Ontario, Canada M5S 1A7;
and TRIUMF, Vancouver, British Columbia, Canada V6T 2A3*
- ³⁵*University of Michigan, Ann Arbor, Michigan 48109, USA*
³⁶*Michigan State University, East Lansing, Michigan 48824, USA*
- ³⁷*Institution for Theoretical and Experimental Physics, ITEP, Moscow 117259, Russia*
³⁸*University of New Mexico, Albuquerque, New Mexico 87131, USA*
³⁹*Northwestern University, Evanston, Illinois 60208, USA*
⁴⁰*The Ohio State University, Columbus, Ohio 43210, USA*
⁴¹*Okayama University, Okayama 700-8530, Japan*
⁴²*Osaka City University, Osaka 588, Japan*
- ⁴³*University of Oxford, Oxford OX1 3RH, United Kingdom*
^{44a}*Istituto Nazionale di Fisica Nucleare, Sezione di Padova-Trento, I-35131 Padova, Italy*
^{44b}*University of Padova, I-35131 Padova, Italy*
- ⁴⁵*LPNHE, Université Pierre et Marie Curie/IN2P3-CNRS, UMR7585, Paris, F-75252 France*
⁴⁶*University of Pennsylvania, Philadelphia, Pennsylvania 19104, USA*
^{47a}*Istituto Nazionale di Fisica Nucleare Pisa, I-56127 Pisa, Italy*

^aDeceased.^bVisitor from University of Massachusetts Amherst, Amherst, MA 01003, USA.^cVisitor from Universiteit Antwerpen, B-2610 Antwerp, Belgium.^dVisitor from University of Bristol, Bristol BS8 1TL, United Kingdom.^eVisitor from Chinese Academy of Sciences, Beijing 100864, China.^fVisitor from Istituto Nazionale di Fisica Nucleare, Sezione di Cagliari, 09042 Monserrato (Cagliari), Italy.^gVisitor from University of California Irvine, Irvine, CA 92697, USA.^hVisitor from University of California Santa Cruz, Santa Cruz, CA 95064, USAⁱVisitor from Cornell University, Ithaca, NY 14853, USA.^jVisitor from University of Cyprus, Nicosia CY-1678, Cyprus.^kVisitor from University College Dublin, Dublin 4, Ireland.^lVisitor from University of Edinburgh, Edinburgh EH9 3JZ, United Kingdom.^mVisitor from University of Fukui, Fukui City, Fukui Prefecture, Japan 910-0017.ⁿVisitor from Kinki University, Higashi-Osaka City, Japan 577-8502.^oVisitor from Universidad Iberoamericana, Mexico D.F., Mexico.^pVisitor from University of Iowa, Iowa City, IA 52242, USA.^qVisitor from Kansas State University, Manhattan, KS 66506, USA.^rVisitor from Queen Mary, University of London, London, E1 4NS, England.^sVisitor from University of Manchester, Manchester M13 9PL, England.^tVisitor from Muons, Inc., Batavia, IL 60510, USA.^uVisitor from Nagasaki Institute of Applied Science, Nagasaki, Japan.^vVisitor from University of Notre Dame, Notre Dame, IN 46556, USA.^wVisitor from Obninsk State University, Obninsk, Russia.^xVisitor from University de Oviedo, E-33007 Oviedo, Spain.^yVisitor from Texas Tech University, Lubbock, TX 79609, USA.^zVisitor from IFIC (CSIC-Universitat de Valencia), 56071 Valencia, Spain.^{aa}Visitor from Universidad Técnica Federico Santa María, 110v Valparaíso, Chile.^{bb}Visitor from University of Virginia, Charlottesville, VA 22906, USA.^{cc}Visitor from Bergische Universität Wuppertal, 42097 Wuppertal, Germany.^{dd}Visitor from Yarmouk University, Irbid 211-63, Jordan.^{ee}On leave from J. Stefan Institute, Ljubljana, Slovenia.

- ^{47b}*University of Pisa, I-56127 Pisa, Italy*
^{47c}*University of Siena, I-56127 Pisa, Italy*
^{47d}*Scuola Normale Superiore, I-56127 Pisa, Italy*
⁴⁸*University of Pittsburgh, Pittsburgh, Pennsylvania 15260, USA*
⁴⁹*Purdue University, West Lafayette, Indiana 47907, USA*
⁵⁰*University of Rochester, Rochester, New York 14627, USA*
⁵¹*The Rockefeller University, New York, New York 10021, USA*
^{52a}*Istituto Nazionale di Fisica Nucleare, Sezione di Roma 1, I-00185 Roma, Italy*
^{52b}*Sapienza Università di Roma, I-00185 Roma, Italy*
⁵³*Rutgers University, Piscataway, New Jersey 08855, USA*
⁵⁴*Texas A&M University, College Station, Texas 77843, USA*
^{55a}*Istituto Nazionale di Fisica Nucleare Trieste/Udine, I-34100 Trieste, I-33100 Udine, Italy*
^{55b}*University of Trieste/Udine, I-33100 Udine, Italy*
⁵⁶*University of Tsukuba, Tsukuba, Ibaraki 305, Japan*
⁵⁷*Tufts University, Medford, Massachusetts 02155, USA*
⁵⁸*Waseda University, Tokyo 169, Japan*
⁵⁹*Wayne State University, Detroit, Michigan 48201, USA*
⁶⁰*University of Wisconsin, Madison, Wisconsin 53706, USA*
⁶¹*Yale University, New Haven, Connecticut 06520, USA*

(Received 3 February 2010; published 30 March 2010)

We present a measurement of the top quark mass and of the top-antitop ($t\bar{t}$) pair production cross section using $p\bar{p}$ data collected with the CDF II detector at the Tevatron Collider at the Fermi National Accelerator Laboratory and corresponding to an integrated luminosity of 2.9 fb^{-1} . We select events with six or more jets satisfying a number of kinematical requirements imposed by means of a neural-network algorithm. At least one of these jets must originate from a b quark, as identified by the reconstruction of a secondary vertex inside the jet. The mass measurement is based on a likelihood fit incorporating reconstructed mass distributions representative of signal and background, where the absolute jet energy scale (JES) is measured simultaneously with the top quark mass. The measurement yields a value of $174.8 \pm 2.4(\text{stat} + \text{JES})^{+1.2}_{-1.0}(\text{syst}) \text{ GeV}/c^2$, where the uncertainty from the absolute jet energy scale is evaluated together with the statistical uncertainty. The procedure also measures the amount of signal from which we derive a cross section, $\sigma_{t\bar{t}} = 7.2 \pm 0.5(\text{stat}) \pm 1.0(\text{syst}) \pm 0.4(\text{lum}) \text{ pb}$, for the measured values of top quark mass and JES.

DOI: 10.1103/PhysRevD.81.052011

PACS numbers: 14.65.Ha, 13.85.Ni, 13.85.Qk

I. INTRODUCTION

Since its early measurements, the large value of the top quark mass (M_{top}) has represented a really striking property of this particle, giving to the top quark a special position within the standard model (SM) and suggesting also possible links to new physics [1]. In fact, apart from being itself a fundamental parameter of the SM, M_{top} is by far the largest mass among the ones of the observed fermions, and this makes the top quark contribution dominant in higher order corrections to many observables. Therefore M_{top} plays a central role in checking the consistency of theoretical predictions of the SM. The higher order corrections apply also to the W boson propagator, and therefore affect the calculated value of the W mass, M_W . As the latter depends logarithmically on the mass of the Higgs boson, precise measurements of M_W and M_{top} allow setting indirect constraints on the value of the mass of this fundamental, but still unobserved particle [2]. Moreover, possible contributions due to some unknown physics might also be constrained. Finally, the present value of M_{top} makes the

Yukawa coupling to the Higgs field of $\mathcal{O}(1)$ and this could indicate a special role of the top quark in the mechanism of electroweak symmetry breaking.

All these reasons make the accurate knowledge of M_{top} a really important issue, but the same is true for the measurement of the $t\bar{t}$ production cross section ($\sigma_{t\bar{t}}$), both as a test for physics contributions beyond the SM and as a test of current next-to-leading-order (NLO) QCD calculations [3]. Usually, measurements of $\sigma_{t\bar{t}}$ rely upon event counting and are performed assuming an *a priori* value for M_{top} . The technique used here allows the simultaneous measurement of both these important and related properties of the top quark.

At the Tevatron Collider at Fermi National Accelerator Laboratory, top quarks are produced mostly in pairs. In the SM the top quark decays into a W boson and a b quark almost 100% of the time, and the topology of the final state resulting from a $t\bar{t}$ event depends on the hadronic or leptonic decay of the two final-state W bosons. In this paper, we consider events characterized by a multijet topology (*all-hadronic* mode) with no energetic leptons. This

$t\bar{t}$ final state has the advantage of a large branching ratio ($\approx 4/9$) and of having no undetectable final-state particles. The major challenge of this channel is the large background from QCD multijet production, which dominates the signal by 3 orders of magnitude after the application of a specific online event selection (trigger). To increase the purity of the candidate sample, requirements based on the kinematical and topological characteristics of SM $t\bar{t}$ events are expressed in terms of an artificial neural network and applied to the data. Further improvement is then obtained from the requirement of at least one jet identified as originating from a b quark using a secondary vertex b -tagging algorithm. Simulations predict that a clear $t\bar{t}$ signal will thus become visible over background in the selected data sample, and the measurement of the top quark mass and the $t\bar{t}$ cross section is made possible in spite of the overwhelming QCD multijet production.

A reconstructed top quark mass is determined by fitting the kinematics of the six leading jets in the event to a $t\bar{t}$ final state. This variable, denoted as m_t^{rec} , does not strictly represent a measurement of M_{top} , but its distribution obtained by a sample of $t\bar{t}$ events is sensitive to M_{top} itself. The jet energy scale (JES) is a factor representing the set of corrections needed to obtain a better estimate of the energy of a parton starting from a jet reconstructed by clusters in the calorimeter. The default JES used in simulated events is obtained by a tuning to the data, but possible discrepancies between data and simulation lead to an uncertainty on this value. The strong correlation existing between the m_t^{rec} distribution and the JES implies therefore a corresponding uncertainty on M_{top} . However, the JES can be calibrated using the selected samples of $t\bar{t}$ candidate events, where a second variable, m_W^{rec} , is reconstructed by the four-momenta of the jets assigned to the W bosons. This variable is related to the well-known value of the W -boson mass, and the JES can be adjusted in such a way that both the m_t^{rec} and the m_W^{rec} distributions for simulated events match the observed data. The inclusion of this procedure, usually referred to as *in situ* calibration, enables a significant reduction of the systematic uncertainty associated with the inaccurate knowledge of the JES, and represents an important improvement of the work described in this paper with respect to the previous CDF analysis by a similar method [4].

The m_t^{rec} and m_W^{rec} distributions are reconstructed in two separate samples of selected data events, defined by the presence of exactly one and two or more b -tagged jets, respectively. The data are then compared to corresponding distributions expected from background and $t\bar{t}$ events simulated with various values of the top quark mass and of the JES to fit for these parameters. In addition, the fitted signal yields are used to derive a measurement of the $t\bar{t}$ production cross section.

The results reported here are based on data taken between March 2002 and April 2008, corresponding to an

integrated luminosity of 2.9 fb^{-1} . This measurement complements other recent determinations of the top quark mass and $t\bar{t}$ cross section by CDF and D0 [5,6] in other final states, and improves the latest CDF measurements in the same channel [4,7].

The organization of the paper is as follows: Section II contains a brief description of the CDF II detector. The trigger and the neural-network-based sample selection are discussed in Sec. III, along with the identification of jets initiated by b quarks (b jets). Sections IV and V present the simulated signal samples and the data-driven method we use for estimating the background from multijet data. Section VI describes how the fundamental variables m_t^{rec} and m_W^{rec} are reconstructed, while in Sec. VII we present the final requirements to define the samples of events used in the measurement. The parametrization of the dependence of the distributions of reconstructed variables on the values of the top quark mass and the jet energy scale are described in Sec. VIII A. The fit to the experimental distributions and its calibration are described in Secs. VIII B and IX, respectively. Section X details the study of the systematic uncertainties on the mass measurement, which is then reported in Sec. XI. We describe in Sec. XII the measurement of the $t\bar{t}$ cross section.

II. THE CDF II DETECTOR

The CDF II detector [8] is an azimuthally and forward-backward symmetric apparatus designed to study $p\bar{p}$ collisions at the Tevatron. A cylindrical coordinate system is used where θ is the polar angle to the proton beam direction at the event vertex, ϕ is the azimuthal angle about the beam axis, and pseudorapidity is defined as $\eta = -\ln[\tan(\theta/2)]$. We define transverse energy as $E_T = E \sin\theta$ and transverse momentum as $p_T = p \sin\theta$, where E is the energy measured by calorimeters, and p is the magnitude of the momentum measured by a tracking system. The detector consists of a magnetic spectrometer surrounded by calorimeters and muon chambers. The charged particle tracking system is immersed in a 1.4 T solenoidal magnetic field with axis parallel to the beam line. A set of silicon microstrip detectors provides charged particle tracking in the radial range from 1.5 to 28 cm, while a 3.1 m long open-cell drift chamber, the central outer tracker (COT), covers the radial range from 40 to 137 cm. In combination, the silicon and COT detectors provide excellent tracking up to about pseudorapidities $|\eta| \leq 1.1$, and with decreasing precision up to $|\eta| \leq 2.0$. Segmented electromagnetic and hadronic calorimeters surround the tracking system, and measure the energy deposit of particles interacting in the calorimeters. The electromagnetic and hadronic calorimeters are lead-scintillator and iron-scintillator sampling devices, respectively, covering the range $|\eta| \leq 3.6$. They are segmented in the central region ($|\eta| < 1.1$) in towers of 15° in azimuth and 0.1 in η , and the forward region ($1.1 < |\eta| < 3.6$) in towers of 7.5°

for $|\eta| < 2.11$ and 15° for $|\eta| > 2.11$, while the coverage in $|\eta|$ increases gradually from 0.1 to 0.6. The electromagnetic calorimeters [9,10] are instrumented with proportional chambers (at large angles) or scintillating strip detectors (in the forward regions), which measure the transverse profile of electromagnetic showers at a depth corresponding to the expected shower maxima. Drift chambers located outside the central hadronic calorimeters and behind a 60 cm iron shield detect muons with $|\eta| \leq 0.6$ [11]. Additional drift chambers and scintillation counters detect muons in the region $0.6 < |\eta| < 1.5$. Multicell gas Cherenkov counters [12] with a coverage of $3.7 < |\eta| < 4.7$ measure the average number of inelastic $p\bar{p}$ collisions and thereby are used to determine the luminosity.

III. MULTIJET EVENT SELECTION AND b TAGGING

The final state of all-hadronic $t\bar{t}$ events is characterized by the presence of at least six jets from the decay of the two top quarks, where additional jets might come from initial- or final-state radiation (ISR or FSR). Events having such a topology are collected using a multijet trigger which relies on calorimeter information. Subsequently, jets are identified during event reconstruction by grouping clusters of energy in the calorimeter using a fixed-cone algorithm with a radius of 0.4 in $\eta - \phi$ space [13]. After a preliminary selection of multijet events, a neural-network selection based on relevant kinematical variables is used to further improve the purity of the sample.

A. Multijet trigger

The CDF trigger system has three levels. The first two levels consist of special-purpose electronic circuits and the third one of conventional programmable digital processors. At level 1, the trigger requires the presence of at least one calorimeter tower with transverse energy $E_T^{\text{tow}} \geq 10$ GeV. At level 2, the total transverse energy, obtained as the sum over all calorimeter towers, $\sum E_T^{\text{tow}}$, must be ≥ 175 GeV. Moreover, the presence of least four clusters of towers, each with transverse energy $E_T^{\text{clus}} \geq 15$ GeV, is required. Finally, the third trigger level confirms the level 2 selection using a more accurate determination of the jet energy, requiring four or more reconstructed jets with $E_T \geq 10$ GeV. Approximately 14×10^6 events satisfy the trigger requirements, corresponding to an events signal-over-background ratio (S/B) of about 1/1200, assuming a theoretical cross section of 6.7 pb for a top quark mass of 175 GeV/ c^2 [3].

B. Preselection and topology requirements

Events satisfying the trigger requirements are reconstructed in terms of their final-state observables (tracks, vertices, charged leptons, and jets). We retain only those events that are well contained in detector acceptance,

requiring the primary event vertex [14] to lie inside the luminous region ($|z| < 60$ cm). We remove events having well-identified energetic electrons or muons as defined in [15], namely, electrons with $E_T > 20$ GeV and muons with $p_T > 20$ GeV/ c .

In order to have jets matching as accurately as possible to the hard scattering partons, we correct jet energies for detector response and multiple interactions [16]. First, we consider the η dependence of detector response and energy loss in the uninstrumented regions. Then, after accounting for the small extra energy deposited by multiple collisions in the same beam-beam bunch crossing, a correction for calorimeter nonlinearity is applied so that the jet energies are equal, on average, to the energy of the particles incident on the jet cone. The total uncertainty on the estimate of the original parton energy, where all uncertainties for the individual corrections are added in quadrature, varies from 8% to 3% with jet transverse energy increasing from 15 GeV to 50 GeV, and remains approximately constant at 3% above 50 GeV. Jets with $|\eta| \leq 2$ and $E_T \geq 15$ GeV, after all corrections are applied, are selected for further analysis.

As the uncertainty on the missing transverse energy, \cancel{E}_T [17], increases proportionally to $\sqrt{\sum E_T}$ [18], its significance is defined as $\frac{\cancel{E}_T}{\sqrt{\sum E_T}}$, where the \cancel{E}_T is corrected for any identified muons, while $\sum E_T$ is obtained by summing the E_T 's of all the selected jets. We then require that $\frac{\cancel{E}_T}{\sqrt{\sum E_T}}$ be < 3 GeV $^{1/2}$ to select events with small \cancel{E}_T . At this stage, called preselection, we are left with about 8.2×10^6 events.

As the topology of the candidate events is determined by the jet multiplicity, we define the signal region by selecting events with a number of jets $6 \leq N_{\text{jets}} \leq 8$, and we also require jet pairs to be separated by at least 0.5 units in the $\eta - \phi$ space. The number of events passing these additional requirements is 1.671×10^6 , with an expected S/B of approximately 1/430.

C. Neural-network-based kinematical selection

To further improve the purity of the signal sample, we use a multivariate approach and take advantage of the distinctive features of signal and background events through a neural network, which takes into account the correlations between the kinematical variables which enter as input nodes in the network. The network uses the MLPFIT package [19] as implemented by ROOT [20] through the *TMultiLayer-Perceptron* class.

A first set of 11 global variables, summarized in Table I, have already been proven to be effective [4] in reducing the QCD background. Studies performed for this analysis on the jet development in the calorimeter have indicated that a good discrimination between quark-initiated and gluon-initiated jets can be accomplished with η moments (M_η)

TABLE I. Input variables to the neural network.

| Variable | Description |
|----------------------------|--|
| $\sum E_T$ | Scalar sum of selected jets E_T |
| $\sum_3 E_T$ | As above, except the two highest- E_T jets |
| C | Centrality |
| A | Aplanarity |
| M_{2j}^{\min} | Minimum dijet invariant mass |
| M_{2j}^{\max} | Maximum dijet invariant mass |
| M_{3j}^{\min} | Minimum trijet invariant mass |
| M_{3j}^{\max} | Maximum trijet invariant mass |
| $E_T^{*,1}$ | $E_T \sin^2 \theta^*$ for the highest- E_T jet |
| $E_T^{*,2}$ | $E_T \sin^2 \theta^*$ for the next-to-highest- E_T jet |
| $\langle E_T^* \rangle$ | Geometric mean over the remaining jets |
| $\langle M_\eta^s \rangle$ | Geometric mean over the untagged jets |
| $\langle M_\phi^s \rangle$ | Geometric mean over the untagged jets |

and ϕ moments (M_ϕ) of a jet, which are defined as

$$M_\eta = \sqrt{\left[\sum_{\text{tow}} \frac{E_T^{\text{tow}}}{E_T} \eta_{\text{tow}}^2 \right] - \eta^2} \quad (1)$$

and

$$M_\phi = \sqrt{\left[\sum_{\text{tow}} \frac{E_T^{\text{tow}}}{E_T} \phi_{\text{tow}}^2 \right] - \phi^2}, \quad (2)$$

where E_T , η , and ϕ are, respectively, the transverse energy, the pseudorapidity, and the azimuthal angle of the jet, while E_T^{tow} is the transverse energy deposited in the calorimeter towers belonging to the jet.

We remove possible biases coming from E_T distributions, which might differ in signal and background events, by deconvoluting the E_T dependence through a rescaling of all moments to a common reference value of $E_T = 50$ GeV. We obtain what we call scaled moments:

$$M_\eta^s = M_\eta \frac{f_q^\eta(50 \text{ GeV})}{f_q^\eta(E_T)} \quad (3)$$

and

$$M_\phi^s = M_\phi \times \frac{f_q^\phi(50 \text{ GeV})}{f_q^\phi(E_T)}, \quad (4)$$

where $f_q^\eta(E_T)$ and $f_q^\phi(E_T)$ are the functions that fit the profiles of M_η vs E_T and of M_ϕ vs E_T in quark-initiated jets from simulated $t\bar{t}$ events.

These scaled moments are quite different for jets coming from a quark or a gluon in simulated $t\bar{t}$ events. Such a behavior has been verified in data events where the jet origin is well known. To take advantage of the large number of jets in a $t\bar{t}$ event, we consider the geometric average of the η moments and of the ϕ moments, see Fig. 1, evaluated using all jets which are not identified as coming from a heavy quark by the criteria explained in Sec. III D.

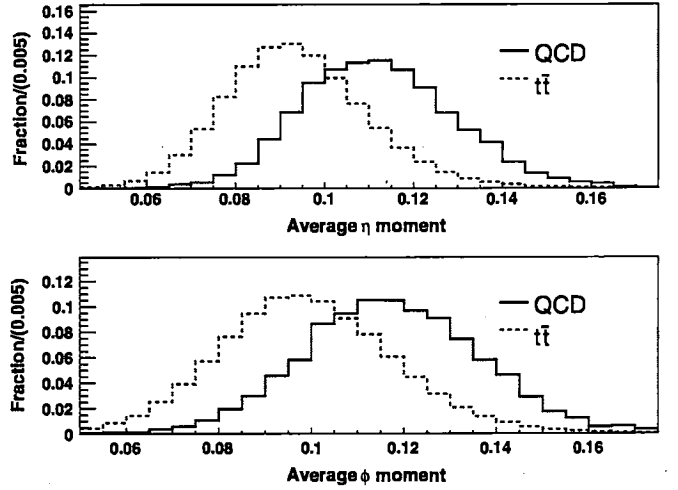


FIG. 1. Geometric average of the η scaled moments ($\langle M_\eta^s \rangle$, upper plot) and of the ϕ scaled moments ($\langle M_\phi^s \rangle$, lower plot) for QCD multijet (solid histogram) and simulated $t\bar{t}$ (dashed histogram) events with $6 \leq N_{\text{jets}} \leq 8$.

The 13 variables are used as inputs to a neural network with two hidden layers with 20 and 10 hidden nodes, respectively, and one output node. The network is trained on same-size samples of signal and background events with $6 \leq N_{\text{jets}} \leq 8$ (about half a million events). In order to model the signal we use the PYTHIA v6.2 [21] leading-order (LO) Monte Carlo generator with parton showering followed by a simulation of the CDF II detector. The reference top quark mass chosen for the training is $M_{\text{top}} = 175$ GeV/c². The background is obtained from the multijet data events themselves, since the signal fraction is expected to be very small before applying the neural-network selection. The value of the output node, N_{out} , is

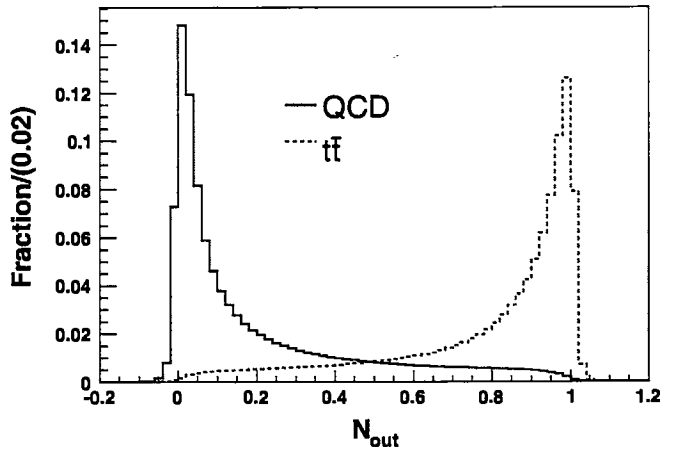


FIG. 2. Neural-network output N_{out} for QCD multijet (solid histogram) and simulated $t\bar{t}$ (dashed histogram) events with $6 \leq N_{\text{jets}} \leq 8$. Histograms are normalized to unity. The neural-network implementation that we use in the *TMultiLayerPerceptron* produces an output which is not strictly bound between 0 and 1.

$$3.7\% = \frac{\text{tagged}}{\text{Sid}} = \frac{P_T \text{ Sid } b + P_{\text{mis}f} \text{ fid } l}{\text{Sid } b + \text{sid } l}$$

$$3.7\% = \frac{\text{tagged}}{\text{fiducial}} = \frac{\text{mista } b}{\text{fid}}$$

T. AALTONEN *et al.*

the quantity we use as a discriminator between signal and background, and is shown in Fig. 2 for the $6 \leq N_{\text{jets}} \leq 8$ sample.

D. Tagging b quarks

In order to enrich the $t\bar{t}$ content in the event sample, we use a b -tagging algorithm based on secondary vertex reconstruction as described in detail in [14,22]. The algorithm identifies a jet likely to contain a hadron with a b quark by reconstructing its decay vertex with at least two high-quality tracks with hits in the silicon vertex detector. A b -tagged jet (*tag*, in brief) must have an associated secondary vertex with a displacement from the primary vertex in the transverse plane larger than 7.5 times the transverse-displacement resolution. This is evaluated for each secondary vertex, but its typical value is about $190 \mu\text{m}$. The tagging efficiencies for jets coming from the fragmentation of b or c quarks are corrected in simulated events according to the efficiency seen in the data, by a factor 0.95 ± 0.04 , both for b jets and c jets. These factors are described in detail in [14].

IV. EVENT SIMULATION

The standard model $t\bar{t}$ events used to study the event selection and to check the performance of the method (Sec. IX) are simulated using PYTHIA v6.2 [21]. Samples generated with input values of the top quark mass, $M_{\text{top}}^{\text{in}}$, ranging from 160 to 190 GeV/c^2 are considered and, for each sample, the event selection is repeated by varying the JES from its default value [16]. The displacement, denoted as ΔJES , is measured relative to the uncertainty, σ_{JES} , on the default value itself, so that the value of JES applied to simulated events is increased by $\Delta\text{JES} \cdot \sigma_{\text{JES}}$ with respect to the default. To test the method, input values $\Delta\text{JES}^{\text{in}}$ ranging from -3 to $+3$ are considered.

Different generators and different values for the model parameters are used to estimate the systematic uncertainties, as described in Sec. X.

V. BACKGROUND ESTIMATE

The background for the $t\bar{t}$ multijet final state comes mainly from QCD production of heavy-flavor quark pairs ($b\bar{b}$ and $c\bar{c}$) and from false tags of light-flavor quark jets. Other standard model processes such as $W/Z + \text{jets}$ have a smaller production cross section and small acceptance due to the selection requirements.

Given the large theoretical uncertainties on the QCD multijet production cross section, a more accurate background estimate is obtained from the data, rather than from Monte Carlo simulations. A tag rate per jet, defined as the probability of tagging a jet whose tracks are reconstructed in the vertex detector (*fiducial jet*), is then evaluated in a sample of events with exactly four jets passing the preselection and therefore still dominated by the background

PHYSICAL REVIEW D 81, 052011 (2010)

($S/B \approx 1/5000$). The rate is parametrized in terms of variables sensitive to both the tagging efficiency for heavy-flavored objects and the probability of false tags: the jet E_T , the number of tracks reconstructed in the silicon vertex detector and associated with the jet, $N_{\text{trk}}^{\text{jet}}$, and the number of primary vertices reconstructed in the event, N_{vert} [4]. By definition, the tag rate estimates the probability that a fiducial jet having, on average, the characteristics of jets from background events is tagged. Its average value is about 3.7%, with negligible uncertainty. However, direct exploitation of the tag rate to predict the number of background events with exactly a given number of tags would give incorrect numbers. This happens because, by construction, this rate is the ratio between the number of tagged jets and the number of fiducial jets in a whole sample of events. Possible correlations among jets in the same event are not considered. As heavy-flavor quarks come in pairs in QCD background, the probability to tag a pair of jets in the same event is therefore larger than the simple product of the tag probabilities of individual jets given by the tag rate.

To account for this we introduce correction factors to obtain a better estimate for the number of 1-tag and ≥ 2 -tag background events. These factors are derived in a control sample dominated by the background (events with six, seven, or eight jets and $N_{\text{out}} \leq 0.25$, with $S/B \approx 1/1300$ for one tag and $S/B \approx 1/400$ for ≥ 2 tags) as the ratio between the observed number of events with n tags (with $n = 1, 2, 3$) and the average expectation obtained by using the tag rate to evaluate the probability for each event to have the same number, n , of tagged jets. These factors represent, therefore, average corrections to the probability for a possible *tag configuration*, that is, for the assumption that among the fiducial jets in an event of the sample selected before the b -tagging requirements (*pretag sample*) only a given subset is actually tagged when the algorithm is applied. Their average values are 0.94, 1.48, and 2.46 for events with one, two, and three tagged jets, with relative statistical uncertainties of 0.4%, 1.1%, and 5.1%, respectively. Similarly to the tag rate, these corrections should be valid for events with the characteristics of background events.

The accuracy of our modeling of the background processes is verified in control samples, i.e. on events with higher values of N_{out} and therefore with a larger fraction of signal events and with possible different kinematics and background composition. As the background prediction is performed using the data in the pretag sample, the presence of $t\bar{t}$ events must also be taken into account. Therefore a correction is applied to derive a better evaluation, $n_{(b,\text{exp})}$, of the background normalization from the raw estimate $n_{(b,\text{raw})}$ directly obtained by the corrected tag rate matrix. This correction must subtract the contribution $n_{t\bar{t}}^{\text{tr}}$ coming from applying the matrix to signal events and included in $n_{(b,\text{raw})}$. Denoting by N_{obs} the number of events observed in

the data sample, by $n_{t\bar{t}}$ the number of signal events in this sample, and assuming that the excess of events with respect to the expected background is totally due to the signal, the correction can be written as

$$\begin{aligned} n_{(b,\text{exp})} &= n_{(b,\text{raw})} - n_{t\bar{t}}^{tr} = n_{(b,\text{raw})} - \frac{n_{t\bar{t}}^{tr}}{n_{t\bar{t}}} \cdot n_{t\bar{t}} \\ &= n_{(b,\text{raw})} - \frac{n_{t\bar{t}}^{tr}}{n_{t\bar{t}}} \cdot (N_{\text{obs}} - n_{(b,\text{exp})}), \end{aligned} \quad (5)$$

which, with $R_{t\bar{t}} \equiv n_{t\bar{t}}^{tr}/n_{t\bar{t}}$, gives

$$n_{(b,\text{exp})} = \frac{n_{(b,\text{raw})} - R_{t\bar{t}} \cdot N_{\text{obs}}}{1 - R_{t\bar{t}}}. \quad (6)$$

$R_{t\bar{t}}$ can be inferred from simulated events and amounts to $0.314 \pm 0.003(\text{stat})$ [$0.067 \pm 0.0014(\text{stat})$] for 1-tag (≥ 2 -tag) events. Further possible discrepancies between the observed and expected number of events are considered as due to the modeling of the background and accounted for as a systematic uncertainty.

VI. MASS RECONSTRUCTION

The simultaneous measurement of the top quark mass and the JES is based on the reconstruction, event by event, of both the top quark and the W masses through a constrained fitting technique. The shapes of the distributions obtained by this procedure are sensitive to the values of both M_{top} and JES. Therefore, for simulated events, they are built using samples corresponding to the different input values of M_{top} and ΔJES listed in Sec. IV.

Moreover, given the different resolution in the reconstructed top quark mass and the W -boson mass, and also the different S/B which can be achieved by requiring events with exactly one or ≥ 2 tags, two sets of distributions are separately derived in these samples.

A. Reconstructed top quark mass

For each event we determine a reconstructed top quark mass, m_t^{rec} , from the four-momenta of selected jets. Sixteen equations can be considered to connect the four-momenta of the two top quarks and their decay products according to the $t\bar{t} \rightarrow b\bar{b}W^+W^- \rightarrow b\bar{b}q_1\bar{q}_2q_3\bar{q}_4$ hypothesis:

$$p_t^\mu = p_{W^+}^\mu + p_b^\mu, \quad (7)$$

$$p_t^\mu = p_{W^-}^\mu + p_b^\mu, \quad (8)$$

$$p_{W^+}^\mu = p_{q_1}^\mu + p_{\bar{q}_2}^\mu, \quad (9)$$

$$p_{W^-}^\mu = p_{q_3}^\mu + p_{\bar{q}_4}^\mu, \quad (10)$$

with $\mu = 0, 1, 2, 3$. There are 13 unknown quantities, i.e., the unknown top quark mass and the three-momenta of the top quarks and of the W bosons, so the kinematics of the events are overconstrained.

The fit is performed using only the six highest- E_T jets (leading jets) of the event and considering their possible assignments to quarks of a $t\bar{t}$ final state. The total number of different permutations giving two doublets of jets corresponding to the W bosons and two triplets of jets corresponding to the top quarks is 90. Since we require the presence of b tags, assigning the tagged jets only to b quarks reduces this number to 30 for 1-tag events and six in case of two or more b tags [23].

For each permutation the kinematics of the event is reconstructed minimizing the following χ^2 function:

$$\begin{aligned} \chi^2 &= \frac{(m_{jj}^{(1)} - M_W)^2}{\Gamma_W^2} + \frac{(m_{jj}^{(2)} - M_W)^2}{\Gamma_W^2} + \frac{(m_{jjb}^{(1)} - m_t^{\text{rec}})^2}{\Gamma_t^2} \\ &\quad + \frac{(m_{jjb}^{(2)} - m_t^{\text{rec}})^2}{\Gamma_t^2} + \sum_{i=1}^6 \frac{(p_{T,i}^{\text{fit}} - p_{T,i}^{\text{meas}})^2}{\sigma_i^2}. \end{aligned} \quad (11)$$

The minimization procedure is performed with respect to seven parameters, i.e., the reconstructed top quark mass m_t^{rec} and the transverse momenta $p_{T,i}^{\text{fit}}$ of the six jets, which are constrained to the measured value $p_{T,i}^{\text{meas}}$ within their known resolution σ_i . The invariant masses of the jet doublets assigned to light-flavor quarks coming from a W , $m_{jj}^{(1,2)}$, and of the trijet systems including one doublet and one of the jets assigned to b quarks, $m_{jjb}^{(1,2)}$, are evaluated by the trial momenta of jets at each step of the minimization. On the contrary, the measured mass M_W and the natural width Γ_W of the W boson as well as the assumed natural width of the top quark, Γ_t , are kept constant to $80.4 \text{ GeV}/c^2$, $2.1 \text{ GeV}/c^2$, and $1.5 \text{ GeV}/c^2$, respectively [24,25].

The permutation of jets which gives the lowest χ^2 value is selected, and the corresponding fitted value of m_t^{rec} enters an invariant mass distribution (*template*) which will be used for the M_{top} measurement.

B. Reconstructed W mass

Reconstructing the mass of W bosons by using dijet systems represents a possibility to obtain a variable, in principle, insensitive to M_{top} which allows, therefore, an independent determination of JES.

To build the m_W^{rec} distributions we use the same procedure and χ^2 expression considered for m_t^{rec} , but now the W -boson mass is also left as a free parameter in the fit (i.e. M_W becomes m_W^{rec}). Again, for each event, the value of m_W^{rec} corresponding to the permutation of the jet-to-parton assignments with the lowest χ^2 enters the distribution.

Using different fits in the reconstruction of m_t^{rec} and m_W^{rec} can lead to selecting different assignments of jets to partons for the two variables in the same event. This is not a problem as the same procedure is followed both on data and simulated events. Reconstructing the top quark mass using a constant value of M_W , as described in Sec. VI A, improves the resolution of the distributions and therefore

the determination of the *true* value of M_{top} . The correlations between the values of m_t^{rec} and m_W^{rec} in the same event are taken into account in the calibration of the likelihood fit used for the measurement (Sec. VIII B).

C. Background templates

In order to reconstruct data-driven background templates we apply the kinematical fitter to the sample of events passing the neural-network selection, but before the requirement of tagged b jets.

The same procedures described in Secs. VI A and VI B are repeated on these events assigning fiducial jets to b quarks and then looping over all possible assignments of other jets to the remaining quarks, performing the fit for each permutation and selecting the reconstructed m_t^{rec} and m_W^{rec} values corresponding to the best χ^2 . These values then enter the templates weighted by the *corrected* probability of the assumed tag configuration; see Sec. V. As for the normalization, the background distributions also need to be corrected for the presence of signal in the pretag sample by subtracting the contribution from $t\bar{t}$ events. The shape of this contribution is obtained from simulated samples and depends on the assumed M_{top} and JES, while the normalization is given by the difference $n_{(b,\text{raw})} - n_{(b,\text{exp})}$, as described in Sec. V.

In order to check how well our modeling describes the background, we consider events in control regions defined by the N_{out} value, in ranges where the signal presence after tagging is still very low. In these regions the templates, i.e. the main elements of our measurement, are reconstructed by the procedure described in the previous sections, both for the signal and the background, as well as other important distributions like N_{out} and the χ^2 of the fit used to build the m_t^{rec} templates. These distributions are then compared to observed data, taking into account the contribution from signal events. The agreement is generally good in all the control regions, and this confirms the reliability of the background model.

Figures 3 and 4 show, as examples, distributions of m_t^{rec} and m_W^{rec} in one of the control regions for 1-tag and ≥ 2 -tag events, where the sum of signal and background is compared to the same distributions reconstructed in the data. In these plots the integral of the signal distributions corresponding to $M_{\text{top}} = 175 \text{ GeV}/c^2$ and the default value $\Delta\text{JES} = 0$ have been normalized to the difference between the observed data and the corrected expected background.

VII. EVENT SAMPLES

In order to obtain the best performance from our method, we performed sets of *pseudoexperiments* (PEs) to find out which requirements on the values of N_{out} and of the χ^2 used to obtain the m_t^{rec} values minimize the statistical uncertainty on the top quark mass measurement. The procedure is similar to the one outlined in Sec. IX, with a

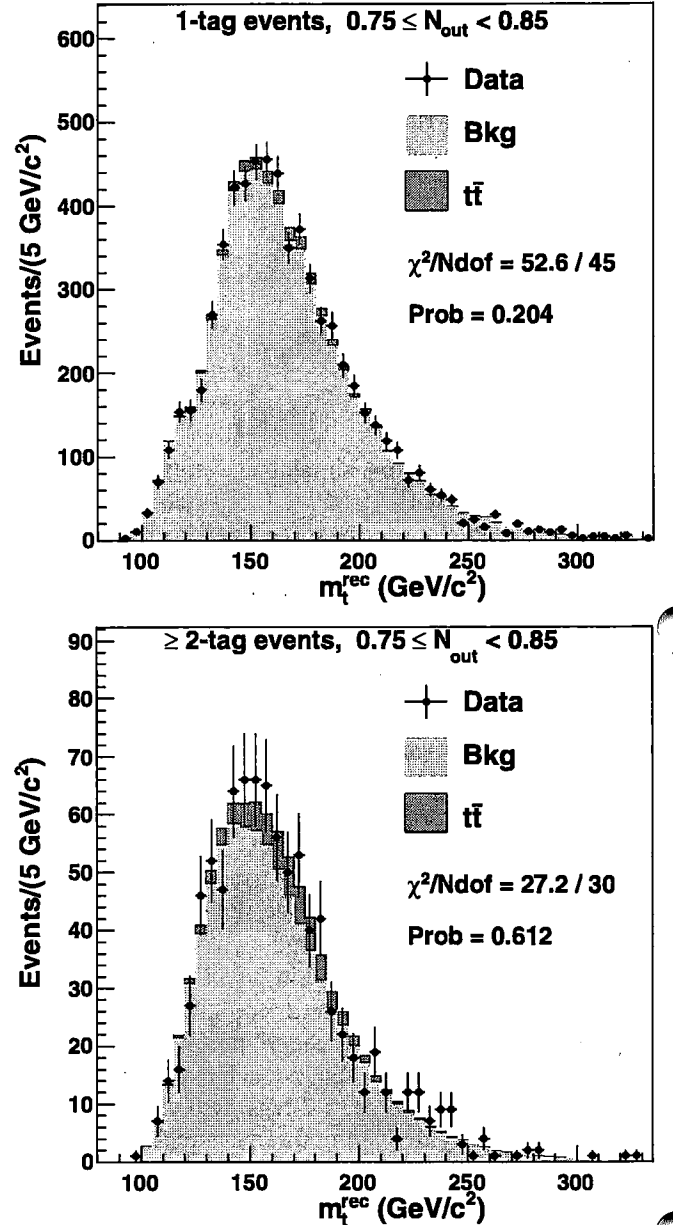


FIG. 3 (color online). Histograms of the reconstructed top quark mass m_t^{rec} for 1-tag events, upper plot, and ≥ 2 -tag events, lower plot, are shown in a control region defined by $0.75 \leq N_{\text{out}} < 0.85$. Along with the data are plotted the expected background and the signal contribution for $M_{\text{top}} = 175 \text{ GeV}/c^2$ and the default value $\Delta\text{JES} = 0$, normalized to the difference between the data and the background. The value of the purely statistical χ^2 probability is reported on each plot.

binned version of the same likelihood. It is applied separately to 1-tag and ≥ 2 -tag samples and considers many different combinations of possible requirements. The smallest values for the uncertainty are obtained using ($N_{\text{out}} \geq 0.90$, $\chi^2 \leq 6$) in the 1-tag sample and ($N_{\text{out}} \geq 0.88$, $\chi^2 \leq 5$) in the ≥ 2 -tag sample so that we add these requirements to the prerequisites described in Sec. III B.

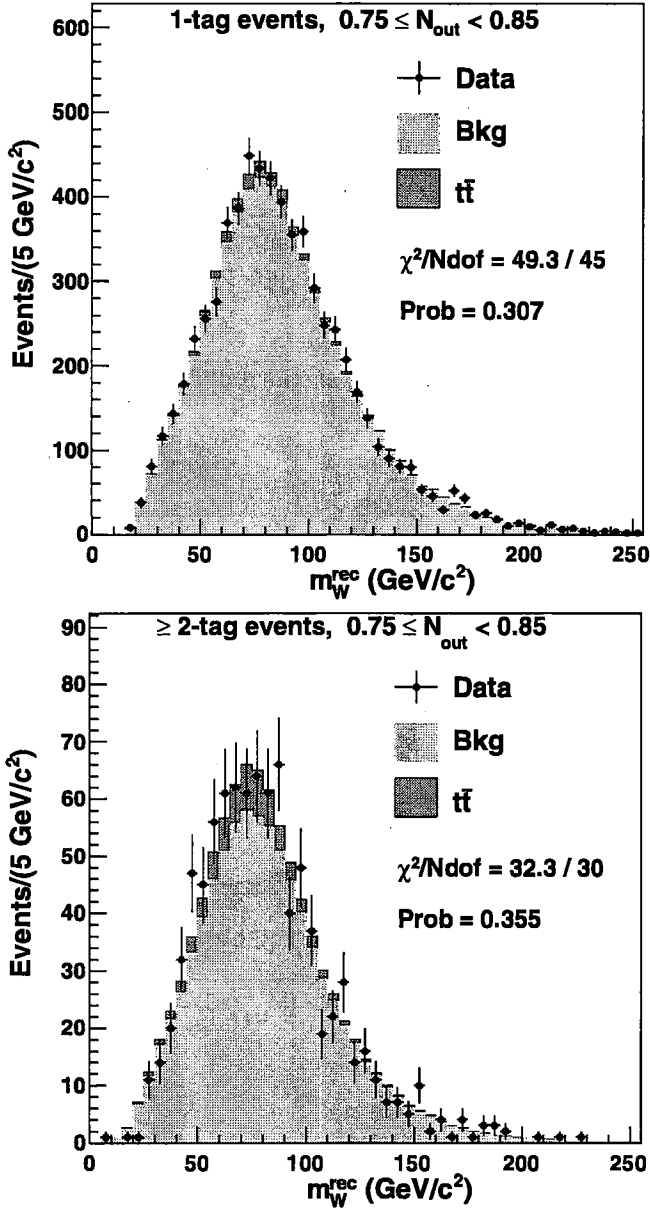


FIG. 4 (color online). Histograms of the reconstructed W mass m_W^{rec} for 1-tag events, upper plot, and ≥ 2 -tag events, lower plot, are shown in a control region defined by $0.75 \leq N_{\text{out}} < 0.85$. Along with the data are plotted the expected background and the signal contribution for $M_{\text{top}} = 175 \text{ GeV}/c^2$ and the default value $\Delta\text{JES} = 0$, normalized to the difference between the data and the background. The value of the purely statistical χ^2 probability is reported on each plot.

The final definition of the samples used in our analysis is summarized in Table II.

After these selections, 3452 and 441 events are observed for the 1-tag and ≥ 2 -tag samples, respectively. We can evaluate the average number of background events expected in the selected samples and their uncertainties, as described in Sec. V. The systematic uncertainties on the

TABLE II. Final definition and requirements for selected event samples.

| Event sample | b tags | N_{out} | m_t^{rec} fit χ^2 |
|---------------|----------|------------------|---------------------------------|
| One tag | = 1 | ≥ 0.90 | ≤ 6 |
| ≥ 2 tags | 2 or 3 | ≥ 0.88 | ≤ 5 |

TABLE III. Number of events observed in the selected data samples and corresponding expected numbers of background and $t\bar{t}$ events. The signal contribution is evaluated for $M_{\text{top}} = 175 \text{ GeV}/c^2$, $\Delta\text{JES} = 0$, and $\sigma_{t\bar{t}} = 6.7 \text{ pb}$.

| Event sample | Observed | Background | $t\bar{t}$ |
|---------------|----------|---------------|------------|
| One tag | 3452 | 2785 ± 83 | 693 |
| ≥ 2 tags | 441 | 201 ± 29 | 193 |

background normalizations are estimated by assuming that the discrepancy between the observed number of events in the data and the sum of the expected contributions from signal and background (where, in this case, the theoretical cross section value of 6.7 pb is considered for $t\bar{t}$ events production) is due to a bad evaluation of the background. This is done separately for 1-tag and ≥ 2 -tag samples, and the resulting relative uncertainties on the expected number of events are $\sigma(n_{(b,\text{exp})}^{1 \text{ tag}}) = 2.9\%$ and $\sigma(n_{(b,\text{exp})}^{\geq 2 \text{ tags}}) = 14.6\%$, respectively. The efficiencies of the full selection on $t\bar{t}$ events corresponding to $M_{\text{top}} = 175 \text{ GeV}/c^2$ and $\Delta\text{JES} = 0$ are 3.6% and 1.0% for 1-tag and ≥ 2 -tag events, respectively. These values are used to evaluate the expected signal contributions of Table III, where $\sigma_{t\bar{t}} = 6.7 \text{ pb}$ is assumed. In the same table, the observed number of events and the expected background in each sample are also summarized.

VIII. LIKELIHOOD FIT

The technique described in Sec. VI allows one to obtain sets of *observed* m_t^{rec} and m_W^{rec} values reconstructed in the data samples with 1 or ≥ 2 tags as well as to build signal and background distributions for the same variables. In order to measure the top quark mass simultaneously with the JES, a fit is performed where an unbinned likelihood function is maximized to find the values of M_{top} , ΔJES , and the number of signal (n_s) and background (n_b) events for each tagging category which give the probability density functions (p.d.f.'s) best describing the data.

A. Probability density functions

The signal templates are fitted by normalized combinations of Gamma and Gaussian p.d.f.'s, and the dependence of the shape on input M_{top} and ΔJES is included, writing the parameters of the p.d.f.'s as linear functions of these

variables. Figures 5 and 6 show examples of the fitted p.d.f.'s superimposed on the m_t^{rec} and m_W^{rec} signal templates, respectively, for different M_{top} and ΔJES values.

The shape of distributions built for the background cannot depend on the characteristics of signal events, and, in particular, on the value of top quark mass. Moreover, as they are obtained from data, the shapes correspond to the reference value of the jet energy scale. For these reasons no dependence on M_{top} and JES is considered in the p.d.f.'s used to fit the background templates. Actually, a very weak dependence is introduced

through the corrections to the shape of the background distributions, performed to take into account the presence of signal events in the pretag sample, as described in Sec. VI C. These effects are taken into account as a systematic uncertainty. Examples of background m_t^{rec} and m_W^{rec} distributions and the corresponding fitted p.d.f.'s are shown in Fig. 7 for ≥ 2 -tag events. Discrepancies between the fitted p.d.f.'s and the corresponding distributions are considered in the calibration procedure, presented in Sec. IX.

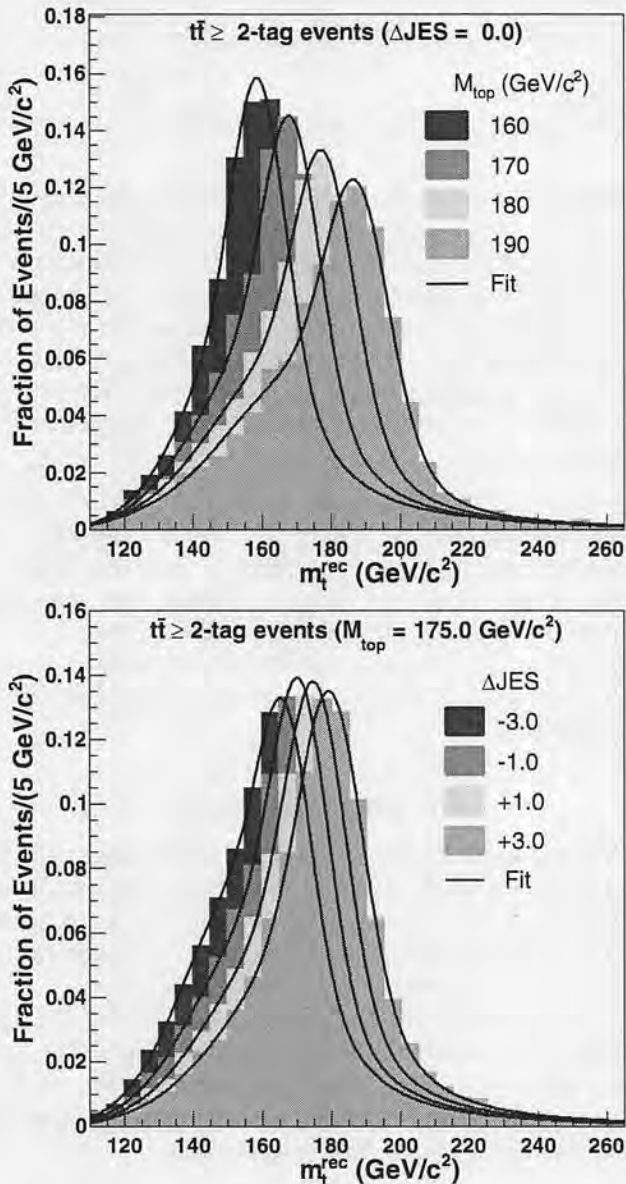


FIG. 5 (color online). Histograms and corresponding fitted probability density functions for the signal m_t^{rec} in ≥ 2 -tag events for a constant ΔJES value ($\Delta\text{JES} = 0$), varying the input top quark mass (upper plot), and for a constant M_{top} value ($175 \text{ GeV}/c^2$), varying the input jet energy scale (lower plot).

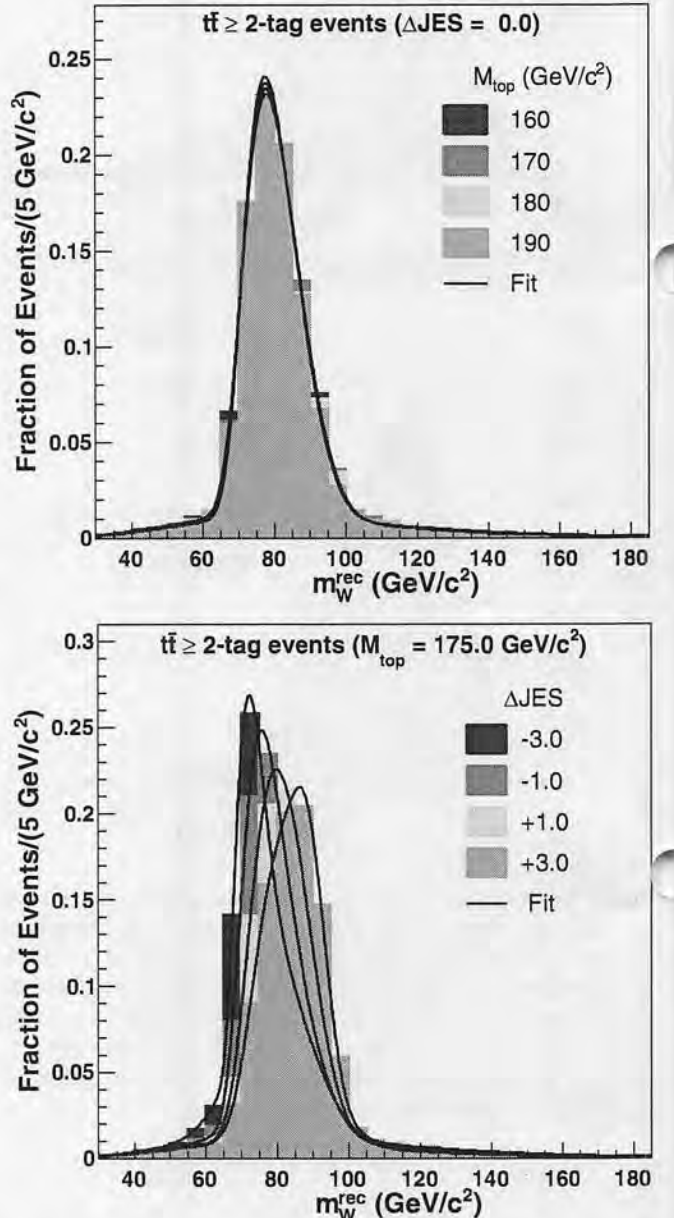


FIG. 6 (color online). Histograms and corresponding fitted probability density functions for the signal m_W^{rec} in ≥ 2 -tag events for a constant ΔJES value ($\Delta\text{JES} = 0$), varying the input top quark mass (upper plot), where the independence of m_W^{rec} on M_{top} is apparent, and for a constant M_{top} value ($175 \text{ GeV}/c^2$), varying the input jet energy scale (lower plot).

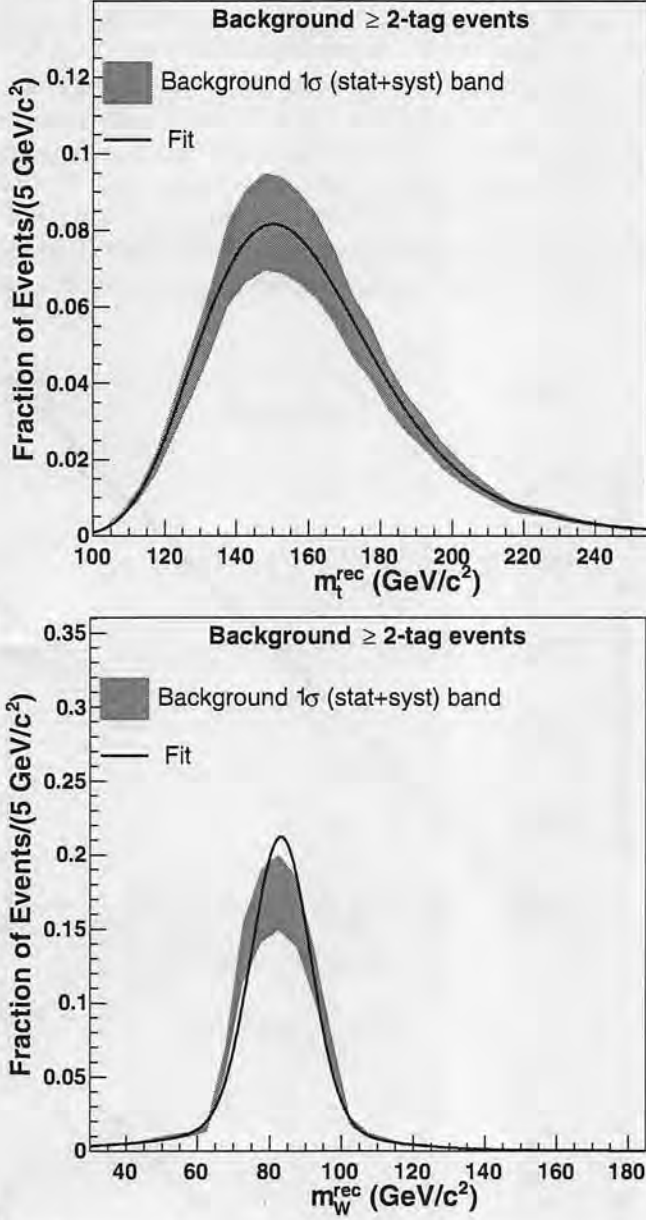


FIG. 7 (color online). Data-driven background histograms of m_t^{rec} (upper plot) and m_W^{rec} (lower plot) for $\geq 2\text{-tag events}$. The bands denote the 1σ uncertainty on the bin contents of the histograms, including both statistical and systematic contributions. The solid lines show the p.d.f.'s fitted to the histograms.

B. The likelihood function

The likelihood function \mathcal{L} is divided into three main parts and can be written as

$$\mathcal{L} = \mathcal{L}_{1\text{-tag}} \times \mathcal{L}_{\geq 2\text{-tags}} \times \mathcal{L}_{\Delta\text{JES}_{\text{constr}}} \quad (12)$$

The $\mathcal{L}_{1\text{-tag}}$ and $\mathcal{L}_{\geq 2\text{-tags}}$ terms further consist of other factors:

$$\mathcal{L}_{1,\geq 2\text{-tags}} = \mathcal{L}_{M_{\text{top}}} \times \mathcal{L}_{\text{JES}} \times \mathcal{L}_{\text{Poisss}} \times \mathcal{L}_{N_{\text{constr}}^{\text{bkg}}} \quad (13)$$

where the four terms on the right side assume, respectively, the following form [the superscripts referring to the tag sample are omitted and $f_s \equiv n_s/(n_s + n_b)$, $f_b \equiv 1 - f_s$]:

$$\prod_{i=1}^{N_{\text{obs}}} f_s \cdot P_{\text{sig}}^{m_t^{\text{rec}}} (m_{t,i} | M_{\text{top}}, \Delta\text{JES}) + f_b \cdot P_{\text{bkg}}^{m_t^{\text{rec}}} (m_{t,i}), \quad (14)$$

$$\prod_{i=1}^{N_{\text{obs}}} f_s \cdot P_{\text{sig}}^{m_W^{\text{rec}}} (m_{W,i} | M_{\text{top}}, \Delta\text{JES}) + f_b \cdot P_{\text{bkg}}^{m_W^{\text{rec}}} (m_{W,i}), \quad (15)$$

$$\frac{e^{-(n_s + n_b)} \cdot (n_s + n_b)^{N_{\text{obs}}}}{N_{\text{obs}}!}, \quad (16)$$

$$\exp \left[-\frac{(n_b - n_{(b,\text{exp})})^2}{2\sigma_{n_{(b,\text{exp})}}^2} \right]. \quad (17)$$

In expression (14) the probability to observe the set $m_{t,i}$, ($i = 1, \dots, N_{\text{obs}}$) of m_t^{rec} values reconstructed in the data is calculated by using the total probability density function resulting from the combination of the parametrized signal and background p.d.f.'s (Sec. VIII A), $P_{\text{sig}}^{m_t^{\text{rec}}}$ and $P_{\text{bkg}}^{m_t^{\text{rec}}}$, respectively, as a function of the free parameters of the fit. In term (15) the same is done for the set of the observed W masses, $m_{W,i}$, ($i = 1, \dots, N_{\text{obs}}$), and the m_W^{rec} p.d.f. The term (16), $\mathcal{L}_{\text{Poisss}}$, gives the probability to observe the number of events selected in the data, given the average number of signal (n_s) and background (n_b) events expected in the sample, as assumed at each step of the likelihood fit. In the last term, (17), the parameter n_b is constrained by a Gaussian to the *a priori* background estimate given in Sec. VII, i.e. $n_{(b,\text{exp})} = 2785 \pm 83$ for 1-tag events and $n_{(b,\text{exp})} = 201 \pm 29$ for $\geq 2\text{-tag}$ events. Finally, the last term in expression (12), $\mathcal{L}_{\Delta\text{JES}_{\text{constr}}}$, is a Gaussian term constraining ΔJES to its *a priori* value:

$$\exp \left[-\frac{(\Delta\text{JES} - \Delta\text{JES}_{\text{constr}})^2}{2} \right]. \quad (18)$$

When the measurement is performed on data, the JES can be constrained to the value independently measured in [16]. Given the meaning of ΔJES , described in Sec. IV, this means that, in this case, $\Delta\text{JES}_{\text{constr}} = 0$.

IX. VERIFICATION AND CALIBRATION OF THE METHOD

We want to investigate the possible presence of biases in the top quark mass and jet energy scale measurements introduced by our method, as well as to have an estimate of its statistical power before performing the measurement on the actual data sample. To do so, we run realistic PEs where *pseudodata* are extracted from simulated signal and data-driven background distributions. A set of 3000 PEs is performed for each simulated value of the top quark mass and of the displacement in the jet energy scale (Sec. IV).

Using the notation introduced in Sec. IV, we refer to these input values as $M_{\text{top}}^{\text{in}}$ and $\Delta\text{JES}^{\text{in}}$, and they represent the *true* values we want to measure. In each PE the actual numbers of signal ($N_{(s,\text{obs})}$) and background ($N_{(b,\text{obs})}$) events in each tagging category are generated with Poisson distributions with mean $n_{(s,\text{exp})} = N_{\text{obs}} - n_{(b,\text{exp})}$ and $n_{(b,\text{exp})}$, respectively, where N_{obs} are the observed number of events in the data samples ($N_{\text{obs}} = 3452$ for 1-tag and $N_{\text{obs}} = 441$ for ≥ 2 -tag events). A set of $N_{(s,\text{obs})}$ and $N_{(b,\text{obs})}$ mass values is then drawn from m_t^{rec} and m_W^{rec} distributions of signal and background and used as input to the likelihood fit (Sec. VIII) that returns simultaneous measurements of M_{top} and ΔJES , denoted as $M_{\text{top}}^{\text{out}}$ and $\Delta\text{JES}^{\text{out}}$. The average of these measurements over the whole set of 3000 PEs represents the best estimate of the input values obtained by the fitting procedure and therefore can be used to study its behavior. We fit the dependence of these averages with respect to the input values over the whole range of simulated $M_{\text{top}}^{\text{in}}$ and $\Delta\text{JES}^{\text{in}}$ as

$$\langle M_{\text{top}}^{\text{out}} \rangle = (A_{00} + A_{01} \cdot \Delta\text{JES}^{\text{in}}) + (A_{10} + A_{11} \cdot \Delta\text{JES}^{\text{in}}) \cdot (M_{\text{top}}^{\text{in}} - 175), \quad (19)$$

$$\langle \Delta\text{JES}^{\text{out}} \rangle = [B_{00} + B_{01} \cdot (M_{\text{top}}^{\text{in}} - 175)] + [B_{10} + B_{11} \cdot (M_{\text{top}}^{\text{in}} - 175)] \cdot \Delta\text{JES}^{\text{in}}. \quad (20)$$

These relations can be inverted to obtain calibration functions to be applied to further measurements and therefore, on average, a more reliable estimate of the true values (2D calibration). The calibrated values resulting from a measurement giving $M_{\text{top}}^{\text{out}}$ and $\Delta\text{JES}^{\text{out}}$ are denoted as $M_{\text{top}}^{\text{corr}}$ and $\Delta\text{JES}^{\text{corr}}$, while the respective uncertainties, obtained by propagating through the calibration the uncertainties from the likelihood fit, are $\delta M_{\text{top}}^{\text{corr}}$ and $\delta\Delta\text{JES}^{\text{corr}}$. A second set of PEs is then performed to test the goodness of the procedure. Table IV shows the coefficients A_{ij} and B_{ij} obtained both from calibrated and uncalibrated PEs compared to their ideal values in the absence of any bias.

In Fig. 8 examples of linearity plots are shown for calibrated PEs. These plots, together with the numbers in

TABLE IV. Coefficients of expressions (19) and (20) as obtained from calibrated and uncalibrated pseudoexperiments. The ideal values in the absence of any bias are also shown.

| | Uncalibrated PEs | Calibrated PEs | Ideal value |
|----------|----------------------|----------------------|-------------|
| A_{00} | 175.47 ± 0.01 | 174.99 ± 0.01 | 175 |
| A_{01} | -0.24 ± 0.01 | 0.00 ± 0.01 | 0 |
| A_{10} | 0.985 ± 0.002 | 1.000 ± 0.002 | 1 |
| A_{11} | 0.009 ± 0.001 | 0.000 ± 0.001 | 0 |
| B_{00} | -0.026 ± 0.003 | 0.002 ± 0.003 | 0 |
| B_{01} | 0.0009 ± 0.0004 | -0.0001 ± 0.0004 | 0 |
| B_{10} | 1.052 ± 0.002 | 0.999 ± 0.002 | 1 |
| B_{11} | -0.0016 ± 0.0002 | 0.0001 ± 0.0002 | 0 |

Table IV, show how the calibration removes any average bias. To check that the uncertainties $\delta M_{\text{top}}^{\text{corr}}$ and $\delta\Delta\text{JES}^{\text{corr}}$ are also unbiased, we consider the width of $M_{\text{top}}^{\text{corr}}$ and $\Delta\text{JES}^{\text{corr}}$ pull distributions, that is, the distributions of deviations of the calibrated values from the true inputs in the PEs, divided by the uncertainties themselves. We find that the uncertainties are both underestimated, and multiplicative correction factors equal to 1.084 for $\delta M_{\text{top}}^{\text{corr}}$ and to 1.115 for $\delta\Delta\text{JES}^{\text{corr}}$ are needed. After these corrections the

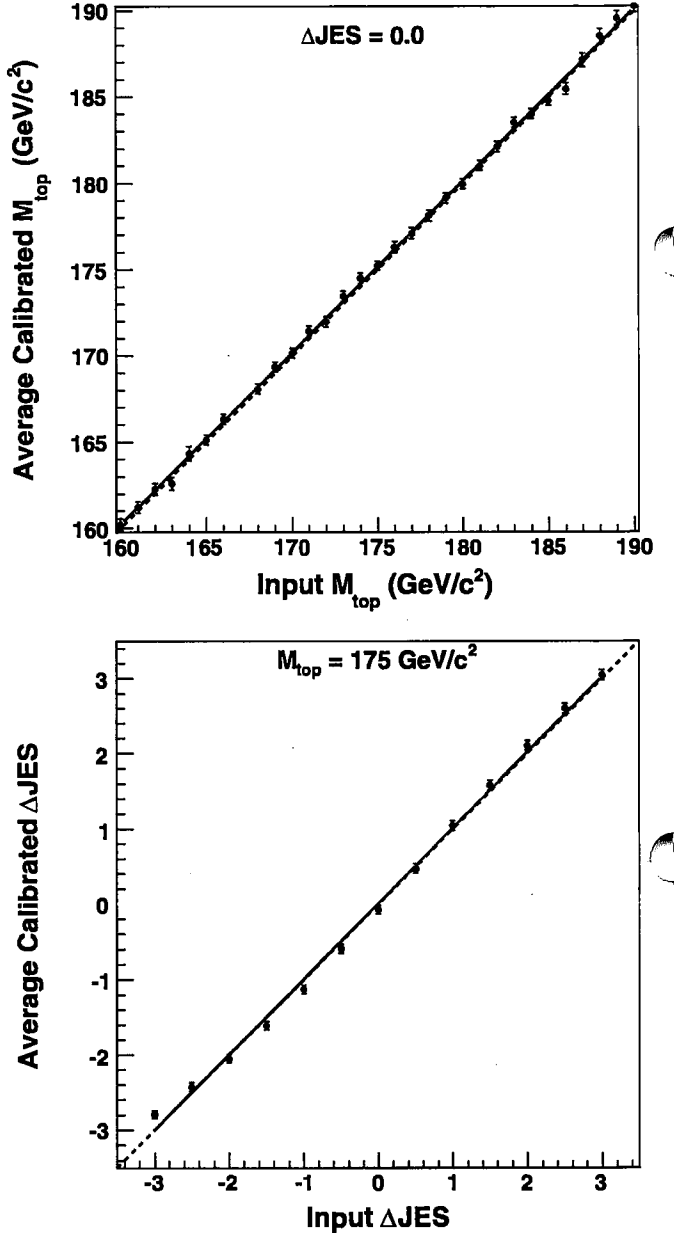


FIG. 8 (color online). Examples of response linearity plots ($\langle M_{\text{top}}^{\text{corr}} \rangle$ vs $M_{\text{top}}^{\text{in}}$, upper plot, and $\langle \Delta\text{JES}^{\text{corr}} \rangle$ vs $\Delta\text{JES}^{\text{in}}$, lower plot) after the 2D calibration. The solid lines represent the linear functions which best fit the response as a function of the input values, while the dashed lines represent the ideal behavior.

average expected uncertainty on the measured top quark mass and jet energy scale displacement for true M_{top} and ΔJES around 175 GeV/c^2 and 0 are

$$\delta M_{\text{top}}^{\text{corr}}(\text{stat} + \text{JES}) = 2.0 \text{ GeV}/c^2, \quad (21)$$

$$\delta\Delta\text{JES}^{\text{corr}}(\text{stat} + M_{\text{top}}) = 0.45. \quad (22)$$

X. SYSTEMATIC UNCERTAINTIES

The possible systematic uncertainties on the top quark mass and the jet energy scale measurements have been studied and are summarized in this section. These arise mostly from the measurement technique itself, from uncertainties in the simulation of the $t\bar{t}$ events, from mismodeling of the detector response, and from uncertainty on the shapes of signal and background templates used to derive the p.d.f.'s and to calibrate the measurement. The uncertainties are usually evaluated by performing PEs, extracting pseudodata from templates built using signal samples where the possible systematic effects have been considered and included. Corrections to the shape of the raw background templates are performed as described in Sec. VI C to obtain the corrected background templates corresponding to the effect one wants to study. On the contrary, nothing is changed in the elements of the likelihood fit, because it is the default procedure that we want to apply to real data and that, therefore, we have to test in case of possible mismodeling of the data themselves. The results from these PEs are then compared to the ones obtained by using default templates, and the shifts in the average $M_{\text{top}}^{\text{corr}}$ and $\Delta\text{JES}^{\text{corr}}$ values are taken as the estimate of the systematic uncertainties. In some cases the statistical uncertainties on the shifts may be larger than the shifts themselves, and therefore we use conservatively the former as the systematic uncertainty. In the following, after the description of each effect, we also quote in parentheses the values of the corresponding uncertainties for the top quark mass and the jet energy scale, respectively. These values are then summarized in Table V.

The 2D calibration removes the average biases, especially related to the parametrization of the templates using smooth probability density functions. Residual biases usually exist at single $(M_{\text{top}}^{\text{in}}, \Delta\text{JES}^{\text{in}})$ points, and have to be taken into account. We therefore consider the shift of the mean of the pull distributions with respect to 0 at each $(M_{\text{top}}^{\text{in}}, \Delta\text{JES}^{\text{in}})$ point to evaluate this *residual bias* systematic uncertainty, which, given the definition of pull in Sec. IX, is defined as a function of the uncertainty on the calibrated measurements. To obtain the proper coverage of both positive and negative biases we evaluate them separately, so that asymmetric uncertainties are finally considered. They are generally given by $(^{+0.37}_{-0.20}) \cdot \delta M_{\text{top}}^{\text{corr}}$ for $M_{\text{top}}^{\text{corr}}$ and $(^{+0.43}_{-0.56}) \cdot \delta\Delta\text{JES}^{\text{corr}}$ for $\Delta\text{JES}^{\text{corr}}$. Specifying the values

TABLE V. Systematic uncertainties and their sizes for the top quark mass and the jet energy scale measurements. The total uncertainty is obtained by the sum in quadrature of single contributions.

| Source | $\delta M_{\text{top}}^{\text{syst}} (\text{GeV}/c^2)$ | $\delta\Delta\text{JES}^{\text{syst}}$ |
|-----------------------------------|--|--|
| Residual bias | $^{+0.8}_{-0.4}$ | $^{+0.18}_{-0.24}$ |
| 2D calibration | <0.1 | <0.01 |
| Generator | 0.3 | 0.25 |
| ISR/FSR | 0.1 | 0.06 |
| <i>b</i> -jet energy scale | 0.2 | 0.04 |
| <i>b</i> -tag SF E_T dependence | 0.1 | 0.01 |
| Residual JES | 0.5 | ... |
| PDF | $^{+0.3}_{-0.2}$ | $^{+0.05}_{-0.04}$ |
| Multiple $p\bar{p}$ interactions | 0.2 | 0.01 |
| Color reconnection | 0.4 | 0.08 |
| Statistics of templates | 0.3 | 0.07 |
| Background shape | 0.1 | 0.02 |
| Total | $^{+1.2}_{-1.0}$ | $^{+0.34}_{-0.37}$ |

obtained in the measurement on the data, described in Sec. XI, we obtain $^{+0.8}_{-0.4} \text{ GeV}/c^2$ on $M_{\text{top}}^{\text{corr}}$, $^{+0.18}_{-0.24}$ on $\Delta\text{JES}^{\text{corr}}$.

The uncertainties on the parameters of the 2D calibration give a small uncertainty on the corrected values $M_{\text{top}}^{\text{corr}}$ and $\Delta\text{JES}^{\text{corr}}$ which can be evaluated by the calibration functions and the values of M_{top} and ΔJES fitted in the data ($< 0.1 \text{ GeV}/c^2$, < 0.01).

Many sources of systematic effects arise from uncertainties in modeling of the hard interaction in simulated events. PYTHIA and HERWIG [26] Monte Carlo generators differ in their hadronization schemes and in their description of the underlying event and multiple interactions. The default signal samples have been generated with PYTHIA, and therefore an uncertainty is obtained by using a sample generated using HERWIG (0.3 GeV/c^2 , 0.25).

Jets coming from possible emission of hard gluons might fall among the six leading jets and populate the tails in the top quark invariant mass distribution. The amount of radiation from partons in the initial or final state is set by parameters of the PYTHIA generator used to simulate signal events. To study these effects, templates are built using samples where the values of the parameters have been changed with respect to the default, to increase or to decrease the amount of radiation [22] (0.1 GeV/c^2 , 0.06).

Since the default jet energy corrections are derived from data samples deficient in heavy flavors [16], an additional uncertainty comes from considering the different properties of *b* quarks. We account for the uncertainties on the *b*-quark semileptonic branching ratios, fragmentation modeling, and calorimeter response to heavy-flavor hadrons (0.2 GeV/c^2 , 0.04).

The different efficiency of the *b*-tagging algorithm on data and simulated events is usually considered by introducing a constant scale factor (*b*-tag SF). The overall

uncertainty on this parameter affects the cross section measurement described in Sec. XII. However, such a scale factor does not need to be considered regarding the top quark mass measurement, because it could slightly change only the population of the signal templates but not their shape. On the other hand, variations of the latter could be caused by the possible dependence of the b -tag SF on the transverse energy of jets, which is then considered as a systematic effect ($0.1 \text{ GeV}/c^2, 0.01$).

The uncertainty on the top quark mass coming from the likelihood fit includes the uncertainty due to the jet energy scale. However, as described in Sec. III B, this uncertainty is the result of many independent effects with different behavior with respect to properties of jets like E_T and η [16], and therefore represents a leading-order correction. Second-order effects can arise from uncertainties on the single corrections applied to the jet energies. To evaluate these possible effects, we build signal templates by varying separately by $\pm 1\sigma$ the single corrections and, for each one of these variations, PEs were performed by using these templates and not applying the constraint $\mathcal{L}_{\Delta\text{JES}_{\text{corr}}}$ in the likelihood fit, as this term is related to effects of the full correction. The resulting uncertainties have been added in quadrature to obtain a *residual* JES uncertainty on the top quark mass ($0.5 \text{ GeV}/c^2$).

The choice of parton distribution functions (PDF) in the proton used in Monte Carlo generators can affect the kinematics of simulated $t\bar{t}$ events and thus the top quark mass measurement. We considered four sources of uncertainties: the difference arising from the use of the default CTEQ5L [27] PDF and one calculated from the MRST group, MRST72 [28]; the uncertainty depending on the value of α_s , evaluated by the difference between the use of MRST72 and MRST75 PDF's; the uncertainty depending on the differences between the LO and NLO calculations of PDF's, evaluated by the difference between using default CTEQ5L (LO) and CTEQ6M (NLO) PDF's; and the uncertainties on PDF's derived from experimental data uncertainties ($^{+0.3}_{-0.2} \text{ GeV}/c^2, ^{+0.05}_{-0.04}$).

The probability to have multiple $p\bar{p}$ interactions during the same bunch crossing is a function of the instantaneous luminosity. This is reflected in the increasing number of primary vertices reconstructed in the events at higher luminosities. We account for the fact that the simulated samples for the signal process do not model the actual luminosity profile of the data by considering the signal distributions for events with 1, 2, 3, and ≥ 4 reconstructed vertices separately. These distributions are then used to obtain the templates by weighted averages, where the weights are evaluated as the fractions of events with 1, 2, 3, and ≥ 4 vertices observed in the data. Moreover, a possible mismodeling of the dependence of the jet energy response as a function of the reconstructed number of primary vertices in simulated events is considered ($0.2 \text{ GeV}/c^2, 0.01$).

Uncertainties from modeling of color reconnection effects [29] are estimated by comparing the results of two sets of PEs performed drawing pseudodata from templates built using two different samples of events simulated by PYTHIA. The samples are generated with two different sets of parameters, corresponding to two different models of color reconnection ($0.4 \text{ GeV}/c^2, 0.08$).

The shapes of the signal and background distributions are affected by uncertainties due to the limited statistics of the simulated events and data samples used to build them. These uncertainties affect the results of a measurement which is performed maximizing an unbinned likelihood where parametrized p.d.f.'s, fitted to default templates, are evaluated. We address this effect, obtaining 100 sets of templates by statistical fluctuations of default ones and performing pseudoexperiments drawing data from each of these sets separately. From each set we obtain an average value for $M_{\text{top}}^{\text{corr}}$ and $\Delta\text{JES}^{\text{corr}}$, and the spread of these values is taken as the systematic uncertainty ($0.3 \text{ GeV}/c^2, 0.07$).

Besides the purely statistical effects, quoted above, the shape of the background templates also has uncertainties due to the corrections for the presence of signal events in the pretag sample, Sec. VI C, and to the systematic uncertainty on the background normalization, Sec. VII. We address this source of systematic uncertainty by the same technique used for the statistical contributions, that is, by obtaining a set of 100 background templates where the content of each bin is separately fluctuated by Gaussian distributions centered on the default bin content and with a width equal to its systematic uncertainty, and taking the spread of results from PEs as the systematic uncertainty ($0.1 \text{ GeV}/c^2, 0.02$).

Table V shows a summary of all the systematic uncertainties and their sum in quadrature, which gives a total systematic uncertainty of $^{+1.2}_{-1.0} \text{ GeV}/c^2$ for the M_{top} measurement and $^{+0.34}_{-0.37}$ for the ΔJES .

XI. TOP MASS AND JES MEASUREMENTS

After the kinematical selection with $N_{\text{out}} \geq 0.90$ (≥ 0.88) and $\chi^2 \leq 6$ (≤ 5), we are left with 3452 (441) events with one (≥ 2) tag(s). The background amounts to 2785 ± 83 (201 ± 29) for events with one (≥ 2) tag(s).

For these events a top quark mass has been reconstructed using the likelihood fit described in Sec. VIII B and applied to the data sample. Once the calibration procedure and corrections are applied, as described in Sec. IX, the best estimate of the top quark mass is

$$M_{\text{top}} = 174.8 \pm 2.4(\text{stat + JES}) \text{ GeV}/c^2, \quad (23)$$

while the value obtained for the jet energy scale displacement is

$$\Delta\text{JES} = -0.30 \pm 0.47(\text{stat + } M_{\text{top}}). \quad (24)$$

We can also evaluate separately the purely statistical contributions, obtaining

$$M_{\text{top}} = 174.8 \pm 1.7(\text{stat}) \pm 1.6(\text{JES}) \text{ GeV}/c^2 \quad (25)$$

and

$$\Delta\text{JES} = -0.30 \pm 0.35(\text{stat}) \pm 0.32(M_{\text{top}}). \quad (26)$$

The plot in Fig. 9 shows the measured values together with the log-likelihood contours corresponding to 1σ , 2σ , and 3σ uncertainty on the value of the top quark mass [24]. The slope of the major axis of the contours denotes that the measurements of M_{top} and ΔJES have a negative correlation, and the value of the correlation coefficient obtained from the likelihood fit is -0.68 .

The plots in Fig. 10 show the m_t^{rec} distributions for the data compared to the expected background and the signal for a top quark mass of $175.0 \text{ GeV}/c^2$ and a jet energy scale displacement of -0.3 , that is, the values of simulated M_{top} and ΔJES as close as possible to the measurements in the data. The signal and background contributions are normalized to the respective number of events as fitted in the data.

The plots in Fig. 11 compare the measured statistical uncertainty, just after the 2D calibration, with the expected distribution from default pseudoexperiments using as inputs $M_{\text{top}} = 175.0 \text{ GeV}/c^2$ and $\Delta\text{JES} = -0.3$. We find

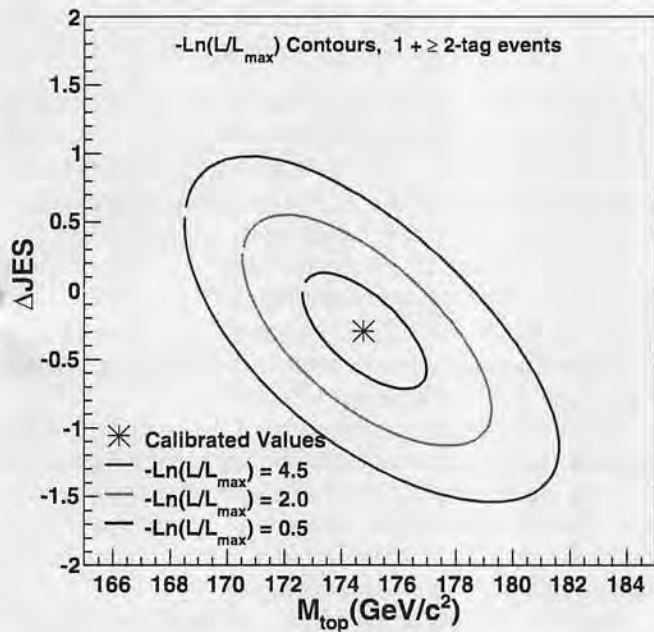


FIG. 9 (color online). Negative log-likelihood contours for the likelihood fit performed for the M_{top} and ΔJES measurements. The minimum is also shown and corresponds to the values measured in the data. The contours are drawn at values of 0.5, 2.0, and 4.5 of the increase of the log-likelihood from the minimum value. These curves correspond to 1σ , 2σ , and 3σ uncertainty on the measurement of the top quark mass.

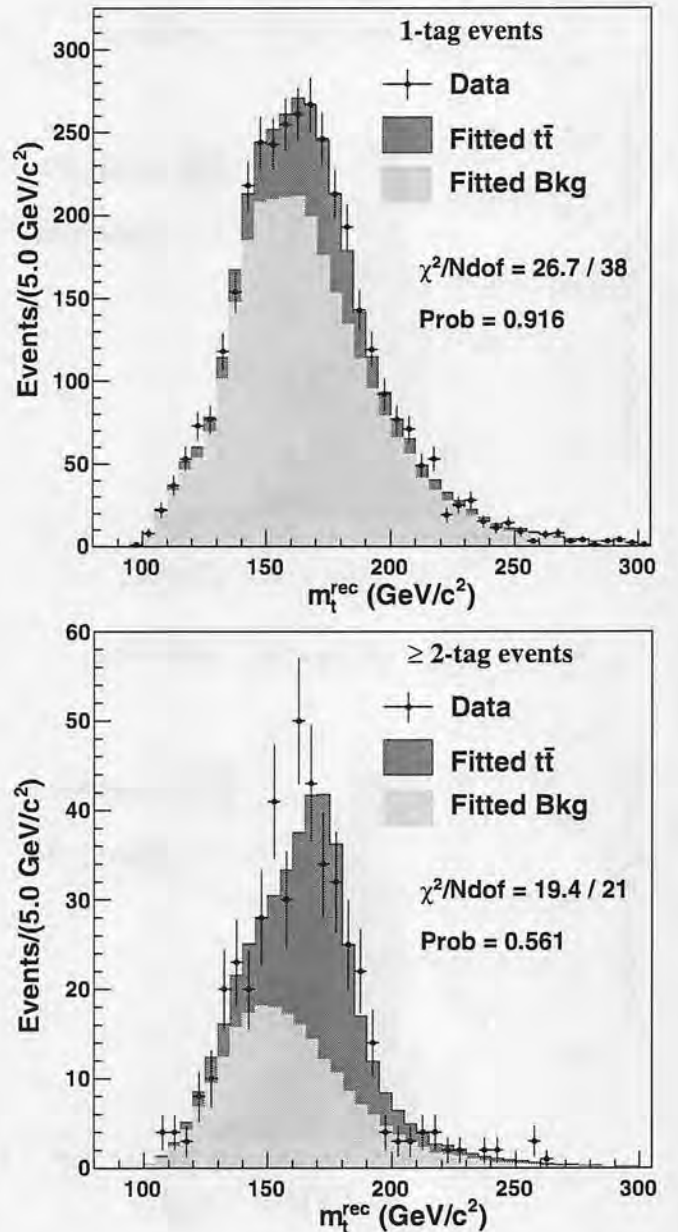


FIG. 10 (color online). Histograms of m_t^{rec} as obtained in the data (black points) for 1-tag (upper plot) and ≥ 2 -tag events (lower plot) are compared to the distributions from signal and background corresponding to $M_{\text{top}} = 175 \text{ GeV}/c^2$ and $\Delta\text{JES} = -0.3$. The expected histograms are normalized to the measured values for the average number of signal and background events. The values of the purely statistical χ^2 and of its probability are reported on each plot, showing the overall agreement between the data and the distributions corresponding to the fitted values of M_{top} and ΔJES .

that the probability of achieving a better sensitivity is 91.6% for M_{top} and 81.2% for ΔJES .

Summarizing, the measured values for the top quark mass and the jet energy scale are

$$M_{\text{top}} = 174.8 \pm 2.4(\text{stat} + \text{JES})^{+1.2}_{-1.0}(\text{syst}) \text{ GeV}/c^2, \quad (27)$$

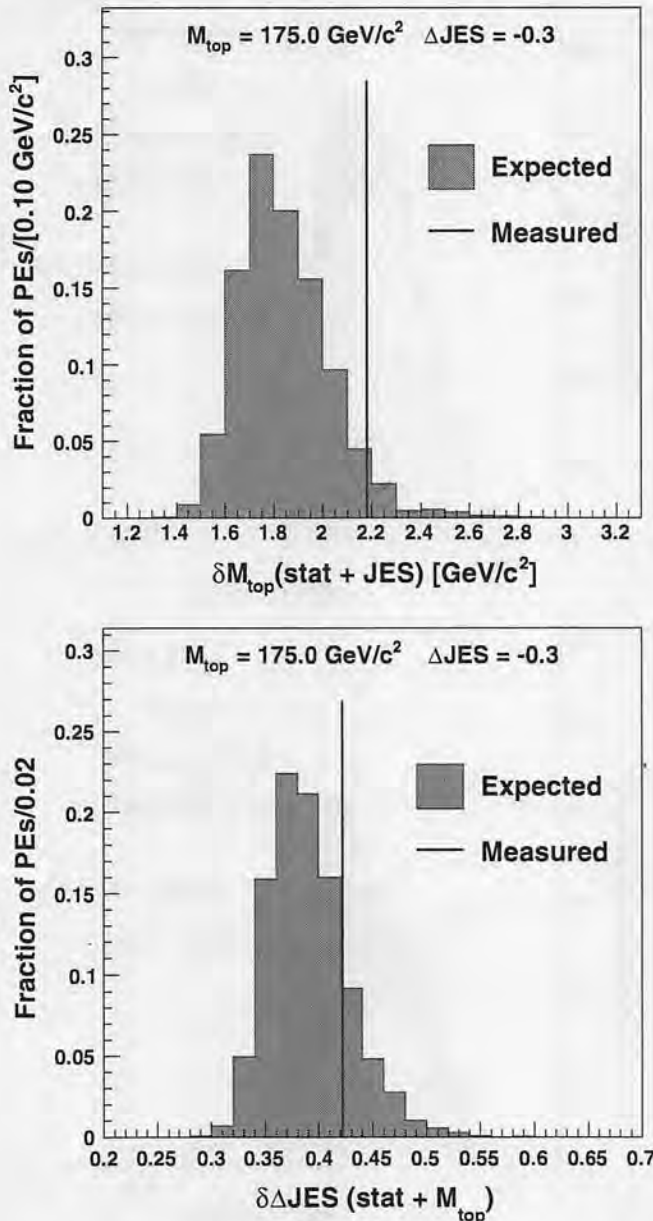


FIG. 11 (color online). Distributions of the uncertainties on the top quark mass (upper plot) and the jet energy scale displacement (lower plot) as expected from default PEs performed using as input values $M_{\text{top}}^{\text{in}} = 175.0 \text{ GeV}/c^2$ and $\Delta\text{JES}^{\text{in}} = -0.3$. The vertical lines indicate the uncertainties obtained in our reported result.

$$\Delta\text{JES} = -0.30 \pm 0.47(\text{stat} + M_{\text{top}})^{-0.34}_{+0.37}(\text{syst}), \quad (28)$$

which, isolating the purely statistical contributions and adding the uncertainties from JES and M_{top} to the respective systematic uncertainties, can also be written as

$$M_{\text{top}} = 174.8 \pm 1.7(\text{stat})^{+2.0}_{-1.9}(\text{syst}) \text{ GeV}/c^2, \quad (29)$$

$$\Delta\text{JES} = -0.30 \pm 0.35(\text{stat})^{+0.47}_{-0.49}(\text{syst}). \quad (30)$$

This measurement of the top quark mass has been used in the current world average [5].

XII. CROSS SECTION MEASUREMENT

The procedure used to measure the top quark mass also returns the average number of signal events expected, given the selected data samples. These results can be turned into a measurement of the $t\bar{t}$ cross section, as follows.

A. The likelihood function

From the number of signal events, $n_s^{1 \text{ tag}}$ and $n_s^{\geq 2 \text{ tags}}$, as obtained from the mass likelihood fit, we derive a measurement of the $t\bar{t}$ production cross section considering the efficiency for selecting a $t\bar{t}$ event in the two tagging categories.

The cross section measurement is performed by maximizing a likelihood function which can be divided into two parts:

$$\mathcal{L} = \mathcal{L}_{1 \text{ tag}} \times \mathcal{L}_{\geq 2 \text{ tags}}, \quad (31)$$

where each term can be expressed as

$$\mathcal{L}_{1, \geq 2 \text{ tags}} = \mathcal{L}_{\sigma_{t\bar{t}}} \times \mathcal{L}_\epsilon, \quad (32)$$

where

$$\mathcal{L}_{\sigma_{t\bar{t}}} = \exp \left[-\frac{(\sigma_{t\bar{t}} \cdot \epsilon \cdot L - n_s)^2}{2\sigma_{n_s}^2} \right] \quad (33)$$

contains all the parameters of the fit, i.e. the production cross section $\sigma_{t\bar{t}}$, the integrated luminosity L , the signal efficiency ϵ , and the signal yield $n_s \pm \sigma_{n_s}$, as given by the mass measurement, while \mathcal{L}_ϵ is a Gaussian term constraining the efficiency within its statistical uncertainty.

The efficiencies are evaluated using a sample of about $4 \times 10^6 t\bar{t}$ events generated with $M_{\text{top}} = 175 \text{ GeV}/c^2$ and assuming $\Delta\text{JES} = -0.3$, i.e. the value we measured by the mass likelihood fit, and are summarized along with signal yields and other parameters in Table VI.

While studying the performance of the procedure, using pseudoexperiments produced assuming a given input cross section, we observe the need to introduce a small correction. The outcome of the fit needs to be multiplied by a factor $k_\sigma = 0.982 \pm 0.008$ in order to obtain an unbiased measurement of the cross section.

From the maximization of the likelihood, we obtain a central value for the $t\bar{t}$ production cross section

$$\sigma_{t\bar{t}} = 7.2 \pm 0.5(\text{stat}) \pm 0.4(\text{lum}) \text{ pb}, \quad (34)$$

evaluated assuming $M_{\text{top}} = 175 \text{ GeV}/c^2$ and $\Delta\text{JES} = -0.3$, close to the values measured in Sec. XI. The first uncertainty is the statistical one, while the second one derives from the 6% uncertainty on the integrated lumi-

TABLE VI. Input variables to the cross section evaluation. For the signal yields, the first uncertainty is the purely statistical one.

| Variable | Input value |
|-----------------------------|--------------------------------|
| Signal yield, one tag | $643 \pm 59 \pm 54$ |
| Signal yield, ≥ 2 tags | $216 \pm 21 \pm 14$ |
| Efficiency, one tag | $(3.55 \pm 0.01)\%$ |
| Efficiency, ≥ 2 tags | $(1.00 \pm 0.01)\%$ |
| Integrated luminosity | $2874 \pm 172 \text{ pb}^{-1}$ |

TABLE VII. Cross section as evaluated assuming different values for M_{top} and ΔJES .

| M_{top} (GeV/c^2) | ΔJES | $\sigma_{t\bar{t}}$ (pb) |
|---------------------------------------|--------------------|--------------------------|
| 175.0 | -0.3 | 7.24 |
| 175.0 | 0.0 | 7.00 |
| 172.5 | 0.0 | 7.21 |
| 170.0 | 0.0 | 7.29 |

nosity. As the signal efficiencies depend strongly on the assumed values for M_{top} and ΔJES , the measured $t\bar{t}$ cross section also has the same dependence. For reference we report in Table VII the cross sections corresponding to other (M_{top} , ΔJES) points with a top quark mass near the current CDF average. In this case we assume $\Delta\text{JES} = 0$, and the systematic uncertainty on JES is increased from 6.1% to 9.2%, corresponding to changing the ΔJES by ± 1 rather than by ± 0.6 units, that is, the sum in quadrature of the uncertainties on the measured jet energy scale, Sec. XI.

B. Systematic uncertainties

Most of the sources of systematic uncertainties affecting the measurement of $\sigma_{t\bar{t}}$ are the same as the ones discussed for the measurement of the top quark mass. We just need to evaluate their effects both on the signal yields and on the signal efficiencies in order to derive the effects on the cross section. There are few other sources of systematic uncertainty specific to a cross section measurement which have not been discussed in Sec. X, because they affect only the signal efficiencies. These include the uncertainty on the calibration constant, k_σ , on the $W \rightarrow \text{hadrons}$ branching ratio (BR) [24], on the trigger simulation, and on the distribution of the primary vertex z coordinate. As for the effect of the JES uncertainty on the efficiency, we have evaluated it by changing the ΔJES by ± 0.6 units with respect to the measured value $\Delta\text{JES} = -0.3$. Residual effects due to individual levels of corrections have been accounted for, too. The relative uncertainties $\Delta\sigma_{t\bar{t}}/\sigma_{t\bar{t}}$ for the individual sources are summarized in Table VIII. Considering their sum in quadrature, the $t\bar{t}$ production cross section amounts to

$$\sigma_{t\bar{t}} = 7.2 \pm 0.5(\text{stat}) \pm 1.0(\text{syst}) \pm 0.4(\text{lum}) \text{ pb}, \quad (35)$$

assuming $M_{\text{top}} = 175 \text{ GeV}/c^2$ and $\Delta\text{JES} = -0.3$.

TABLE VIII. Systematic uncertainties and their relative sizes for the cross section measurement. The total uncertainty is obtained by the sum in quadrature of single contributions.

| Source | $\Delta\sigma_{t\bar{t}}/\sigma_{t\bar{t}}$ (%) |
|--------------------------------------|---|
| Calibration factor | 0.8 |
| Generator | 4.2 |
| ISR/FSR | 0.6 |
| b -jet energy scale | 2.8 |
| b -tag SF E_T dependence | 5.4 |
| PDF | 3.4 |
| Multiple $p\bar{p}$ interactions | 2.5 |
| Color reconnection | 0.8 |
| Templates statistics | 0.8 |
| Background shape | 0.3 |
| Background normalization | 8.2 |
| JES | 6.1 |
| Residual JES | 2.1 |
| Primary vertex | 0.2 |
| BR($W \rightarrow \text{hadrons}$) | 0.8 |
| Trigger | 1.8 |
| Total | 13.7 |

XIII. CONCLUSIONS

Using a very effective neural-network-based kinematical selection and a b -jet identification technique, we measure the top quark mass to be

$$M_{\text{top}} = 174.8 \pm 2.4(\text{stat} + \text{JES})^{+1.2}_{-1.0}(\text{syst}) \text{ GeV}/c^2, \quad (36)$$

and the $t\bar{t}$ production cross section to be

$$\sigma_{t\bar{t}} = 7.2 \pm 0.5(\text{stat}) \pm 1.0(\text{syst}) \pm 0.4(\text{lum}) \text{ pb}. \quad (37)$$

These values represent the most precise measurements to date of M_{top} and $\sigma_{t\bar{t}}$ in the all-hadronic decay channel. The results are consistent with the measurements obtained in other decay channels by CDF and D0 Collaborations [5,6] and, as it concerns $\sigma_{t\bar{t}}$, with the theoretical predictions evaluated at the value of the top quark mass obtained in our measurement [3].

ACKNOWLEDGMENTS

We thank the Fermilab staff and the technical staffs of the participating institutions for their vital contributions. This work was supported by the U.S. Department of Energy and National Science Foundation; the Italian Istituto Nazionale di Fisica Nucleare; the Ministry of Education, Culture, Sports, Science and Technology of Japan; the Natural Sciences and Engineering Research Council of Canada; the National Science Council of the Republic of China; the Swiss National Science Foundation; the A.P. Sloan Foundation; the Bundesministerium für Bildung und Forschung, Germany; the World Class University Program, the National Research Foundation of Korea; the Science and

Technology Facilities Council and the Royal Society, United Kingdom; the Institut National de Physique Nucléaire et Physique des Particules/CNRS; the Russian Foundation for Basic Research; the Ministerio de Ciencia e

Innovación, and Programa Consolider-Ingenio 2010, Spain; the Slovak R&D Agency; and the Academy of Finland.

- [1] S. Heinemeyer *et al.*, J. High Energy Phys. 09 (2003) 075.
- [2] LEP Electroweak Working Group, Tevatron Electroweak Working Group, and SLD electroweak and heavy flavour groups, arXiv:0911.2604.
- [3] M. Cacciari *et al.*, J. High Energy Phys. 09 (2008) 127; N. Kidonakis and R. Vogt, Phys. Rev. D **78**, 074005 (2008); S. Moch and P. Uwer, Nucl. Phys. B, Proc. Suppl. **183**, 75 (2008).
- [4] T. Aaltonen *et al.* (CDF Collaboration), Phys. Rev. D **76**, 072009 (2007).
- [5] Tevatron Electroweak Working Group for CDF and D0 Collaborations, arXiv:0903.2503.
- [6] T. Aaltonen *et al.* (CDF Collaboration), Phys. Rev. D **79**, 112007 (2009); **79**, 052007 (2009); V. Abazov *et al.* (D0 Collaboration), Phys. Rev. Lett. **100**, 192004 (2008); Phys. Lett. B **679**, 177 (2009).
- [7] T. Aaltonen *et al.* (CDF Collaboration), Phys. Rev. D **79**, 072010 (2009); Phys. Rev. Lett. **98**, 142001 (2007).
- [8] D. Acosta *et al.* (CDF Collaboration), Phys. Rev. D **71**, 032001 (2005).
- [9] L. Balka *et al.*, Nucl. Instrum. Methods Phys. Res., Sect. A **267**, 272 (1988).
- [10] M. Albrow *et al.*, Nucl. Instrum. Methods Phys. Res., Sect. A **480**, 524 (2002).
- [11] G. Ascoli *et al.*, Nucl. Instrum. Methods Phys. Res., Sect. A **268**, 33 (1988).
- [12] D. Acosta *et al.*, Nucl. Instrum. Methods Phys. Res., Sect. A **494**, 57 (2002).
- [13] F. Abe *et al.* (CDF Collaboration), Phys. Rev. D **45**, 1448 (1992).
- [14] D. Acosta *et al.* (CDF Collaboration), Phys. Rev. D **71**, 052003 (2005).
- [15] A. Abulencia *et al.* (CDF Collaboration), Phys. Rev. D **74**, 072006 (2006).
- [16] A. Bhatti *et al.*, Nucl. Instrum. Methods Phys. Res., Sect. A **566**, 375 (2006).
- [17] The missing transverse energy \cancel{E}_T is calculated as the vector sum of the energy in each calorimeter tower multiplied by a unit vector in the azimuthal direction of the tower. If isolated high momentum muons are found in the event, the \cancel{E}_T is corrected by subtracting the muon energy in the calorimeter and adding the muon p_T to the vector sum. \cancel{E}_T is defined as the magnitude of \cancel{E}_T .
- [18] D. Acosta *et al.* (CDF Collaboration), Phys. Rev. Lett. **96**, 202002 (2006).
- [19] MLPFIT: A Tool for Multi-Layer Perceptrons, <http://schwind.home.cern.ch/schwind/MLPfit.html>.
- [20] R. Brun and F. Rademaker, ROOT Version 4.00/08, <http://root.cern.ch/>.
- [21] T. Sjöstrand *et al.*, Comput. Phys. Commun. **135**, 238 (2001).
- [22] A. Abulencia *et al.* (CDF Collaboration), Phys. Rev. D **73**, 032003 (2006).
- [23] The ≥ 2 -tag sample actually consists of events with two or three tagged jets. When three tags are present, the two leading ones are assigned to b quarks.
- [24] C. Amsler *et al.* (Particle Data Group), Phys. Lett. B **667**, 1 (2008).
- [25] S. M. Oliveira, L. Brucher, R. Santos, and A. Barroso, Phys. Rev. D **64**, 017301 (2001).
- [26] G. Marchesini *et al.*, Comput. Phys. Commun. **67**, 465 (1992); G. Corcella *et al.*, J. High Energy Phys. 01 (2001) 010.
- [27] H. L. Lai *et al.*, Eur. Phys. J. C **12**, 375 (2000).
- [28] A. D. Martin, R. G. Roberts, W. J. Stirling, and R. S. Thorne, Eur. Phys. J. C **4**, 463 (1998).
- [29] P. Skands and D. Wicke, arXiv:0807.3248; P. Skands, arXiv:0905.3418.